IMPINGING JET HEAT TRANSFER
AND THERMAL DEFORMATION FOR
CALENDER ROLLS

by

Ian A. Journeaux

A Thesis Submitted to the Faculty of Graduate Studies
and Research in Partial Fulfillment of the
Requirements for the Degree of
Doctor of Philosophy

Department of Chemical Engineering
McGill University
Montreal, Quebec
Canada

September 1990

ABSTRACT

The heat transfer characteristics of turbulent impinging jets, typical of those used in paper machine cross machine directicn caliper profile control were measured. The effect of jet entrainement on the impingement heat transfer by unconfined jets was successfully scaled using a jet thermal entrainement factor. The addition of a confinement plate to an existing unconfined impinging jet control system was shown to improve the average heat transfer by 33% and 80% for a nozzle-to-impingement surface spacing of 2 and 1 respectively.

The thermal deformation of calender roll under control actuators was predicted numerically using finite volume and finite element techniques. The most desirable steady state control charateristics, i.e high peak deformation and small width of deformation, were obtained on unheated rolls of minimum practical thickness. The results indicate that control actuator spacings less than 0.2m provide negligible control advantage.

Experiments were performed on a double calender stack of a production newsprint machine to determine the optimal position for cross-machine direction calender control actuators which would minimize the response time and maximize the magnitude of the response. Control on the queen roll and the two rolls immediately above it produces the strongest response. The king roll and the top roll, each of which affects only one nip, are shown to be poor choices for the placement of control actuators. When two calenders are used in succession, the actuators should be placed in the first stack. Calender roll design must be considered when choosing the location for control actuators.

RÉSUMÉ

On a étudié experimentallement le transfer de chaleur de jet d'air turbulent, typique des actionneur utilise dans un système de contrôle du profil d'épaisseur sur une machine a papier. Effect d'entraînement par le jet d'aire non contenu sur le transfer de chaleur peut être gradué en utilisant un factor d'entrainement thermique. L'addition d'une plac de confinement peu améliorer le transfer chaleur par 33% et 80% correspondant a des distance buse-rouleau de 2 et 1 respectivement.

La déformation de rouleau de calandres par des actionneurs ont été calculé numériquement en utilisant des techniques de volume fini et d'element fini. Les characteristics optimale de control, soit une deformation maximal et une largeur de control minimal, ont été obtenu avec des rouleau non chauffer et d'eppaiseur de coquille le minimum possible. Les resulat indique que des actioneurs espacé de moin que 0.2m ne resulte pas dans une éfficacité de contrôle superiere.

Des essais ont été effectués sur des calandres jumelées d'une machine à papier commerciale afin de déterminer la position optimale des actionneurs (jets d'air refroidissant) d'un système de contrôle du profil d'épaisseur. L'objectif de cette étude était de minimiser le temps de réponse des actionneurs et de maximiser l'effet du système de contrôle. L'efficacité est maximale lorsque les actionneurs sont situés à partir du second rouleau inférieur jusqu'aux rouleaux supérieurs. Les rouleaux inférieur et supérieur s'avèrent être un mauvais emplacement car ils n'affectent qu'une seule pince. Lorsque deux calandres identiques sont utilisées successivement, il est préférable d'installer les actionneurs sur la première calandre. Le type de rouleaux est aussi un factor important dans le choix de l'emplacement des actionneurs. Les résultats de cette étude demeurent valables quelque soit le système d'actionneurs utilisé.

ACKNOWLEDGEMENTS

I would like to express my heartfelt gratitude to Dr. R.H. Crotogino and Dr. W.J.M. Douglas for their continuous encouragement, advice and financial support during the completion of this thesis.

I would also like to thank the research group members; Dr. A.R.P van Heiningen, Dr. A.S. Mujumdar, C. Ercan, B. Huang, N. Poirier, O. Polat and S. Polat for all the discussions, useful suggestions and especially their friendship.

I would like to acknowledge the many friends I made during my stay at McGill, for the conversations and discussions which helped me grow on a personal and technical level.

I would like to express my appreciation to the Pulp and Paper Research Insitute of Canada and the Paper Industries Management Association for their scholarship support.

I would like to thank the personnel at the machine shops in the Chemical Engineering Department and at the Pulp and Paper Research Institute of Canada for their help in constructing the equipment.

I wish to thank R.K. Stevens of Abitibi-Price and J.D. McDonald, formerly with Abitibi-Price and now with the Pulp and Paper Research Institute of Canada, for their assistance in making the measurements on the paper machine.

Not to be forgotten, I would like to thank my parents, my wife, Laurie, and my son, William, for being with me during this part of my life.

TABLE OF CONTENTS

CHAPTER 4. IMPINGING JET HEAT TRANSFER IN CALENDER CONTROL SYSTEMS

CHAPTER 5. HEAT TRANSFER AND THERMAL EXPANSION IN PAPER PAPER MACHINE CALENDER ROLLS

CHAPTER 6. THE EFFECT OF ACTUATOR POSITION ON PERFORMANCE OF A CD CALENDER CONTROL SYSTEM: AN EXPERIMENTAL STUDY ON A COMMERCIAL CALENDER

LIST OF FIGURES

LIST OF TABLES

NOMENCLATURE

a - intercept in sensor calibration, Ω

$a_{E,W,P}$ - coefficients in finite difference equations

c_p - heat capacity, J/kg/K

d - nozzle diameter, mm

d_f - film thickness, μm

L - length of film, mm

h - heat transfer coefficient, $W/m^2/K$

H - Nozzle to impingement surface spacing, mm

I_p - calender control performance index, $|W_{\Delta r}/\Delta r_p|$, mm/$\mu$m

ℓ - axial length of cylinder, mm

Mv_s - mass velocity ratio, $\frac{\rho_s V_s}{\rho_j V_j}$

N - number of adjacent control jets

n - number of layers in finite difference procedure

P_b - barometric pressure, Pa

P_s - static pressure, Pa

P_{line} - axial line pressure in a calender nip, Pa/m

q_c - external heat flux due to control jets, W/m^2

q_i - internal surface heat flux, W/m^2

q_p - heat flux due to heat up of the paper web and evaporation of water

q_z - axial heat flux, W/m^2

q_{sm} - maximum self heating heat flux, W/m^2

r - radial position relative to jet centerline

r_o - outside roll radius, mm

r_i - internal roll radius, mm

Δr - local radial thermal roll deformation, μm

Δr_p - maximum radial thermal roll deformation equals the steady state value of $\Delta r|_{z=0}$, μm

$\Delta r|_{z=0}$ - radial thermal roll deformation under actuator centerline, μm

Δr_{p10} - radial thermal roll deformation 10 minutes after a control action, μm

R_s - sensor resistance

R_v - Wheatstone bridge variable resistance, Ω

R_1, R_2 - Wheatstone bridge measurement range resistances, Ω

S - nozzle-to-nozzle separation, mm

s - shell thickness, $(r_o - r_i)$, mm

t - time, s

Δt - sampling period, s

T - temperature, °C

T_a - ambient temperature, °C

T_j - jet temperature, °C

T_∞ - ambient temperature removed from direct influence of the impinging jets

T_s - impingement surface temperature, °C

T_{sp} - external roll surface peak temperature, °C

T_{sb} - external roll surface base temperature, °C

ΔT_{sp} - peak difference in roll surface temperature $|T_{sp} - T_{sb}|$, °C

ΔT_s - Temperature fluctuation at impingement surface, °C

ΔT_{x_δ} - Temperature fluctuation at penetration depth, °C

V - velocity, m/s

V_{out} - fluctuating bridge output voltage, μV

V_a - Wheatstone bridge voltage source, V

w - external surface temperature peak width, mm

$W_{\Delta r}$ - width of deformation, mm

W_T - width of surface temperature peak, mm

x - axial position from jet centerline, mm

x - distance, mm

x_δ - penetration depth, mm

Δx - grid point separation, mm

y - circumferential position from jet centerline, mm

z - axial position from jet centerline, mm

Dimensionless Groups

Bi - Biot Number, $\frac{h\ l}{k}$

Fo - Fourier number, $\frac{\alpha\ t}{l^2}$

$\frac{H}{d}$ - dimensionless nozzle-to-impingement surface spacing

$\frac{S}{d}$ - dimensionless nozzle-to-nozzle spacing

Nu - Nusselt number, $\frac{h\ d}{\lambda_s}$

Nu_o - stagnation Nusselt number

$\overline{Nu}_c$ - circumferentially averaged Nusselt number

$\overline{Nu}_r$ - radially averaged Nusselt number

Re - Reynolds number, $\frac{d\rho V}{\mu}$

Nu_{max} - maximum Nusselt number

$\frac{x}{d}$ - dimensionless axial position

$\frac{y}{d}$ - dimensionless circumferential position

Greek letters

$\mathcal{A}$ - sensitivity, volts/K

α - thermal diffusivity, m^2/s

δ_f	-	resistivity, $\Omega \cdot mm$
ψ	-	Jet impingement angle relative to normal
ϑ	-	Jet impingement point relative to outgoing nip
Φ	-	angular position relative to jet centerline
ν	-	poisson ratio
τ	-	deformation time constant, s
λ	-	thermal conductivity, W/m/K
λ_{sub}	-	thermal conductivity of substrate, W/m/K
ω	-	rotations per second, s^{-1}

Superscripts/Subscripts

a	-	average
e,w	-	evaluated at respective control volume face
E,W	-	evaluated at respective control volume node
j	-	evaluated at jet conditions
s	-	evaluated at surface conditions
o	-	previous time step
n	-	current time step
1,2,3	-	layer number

CHAPTER 1

INTRODUCTION

1.1 Background

Impinging jets are commonly used in a variety of industrial applications where high heat or mass transfer rates are required. The possible applications include processes such as the annealing of metals, tempering of glass, cooling of electronic components and turbine blades and drying of paper and textiles. Another important application, which is the subject of this thesis, is the control of the paper machine calendering operation.

Calendering is the final step in the manufacture of many grades of paper. After the paper has been formed, pressed and dried, it is rough and bulky. The calendering operation reduces the thickness of the paper and gives it the surface properties required for its end use (e.g. printing).

The paper machine calender stack is essentially a rolling mill consisting of a vertical stack of cast iron rolls. The paper issuing from the dryer section enters the top nip of the calender stack and is compressed as it proceeds down through each nip of the stack.

Of the variables which affect the thickness reduction of the paper in the calender, the most important ones are the pressure exerted on the paper in the nips and the temperature of the paper in the nip. Cross-machine (CD) control of the paper thickness uniformity is accomplished by adjustments in these variables. Roll temperatures, and consequently local nip pressures, are controlled by locally heating and/or cooling the rolls using hot or cold air jets or induction heaters. The rolls are cooled where less paper thickness reduction (i.e. thicker paper) is required. When a roll is cooled, the local roll diameter is reduced, by thermal deformation, and the nip pressure is relieved. Where thinner paper is required, the rolls can be heated, causing the reverse effects.

The complex interactions of the calendering parameters, the control variables and their effect on the resulting thickness profiles have been understood qualitatively by papermakers, who have been adjusting the CD profiling systems manually for many years. However, very little quantitative information is available which might help in the design and optimization of control systems.

There exists a large body of fundamental knowledge about the heat/mass transfer characteristics of impinging jets which has been comprehensively reviewed in the recent literature (Obot[1980], Saad[1981]). However, the literature dealing with their application to industrial processes is somewhat less extensive. The design of paper dryers, for example, is frequently cited as an application of the fundamental work on impingement heat and mass transfer (Holik[1971), Martin[1977], van Heiningen[1982], Obot[1980], Polat[1988]). The application of these fundamentals to the problem of paper machine calender control have, with one exception, been very superficial and qualitative (Lyne et al.[1976], Mitchell and Sheahan[1978], Crotogino et al.[1982]). The exception, is the exploratory work of Pelletier[1984,1987].

The conversion of the heat flux at the calender roll surface into a control response, i.e. a local change in paper thickness, depends on how the heat is distributed within the calender roll and the corresponding local thermal deformation of the calender roll. Only a few studies have dealt with the actual calender roll deformation, either numerically (Brierly[1975], Aro[1984]) or experimentally (Lyne[1976]). Provided appropriate boundary conditions can be specified, the problem can now be solved using well-tested numerical techniques available in commercial software.

1.2 Objectives and Scope

The primary objective of this work is to provide a better fundamental basis for the design and optimization of paper machine calender control systems. To reach this objective, two studies were undertaken. The first is an experimental study of the factors affecting the heat transfer between impinging air jets and calender rolls. The second involves the numerical simulation of the heat transfer inside calender rolls and the resulting thermal deformation, as a function of the experimentally obtained impingement heat transfer boundary condition.

The objectives of the experimental impingement heat transfer study were:

1. To determine to what extent the current impingement heat transfer literature could be applied to calender control using impingement air systems, where impingement geometry and surface motion might play an important role.
2. To investigate the effect of ambient temperature on the impingement heat transfer performance.
3. To determine the effect of jet Reynolds number of the impingement heat transfer.
4. To study the effect of the impingement jet geometry on

the heat transfer profiles. The geometric variables included:

a) Nozzle-to-roll spacing

b) Nozzle-to-nozzle spacing

c) Jet impingement angle relative to normal impingement

d) Jet impingement position relative to the in-going and out-going nips

e) Semi-confinement of the impinging jet

f) Use of a jet array vs. single row of jets

The objectives of the numerical study on calender roll thermal deformations were:

1. To determine numerically, the thermal deformations possible with calender control systems.

2. To determine which roll design has the greatest potential for roll diameter correction given a specified internal heat transfer boundary condition.

3. To evaluate how changes in the impingement heat transfer boundary condition affect the local calender roll deformation.

A further objective was to determine the most favorable roll in a calender stack at which to attempt the cross-machine thickness correction. This objective was met with an experimental study carried out on a commercial newsprint machine calender.

To meet the overall objective of this study, recommendations and practical guidelines for the design and optimization of calender control systems will be made based on the results of this study.

CHAPTER 2

LITERATURE REVIEW

2.1 Introduction

The primary objective of this work is to provide a better fundamental basis for the design and optimization of paper machine calender control systems. To provide the background required for this study, two subject areas are reviewed:

i) calendering technology
ii) fundamentals of jet impingement heat transfer

The discussion of the calendering technology will provide the required information to understand the calender control problem being studied. The discussion of the fundamentals of impingement heat/mass transfer will provide the background for the solution of the problem.

2.2 Calendering of Paper

2.2.1 Papermaking

The papermaking process is illustrated in Figure 2.1, which shows a schematic representation of the cross-section of a modern pap.r machine. There are four primary operations:

1. Forming and drainage
2. Pressing
3. Drying
4. Calendering

In the forming and drainage operation, the dilute fiber suspension issues as a jet from a headbox and is deposited onto a continuously moving forming screen. As the water is removed from the suspension by a

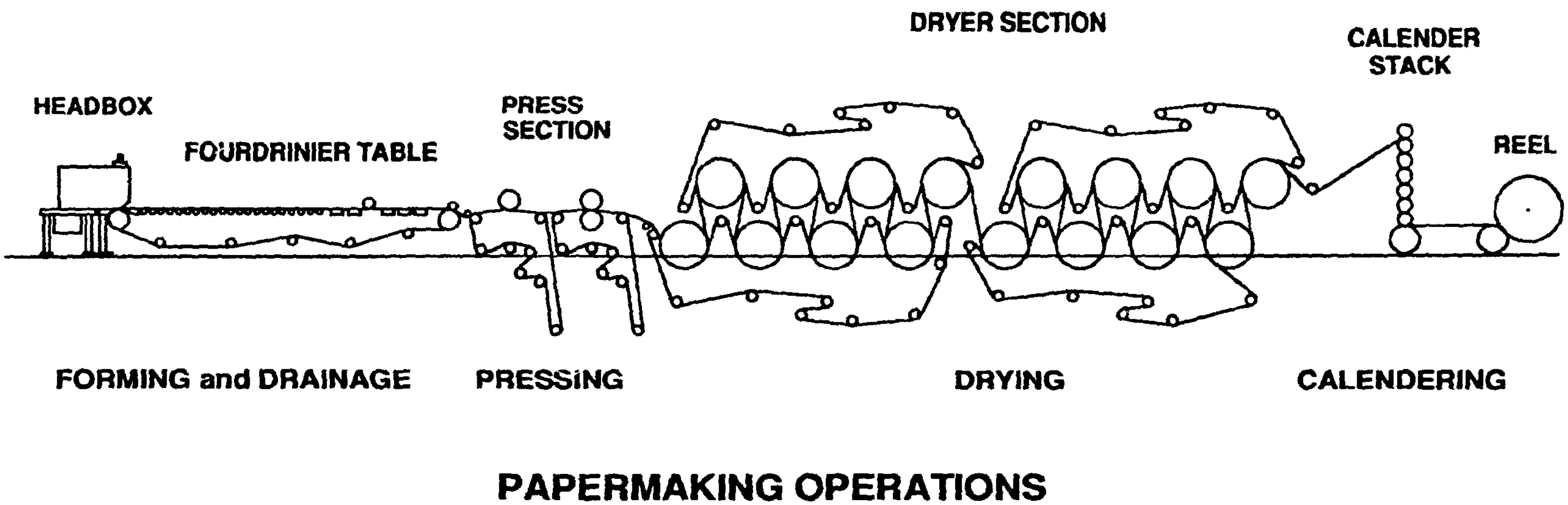

Figure 2.1 The papermaking process

combination of gravity, suction, pressure and/or centrifugal forces, a fiber web is formed.

After the paper web has been dewatered to a solids content range of 10-20%, it is contacted with a felt which carries it into a series of presses, where the web is consolidated and further dewatered to a solids content, typically in the range 40-45%.

After pressing, the paper is dried, usually by contacting the paper with a series of steam-heated drying cylinders. The paper will normally leave the dryer section with a moisture content in the range of 5-8%.

The final operation for many grades of paper is calendering. Here, the sheet is subjected to a series of rapid compressions in the calender stack, which transforms the rough, bulky sheet issuing from the dryer section into a sheet with the surface properties and sheet thickness suitable for its end use (e.g. printing).

After calendering, the paper is wound onto a reel. In an off-machine operation, these reels are cut to the desired width while being rewound into rolls suitable for shipment to the customer. Some grades of paper require additional finishing operations, such as off-machine coating and/or supercalendering, prior to being rewound and prepared for shipping.

2.2.2 The Calendering Operation

The paper machine calender, shown in Figure 2.2, consists of a vertical stack of cast iron rolls. The paper is compressed as it passes through successive nips from the top to the bottom of the calender and becomes progressively thinner and smoother. A review of the parameters affecting this operation and a description of the major components of a modern calender was presented by Crotogino[1981].

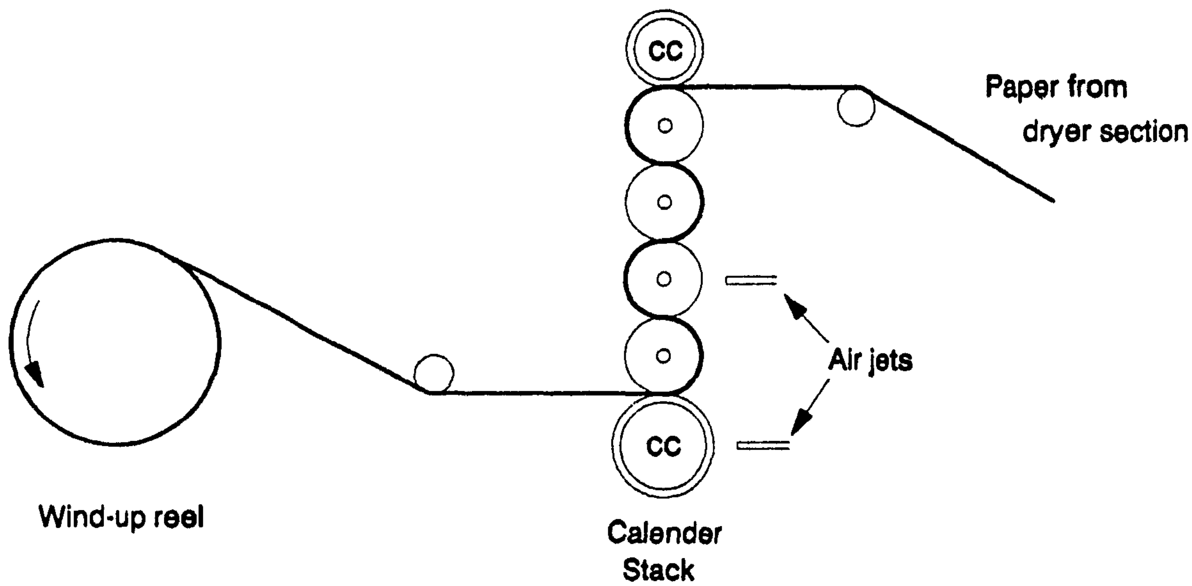

Figure 2.2 A paper machine calender stack

The web thickness reduction which occurs in a calender nip is affected by the nip load, the machine speed, the roll diameters, the web and the calender roll temperatures, the web moisture content and the initial bulk. A long-standing equation used to predict the thickness reduction was proposed by Macken et al.[1941]. However, it only considered the effect of one parameter, the nip load applied in the calender.

$$t_f = \frac{1}{\frac{1}{t_i} + mP^n} \tag{2.1}$$

where t_f - out-going web thickness,

t_i - in-going web thickness

P - nip pressure

m, n - empirical constants

Based on experimental work with a platen press, Peel and co-workers[1969,1972], proposed correlations which accounted for the effects of pressure, dwell time, web temperature and web moisture content. The engineering application of these equations was limited since the dwell time and maximum pressure in the calender nip cannot readily be measured. Kerekes[1976,1977] proposed modified versions of these equations, replacing dwell time and pressure with the measurable variables nip load, roll radius and machine speed.

Crotogino[1980,1982,1983] proposed a comprehensive calendering equation which accounted for all the factors affecting sheet bulk reduction including the initial bulk of the paper entering a nip. With the incorporation of initial bulk, the equation could be applied successively to each nip of a calender stack to calculate the total bulk reduction in a multi-nip calender. The resulting equation is

$$\varepsilon = A + \mu B_i \tag{2.2}$$

where

$$\varepsilon = \frac{t_i - t_f}{t_f} = \frac{B_i - B_f}{B_i} \tag{2.3}$$

$$\mu = a_o + a_L \log L + a_S \log S + a_R \log R + a_\theta \theta + a_M M \tag{2.4}$$

and
B_i - initial web bulk, cm^3/g
B_f - final web bulk, cm^3/g
L - nip load, kN/m
M - web moisture content, %
R - effective roll radius, $R = \dfrac{2R_1R_2}{R_1 + R_2}$, m
S - machine speed, m/min
θ - web temperature, $^\circ C$

The coefficients A, a_o, a_L, a_S, a_R, a_θ, a_M must be determined experimentally. They reflect the viscoelastic behavior of the paper and are dependent on the furnish used (i.e. the wood species, pulping method used, etc.) and to some extent on the papermaking operations before calendering.

The calendering equation uses the cross-machine (CD) average values of the independent parameters, in Equations 2.2 to 2.4, to calculate an average bulk reduction. It cannot provide any precise quantitative information on the cross-machine variations in the bulk reduction. While, in principle, it is possible to measure the local paper web and calender roll temperature, as well as the entering bulk and moisture content across the width of the calender, the local nip load cannot be measured. It is established by the nip shape and the local stress/strain behavior of the paper under compression in the nip. The calendering equation describes the bulk of the paper after it has left the nip, not the paper in the nip. However, as it is reasonable to expect that an in-nip calendering equation would have the same form, the calendering equation can give qualitative insight into the CD control problem.

The cross-machine direction control of the calendering process is required to compensate for CD variations in the basis weight, moisture content and temperature of the paper entering the calender. Also, there are differences in the local nip pressures due to calender roll grinding tolerances and roll deflections. These CD variations in the local calendering conditions, if left uncorrected, result in paper of varying surface properties and thickness. The variations in the surface properties results in uneven ink transfer when the paper is printed, while machine direction (MD) streaks of high or low sheet thickness, when built up over hundreds and thousands of revolutions on the windup reel, produce hard or soft areas in the reel. The CD variations in reel hardness can cause roll structure problems when the paper is rewound and cut into rolls suitable for use in a printing press.

A more thorough review of the mechanism of cross-machine direction calender control will be presented later.

2.2.3 Calendering Equipment

A typical paper machine calender stack, as shown in Figure 2.2, consists of a vertical stack of from two to eight chill cast iron rolls. The roll diameters vary from approximately 300 mm for rolls found on old, narrow and slow paper machines to 800 mm for modern, wide and fast machines. The pressure in the nips, or the nip load is a consequence of the weight of the rolls. Provisions can be made to augment or relieve the gravity loading at appropriate intermediate positions in the stack.

Provisions are also made on most modern calenders to heat some of the rolls.

There are a variety of different types of calender rolls currently in use. They can be classified into three general categories:

1. solid rolls
2. heat transfer rolls
3. variable crown rolls

Solid rolls are primarily used on older calender stacks and are not common in newer installations. The only advantage associated with solid rolls is their weight, which contributes to higher nip loads, but with the larger roll diameters used in newer calenders, the weight of solid rolls can be excessive. As a general practice, solid rolls in existing calender stacks are being replaced by either heat transfer or variable crown rolls.

Some calender rolls are heated to promote bulk and roughness reduction in the paper web. The three most common types of heat transfer rolls are shown in Figure 2.3.

Of the heat transfer rolls, the simplest design is the center-bored roll (Figure 2.3.a) Typically the roll is heated by passing steam through the center bore. The heat transfer rates in this type of roll are relatively low due to the limited internal heat transfer area and the thick shell.

Modern heat transfer rolls, such as the double walled rolls (Figure 2.3.b) or the peripherally bored rolls (Figure 2.3.c) achieve much higher heat transfer rates by increasing the internal heat transfer area and reducing the effective shell thickness. The heating fluid (typically pressurized water), is passed through the heating channel at high

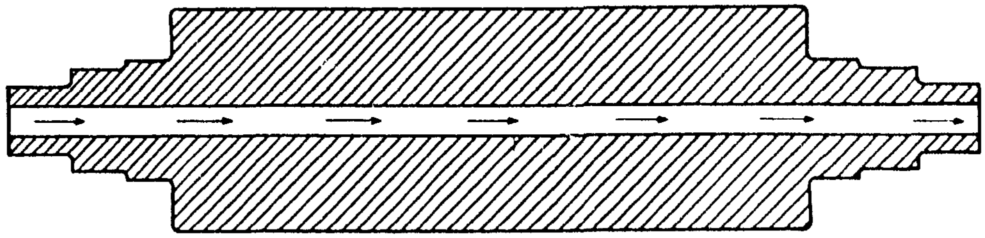

a) center bored roll

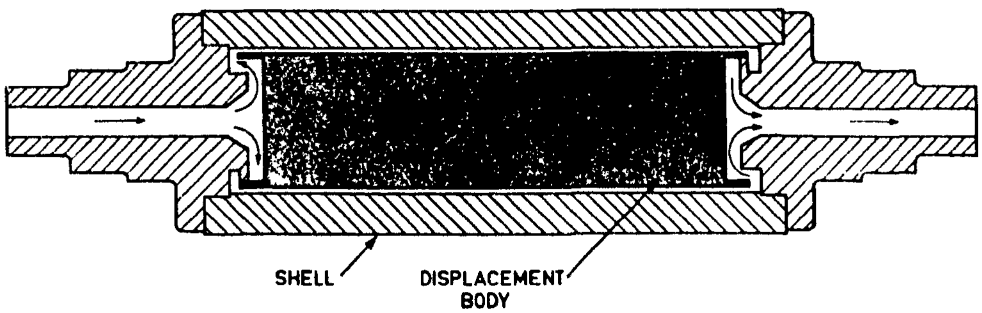

b) double walled roll

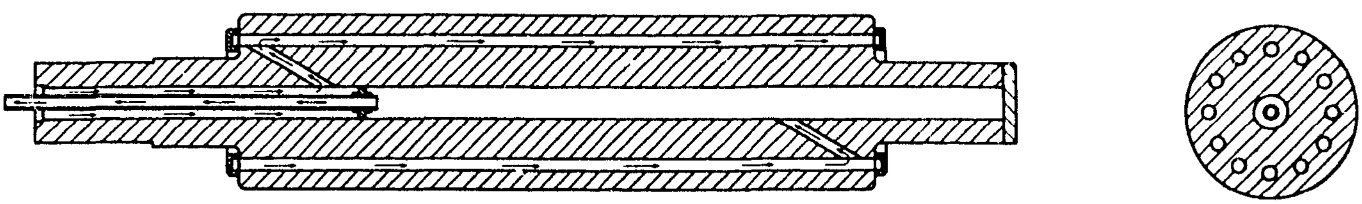

c) peripherally bored roll

Figure 2.3 Various heat transfer roll designs velocity, ensuring high heat transfer rates and uniform axial temperatures. There are a number of other heat transfer roll designs available which are primarily variation of the three basic types shown in Figure 2.3.

Variable crown rolls are used in calenders to compensate for the tendency of the bottom roll (king roll) in a stack to sag under its own weight and the weight of the rolls above it. They can also be used to prevent a roll from bending when additional load is applied (or relieved) through its bearing housings. Crown-controlled rolls (CC rolls), a type of variable crown roll, are shown in Figure 2.2 in the king roll position and at the top of the calender where loading in the calender stack can be increased or relieved.

Although there is an increasing number of designs for variable crown rolls, all share certain features. As shown in Figure 2.4, they consist of a hollow cylinder, which is supported on hydraulic or hydrostatic bearing systems across the entire width of the machine. The forces which are applied externally are transferred through the shell and the hydraulic support elements to the stationary central beam. The design of the rolls vary primarily in the choice of a internal hydraulic loading system.

Another type of roll, which should be mentioned here is the soft calender roll. Soft rolls are covered with material which has a hardness similar to that of paper under compression in the calender nip. The roll covering is typically of an elastomeric material or paper under extremely high radial compression. These roll are typically used in off-line super calenders or gloss calenders, but their use has recently been extended to on-machine calendering (Crotogino and Gratton[1987]). Overheating of the roll covering material, due to the heat generated

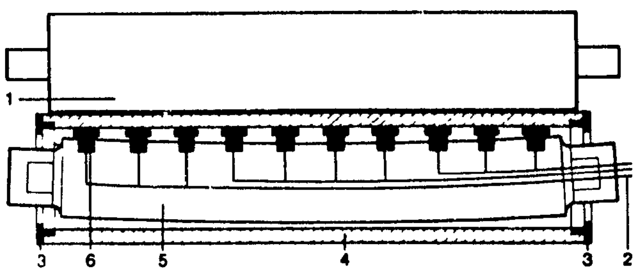

1. Opposing roll
2. Oil supply (zone control)
3. End bearings
4. Roll shell
5. Beam
6. Hydrostatic bearings

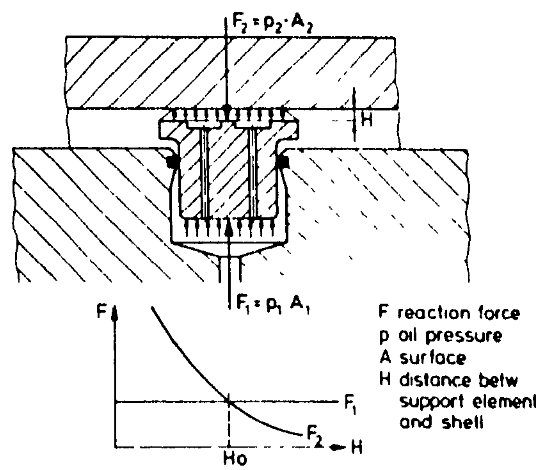

Figure 2.4 The Nipco variable crown roll

within the material as a result of rolling friction or heat transfer from the paper, can damage the roll covering material. Cooling of these rolls with air jets is an increasingly important application of the impingement heat transfer results discussed in this thesis.

2.3 Calender Control Systems

2.3.1 Sensors and Actuators

The entire calendering operation must be controlled to produce uniform paper thickness and surface properties across the width of the machine, since machine direction streaks of high or low sheet thickness will build up to produce hard or soft spots on the windup reel.

Traditionally, reel hardness has been measured by striking the windup reel with a wooden bat. Based on the sound and feel, the operator can adjust the CD calender control system manually. Two sensor types have been developed: the Backtenders Friend (BTF), which measures the reel hardness directly (Cherewick and Walker[1974]) and web thickness gauges.

The CD control of the calendering process is performed by locally adjusting the nip load and/or sheet temperature. Local heating of the calender roll results in a larger roll diameter, higher nip pressures and thus greater paper thickness reduction. The reverse is true when the calender roll is cooled.

Impinging air jets have been the standard actuator system for calender control. A variety of impingement type calender control systems are available including unconfined/confined in single row and multiple jets geometries, as illustrated in Figure 2.5, with each having its stated advantages. These sensors will be discussed in greater detail later.

The most common new air actuator systems involve the use of semi-confined jets or arrays of nozzles (Higham[1986] and Boissevain[1986]). Rather than adjusting the air flow, these systems maintain a constant air flow and modulate the temperature of the air.

Another recent innovation is the Cal Coil© system (Larive and Lindstrom[1986]) which uses AC induction heaters as actuators. Cal Coil© actuators, used alone, or in combination with an air impingement actuator system, are gaining popularity, particularly with new installations due to high heat transfer efficiencies.

A third approach to calender control has recently been proposed, and involves the evaporation of a mist of water in the air near the calender roll surface. This technique, although promising since it uses the latent heat of evaporation as a heat sink, has not received wide spread acceptance due to potential problems if the the water mist does not completely evaporate in the boundary layer and deposits on the paper or the calender roll.

2.3.2 Impingement Jet Geometry and Positioning

The literature dealing with air jet actuators for CD calender control is largely speculative in nature. Experimental data that have been published are frequently contradictory and cannot readily be generalized to the wide variety of calendering configurations available.

Kahoun et al.[1965] proposed using cool air impinging directly on the web entering the calender stack, as a means of controlling reel building. They reported that more effective control had been achieved with a faster response time than when air was directed onto calender rolls. They speculated that

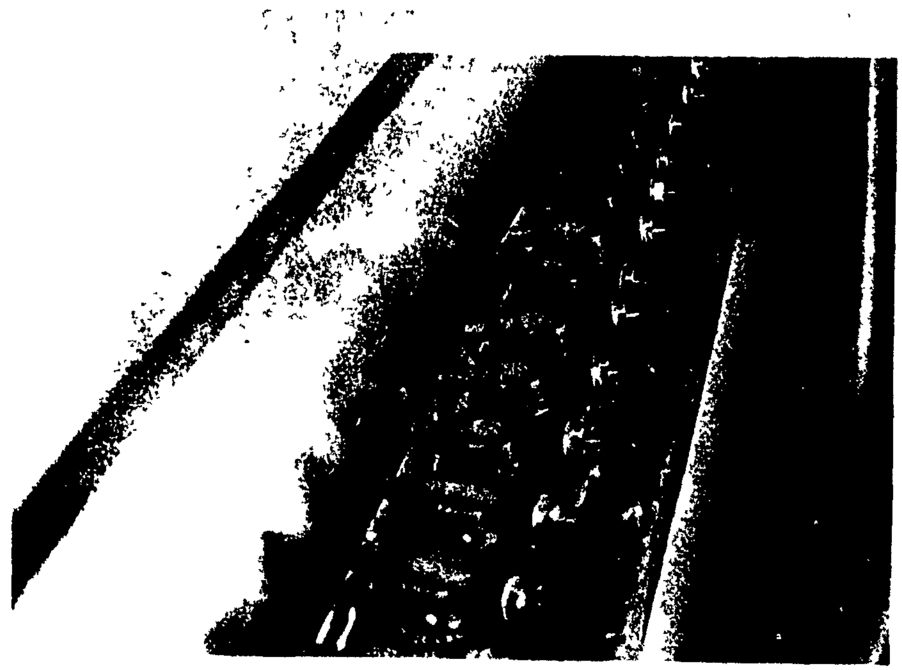

Figure 2.5(a) Industrial calender control air nozzles
12 mm nozzle diameter

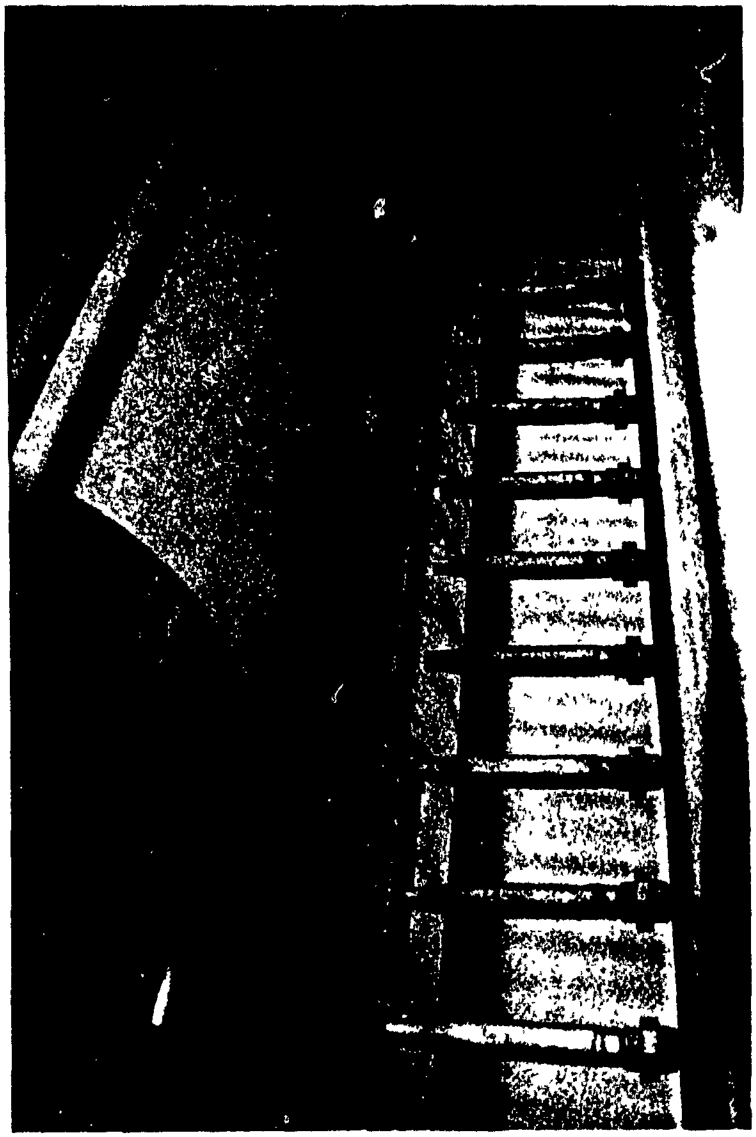

Figure 2.5(b) Industrial calender control air nozzles
25.4 mm nozzle diameter

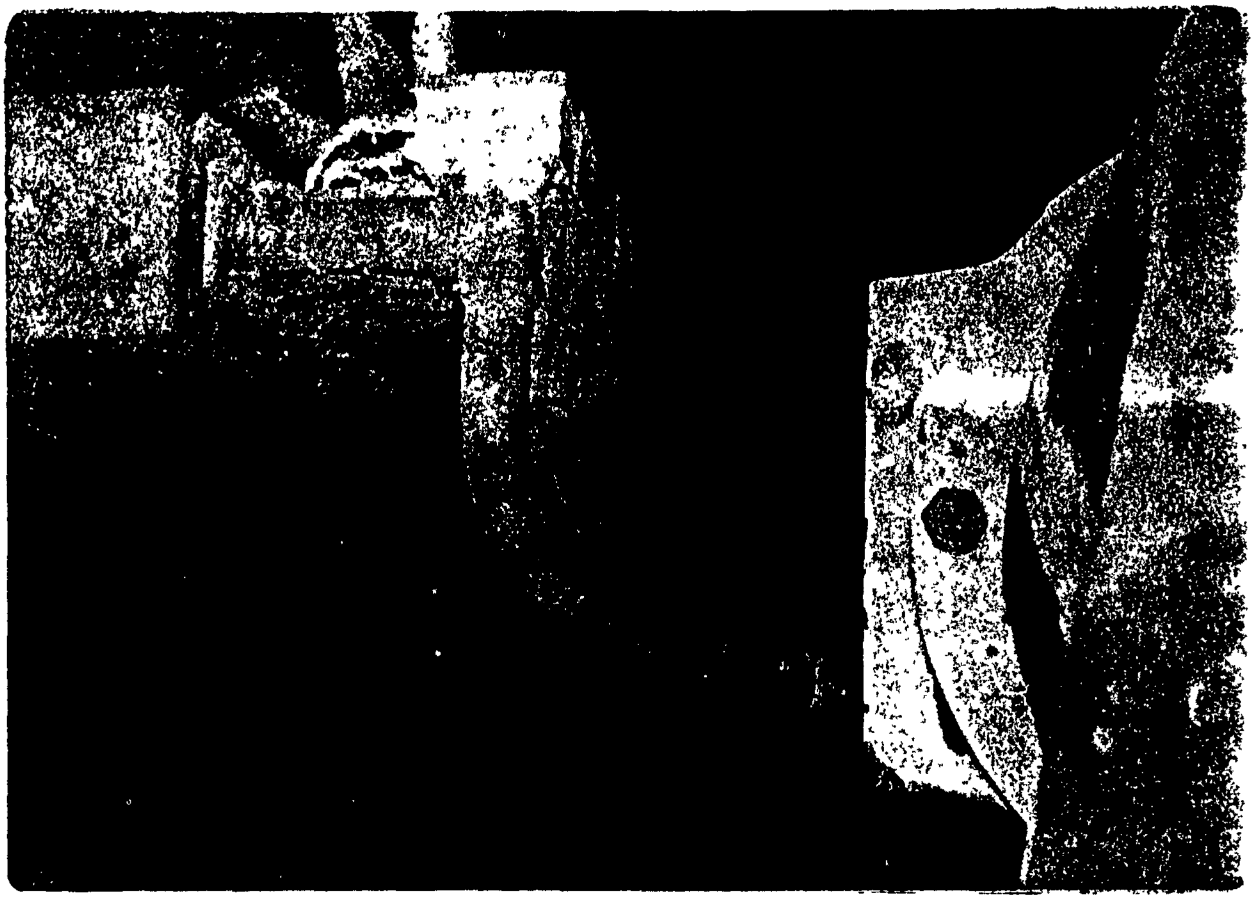

Figure 2.5(c) Industrial calender control air nozzles

12mm x 50mm rectangular nozzle

i. the high heat transfer efficiency to the paper.

ii. the ability of the cooled web to change the temperature of several rolls in the calender.

Bryan[1972] considered the air flow patterns around a calender stack, Figure 2.6, and concluded that the most efficient heat transfer required the break-up of the boundary layer carried with the roll surface. He argued that the jet velocity required to do this was dependant on the position of the jets relative to the in-going and out-going nips and proposed that the low pressure zone associated with the outgoing nip would be the most effective location. No direct evidence supporting this hypothesis was presented.

Lyne et al.[1976] reported results obtained on a production calender stack, with the conditions as described in Figure 2.7. On the 1000mm diameter crown controlled king roll, Lyne observed a surface temperature change of 1.5°C and a resulting web caliper change of 1.5μm. No surface temperature or web caliper changes were observed using the smaller, lower flow rate nozzle on the 750mm diameter, solid queen roll. Lyne argued that the lack of an effect on the queen roll is due to the damping effect of the heat removed by the paper web on the surface temperature change. Based on these arguments the king roll was recommended as the optimum location for calender profile control. The direct comparison of the king and queen roll results and their generalization was somewhat misleading since jet Reynolds number for the smaller nozzle used on the queen is half and has about 15% of the mass flow rate of the larger nozzle used on the king roll.

Mitchell and Sheahan[1978] carried out experiments on a production calender stack, configured as shown in Figure 2.8, to investigate the

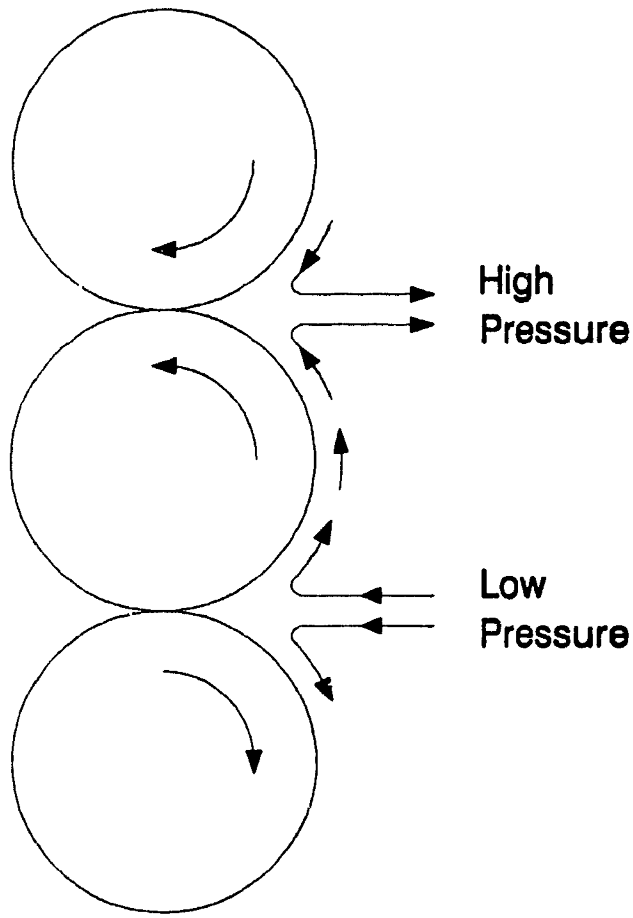

Figure 2.6 Air flows around a calender stack

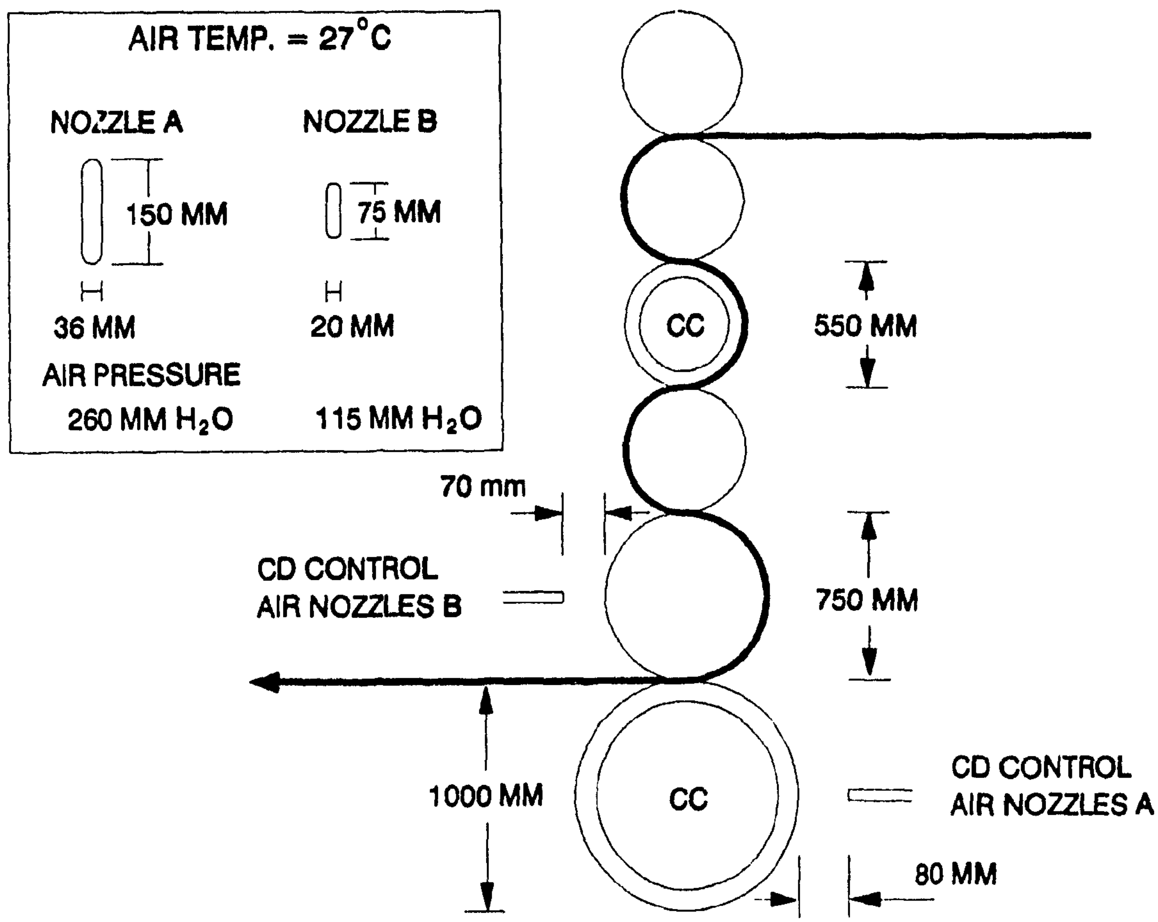

Figure 2.7 Calender stack configuration used in a calender performance mill trial by Lyne et al.[1976]

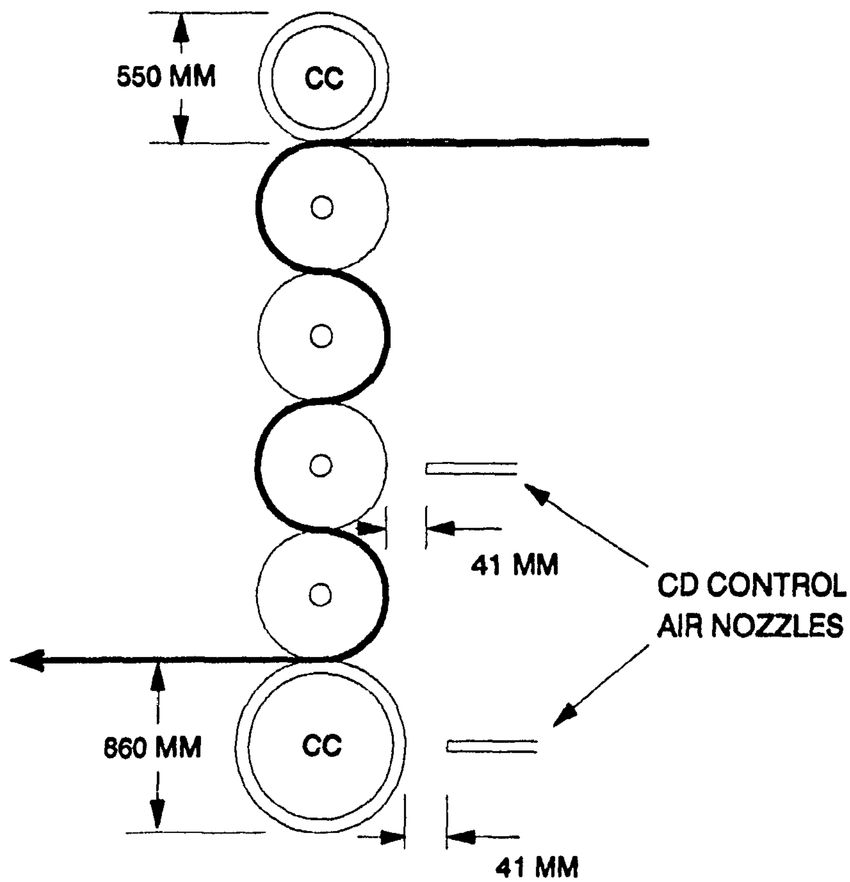

Figure 2.8 Calender stack configuration used in mill trial by Mitchell and Sheahan[1978]

summarized in Figure 2.9. The numbers shown at various locations in a double calender stack represent the effectiveness of a control system in that position relative to the performance of a control system located on the king roll of the second calender.

Fjeld and Hickey agree with the analysis of Lyne et al. in that the damping effect of the heat removed with the paper during a half wrap of a calender would not be present if the control system were on the top roll or at the king roll. However, they contradict Lyne et al. by arguing that although the bottom nip may have pressures up to ten times greater than the top nip, the potential for average caliper change and thus the control bandwidth would be drastically decreased.

Lyne et al. argued that the caliper correction made with the king roll are final. Fjeld and Hickey discounted this argument by pointing out that in feedback control (typical for paper machine caliper control systems) the location where the caliper correction is made is irrelevant. This argument is valid provided the actuators are powerful enough to make the appropriate correction at any position in the system and ignores the relative effectiveness of the actuators at different positions in the calender stack.

Although the literature dealing with the fundamentals of impingement heat transfer is quite extensive, the direct application of this data to the calender control problem is not immediately obvious due primarily to the unknowns associated with:

i. the effect of ambient temperature on impingement heat transfer.

ii. the effect of the high velocity of the impingement surface relative to the impinging air jet velocity.

effect of cooling impingement air showers on the roll surface temperature profiles. They observed that an impingement air jet placed on the crown controlled king roll of the calender stack produced a surface temperature drop of 5.0°C while a similar air jet placed on the third roll only produced a 1.7°C change with an additional temperature drop of 0.3°C on the king roll. These surface temperature changes resulted in 30% and 20% drops in the reel hardness as measured with the on-machine calender control system. It is not mentioned if the intermediate rolls on the calender stack were heated.

As to the lateral separation of the nozzles, Mitchell and Sheahan[1978] observed that the surface temperature drop achieved with a nozzle separation of 100mm was only 20% higher than that using a nozzle separation of 200mm using the same jet velocity and thus half the total air flow rate. They concluded that a fair amount of air is wasted when using the closer nozzle separation. Confusing these results, is the possibility that the calender control system may have been air supply limited. This may have lead to decreased jet velocities for the closer nozzle separation.

Fjeld and Hickey[1984] discussed the optimum location of calender profiling systems. Based primarily on computer control arguments, they recommend the use of calender control systems on the upper rolls of a calender stack as providing

i. high speed response and good spatial resolution in the cross-machine direction

ii. wide control band and

iii. highest potential for relative decrease in caliper

Their recommendations for the placement of control systems are

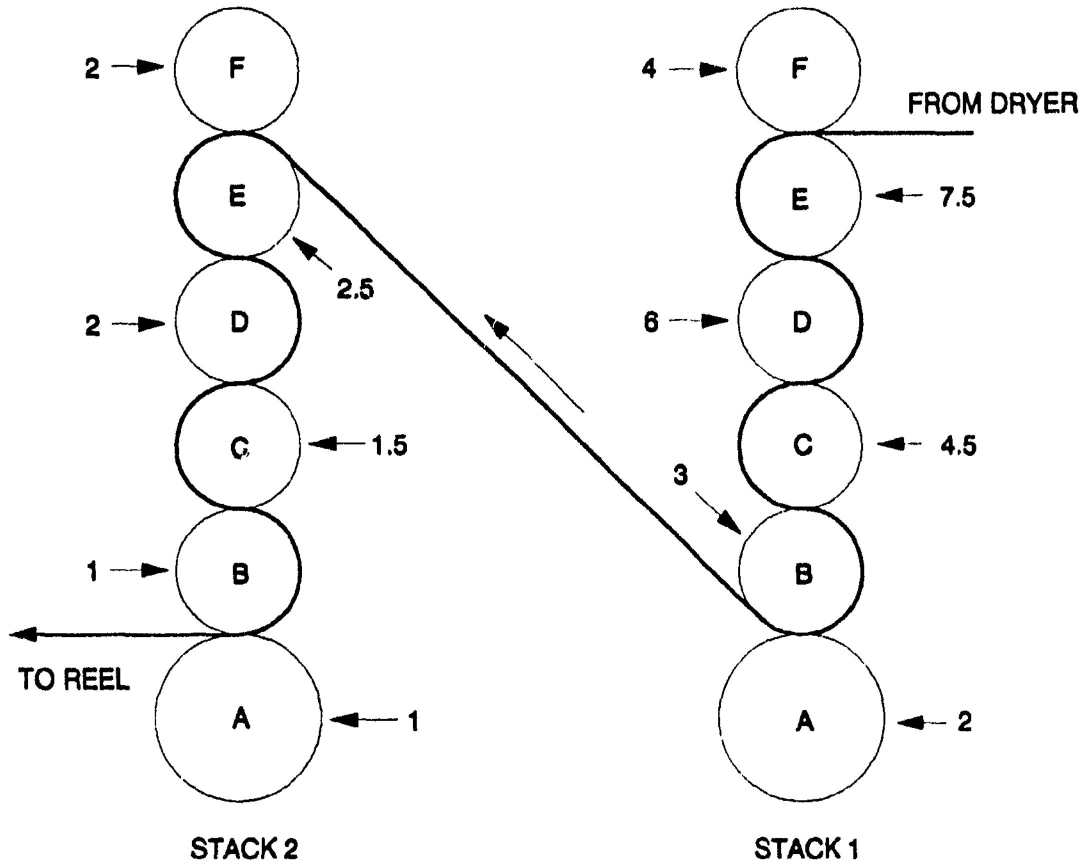

Figure 2.9* Relative performance of calender stack control systems relative to the last nip of the second stack - Fjeld and Hickey[1984]

iii. the effect of complicated air flow patterns around the calender stack.

The only study of impingement heat transfer as it applies to the calender control problem is that of Pelletier et al.[1984,1987]. The experimental results demonstrated the importance of entrainment of ambient temperature air by the unconfined jets on the resulting impingement surface heat transfer. Pelletier et al.showed that over the range investigated, the circumferential position and angle of inclination of the impinging jets relative to the roll surface had only a minor influence on average heat transfer.

2.3.3 Roll Deformations

None of the calender control literature deals with the effect of calender roll design (i.e. shell or solid) or internal calender operating parameters (i.e. heated, unheated, crown controlled) on the performance of a caliper control system. Mitchell and Sheahan[1978] noted the very much slower response of a solid calender roll as compared to a shell type roll. Lyne et al.[1976] acknowledged the effect of roll design and speculated that unheated hollow rolls will have a larger change in radius per $^{\circ}$C than either solid or heated rolls.

The thermoelastic deformations of hollow and solid cylinders is discussed extensively (Boley[1972], James[1964], Valentin and Carey[1970], Emery and Carson[1971] amongst others). The primary concern has often been the study of nuclear fuel rods, which have internal heat generation. The literature available on the prediction and or measurement of the roll deformations experienced under typical calender operating conditions is very limited.

Brierly[1975], using numerical techniques, predicted the temperature distribution and thermal deformation of a calender roll. The boundary conditions used consisted of a specified internal surface temperature and external temperature profile with no traction (no external forces) boundary conditions on all sides. The external temperature profile was specified as

$$T_s = T_{sp} - \frac{2z}{w} \Delta T_p \qquad 0 \le z \le \frac{w}{2}$$

$$T_s = T_{sm} \qquad \frac{w}{2} \le z \le \frac{\ell}{2}$$

where T_s - surface temperature, $^\circ C$

ΔT_p - peak surface temperature difference, $T_{sp}-T_{sm}$, $^\circ C$

T_{sp} - roll surface peak temperature, $^\circ C$

T_{sm} - roll surface minimum temperature, $^\circ C$

w - peak width, mm

z - axial position, mm

The calculated displacement fields were found to be dependant on the mesh size used, with the errors, estimated by Brierly, to be about ±2.75%.

Brierly found that for peak widths greater than 250-500mm, the peak roll deformation, Δr_p, was unaffected by the peak width, w. He proposed an empirical correlation for the roll radius change, Δr, as a function of the temperature change and peak width, in the form

$$\frac{\Delta r}{\Delta T_p} = \left\{ 1 - \exp - \left(\frac{w}{\lambda} \right)^p \right\} \qquad (2.5)$$

where Δr - roll radius change

$$\left.\begin{array}{l} k \\ \lambda \\ p \end{array}\right\} \quad \text{constants dependant or roll geometry and internal temperature}$$

The application of this equation to actual calendering conditions was not verified.

Given the stress boundary conditions of no traction on all surfaces, which allows axial expansion, he makes no mention of any edge distortions, such as the "OXBOW effect" discussed by D'Amato[1980]. This effect, illustrated in Figure 2.10, is caused by the difference between the inside and outside surface axial expansion which results in a buckling at the calender roll surface.

The only reference to experimental measurements of the thermal deformations of calender rolls under air jets is the work of Lyne et al.[1976]. Using a holographic interferometry technique, thermal deformations of a solid 0.5m diameter roll under the influence of a single heating jet were obtained for several operating conditions. The roll radius change at the impingement jet induced temperature peak was characterized as 1.4μm per $^{\circ}C$ surface temperature change for the 0.5m diameter roll.

These results are not directly comparable with the Brierly's numerical results since the calender roll was solid, as compared to the heated shell considered by Brierly. Also the ΔT_p values are modest when compared to the assumptions made by Brierly.

2.3.4 Prediction of CD Paper Web Thickness

Haglund[1975] proposed a numerical model to describe the effects of cross-direction variations in the calendering and in paper properties on the thickness profile of the outgoing sheet. The local cross-machine

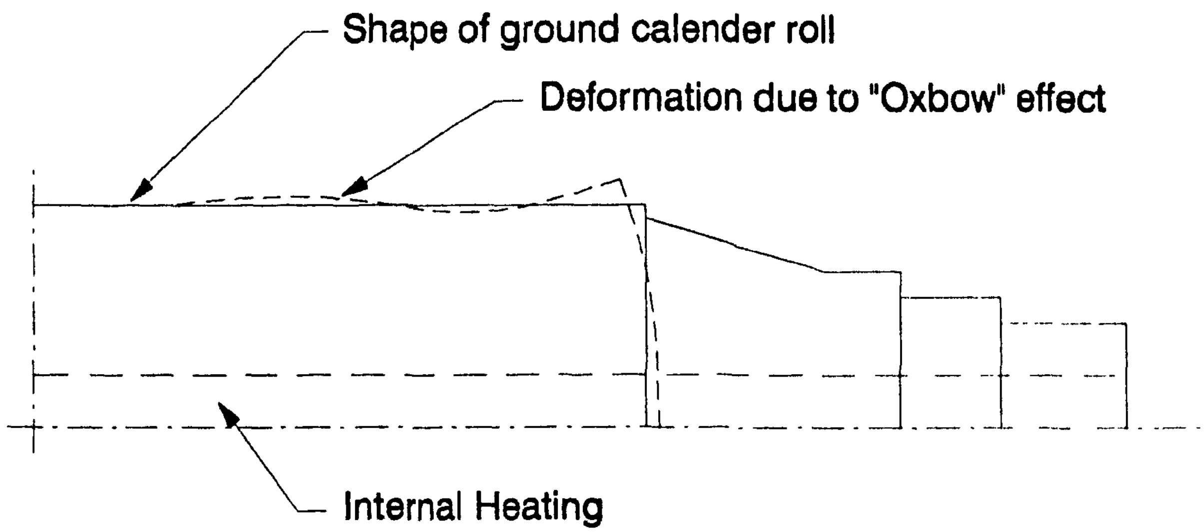

Figure 2.10 The "OXBOW" effect

calendering conditions were linked using the line pressure distribution, resulting calender roll deflections and the local roll deformations.

This procedure requires a conversion from the measurable applied line pressure, P_{line}, to the resulting pressure distribution in a calender nip. Robertson and Haglund[1974] showed that the relationships for t_p and t_r proposed by Colley and Peel[1972] could be applied to a rolling nip using a method developed by Mardon et al.[1965] which related the maximum pressure in the nip, P_{max}, to the line pressure. This procedure is implicit and requires a large amount of experimental data. For this reason, Haglund used the simplification suggested by Robertson and Haglund, where the pressure pulse in the nip is approximated by a rectangular pulse.

This model produced the interesting prediction that an incoming streak of high basis weight might result in a outgoing low thickness streak, due to the resulting load concentration. Based on the model predictions, Haglund concluded that successful calender control would require control of the roll radius profile in the range, $\Delta r \leq 1$ μm.

Derezinski[1981], using the approach of Haglund et al. developed a model of a complete calender stack incorporating the effect of heat transfer within the calender stack on the local roll deformations and web caliper reductions. As in Haglund's analysis, difficulties were encountered in describing the line pressure distribution along the calender nip as a function of the local web thickness and calender roll diameter. Also the bending of the calender roll due to nip pressure distribution was not included.

2.4 Impinging Jets

Two separate aspects of impinging jets will be discussed in this section:

- the flow characteristics of turbulent impinging jets.
- the heat and mass transfer under axisymmetric jets impinging on impermeable surfaces with emphasis on the research of particular relevance to this study.

2.4.1 Flow Characteristics of Axisymmetric Jets

The flow field associated with turbulent impinging jets can be divided into three distinct regions (Poreh and Cermak[1959]). These flow regimes are shown in Figure 2.11 and consist of the free jet, the impingement (or stagnation) and the wall jet regions. A concise description of each flow regime is provided below.

(a) The Free Jet Region

The free jet has undergone extensive analysis, both analytical and experimental, with information readily available in many standard texts (Schlichting[1968] anc Abramovitch[1963]). In an axisymmetric jet, the free jet region is composed of three parts:

i. Potential core
ii. Developing or transition flow
iii. Developed flow

The potential core is characterized as a region where the jet center line velocity remains unchanged from the jet velocity at the nozzle exit. The length of the potential core has been estimated at up to six nozzle diameters, with this length being a strong function of the jet Reynolds number, Re, and the nozzle geometry (Obot[1980]). It has

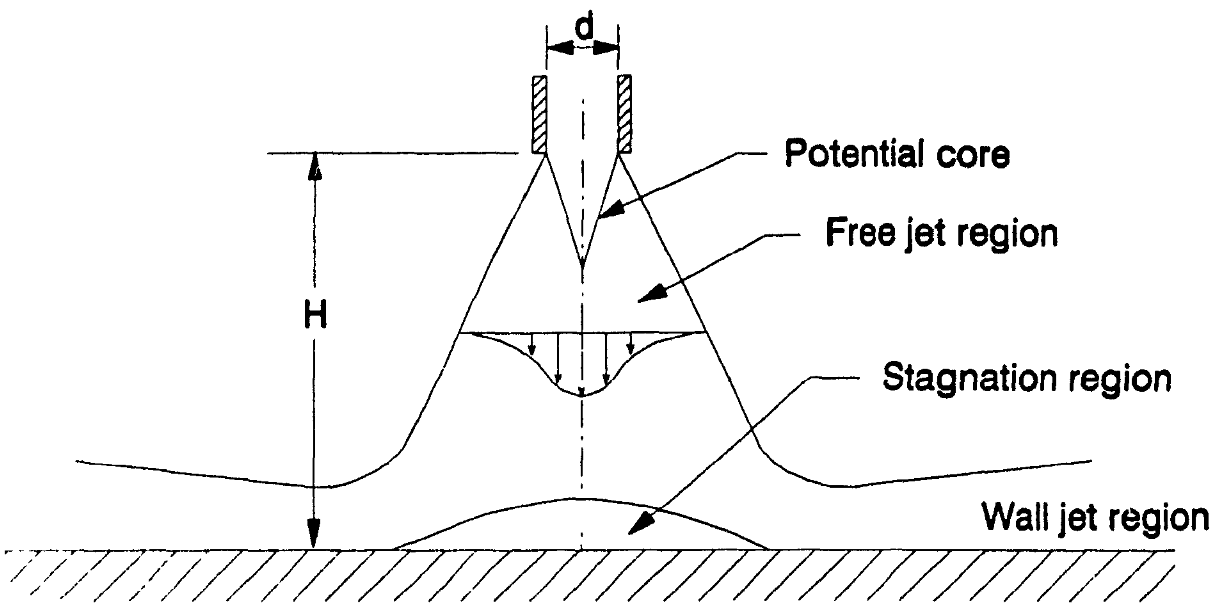

Figure 2.11 Flow regimes in an axisymmetric impinging jet

been proposed that the stagnation heat transfer tend to reach a maximum when the nozzle-to-impingement surface separation, h, corresponds to the length of the potential core.

If the nozzle-to-impingement surface spacing is large enough, there will also exist a region of developed flow where the jet can be characterized by the rate at which the jet centerline velocity decays and the rate at which the jet spreads as the distance from the nozzle exit increases.

(b) Impingement Region

When the free jet begins to be affected by the impingement surface, the impingement (or stagnation) region begins. It is in this region that the hydrodynamics of the impinging jet are the most complex. The sudden change in jet flow direction leads to a rapid decrease in the jet axial velocity and increase in the axial turbulence intensity. The sudden change in jet flow direction also gives rise to increased static pressures. The strong pressure gradients which can occur in this region create conditions favorable for the creation of a laminar boundary layer, even for cases where there is a high degree of jet turbulence.

The dimensions of the impingement region for axisymmetric jets has been the subject of several studies (Poreh and Cermak[1959], Tani and Komatsu[1966], Chia[1972] and Belatos[1977]) but as the definitions are inherently arbitrary, the dimensions vary somewhat between researchers.

Obot[1980] confirmed that the approach of Tani and Komatsu[1966] was the most realistic method to describe the extent of the impingement region. For the height of the impingement region the point at which the impinging jet deviates from the corresponding free jet profile was selected, which Tani and Komatsu found to lie between 1.6 and 2.2 nozzle diameters for the H/d range $4 \leq H/d \leq 12$. The radial extent of the stagnation region was defined as the point at which the impingement surface pressure gradients approached zero. Using this definition they found that the stagnation region extended out radially 1.6 to 3d from the jet centerline. These definitions may appear to be imprecise but they agree quite well with the actual flow separation shown in Figure 2.11.

(c) Radial Wall Jet

The radial wall jet region is the region which extends beyond the stagnation region where the jet spreads out over the impingement surface and is characterized by negligible pressure gradients. The radial velocity reaches a maximum as the flow leaves the stagnation region. The decreased pressure gradients cause the laminar boundary layer (established in the stagnation region) to become turbulent. An extensive review of the available literature characterizing radial wall jets was carried out by Obot[1980].

2.4.2 Heat and Mass Transfer Under Axisymmetric Impinging Jets

The impingement heat/mass transfer literature for axisymmetric jets is quite extensive. In the recent past there have been several comprehensive reviews (Obot[1980] and Saad[1981]) which have critically evaluated the current literature. The objective of this review is to present the background information required to place this study in perspective.

The discussion of axisymmetric impingement heat transfer will at first be restricted to the case of isothermal impingement, where the impinging jet is at the same temperature as the surroundings. This condition is common to most of the available impingement literature and its understanding is crucial to the understanding of the effect of ambient temperature on the heat transfer, which will be described in a following section. The effects of semi-confinement, surface motion and angle of inclination on the impingement heat transfer will also be discussed in separate sections.

(a) Impingement Heat/Mass Transfer

i. Local Nusselt number profiles

The classic experimental Nu profiles of Gardon and Cobonpue[1962] and Gardon and Akfirat[1965] for impinging axisymmetric jets illustrate many characteristics typical of impingement heat transfer. These results are reproduced in Figures 2.12 and 2.13 and illustrate the effect of nozzle-to-impingement surface spacing, H/d, and jet Reynolds number, Re_j, on the local heat transfer profiles. The general shape of these profiles have been observed by many researches including Koopman and Sparrow[1975] and Obot[1981] amongst others.

The results for $H/d \leq 4$ have several distinct features. There is a central minimum at the stagnation point and off stagnation maxima located near $r/d = 0.6$ and 1.9 with an intervening minimum near $r/d = 1.2$. The central minimum has been attributed to low radial velocities in the region $r/d \leq 0.5$. The inner maximum has been attributed by Kezios[1956] to a minimum in the boundary layer thickness of the developing wall jet in the annular region at $r/d = 0.6$, while Gardon and Akfirat state that they are "not caused by turbulence but by some mechanism inherent in the flow of impinging axisymmetric jets, regardless of whether or not they (the jets) are laminar or turbulent."

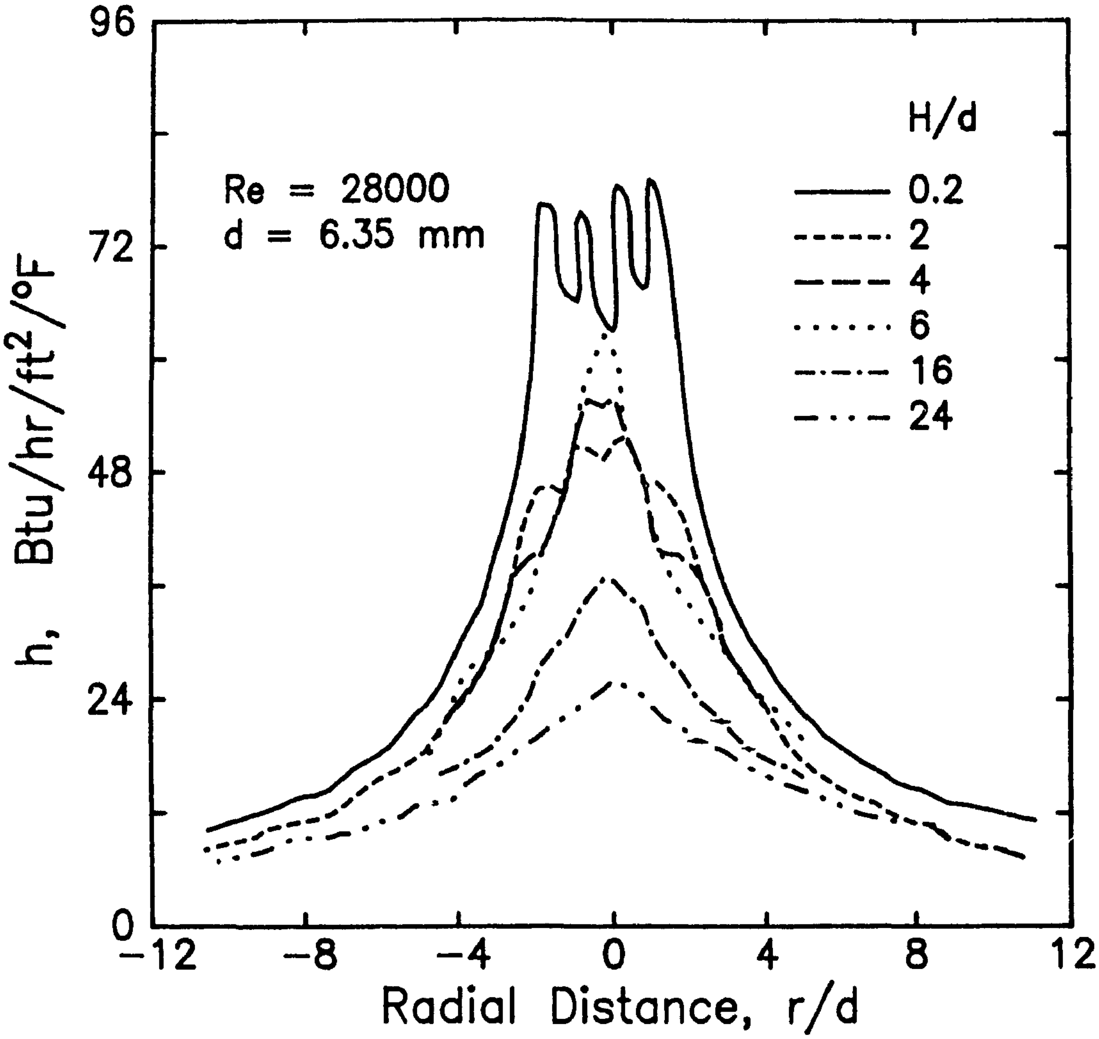

Figure 2.12 Effect of H/d on profiles of heat transfer coefficient - Gardon and Cobonpue[1962]

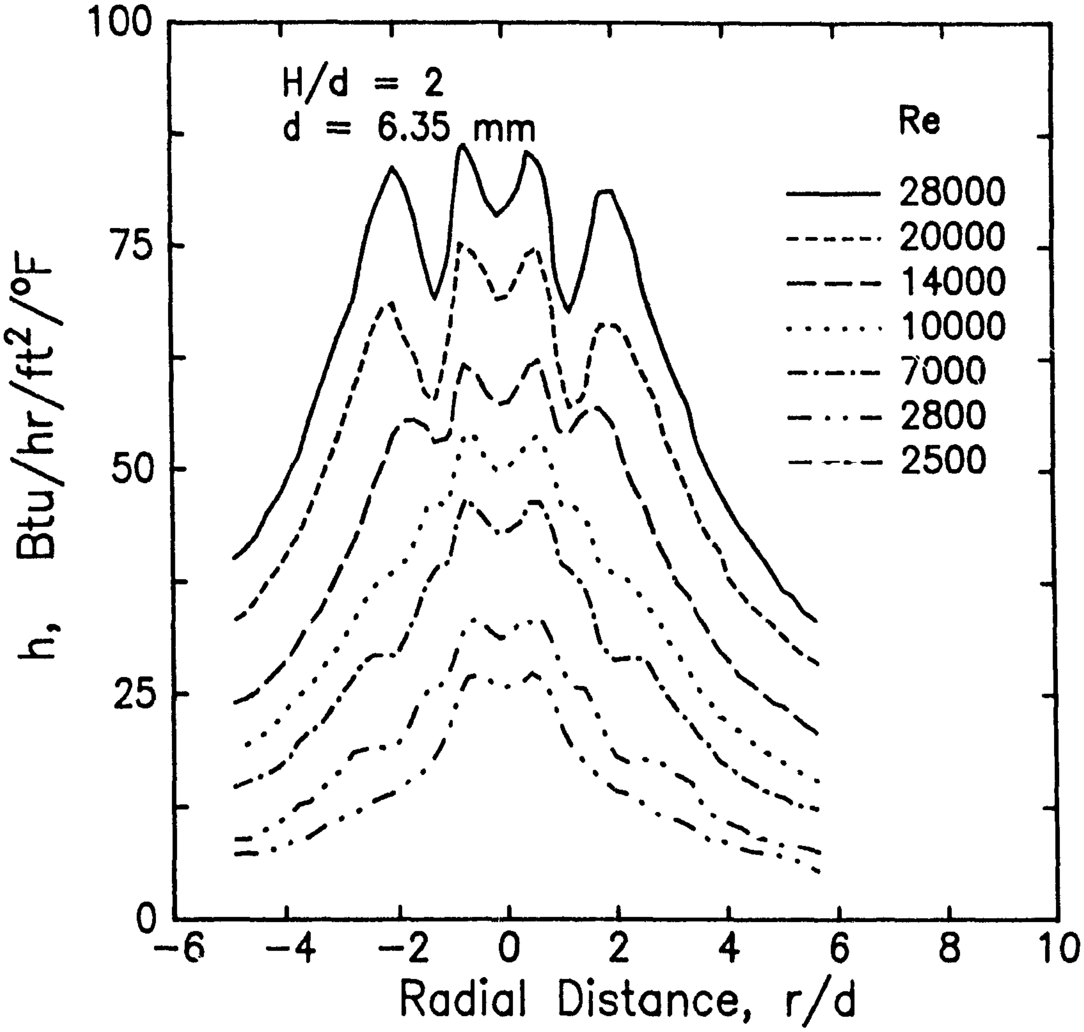

Figure 2.13 Effect of Re on profiles of local heat transfer coefficient - Gardon and Akfirat[1965]

As the flow moves radially away from the jet centerline, the thickening boundary layer together with the radial spreading of the jet is sufficient to produce the local heat transfer minimum near $r/d = 1.2$. The outer heat transfer maximum has been attributed by Gardon and Akfirat to the transition from a laminar to a turbulent boundary layer. As noted earlier, the pressure gradients within the stagnation region for lower H/d and higher Re are favorable for the existence of a laminar boundary layer regardless of the jet exit turbulence conditions. As the flow spreads radially over the impingement surface the pressure gradients are relieved allowing the transition to a turbulent boundary layer.

As shown in Figure 2.12, when H/d is increased, the secondary maximum at $r/d = 1.9$ decreases in prominence, where between $H/d = 4$ and 6 only vestigial shoulders exist and for $H/d \geq 8$ only the characteristic bell shaped profile remains.

As to the influence of jet Reynolds number on the Nusselt profiles, Figure 2.13 shows that the sharpness of the maxima and minima are accentuated at lower H/d and higher Re. Comparison of the profiles show that the outer maxima increasing faster than the inner peaks as Re is increased. Since the heat transfer is higher in turbulent flow as compared with laminar flow it follows that the inner peaks (where laminar flow conditions exist) must increase more slowly.

ii) Stagnation Nusselt number, Nu_c

The stagnation point Nusselt number, Nu_o, has been exhaustively studied and numerous correlations have been proposed particularly for larger H/d, which is of limited interest in this study. A critical analysis of the predictive equations available was performed by

Obot[1982] who reconciled many existing differences. The existence of a maximum in Nu_o near $H/d = 8$ is probably the incentive for proposing correlations for $H/d \geq 8$, even though many several researchers extended their experimental investigations to the range $H/d \leq 8$.

For axisymmetric jets, the existence of a maximum stagnation point heat and mass transfer coefficient as a function of H/d has been well documented in the literature. Gardon and co workers[1962, 1965, 1966], Nakatogawa et al.[1970], Koopman and Sparrow[1975] attribute the presence of this maximum to successively, an initial increase in the fluctuating velocity component, u', as a result of entrainment and mixing over the potential core and transition regions, the existence of a maximum in the u' vs z/d profile, followed by a decrease in both axial mean and fluctuating velocities (U and u') as z/d is further increased. On the other hand, Obot[1980] and Donaldson et al.[1971] attribute the maximum in Nu_o to a corresponding maximum in the stagnation point radial velocity gradient with the optimum separation, H/d, a function of the nozzle geometry. The maximum in Nu_o has been documented by the above researchers to lie in the range $4 \leq H/d \leq 8$ with the usual value being quoted as $H/d = 5$. Obot observed a maximum in Nu_o at $H/d = 8$ for contoured and long sharp-edged entry nozzles and $H/d = 4$ for short sharp-edged entry nozzles.

For the industrially important case of $H/d \leq 8$, the only existing correlation is that of Obot:

$$Nu_o = 1.15\, Re^{0.41} \left(\frac{h}{d}\right)^{0.18} \tag{2.7}$$

valid over the range $15,000 \leq Re \leq 60,000$. Obot[1980] also proposed a correlation based on the experimental data of den Ouden and Hoogendoorn[1974] and Garden and Akfirat[1965] for $H/d \leq 8$ and obtained:

$$Nu_o = 0.64\ Re^{0.52} \tag{2.8}$$

These are compared with the data of Gardon and Akfirat, den Ouden and Hoogendoorn, Hrycak[1978], Murray and Patten[1978], Nakatogawa et al.[1970] and Obot in Figure 2.14.

The data fall into essentially three groups. The data of Nakatogawa et al. and Obot are in close agreement, as are the data of den Ooden and Hoogendoorn, Gardon and Akfirat and Murray and Patten. The differences between these two groups has been attributed by Obot to differences in the nozzle exit profiles for both the mean velocity and turbulence level. The data of Nakatogawa et al. and Obot is for similar nozzle exit flow conditions and the agreement is quite good. The results of Gardon and Akfirat are probably for a contoured inlet nozzle of $\ell/d = 18$ (if similar to the nozzle used by Gardon and Cobonpue[1963]), which do not have comparable nozzle exit profiles. All these results are much lower (by a factor of 2) than the experimental data of Hrycak's which, as argued by Obot, can be totally disregarded since the differences cannot be attributed to nozzle geometry or other reported experimental condition. The influence of nozzle geometry was documented by Obot for a wide variety of nozzle geometries, with short sharp edged inlet nozzle or long tubes resulting in higher heat transfer, but no nozzle geometry could be found to produce the high heat transfer observed by Hrycak.

iii) Average Nusselt number, $\overline{Nu}_r$

The $\overline{Nu}_r$ distributions are of particular interest for design purposes but are of limited use in the analysis of the causative flow phenomena with the local Nu profiles yielding much more insight.

In general, it is usually quoted in the literature that $\overline{Nu}_r$ decreases as the nozzle-to-impingement surface spacing, H/d, increases,

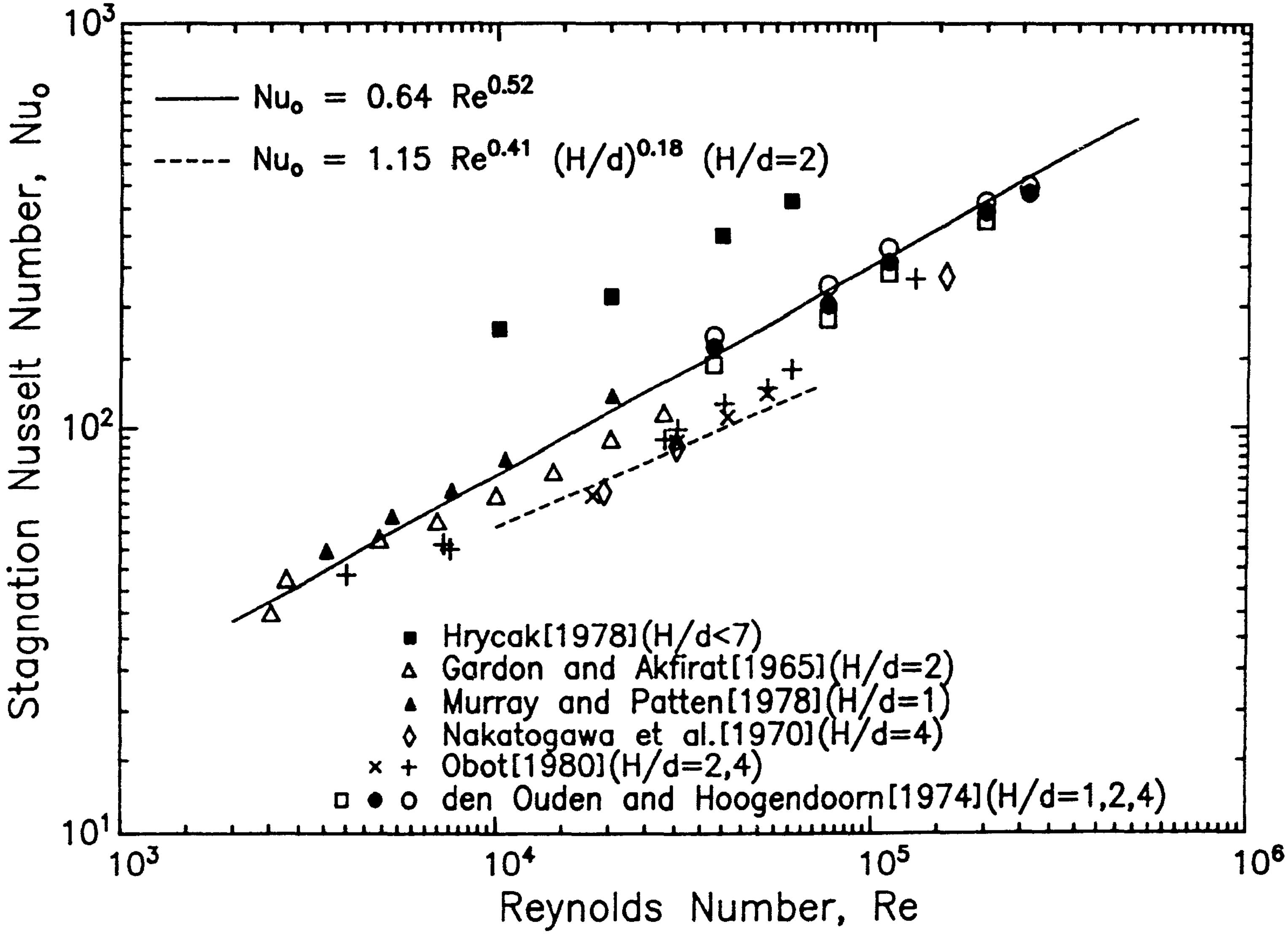

Figure 2.14 Comparison of experimental stagnation Nusselt numbers, Nu_o for circular turbulent jets where H/d < 7.

but again, as with the stagnation Nusselt number, the number of data available for $H/d \le 8$ are limited. The importance of nozzle geometry, as documented by Obot precludes the use of many correlations since they are for unknown nozzle configurations. The only recommended correlation is that of Obot[1980] for unconfined contoured entrance nozzle.

$$\overline{Nu}_r = 0.099\ Re^{0.79} \left(\frac{h}{d}\right)^{-0.19} \left(\frac{r}{d}\right)^{-0.48} \tag{2.9}$$

valid for $15000 \le Re \le 60000$

$1.7 \le r/d \le 13.9$

$2 \le H/d \le 12$

In the literature it is often the practice to represent the averaging area in terms of the ratio, heat transfer area to nozzle area, termed open area or f. The radial averaging distance, r/d is related to the open area by the function

$$\left(\frac{r}{d}\right) = (4\ f)^{-0.5} \tag{2.10}$$

(b) Effect of Ambient Temperature

In an unconfined or semi-confined system, the temperature of the impingement air is often different from that of the surrounding ambient air. If the ambient temperature lies between the jet and impingement surface temperatures ($T_j > T_a > T_s$ or $T_j < T_a < T_s$), as is usually the case, the entrainment of the surrounding air by the jets reduces the effective fluid-to-surface temperature difference leading to a corresponding decrease in the heat transfer at the impingement surface.

Traditionally heat transfer coefficients have been defined in terms of the jet-to-surface temperature difference so that the effect of jet entrainment is buried in the reported values of the heat transfer coefficients. There has been little work done to quantify this effect.

Schauser and Eustis[1963], working with a two-dimensional jet, used integral techniques to analyze the effect of thermal entrainment on a single impinging jet. They presented experimental results limited to the cases $T_j = T_a \neq T_w$ and $T_j \neq T_a = T_w$.

Bouchez and Goldstein[1975] suggest that the analysis used in film cooling problems could be used in non-isothermal impinging jet problems to remove the effect of entrainment on h.

Striegel and Diller[1982],[1984] developed an analytical correlation to determine the effect of thermal entrainment on the local heat transfer to a single, plane, turbulent impinging jet with a temperature different from the surrounding fluid. For their analysis they define a dimensionless entrainment factor, F,

$$F = \frac{T_j - T_a}{T_j - T_s} \qquad (2.11)$$

With the proposed definition of entrainment factor, analytical models for the limiting cases, $T_a = T_j$, $F = 0$, (limited effect of thermal entrainment), and $T_a = T_s$, $F = 1$, (large effect of thermal entrainment), were developed. Solutions for intermediate values of F were obtained by linearly superimposing the limiting cases. The model involved four parameters which were determined by comparing experimental local heat transfer profiles with the analytical solutions.

Strigel and Diller found that when the effect of thermal entrainment was included, a single jet model would successfully predict the heat transfer for widely spaced multiple jets.

The recent work of Hollworth et al.[1984, 1985] to quantify the effect of thermal entrainment uses a film cooling approach. The similarity between film cooling and non-isothermal impingement was first noticed by Florschuetz and Metzger[1982]. In film cooling, a coolant is introduced onto a solid surface forming a blanket with insulates the solid from the surrounding fluid.

Using this approach, Hollworth et al. showed that the local heat transfer coefficient profile is not a function of the jet-to-ambient temperature difference when h is defined in terms of the difference between the local recovery temperature (film temperature measured for an adiabatic surface for a given flow geometry) and impingement surface temperature. Figures 2.15 and 2.16 show how the local Nu profiles for different temperature mismatches ΔT_{ja}, collapse on to one another when the recovery temperature is used instead of the jet temperature.

Hollworth et al. proposed the following equation to specify the heat transfer coefficient:

$$q = h\,(T_a - T_s) + h\,\phi\,(T_j - T_a) \tag{2.12}$$

where $$\phi = \alpha \cdot \beta = \left[\frac{T_{rm} - T_a}{T_j - T_a}\right] \cdot \left[\frac{T_r - T_a}{T_{rm} - T_a}\right] \tag{2.13}$$

α - dimensionless stagnation point recovery temperature
β - dimensionless local recovery temperature
T_r - local recovery temperture
T_{rm} - recovery temperature at the stagnation point

which reduces down to

$$q_c = h\,(T_a - T_s) + h\,(T_r - T_a) \tag{2.14}$$

where h is solely a function of Re, H/d and r/d.

The primary difficulty with this approach is the determination of the recovery temperature, which must be obtained on an adiabatic surface

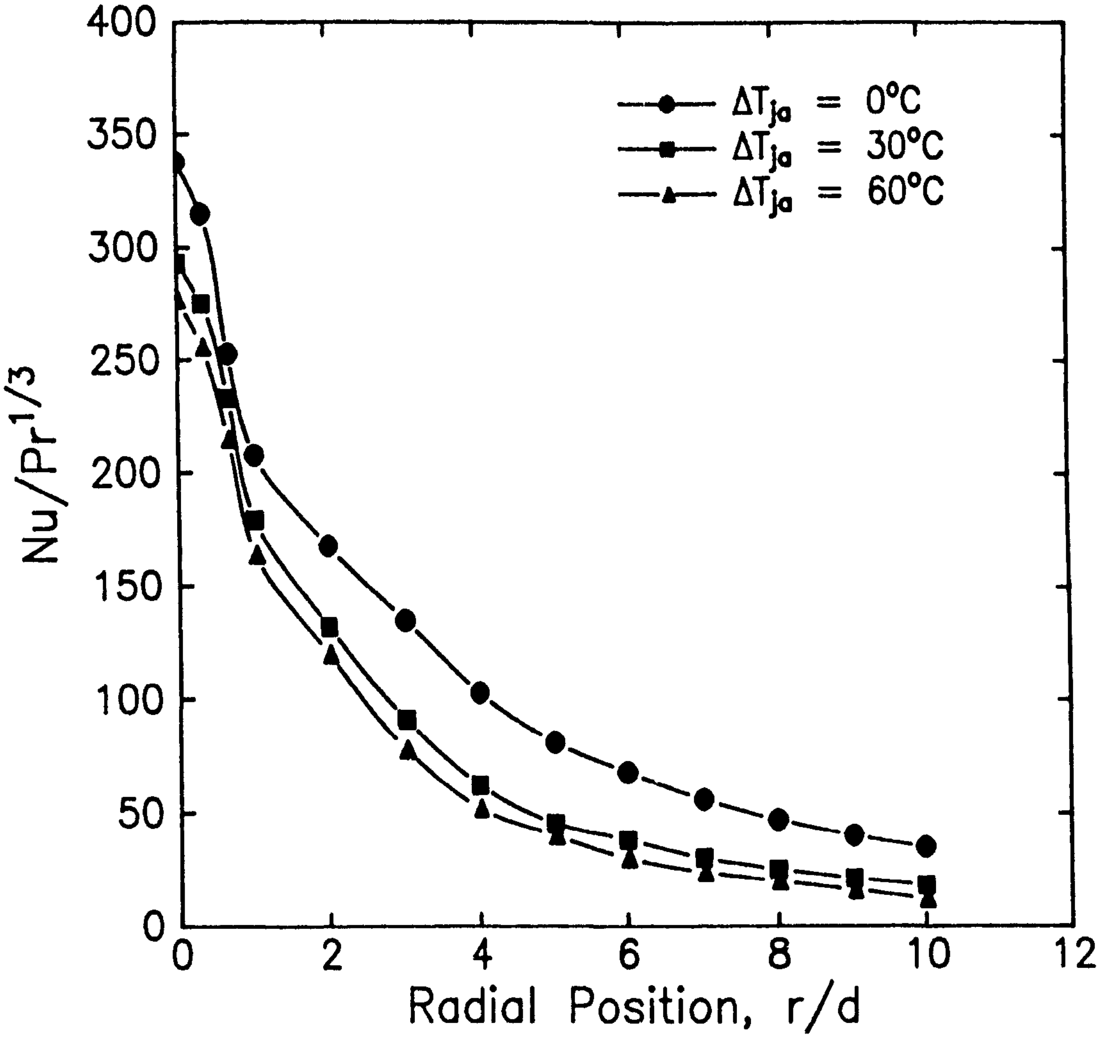

Figure 2.15 Effect of entrainment on heat transfer profiles for $H/d = 5$ and $Re = 60000$ based on $T_j - T_s$ - Hollworth et al.[1985]

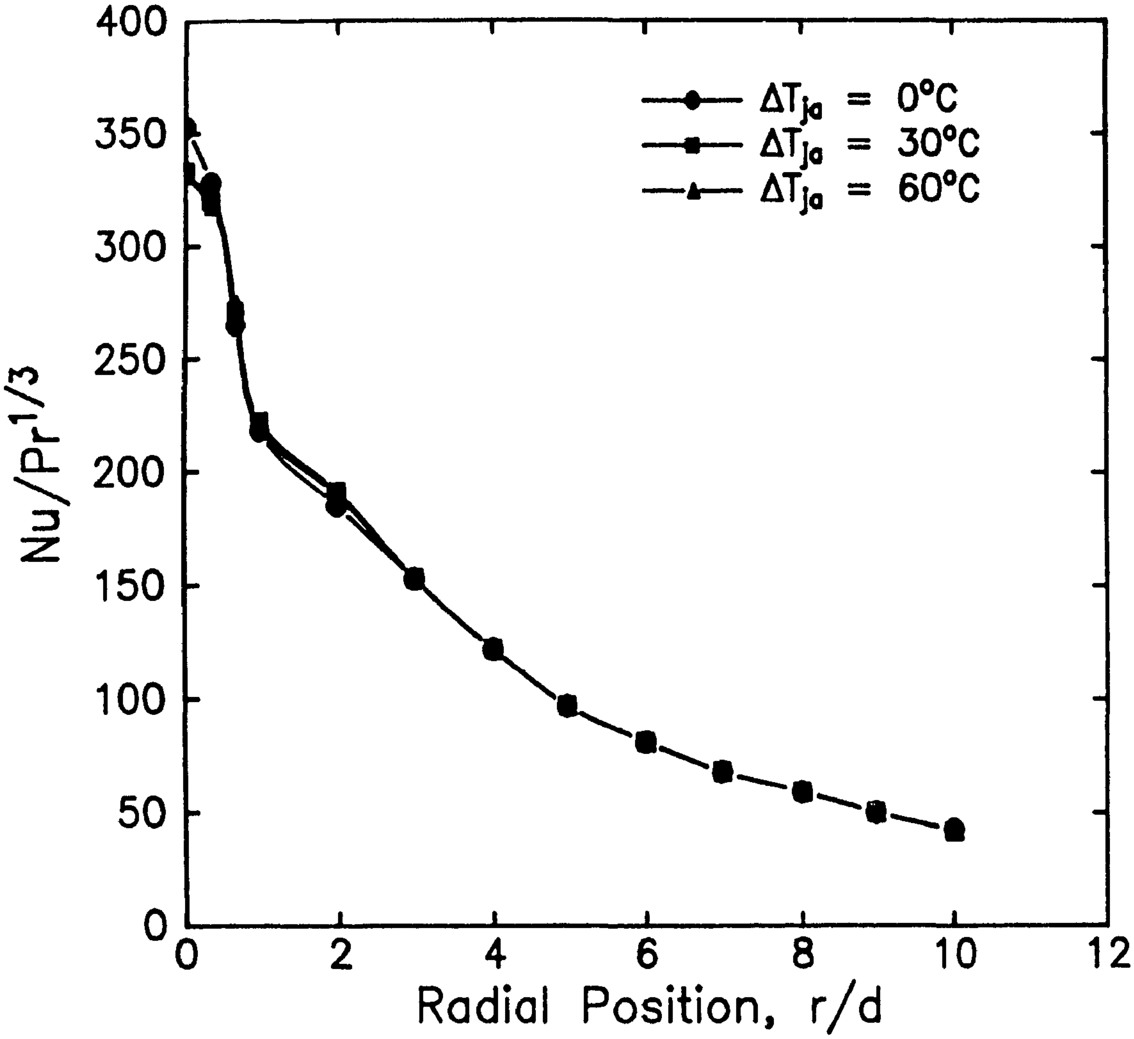

Figure 2.16 Effect of entrainment on heat transfer profiles for H/d = 5 and Re = 60000 based on $T_r - T_s$ - Hollworth et al.[1985]

under the same conditions as when the heat transfer measurements are made.

(c) Effect of Semi-Confinement

Sparrow et al.[1975], using circular jets with a Reynolds number in the range 38,000 to 115,000, under conditions of low cross flow, Folayan[1976], using a two dimensional slot jet at a fixed Re = 7100 and Obot[1980] using circular jets in the range $15000 \le Re \le 60000$, studied the effect of semi-confinement on the heat transfer characteristics. All observed limited effect of confinement on Nu_o for low H/d (or H/w). Sparrow et al., in the range $5 \le H/d \le 12$ observed a tendency for higher Nu_o for Re > 38000 while Obot and Folayan observed slightly lower Nu_o with confinement.

The presence of a confinement plate prevents the entrainment of the air which surrounds the nozzle upstream of the nozzle exit plane. For this reason, under semi-confined conditions the jet would be expected to decay, and spread at a somewhat slower rate. For H/d's less that length of the potential core region of the jet, Nu_o might expect to be unaffected by confinement since the core region is not affected by mixing. For larger H/d, the reduced mixing associated with the presence of a confinement plate could lead to higher Nu_o since the jet arrival velocity would be higher.

With respect to the Nu profile away from the stagnation point, all three observed somewhat lower heat transfer with the effect of confinement decreasing with increasing Re_j. This can be directly attributed to the decreased volume of flow entrained by the jet. The data provided by Crow and Champagne[1971] indicate that an unconfined jet entrains an amount of surrounding fluid equal to 30% of the jet flow at a distance 2d downstream from the nozzle exit.

Under conditions when $T_j \neq T_a$, the presence of confinement can be expected to have little effect on the stagnation Nusselt number for small H/d, again due to the limited effect of jet mixing when the nozzle to impingement surface spacing is within the potential core regardless of the presence of a confinement plate. But for locations other than the stagnation point, there must exist a point at which the increased heat transfer due to higher fluid flow in the absence of confinement is balanced by the lower thermal degradation of the jet flow due to the restricted interaction between the jet and the surrounding fluid when confinement is present. This balancing point has not been documented in the literature.

(d) Effect of Surface Motion

The effect of surface motion on impingement heat transfer has received relatively little attention even though it is encountered in a variety of engineering situations. The experimental work of Maxwell and Nash[1973], using a rotating cylinder, and Popiel et al.[1974] and Metzger and Grochowsky[1977], using a rotating disk were performed using unconfined axisymmetric jets. Fechner[1971] and Zhang[1986] reported on the heat transfer under unconfined slot jets impinging on a cylinder while Subba Raja and Schlunder[1977] and Hardisty[1980] used a continuously moving flat surface. van Heiningen[1982], Polat[1988] and Huang[1988] reported on the effects of surface motion on the heat transfer characteristics of a confined slot jet.

The variable surface motion can be represented using the dimensionless surface velocity mass ratio, M_{vs}, defined as

$$M_{vs} = \frac{\rho_s V_s}{\rho_j V_j} \qquad (2.15)$$

Hardisty reported that the effect of surface motion on the impingement flow field was negligible for the practical situations encountered in ink drying. The work of van Heiningen[1982] and Polat[1988] showed that for $M_{vs} \leq 0.1$, the surface motion had limited effect on the local Nu profile while further increases in M_{vs} resulted in a slight increase in Nu_o (< 10%) but no significant displacement of its position and a skewing of the Nusselt profile in the direction of surface motion.

With respect to $\overline{Nu}$, Fechner observed a slight increase (<10%) in $\overline{Nu}$ as M_{vs} was increased while van Heiningen reported the opposite effect with good agreement of the value of $\overline{Nu}$ corresponding to $M_{vs} = 0$. The different trends was discounted by van Heiningen as attributable to an equipment specific problem. Subba Raju and Schlunder[1977] observed an increase of 1.5 to 2 times the average heat transfer observed by Fechner and van Heiningen for very small values of surface motion, i.e. $M_{vs} \ll 0.1$. The agreement between the data of Fechner and van Heiningen would indicate that the large increases in $\overline{Nu}$, observed by Subba Raju and Schlunder, are unrealistic.

(e) Effect of Impingement Angle

The heat transfer characteristics under conditions where the impinging jet is not necessarily normal to the impingement surface, Figure 2.17, has been studied by Perry[1954], McMurray et al.[1966], Folayan[1976], Pelletier et al.[1984,1987] and Goldstein and Franchett[1988] for axisymmetric jets, and Korger and Krizek[1972] and Huang[1988] for slot jets. Perry and Pelletier reported that $\overline{Nu}$ was a maximum for normal impingement, $\phi = 0$. Korger and Krizek observed

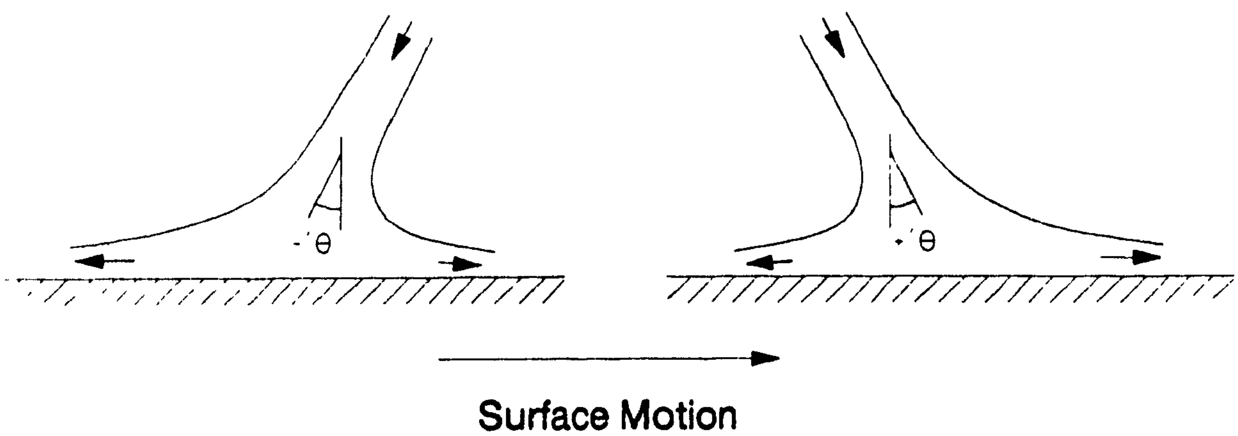

Figure 2.17 Definition of impingement angle relative to the impingement surface motion.

that while the local mass transfer profile was dependant on the angle of impingement the average mass transfer rate was unaffected. Huang showed that for a confined slot jet angle of impingement over the range $\pm 15^{\circ}$ has little effect on average Nu, while inclination by 30° from normal results in a substantial lowering of average heat transfer.

Goldstein and Franchett, using a temperature sensitive liquid crystal technique, generated very detailed profiles of local Nusselt number over the range $10000 \le Re \le 30000$, $4 \le H/d \le 10$ and nozzle inclinations in the range $0 - 60^{\circ}$. They proposed a correlation of the form

$$Nu = A\, e^{-(B + C \cos\Phi)(r/d)^{0.75}} Re^{0.7} \qquad (2.16)$$

where r, Φ - cylindrical coordinates about the jet axis for contours of constant Nu

A - function of jet inclination and H/d

B, C - functions of jet inclination

for the distribution of local Nusselt number. An additional parameter, E, was used to account for the shift in the location of the peak Nusselt number relative to the geometric interssection of the jet axis and the impingement surface. They observed a maximum in Nu_o for normal impingement.

McMurray et al. and Folayan both observed a maximum in Nu_o at an impingement angle of 30° from normal impingement. Baines and Keffer[1976] in a study on the effects of angle of impingement on surface shear stress, using a two dimensional jet, found a maximum in the shear stress for a jet inclination of about 20° directed against the surface motion. Using a simple form of Reynolds analogy, they interpreted the surface shear stresses observed in terms of overall heat transfer coefficients. As was pointed out by van Heiningen et al.[1976] and Black and Hardisty[1976] the Reynolds analogy in invalid in the stagnation region.

2.5 Conclusions

The limited published literature dealing with calender cooling does not provide adequate or consistent guidelines for the design of calender control systems. The few measurements which are available can not be generalized and extrapolated to other calender stack configurations. The discussion relating to the positioning of calender control actuators in the calender stack and, in the case of impingement systems, the positioning relative to the calender roll itself, are speculative and contradictory with little regard being paid to the type of calender roll involved.

There is a wide body of literature dealing with the fundamental aspects of impingement heat transfer. The heat transfer coefficients for single round impinging jets as a function of the nozzle orientation relative to the impingement surface, impingement surface motion, jet flow rate, thermal jet entrainment and jet confinement have been studied have been documented. However, all of these elements are present in the calender control problem and the combined effects of these variables on the impingement heat transfer cannot be predicted from the information available on the individual effects.

The current study was undertaken to determine to what extent the current impingement heat transfer literature could be applied to the impingement calender control problem and provide a better fundamental basis for the design and optimization of paper machine calender control systems.

CHAPTER 3

EXPERIMENTAL EQUIPMENT AND PROCEDURES

3.1 Overall Design Concept

The CALCON (CALender CONtrol) experimental facility was built by Pelletier [1984] for the study of local and average heat transfer from a horizontal row of unconfined circular air jets impinging on the surface of a roll in a vertical stack of rotating rolls. This experimental apparatus was designed to closely simulate the air side heat transfer which occurs during the control of cross-machine paper thickness in paper machine calender stacks when using impinging air jets to locally cool or heat one or more rolls in the calender stack. The technique used to obtain the local heat transfer rates on a moving surface was proposed and developed by van Heiningen [1982].

For the present study, several modifications to the equipment were made:

i. The nozzle positioning subsystem was modified to allow more accurate positioning of the impingement nozzles relative to the impingement surface.

ii. The air supply system was modified to use external air obtained from outside the laboratory, to prevent the gradual increase in jet temperature due to the recirculation of air through the fan.

iii. A simplified procedure for building the sensor was introduced to facilitate the quick replacement of damaged sensors.

The experimental equipment is shown schematically in Figure 3.1. It consisted of three vertically stacked rolls, with the heat transfer sensor located on the surface of the middle roll. The rolls were not touching ($\approx$ 1mm gap) to protect the sensor but by using a chain drive, they rotated at the same speed and direction as though they were touching. On either side of the center roll was a row of nozzles used to direct cold air on the roll surface from one side and hot air onto the other. When the system reached a quasi-steadystate, the roll surface temperature cycled with a maximum peak-to-peak temperature variation of the order $\pm$ 2°C as the surface was exposed to the heating and cooling air jets with the average roll surface temperature intermediate to that of the jet temperatures. Thus, on average, the roll surface could be considered adiabatic.

The circumferential surface temperature profile was measured by the heat flux sensor, a gold thin film resistance thermometer capable of resolving 0.001°C at a 5kHz sampling rate, and recorded using a high speed data acquisition system. The temperature profile obtained was used as a boundary condition for the solution of the transient heat conduction equation, from which the local circumferential heat flux profile was calculated [van Heiningen, 1982]. A detailed description of each of the subsystems is provided in the subsequent sections of this chapter.

The photograph shown as Figure 3.2 provides a general view of the experimental facility. The separate heating and cooling subsystems were located above the main calender assembly with the heating distribution header located in the foreground. The cooling header was located on the opposite side of the equipment.

The range of the experimental parameters were chosen based on current industrial operation of calender control systems. The main flow

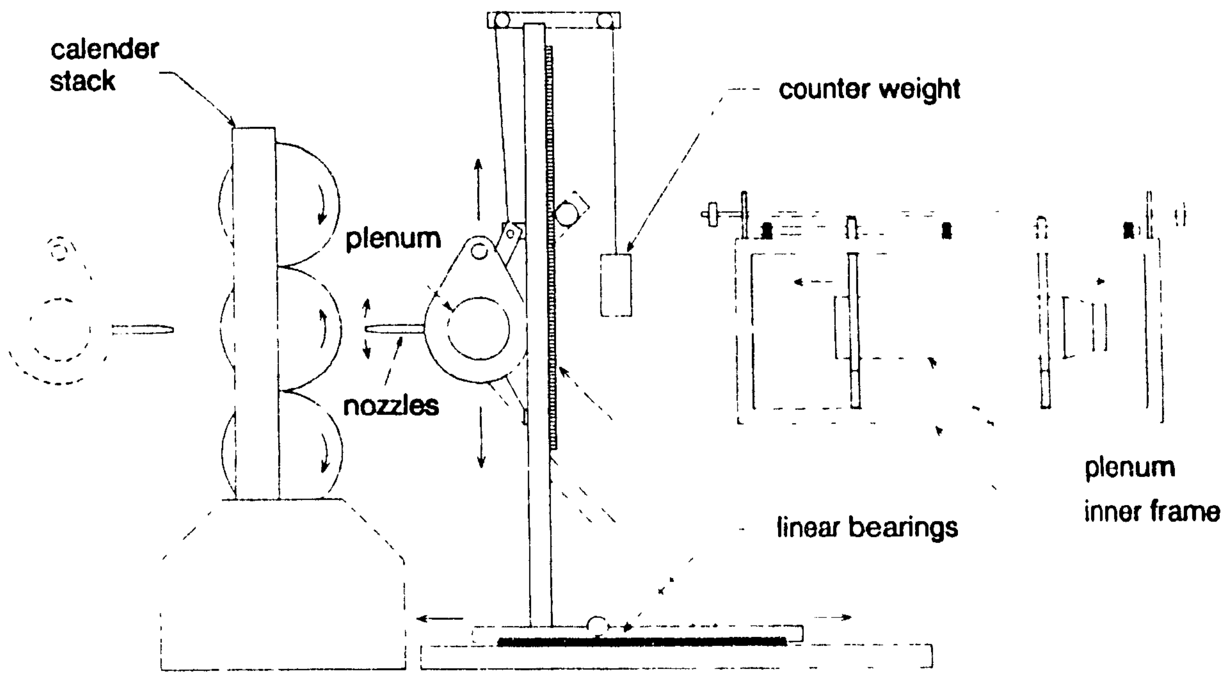

Figure 3.1 A schematic of the CALCON model calender stack

Figure 3.2 Photo of CALCON experimental setup

parameter, jet Reynolds number, Re_j, was varied from 22000 to 118000. This covers the range of industrial operating conditions, with Re_j = 90000 being typical for the nozzles used in this study.

The other parameters to be investigated included the nozzle-to-roll spacing, H/d, the nozzle-to-nozzle spacing, S/d, the jet impingement angle, ψ, the angular position of the jet impingement point, θ , the degree of jet confinement, Y_c, and the effect of ambient temperature.

The schematic diagram, shown in Figure 3.1, provides an overall illustration of the CALCON apparatus The subsystems included the air supply system, the model calender stack and nozzle positioning system, the heat flux sensor and the data acquisition system. A detailed description of each of the subsystems is provided.

3.2 The Model Calender Stack

The model calender stack consisted of three polyvinylchloride (PVC) rolls, each with a diameter of 558mm, a length of 813mm and a wall thickness of 12mm. The diameter was chosen as to correspond to typical roll diameters used in some commercial paper machine calender stacks.

Although paper machine calender rolls are normally made of chilled cast iron, PVC was chosen as the roll material for the model calender to satisfy the special requirements of the heat flux sensor, which will be discussed in Section 3.4. The impingement heat transfer coefficient, in the case of an adiabatic impingement surface (closely approximated in this equipment), is an aerodynamic property, and thus independent of the choice of calender roll material.

Each roll was mounted on 17mm end plates which were attached to hollow 38mm diameter axles. The roll axles were mounted on the calender frame using ball bearing pillow blocks.

The calender rolls were driven using a chain drive with the lower roll driven using a non-slip belt from a 1.2kW variable speed D.C. motor. In an actual machine calender, only one roll is driven with the other rolls rotating by frictional contact with the driven roll. This was not possible on the model calender stack, as contact between the rolls would damage the heat flux sensor, which was mounted on the surface of the middle roll.

3.3 The Air Supply System

The air supply to the nozzles was provided by an 11kW turboblower, capable of delivering 0.9m^3/sec at 10kPa. To reduce the noise level in the laboratory, the fan and air intake were located in a specially constructed shed on an outside wall of the building. The air from the fan was divided into two streams, one passing through a heater, the other through a cooler, before continuing to the respective distribution headers and nozzles.

The heater consisted of six separate 1kW, 110V heating elements for a total of 6kW. Each heater element was controlled separately; five elements had on-off controls while the 6th was attached to a potentiometer for fine adjustment of the nozzle exit temperature.

The cooler used in this equipment consisted of a 7kW, water cooled air conditioner, that had been modified for this equipment by removing the built in fan. The air conditioner was designed to operate on a duty cycle, which caused unacceptably large outlet air temperature fluctuations. Hence it was operated a full capacity during the experimental runs. The temperature of the cold air was therefore dependant on the supply air temperature and was primarily determined by outside weather conditions. This limited both the choice and the control of the experimental conditions. However, in normal operation the experimental conditions remained sufficiently stable for the duration of the daily experimental runs.

The distribution headers used on the heating and cooling sides of the equipment were designed with five nozzle openings, with center-line spacings of 100 mm. This permitted the selection of two different nozzle-to-nozzle spacings, $S/d = 4$ and $S/d = 8$. Each nozzle opening was fitted with a flow control valve which consisted of a cylindrical plug with three V-shaped openings. The plugs fit snugly inside the nozzle openings and were inserted or retracted using threaded rods.

The shape and dimensions of the nozzles used in this study are shown in Figure 3.3. These nozzles were chosen because they were readily available and are widely used in commercially available calender control systems. The nozzles consisted of a 41mm ID, 210mm long (1.5in. schedule 40 aluminum pipe) straight section, followed by a 70mm long converging section and a 25mm ID, 25mm long nozzle tip. The converging section and nozzle tip were fabricated from cast aluminum. The total length of the nozzle assembly was 305mm.

For experimental purposes, the nozzle exit velocity, V_j, was measured using a static pressure tap located 150mm upstream from the nozzle exit. The correlation relating V_j to the nozzle static pressure was obtained by comparing the nozzle static pressure, P_s, to the jet centerline nozzle exit velocity as measured using a 3mm dia. pitot tube at a position 5mm downstream of the nozzle exit. The nozzle exit velocity profiles, in the horizontal and vertical planes were measured and found to be flat (see Section 3.7), thus the jet centerline velocity adequately characterizes the jet. The resulting calibration was:

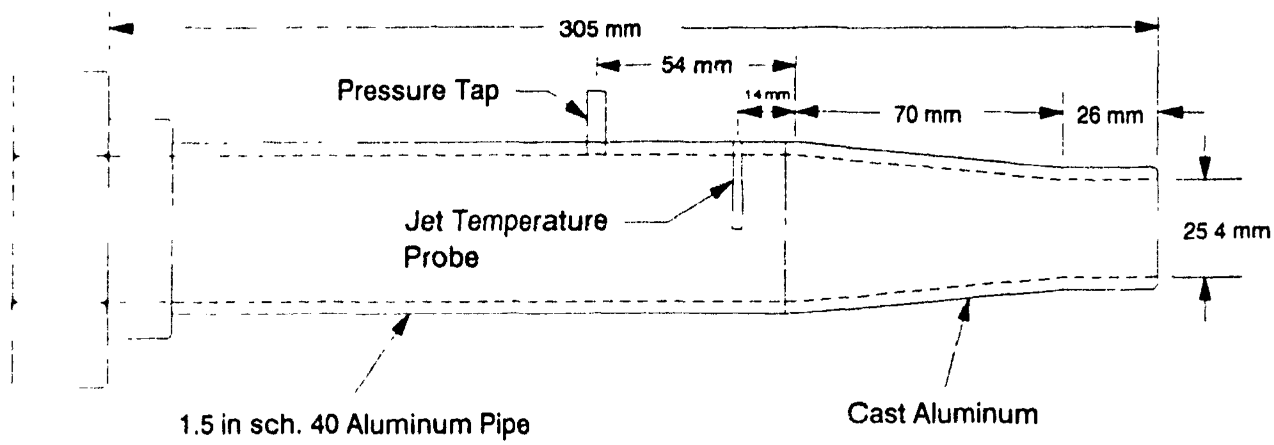

Figure 3.3 Impingement nozzle design

$$V_j = 26.438 \left[\frac{P_s T_j}{P_b}\right]^{1/2} \tag{3.1}$$

where: V_j - jet velocity (m/s)
P_s - static Pressure (Pa)
T_j - jet temperature (K)
P_b - barometric pressure (Pa)

As shown in Figure 3.4, the calibration was independent of the nozzle used.

The jet temperatures were measured using chromel/constantan thermocouples located 100 mm upstream from the nozzle exits. The thermocouple output was monitored with a digital voltmeter equipped with electronic cold junction compensation.

The nozzle support system used in this equipment, differs substantially from that described by Pelletier[1984]. Positioning of the nozzles in Pelletier's equipment was difficult and inaccurate. Also, vibrations were transmitted from the calender to the nozzles since they were attached directly to the model calender frame.

For this work the nozzle support system was redesigned to be free standing. Rack and pinion mechanisms and linear bearings were used to provide smooth accurate positioning of the nozzles in all directions. Locking mechanisms were provided to fix the assembly in the desired position. A rack and pinion and counter weight was used to move the nozzle assemblies in the vertical direction. A rack and pinion was also used to adjust the nozzle-to-calender stack separation. Linear bearings were used to move the nozzle assemblies in the axial direction relative to the calender rolls.

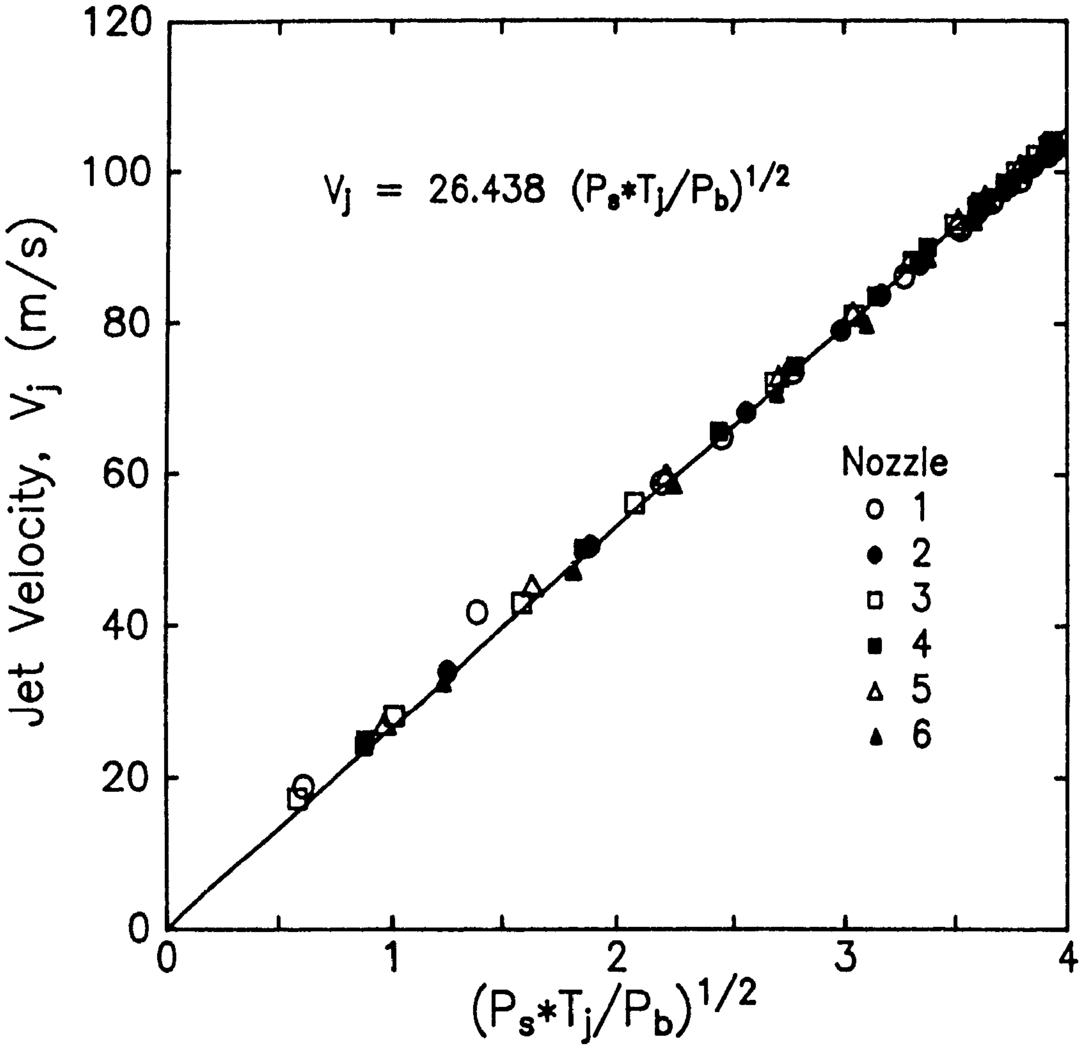

Figure 3.4 Impingement nozzle flow rate calibration

3.4 The Heat Flux Sensor

3.4.1 Measurement Technique

The technique for determining the local heat transfer for air jets impinging on a rotating surface was developed by van Heiningen[1982]. The heat flux sensor consisted of a gold thin film resistance thermometer. The gold film was deposited directly onto a substrate made of the same material as the roll, and thus the heat flux sensor assembly had the same thermal response characteristics as the roll. The sensor was mounted flush with the roll surface in the center of the middle roll. A friction fit prevented the sensor from moving due to centrifugal forces.

The thin film resistance thermometer was capable of resolving 0.001°C at a 5kHz sampling frequency. Hence, even at the high rotational speeds used in this study (up to 600rpm), instantaneous local surface temperature profiles consisting of 500 individual temperature measurements were recorded.

The surface heat flux, q_o, was obtained by solving the one dimensional transient heat conduction equation for a semi-infinite solid, as given in Equation 3.2, using the average circumferential surface temperature profile as a boundary condition.

$$\frac{\partial T}{\partial t} = \alpha \frac{\partial^2 T}{\partial^2 x} \qquad (3.2)$$

Since the temperature profile is periodic, the circumferential position is proportional to the time, t, used in equation 3.2, and is directly related to the sampling frequency.

The surface heat flux, q_o, was then obtained using the calculated temperature gradient at the roll surface.

$$q_o = -\lambda_{sub} \left.\frac{\partial T}{\partial x}\right|_{x=0} \tag{3.3}$$

The numerical procedures used to calculate the surface heat flux are discussed in Section 3.6.2.

The local heat transfer coefficient, h, was defined using the jet to local surface temperature difference

$$h = \frac{q_o}{(T_j - T_s)} \tag{3.4}$$

where T_j - jet temperature

T_s - local surface temperature

The local Nusselt number was defined as

$$Nu = \frac{h\ d}{\lambda_j} \tag{3.5}$$

where d - nozzle diameter

λ_j - conductivity of air at jet temperature

3.4.2 Manufacture of the Heat Flux Sensor

The original selection of polyvinylchloride as a construction material for the model calender stack was based on requirements of the heat flux sensor. Since the gold film was deposited directly on the substrate, the substrate had to be electrically insulating. Also, the material had to be isotropic with respect to its thermal properties to facilitate the solution of Equation 3.2. Polyvinylchloride met these criteria and was available in a pipe of the appropriate diameter for this study.

The original sensor used in the CALCON equipment (Pelletier, [1984]) was fabricated using a time-consuming photo fabrication technique. The fragility of the sensor meant that the sensor had to be replaced frequently. Hence, a more time efficient manufacturing technique was developed. The new procedure involved the following steps:

i) Silver lead wires were glued in place so that the lead wires were flush with the substrate surface.

ii) A much wider film pattern was laid out between the leads using a thin metal mask.

iii) The substrate was placed in the vacuum deposition equipment and gold was deposited until a finite resistance across the lead wires was detected.

iv) The electrical conduction between the silver lead wires and the gold film was further enhanced by painting the connections with electrically conductive paint [Conductive Silver 200, Degussa].

v) To stabilize the sensor resistance (gold film and silver paint) the sensor was cured at 70°C in a convection oven. The maximum curing temperature was determined by the PVC.

This procedure allowed the relatively rapid production a new sensor and produced a sensitivity of about 0.5 Ω per °C. Figures 3.5 and 3.6 show respectively a schematic and a picture of the resulting sensor.

The sensitivity, $\mathcal{A}$ of a thin film resistance thermometer is proportional to the film length and inversely proportional to the square root of the film thickness. The relationship, as derived by van

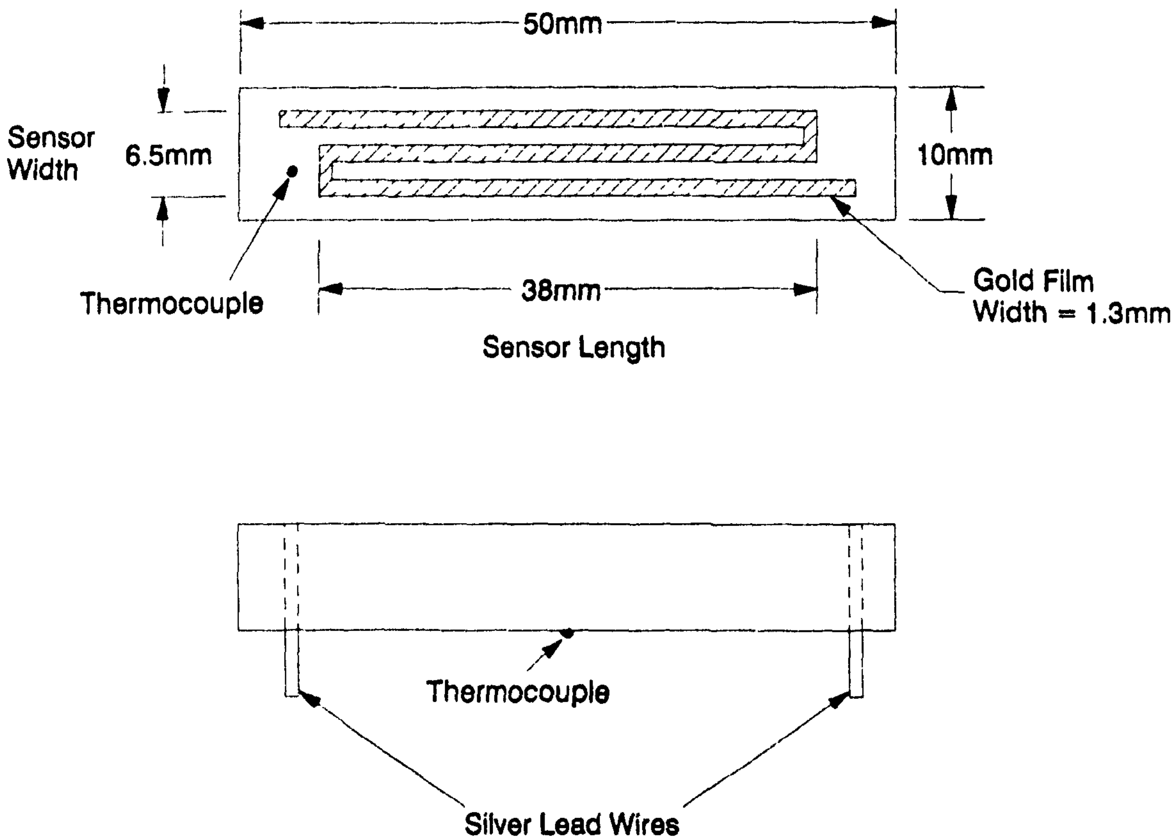

Figure 3.5 Schematic of the heat flux sensor

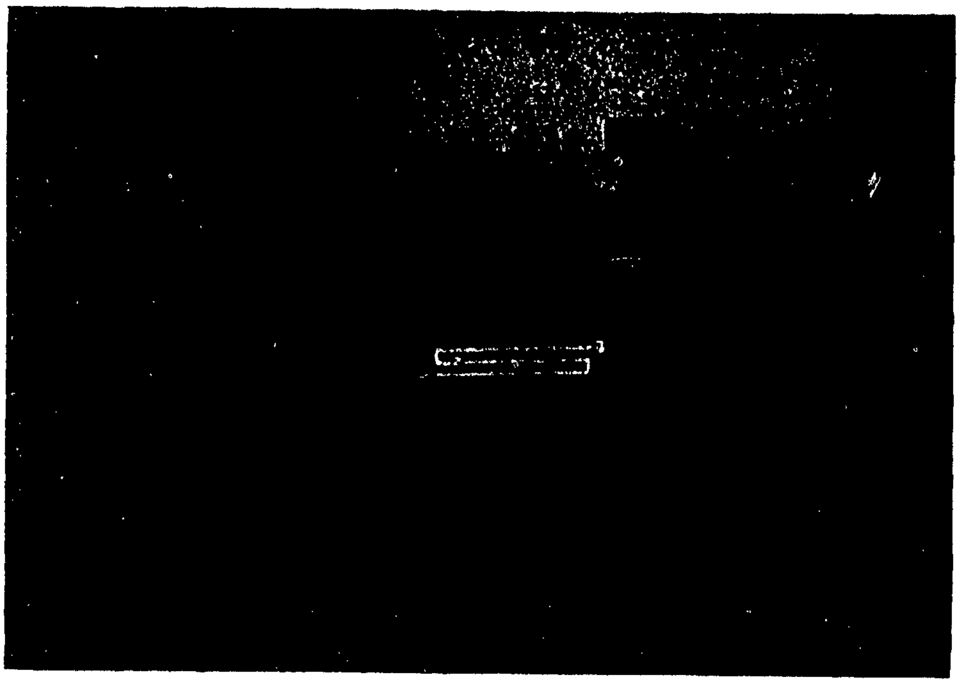

Figure 3.6 Picture of the heat flux sensor

Heiningen[1982], is:

$$\mathcal{A} = \alpha_t L \left(\frac{\delta_f \, q_{sm}}{d} \right)^{1/2} \tag{3.6}$$

where:

α_t	-	temperature coefficient of resistance
L	-	length of film
δ_f	-	resistivity
q_{sm}	-	maximum self-heating heat flux
d	-	film thickness

Decreasing film thickness and increasing film length, increases the film temperature sensitivity. Although the new sensor was much shorter than that used by Pelletier[1984], it had a similar temperature sensitivity by virtue of the reduced film thickness. Based on Equation 3.6, the film thickness on the new sensor was approximately one tenth that used by Pelletier. This made the film more fragile but the relative ease with which the sensor could be manufactured made the increased fragility acceptable.

For calibration purposes, a fine wire (0.1mm diameter) Chromel-Constantan thermocouple was mounted on the surface of the substrate near the gold film. The thermocouple was glued in place using a high thermal conductivity epoxy adhesive (TRA-BOND 2151, TRA-CON Inc.).

3.4.3 Calibration of the Heat Flux Sensor

Even after curing in a low temperature oven, the resistance of the gold film used in the heat flux sensor was found to decrease with time. The change in resistance and thus the calibration of the sensor was due to the gold film not being sufficiently cured. To avoid distortion of the sensor during curing, the curing temperature was kept well below the glass transition temperature of PVC, 79°C, which was insufficient to fully stabilize the gold film and silver paint. Consequently, an efficient and reliable calibration technique was developed, which minimized the risk of damaging the sensor. This calibration was carried out frequently and was updated each day before a series of experiments was undertaken.

The sensor calibration technique originally used by Pelletier[1984], who also encountered this problem, required the removal of the sensor from the equipment. This was considered excessively risky and time-consuming. Instead a technique was developed whereby the sensor could be calibrated while installed in the roll in the model calender stack.

i. The resistance of the sensor was measured at room temperature.

ii. The sensor was then placed directly under an impinging jet and heated to a steady-state surface temperature, which was measured using the surface thermocouple.

iii. This procedure was repeated at several impingement air temperatures, to produce calibration curves like that shown in Figure 3.7.

The calibrations could be expressed in terms of a straight-line relationship of the form:

$$R_s = a + b\,T \tag{3.7}$$

where: R_s - sensor resistance (Ω)
T - temperature (°C)
a - intercept (Ω)
b - sensitivity (Ω/°C)

As shown in Figure 3.7, the sensitivity of the calibration (i.e. the slope of the calibration curve) was constant with a value of 0.5073 $\Omega/^{\circ}C$. Thus, for calibration purposes, the position of the curve (i.e. the intercept) could be determined daily with a single point calibration at room temperature.

Figure 3.8 and 3.9 show the sensitivity of the Nu profiles to the calibration intercept. As shown in Figure 3.8, if both the heating and the cooling side of the equipment operated under similar conditions the differences in the Nusselt profiles and $\overline{Nu}$ under each jet were small. The heating and cooling $\overline{Nu}$ differ by less than 10%. If the calibration used is in error by 5%, the same experimental results show there is a dramatic difference between the Nu profiles, Figure 3.9. Using this calibrations results in a differences of ≅ 35% in $\overline{Nu}$ This error magnification, apparent in the circumferential Nu profile, provided a method of verifying the sensor calibration once a set of experimental runs was started. By maintaining a constant set of operating conditions on the cooling side sharp changes in the sensor calibration during a set of experimental runs could be monitored. Clearly, the daily updating of the sensor calibration intercept, with periodic verification of the sensor sensitivity, (i.e. weekly or biweekly) was an acceptable procedure which ensured reproducible results.

3.4.4 Signal Conditioning

The signal conditioning instrumentation is shown in Figure 3.10. The fluctuating component of the sensor resistance was measured using a 4-decade Wheatstone bridge. A 1.2218V, low noise, high precision electronic power supply was used as a voltage source. The voltage level was specified such that the self-heating heat flux of the sensor be

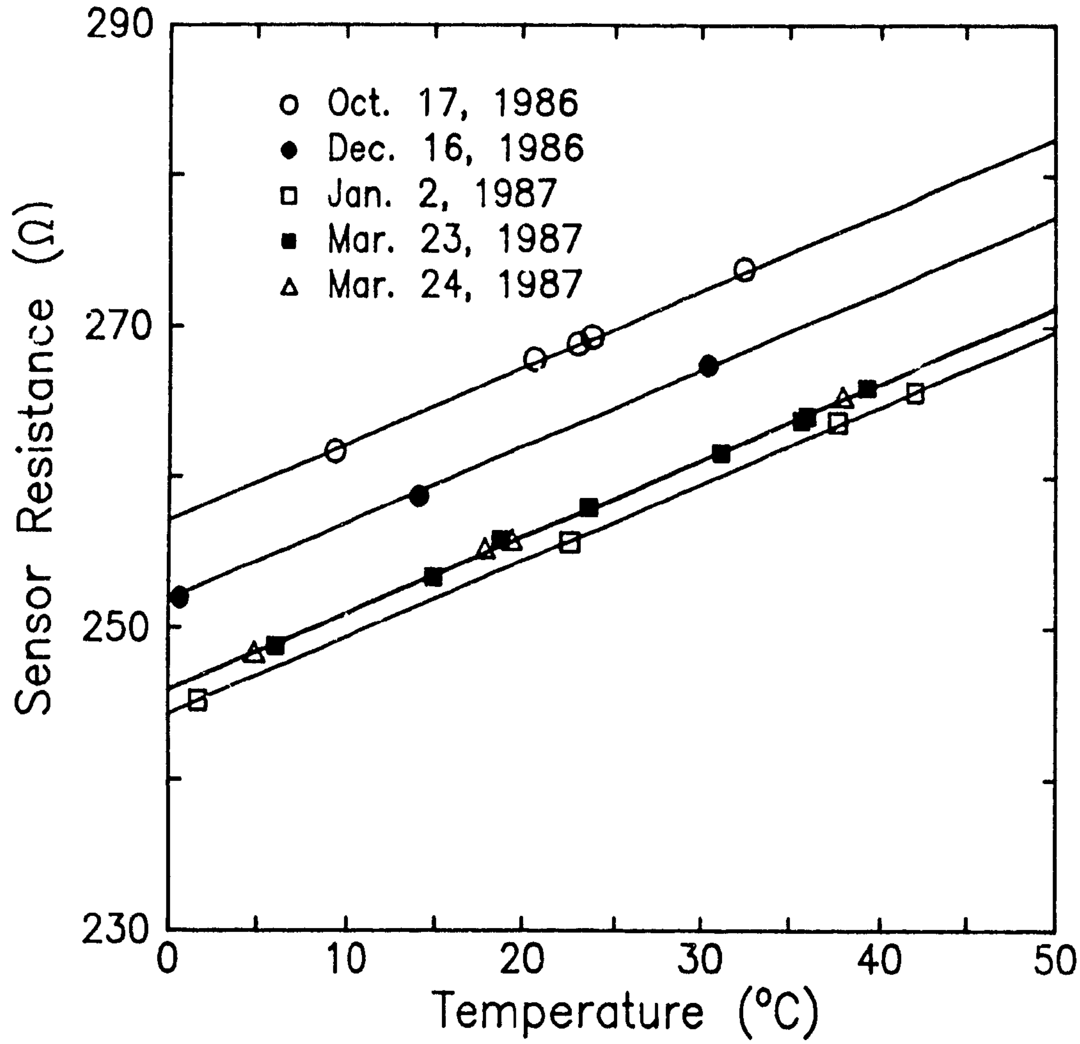

Figure 3.7 Sensor calibration as a function of time (months)

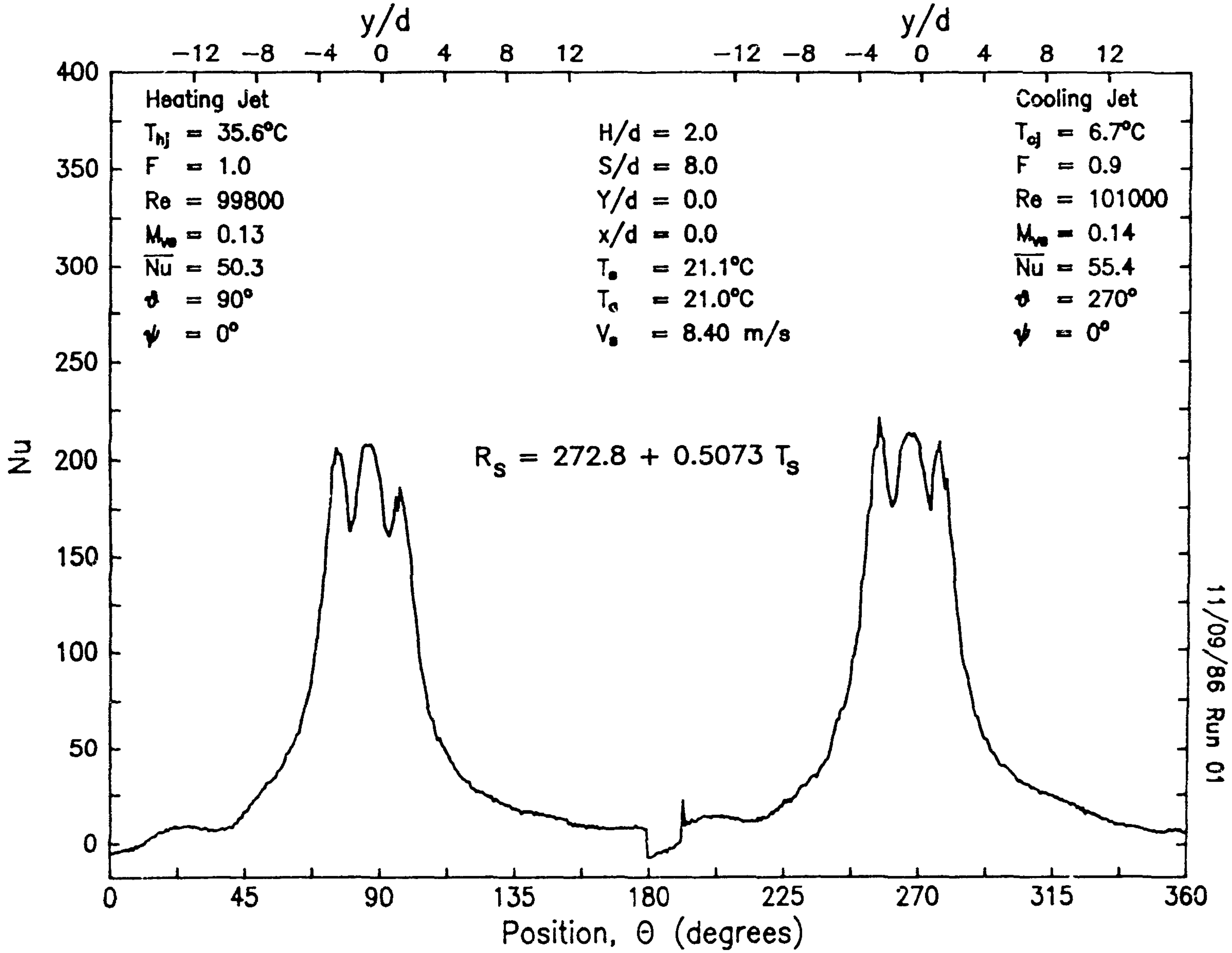

Figure 3.8 Experimental Nusselt profile for H/d = 2 obtained with correct sensor resistance to surface temperature calibration

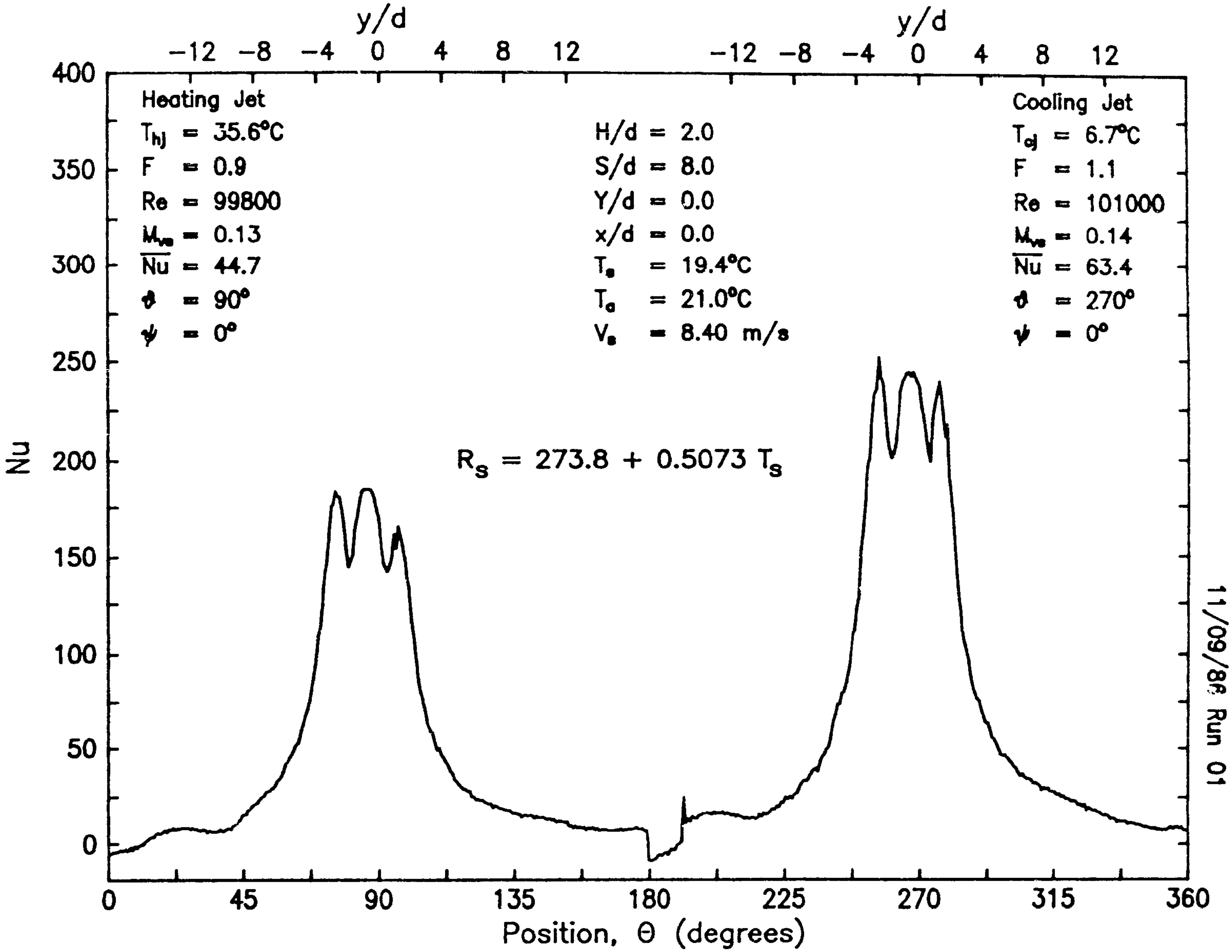

Figure 3.9 Experimental Nusselt profile obtained with a 5% error in sensor calibration intercept. The experimental data is the same as that in Figure 3.4.4

negligible with respect to the impingement convective heat flux. These calculations have been carried out for a similar sensor by van Heiningen[1977].

The fluctuating Wheatstone bridge output voltage is related to the sensor resistance by the relationship:

$$V_{out} = \frac{V_a \left[R_s + \frac{R_v}{10} \right]}{(R_s + R_1) \left[1 + \frac{R_v}{R_2} \right]} \tag{3 8}$$

where:

V_{out}	-	fluctuating bridge output (μV)
V_a	-	Whetstone bridge voltage source (V)
R_s	-	sensor resistance (Ω)
R_v	-	variable resistance (Ω)
R1, R2	-	measurement range resistances (set to 90.909Ω and 909.09Ω respectively)

The output voltage, V_{out}, was amplified 2500 times by a low noise differential amplifier (DANA Model 2860). The high frequency noise was subsequently removed using a low pass filter. The filter cut off frequency was selected to be half of the sampling frequency (i.e. the Nyquist frequency). The number of samples per revolution was fixed at 500 thus the sampling frequency was a function on the roll rpm The signal was acquired using a micro-computer based, 12 bit, high speed analog-to-digital converter (Data Translation DT-2801A).

In operation the variable resistance, R_V, was adjusted such that the output voltage is near zero but always positive. This allowed the signal to be further amplified, using an amplifier on the A/D system

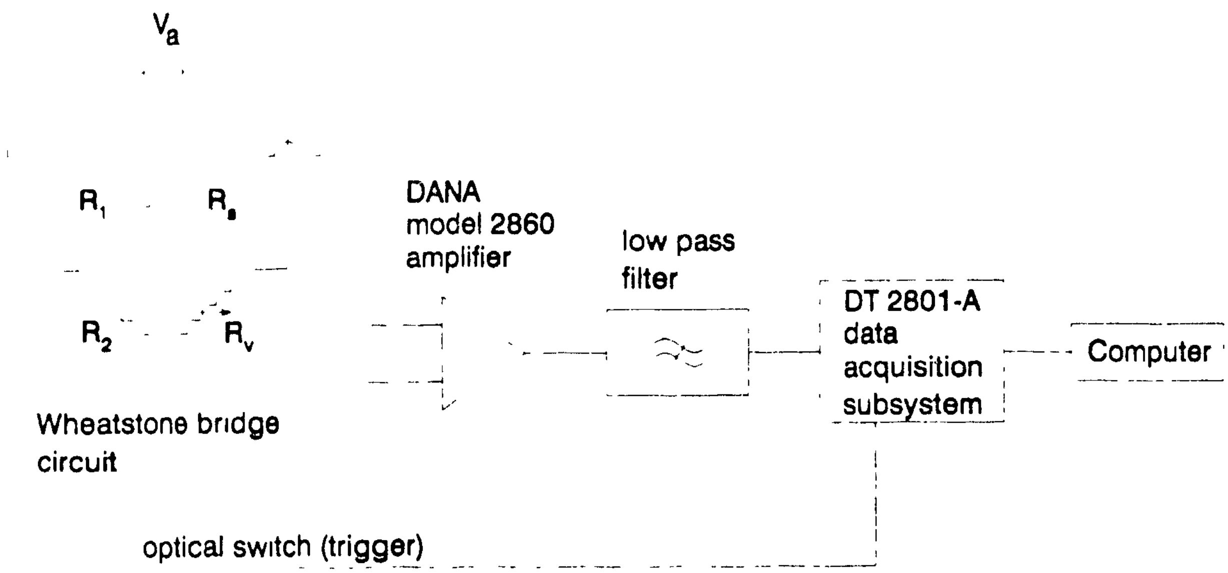

Figure 3.10 Signal conditioning circuitry used in data acquisition system

itself, to a value less than 10V, the maximum input voltage for the A/D converter.

Due to the extremely low signal output levels obtained from the Wheatstone bridge circuit, reducing the signal to noise ratio was a priority. The noise level in the heat flux sensor was reduced to ± 10μV on a peak to peak signal level of 1V (after a gain of 2500). The measures used to reduce the signal to noise ratio are described in Appendix **A**.

3.5 Other Sensors

3.5.1 Sensor Position Signal

An optical position sensor was mounted on the central wall to identify the circumferential location of the sensor and to measure the roll rpm. It consisted of a small lever on the circumference of the calender roll which would pass through a slotted optical switch once per revolution.

The roll rpm was monitored by acquiring the optical switch signal at a specified sampling frequency and calculation the time between switch closures. Once the rpm had stabilized at the required value, the optical switch signal was used to trigger the acquisition of sensor data and provided a method of aligning the acquired data for averaging.

3.5.2 Temperature Measurement

Temperatures were monitored at various locations throughout the equipment using chromel-constantan thermocouples. The fixed locations were:

- one in each nozzle, located 100mm upstream from the nozzle exit.
- one mounted on the surface of the heat flux sensor near the

gold film.

- one located on the interior surface of the heat flux sensor.

The ambient temperature was monitored at 3 separate locations

- in the plane of the nozzle exits, one nozzle diameter from the edge of the central nozzle.
- 10 nozzle diameters up stream of the central jet midway between the nozzle exits and the plenum.
- a location, removed from the direct influence of the impinging jets, corresponding to a T_∞.

The actual temperature to be monitored was selected using a multiple position rotating thermocouple switch (Omega), with the switch output going to an calibrated electronic cold junction compensator (Omega). The temperatures were recorded at the same time as the surface temperature measurements were being taken

3.5.3 Pressure Measurements

The local roll surface pressure was measured with a differential pressure transducer (Kulite XT-190-5). The pressure inside the roll (i.e. atmospheric) used as the reference pressure. The transducer was mounted flush with the impingement surface at the center of the middle roll opposite (i.e. 180° from) the heat flux sensor. The transducer had a sensitivity of 0.0025mV/Pa when a 10V excitation voltage was used and has a compensated temperature range of 20-90°C. The response time of the transducer was too slow to obtain useful pressure profiles at normal operating conditions (i.e. rpm = 300). For this reason the pressure profiles were obtained at low rpm (50rpm) and was strictly used in the evaluation of jet symmetry.

3.6 Data Acquisition System and Procedures

A sophisticated computer program was developed to perform the data acquisition, data reduction and provide on-linea graphical display of the resulting profiles. The immediate processing of the experimental data as it was acquired allowed a quick overview of the experimental results, to determine if potential problems in the data existed. A flow sheet describing the data acquisition program is shown in Appendix B

3.6.1 Acquisition of Local Surface Temperature Profile

The local surface temperature profile were calculated from the data measured and averaged over 50 rotations to reduce the random noise in the signal. The 50 rotations produced an acceptable average profile in small enough time interval that drift in the experimental conditions (i.e. particularly temperature shifts in the nozzle exit temperature) were negligible. The optical switch was used to start the acquisition of the sensor signal for the duration of one rotation at the sampling frequency required to produce the desired number of samples per revolution. The rpm at the start of the data acquisition is used to calculate the sampling frequency.

The number of samples per revolution was set to 500, which corresponds to about two samples per sensor width and five samples per nozzle diameter. The 50 circumferential profiles were measured in rapid succession with the total acquisition time at 300rpm of less than 30s.

Since all sensor acquisition was started at the same circumferential location, the measurements made during the individual rotations could be directly superimposed for averaging. The average resistance was converted to temperature using equation (3.4). Averaging of the resistance profile was equivalent to averaging the heat flux profile since the conversion of resistance to temperature and finally to heat flux requires only linear operations. The consequence of this was a dramatic reduction ($\approx$ 90%) in the data storage requirements.

3.6.2 Calculation of Instantaneous Local Heat Flux

The instantaneous local heat flux was calculated from the experimentally determined local surface temperatures by treating the sensor substrate as a semi-infinite slab and solving the one-dimensional unsteady heat conduction equation (Equation 3.2). An explicit finite difference procedure, as described by Patankar [1980], was used to obtain the temperature distribution within the sensor substrate. The resulting equations are of the form:

$$a_P T_P^n = a_E T_E^o + a_W T_W^o + a_P^o T_P^o \tag{3.9}$$

where:

$$a_E = \frac{\lambda_s}{(\delta x)_e} \qquad a_W = \frac{\lambda_s}{(\delta x)_w}$$

$$a_P^o = \frac{\rho \, cp_s \, \Delta x}{\Delta t} \qquad a_P = a_E + a_W + a_P^o$$

e,w - indicate evaluated at control volume face
o - indicates previous time step
n - indicates new time step

Figure 3.11 describes the grid point cluster for this one dimensional problem.

For numerical stability when using an explicit scheme to solve Equation 3.5, the Fourier number, Fo, must satisfy the condition:

$$Fo = \frac{\Delta t \ \alpha_s}{(\Delta x)^2} \geq \frac{1}{2} \tag{3 10}$$

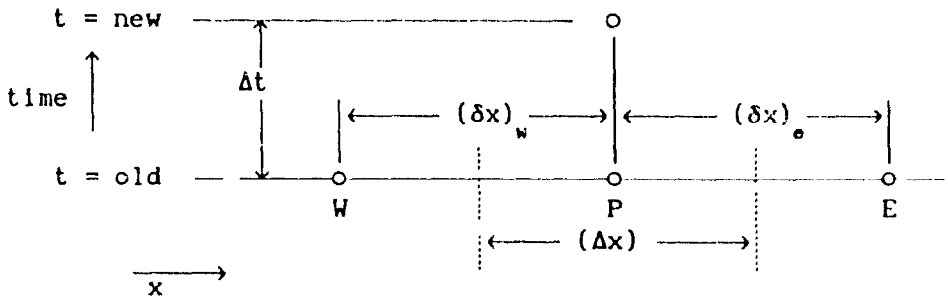

Figure 3.11 Grid-point cluster for one-dimensional unsteady problem.

Since Δt is specified in this problem by the sampling frequency, the distance between neighboring grid points, Δx, is given by:

$$\Delta x = \sqrt{2 \ \alpha_s \ \Delta t} \tag{3.11}$$

The combination of equations 3.9, 3.10 and 3.11 yields:

$$T_P^n = \frac{(T_E^o + T_W^o)}{2} \tag{3.12}$$

The surface heat flux, q_o, can be calculated using a second order approximation of the derivative at the surface:

$$q_o = \frac{\lambda_s}{\Delta x} (-3 \ T_1^n + 4 \ T_2^n - T_3^n) \tag{3.13}$$

The initial condition used to solve Equation 3.2 was the average cylinder temperature. Since the problem is cyclic in nature, the initial boundary condition used to solve equation (3.5) is arbitrary, and requires only that enough iterations be performed to remove the effect of the choice of initial condition. Solving for the temperature profile through six complete revolution, using the average roll surface temperature distribution as an initial condition, was found to be sufficient to remove any effect due to the initial conditions.

The internal boundary condition is that of a semi-infinite solid. Assuming a sinusoidal surface temperature variation of frequency, ω, the thermal penetration depth (Chapman [1967]) where the amplitude of the temperature fluctuation is 0.1% of that at the heat transfer surface is

$$x_\delta \quad = \quad -\ln(0.001)/(\alpha_s/\omega)^{1/2} \qquad (3.14)$$

For even the slowest rpm used, x_δ , determined using Equation 3.14, is only 2mm which is much less than the sensor substrate thickness, 14mm. Thus, semi-infinite heat transfer analysis is justified. The number of finite difference grid points, n, used in the finite difference solution is given by

$$n \quad = \quad \text{integer of } (\ x_\delta/\Delta x\ ) + 1 \qquad (3.17)$$

The local values of the local heat transfer coefficient, h_j and Nusselt number, Nu, were evaluated using the definitions given in Equations 3.4 and 3.5 where the value of T_j used in the equations is that of the hot or cold jet, depending on the position of the sensor.

The numerical procedures for the calculation of the radial temperature profile and surface heat flux require accurate values for the thermal properties of the substrate. The thermal behavior of PVC is not well documented and can be a function of the additives used. For this reason the thermal conductivity, λ, heat capacity, Cp_s, and density, ρ, of the PVC substrate were measured experimentally. The results obtained are in good agreement with the existing literature indicating that, if additives were used, they had little effect on the thermal properties of the PVC The procedures used to measure these thermal properties, the experimental data and comparisons with the available literature are presented in Appendix C.

3.6.3 Display of Circumferential Profiles

The circumferential profiles of resistance, temperature, heat flux and Nusselt number were displayed online using MPPS-PC (McGill Package of Plotting Subroutines for the IBM personal computer). This computer package allows the easy integration of sophisticated graphics routines to any Fortran program. The same routines were used to create the hard copy output. Typical output profiles were shown earlier in Section 3.4.3 as Figures 3.8 and 3.9.

3.7 Jet Flow Characteristics

3.7.1 Symmetry of Flow Under the Impinging Jets

There are several methods of verifying the impinging jet symmetry. These include impingement surface heat transfer and pressure distribution and the impinging jet velocity and temperature profiles.

(a) Impingement surface heat transfer distribution

During the experimental program a complete profile, in cartesian coordinates relative to the jet centerline, of the local heat transfer at the impingement surface was obtained by sampling the circumferential heat transfer profile at various axial positions along the impingement surface. Since the sensor is much larger in the axial direction than in the circumferential direction, (1.45d versus 0.27d) the data is obtained at a much wider interval in the axial direction (2 samples per nozzle diameter in the axial direction versus 9 samples in the circumferential direction). Comparison of the jet centerline Nu profiles, Figures 3.12 and 3.13, obtained in the circumferential and axial directions, for H/d = 2 and 4 and a jet-to-jet spacing, S/d = 8, show that the jet is quite axisymmetric. The aspect ratio of the sensor, shown if Figure 3.14 explains why the local minimum and maximum, at y/d = 1.05 and y/d = 1.85 respectively, do not appear in the axial direction profile. Contour plots of the local Nu profile over the impingement surface for several H/d, Figures 3.15 to 3.17, clearly show the axisymmetry.

(b) Impingement surface static pressure distribution

The surface pressure profiles under an impinging jet at low RPM, as a function of circumferential and axial position were measured using a pressure transducer, to provide an indication of the jet symmetry. Although the impingement surface static pressure distribution is less sensitive to asymmetry, the results shown in Figure 3.18, indicate a high degree of axial symmetry about the jet impingement point.

(c) Jet velocity profile

The nozzles used in this study (Figure 3.3) consisted 210mm long straight section with an inside diameter of 41mm followed by a 100mm converging section and a 25.4mm long, 25.4mm diameter nozzle exit section. The jet flow was expected to be very turbulent, because of the flow control valve located immediately upstream of the nozzle and the high jet Reynolds number. Figure 3.19 shows the jet velocity profile obtained in the vertical and horizontal planes at a position 5 mm

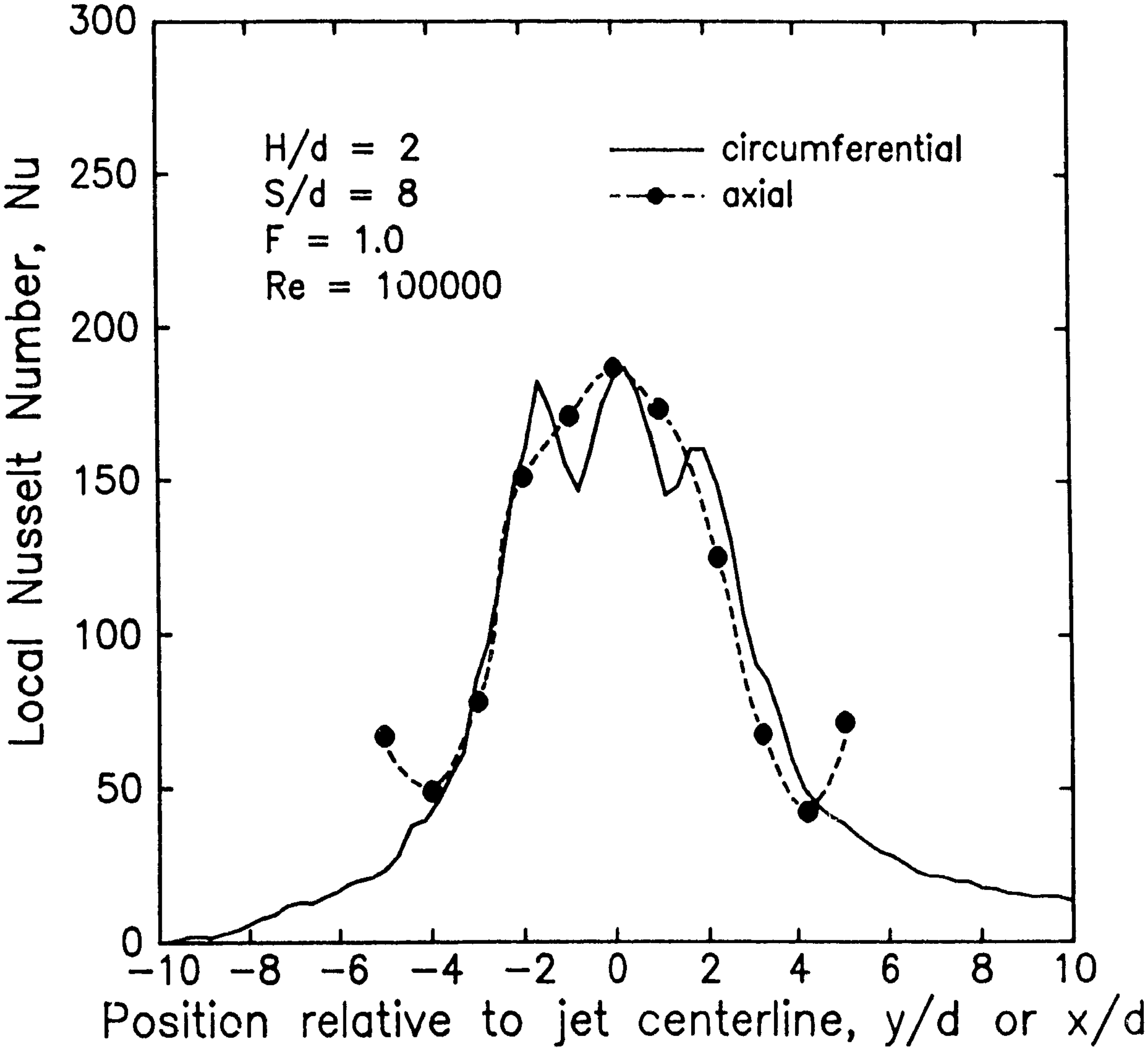

Figure 3.12 Axial vs circumferential Nusselt number profile for H/d-2

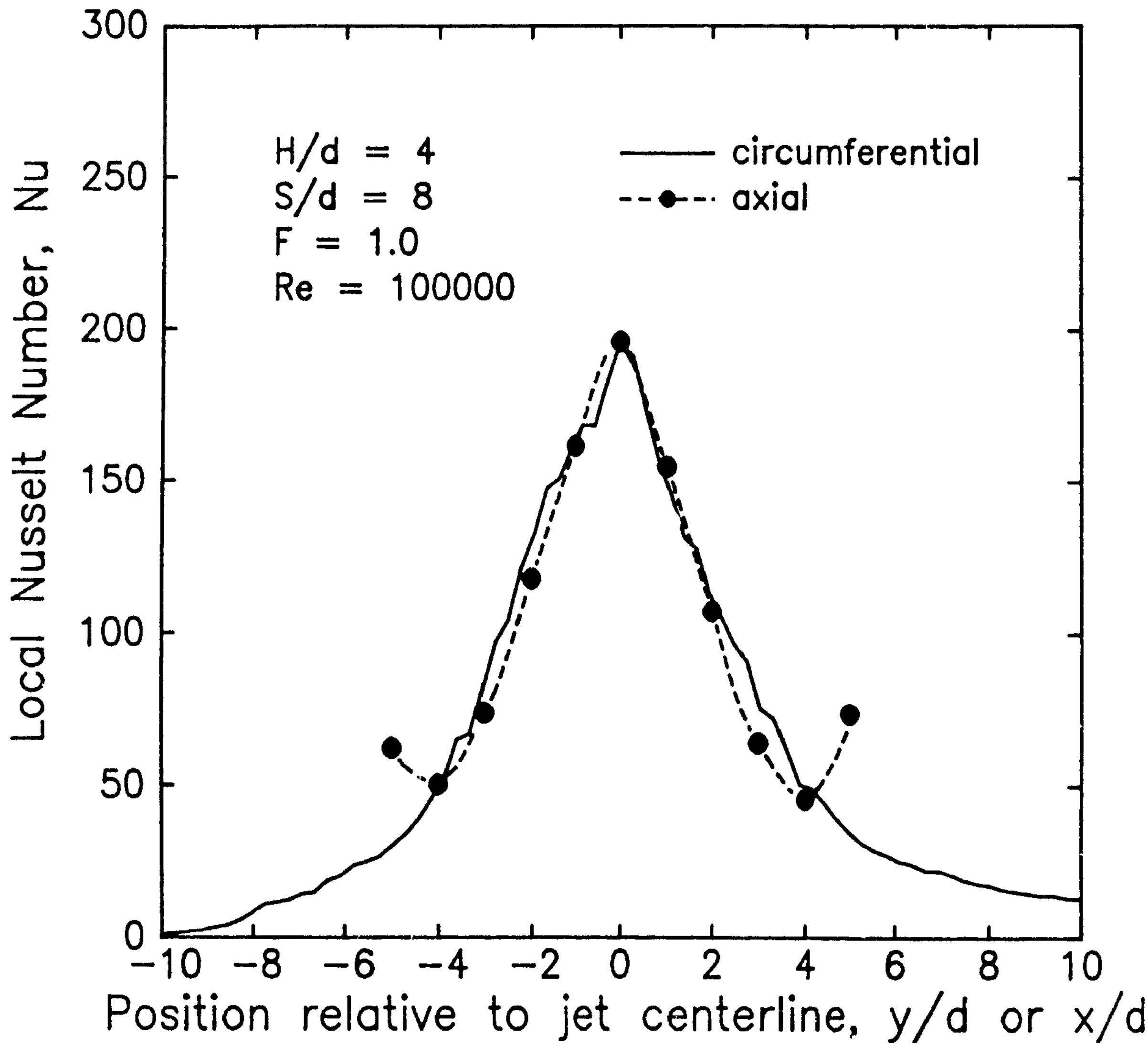

Figure 3.13 Axial vs circumferential Nusselt number profile for H/d=4

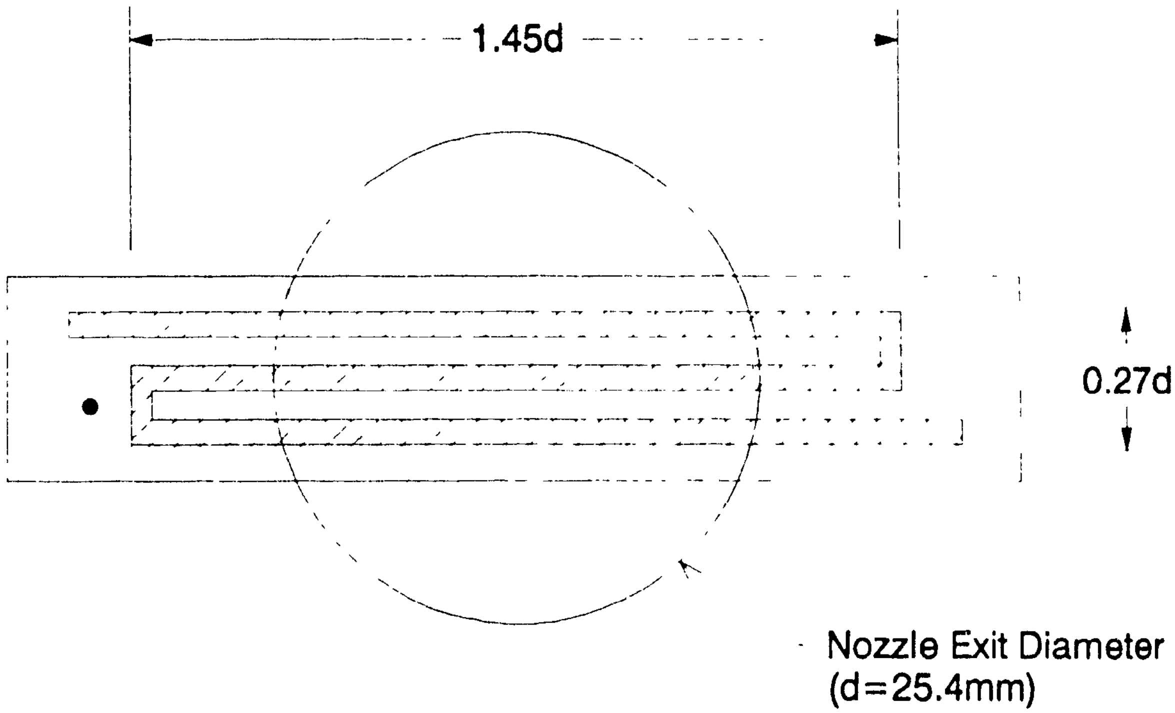

Figure 3.14 Comparison of the dimensions of the heat flux sensor and the nozzle exit diameter

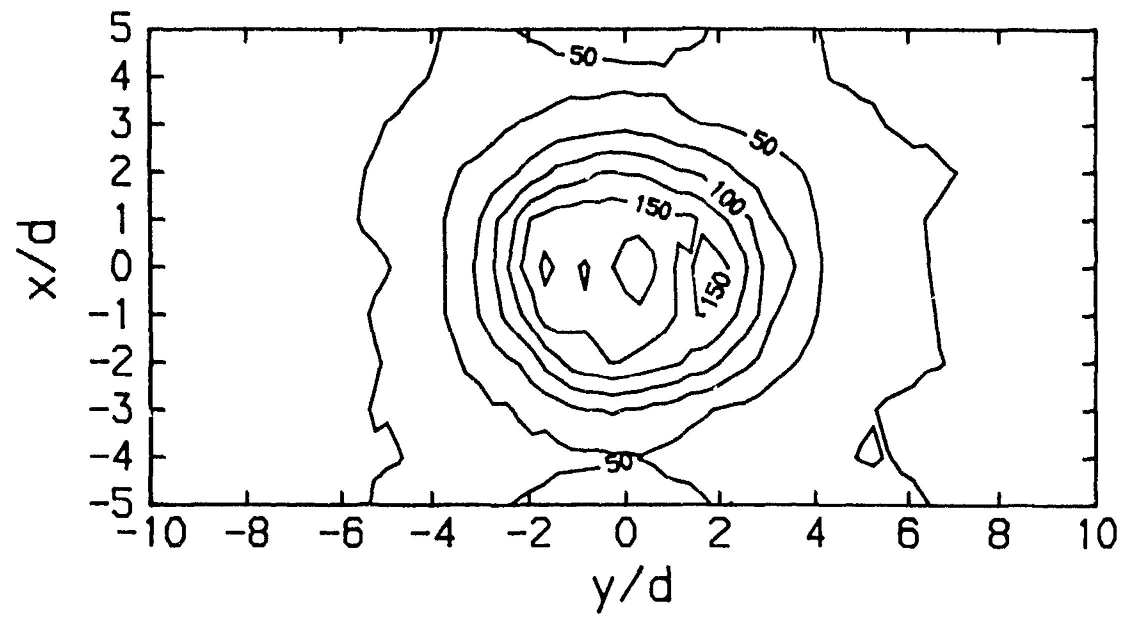

Figure 3.15 Contour plot of local Nusselt number at H/d=2

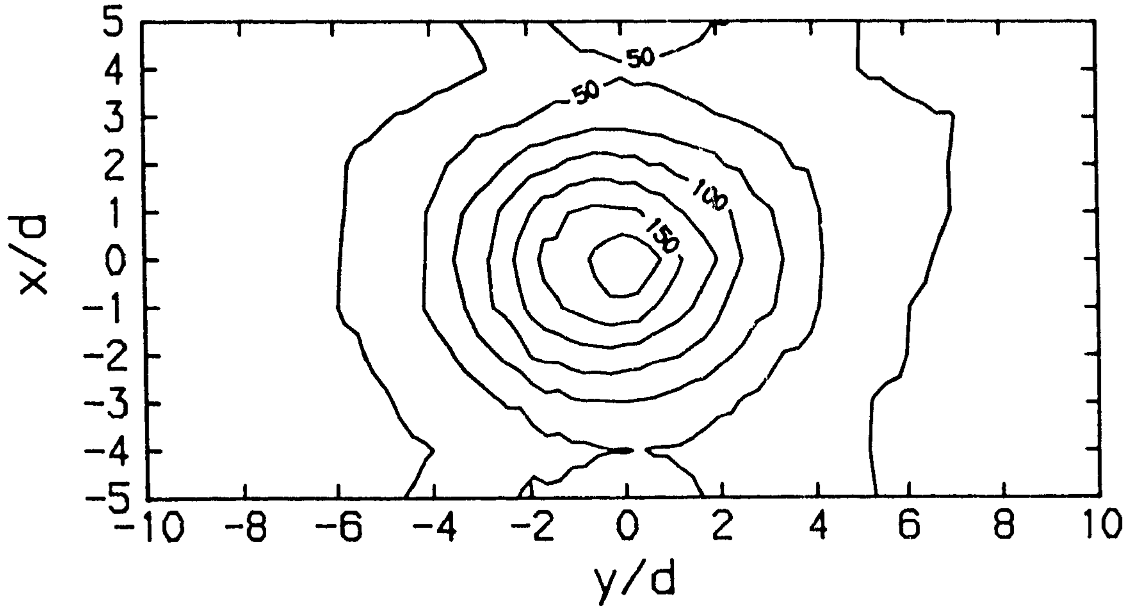

Figure 3.16 Contour plot of local Nusselt number at H/d=4

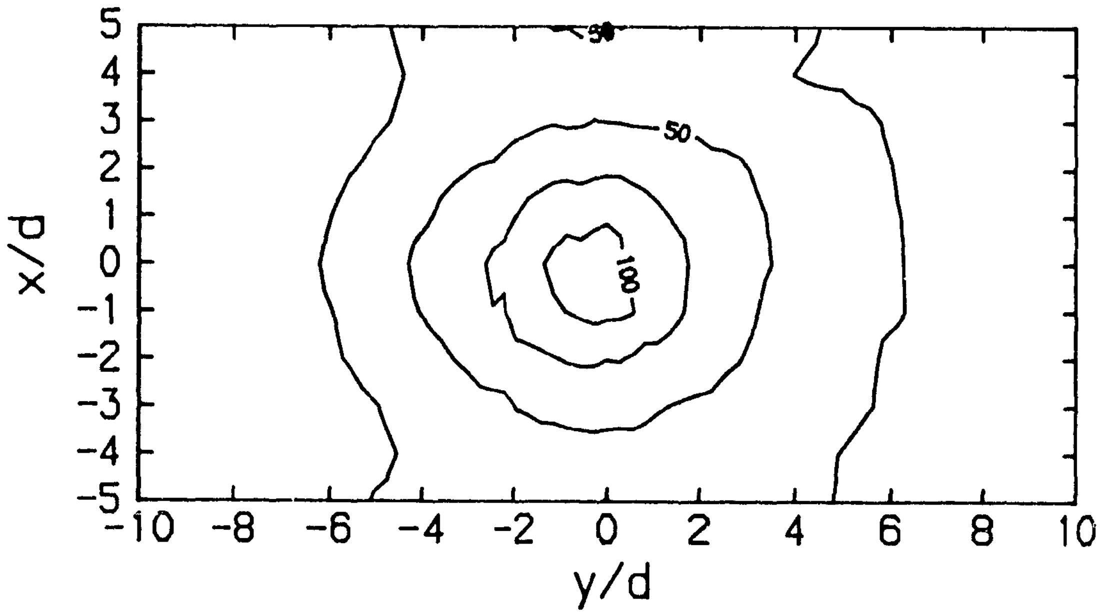

Figure 3.17 Contour plot of local Nusselt number at H/d=8

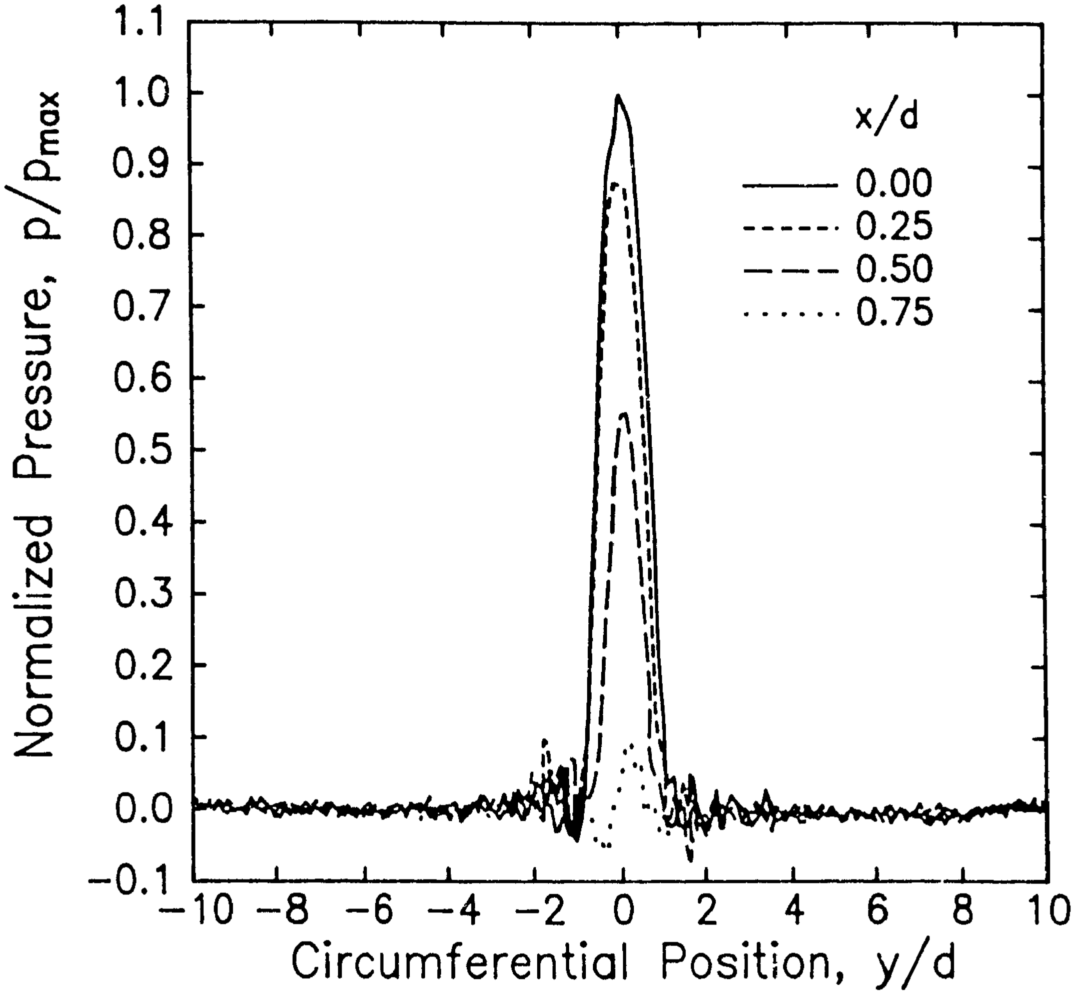

Figure 3.18 Static pressure distribution measured at the impingement surface as a function of circumferential, y/d, and axial, x/d, position.

downstream of the nozzle exit. The profiles were obtained by traversing the jet with a 3mm diameter pitot tube. The jet velocity can be considered uniform over the jet exit area.

(d) Jet temperature profile

The accurate determination of the Nu profiles requires an accurately known and uniform jet exit temperature profile. Under normal operating conditions (i.e. jet to surface temperature difference of the order of 10 to 20°C.) an error of 0.5°C will result in errors of $\pm$ 2.5-5% in the Nusselt number profiles. Figure 3.20 shows the jet temperature profiles in the horizontal and vertical planes measured 5mm downstream of the nozzle exit. As expected due to the high turbulence levels the temperature profiles were flat with a maximum difference of 0.2°C (<1%). This is well within the acceptable experimental error of this study.

Based on these observations the profiles obtained for normal impingement ($\psi = 0^\circ$) under unconfined conditions can be considered to be axisymmetric.

3.7.2 Confined Impinging Jet Pressure Recovery

When an impinging jet is confined, the jet flow can experience pressure recovery where the pressure drop across the nozzle is greater than pressure difference between the nozzle and the exhaust ports. The importance of pressure recovery when using confined slot jets was discussed extensively by van Heiningen [1980, 1982]. For confined axisymmetric jets, the wall jet velocity is inversely proportional to the radial position away from the nozzle centerline which is unfavorable for pressure recovery. Thus for axisymmetric jets the effect of jet

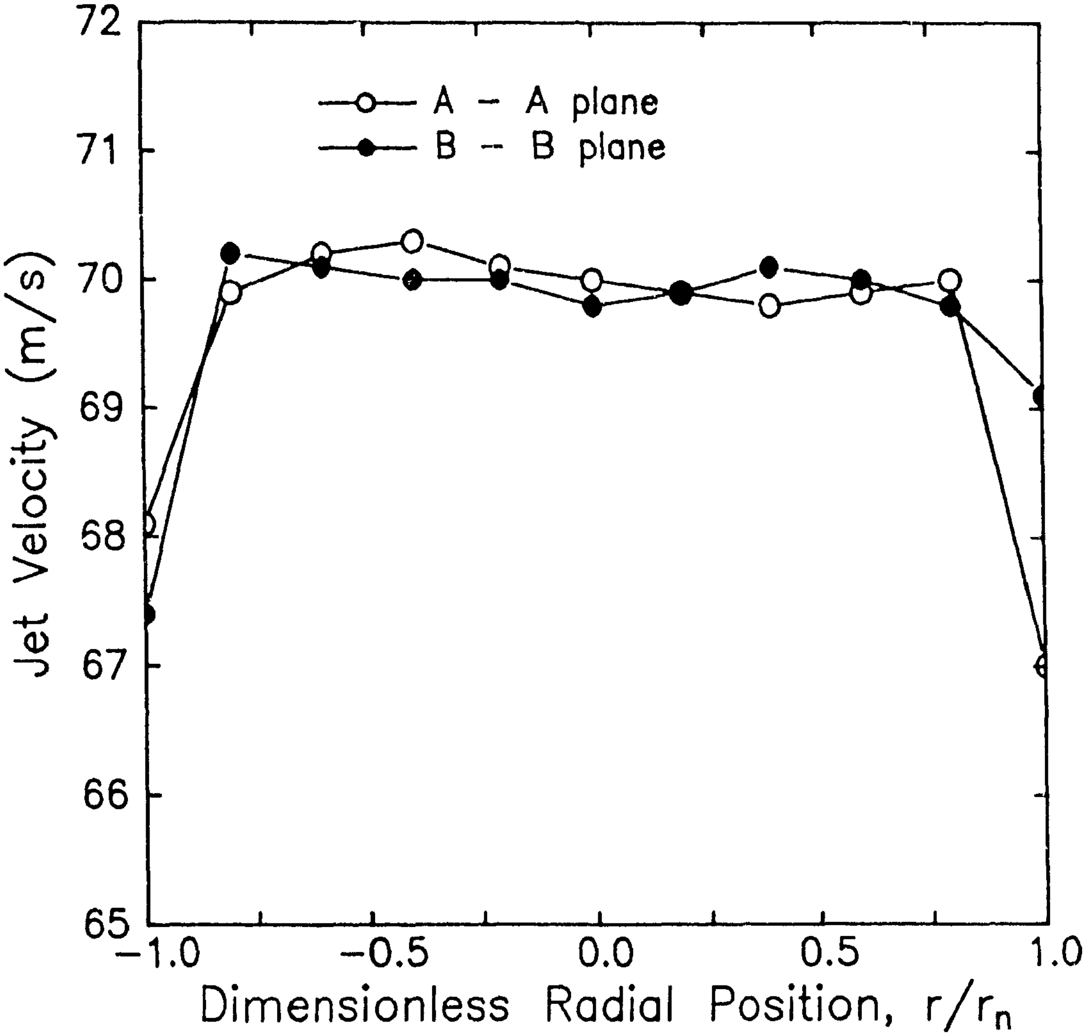

Figure 3.19 Velocity distribution at the nozzle exit in the horizontal, A-A, and vertical, B-B, planes.

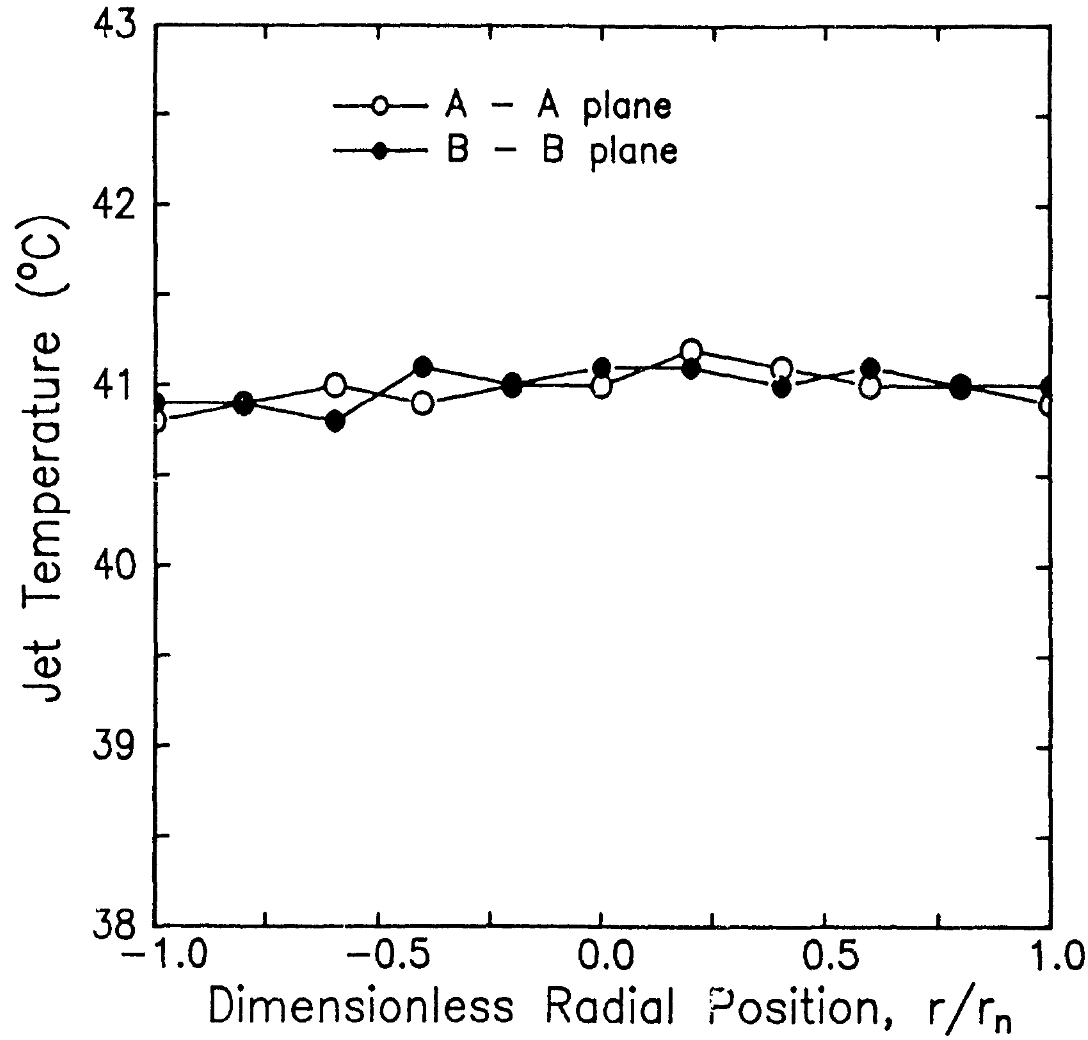

Figure 3.20 Temperature distribution at the nozzle exit in the horizontal, A-A, and vertical, B-B, planes.

confinement on the pressure drop across the nozzle exit can normally be considered negligible. As shown in Figure 3.21, where pressure drop across the nozzle is compared to the static pressure in the impingement nozzle, the pressure recovery was less than 6% for $H/d \geq 1$ and less than 3% for $H/d \geq 2$.

3.7.3 Effect of Inlet Air Humidity

An unexpected result of the many qualification runs was the uncovering of an effect of inlet air humidity. In the current experimental setup the inlet air to the fan was outside the building. Under conditions of high relative humidity (as experienced during the summer months) the air cooler could bring the air temperature down below the dew point and cause the formation of a water mist in the air stream. This phenomena was first observed when air conditions caused water to condense and seep through the cloth flexible ducting used between the air cooler and the nozzle header.

Figure 3.22 shows Nusselt number profiles obtained under conditions leading to condensation in the cooling side of the air supply system. The cooling side Nu profiles are seen to be approximately 30% higher than the Nu profiles on the heating side for similar operating conditions. This difference is not evident in Figure 3.23, which shows results measured under conditions where no condensation occurred in the air system.

The increase in heat transfer is caused by the evaporation of the water mist in the boundary layer near the roll surface, lowering the film temperature, which increases the effective driving force for heat transfer. Since the Nu profiles are based on the jet temperature, the actual driving force is underestimated, resulting in higher Nu profiles.

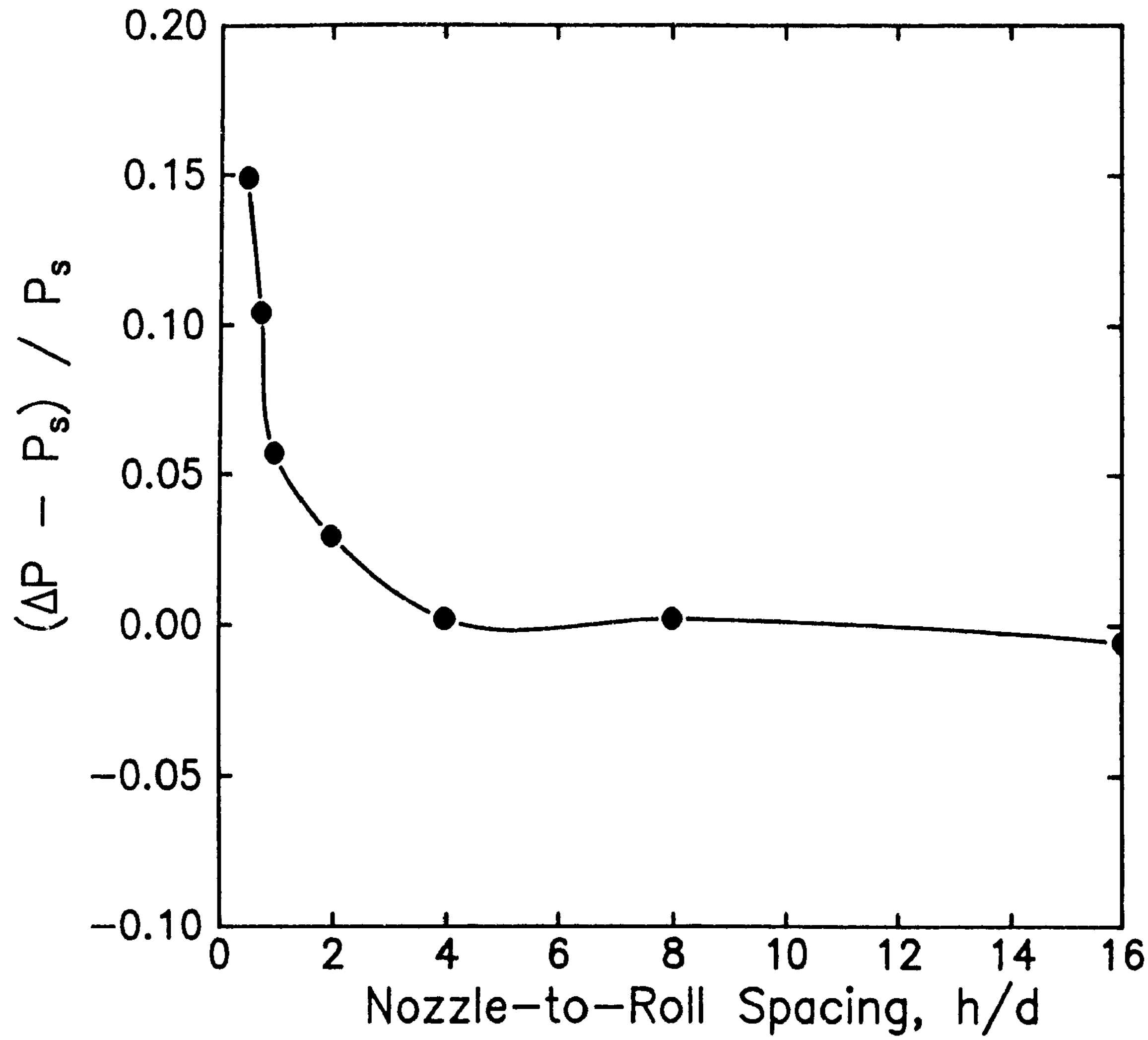

Figure 3.21 Difference between the pressure drop across nozzle exit, ΔP, and the nozzle static pressure, P_s, as a function of H/d when a confinement plate is used

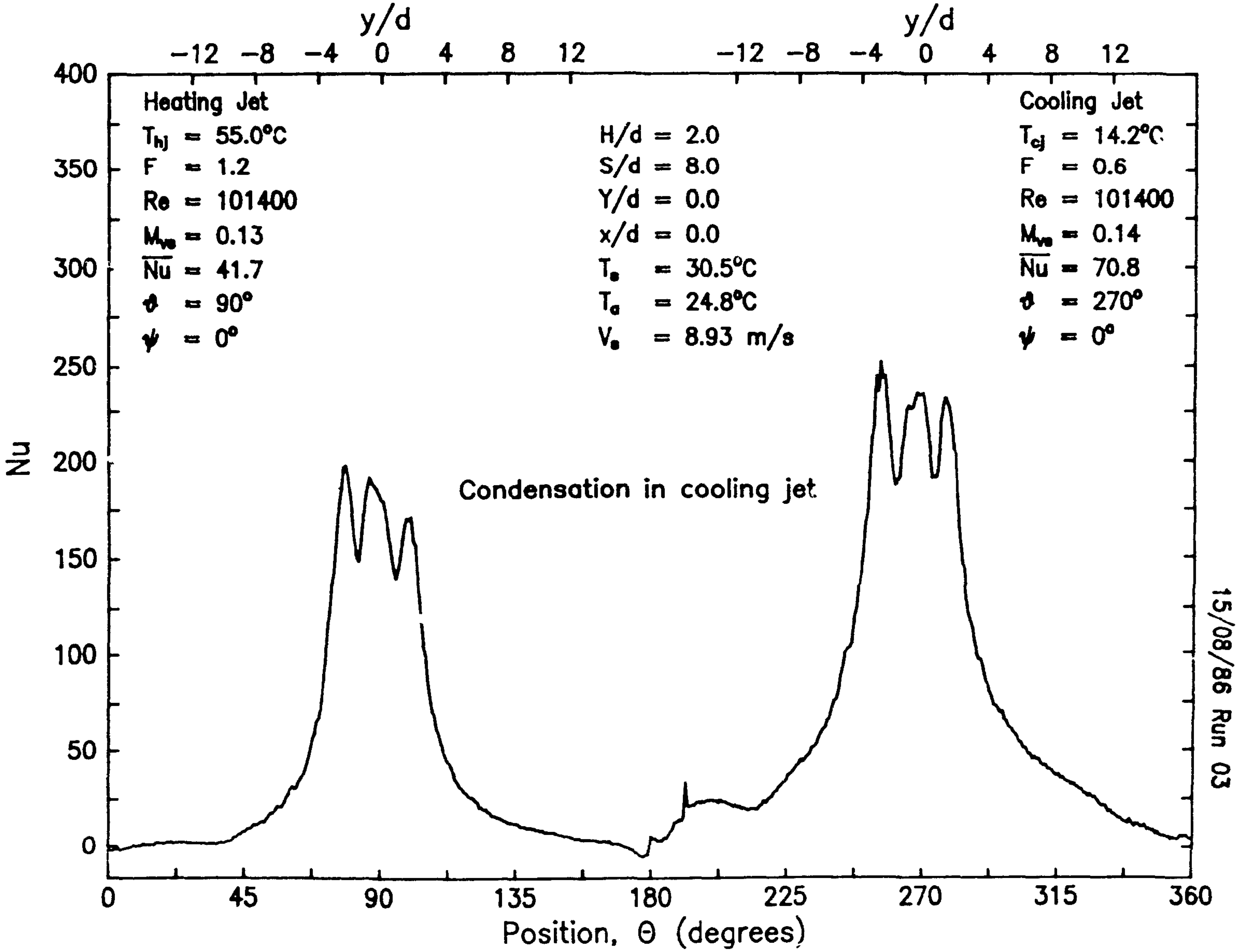

Figure 3.22 Experimental Nusselt profile obtained when there was condensation in the cooling air supply system

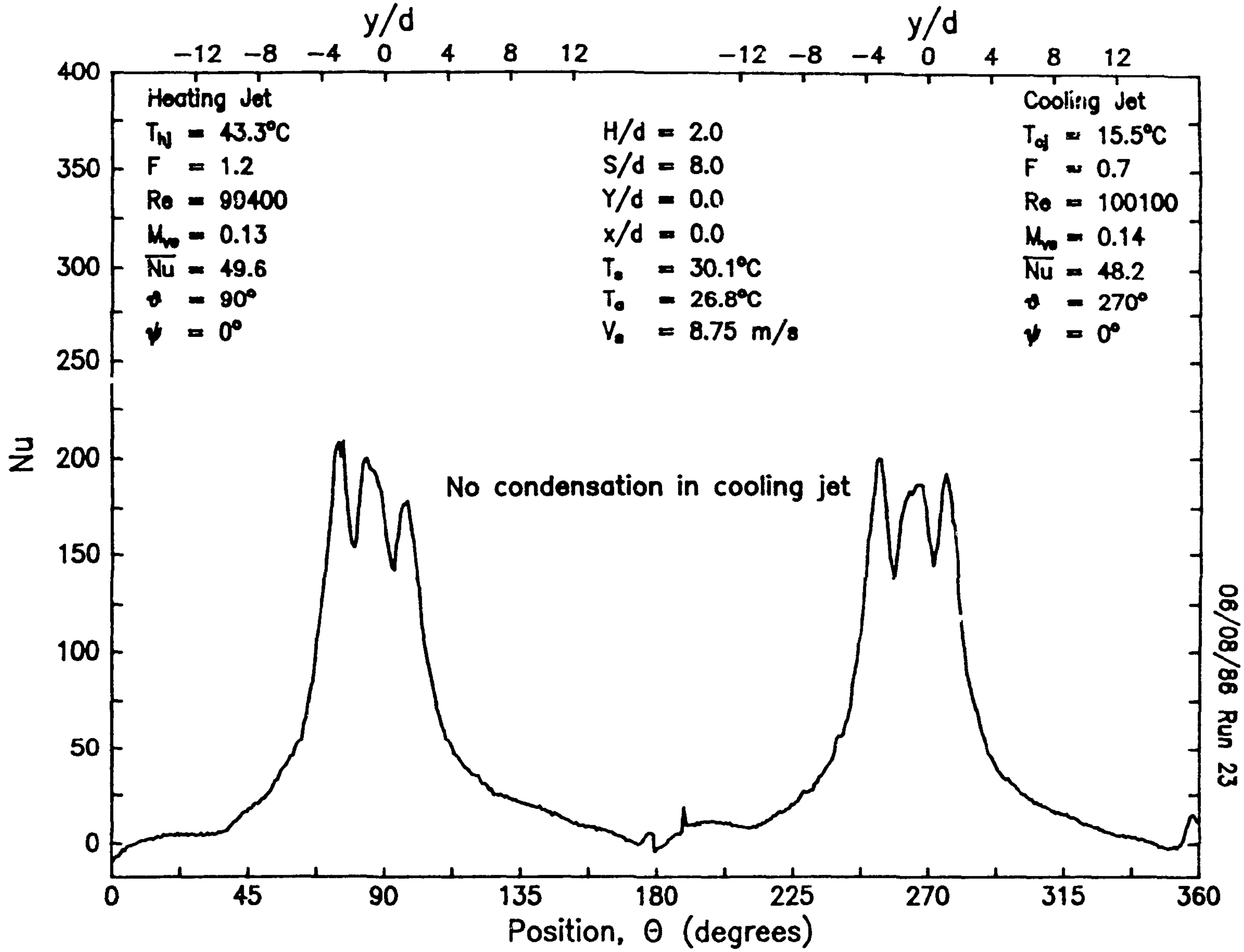

Figure 3.23 Experimental Nusselt profile obtained when there was no condensation in the cooling air supply system

A calender cooling control system, using this evaporative cooling phenomena, has been marketed but under the brand name Mystifier, but it has not received wide spread acceptance, due to perceived problems with the water mist condensing in the paper and/or calender roll and changing the paper web cross direction moisture profile.

For the experimental measurements reported here, condensation is not a factor since experiments were only performed under condition when condensation would not occur. The presence of condensation was determined by using similar operation conditions on the heating and cooling sides and observing the resulting Nu profiles for differences.

CHAPTER 4

IMPINGING JET HEAT TRANSFER IN CALENDER CONTROL SYSTEMS

4.1 Impinging Jets and their Application in Paper Calenders

Impinging jets are commonly used in industrial processes for their high heat and mass transfer characteristics. Applications include processes such as the annealing of metals, tempering of glass, drying of paper and textiles, cooling of electronic components and turbine blades and, of primary interest in this study, the control of paper machine calender stacks using localized heating and/or cooling.

A paper machine calender stack, Figure 4.1, consists of a vertical stack of from two to eight chill cast iron rolls of diameter between 300 and 800mm. As it passes through the nips of the calender stack the web of paper is subjected to a series of rapid compressions, transforming the rough bulky sheet issuing from the dryer section of a paper machine into a sheet with the desired surface properties and thickness.

Cross-machine direction (CD)control of the calendering process is required since variations in moisture content and temperature affect the rheological properties of the paper. Also, there are differences in the local nip pressure due to CD variations in basis weight, calender roll grinding tolerances, thermal deformations and roll deflections. If left uncorrected, these variations cause the surface properties, and thus printing properties, of the paper to vary across the width of the machine. Paper thickness variations when built up over hundreds of layers cause hard or soft regions in the reel which lead to problems

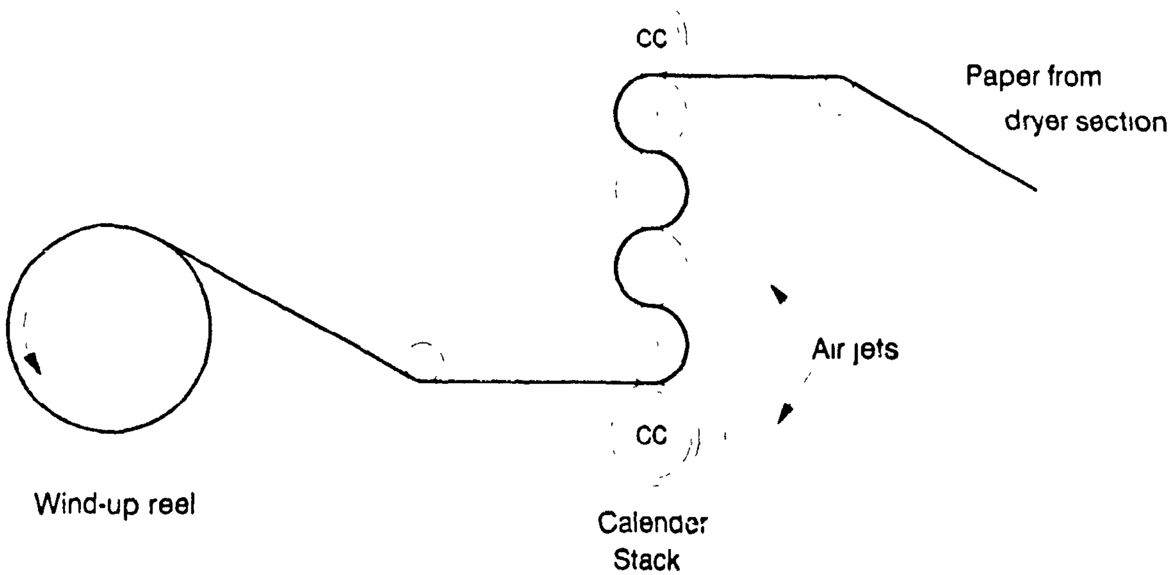

Figure 4.1 A paper machine calender stack.

during rewinding and during high speed unwinding in the press room.

Cross machine direction control of calendering is performed by locally adjusting the nip load and/or sheet temperature. Local heating of the calender roll increases the roll diameter and thereby the nip pressure, thus producing a greater paper thickness reduction. The converse applies when the calender roll is locally cooled.

Traditionally most calender control systems used impinging air jets for locally heating or cooling calender rolls. Although many such systems are still in use, the current state of the art in CD calender control are induction heating systems. On the other hand, air systems have found an important new application in the control of soft calenders. The heat generated in the soft plastic covers as they are repeatedly compressed and the uneven cross direction temperature profile which may be introduced with the paper from the dryer section must be controlled carefully to prevent damage to the soft covers. This has generally been accomplished using cooling air jets.

Little is known about the heat transfer characteristics of the air jets used to control paper thickness in commercial calenders. The paper industry literature on this subject, reviewed in Chapter 2, is largely speculative in nature (Kahoun et al.[1964], Bryan[1972]). The extensive literature on the fundamentals of impinging jets has recently been reviewed by Obot [1981], Polat [1988], Huang [1988] and in Chapter 2 of this thesis. However, it is not clear whether the results available for heat transfer for single round jets impinging on stationary flat surfaces, for example, can be applied directly for impingement from arrays of round jets on cylinders rotating at high speed.

To apply to the calender control problem the large body of knowledge available on the subject of impingement heat transfer, specific information is required for the case of round jets impinging on rotating cylinders. In addition to determining the effects on heat transfer of the basic flow and geometric parameters, measurement of the effects of ambient air temperature, impingement surface speed, jet location and jet confinement is required. These questions are addressed in the present study.

4.1.1 Literature Review

Although the literature on the fundamentals of impingement heat transfer is quite extensive, direct application of this data to the special constraints of the calender control problem is subject to uncertainty. For example, there is considerable speculation as to what calender impingement configurations result in the highest heat transfer rates, an important industrial problem which cannot be resolved with the available studies.

The only measurement of heat transfer rate between multiple round jets and a calender roll was in the exploratory study by Pelletier et al. [1984, 1987]. These results clearly demonstrate the importance of entrainment of ambient air by unconfined jets on impingement heat transfer rates. Unconfined jets entrain substantial amounts of the surrounding air, Obot [1981], so when jets are used for heating or cooling an impingement surface, such entrainment will always affect the heat transfer rate. Even in the special case of a jet discharging into air of the same temperature as the nozzle exit, impingement heat transfer would be expected to be different between unconfined and confined jets because of the correspondingly different flow fields. Besides this flow field effect, there is generally a thermal effect as described below.

When an unconfined heating jet discharges from a nozzle into air of temperature less than that at the nozzle exit, or when a cooling jet discharges into air warmer than the jet temperature at the nozzle exit, the entrainment of surrounding air by the jet reduces the effective temperature difference for impingement heat transfer, thereby reducing transfer rates. Because impingement heat transfer coefficients are traditionally defined with ΔT_{js}, the difference between the nozzle exit temperature, T_j, and impingement surface temperature, T_s, the effect of entrainment appears implicitly in the values of h.

Although important in equipment design, little has been done to quantify the effect of entrainment. Schauser and Eustis [1963] used integral solutions to analyze the thermal effect of entrainment for a single impinging jet and compared their analytical work with experimental results for unconfined air jets discharging into air at

i) the nozzle exit temperature

ii) the impingement surface temperature.

Vlachopoulos and Tomich [1971] numerically predicted velocity and temperature profiles in the wall jet for a single heated axisymmetric air jet issuing into a cool environment and calculated heat transfer based on empirical correlations. As the specific thermal boundary conditions used in the experiments were unspecified, it is not possible to interpret the results.

Kataoka et al.[1976] investigated the influence of the surrounding fluid on impinging jet cooling with a slot jet and found that the surrounding fluid temperature had to be taken into account. They observed that if the arriving fluid temperature was used in the calculation of heat transfer coefficients, then results were in good agreement with Gardon and Akfirat[1965] for H/w > 8.

Striegel and Diller [1982] proposed analytical models to predict heat transfer from unconfined turbulent slot jets discharging into fluid at a different temperature and generated some experimental results to support their models. They defined a thermal entrainment factor or nondimensional temperature mismatch, F, as

$$F = \frac{T_j - T_a}{T_j - T_s} \tag{4.1}$$

With the use of this thermal entrainment factor they successfully extended single jet results to a multiple jet configuration. As one would expect they observed the strongest effect of F in the wall jet region.

Hollworth and Wilson [1984] and Bouchez and Goldstein [1975] discussed the similarity between impingement heat transfer and film cooling where a coolant introduced on a solid surface insulates the surface from the ambient fluid. The performance of film cooling systems is typically characterized by a film effectiveness, η, defined as

$$\eta = \frac{T_j - T_r}{T_j - T_s} \tag{4.2}$$

The recovery temperature, T_r, is usually measured or predicted for an adiabatic surface, then applied to calculate the heat transfer rate for a non-adiabatic surface. This approach is attractive since it attempts to define the heat transfer using a local temperature driving force. Unfortunately, the difficulty of measurement of the recovery temperature, in industrial applications, limits the use of this approach.

Hollworth and Gero [1985] showed that the local heat transfer coefficient is not a function of the temperature mismatch, ΔT_{ja}, between the nozzle exit and ambient fluid, provided the heat transfer coefficient is defined in terms of the difference between the local recovery temperature and the impingement surface temperature, ΔT_{rs}. As in the case of film cooling, the problem is to measure or predict the local recovery temperature for use in calculating the local Nusselt number.

The effect of surface motion on local impingement heat transfer profiles for confined slot jets has been determined by van Heiningen [1982] and Polat [1988] using the non-dimensional mass velocity ratio,

$$M_{vs} = \frac{\rho_s V_s}{\rho_j V_j} \tag{4.3}$$

which appropriately characterizes surface motion. They observed that the Nu profile becomes skewed in the direction of surface motion for M_{vs} above about 0.13. As typically the M_{vs} ratio can be as large as 0.25 in calender control systems, surface velocity was included as a variable with the round jets of the present study.

The presence of complex air flow patterns around the calender stack has led to speculation about the effect of impingement geometry on heat transfer. Experiments by Mitchell and Sheahan [1978], on an operating calender stack, indicated that the calender control system performance, measured by observing the resulting change in paper thickness, improved when the nozzle-to-calender roll spacing was reduced. Bryan [1972] hypothesized that the most effective heat transfer from air jets would occur when the boundary layer was removed by the jet. He reasoned that the jet velocity required to do this was a function of the boundary layer thickness and thus dependant on the nozzle location relative to the in-going and out-going nips. He concluded that the highest heat transfer would occur when the jet was directed into the low pressure area associated with the outgoing nip.

4.2 Experimental

4 2 1 Equipment and Procedures

The CALCON (CALender CONtrol) experimental facility was built by Pelletier et al. [1987] for the study of local and average heat transfer from a horizontal row of circular air jets impinging on the surface of a roll in a vertical stack of rotating rolls. This experimental apparatus was designed to simulate closely the air side heat transfer which occurs during the cross-machine direction control of paper machine calender stacks when using impinging air jets to locally cool or heat one or more rolls in the calender stack. The technique used to obtain local heat transfer rates on a moving surface was proposed and developed by van Heiningen et al.[1985]. For the present study, several modifications to the CALCON equipment were made:

i. The nozzle positioning subsystem was modified to allow more accurate orientation of the nozzles relative to the impingement surface.

ii. The air supply system was modified to use air from outside instead of inside the laboratory, thereby lowering the temperature of the cooling jet, previously too close to the roll surface temperature.

iii. The manufacturing procedure for the heat flux sensor was simplified to reduce the time required to replace damaged sensors.

The experimental equipment, Figure 4.2, consists of three vertically stacked rolls (diameter: 558 mm) with the heat flux sensor

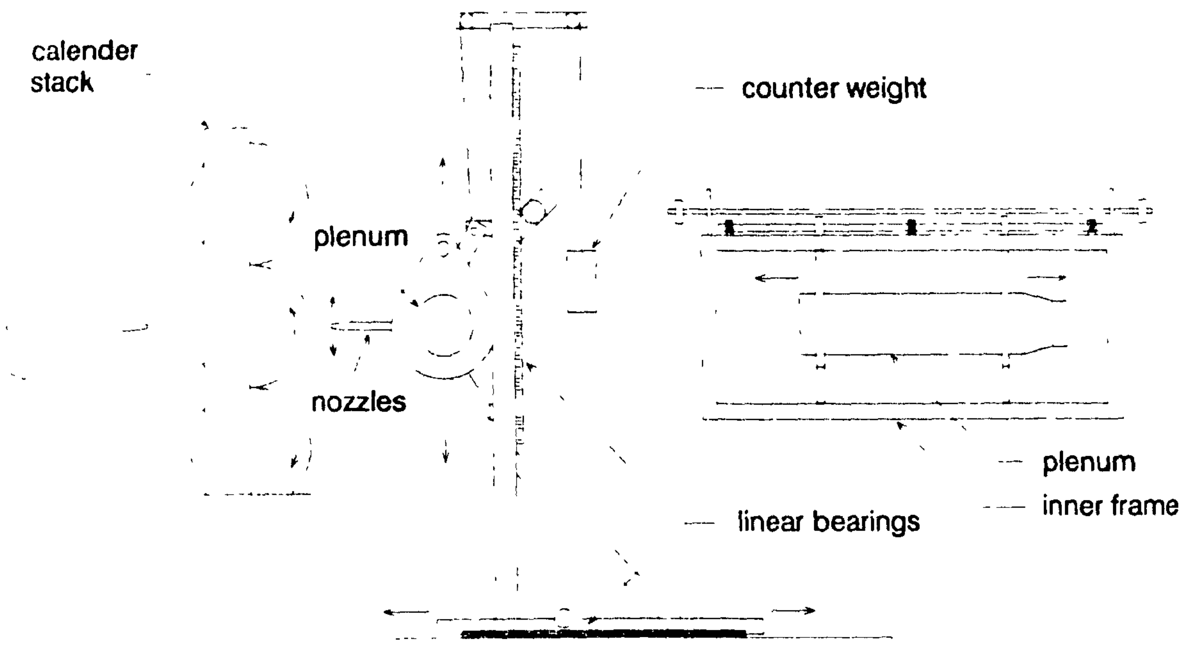

Figure 4.2 Schematic of the CALCON experimental facility.

located on the surface of the middle roll. To protect the sensor the rolls do not touch (≃ 1mm gap). Roll rotation is accomplished using a chain drive so all rotate at the same speed. On either side of the center roll is a row of nozzles (nozzle exit diameter: 25.4 mm) one for heating jets, the other for cooling jets. The nozzle support systems permitted two nozzle-to-nozzle separations, i.e. $S/d = 4$ and $S/d = 8$. When the system reaches a quasi-steady state, the roll surface temperature undergoes cyclic variations in the order of $\pm 2^\circ C$ around a steady average temperature intermediate between the heating and cooling jets. Convective heat transfer coefficients thus obtained correspond to an adiabatic surface boundary condition.

The circumferential surface temperature profile, composed of 500 data points, was measured by the heat flux sensor, Figure 4.3, a gold thin film resistance thermometer capable of resolving $0.001^\circ C$ at a 5 kHz sampling rate. A personal computer based system was used for data acquisition. This circumferential temperature profile was used as a boundary condition for solution of the transient heat conduction equation, from which the local heat flux and Nusselt number profiles could be calculated [van Heiningen et al. 1985]. An essential constraint that enables determination of the surface heat flux by such a sensor is that the heat transfer surface behaves as a semi-infinite solid with the temperature variations at the impingement surface not reaching the other surface.

In the photograph, Figure 4.4, the air supply systems are located above main calender assembly, the heating distribution header in the foreground, the cooling header on the opposite side of the equipment.

The equipment and procedures are detailed in Chapter 3.

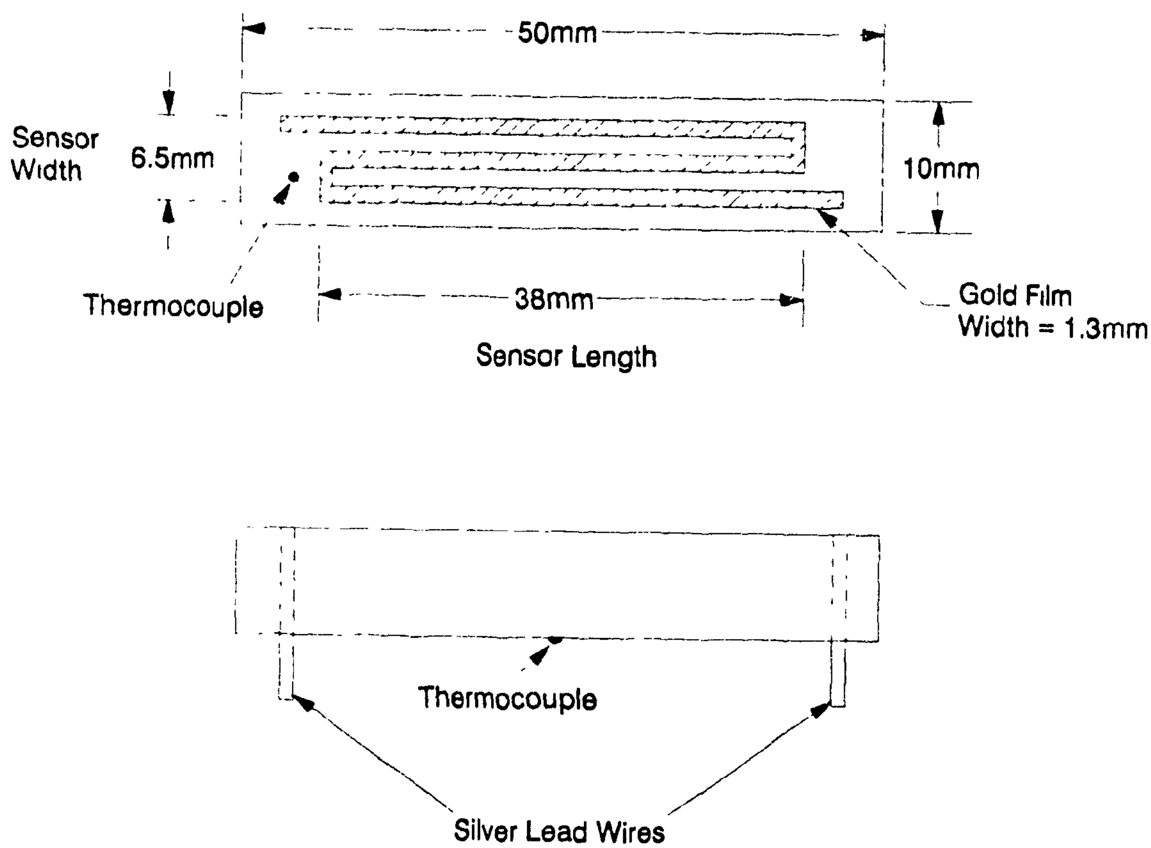

Figure 4.3 The heat flux sensor.

Figure 4.4 Photograph of the CALCON experimental facility.

4.2.2 Experimental Program

The four major topics were:

1. An extensive study of the primary variables affecting heat transfer between unconfined air jets and the calender roll, covering the variables of jet Reynolds number, Re; nondimensional jet-to-impingement surface spacing, H/d; nondimensional jet-to-jet spacing, S/d; and thermal entrainment, characterized using the nondimensional temperature mismatch factor, F.

2. The effects of jet orientation on heat transfer between unconfined air jets and the calender rolls in terms of two position variables, the nozzle circumferential position, ϑ, and nozzle inclination, ψ.

3. The difference in heat transfer performance characteristics between unconfined and confined jets.

4. Consideration of the potential for increasing heat transfer performance by using a staggered array of nozzles instead of the standard in-line array, as suggested by Pelletier et al. [1987].

The geometric variables, H/d, S/d, ϑ, ψ, and Y/d are shown in Figure 4.5. The sign convention for nozzle inclination, ψ, is specified relative to surface motion with ψ positive for a nozzle inclined in the direction of surface motion and vice versa, a convention consistent with the work of Pelletier et al.[1985] and Huang[1989]. For the circumferential position variable, ϑ = 0 and 180 are on the plane passing through the centers of the vertically stacked rolls. Thus the positions of the heating and cooling jet nozzles are at $\vartheta^{\circ} = 90$ and $\vartheta = 270^{\circ}$.

Jet Reynolds number is specified for fluid properties at the nozzle exit. The range of Re used corresponds to nozzle exit velocities in the

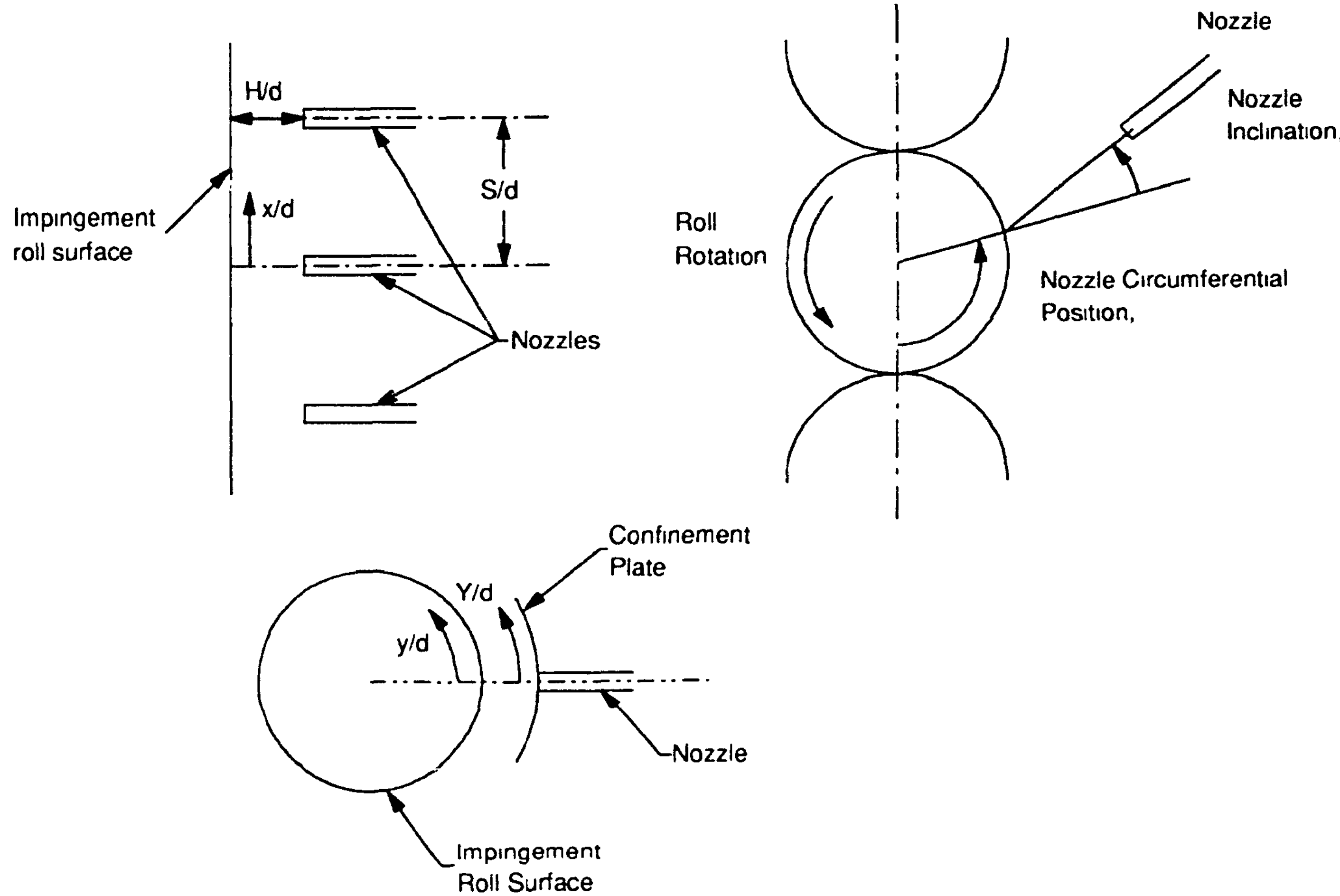

Figure 4.5 Definition of the geometric parameters: nozzle to roll spacing, H/d; nozzle to nozzle spacing, S/d, jet confinement, Y_c; nozzle circumferential position, ϑ; nozzle inclination, ψ

range 15 - 85m/s. The maximum value of the impingement surface motion parameter, M_{vs} = 0.65, at the maximum value of the jet Reynolds number, Re = 118,000, would correspond to an impingement surface speed of v_s = 81m/s. The thermal entrainment factor, F, is that defined by Striegel and Diller[1982] (Equation 4.1).

The range of experimental parameters, Table 4.1, was chosen to reflect current industrial practice for paper machine calender control systems.

Table 4.1: Range of Experimental Parameters

Variable	Range
Nozzle to Impingement Surface Spacing, H/d	$1 < H/d < 8$
Nozzle to Nozzle Spacing, S/d	S/d of 4, 8
Extent of Confinement, Y/d	$0.0 < Y/d < 5.75$
Jet Reynolds number, Re	$22000 < Re < 118000$
Circumferential Nozzle Position , ϑ	$60^\circ \le \vartheta \le 120^\circ$
Nozzle Inclination, ψ	$-45^\circ < \psi < 30^\circ$
Impingement Surface Motion, M_{vs}	$0.02 < M_{vs} < 0.65$
Thermal Entrainment Factor, F	$-0.1 < F < 1.35$
Jet to Surface Temperature difference, $T_j - T_s$	$3 < T_j - T_s < 30$

4.2.3 Sample Experimental Data

A typical circumferential profile of local Nu for unconfined jets ($Y/d = 0$) at the jet centerline, $x/d = 0$, is shown in Figure 4.6. Each such profile shown here is in fact the average for the data collected over 50 successive rotations. On each rotation the sensor moves from $\vartheta = 0^\circ$ to $\vartheta = 360^\circ$, passing first through the heating then through the cooling jet impingement regions. Negative values of y/d indicate the region where the impingement surface is approaching the impingement region (termed the upstream side of the profile) while positive y/d corresponds to the region leaving the jet impingement point (termed the downstream side). The general features of these profiles of local Nu are not discussed here because the existence of off-stagnation minima and maxima and their causes are well known and have been described for round jets most recently by Obot[1981]. These Nu profiles, besides providing information regarding local conditions, form the basis for the integrated average Nusselt number used in most of the discussion.

Examination of heat flux profiles for heating jets, Figure 4.7, shows that, for the range of nozzle exit temperatures (19°C to 55°C) and jet confinement ($0 \le Y/d \le 5.75$) which are the experimental limits in this study, 90% ($\Delta T = 4.89^\circ$C, $Y/d = 0$) to 97% ($\Delta T = 23.1^\circ$C, $Y/d = 0$ and $\Delta T = 12.5^\circ$C, $Y/d = 5.75$) of heat occurs in the range $y/d = \pm 10$. To avoid including regions where heat transfer is dominated by ambient temperature effects, profiles in all subsequent figures were limited to the range $y/d = \pm 10$.

On the cooling jet of the equipment the air temperature could not readily be controlled as the air cooler was best operated at constant load. Although the cooling nozzle exit temperature varied as inlet air temperature changed, the rate of T change was never greater than small

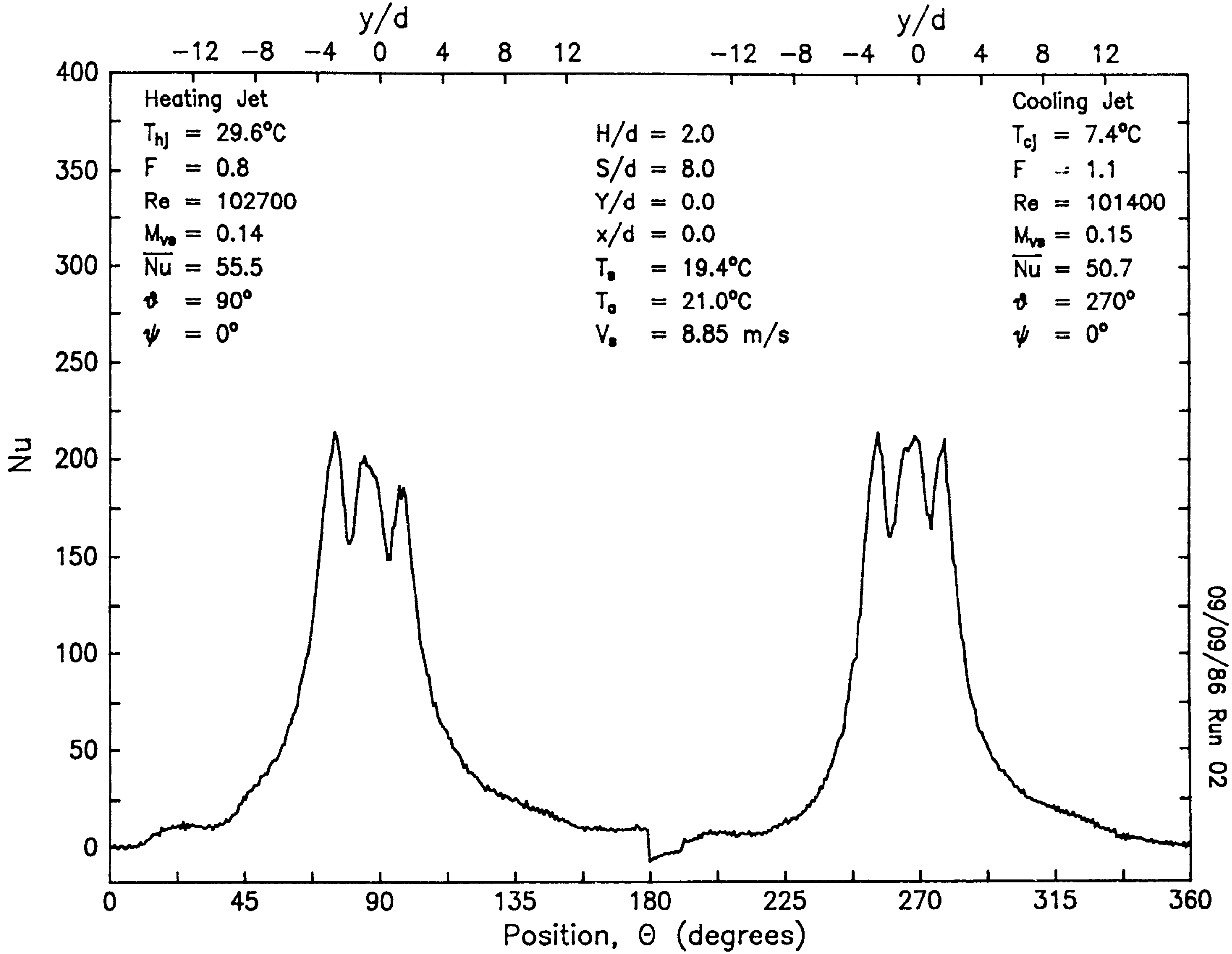

Figure 4.6 Typical complete circumferential profile of local Nusselt number at the jet centerline, x/d = 0, of the middle jet.

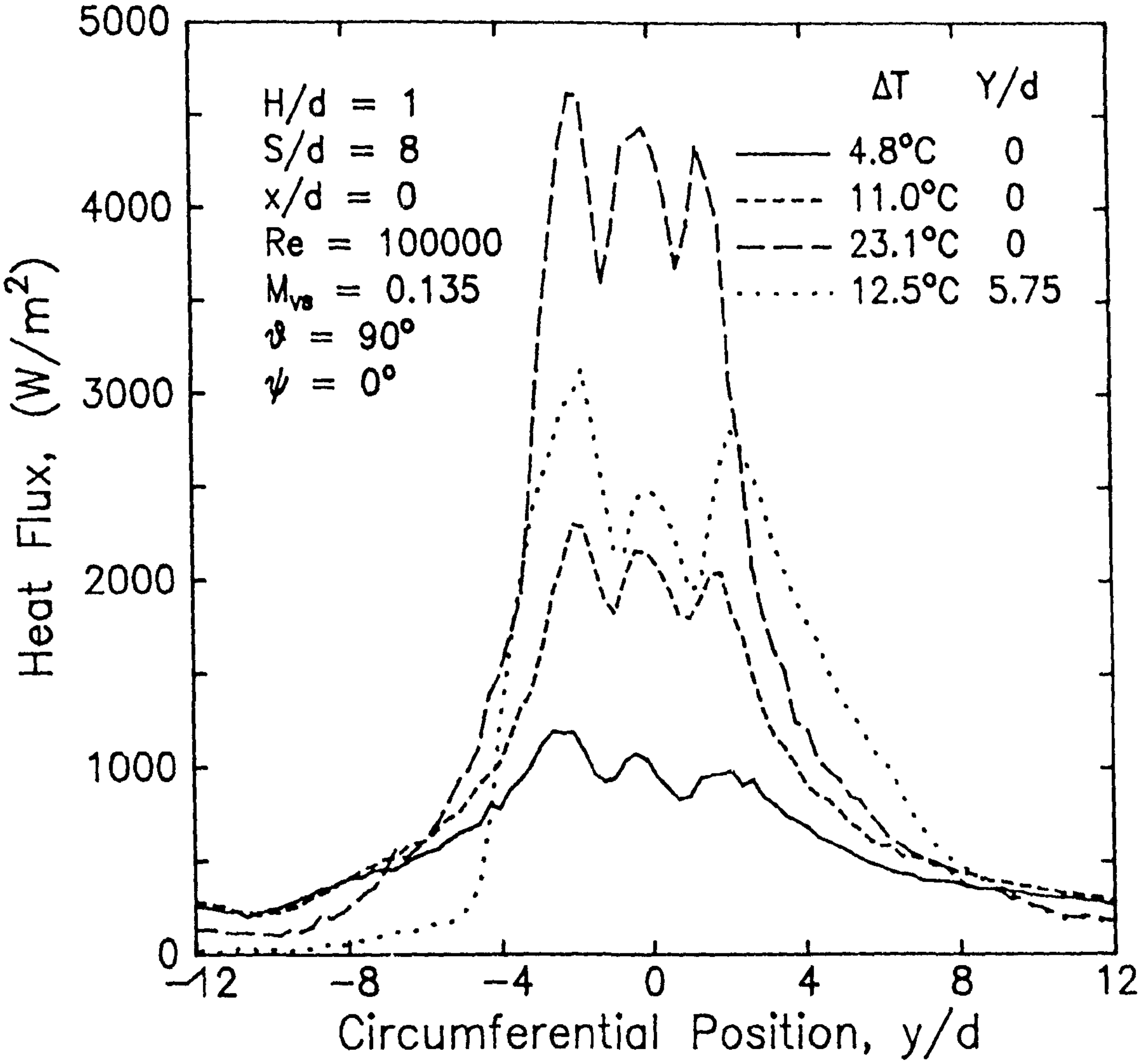

Figure 4.7 Circumferential heat flux profiles.

relative to the duration of an experimental run (<2 min). On the heating side, the air temperature could be varied readily from room temperature to approximately 65°C. Since T_j of the heating jet could be precisely controlled, most of the experimental data are for the heating side. The cooling side was used to monitor the condition of the heat flux sensor. Under constant or slowly changing operating conditions, changes in the calibration of this very fragile sensor could be monitored and thus the time when a recalibration was needed could be conveniently detected.

4.2.4 Effect of Surface Motion

The effect of surface motion on the circumferential profile of local Nusselt number, at the nozzle centerline, x/d = 0, is shown in Figures 4.8 and 4.9. As in the studies of van Heiningen [1982], Huang[1988] and Polat [1988], surface motion is characterized by the nondimensional mass flux ratio,

$$M_{vs} = \frac{\rho_s V_s}{\rho_j V_j} \tag{4.4}$$

which is consistent with the characterization of crossflow used by Bouchez [1973] and Sparrow et al. [1975].

Figure 4.8 shows that for the axisymmetric jets used here there is no significant effect of impingement surface motion on Nusselt number profile for M_{vs} up to 0.26 at Re = 100000. At that Reynolds number the M_{vs} range corresponds to impingement surface velocity up to V_s = 14.3 m/s. There are no discernable effects of M_{vs} on the magnitude of the heat transfer or on the location of the stagnation point or the off-stagnation maxima and minima.

The work of van Heiningen [1982] and Polat [1988] showed that for a

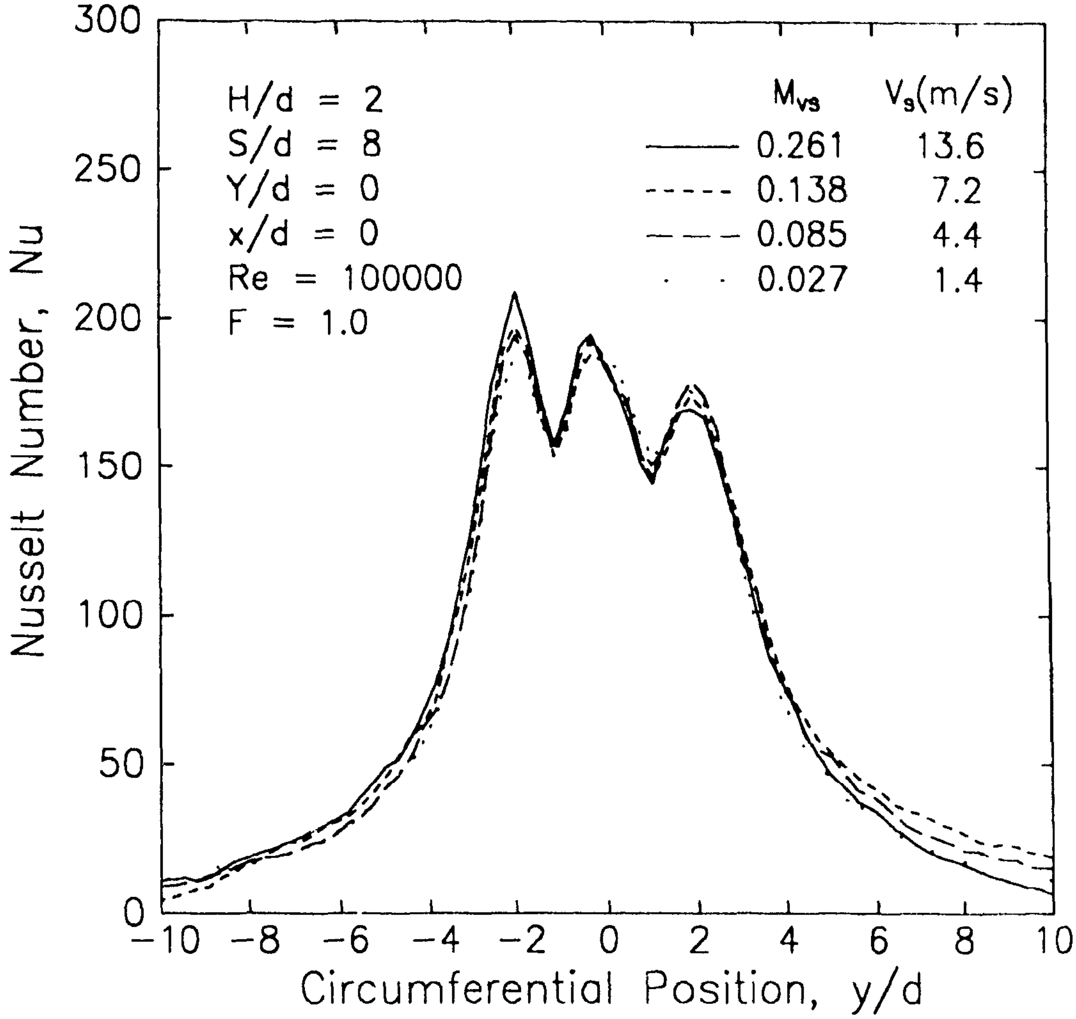

Figure 4.8 Effect of impingement surface speed on local Nu profile at constant jet Reynolds number.

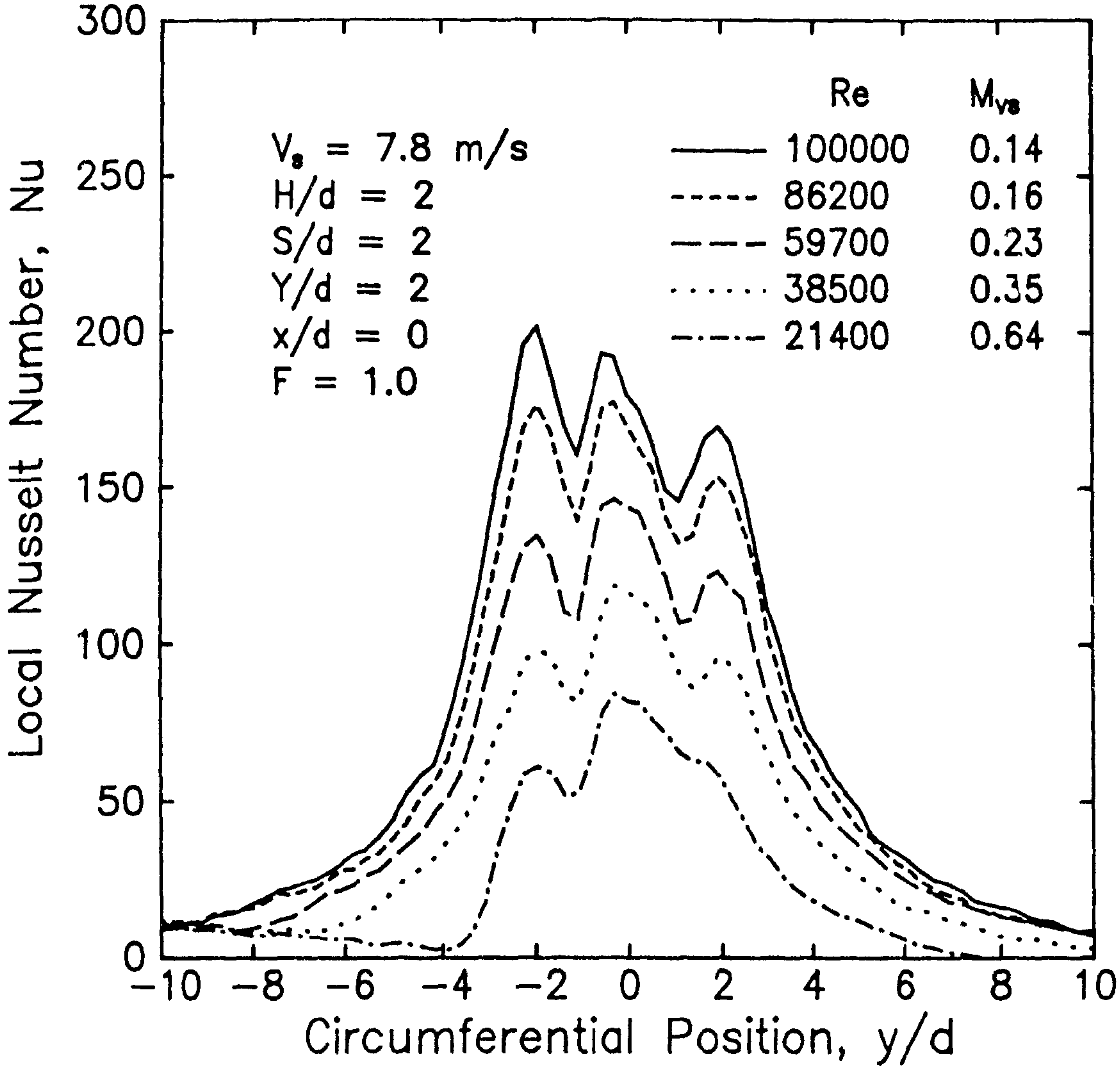

Figure 4 9 Effect of jet Reynolds number and surface motion, M_{vs}, on local Nu profile at constant impingement surface speed.

slot jet the Nu profile becomes skewed in the direction of surface motion at values of M_{vs} near 0.13. Because a slot jet maximizes the effect of a moving impingement surface on the jet, it would be expected that the threshold value of M_{vs} which would cause skewing of the profiles would be higher for a round jet than a slot jet, as established by the present results.

To increase the range of M_{vs} values to 0.64, Re was reduced to 21400 from 100000, with the surface speed held constant at 7 8m/s. Figure 4.9 shows that the Nu profiles remain symmetrical at M_{vs} = 0.35 but are significantly asymmetrical when surface motion is increased to M_{vs} = 0.64. At this value of M_{vs} the wall jet region on the approaching side of the Nu profile, always shown with negative y/d, is displaced in the direction of surface motion. On the downstream side, surface motion as high as M_{vs} = 0.64 suppresses the off-stagnation minimum and maximum As the associated boundary layer phenomena have been well described by Polat[1988] and Huang[1988], this aspect is not discussed here.

As M_{vs} is increased, the decrease in Nu profiles on the upstream side of the stagnation point, as also observed by van Heiningen[1982] and Polat[1988] for confined slot jets, is attributed to a decrease in the actual film temperature driving the heat transfer, due in turn to the entrainment of a boundary layer of air by the impingement surface motion. Since impingement Nu is traditionally defined in terms of the jet to surface temperature difference, ΔT_{js}, this decrease in heat flux is reflected by a corresponding reduction in Nu.

Although the mechanism whereby surface motion affects Nu profiles may be the same for round and slot jets, the latter are more sensitive to surface motion. Thus according to van Heiningen and Polat, profiles are affected at values of M_{vs} as low as 0 1 for slot jets but, as the present study indicates, not until this parameter is in the range $0.35 \leq M_{vs} \leq 0.64$ for round jets. In the case of slot jets, air entrained by the surface motion must either reverse direction as it approaches the jet centerline or, given the right conditions, pass under the jet. For round jets, the air entrained by the surface motion has less effect since it may continue from the approach to the leaving side by simply deflecting off the jet centerline. There is, therefore, less thermal degradation of the impinging jet air flow and thus less effect of surface motion on impingement heat transfer for round as compared to slot jets..

For impingement on stationary surfaces, stagnation Nusselt number, Nu_o, varies as the square root of Reynolds number. A plot of the $Nu_o/Re^{0.5}$ - M_{vs} data, Figure 4.10, shows no effect of surface motion on the stagnation point Nusselt number for $M_{vs} < 0.35$, with an average value of $Nu/Re^{0.5} = 0.59$. At $M_{vs} = 0.64$ the value of $Nu/Re^{0.5}$ is slightly lower by only 3%, a difference within the experimental error.

Another illustration of the lack of a surface motion effect is provided by comparing the local Nusselt number profiles which result from switching the roll rotation from clockwise to counterclockwise, Figure 4.11. The small difference between these profiles is well within measurement error. It interesting to note that in both cases the secondary maximum for negative y/d is higher than that on the positive side The profile obtained with counterclockwise rotation has been flipped so that on Figure 4.11, the same y/d corresponds to the same physical location on the roll surface. Thus the negative y/d side for clockwise rotation is where the surface is approaching the nozzle while for counterclockwise rotation, negative y/d corresponds, exceptionally, to the surface leaving the nozzle. Therefore the slight skewing of the

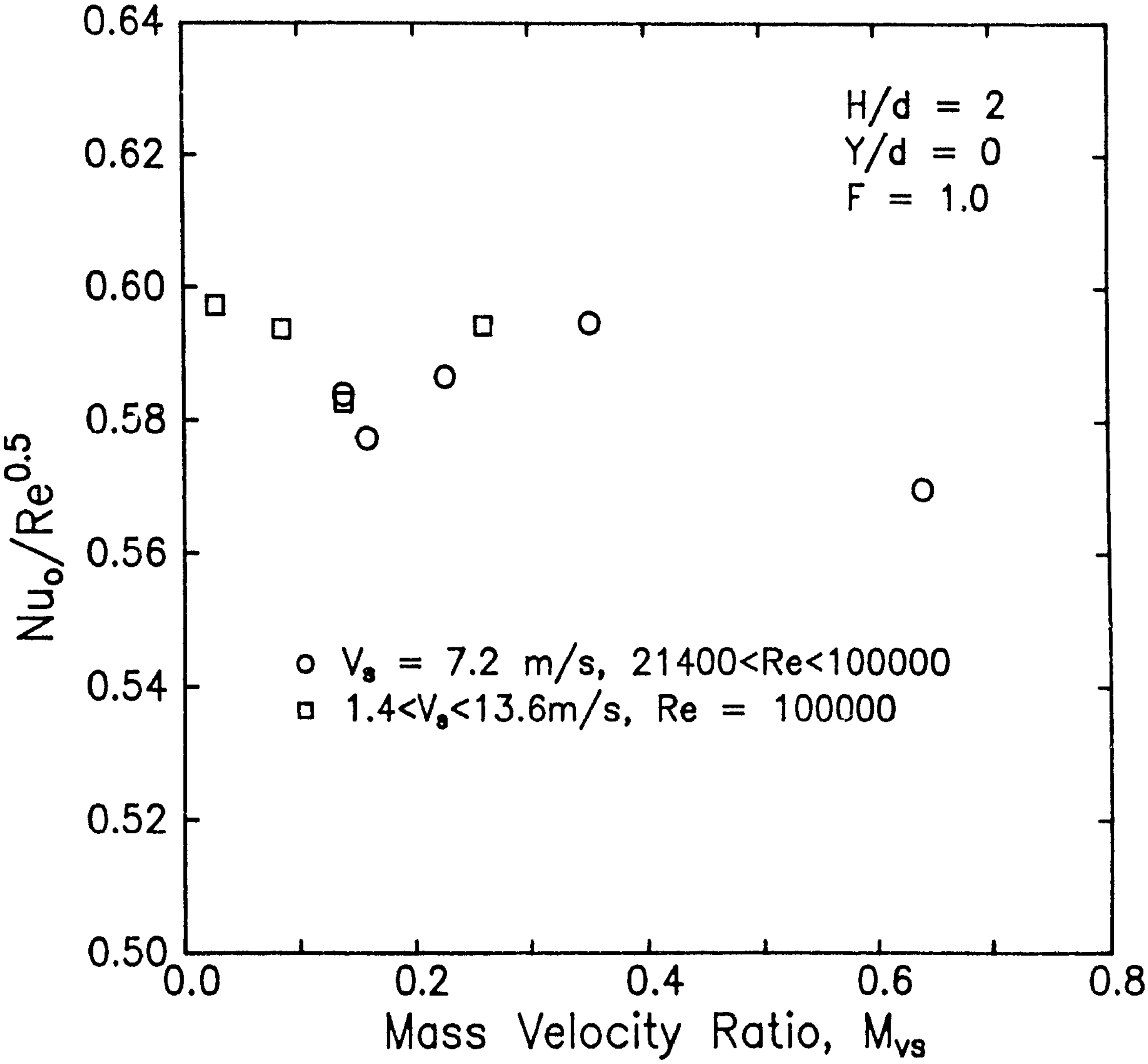

Figure 4.10 The effect of M_{vs} on the ratio $Nu_o/Re^{0.5}$

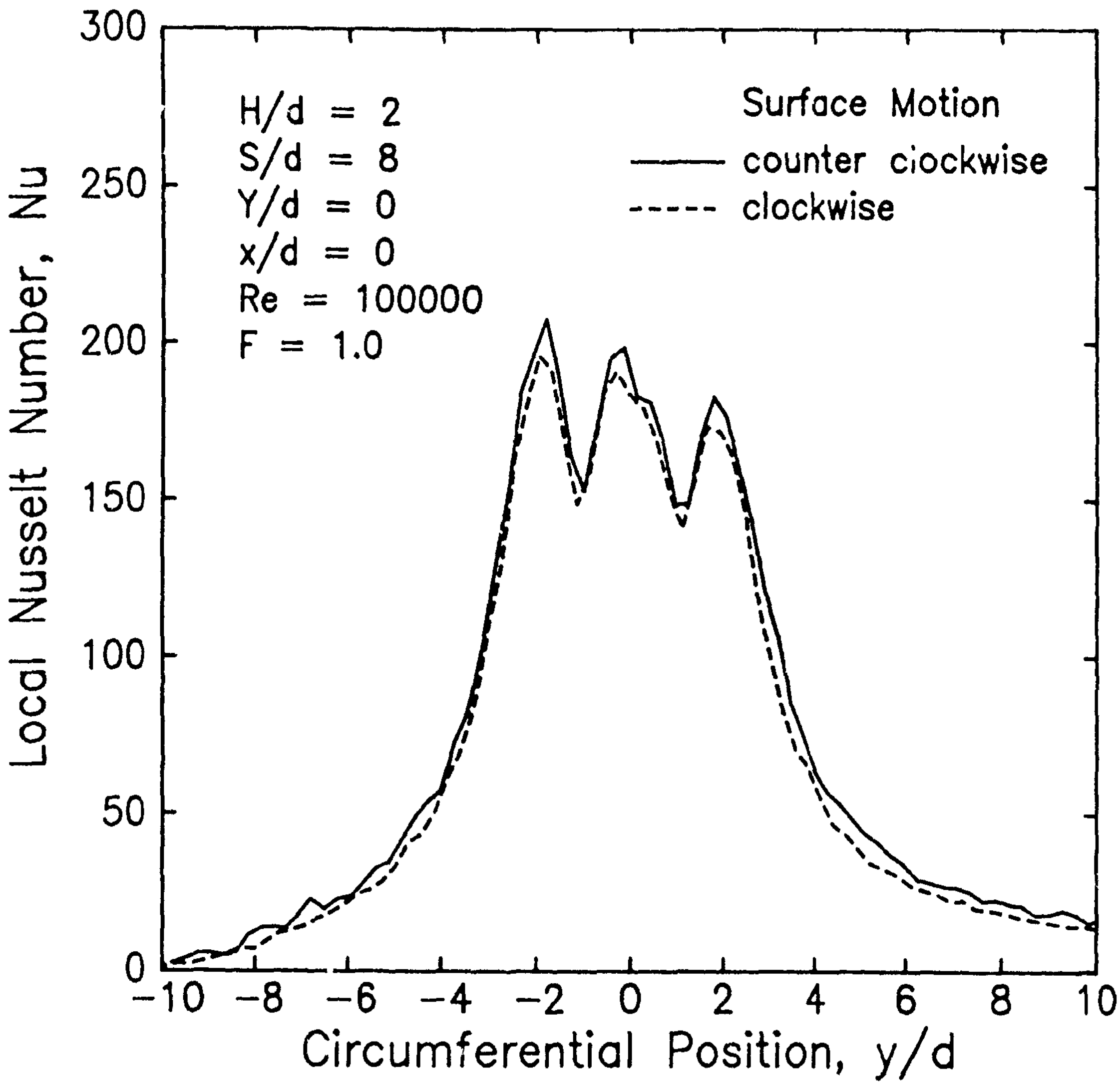

Figure 4.11 Local Nusselt number profiles obtained by changing the direction of surface motion.

Nusselt profile is clearly not caused by surface motion or any sensor asymmetry, but is due to either a slight nozzle misalignment or to imperfect symmetry of the industrial calender control nozzles used in the present study.

The conclusion from these observations is that over the range of jet Reynold number ($60000 < Re < 118000$) and surface velocity up to 14.3 m/s, a range of interest for calender control, the effect of paper machine speed on impingement heat transfer at the calender roll is sufficiently small to be neglected.

4.3 Heat Transfer Under Unconfined, Normally Impinging Jets

4.3.1 Circumferential Profile of Local Nusselt Number

(a) General Features

The effect of Re and H/d on the circumferential distribution of local Nusselt number at the axial position corresponding to the nozzle centerline, $x/d = 0$, is shown in Figures 4.12 and 4.15 for impingement heat transfer with a thermal effect of entrainment corresponding to a temperature mismatch, $F = 1.0$. This value of F is chosen frequently for comparison purposes in the present study because in typical industrial calender control systems the temperature mismatch is usually in the range, $0.75 \leq F \leq 1.2$, with heating jets slightly greater than 1.0 and cooling jets slightly less than 1.0. As these profiles illustrate the characteristics of axisymmetric impingement heat transfer profiles, which are well known, the results (the base case of the present study) are discussed only briefly. Thus at combinations of sufficiently high Re and sufficiently low H/d, the previously studied occurrence of minima and maxima at y/d of about ±1.2 and ±2.0, respectively, is seen again

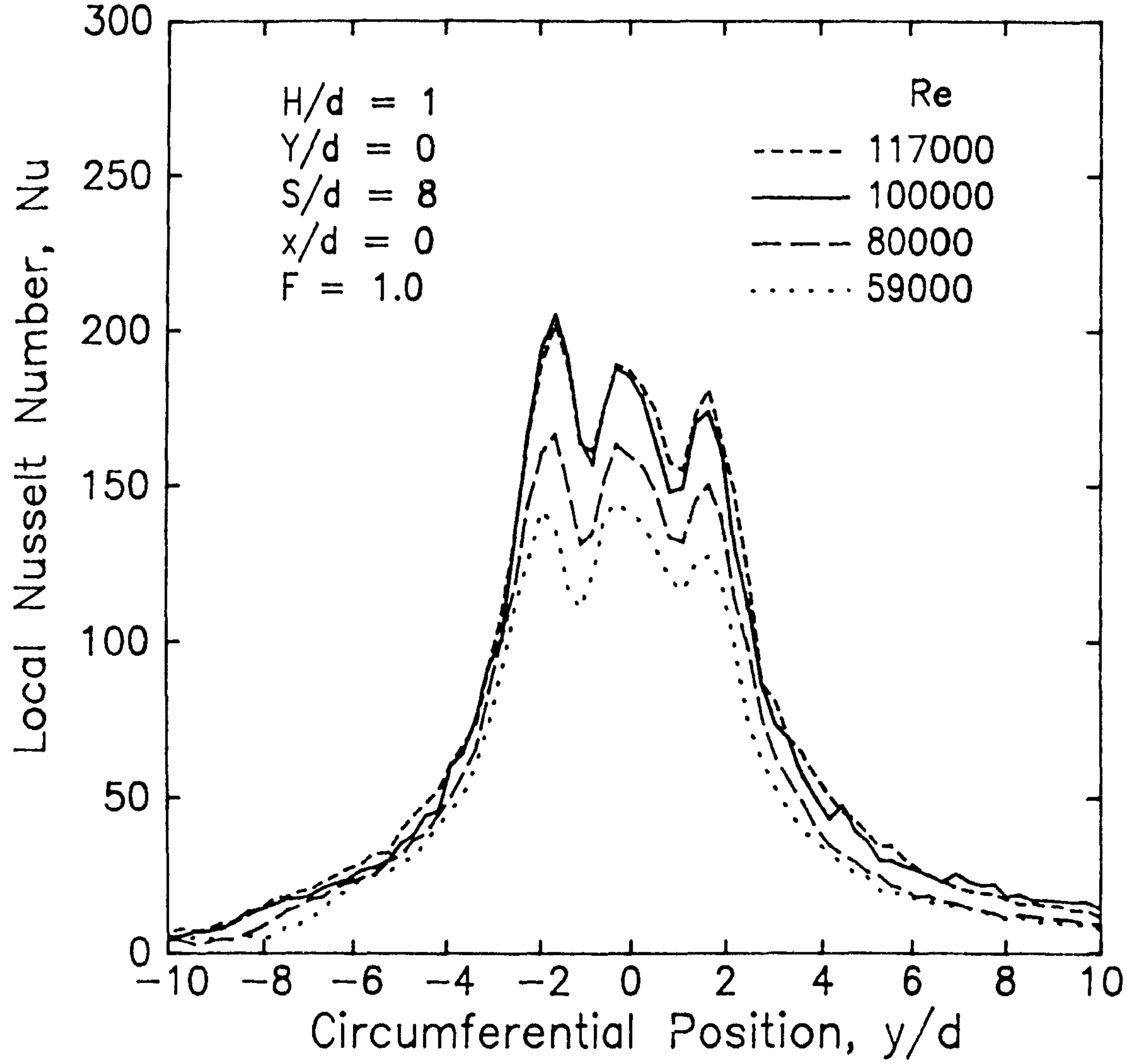

Figure 4.12(a) Effect of jet Reynolds number, Re, on circumferential profiles of local Nusselt number of unconfined jets: H/d = 1 and F = 1.0.

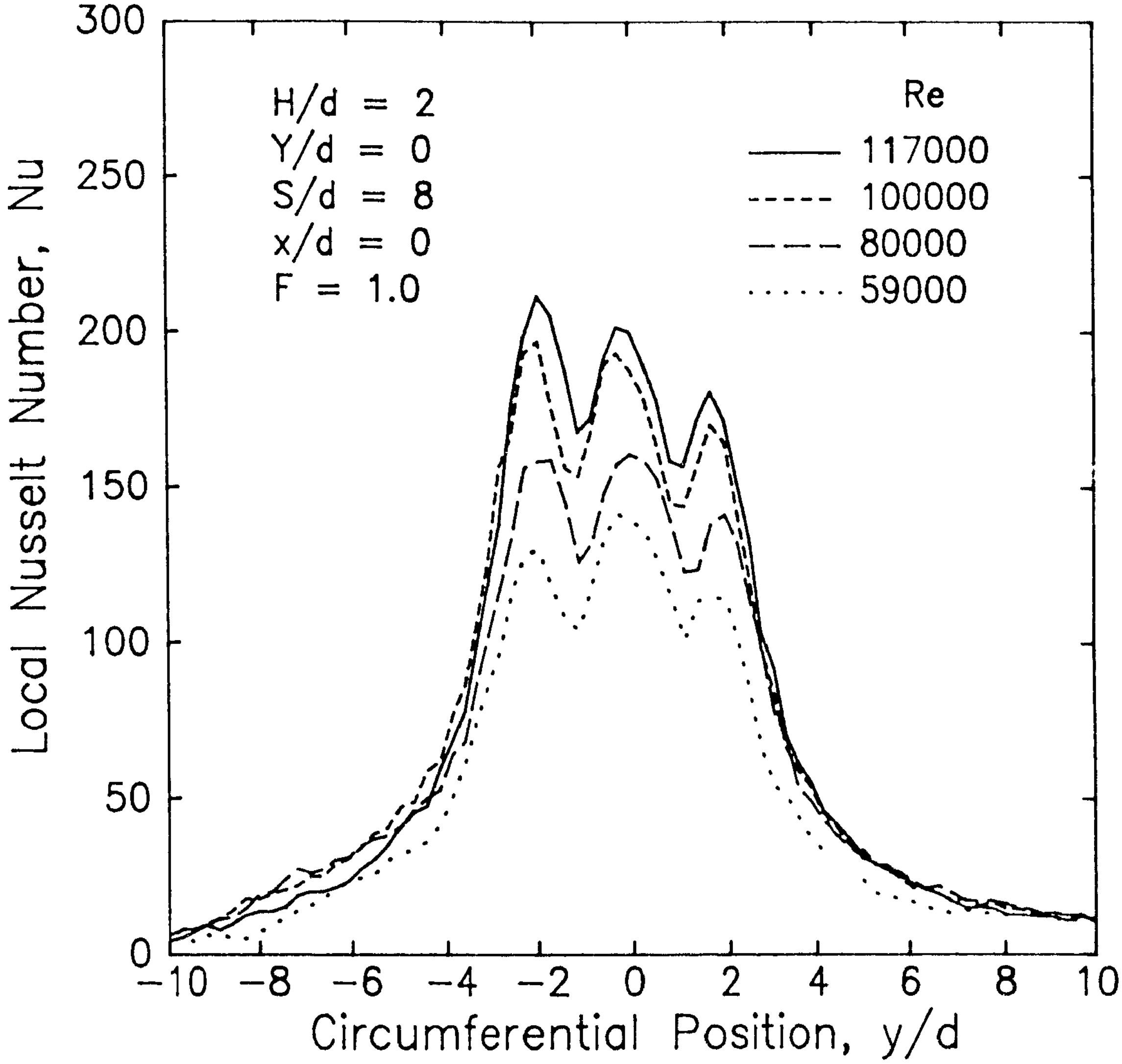

Figure 4 12(b) Effect of jet Reynolds number, Re, on circumferential profiles of local Nusselt number of unconfined jets H/d = 2 and F = 1.0.

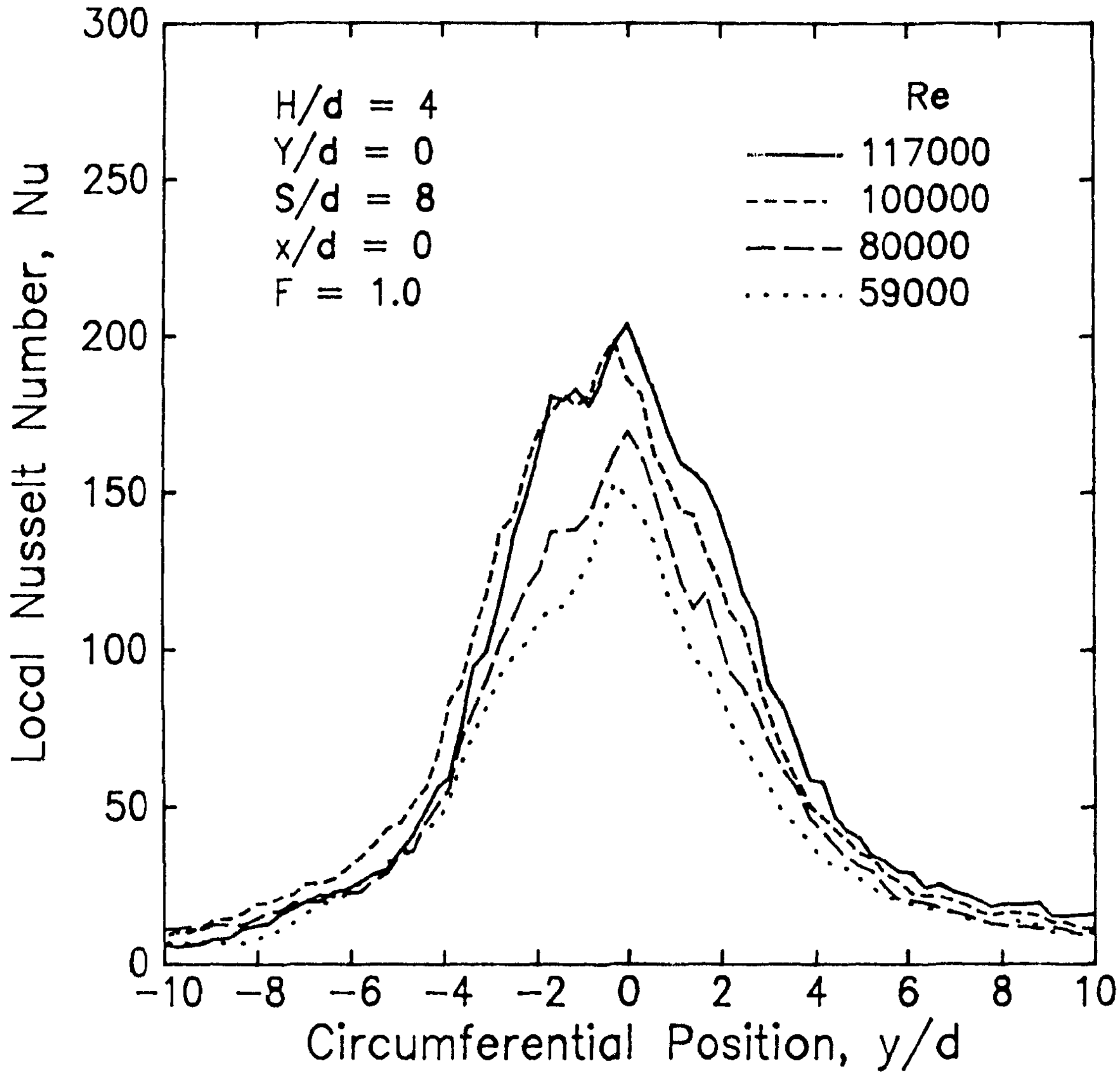

Figure 4.12(c) Effect of jet Reynolds number, Re, on circumferential profiles of local Nusselt number of unconfined jets: H/d = 4 and F = 1.0.

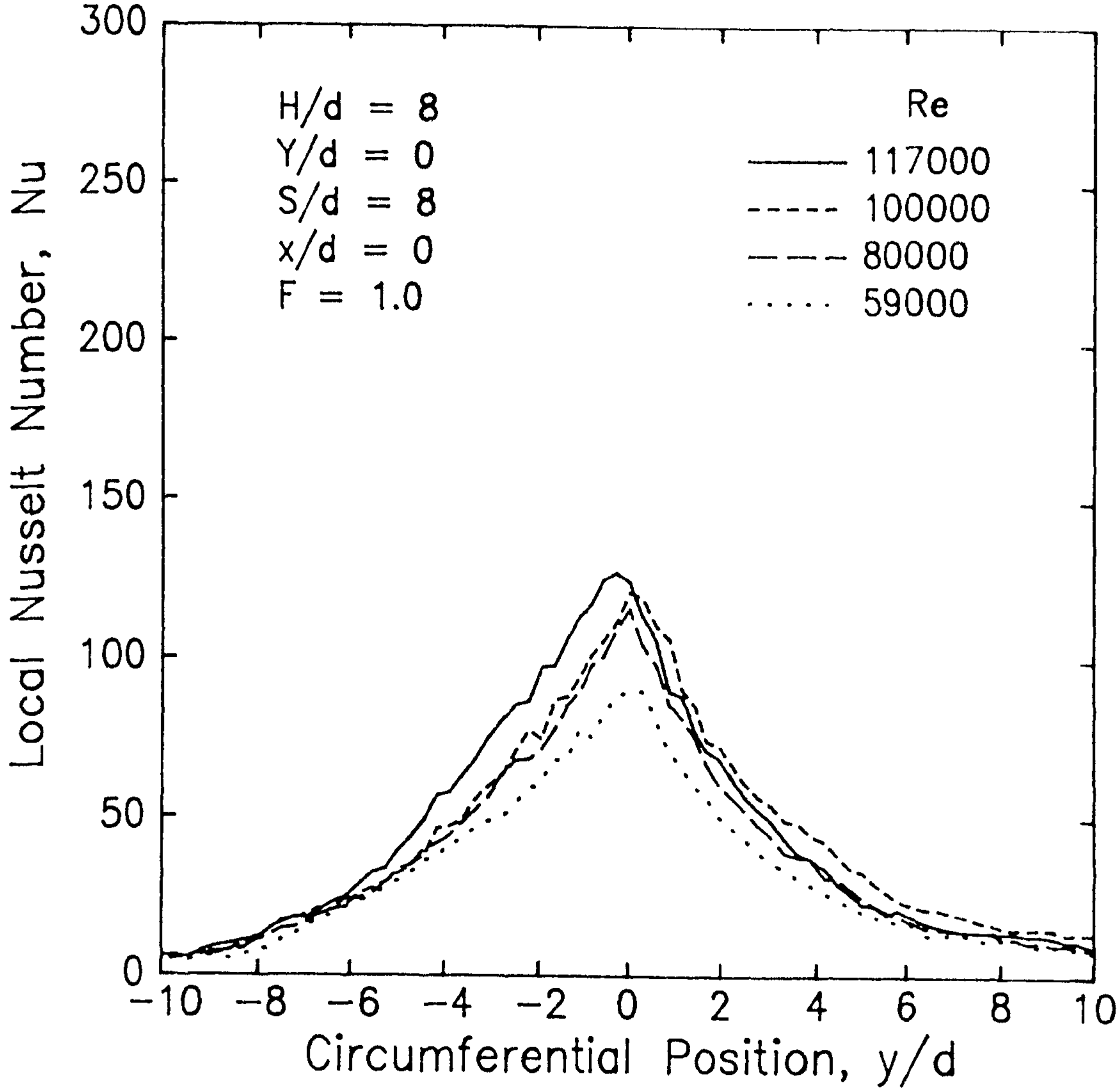

Figure 4.12(d) Effect of jet Reynolds number, Re, on circumferential profiles of local Nusselt number of unconfined jets H/d = 8 and F = 1.0.

chere for the conditions of Figure 4.12. For this range of Re, these off-stagnation features are prominent at spacings, H/d, of 1 and 2, are barely discernible at H/d = 4, while by H/d = 8, Figure 4.12(d), they do not occur. For H/d $\leq$ 2, Figures 4.12(a) and 4.12(b) show that the values of Nu at the off-stagnation maxima are more sensitive to Re than is stagnation point. The slight skewing of the Nu profile in the impingement region, apparent for the close H/d spacings of Figures 4.12(a) and 4.12(b), which disappears for Re < 40000 was analyzed in connection with Figure 4.11.

These characteristics are in agreement with the work of Gardon and Cobonpue[1962], Gardon and Akfirat[1965], Koopman and Sparrow[1975] and Obot[1980]. The profiles obtained by Gardon and co-workers, generally acknowledged as being among the best available, are shown in Figures 4.13 and 4.14. The absence in the present results of the stagnation point minimum they found can be attributed to sensor averaging since the stagnation point minima has a diameter of about 0.6d while the dimensions of the sensor used in the present study is 0.27d by 1.45d in the circumferential and axial directions respectively.

None of the present results show a minimum in local Nu near y/d = 5.2 that was reported by Obot [1980]. As that is the only study to report such a minimum, it may be attributed to some equipment specific effect.

The effect of nozzle to roll spacing, H/d, on the circumferential profile of local Nu is shown in Figure 4.15 for the measurements made at Re = 100000 and F = 1.0. At this Re the off-stagnation maxima begin to disappear as nozzle spacing, H/d, is increased from 2 to 4. The vestigial shoulders remaining at H/d = 4 have completely disappeared when H/d = 6. The behavior of the stagnation point Nusselt number, Nu_o, is discussed in Section 4.3.2.

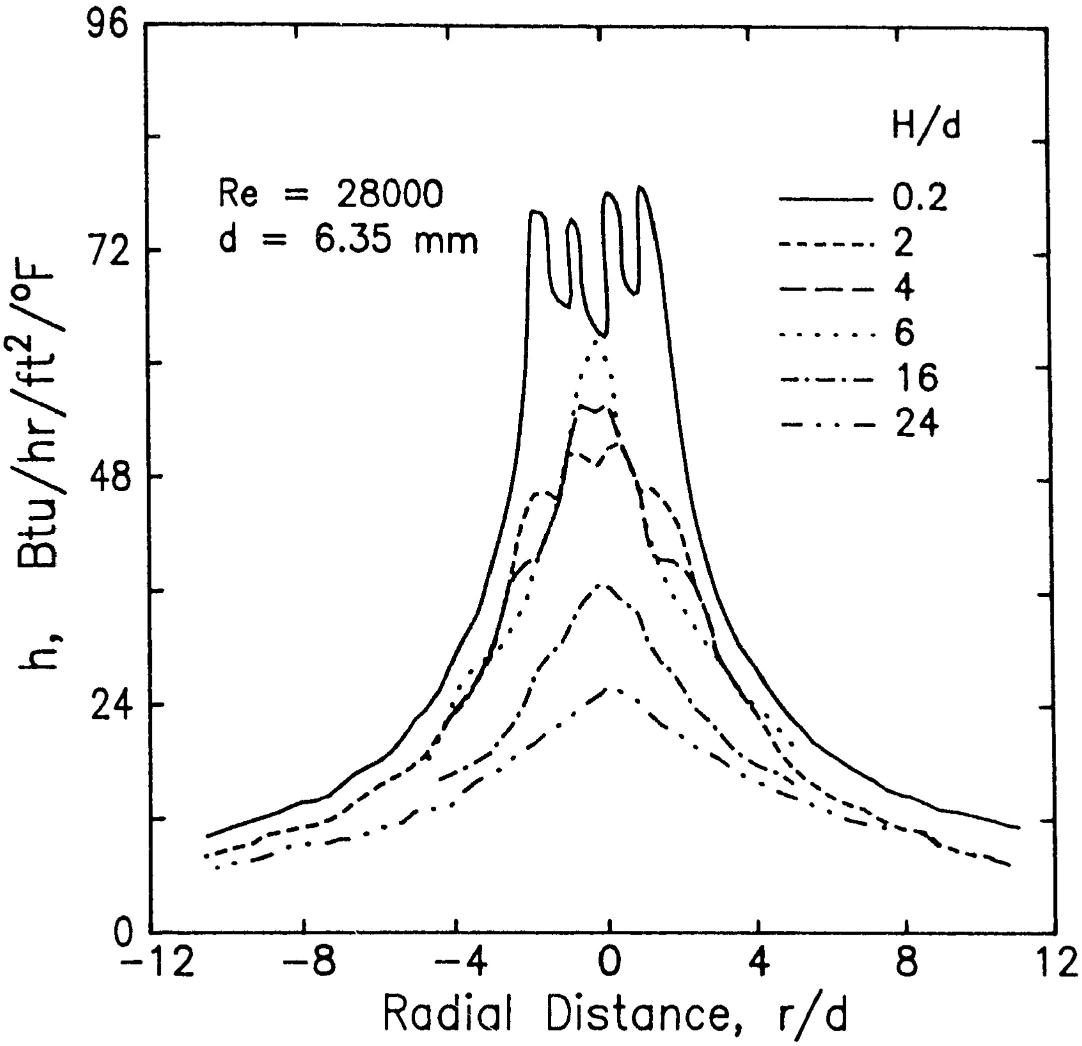

Figure 4.13 Effect of H/d on profiles of local heat transfer coefficient for Re = 28000 - Gardon and Cobonpue [1962]

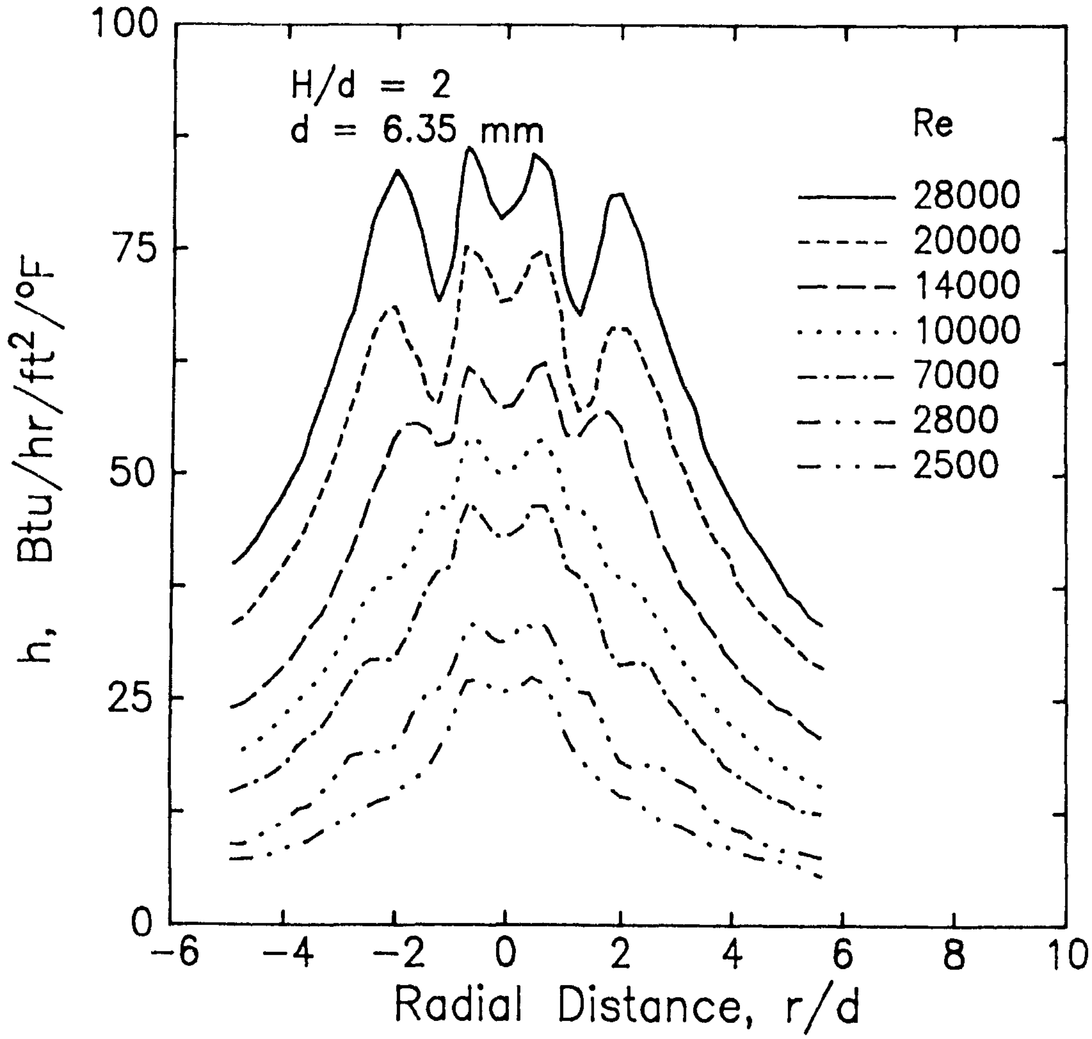

Figure 4.14 Effect of Re on profiles of local heat transfer coefficient for H/d = 2 - Gardon and Akfirat[1962].

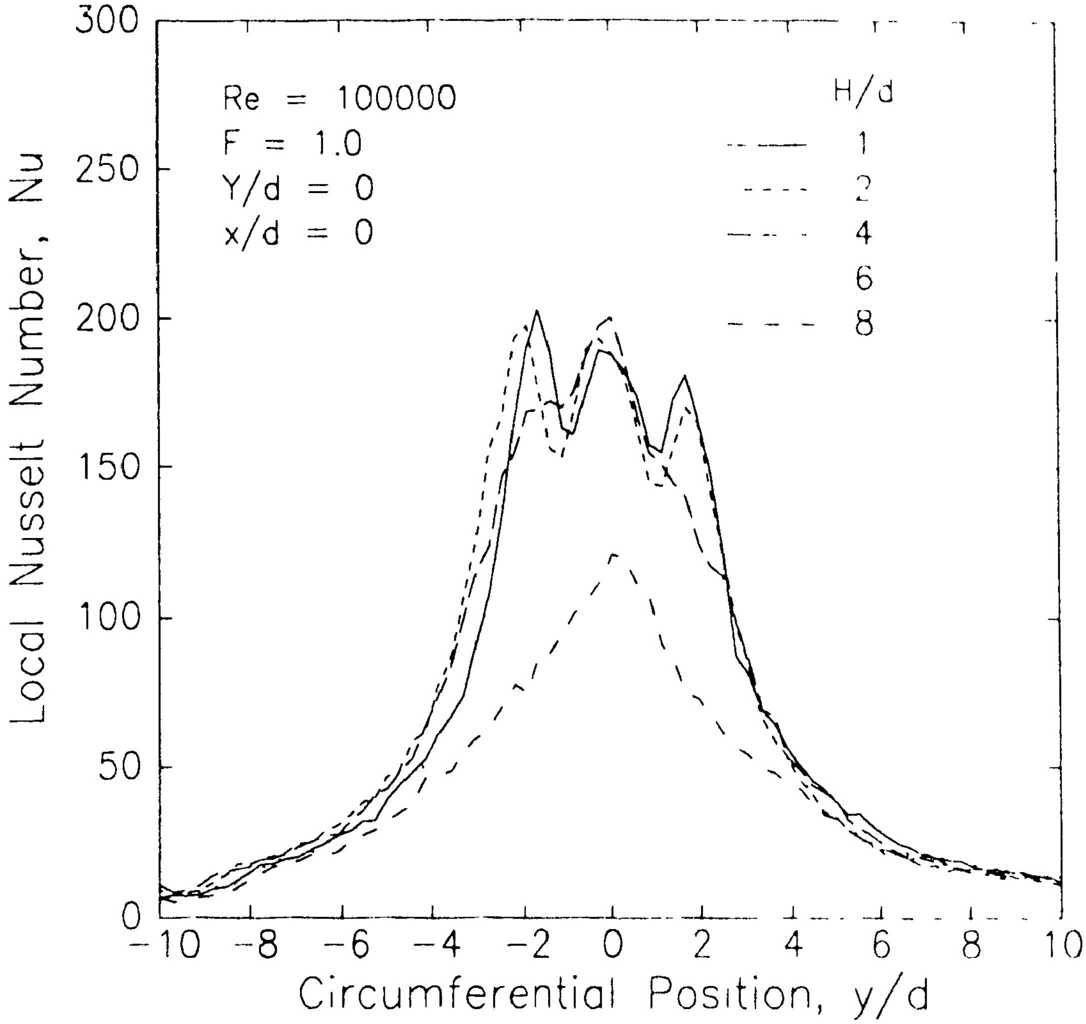

Figure 4.15 Effect of nozzle-to-impingement surface spacing, H/d, on profiles of local Nusselt number for unconfined jets at Re = 100000 and F = 1.0.

(b) Effect of Entrainment

The effect on circumferential profiles of local Nu which is caused by the entrainment by unconfined jets of air at ambient temperature is shown in Figures 4.16(a) to 4.16(d) for a fixed Re = 100000 and a range of nozzle to roll spacings, H/d, from 1 to 8. Nusselt number is defined using jet to impingement surface temperature difference, $(T_j - T_s)$ or ΔT_s, with the physical properties evaluated at T_j. This standard Nusselt number is strongly dependant on the temperature mismatch, $(T_j - T_a)$ or ΔT_a, expressed here nondimensionally as F, the ratio $\Delta T_a / \Delta T_s$. With this definition, when the ambient temperature is the same as the nozzle exit temperature, F = 0.0. F increases as T_a drops below T_j for a heating jet and as T_a increases above T_j for a cooling jet, in both cases with a degradation of the heat transfer by entrainement. In the opposite, but less frequent case, F becomes negative and impingement heat transfer is enhanced by entrainement

With increasing temperature mismatch, F, the strong reduction in heat transfer over the entire circumferential profile at the larger nozzle to impingement surface spacing, H/d of 4 and 8, is readily understandable. These spacings provide for substantial entrainment and thus degradation of the temperature driving force for heat transfer at the impingement surface. While the absolute reduction in local Nu for a specific temperature mismatch, F, is about uniform over the entire profiles, Figure 4.14(c) and 4.14(d), the relative reduction increases strongly from the stagnation point to the wall jet region. This trend is as expected, because degradation of the local potential for heat transfer caused by entrainment increases with the time available for entrainment, hence with distance from the stagnation point.

With increasing temperature mismatch, F, at close nozzle to

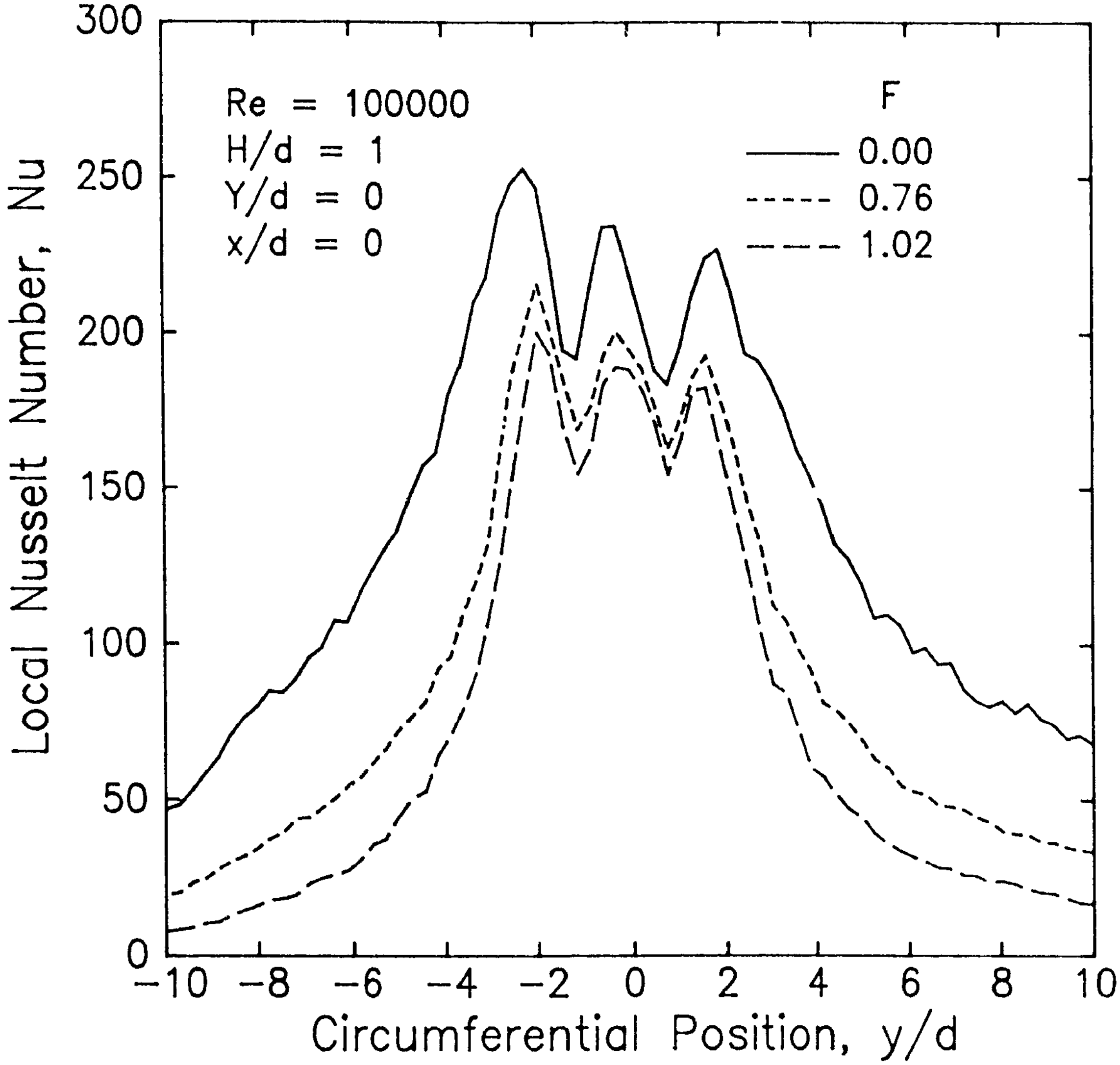

Figure 4.16(a) Effect of jet thermal entrainment factor, F, on circumferential profiles of local Nusselt number of unconfined jets: H/d = 1 and Re = 100000.

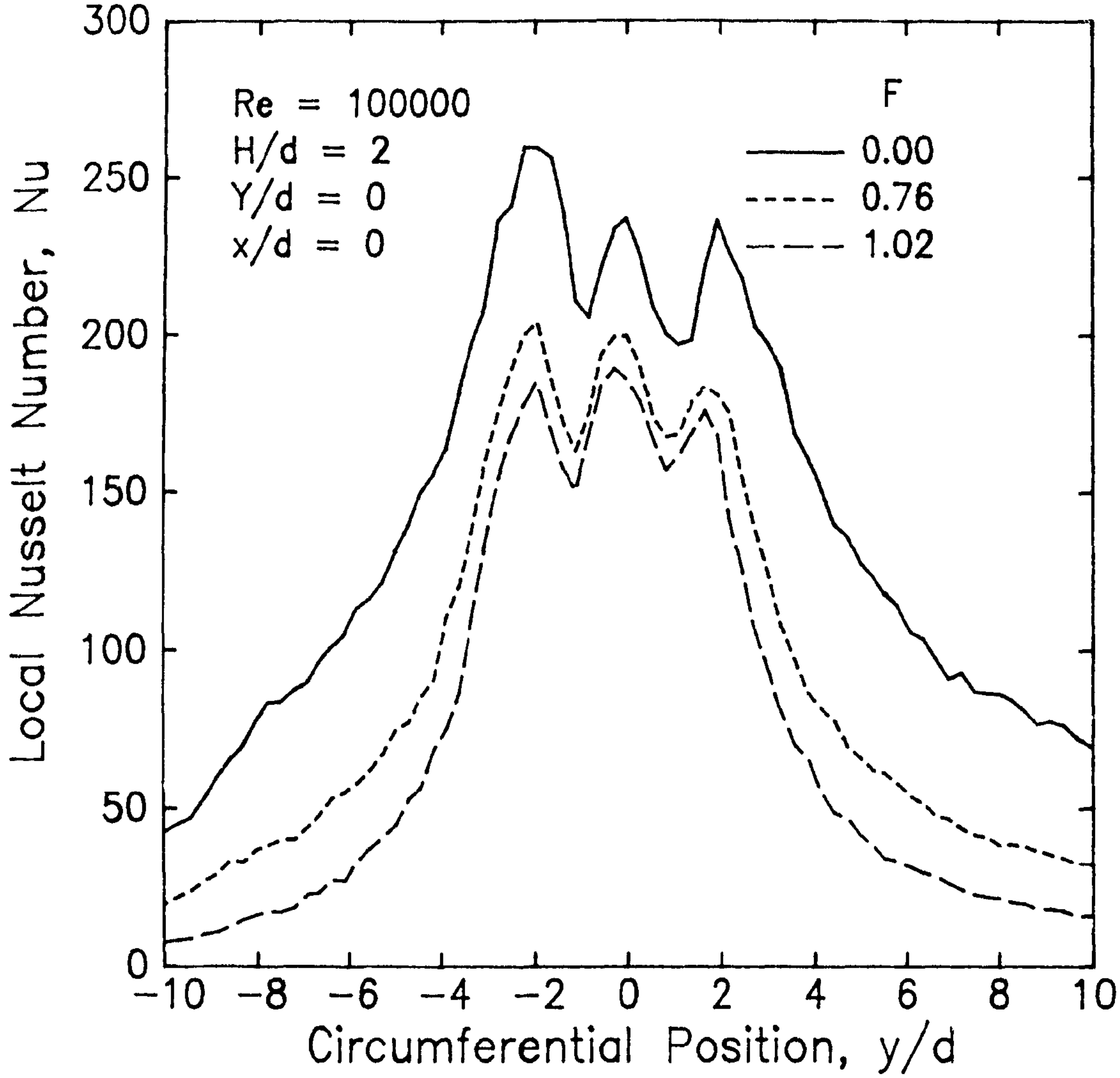

Figure 4 16(b) Effect of jet thermal entrainment factor, F, on circumferential profiles of local Nusselt number of unconfined jets: H/d = 2 and Re = 100000.

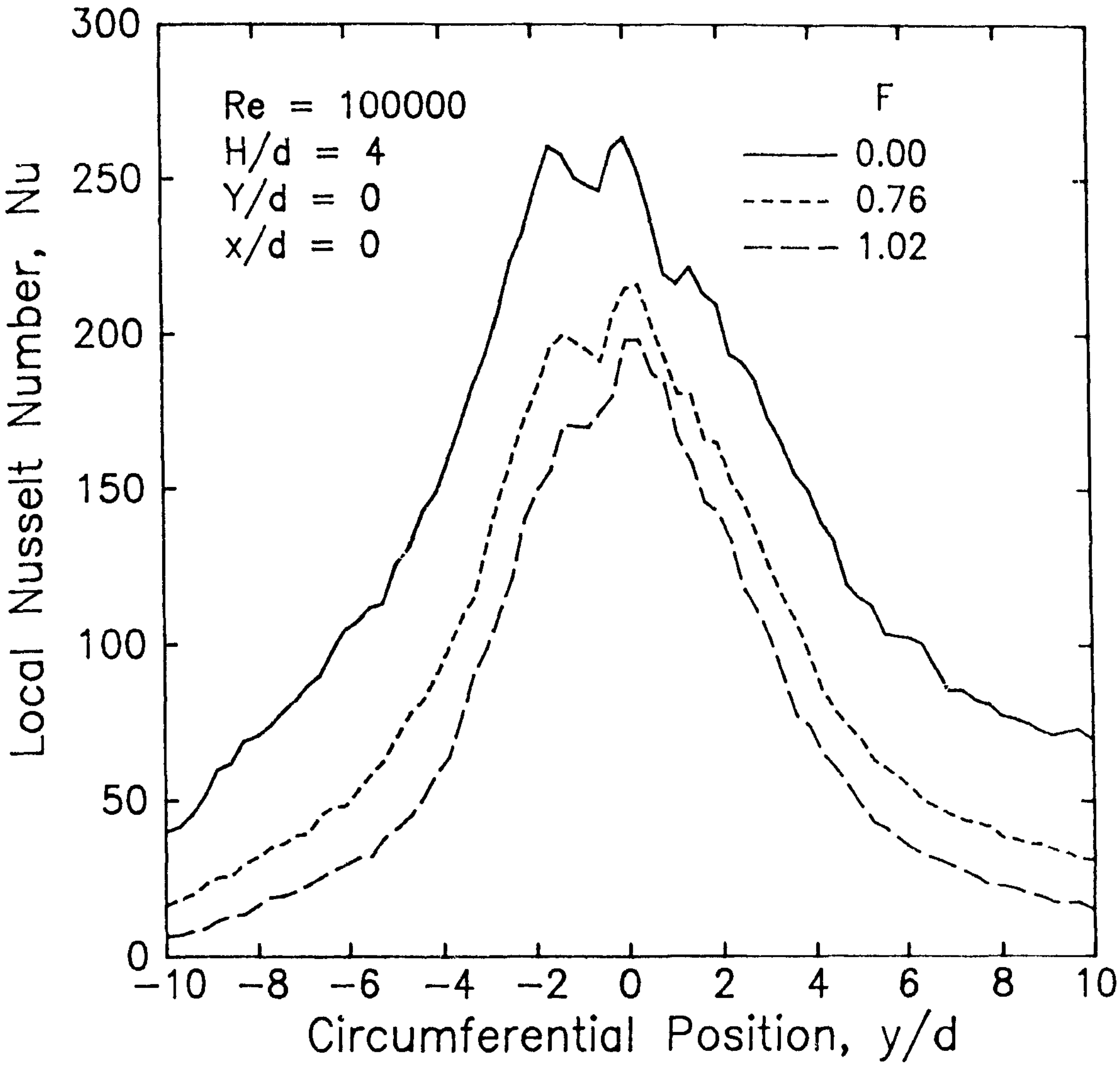

Figure 4.16(c) Effect of jet thermal entrainment factor, F, on circumferential profiles of local Nusselt number of unconfined jets: H/d = 4 and Re = 100000.

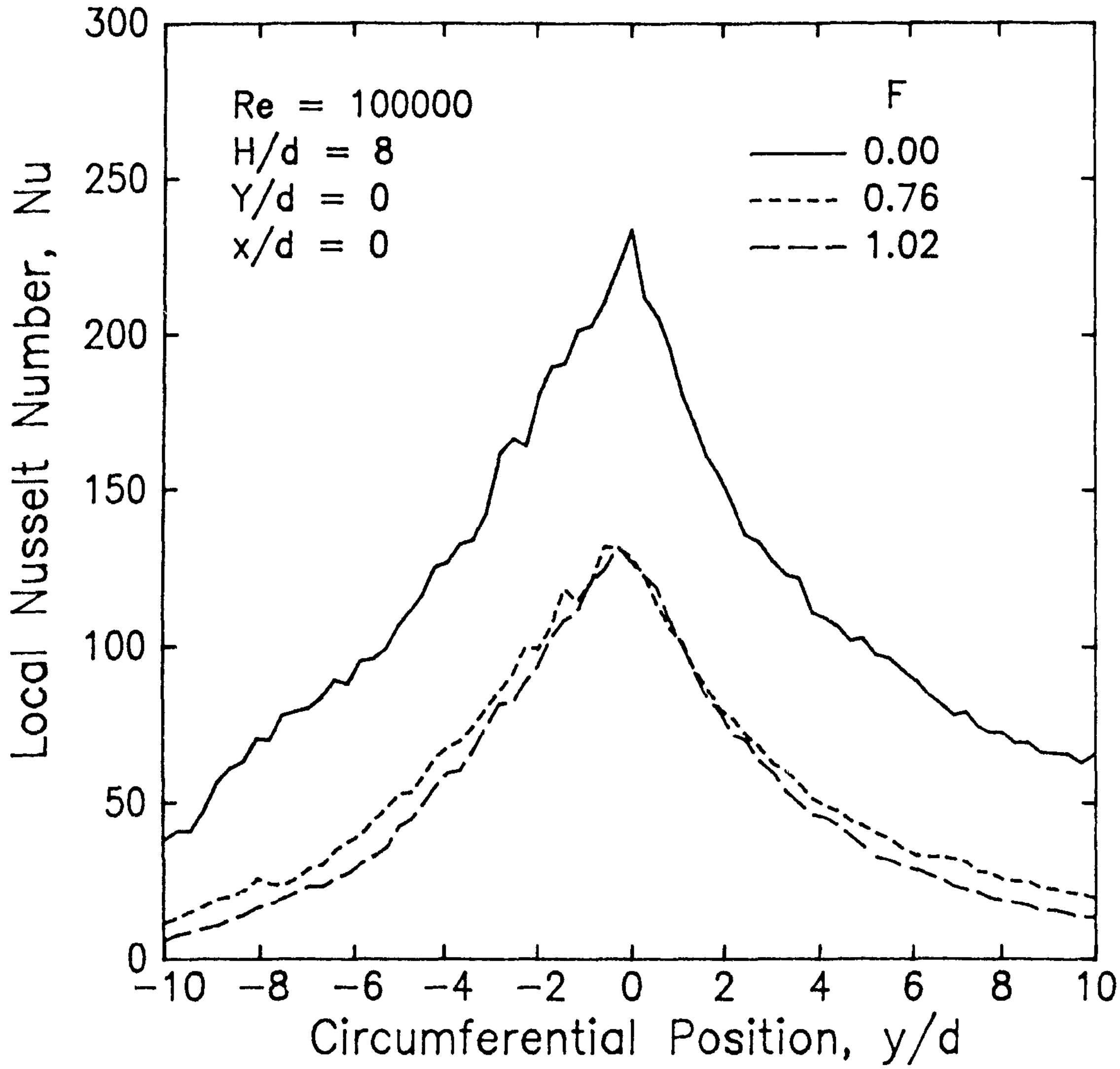

Figure 4.16(d) Effect of jet thermal entrainment factor, F, on circumferential profiles of local Nusselt number of unconfined jets: H/d = 8 and Re = 100000.

impingement surface spacings, H/d of 1 and 2, Figures 4.14(a) and 4.14(b), the decrease in local circumferential Nu profile in the wall jet region is not much different from that for large H/d. This would be expected considering the mechanism of degradation of heat transfer driving force by the total distance over which entrainment acts, i.e. over the total distance H/d plus y/d. However, in the impingement region of y/d out to about ±2, it would seem surprising to find that local Nu is still reduced significantly with H/d of 1 and 2. This aspect of the results may be understood by reference to the heat flux sensor size relative to the jet size, Figure 4.17. The sensor provides much better resolution in the circumferential direction (0.27d wide) than in the axial direction (1.45d long). The fact that in the axial direction a substantial fraction of the sensor is outside the potential core means that this part of the sensor is influenced by thermal entrainment even at very close nozzle to impingement surface spacings. This explanation is confirmed when the effect of entrainment is reduced through the use of a confinement surface, as described in Section 4.5.

4.3.2 Stagnation Point Heat Transfer

The effect of the thermal entrainment factor, F, and nozzle to impingement surface spacing, H/d, on the stagnation point Nusselt number, Nu_o, are shown in Figures 4.18 to 4.20. Figure 4.18(a) shows that for all values of the thermal entrainment factor, Nu_o reaches a maximum for H/d in the range 4-5. For the case of a single axisymmetric jet, the presence of a maximum in the Nu_o - H/d relation, documented by Gardon and co-workers (1962, 1965, 1966), Nakatogawa et al. (1970), Koopman and Sparrow (1975) and others, is attributed to increasing turbulence at the jet centerline, dominant at lower H/d, and decreasing

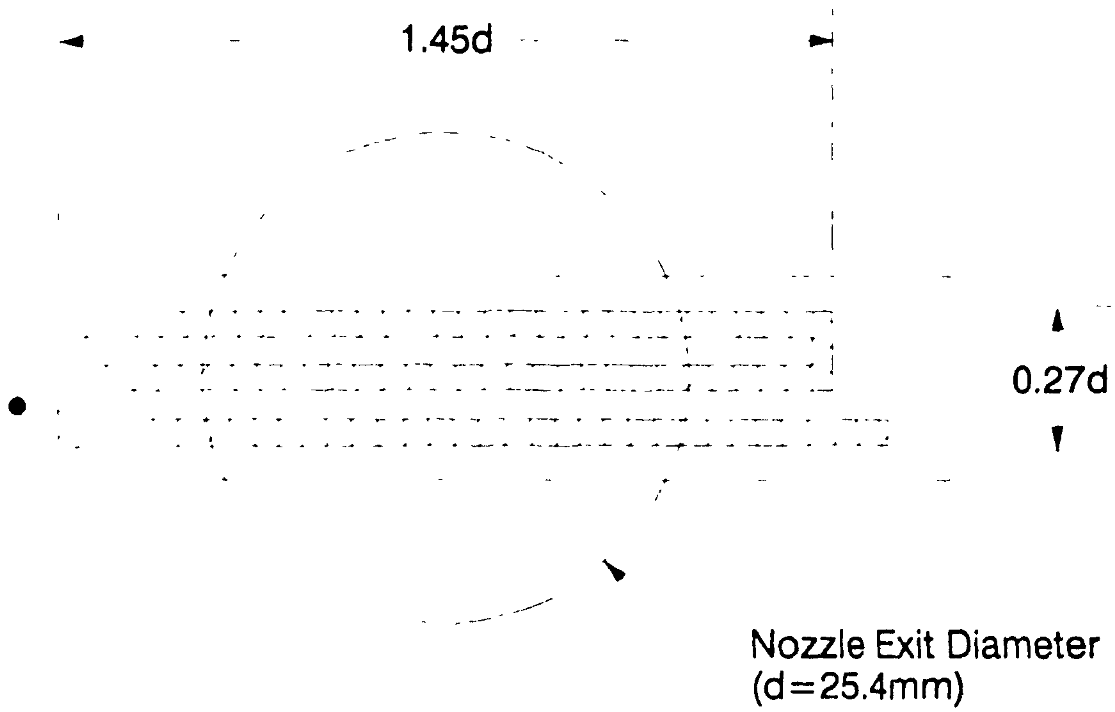

Figure 4 17 Comparison of impingement nozzle and heat flux sensor dimensions.

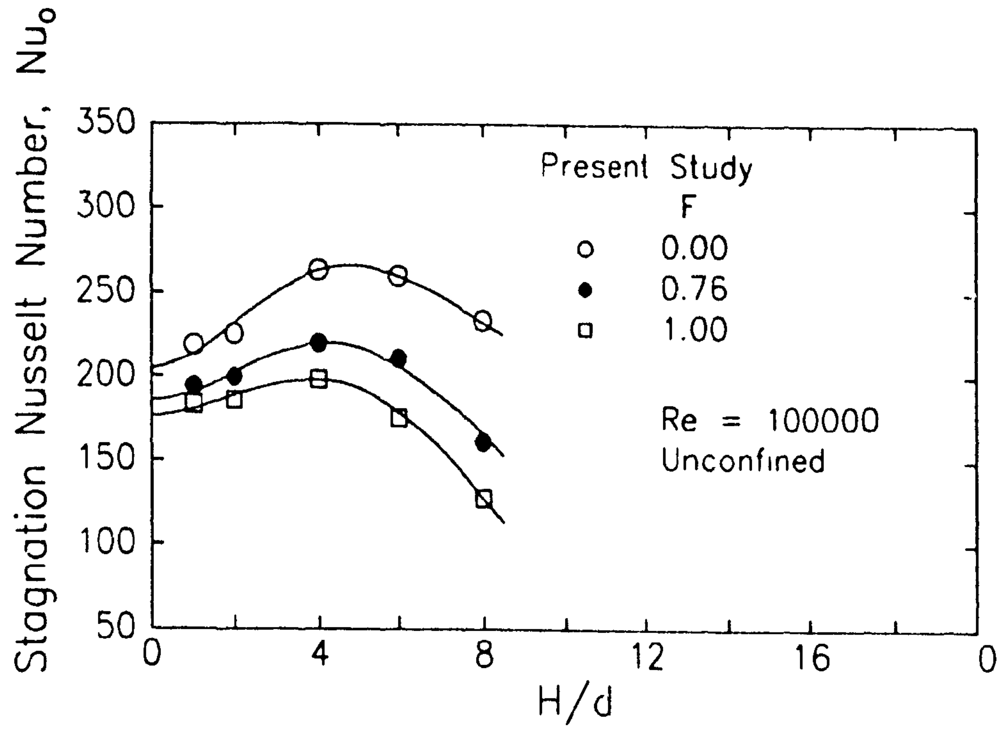

Figure 4.18(a) Effect of thermal entrainment factor, F, on the Nu_o - H/d relationship for unconfined jets

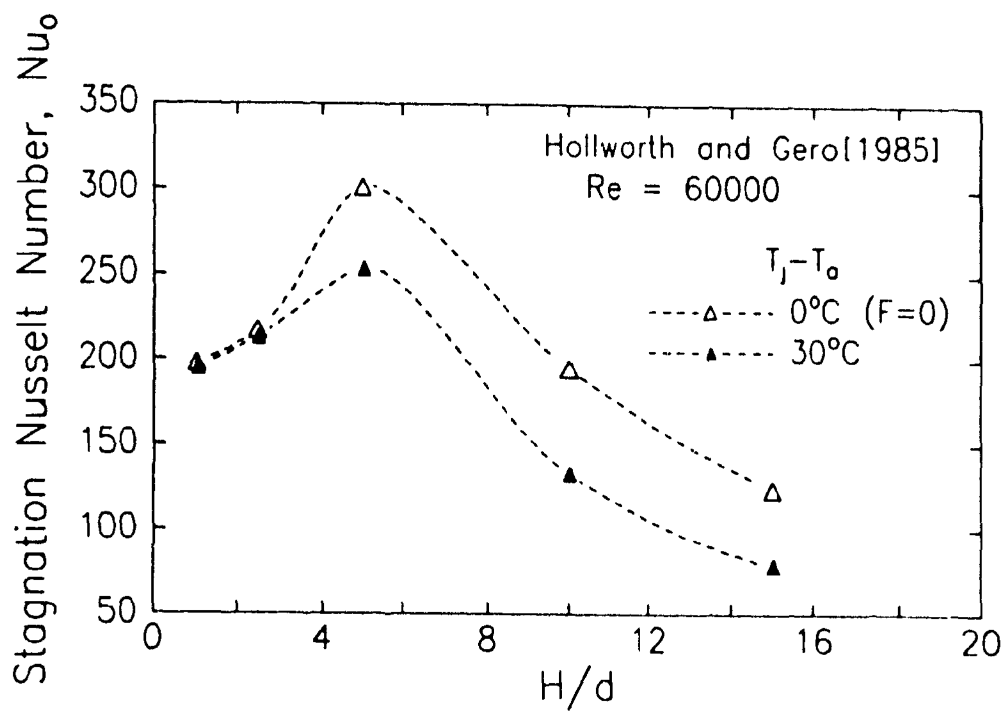

Figure 4.18(b) Effect of temperature mismatch, $T_j - T_a$, on the Nu_o - H/d relationship for orifice jet with an aspect ratio, L/d, of 1, Hollworth and Gero[1985]

mean velocity at the jet centerline at higher H/d. Obot[1980] showed the importance of nozzle geometry on the location of the maximum. It is generally reported the Nu_o reaches a maximum for a spacing of about H/d = 8. The finding here is that the maximum Nu_o occurs at an H/d around 4 or 5 which is in qualitative agreement with the results of Hollworth and Gero[1985], Figure 4.18(b), for a square edged orifice with an aspect ratio (l/d) of 1. The industrial nozzles of the current study, Figure 3.4, were chosen because they are used in paper machine calender control systems. The converging section and use of cast aluminum with rough surfaces would contribute to high nozzle exit turbulence, to a shorter potential core, and hence to the Nu_o maximum occurring at a closer H/d spacing.

Figure 4.19 shows that Nu_o decreases slightly with increasing F for H/d ≤ 4. As pointed out in the previous section in connection to Figure 4.17, the size of the sensor in the axial direction (1.45d) contributes to the small apparent effect of entrainment on Nu_o for small H/d At H/d = 8, Figure 4.19 shows that Nu_o is much more sensitive to entrainment, as has already been discussed.

The agreement of the current results for the Nu_o - Re relationship, Figure 4.20, with the extensive record of such measurements is very good. The differences which do exist derive from numerous sources, i.e. the size of the heat flux sensor, nozzle geometry, nozzle exit profiles in velocity, turbulence intensity and other turbulence variables, and the T - T_s - T_a relationships represented here by the nondimensional temperature mismatch factor, F. For example, the sensor used by Gardon and Akfirat was of diameter 0.071d, while that of the current study was 0.27d x 1 45d. As indicated by Obot, the flow conditions of Gardon and Akfirat were probably for a contoured inlet nozzle of length 18d, and

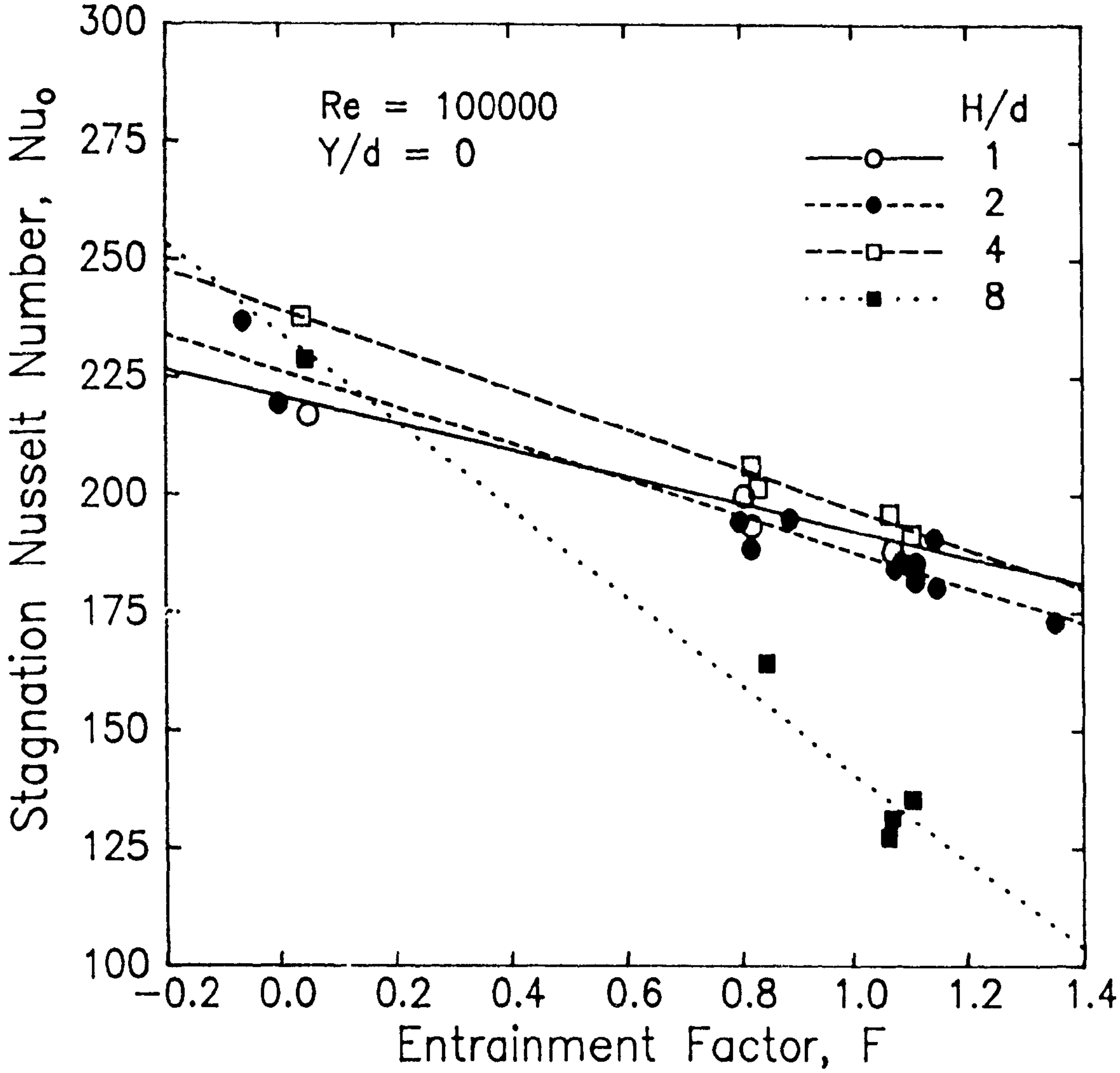

Figure 4 19 Effect on Nu_o of thermal entrainment factor, F, for a range of nozzle-to-impingement surface spacing , H/d.

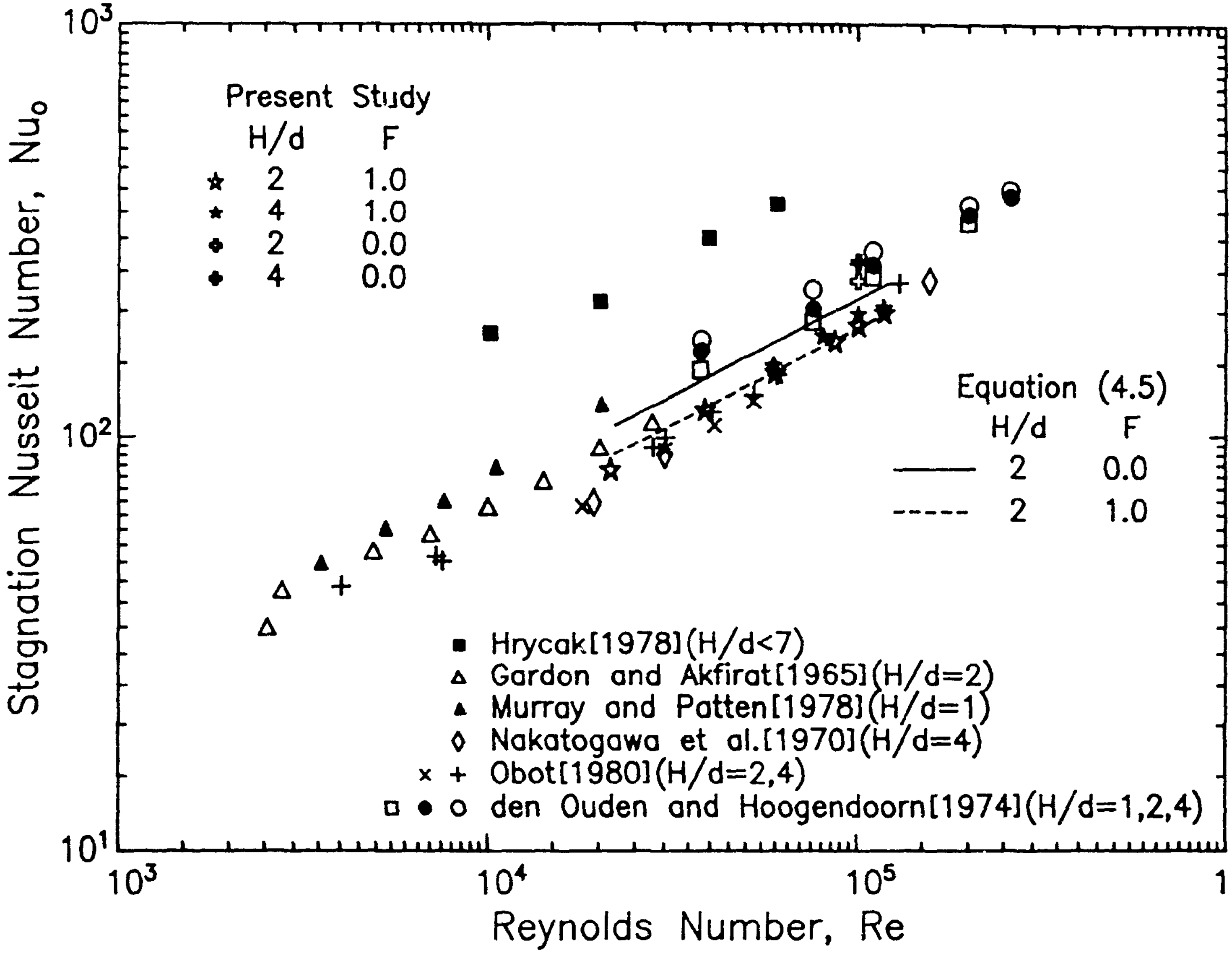

Figure 4 20 Comparison of Nu_o results with previous studies for close nozzle spacing thus would not be directly comparable with the nozzles used here.

A correlation of the following form for stagnation Nusselt number for the H/d ≤ 4 region was obtained using a nonlinear regression program based on a standard Marquart algorithm.

$$Nu_o = \left[a + b \left(\frac{H}{d}\right)^{c} F \right] Re^{d} \left(\frac{H}{d}\right)^{e} \qquad (4.4)$$

which reduces to the commonly used equation when F = 0.0. The results obtained in the Re range 22000 to 118000 yield the following equation.

$$Nu_o = \left[0.962 - 0.100 \left(\frac{H}{d}\right)^{0.53} F\right] Re^{0.46} \left(\frac{H}{d}\right)^{0.[illegible]6} \qquad (4.5)$$

The fit of this equation to the experimental results is shown in Figure 4.21. The correlation coefficient, r^2, for this regression is 0.96. Equation 4.5, for F=0.0 and F=1.0, is compared in Figure 4 20 with results reported for small H/d.

For the case where the ambient temperature, T_a, equals the jet temperature, T_j, or F = 0, Equation 4.5 reduces to

$$Nu_o = 0.962\ Re^{0.46} \left(\frac{H}{d}\right)^{0.[illegible]6} \qquad (4.6)$$

The present results for F = 0 compare quite well with those reported by Obot [1982] and Nakatogawa [1978] and are in the range of 4-8% lower than the results of Gardon and Akfirat [1965] and Murray and Patten [1978].

Obot proposed the relationship:

$$Nu = 1.15\ Re^{[illegible]4} \left(\frac{H}{d}\right)^{[illegible]} \qquad (4.6a)$$

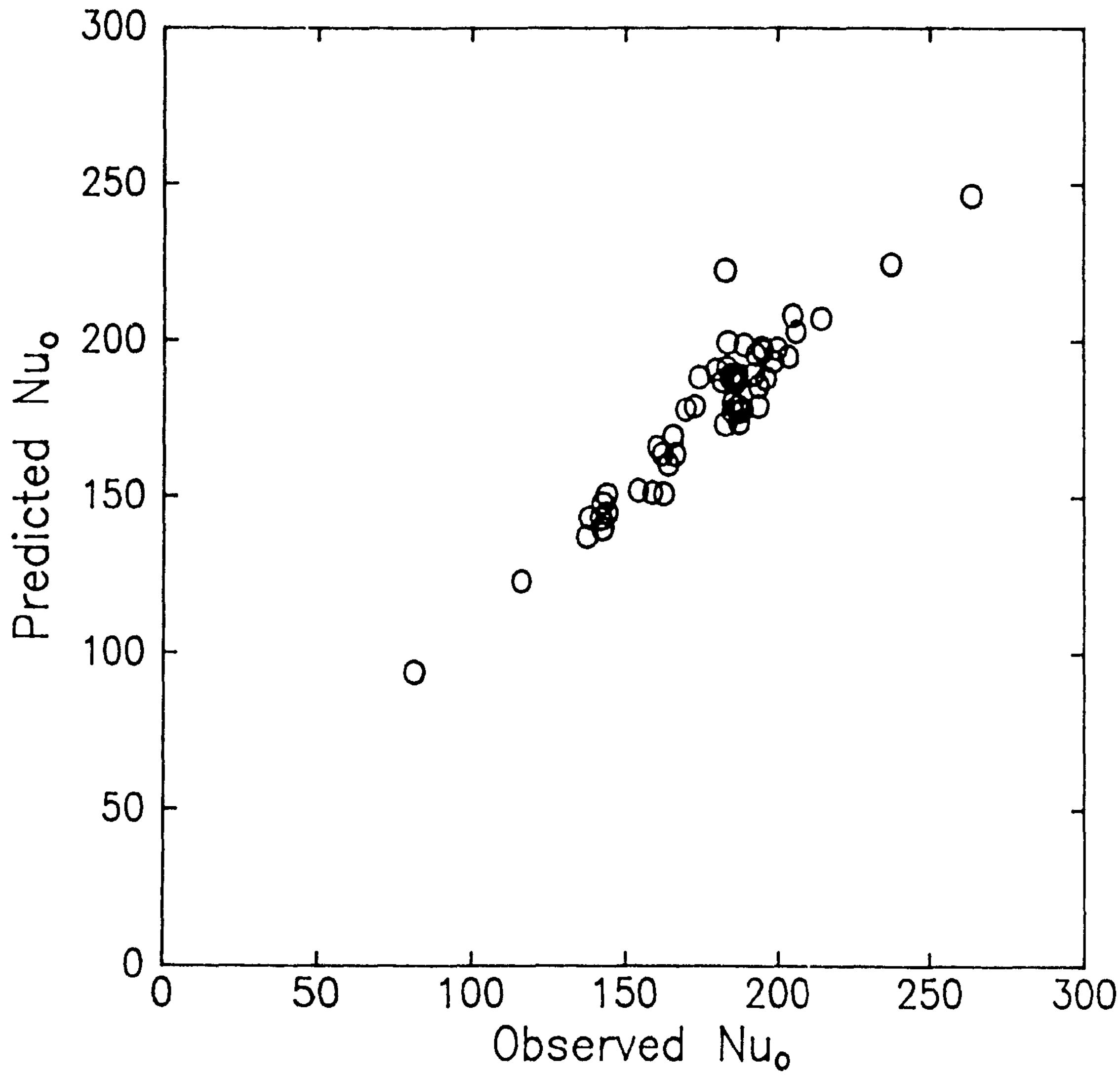

Figure 4.21 Comparison of experimental Nu_o values with those from Equation 4.5, for $H/d \leq 4$ and $0 \leq F \leq 1.2$.

valid for $15{,}000 < Re < 60{,}000$ and $2 \leq H/d \leq 8$ The agreement with Equation 4 6 is excellent. Obot [1980] performed a logarithmic best fit of the data of Ouden and Hoogendoorn [1974] (for H/d = 1, 2 and 4) and Gardon and Akfirat [1965] (for H/d = 2) and obtained.

$$Nu_c = 0.64\ Re^{0.52} \qquad (4.7)$$

As argued by Obot, the modest differences between the proposed correlation, Equation 4.5, with the results of Ouden and Hoogendoorn and Gardon and Akfirat can be attributed to differences in the nozzle exit flow conditions. To that observation one should now add the differences due to varying values of the thermal entrainment factor, F

4.3.3 Radial Average Nusselt Number

Although profiles of local Nu and values of Nu at specific points such as at the stagnation point, and at the off-stagnation minima and maxima are important in the analysis of impinging jets, average heat transfer provides another essential perspective, particularly for process design.

All profiles of local Nu shown to date have been circumferential profiles at the jet centerline, x/d = 0 As shown in Chapter 3, with the nozzle set perpendicular to the roll and in the absence of confinement, profiles of local Nu are effectively axisymmetric over the range of nozzle exit and impingement surface velocities investigated Under these circumstances, evaluation of the radial average Nusselt number, $\overline{Nu}_r = \int Nu\ r\ dr$, can be simplified by taking the circumferential profile at x/d = 0 as a satisfactory approximation of the Nu profile in any radial direction.

The Figure 4.22 profiles as a function of Re and H/d are the $\overline{Nu}_r$ equivalents of the Figure 4.12 circumferential profiles of local Nu, and show the same features, although somewhat attenuated by the integration. At r = 0, these profiles converge, as $\overline{Nu}_{r=0} = Nu_o$. Values of $\overline{Nu}_r$ become of practical interest only for values of r significantly larger than the nozzle radius, d/2. For the same reasons noted earlier for the local Nu profiles, the $\overline{Nu}_r$ profiles were extended to 10d from the jet centerline, i.e. avoiding the larger areas where heat transfer rates are too low to be of interest.

The $\overline{Nu}_r$ profiles of Figure 4.23 show that at Re = 100000 and F = 1, $\overline{Nu}_r$ is essentially independant of H/d for spacings up to 4, with a significant drop off in $\overline{Nu}_r$ for H/d of 6 and higher.

The very large effect of thermal entrainment, F, on $\overline{Nu}_r$ is shown by the Figure 4.24 profiles, analagous to those of Figure 4.16 for profiles of local Nu. The information is condensed to illustrate, on Figure 4.25, the radial average Nusselt number - H/d relationship for a single averaging distance, i.e. $\overline{Nu}_{r,d}$ for $(r/d)_a$ = 10.

Figure 4 25 may be contrasted with the corresponding Nu_o - H/d relationship, Figure 4.18. Thus for the nozzles used in the present study the Nu_o - H/d relation passes through a well-defined maximum at H/d around 4 or 5, while no maximum occurs for $\overline{Nu}_r$. The independance of $\overline{Nu}_r$ for H/d ≤ 4 was noted earlier with the profiles of Figure 4.23. The strong detrimental effect of jet entrainment is apparent from Figure 4 25, which shows that the radial average heat transfer drops by 65% as the entrainment factor, F, increases from 0 to 1. In typical calendering configurations the entrainment factor is in the range 0.75 ≤ F ≤ 1.2 Thus these results establish the not generally appreciated importance of entrainment in the design of impinging jet

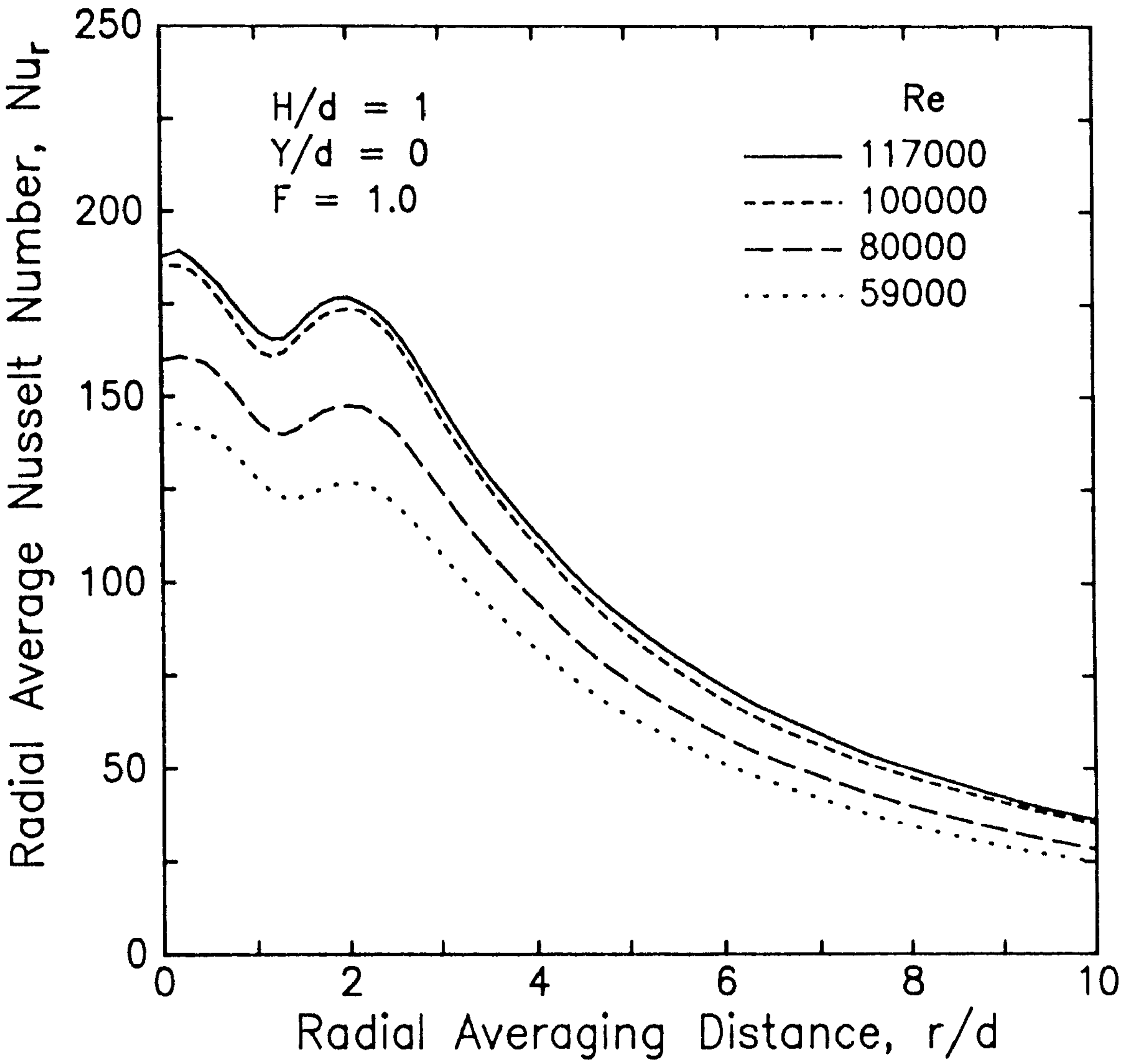

Figure 4.22(a) Effect of jet Reynolds number, Re, on radial average Nusselt number of unconfined jets: H/d 1 and F 1.0

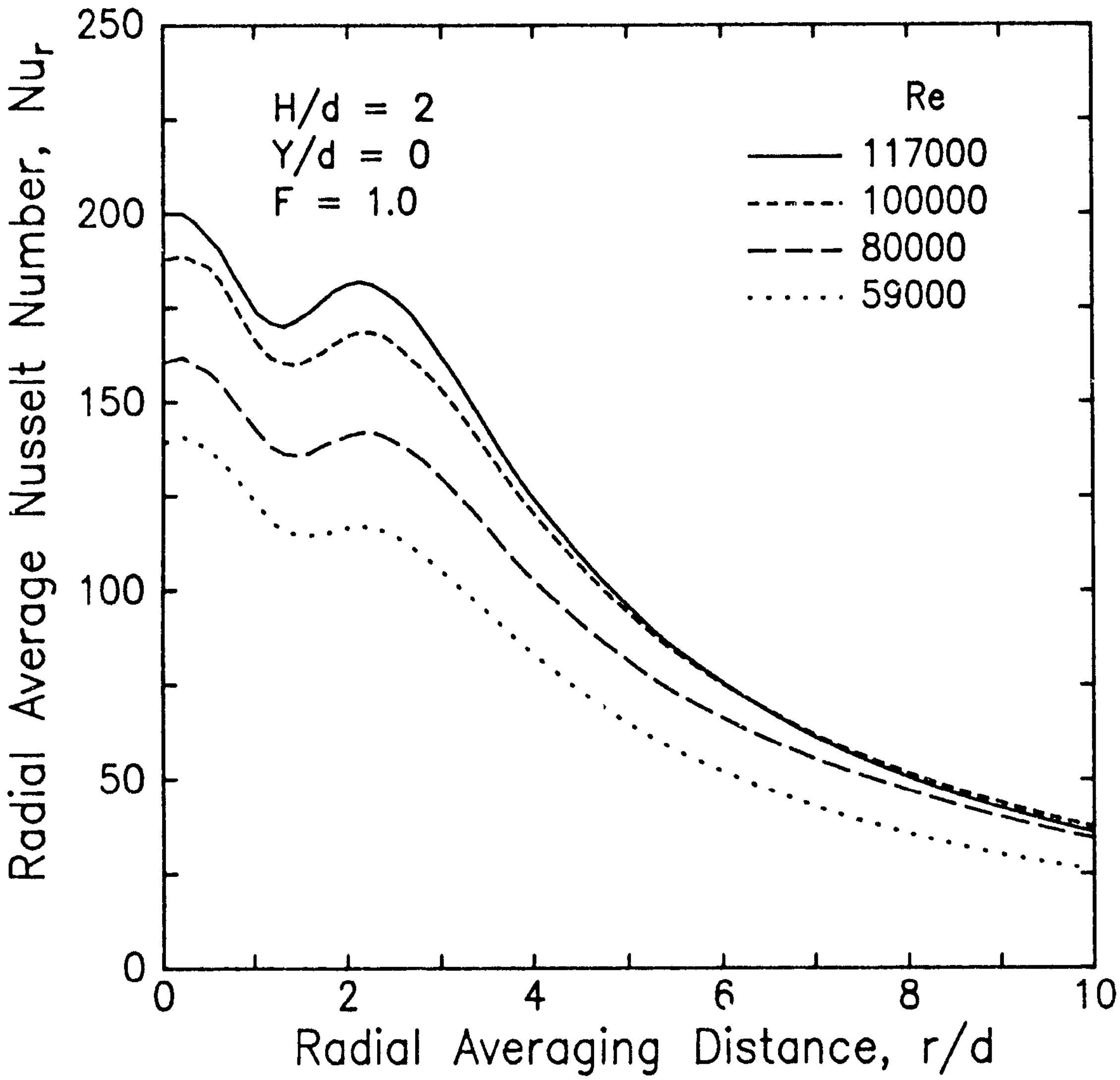

Figure 4.22(b) Effect of jet Reynolds number, Re, on radial average Nusselt number of unconfined jets: H/d = 2 and F = 1.0.

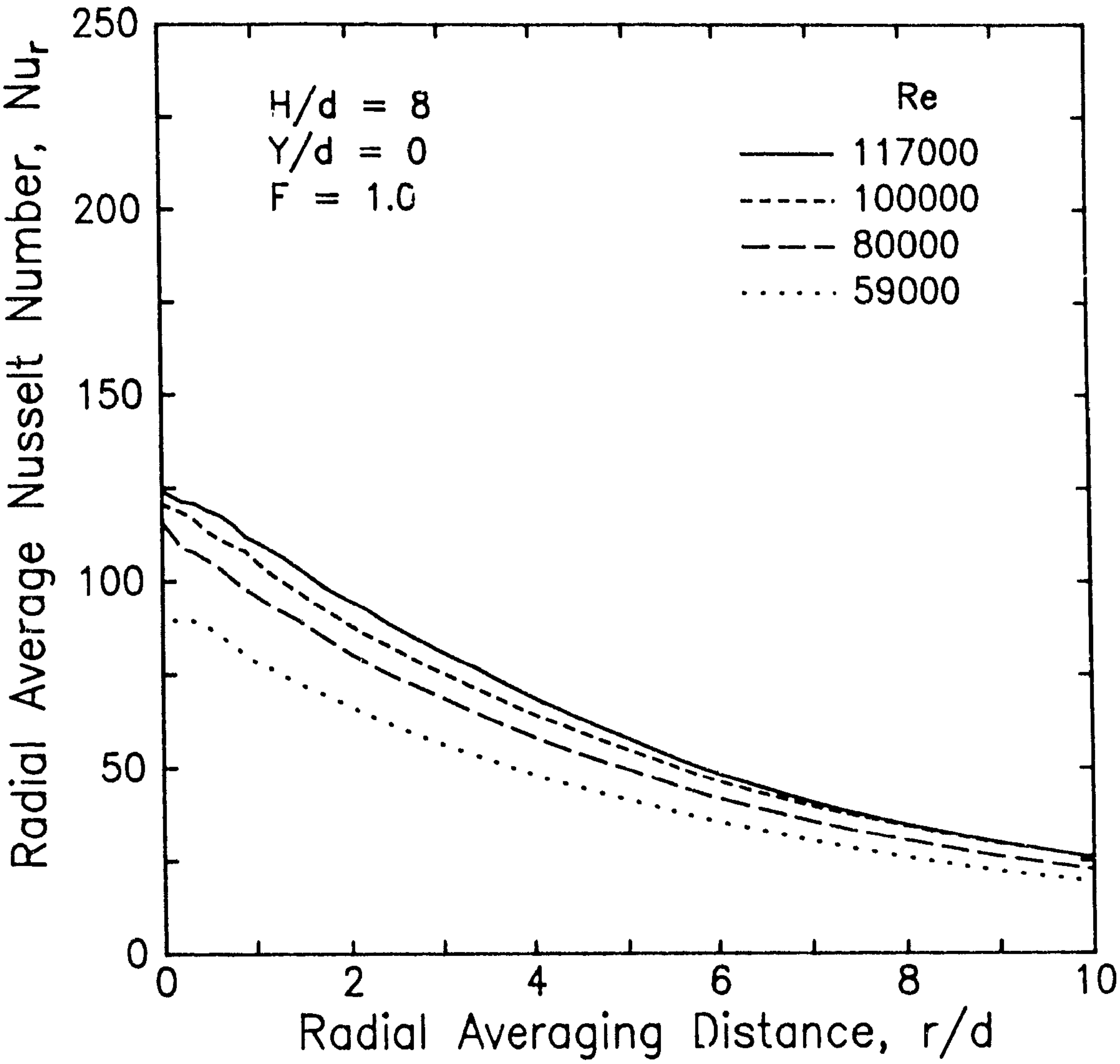

Figure 4 22(c) Effect of jet Reynolds number, Re, on radial average Nusselt number of unconfined jets. H/d - 4 and F - 1 0.

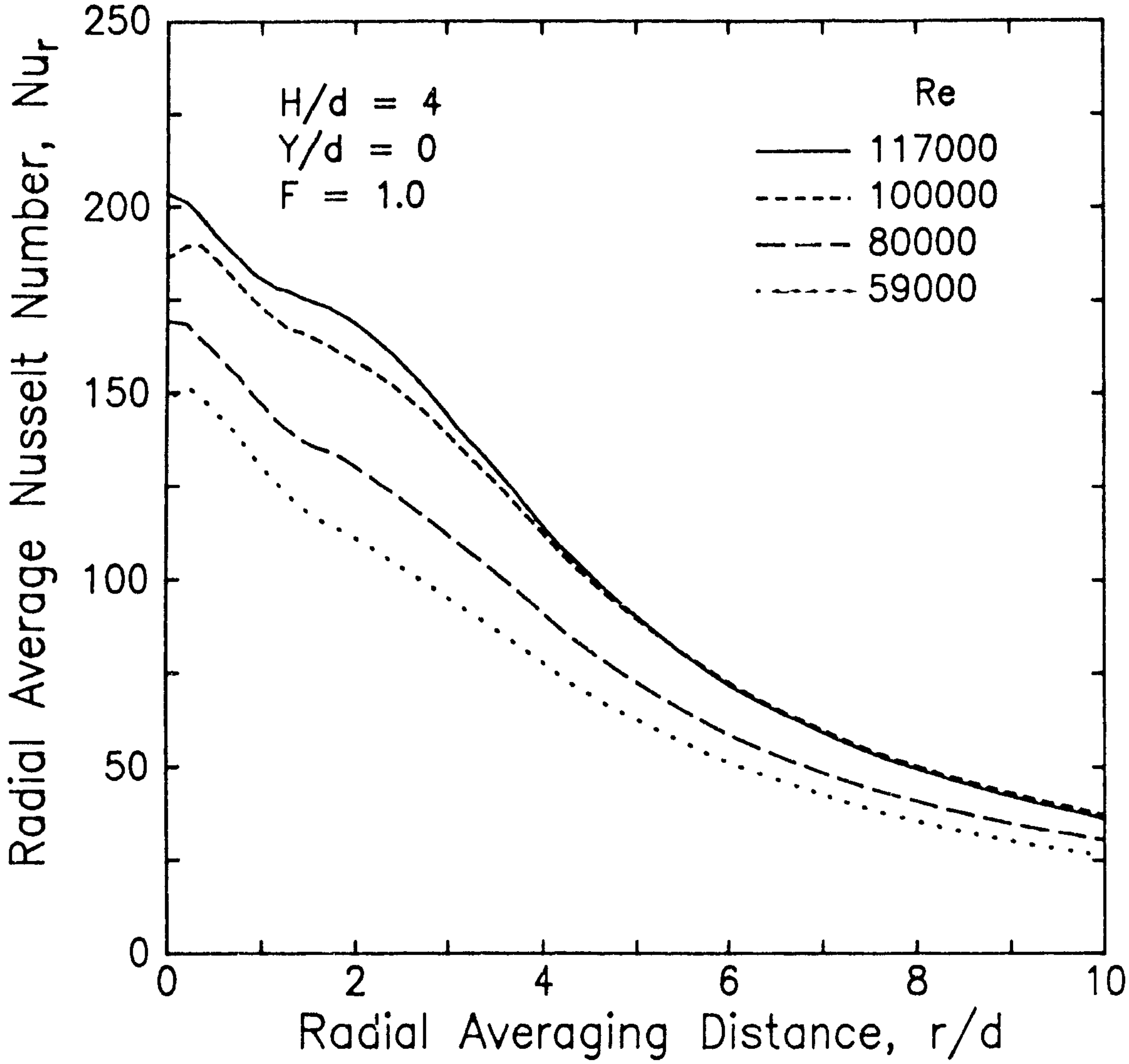

Figure 4 22(d) Effect of jet Reynolds number, Re, on radial average Nusselt number of unconfined jets: H/d = 8 and F = 1 0.

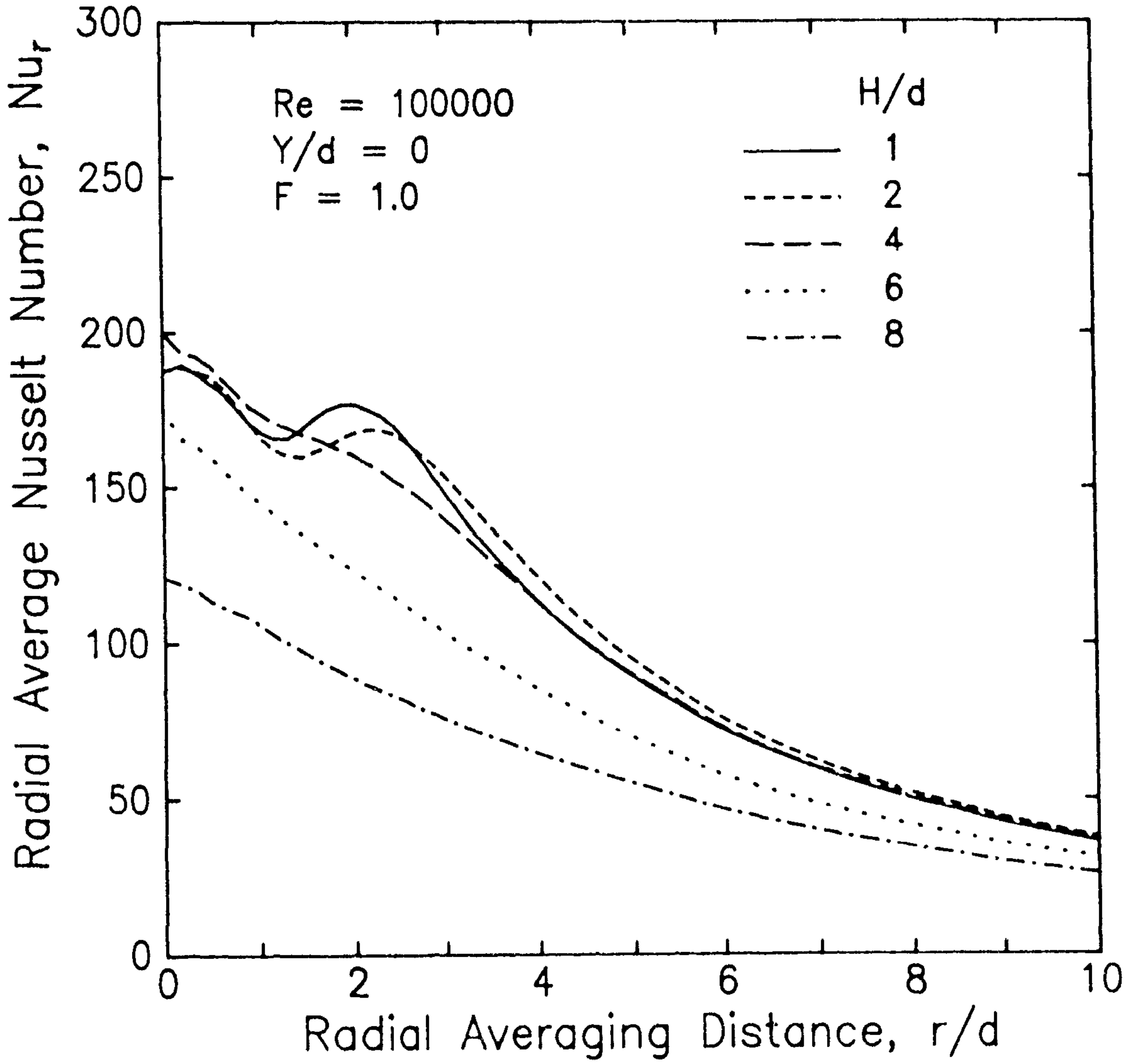

Figure 4.[illegible]3 Effect of nozzle-to-impingement surface spacing, H/d, on radial average Nusselt number of smooth round jets, Re = 100000 and F = 1.0

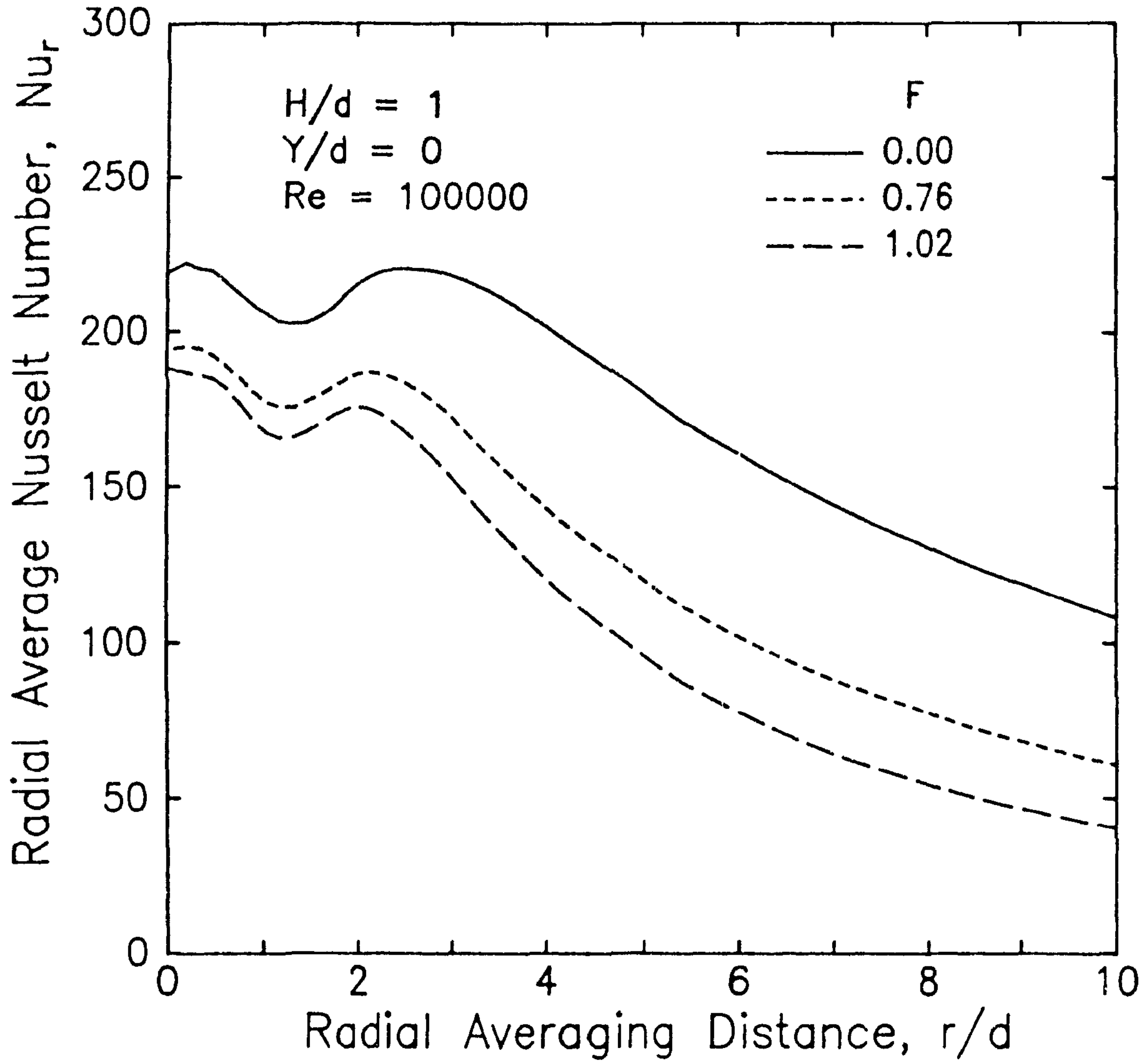

Figure 4.14(a) Effect of thermal entrainment factor, F, on radial average Nusselt number of unconfined jets H/d = 1 and Re = 100000.

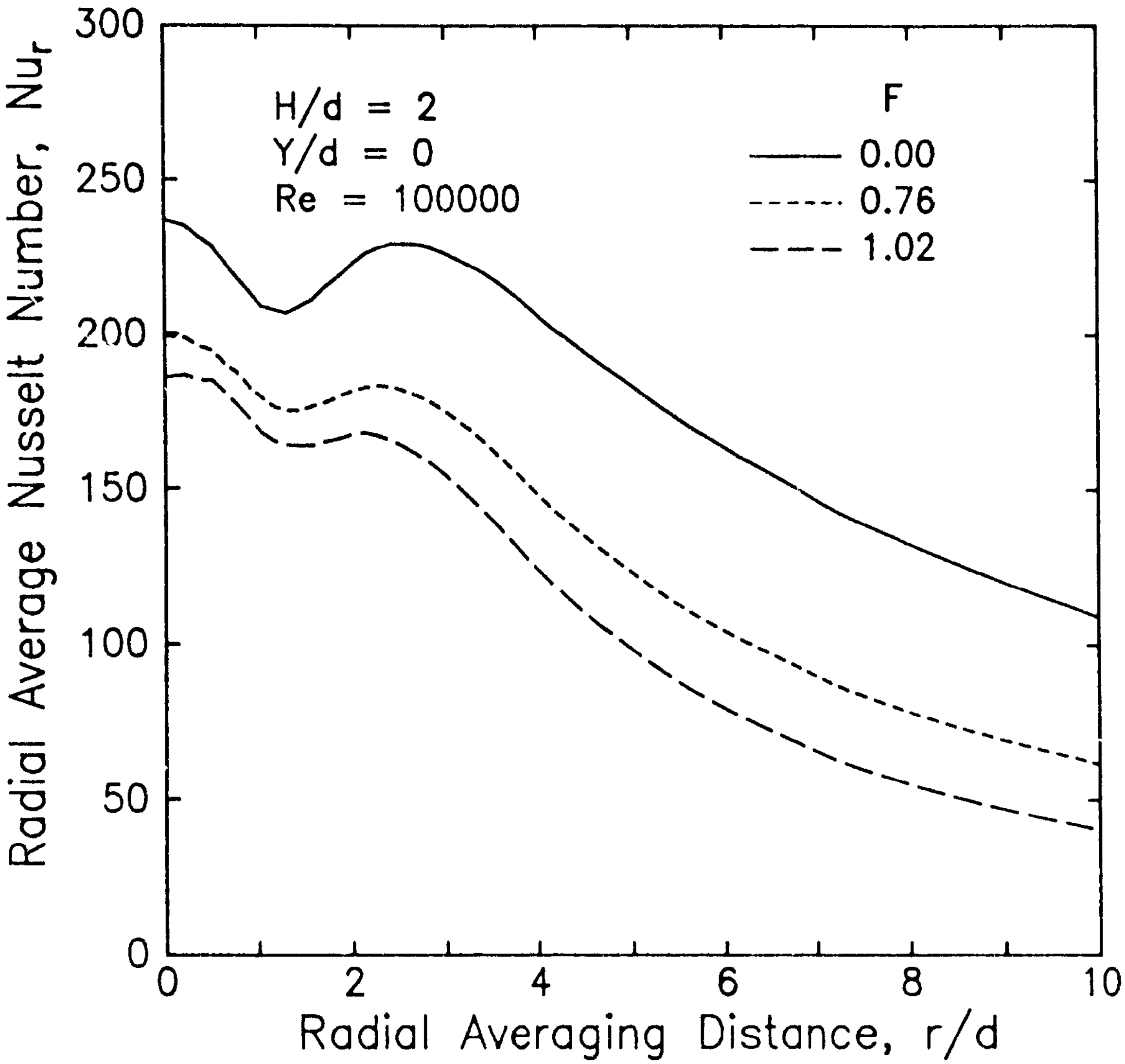

Figure 4.24(b) Effect of thermal entrainment factor, F, on radial average Nusselt number of unconfined jet, H/d = 2 and Re = 100000

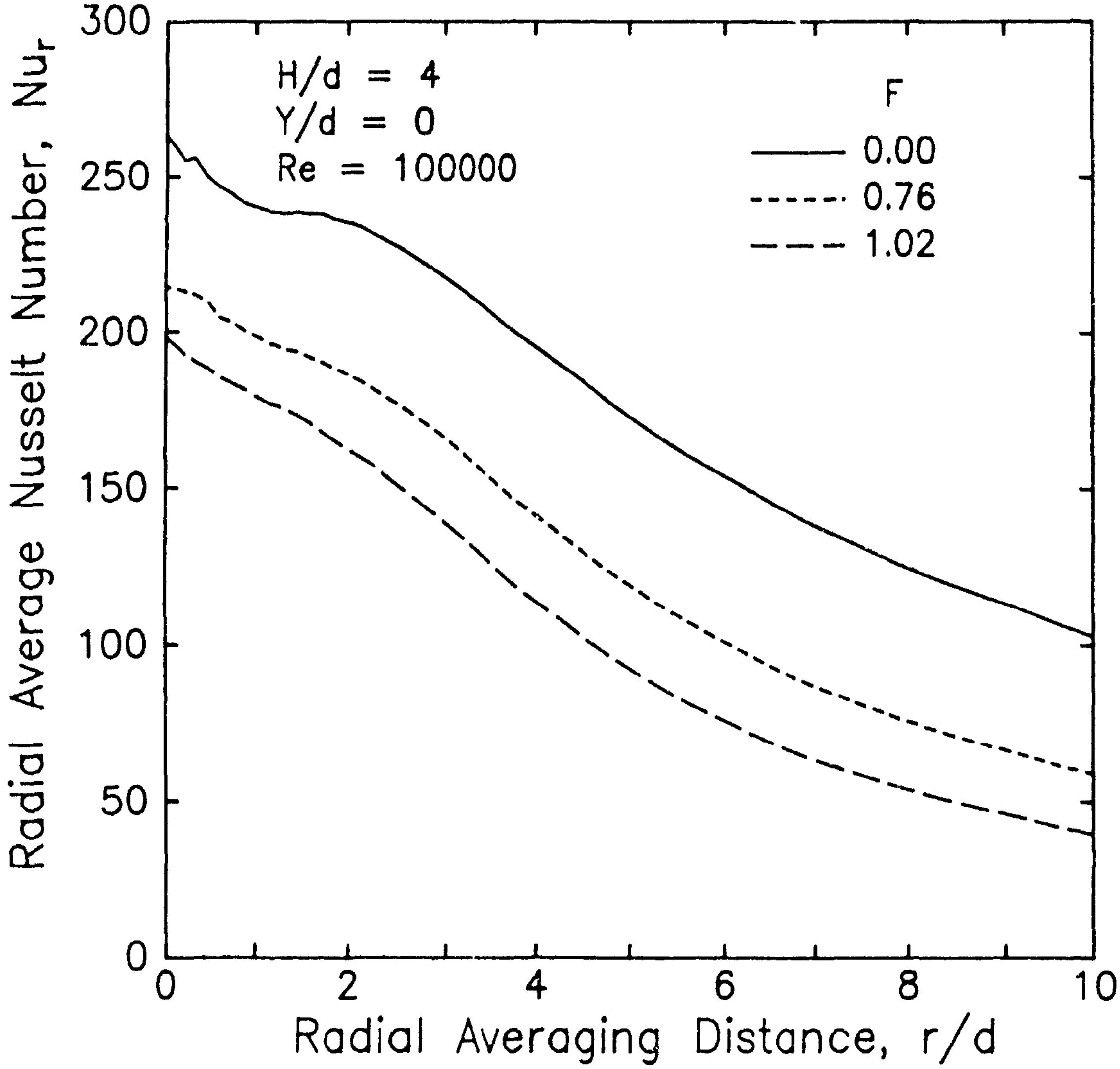

Figure 4.24(?) Effect of thermal entrainment factor, F, on radial average Nusselt number of unconfined jets: H/d = 4 and Re = 100000

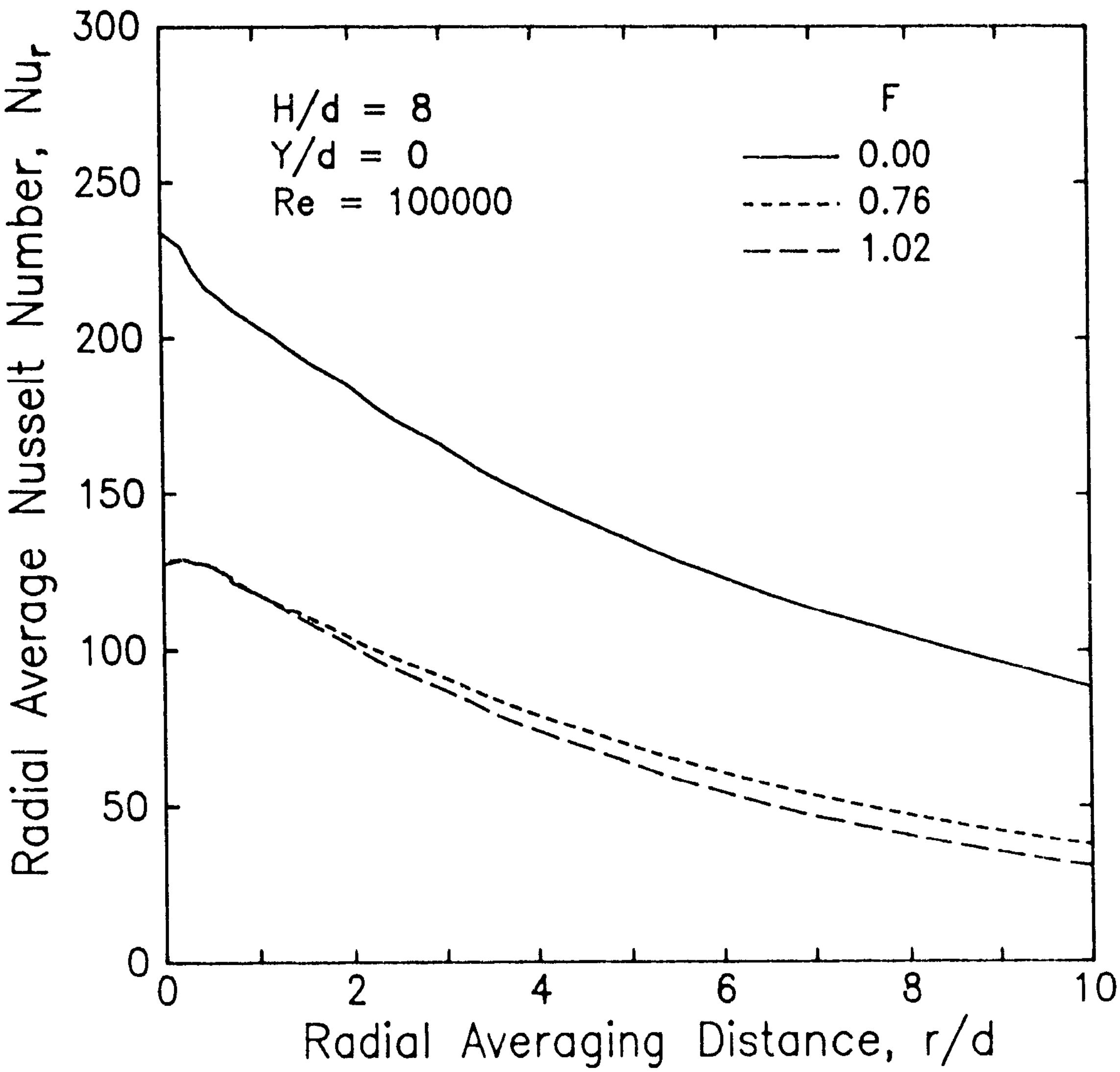

Figure 4.24(d) Effect of thermal entrainment factor, F, on radial average Nusselt number of unconfined jets, H/d = 8 and Re = 100000

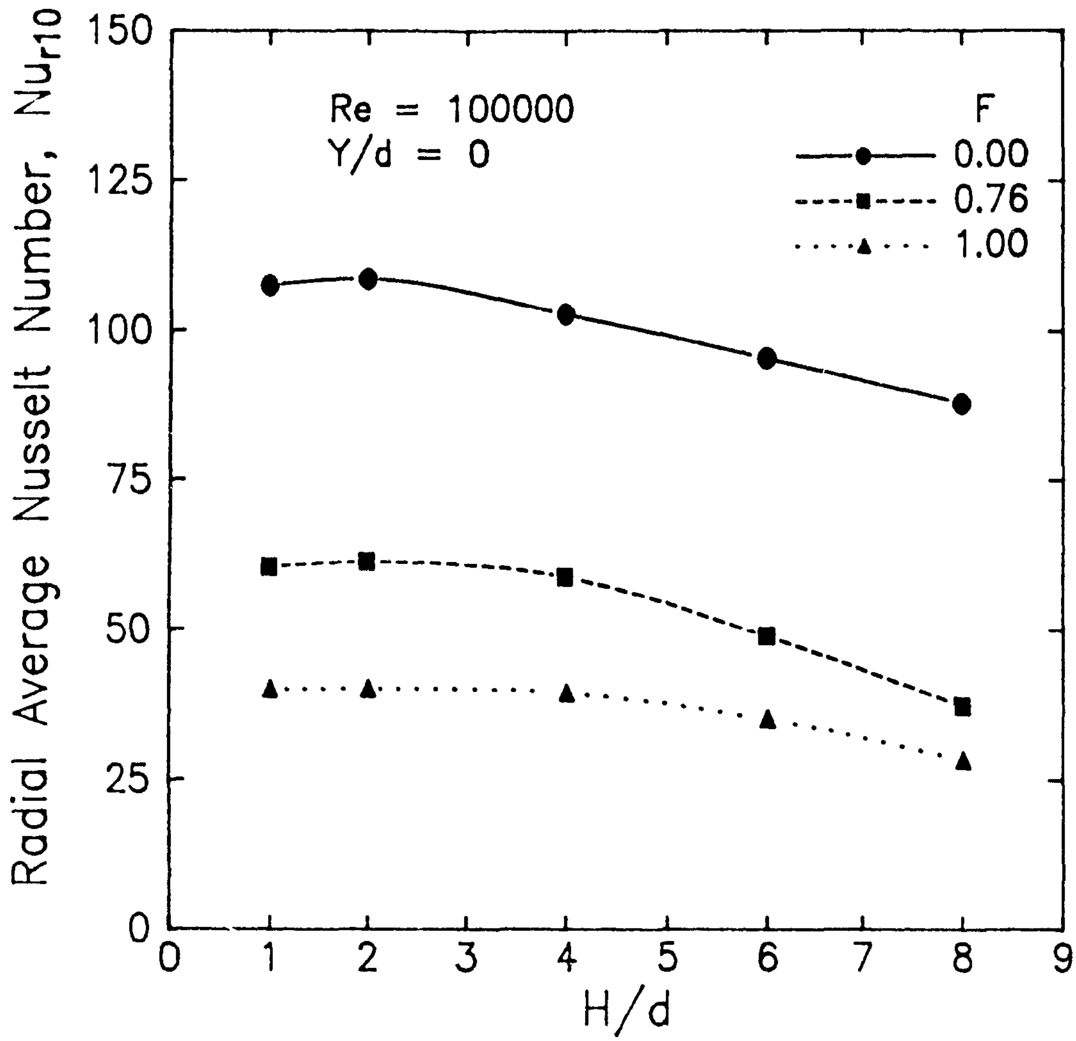

Figure 4.25 Effect of thermal entrainment factor, F, on the radial average Nusselt number - H/d relationship: r/d = 10.

calender control systems.

A correlation for $\overline{Nu}_r$ is complicated by the existence of maxima and/or minima in r/d. For this reason the correlation is restricted to r/d > 3, just beyond the location of the maxima in $\overline{Nu}_r$. This is not a particularly important limitation on the resulting regression since in impinging jet applications, the averaging area is usually larger than r/d = 3. A nonlinear regression, performed using the procedure described in Section 4.2.2, gives

$$\overline{Nu}_r = \left[0.133 - 0.0227\left(\frac{r}{d}\right)^{0.59} F\right] Re^{[illegible]} \left(\frac{r}{d}\right)^{-0.63} \tag{4.9}$$

valid over the range $35000 \le Re \le 117000$

$1 \le H/d \le 4$

$3 \le r/d \le 10$

$0 \le F \le 1.1$

for which the correlation coefficient is 0.92. The effect of H/d on Nu_r in the industrially important range $H/d \le 4$, as would be anticipated from Figure 4.25, was found to be negligible. Figures 4.26(a) [illegible] 4.26([illegible]) illustrate the effectiveness of the proposed correlations. Figure 4.26(c) portrays the dramatic negative effect of thermal entrainment on average Nusselt number.

Few correlations are available for spacings, $H/d \le 8$ and for r/d large enough to be of interest in industrial applications. [illegible] (198[illegible]) proposed the following correlation for his data

$$\overline{Nu}_r = 0.113\, Re^{[illegible]} \left(\frac{r}{d}\right)^{[illegible]} \left(\frac{H}{d}\right)^{[illegible]} \tag{4.10}$$

valid over the range $1[illegible]000 \le Re \le 60000$, $1.7 \le r/d \le [illegible]$ and

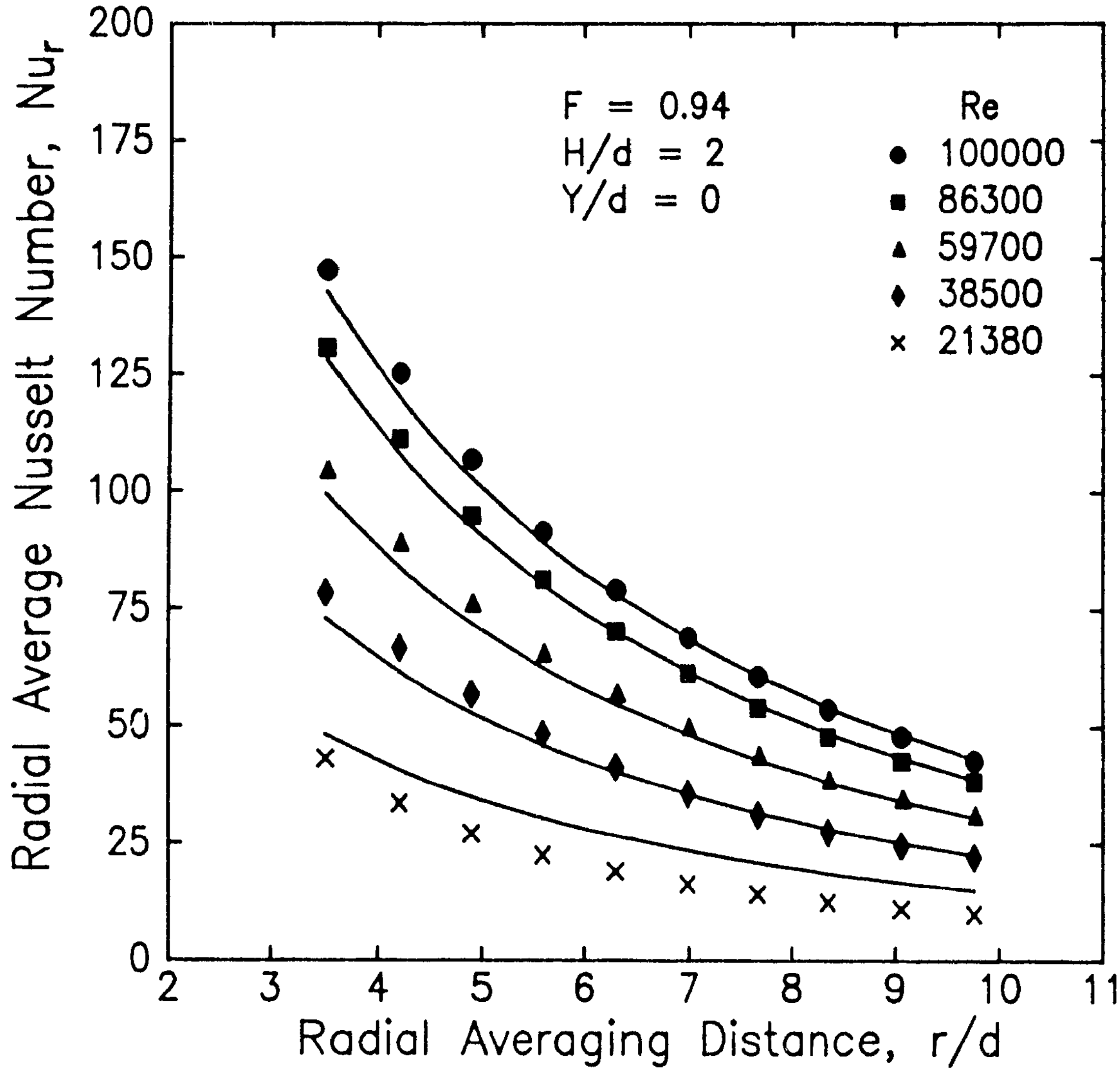

Figure 4.26(a) Comparison of $\overline{Nu}_r$ measurements with those from Equation 4.9: Effect of Re for H/d = 2, F = 0.94.

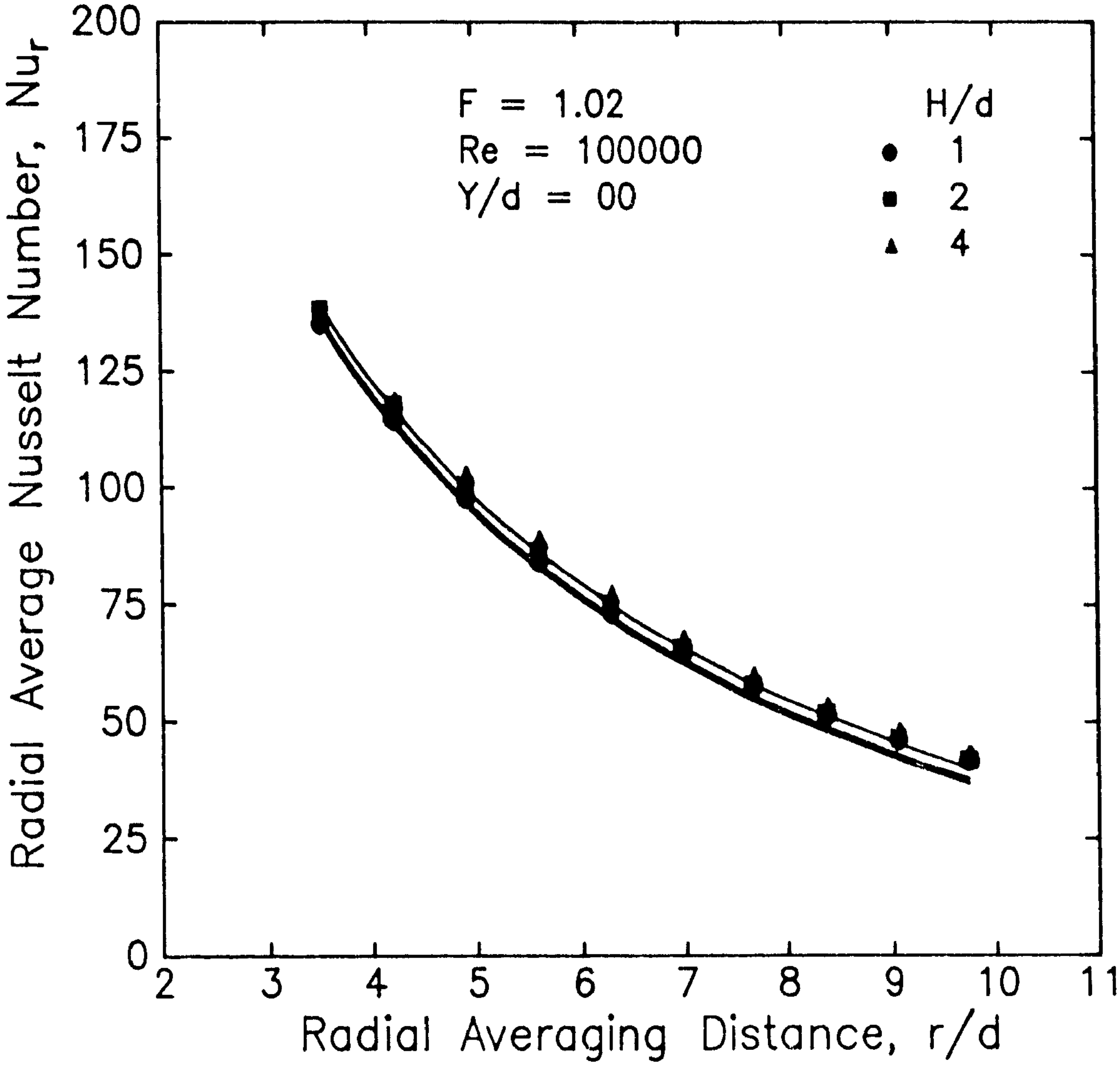

Figure 4.26(b) Comparison of $\overline{Nu}_r$ measurements with those from Equation 4.9 Effect of H/d for Re = 100000, F = 0.94

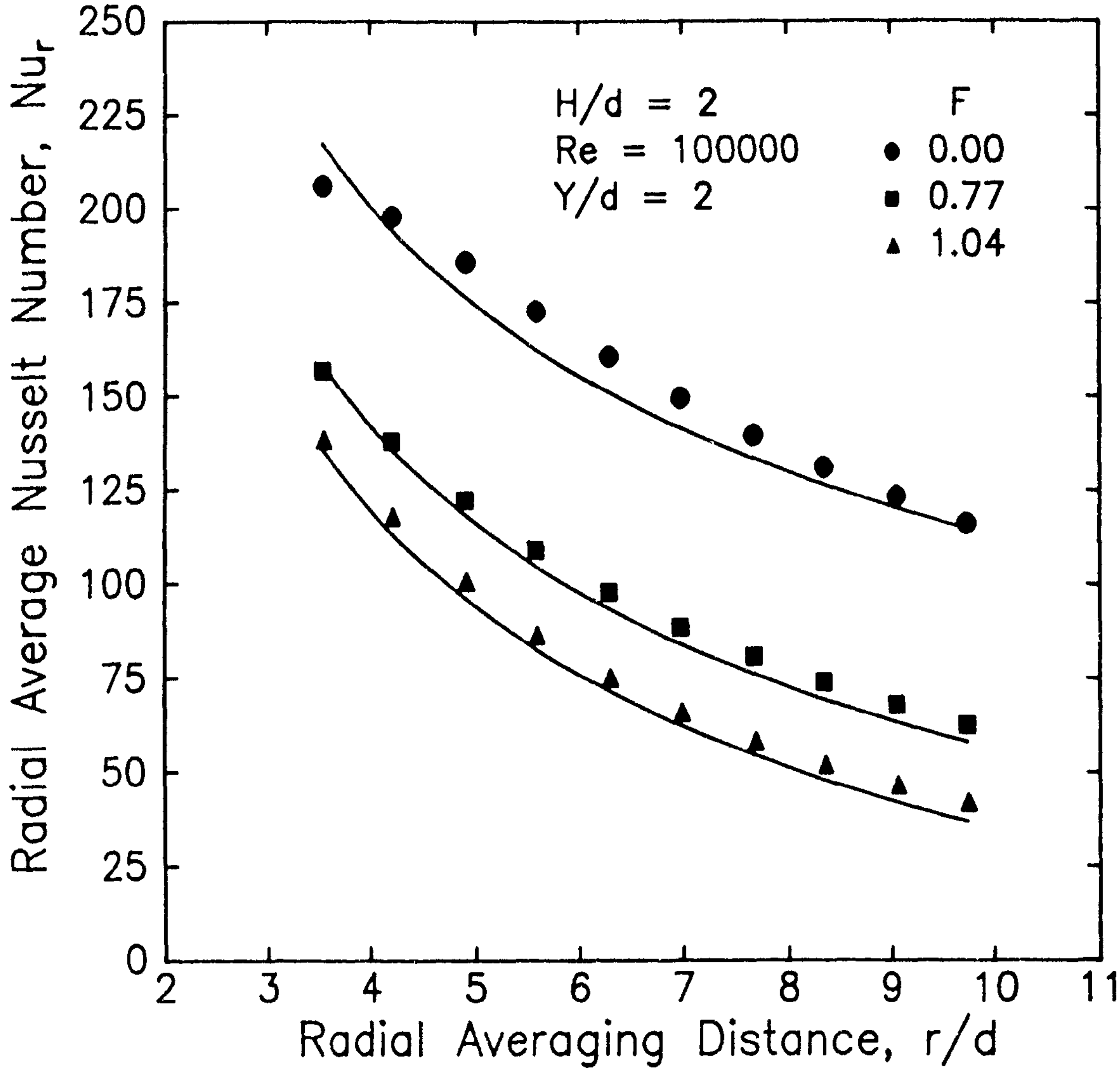

Figure 4.26(c) Comparison of $\overline{Nu}_r$ measurements with those from Equation 4.9: Effect of F for H/d = 2, Re = 100000.

$2 \le H/d \le 12$. This is in good agreement with the current correlation for the case of no thermal entrainment, $F = 0$, for which Equation 4.9 reduces to

$$\overline{Nu}_r = 0.133\ Re^{0.\text{[illegible]}} \left(\frac{r}{d}\right)^{-0.63} \qquad (4.11)$$

4.3.4 Circumferential Average Nusselt Number

For a round jet impinging on a rotating cylinder, however, there exists another basis for averaging the heat transfer, i.e. the heat transfer averaged over circumferential area of the roll, for a specified axial length of the roll. In the present case the relavant axial length is evidently $(x/d)_a = \pm(S/d)/2$, covering the nozzle to nozzle axial spacing. Thus the radial jet based average Nusselt number was designated $\overline{Nu}_r$, and the roll circumferential based average Nusselt number is denoted $\overline{Nu}_c$. For the calender control application of interest in the present study, it is clearly the circumferential average Nusselt number, $\overline{Nu}_c$, which is more important. The basic definition is evidently $\overline{Nu}_c = \int\int Nu\, dxdy$. Figure 4.27 compares the respective averaging areas for $\overline{Nu}_r$ and $\overline{Nu}_c$.

The calculation of the double integral, $\overline{Nu}_c$, can be accomplished in two ways. In the simple case where the impingement heat transfer from the impinging jet to the cylindrical surface calender roll can be considered axisymmetric, the circumferential Nu profile at $x/d = 0$ can be used to calculate a local Nu value at each x-y grid position covering the entire averaging area, circumferentially to $\pm(y/d)_1$, and axially to $\pm(x/d)_a$ or S/d. When this simplification does not apply, Nu circumferential profiles at a number of axial positions over the S/d range must be measured.

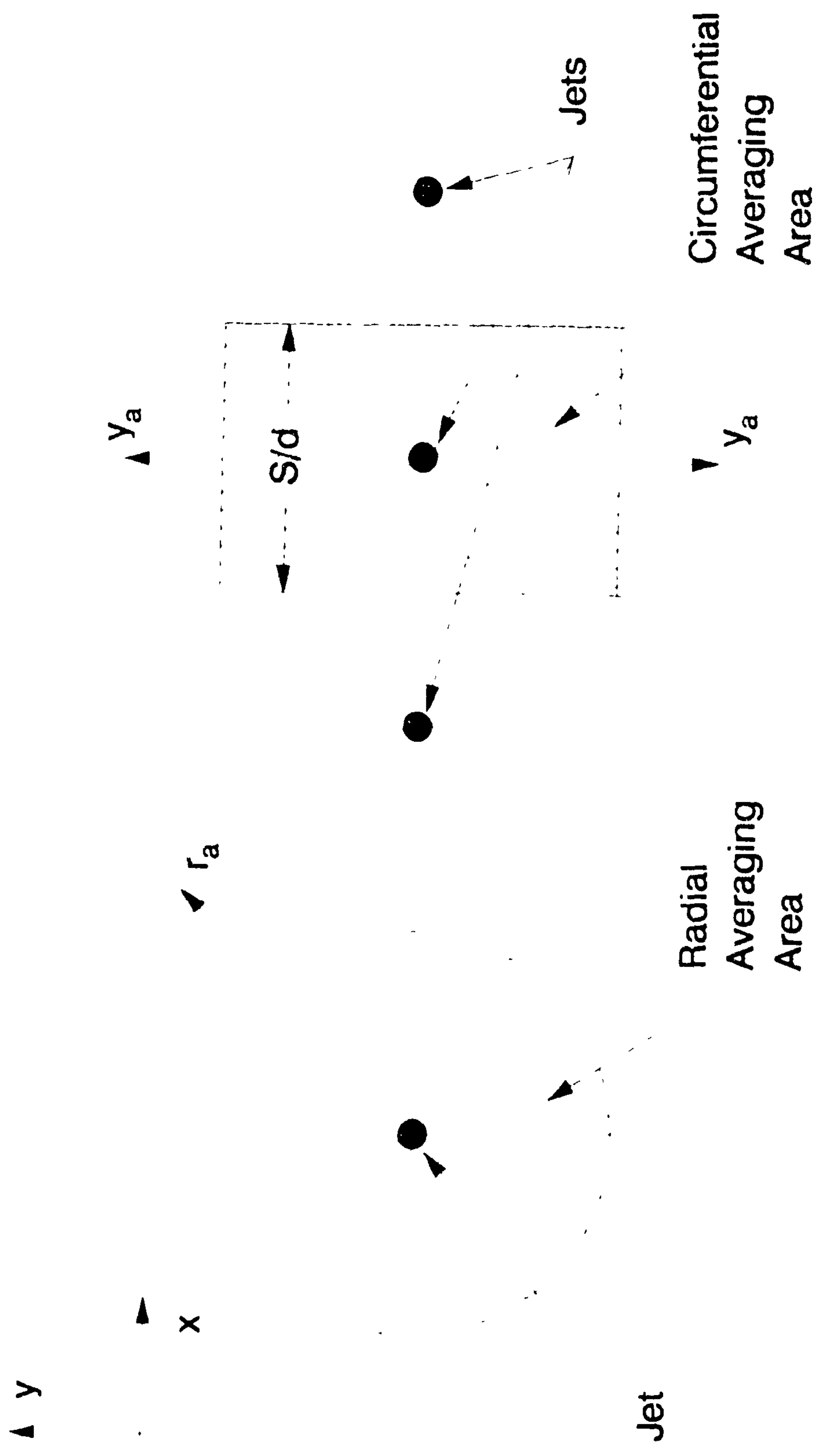

Figure 4.27 Comparison of the averaging areas used to calculate the radial, $\overline{Nu}_r$, and circumferential, $\overline{Nu}_c$, average Nusselt numbers.

For the case of unconfined jets impinging normal to the roll surface, a number of verifications established that it was acceptable to assume the Nu profile was axisymmetric, so $\overline{Nu}_c$ could be determined from a single circumferential Nu profile determined at $x/d = 0$. Typical verifications, Figure 4.28(a), (b) and (c), show the agreement is excellent, particularly as the averaging area is increased.

In the non-axisymmetric heat transfer case, which always applies for confined jets or with jets not impinging normal to the roll surface, determination of $\overline{Nu}_c$ requires the measurement of the Nu circumferential profiles at a sufficient number of axial positions over the axial range $\pm(S/d)/2$.

Typical profiles of $\overline{Nu}_c$, Figures 4.29(a)-(c), illustrate the effect of Re, H/d and F and correspond to the circumferential profiles shown in Figures 4.12(b), 4.15 and 4.16(b) respectively. The profiles of Nu generally show similar trends to those apparent in earlier figures of $\overline{Nu}_r$. The maximum in $\overline{Nu}_r$ at $r/d = 2$, is no longer apparent since the averaging area in the axial direction, $x/d = \pm 4$, is large enough to average out the maximum in the local Nu profiles which occurs near $r/d = 2$.

The correlation obtained for the circumferential average, $\overline{Nu}_c$, is

$$\overline{Nu}_c = \left[0.114 - 0.0234\left(\frac{x}{d}\right)^{0.28}\left(\frac{y}{d}\right)^{0.28} F\right] Re^{0.7} \left(\frac{x}{d}\right)^{-0.32} \left(\frac{H}{d}\right)^{0.32} \qquad (4.12)$$

or, in terms of the nozzle-to-nozzle separation, S/d,

$$\overline{Nu}_c = \left[0.142 - 0.0241\left(\frac{S}{d}\right)^{0.28}\left(\frac{y}{d}\right)^{0.28} F\right] Re^{0.7} \left(\frac{S}{d}\right)^{-0.32} \left(\frac{H}{d}\right)^{-0.32} \qquad (4.13)$$

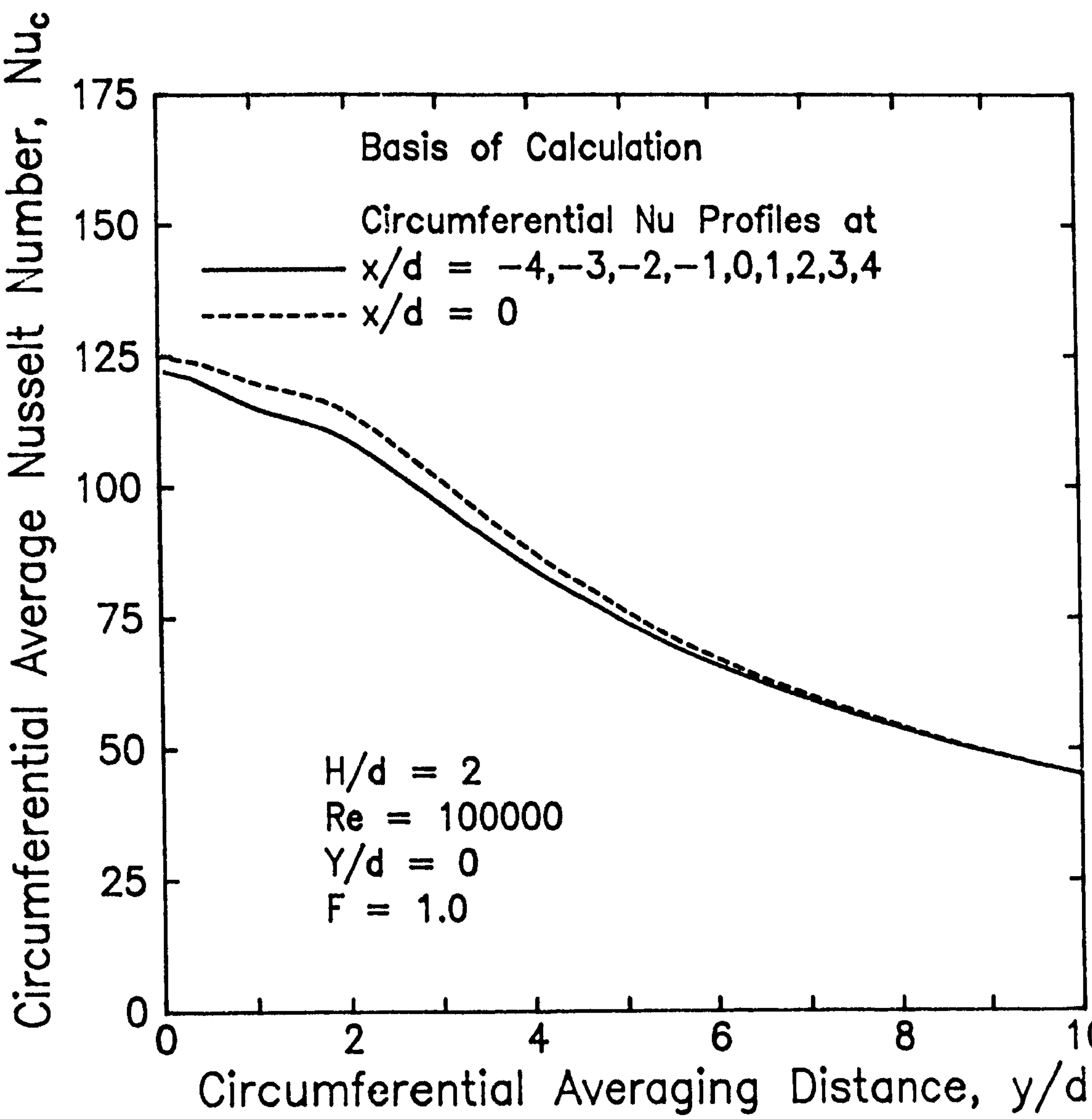

Figure 4.28(a) Comparison of the methods of calculating $\overline{Nu}_c$: Unconfined, normally impinging jets, H/d = 2, Re = 100000.

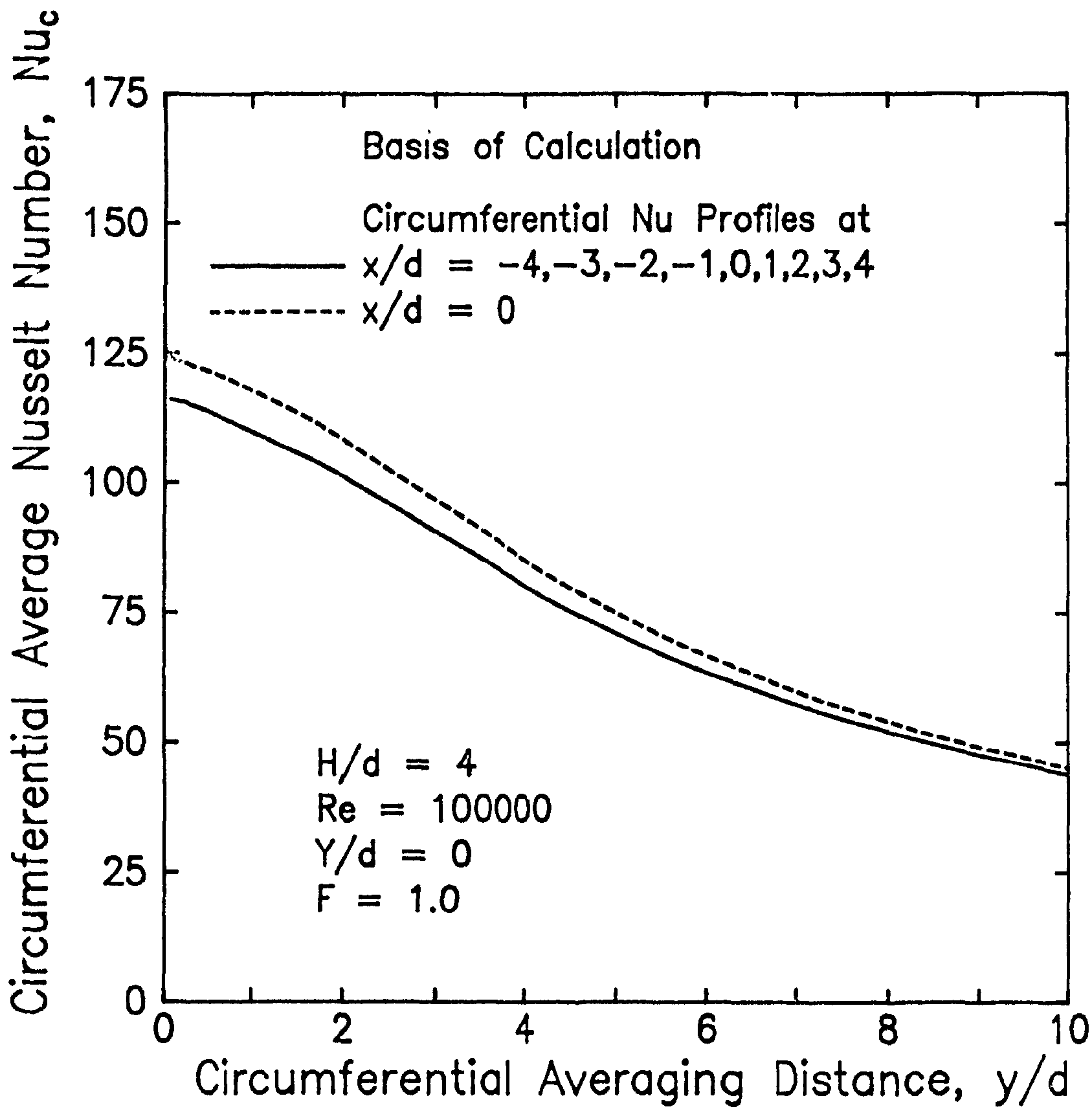

Figure 4.?8(b) Comparison of the methods of calculating $\overline{Nu}_c$: Unconfined, normally impinging jets, H/d = 4, Re = 100000.

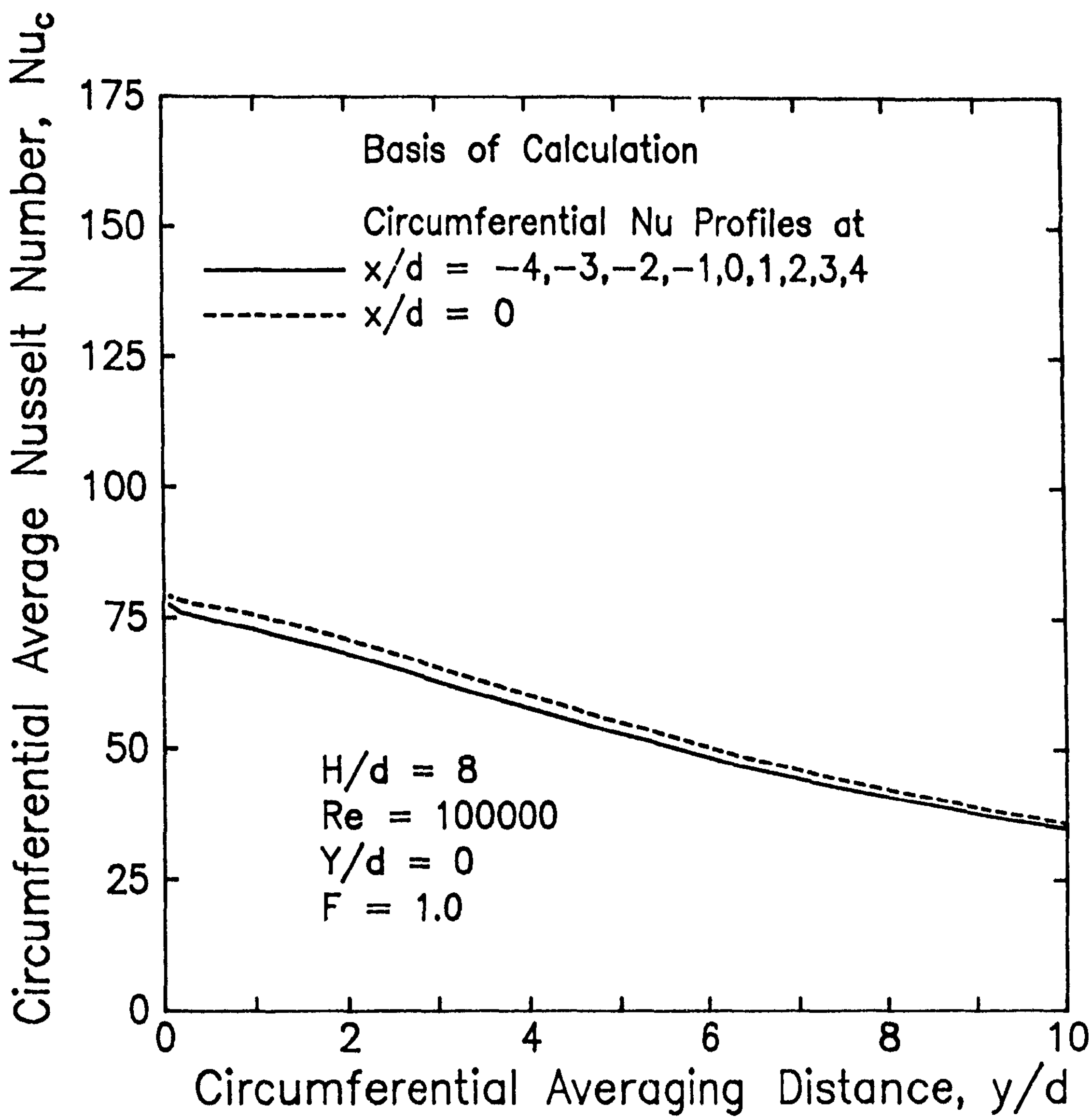

Figure 4.28(c) Comparison of the methods of calculating $\overline{Nu}_c$: Unconfined, normally impinging jets, H/d = 8, Re = 100000.

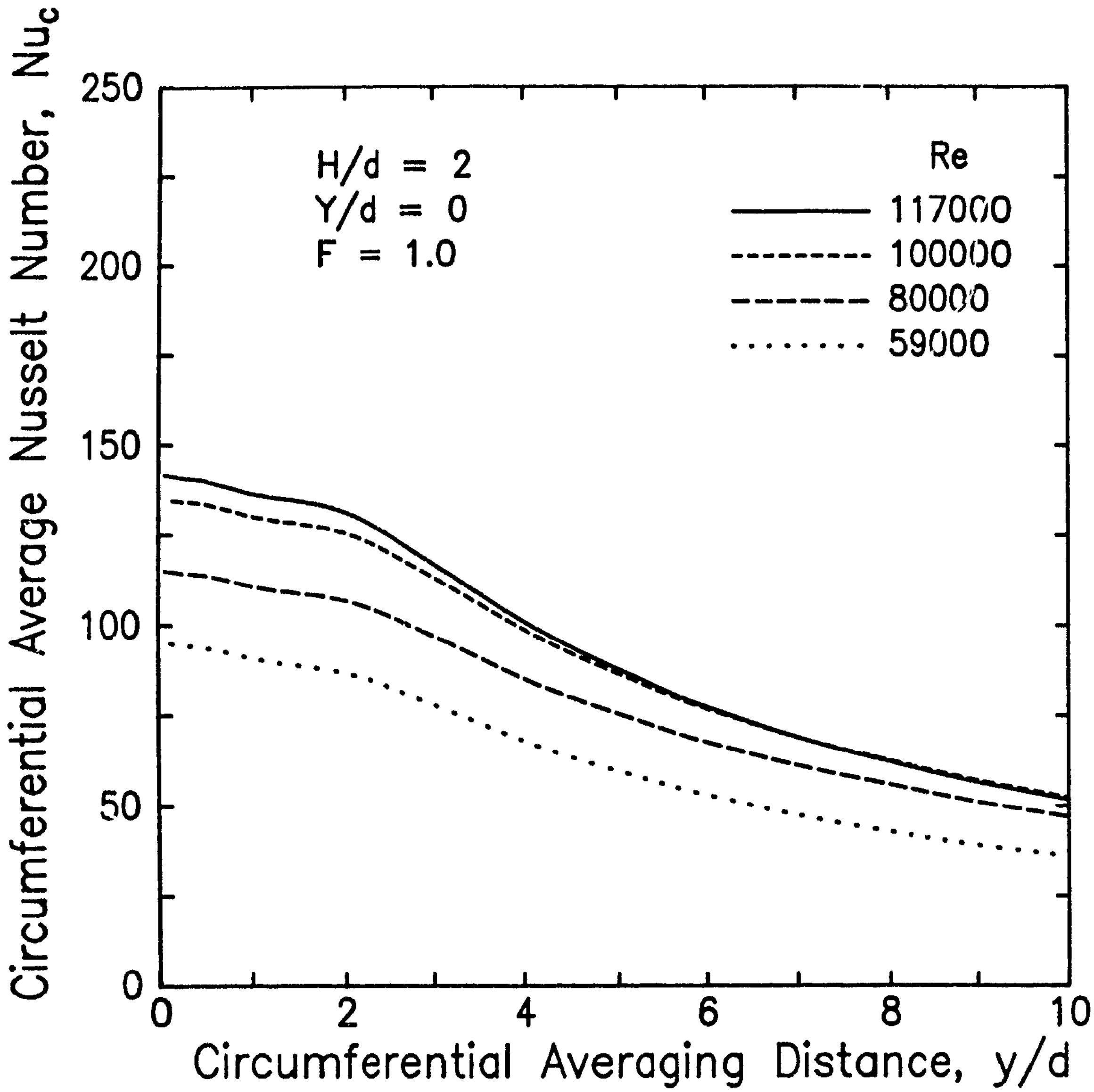

Figure 4.29(a) Effect of jet Reynolds number, Re, on circumferential average Nusselt number of unconfined jets: H/d = 2 and F = 1.0.

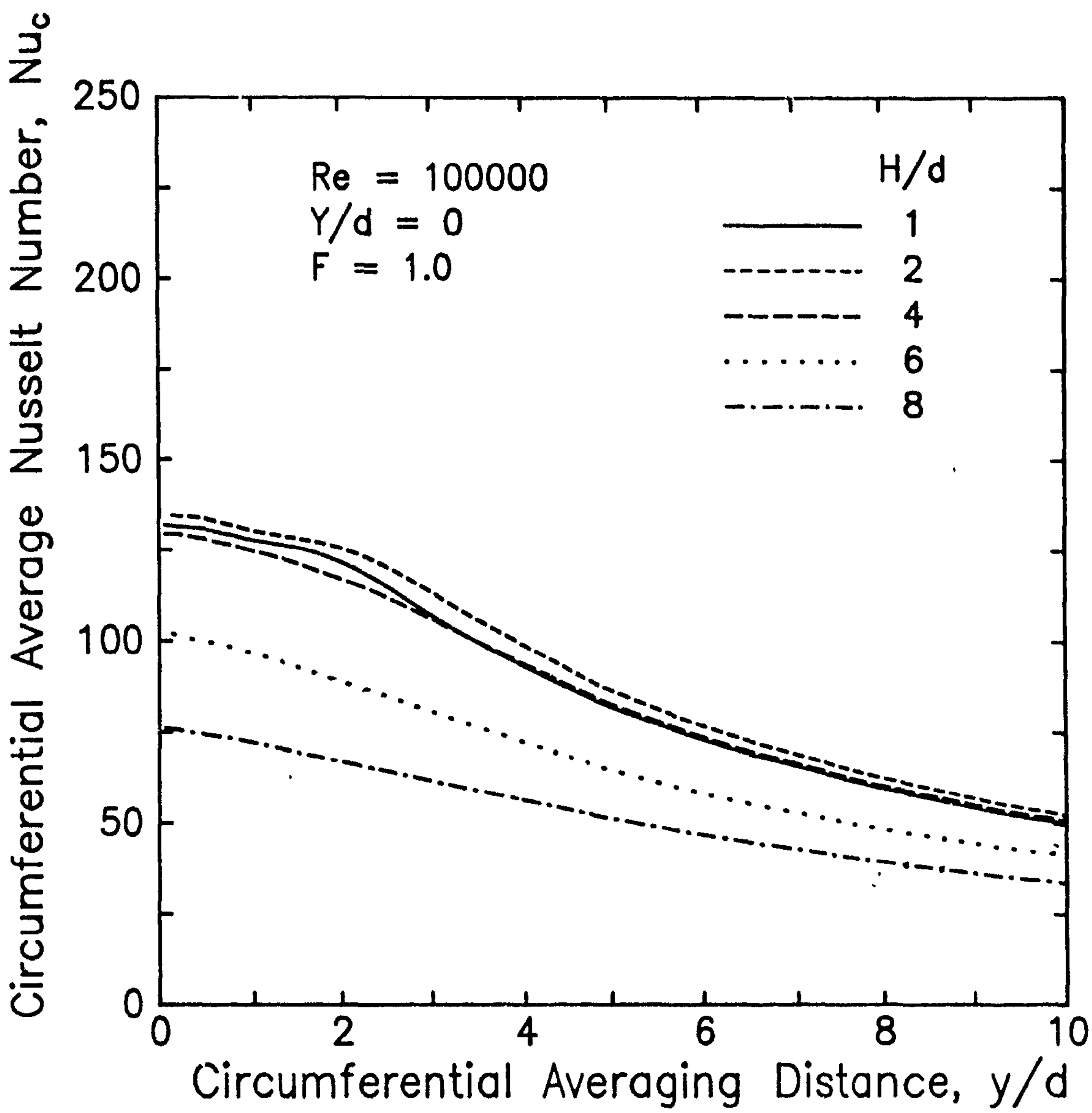

Figure 4.29(b) Effect of nozzle-to-impingement surface spacing, H/d, on circumferential average Nusselt number of unconfined jets: Re = 100000 and F = 1.0.

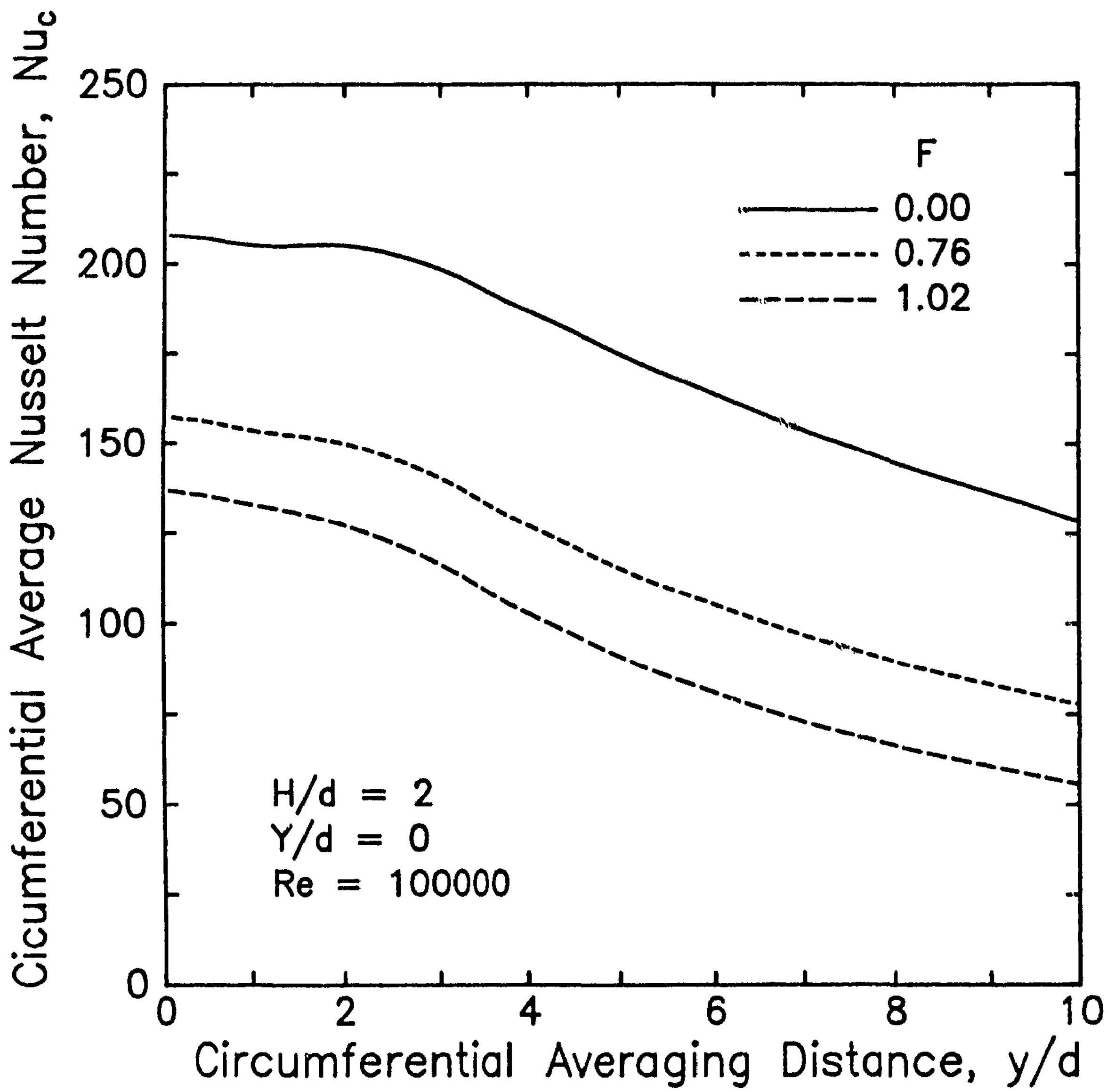

Figure 4.29(c) Effect of thermal entrainment factor, F, on the circum ferential average Nusselt number of unconfined jets: H/d = 2 and Re = 100000.

which is valid of the range

$$35000 \le Re \le 117000$$
$$1 \le H/d \le 4$$
$$3 \le (y/d)_a \le 10$$
$$2 \le (x/d)_a \le 10 \text{ (or } 4 \le S/d \le 20)$$
$$0 \le F \le 1.1$$

The correlation coefficient was 0.91.

As most of the impingement heat transfer to the calender roll is accomplished by $(y/d)_a = 10$ (or $y/d = \pm 10$), the above correlation can be rewritten for $(y/d)_a = 10$ as:

$$\overline{Nu}_c = \left[0.068 - 0.0219\left(\frac{S}{d}\right)^{0.28} F\right] Re^{0.71} \left(\frac{S}{d}\right)^{-0.32} \qquad (4.14)$$

As expected, the Reynolds number exponent in both the radial (Equation 4.9) and the circumferential (Equation 4.12 - 4.14) averages are similar (in this case, equal) since one would not expect the relatively small differences in averaging area, between a rectagular or square area and a circular area (Figure 4.27), to have a pronounced effect on the Reynolds number behavior, for r/d or $(x/d)_a$, $(y/d)_a$ greater than 3.

This lack of an effect of change in averaging area is further illustrated when Equation 4.12 is rewritten for $(x/d)_a = (y/d)_a$, corresponding to a square averaging area, $\pm x/d$ by $\pm y/d$ in size. This results in

$$\overline{Nu}_c = \left[0.114 - 0.0234\left(\frac{x}{d}\right)^{0.56} F\right] Re^{0.71} \left(\frac{x}{d}\right)^{-0.64} \qquad (4.10c)$$

where only the coefficients associated with F are changed by any significant amount.

The relationship between $\overline{Nu}_{c10}$ and the entrainment factor, F, as a function of H/d is shown in figure 4.30. The value of $\overline{Nu}_{c10}$ for F = 1.0 is less than 45% of that at F = 0, over the range $1 \le H/d \le 8$, illustrating the severe heat transfer performance decrease in typical unconfined impinging jet heat transfer applications.

The value of $\overline{Nu}_c$ for $(y/d)_a = 10$, termed $\overline{Nu}_{c10}$, as a function of Re and H/d is shown in Figure 4.31. For any given Re or entrainement factor, F, the highest average heat transfer occurs for H/d < 4, with a modest maximum near H/d = 2.

The circumferential average is of particular interest in the design of impingement jet calender control systems since it reflects the heat transfer over the circumference of the calender roll under the influence of the calender control system.

4.4 Effect of Nozzle Orientation Relative to Calender Roll

Air movement caused by the high velocity of the calender roll surfaces and by the presence of converging and diverging nips leads to complex air flow patterns around a paper machine calender stack, Figure 4.32. There has been considerable unsubstantiated speculation in the calender control literature about the potential benefits that might derive from "optimum" nozzle positioning relative to the rolls. Few published data relate the impinging jet heat transfer to the overall machine calender geometry. The limited data of Pelletier et al.[1984, 1987] suggested the effect of these geometric variables might be small.

The two geometric variables which specify impingement positioning, Figure 4.5, are the circumferential impingement position relative to the diverging nip, ϑ, and the nozzle inclination, ψ, relative to normal impingement.

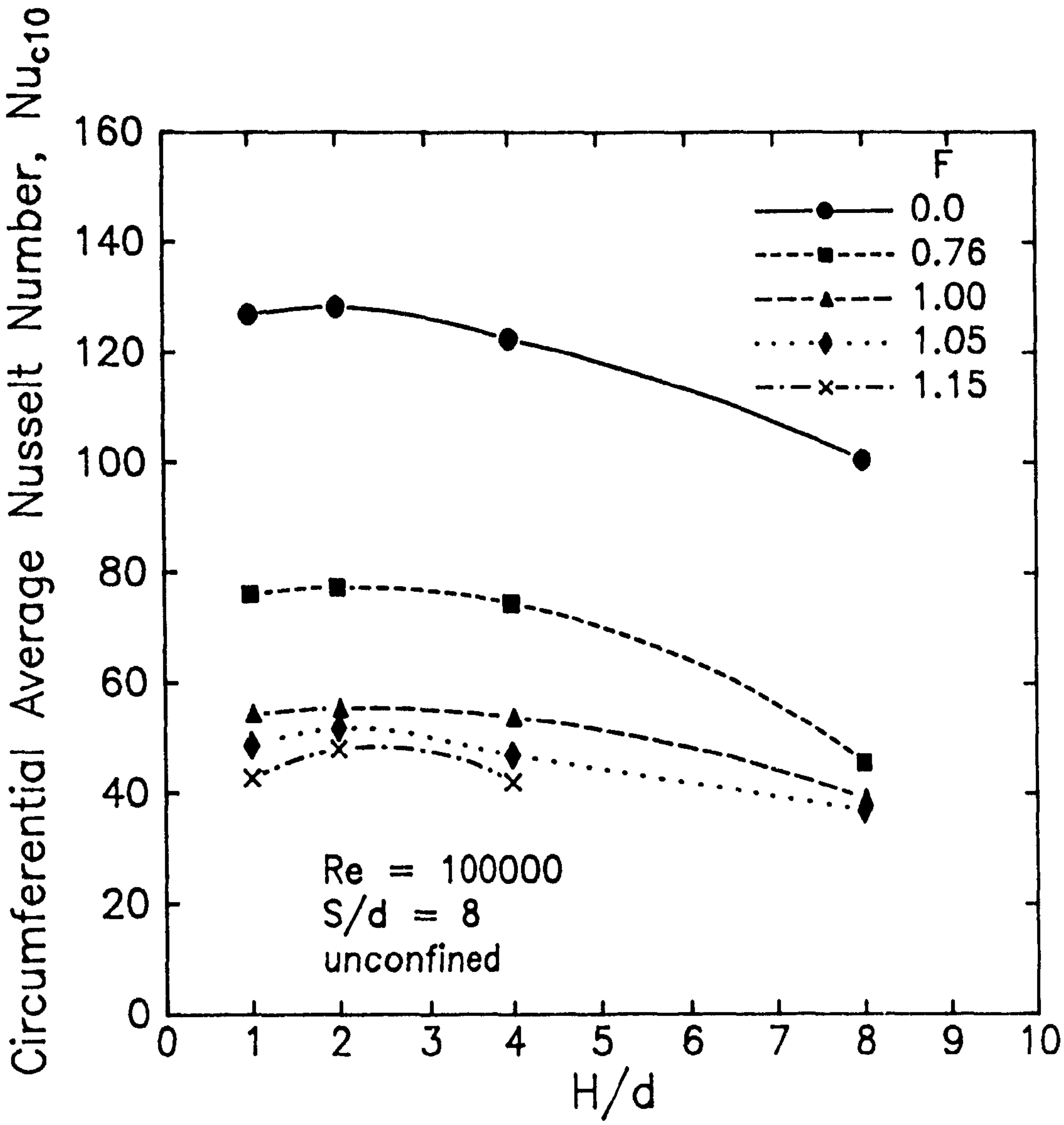

Figure 4.30 Effect of thermal entrainment factor, F, on the circumferential average Nusselt number - H/d relationship: $(y/d)_a = 10$.

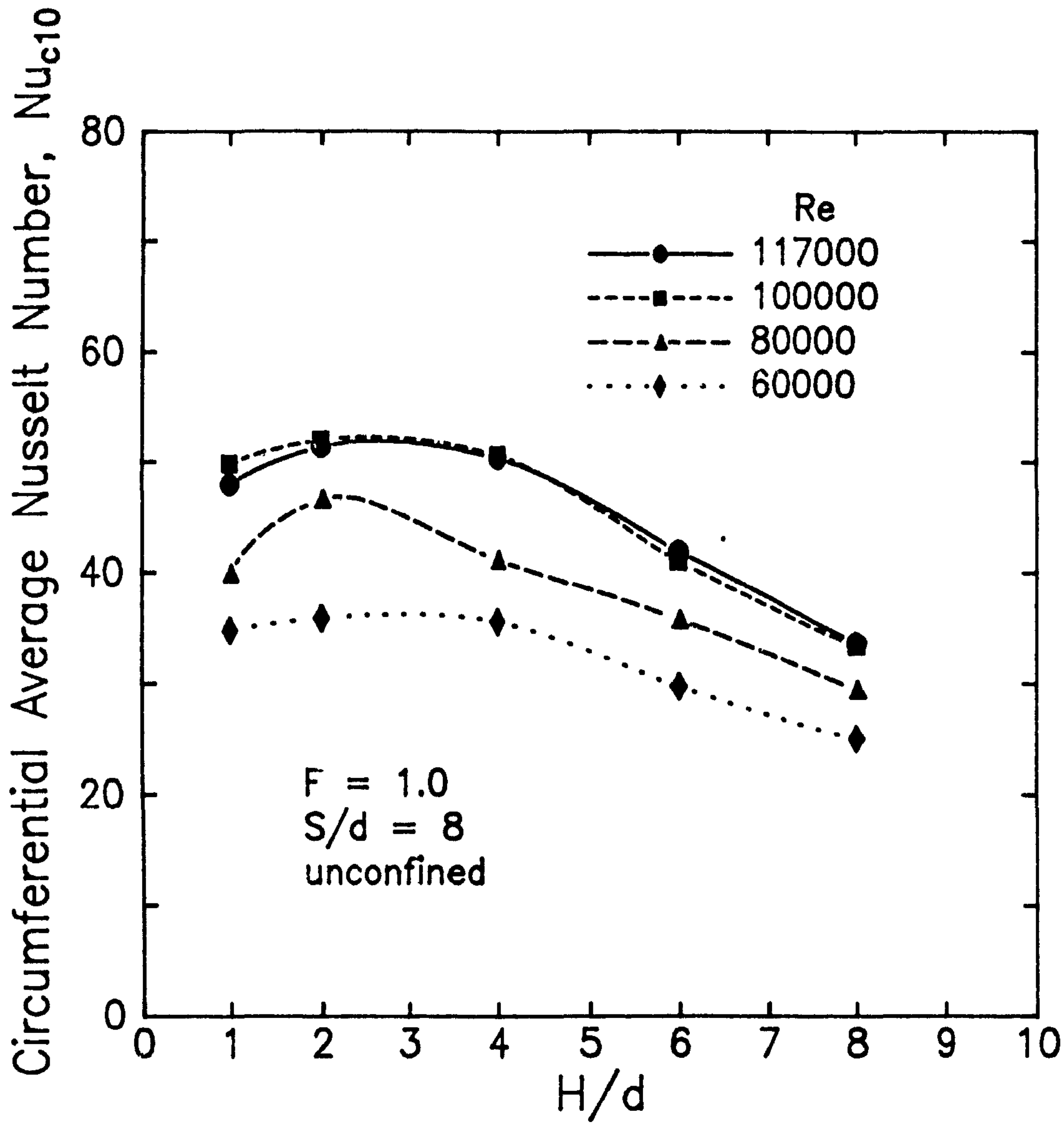

Figure 4.31 Effect of Reyolds number, Re, on the circumferential average Nusselt number - H/d relationship: $(y/d)_a = 10$.

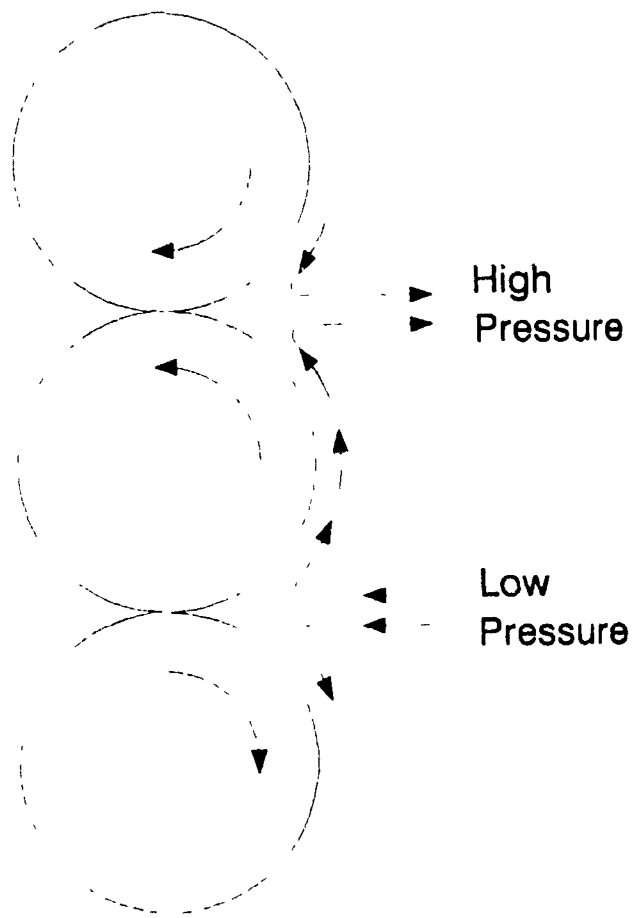

Figure 4.32 Air flow patterns around a calender stack.

4.4.1 Effect of Circumferential Impingement Position

The circumferential Nu profiles passing through the nozzle centerline, $x/d = 0$, are shown in Figure 4.33. All the profiles, with the exception of the neutral position, $\vartheta = 90^\circ$, are shifted such that the impingement points are matched, hence the designation y'/d rather than y/d. The corresponding radial average Nusselt number profiles are shown in Figure 4.34. Clearly there is little effect of ϑ on the Nu profiles in the range $\pm 30^\circ$ ($\pm$ 5.75 d) from the neutral position. As pointed out earlier, with $\vartheta = 90^\circ$ heat transfer becomes independent of jet temperature by about 10d from the nozzle center line. With the roll and nozzle diameters used here, the 180° angular displacement from nip to nip corresponds to a circumferential distance of $\simeq$ 34d. Therefore the ϑ positions of 60° and 120° still leave about 11d from the jet centerline to the nearest nip. The lack of any significant effect on heat transfer rate of varying circumferential impingement position within the range $60^\circ \leq \vartheta \leq 120^\circ$ indicates that within about 10d of the centerline the jet flow field completely dominates that created by the rotating rolls, Figure 4.32.

In Figure 4.33 some minor effects of the nips on the local Nu profiles can be seen in the profiles for $\vartheta = 60^\circ$ and $\vartheta = 120^\circ$. For $\vartheta = 60^\circ$, a sudden drop in the Nu profile can be observed at $y/d = -6$ which is within 5d - 6d of the diverging nip. For the $\vartheta = 120^\circ$ nozzle position, a drop can also be observed at $y/d = 8$. However these effects do not affect $\overline{Nu}_r$, Figure 4.34.

These experimental observations contradict the hypothesis of Bryan[1972] that impingement heat transfer rate would be sensitive to circumferential position of the jet. The absence of such an effect is however consistent with the earlier observation, Section 4.2.4, of the

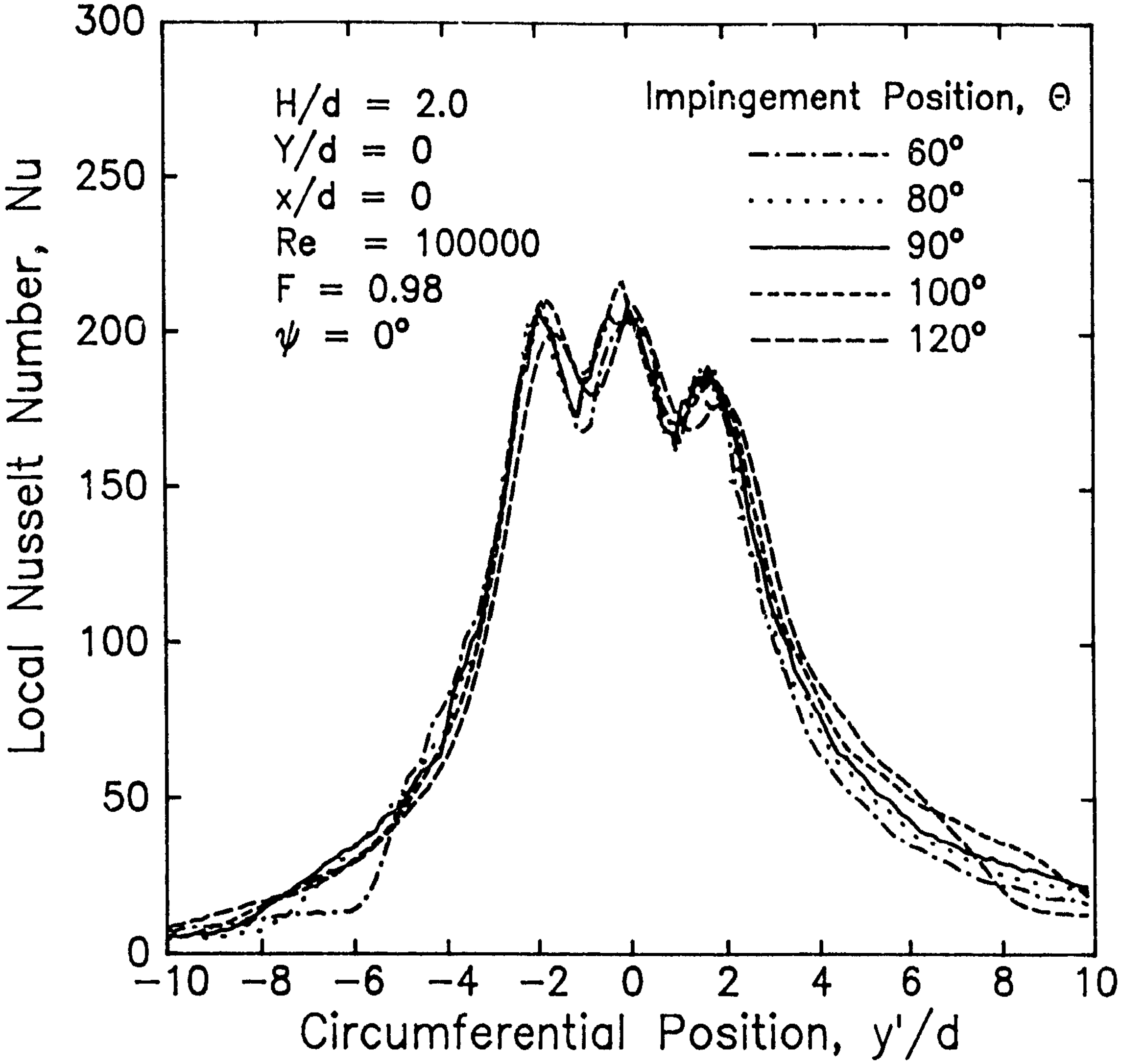

Figure 4.33 Effect of circumferential impingement position, θ, on profiles of local Nusselt number.

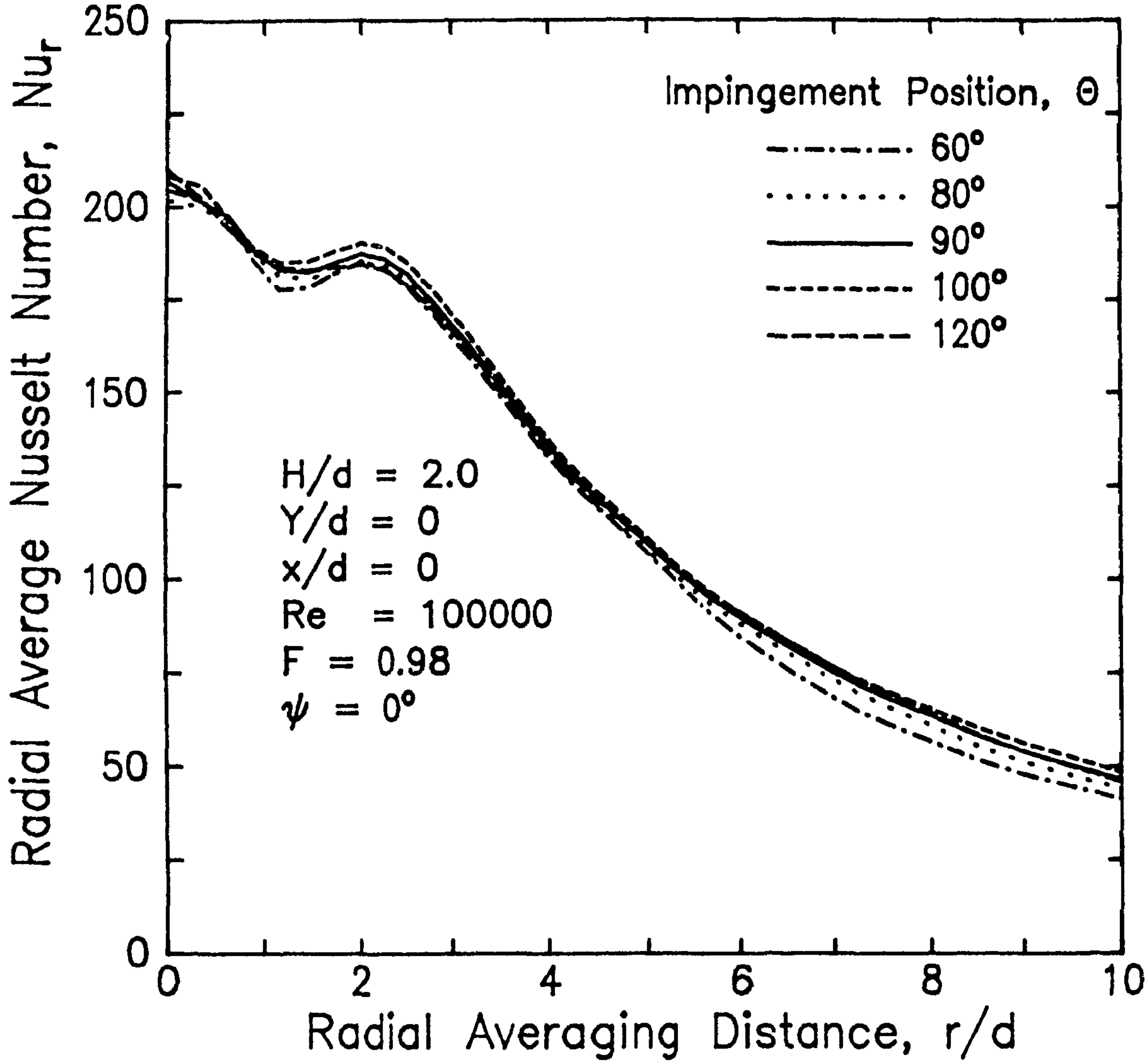

Figure 4.34 Effect of circumferential impingement position, θ, on radial average Nusselt number, $\overline{Nu}_r$.

lack of an effect of surface motion. The surface motion variable, M_{vs} has no effect on heat transfer over the industrially significant range, $0.1 < M_{vs} < 0.3$. Thus the air dragged by calender roll rotation is not able to affect the impingement heat transfer.

Bryan proposed that the most effective position would be with the impingement control nozzles directed into the low pressure zone of the diverging nip, the position of the thinnest boundary layer. This configuration could not be studied on the present equipment because of the existence of a 1mm gap between the rolls, required to avoid damaging the thin film sensor. However, the lack of an observed effect of the surface boundary layer on impingement heat transfer discounts this hypothesis since the only thing gained by this configuration is the reduced boundary layer. Furthermore, the nozzle inclination relative to the roll surface at the impingement point will be high, which, as shown in Section 4.4.2, is detrimental to the impingement heat transfer.

4.4.2 Effect of Nozzle Inclination

The possibility of a maximum in heat transfer coefficient for an impingement angle other than normal to a moving impingement surface was proposed by Baines and Keffer[1976]. With a slot jet they found a maximum in shear stress for the nozzle inclined against the direction of surface motion. Huang[1988] showed that for a confined slot jet, angle of impingement over the range $\pm 15^\circ$ has little effect on average Nu, while inclination by 30° from normal results in a substantial lowering of average heat transfer.

(a) Circumferential Profile of Local Nusselt Number

The direction of surface motion and the orientation of the nozzle relative to the roll are shown on the profiles of Figures 4.35 and 4.36 for nozzle-to-roll spacings, H/d of 2 and 4. With positive values of nozzle inclination, ψ, the jet is directed in the same direction as the impingement surface motion, and vice versa.

With increasing nozzle inclination the Nu profile is skewed in the direction of the jet flow. The profiles lose their symmetry as Nu decreases more rapidly on the side from which the jet arrives.Thus on the jet arrival side the off-stagnation maximum for H/d = 2 is suppressed and merges with the stagnation point maximum. Also, with increasing nozzle inclination there is a steady increase in Nu_{max} with H/d = 2, but for H/d = 4 the Nu_{max} is independent of nozzle inclination. For confined slot jets, Huang[1988] observed effects of nozzle inclination on local Nu profiles similar to those found here for round jets. With inclined nozzles there is an uneven split in the jet flow, and Nu decreases on the side with the smaller flow.

Another feature of the local Nu profiles for H/d = 2 appears to be the result of surface motion. For negative values of ψ, where the jet is directed against the surface motion, the off-stagnation maximum on the side from which the jet arrives is seen to decrease more slowly than the corresponding maximum for positive ψ. With the jet directed against the surface motion, the velocity gradients near the impingement surface are higher, aiding the transition from a laminar to a turbulent boundary layer, resulting in a higher off-stagnation maximum.

(b) Stagnation or Maximum Nusselt Number

Stagnation or maximum Nusselt number from Figures 4.35 and 4.36 is shown in Figure 4.37 as a function of the angle of inclination. For H/d=2, where there exist off-stagnation maxima, it is difficult to

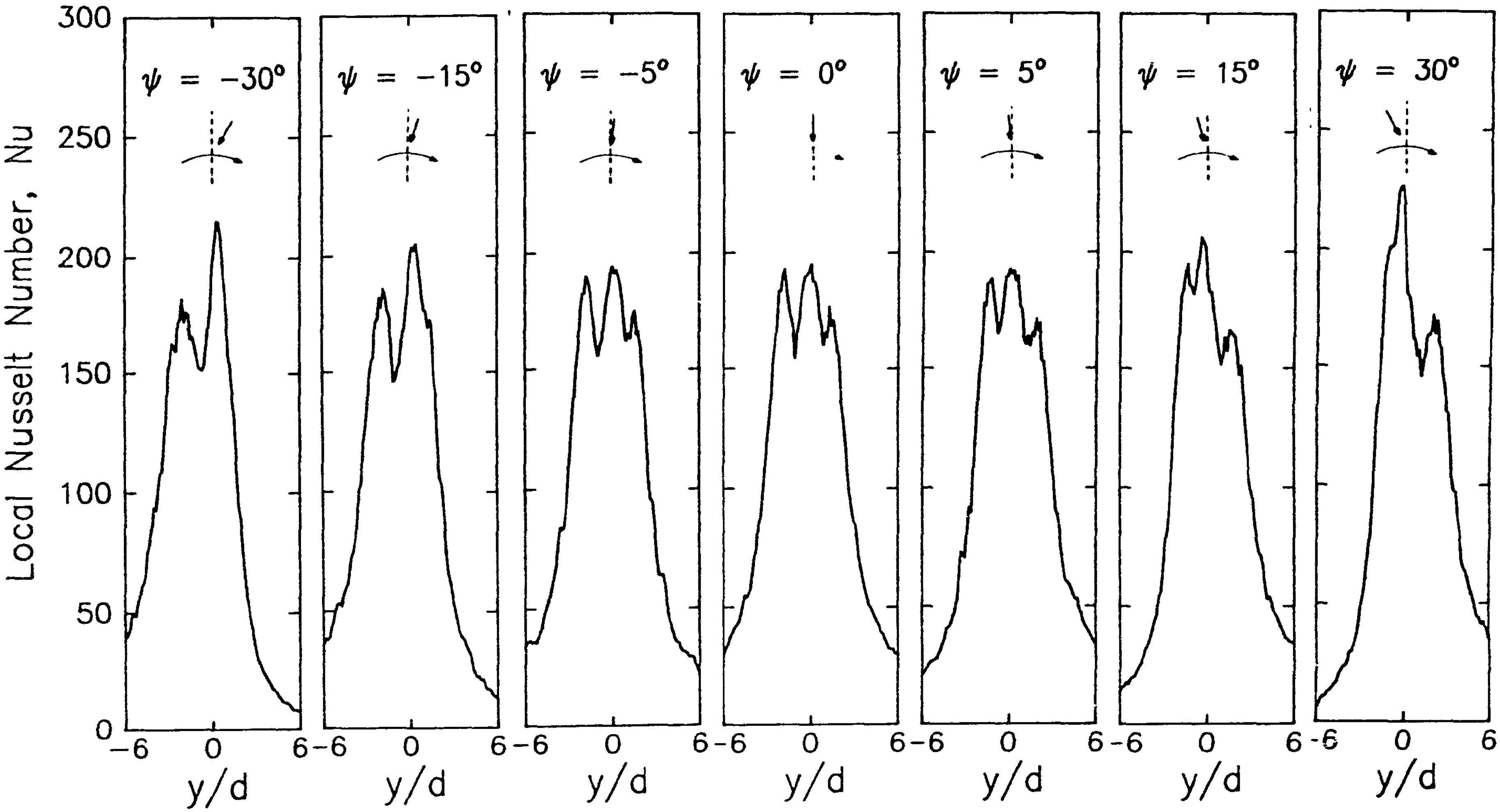

Figure 4.35 Effect of nozzle inclination, ψ, on the profile of local Nusselt number for an unconfined jet: $H/d = 2$, $Re = 100000$, $F = 0.98$.

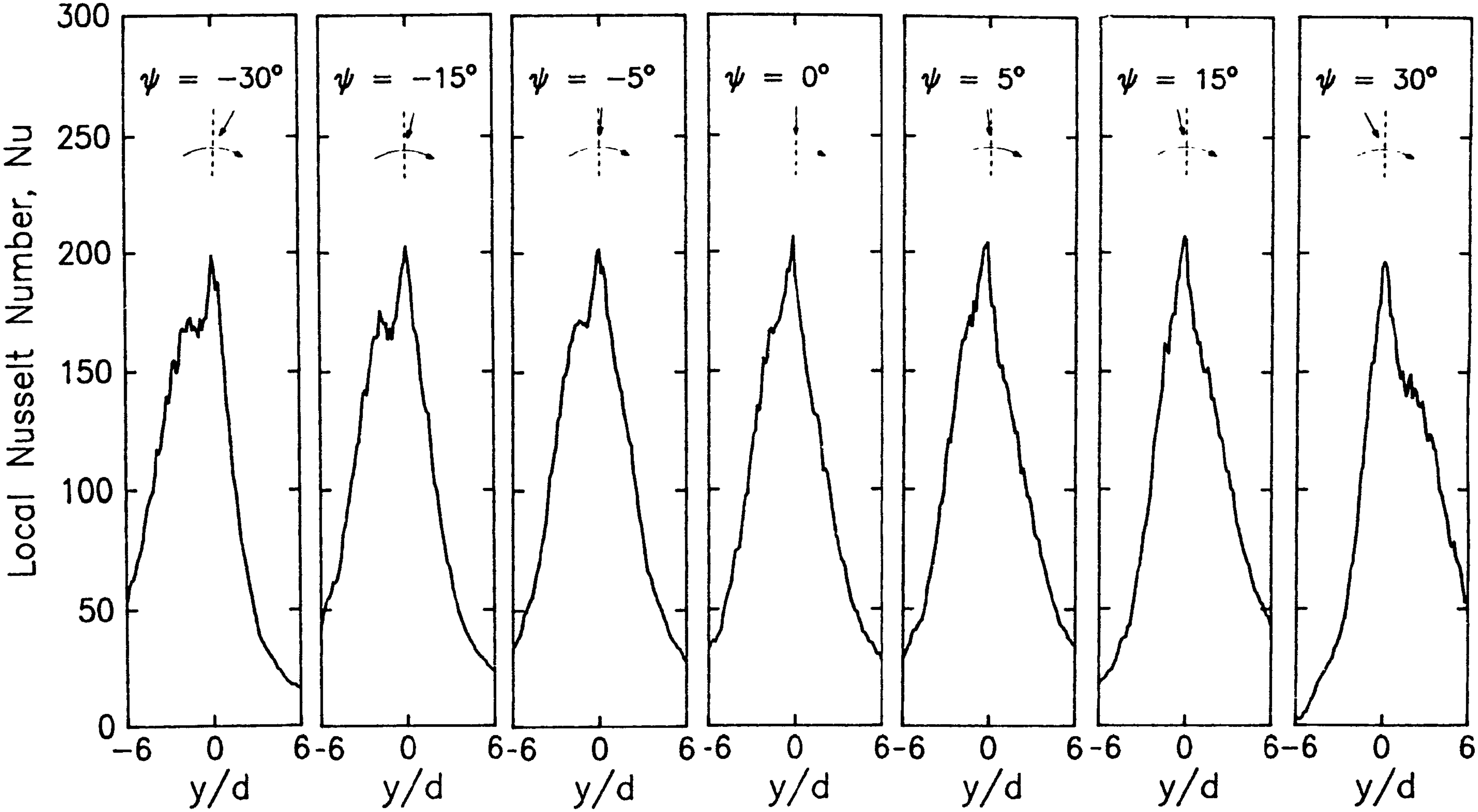

Figure 4.36 Effect of nozzle inclination, ψ, on the profile of local Nusselt number for an unconfined jet: $H/d = 4$, $Re = 100000$, $F = 0.98$.

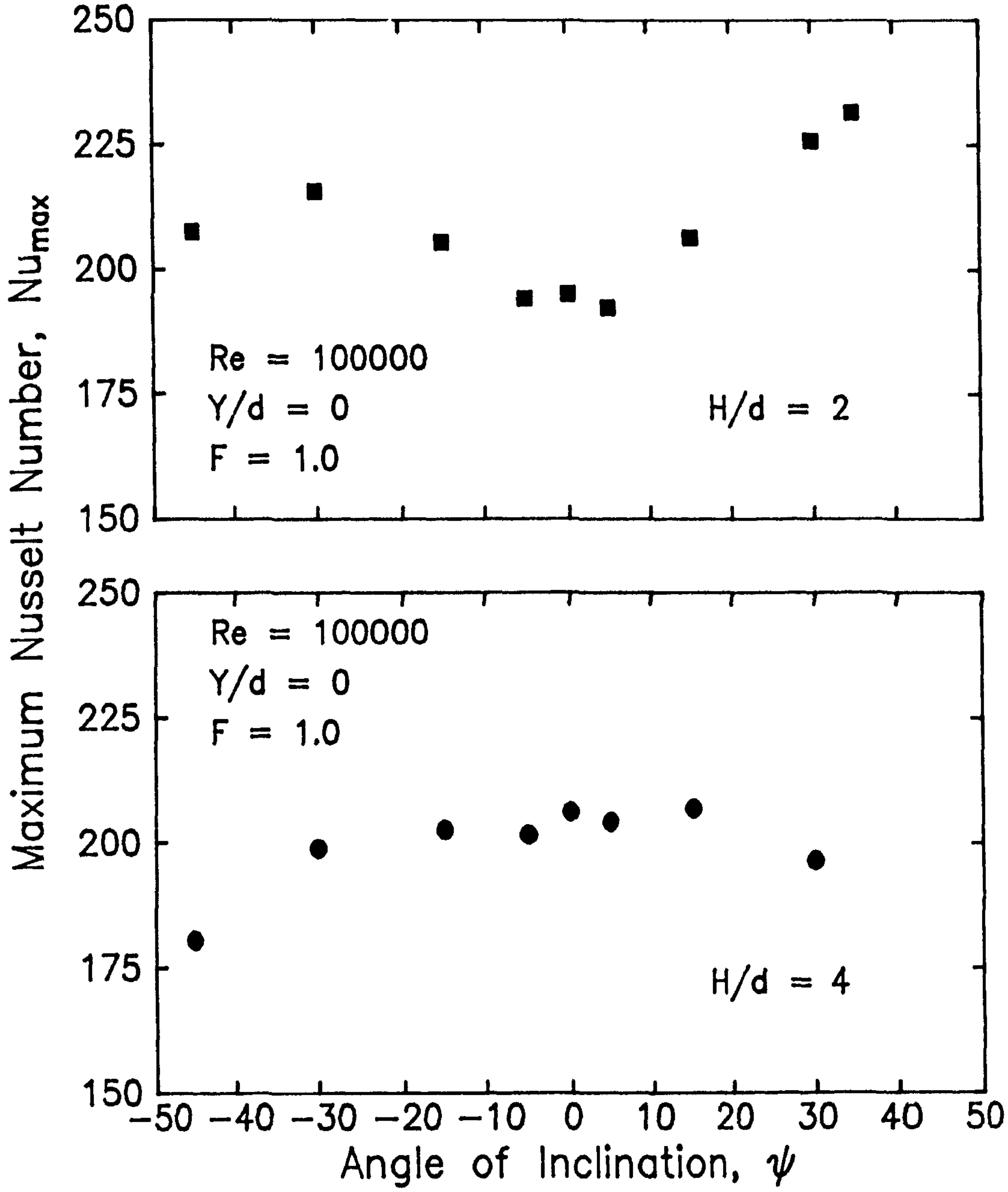

Figure 4.37 Effect of nozzle inclination, ψ, on maximum Nusselt number, Nu_{max}.

locate the position of Nu_o for jet inclinations other than 0°. When the impingement surface is moving there is no true stagnation point since the boundary layer does not change directions but always moves in the direction of surface motion. Thus, for jet inclinations other than normal, the position of the stagnation point Nu_o is difficult to determine. For this reason the maximum in local Nusselt number, designated Nu_{max}, will be used. For larger H/d, there exists only a single maximum which coincides with the stagnation point.

For H/d = 4, Nu_{max} exhibits a very shallow maximum for normal impingement, with less than 5% change over the range $-30^\circ \le \psi \le 30^\circ$. For H/d = 2, Nu_{max} appears to reach maxima for ψ near $\pm 35^\circ$.

Figure 4.38 shows the effect of nozzle inclination on the displacement of Nu_{max} from the intersection of the jet centerline at the impingement surface, termed the geometric jet impingement point. The displacement is symmetrical, with a maximum of 0.5d. This effect has been observed by Korger and Kreizek[1972] using mass transfer measurements under slot jets and was shown analytically for slot jets by Schauer and Eustis[1963], in both cases for stationary impingement surfaces. However, slot jets are much more sensitive in this respect. Thus where the present study established that the point of Nu_{max} is shifted by less than 0.5d for a nozzle inclination of about 40°, Huang[1988] showed that for comparable nozzle spacings, Nu_{max} for slot jets is shifted by around three times the nozzle width.

(c) <u>Circumferential Average $\overline{Nu}_c$</u>

As noted in Section 4.3.4, for a round jet impinging on a cylinder, two average Nusselt numbers can be defined, $\overline{Nu}_r$, defined relative to the nozzle centerline and $\overline{Nu}_c$ relative to the impingement surface. As the

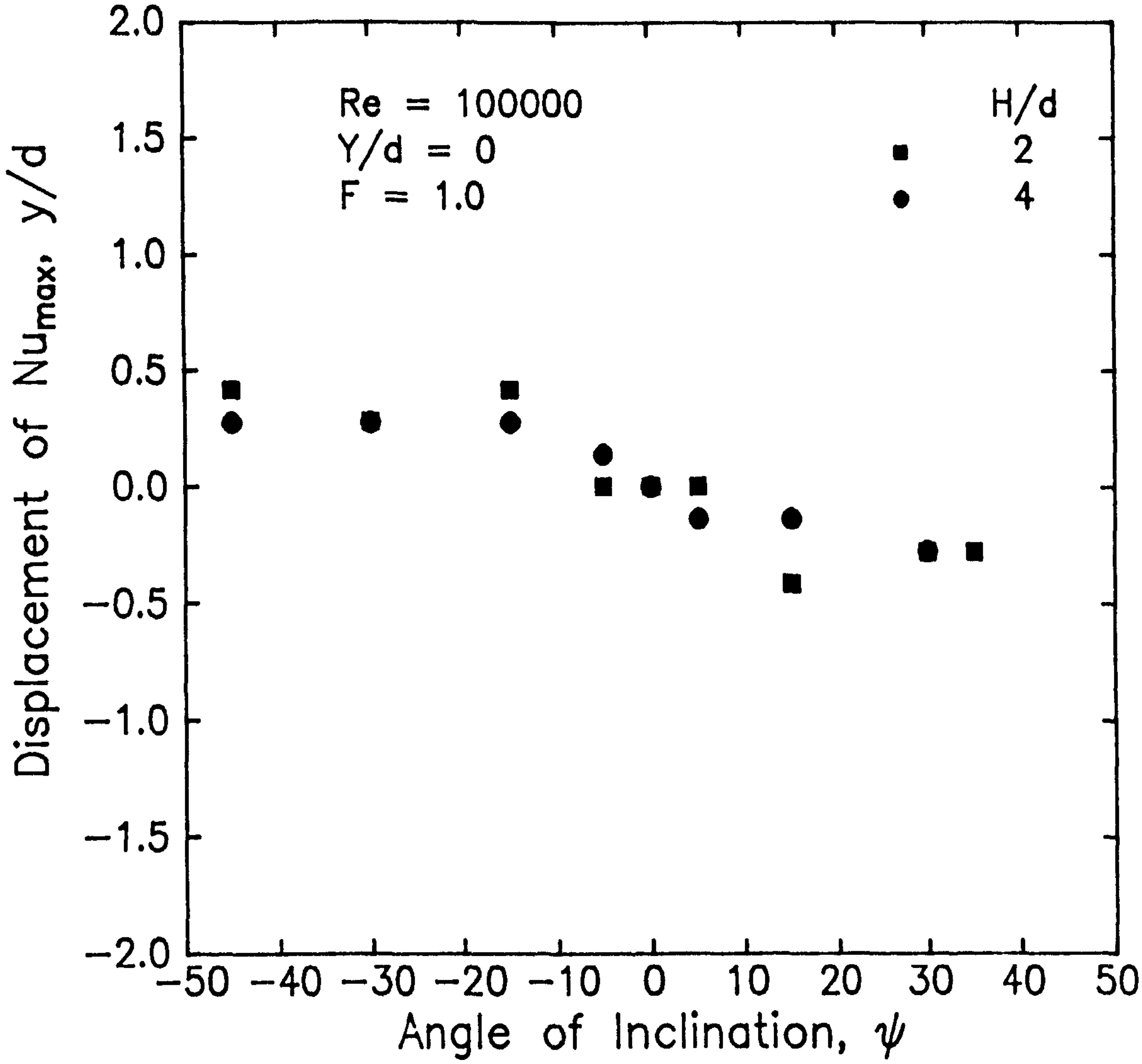

Figure 4.38 Effect of nozzle inclination, ψ, on the position of the maximum Nusselt number, Nu_{max}.

radial average $\overline{Nu}_r$ is meaningful only for axisymmetric impingement, the circumferential average, $\overline{Nu}_c$, must be used to evaluate the effect of nozzle inclination. For a jet-to-jet spacing of 8 d, $\overline{Nu}_c$ is calculated over an axial distance of ± 4 d on either side of the jet centerline.

Figures 4.39 and 4.40 illustrate the effect of nozzle inclination on the profiles of $\overline{Nu}_c$ for two nozzle-to-roll spacings. For calender roll temperature control the only interest is in the total heat transfer at the roll. In Section 4.4.1 it was noted that for the roll and nozzle diameters used here, the circumferential distance between nips is about 29d. As it was demonstrated earlier, the heat transfer beyond y = ±10d is negligible when compared to that occurring within y = ±10d for the range of experimental conditions in this study, making this value of y is an appropriate limit for the extent of calender roll circumference to use for comparison. Thus Figure 4.41 shows the circumferential average Nusselt number evaluated for ±10d. This circumferential distance of 20d accounts for essentially all of the heat transfer between the impinging jets and the roll. As documented in Section 4.3, for constant F, $\overline{Nu}$ is independent of H/d in the range H/d ≤ 4. In Figure 4.41, the values of $\overline{Nu}_{c10}$ at H/d = 2 are somewhat lower because of the deleterious effect of the higher thermal entrainment factor, F. Although the differences in $\overline{Nu}_{c10}$ with nozzle inclinations are not large, from Figure 4.41 it is clear that the highest heat transfer coefficient at the calender roll is with $\psi = 0^\circ$, i.e. for normal impingement. Contrary to previous speculation, the present measurements establish that there is no advantage to be gained from inclining the nozzles away from normal impingement on calender rolls.

This limited effect of jet inclination on average Nusselt number is consistent with Korger and Krizek who found the average mass transfer to

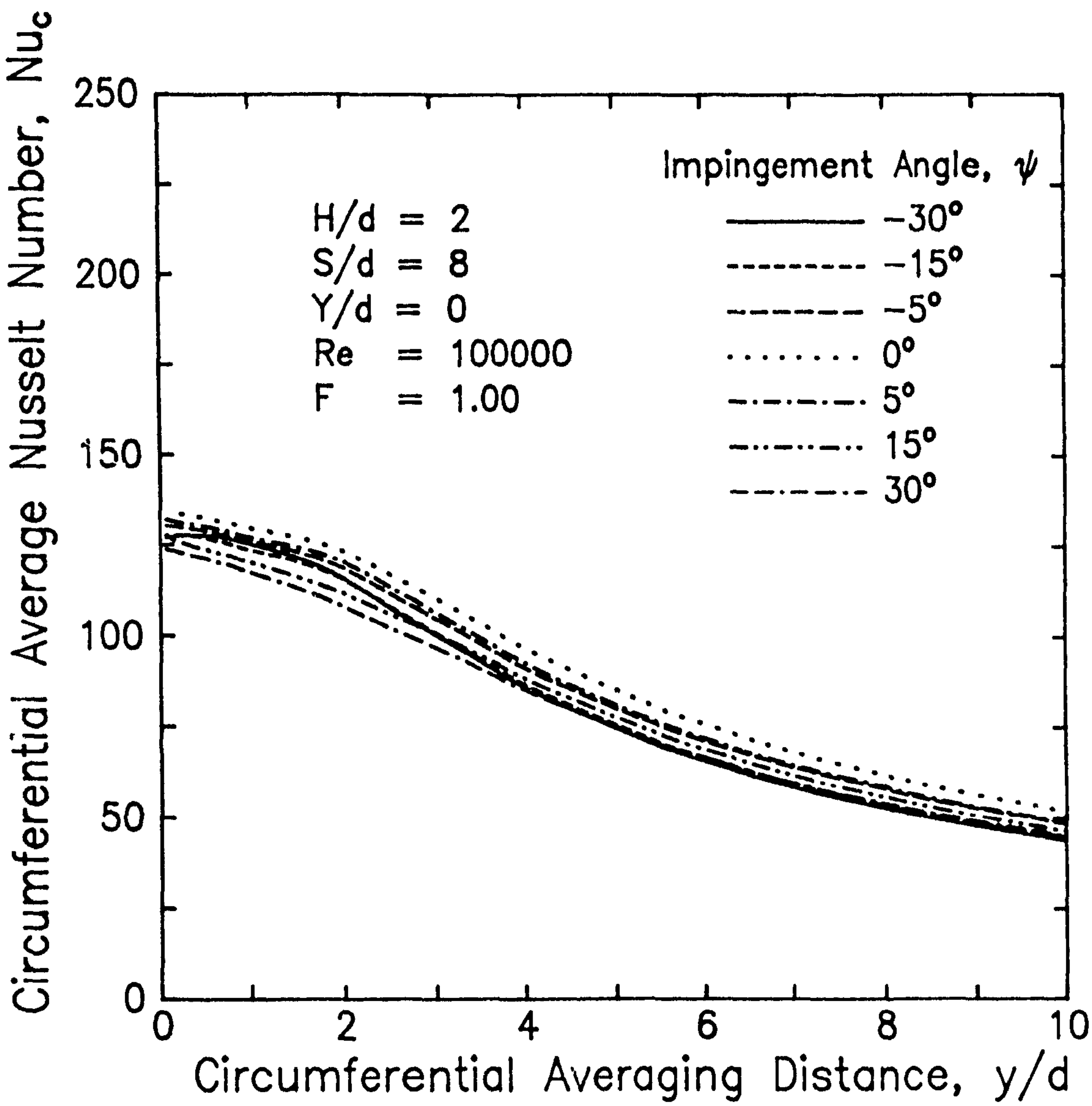

Figure 4.39 Effect of nozzle inclination, ψ, on circumferential average Nusselt number, $\overline{Nu}_c$, of unconfined jets: H/d = 2.

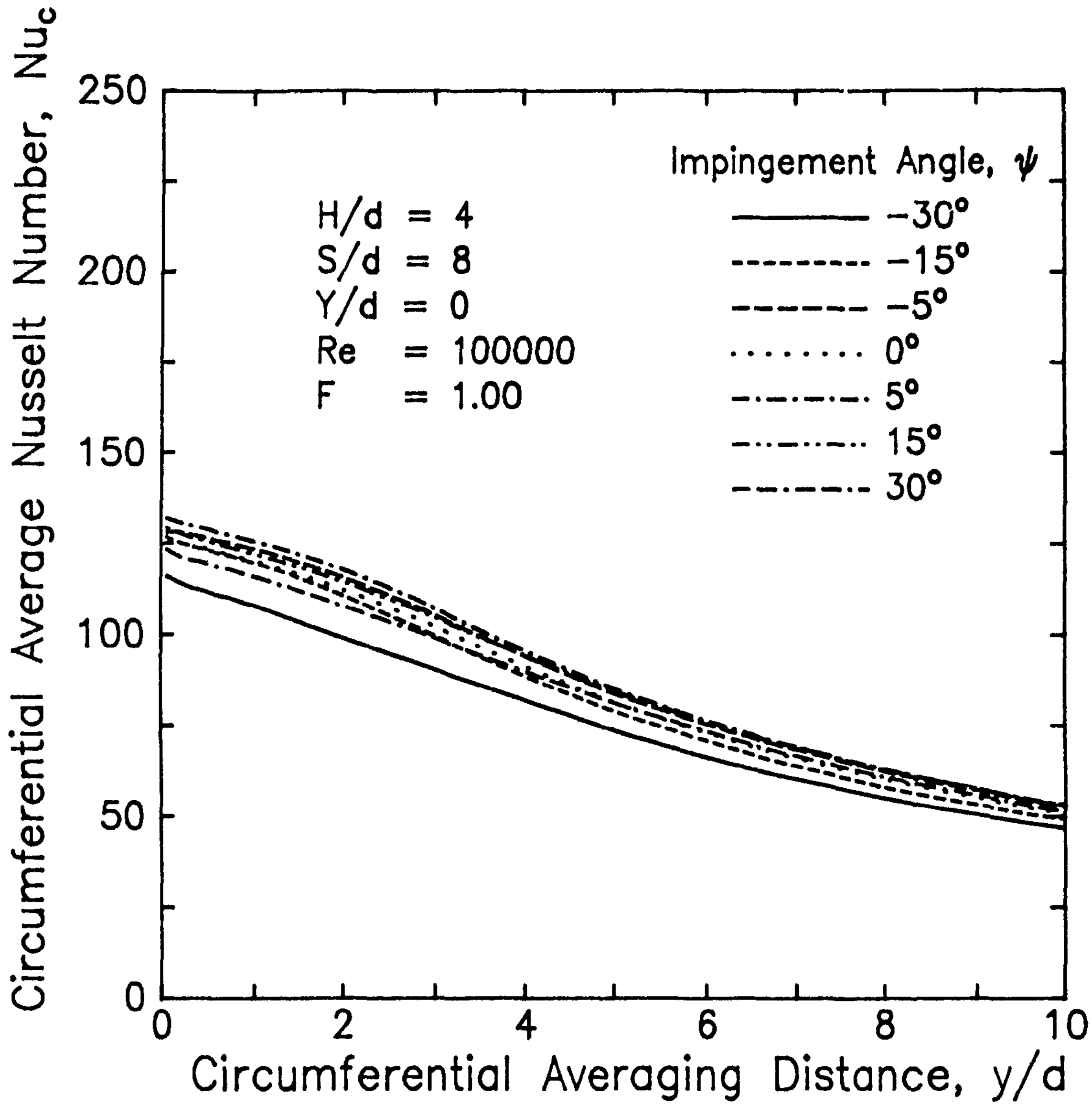

Figure 4.40 Effect of nozzle inclination, ψ, on circumferential average Nusselt number, $\overline{Nu}_c$, of unconfined jets: H/d = 4.

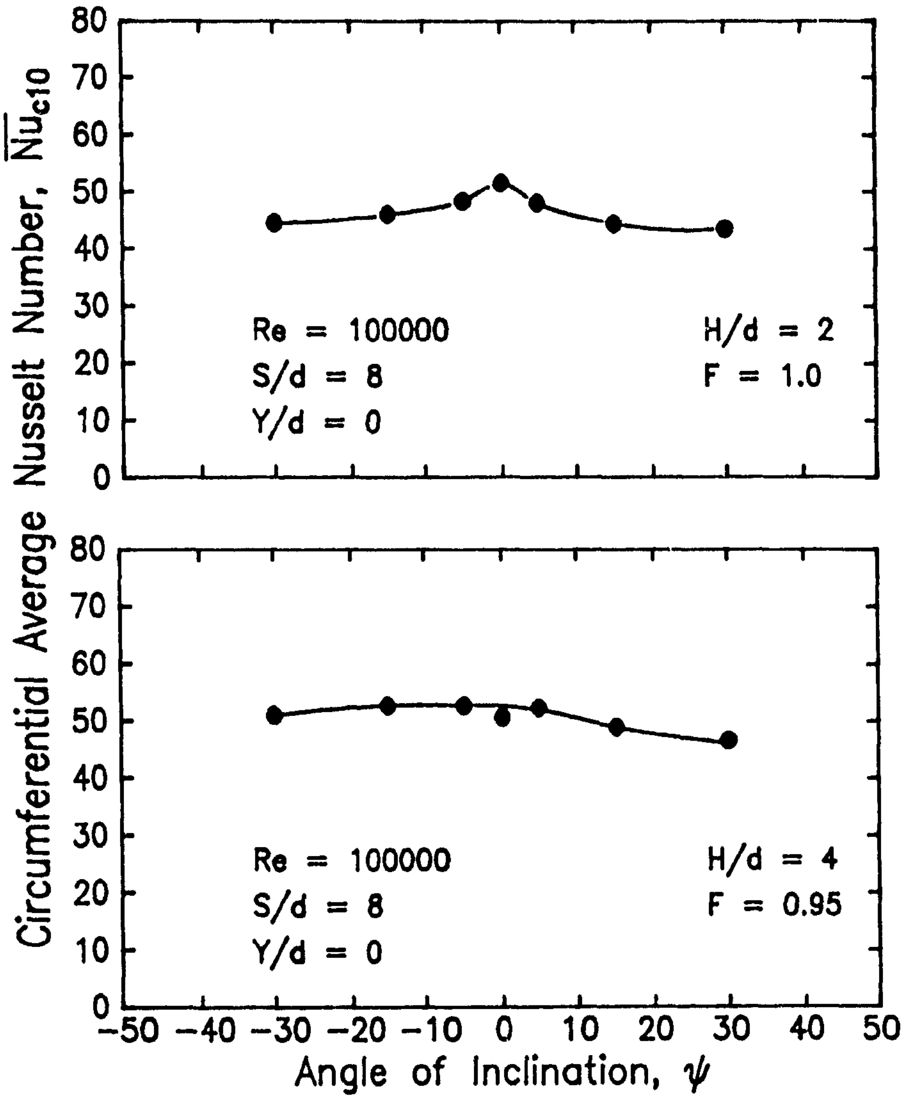

Figure 4.41 Effect of nozzle inclination, ψ, on circumferential average Nusselt number at $(y/d)_d = 10$, $\overline{Nu}_{c10}$, for unconfined jets.

be independent of ψ over the range $0^\circ \le \psi \le 30^\circ$. Likewise for confined slot jets on fast and slow moving impingement surfaces, Huang[1988] found that with respect to average Nusselt number there was no advantage for inclining the jets within $\pm15^\circ$ from perpendicular and a strong disadvantage for nozzles inclined greater than $\pm30^\circ$ from normal.

4.5 Effect of Confinement

Although for most industrial applications confinement of impinging jets is considered a requirement for reasons of thermal efficiency, this has not been the practice in calender control systems until quite recently. Jet thermal entrainment has been demonstrated by the present study to be an important design variable because of its strongly detrimental effect on impinging jet heat transfer. However, even in the thermally neutral case of F = 0, there remains an effect of entrainment on the flow field and hence on the heat transfer for unconfined jets. Therefore it is of interest to document the heat transfer characteristics with the impingement surface isolated from all direct effects of the external environment by use of a jet confinement surface set flush with the nozzle exit and extending parallel to the impingement surface.

For a temperature mismatch of $\Delta T_{ja} = 0$, or $F = 0$, the presence of confinement has been documented by Obot[1982] and Sparrow et al.[1975] to decrease heat transfer, attributed to decreased jet flow without entrainment. For a jet Reynolds number of 100000, the data of Crow and Champagne [1971] show that, at a position 2d downstream of the nozzle exit, an unconfined round jet has entrained an amount of surrounding fluid equal to about 30% of the nozzle exit fluid. Therefore the present experiments were designed to examine the sensitivity of impingement heat experiments were designed to examine the sensitivity of impingement heat transfer to the combination of these thermal and flow field effects. Results are presented for jets with the limits of confinement, Y/d, (i.e. nondimensional extent of confinement circumferentially on either side of the jet centerline) of 0, 3.0, 4.5 and 5.75. The geometry of the confinement surface is shown in Figure 4.42.

4.5.1 Circumferential Profile of Local Nusselt Number

For a thermal entrainment factor of F = 1.15, Figures 4.43(a) - 4.43(c) show the effect of jet confinement on the circumferential distributions at the axial position corresponding to the jet centerline for local Nusselt number with H/d = 1, 2 and 4 and Re = 100000. The effect is most pronounced at the closest spacing, H/d = 1, and largest confinement, Y/d = 5.75. The Nusselt number at the stagnation point and the off-stagnation minima are essentially independent of jet confinement. However, as the confinement is increased to Y/d = 4.5, the secondary maxima grow and move outwards, with the whole profile broadening. With a further increases in confinement to Y/d = 5.75, the increase in heat transfer occurs almost exclusively on the side downstream from the stagnation point (i.e. at positive y/d) with little or no increase occuring on the upstream side. The same trends are substantially diminished at H/d = 2, and almost vanish at H = 4.

On the upstream side, the presence of a sharp break in the local Nusselt profile near y/d = 5 combined with the lack of an increase in the heat transfer profile when increasing confinement from Y/d = 4.5 to 5.75, indicates that the boundary layer entering the impingement area with the moving surface successfully insolates the roll from the impingement jet air. The transition point from heat transfer dominated

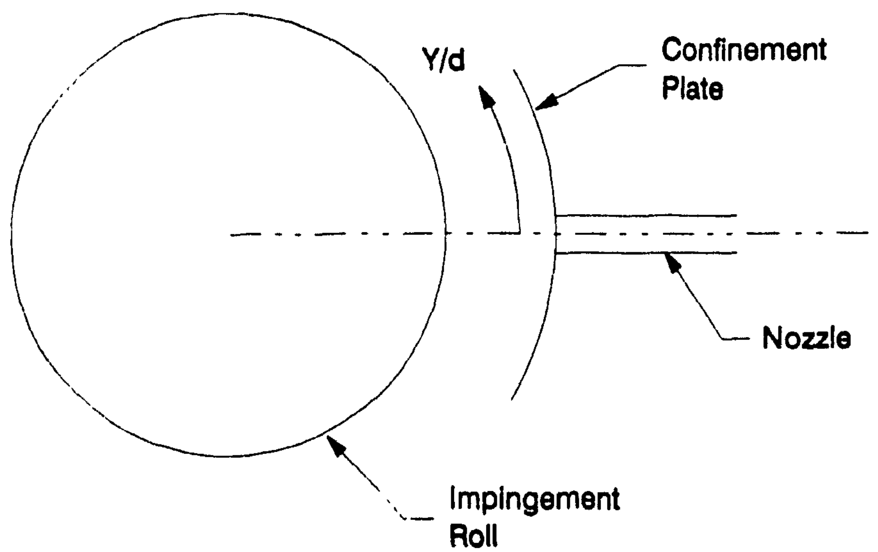

Figure 4.42   Jet confinement geometry.

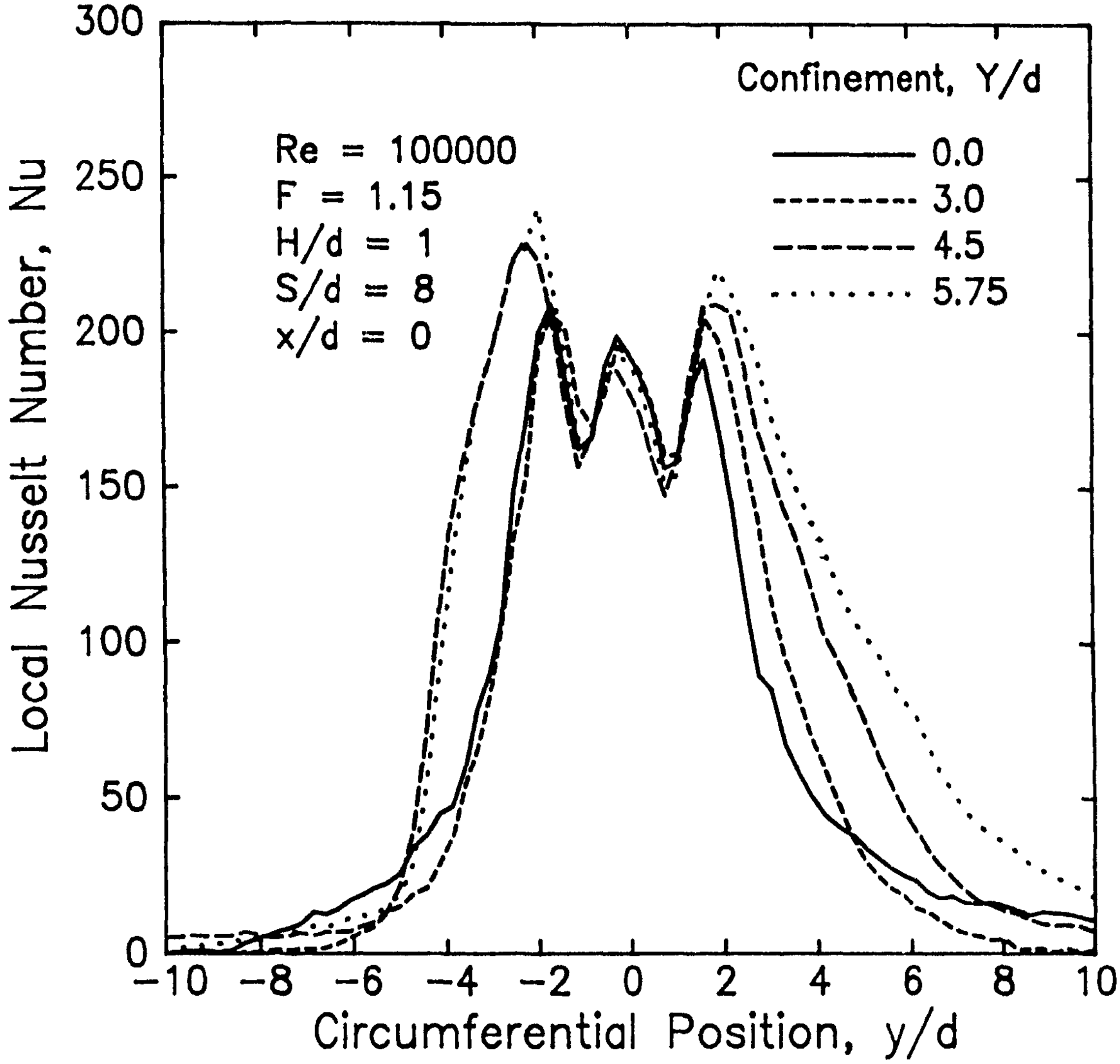

Figure 4.43(a) Effect of confinement, Y/d, on the profile of local Nusselt number: H/d = 1, Re = 100000.

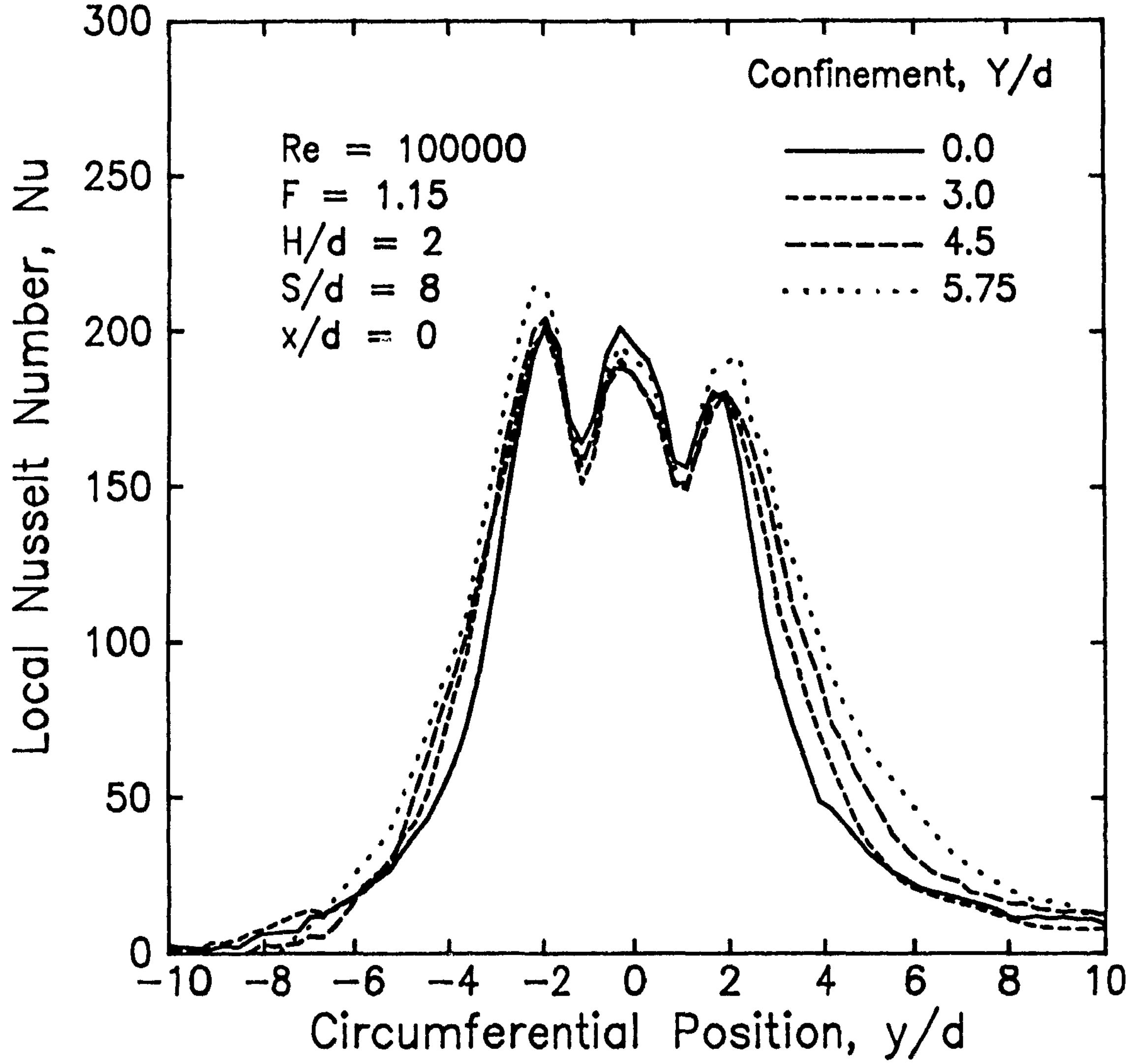

Figure 4.43(b) Effect of confinement, Y/d, on the profile of local Nusselt number: H/d = 2, Re = 100000.

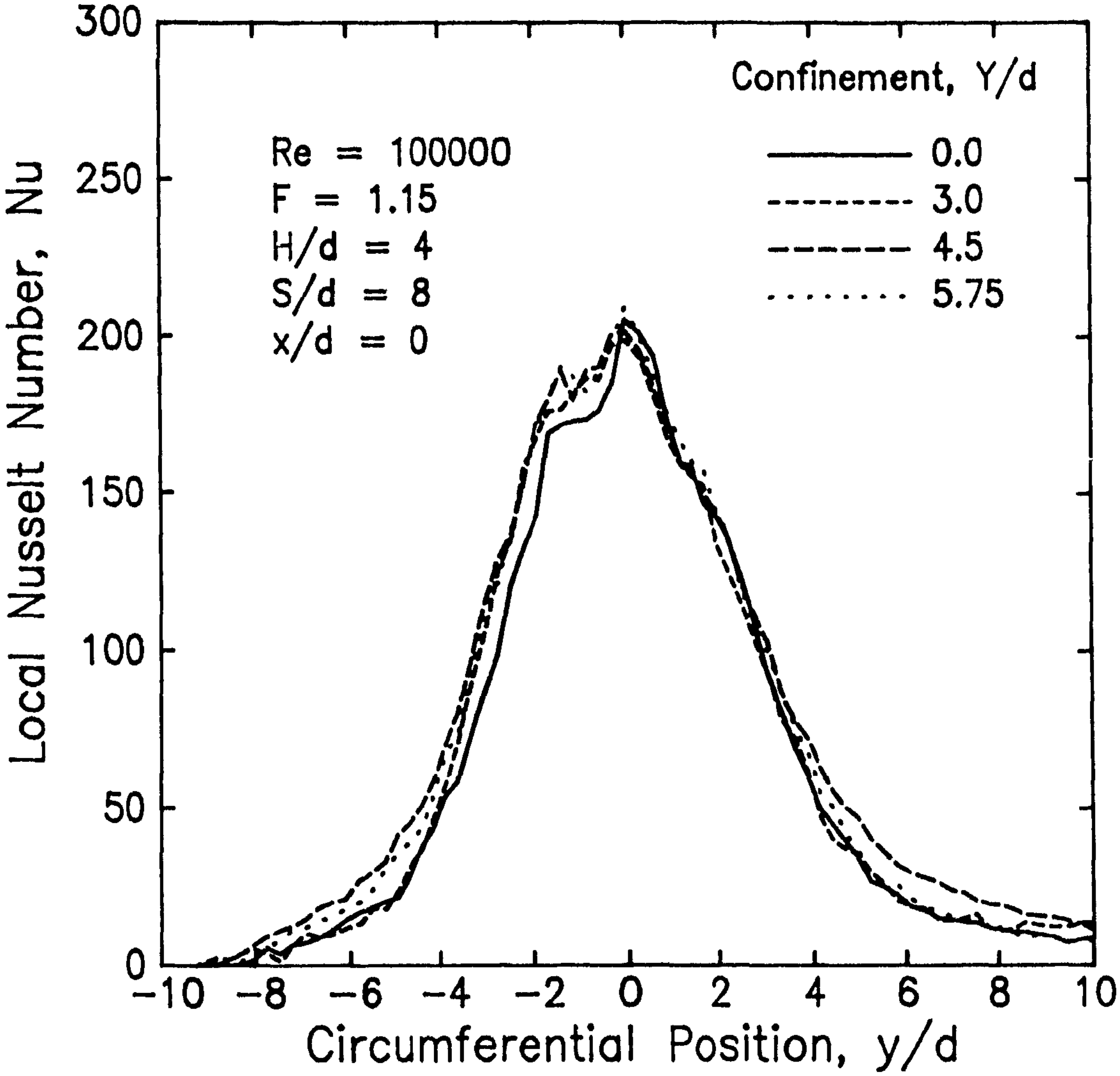

Figure 4.43(c) Effect of confinement, Y/d, on the profile of local Nusselt number: H/d = 4, Re = 100000.

by the impingement air to one dominated by the boundary layer associated with the moving surface occurs near $y/d = -5$. The location of the transition point is a function of Reynolds number, Figure 4.44(a), with the transition near 4.5 at Re = 60000 and 5.5 at Re = 118000.

On the downstream side, confinement helps establish a layer of air which travels with the impingement surface, inhibiting the mixing of the cooler ambient air with the hotter impingement air at locations beyond the confinement surface.

At the maximum extent of confinement tested, $Y/d = 5.75$, Figures 4.44(a) - 4.44(c), portray Nusselt number profiles at $x/d = 0$ for H/d of 1, 2 and 4, over a wide Reynolds number range. Comparison with the corresponding Nu profiles for unconfined jets, Figures 4.13(a) - (c), confirms the same effects noted above for Figures 4.44. Thus relative to the unconfined case, with confinement of $Y/d = 5.75$ the value of Nu at the off-stagnation maximum is increased and occurs further from the stagnation point, with the Nu profile correspondingly broadened. These effects are strongest at $H/d = 1$, are still important at $H/d = 2$ and become minimal at $H/d = 4$. The location of the local Nusselt minima at $y/d = 1.1$ is unaffected by H/d, Re and Y/d. The position of the off-stagnation maxima is near $y/d = 1.8$ for unconfined jets, independent of Re, while it shifts away from the stagnation point with increasing confinement.

Obot [1980], using short, contoured inlet, circular nozzles with a circular confinement plate of radius $R/d = 8.7$, jet Reynolds number in the range 30000 - 53000 and with a thermal entrainment factor likely about $F = 0$, found that heat transfer, relative to the corresponding unconfined jet, decreases by about 10%-15%. There is of course no contradiction between the finding that confinement reduces heat transfer

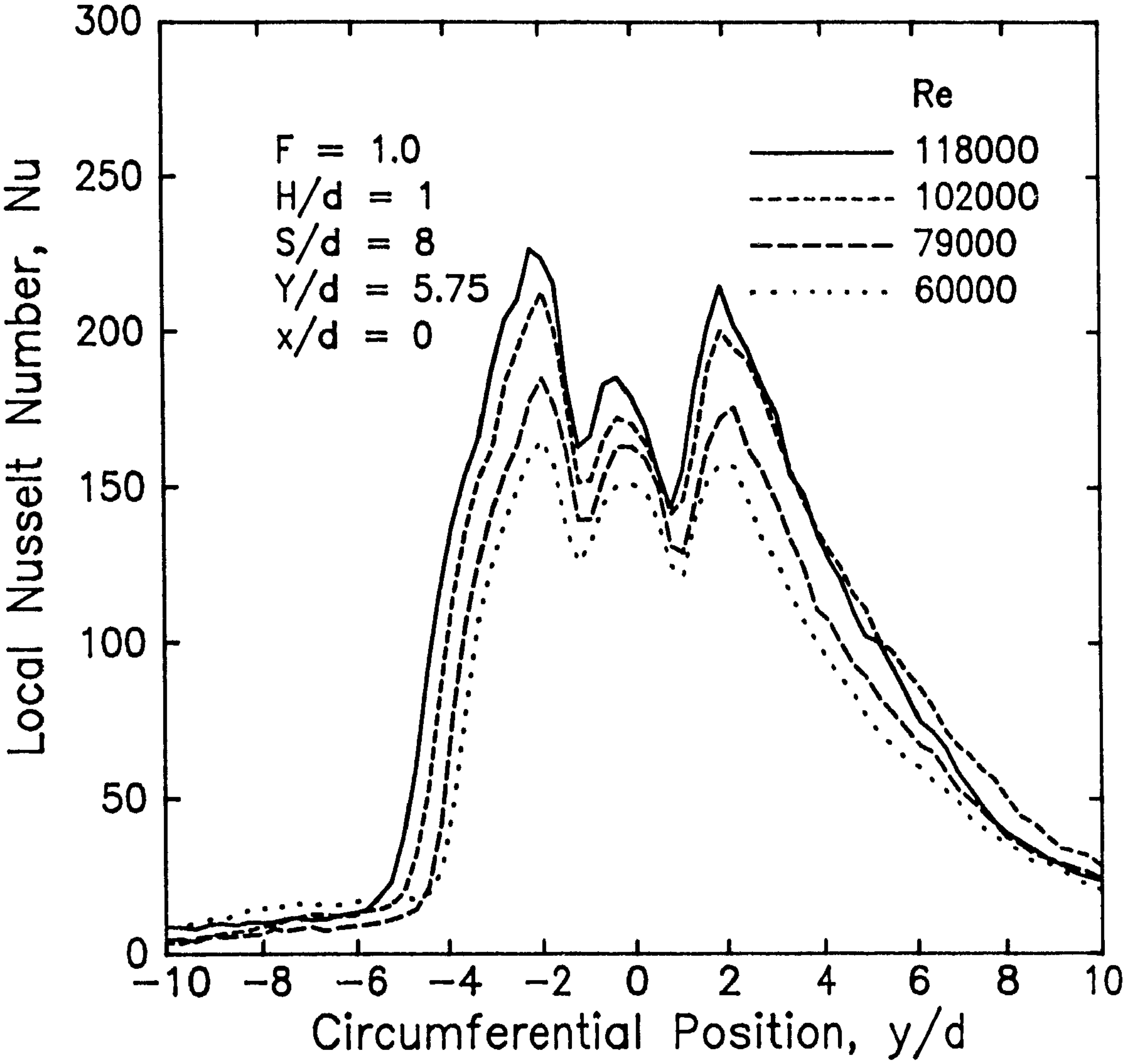

Figure 4.44(a) Effect of Re on the profile of local Nusselt number for the maximum extent of confinement, Y_c = 5.75: H/d = 1.

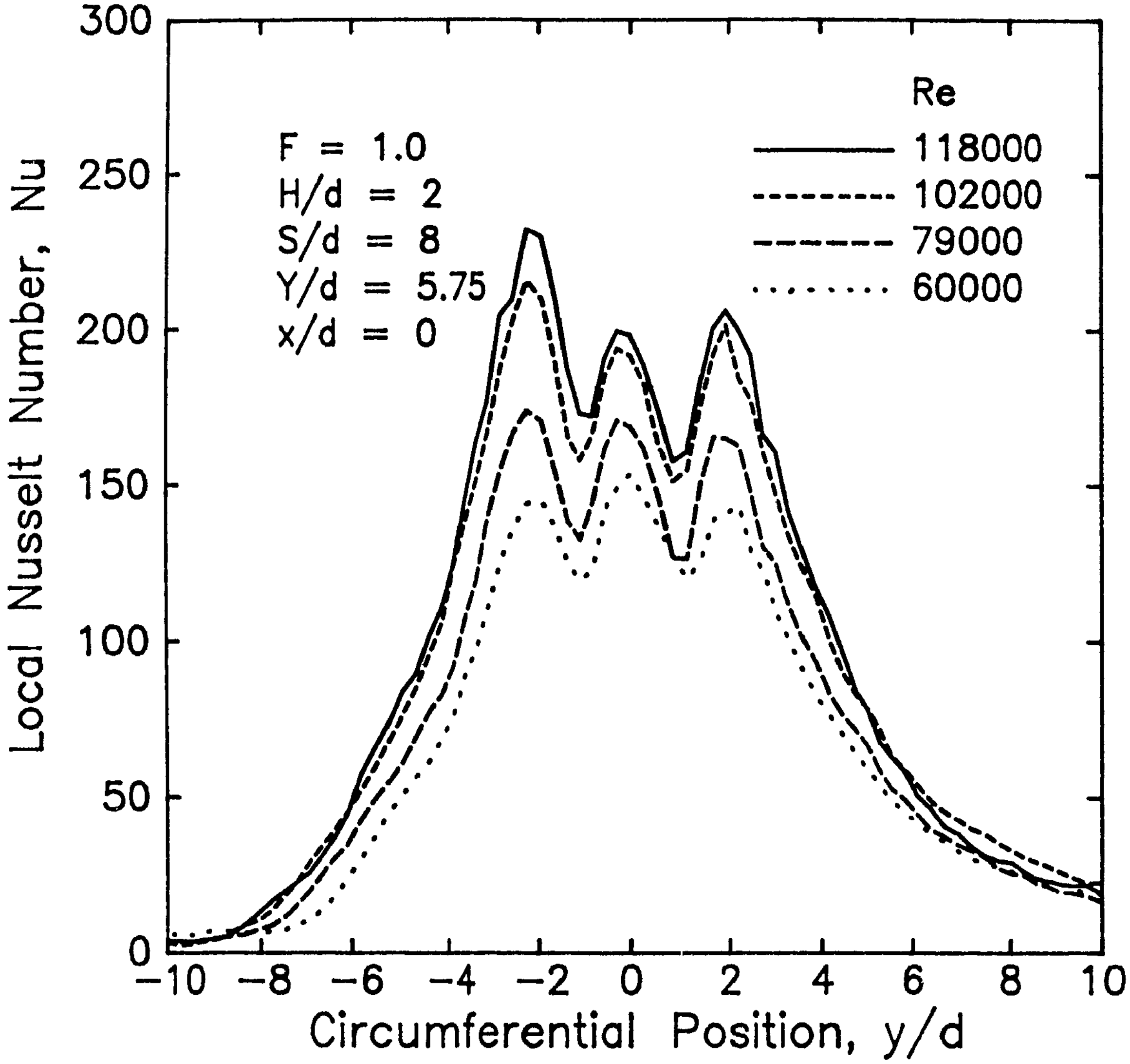

Figure 4.44(b) Effect of Re on the profile of local Nusselt number for the maximum extent of confinement, Y_c = 5.75: H/d = 2.

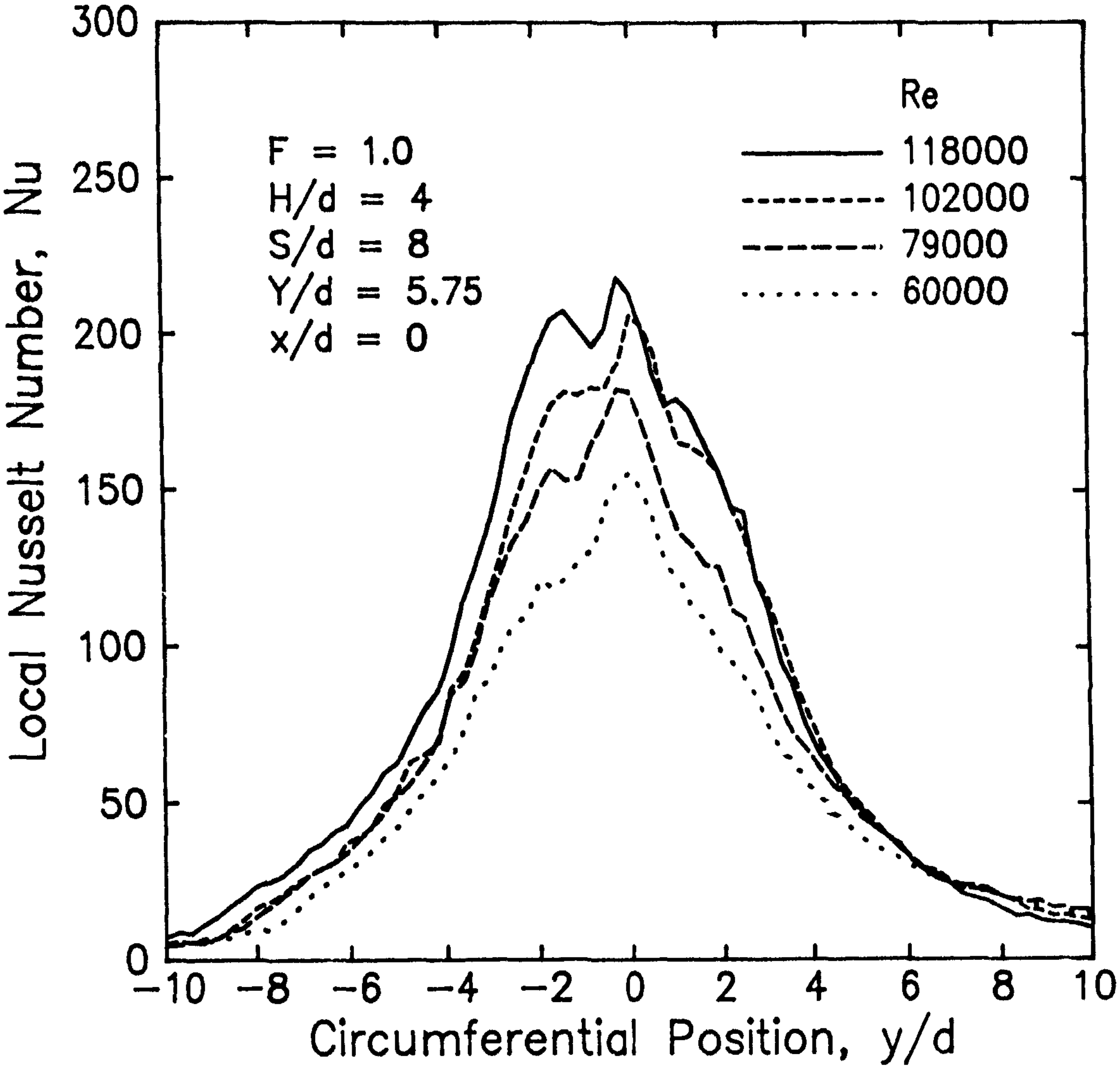

Figure 4.44(c) Effect of Re on the profile of local Nusselt number for the maximum extent of confinement, Y_c = 5.75: H/d = 4.

for F = 0 but increases heat transfer for higher thermal entrainment factors in the range 0.75-1.15 as tested here. With $F \leq 0$, the absence of a confinement plate enhances heat transfer because the entrained fluid contributes to the heat transfer at the impingement surface. With F in the range 0.75 - 1.15, the use of unconfined jets can only produce a decrease in heat transfer due to the thermal degradation of the jet by the unfavorable ambient fluid temperature, as is documented in the heat transfer profiles reported here.

4.5.2 Circumferential Average Nusselt Number

The effects of confinement on calender roll impingement heat transfer that are seen on the profiles of local Nu at x/d = 0 are expressed quantitatively in terms of the circumferentially averaged Nusselt number, $\overline{Nu}_c$, on Figures 4.45(a) -4.45(c). Consistent with the earlier profiles of local Nu, the extent of the increase in calender roll heat transfer by confinement for the case of a high thermal entrainment factor, F = 1.15, is seen to be highest for H/d = 1, still substantial at H/d = 2, and small at H/d = 4. At the standard extent of roll circumference for comparisons of y/d = ±10, $\overline{Nu}_{c10}$ is increased relative to the unconfined jet case by 80% at H/d = 1, by 33% at H/d = 2 and by 15% at H/d = 4.

The reason why the increase in $\overline{Nu}_c$ with y/d is highly nonlinear can be understood only by reference to the boundary layer phenomena which characterize impinging jet flows. At Y/d = 3, where the confinement surface extends just past the secondary maximum located near y/d = ±2, the surface is too small to protect from entrainment that part of the impingement surface which, when protected, contributes to the increase in heat transfer. Thus for Y/d in the range 0 - 5.75, there is little or

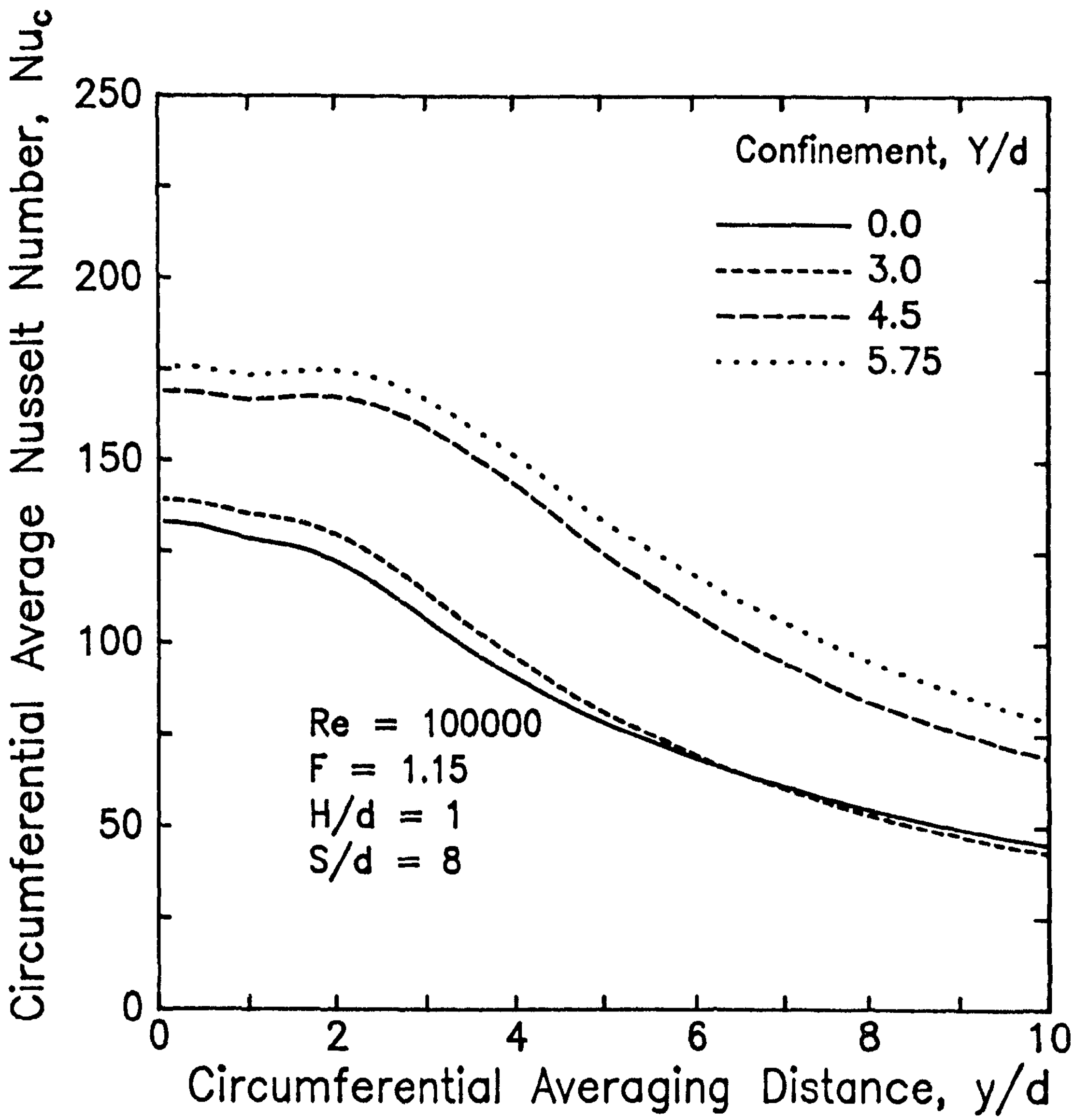

Figure 4.45(a) Effect of confinement, Y/d, on circumferential average Nusselt profile, $\overline{Nu}_c$: H/d = 1 and Re = 100000.

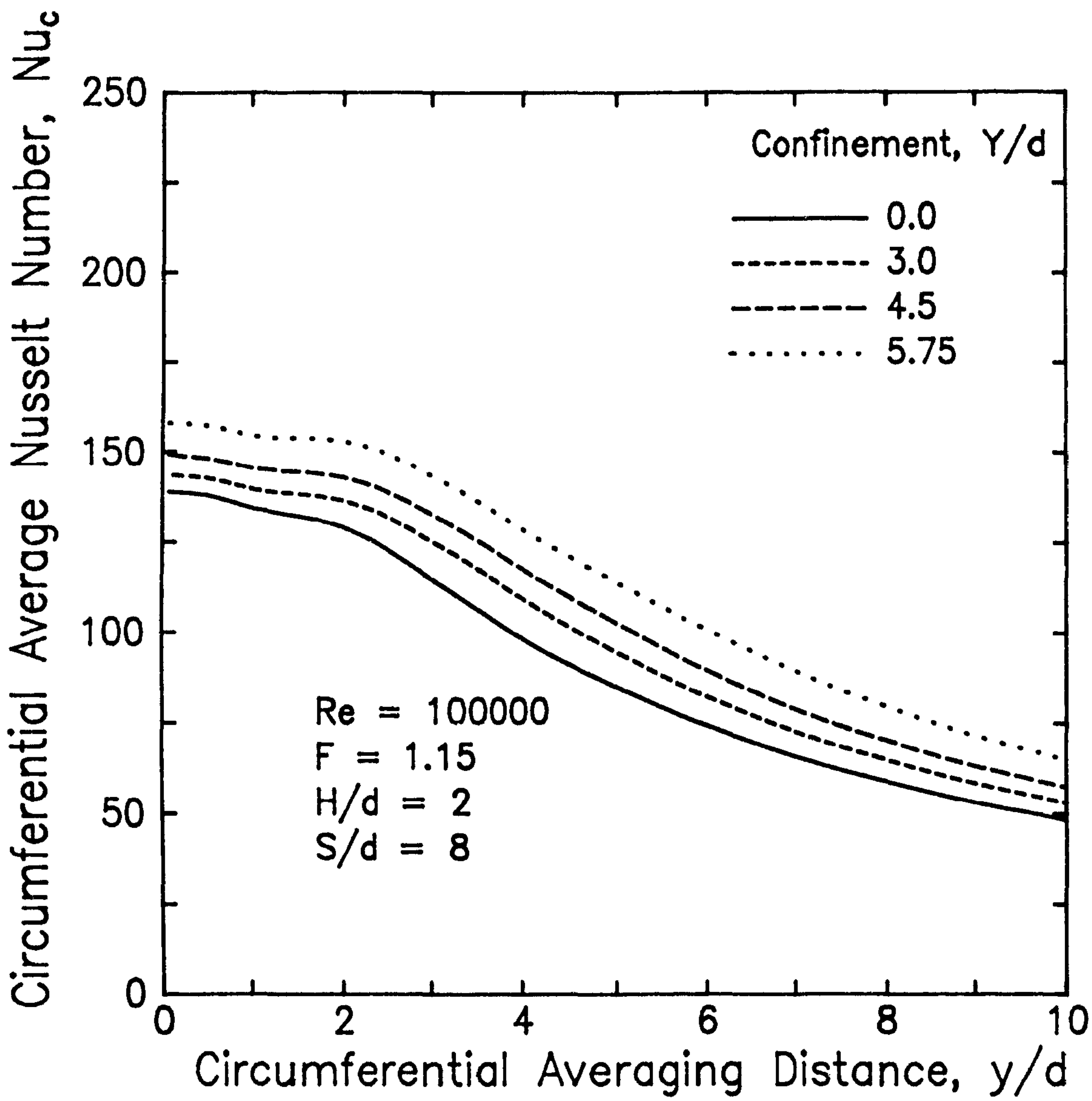

Figure 4.45(b) Effect of confinement, Y/d, on circumferential average Nusselt profile, $\overline{Nu}_c$: H/d = 2 and Re = 100000.

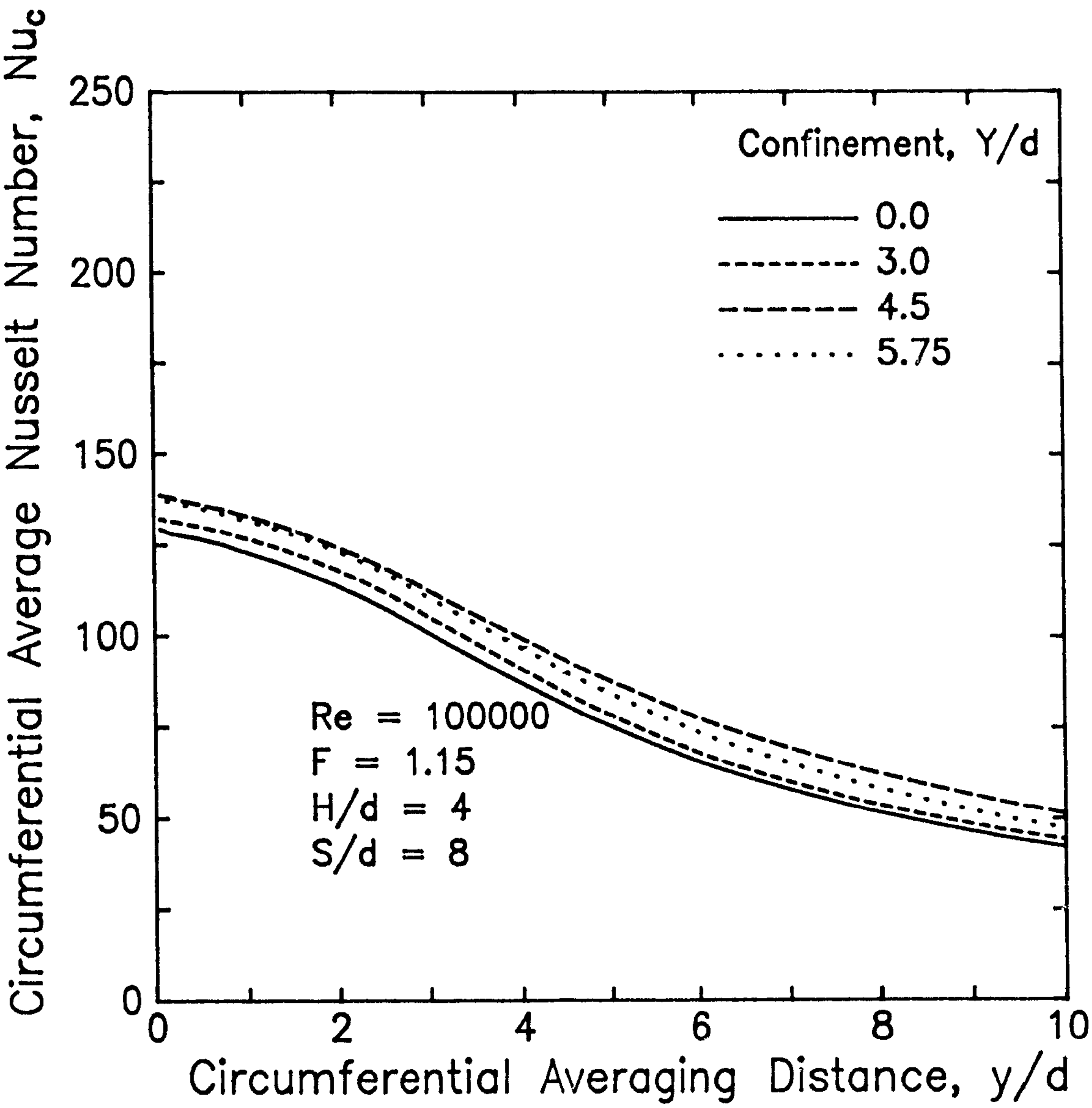

Figure 4.45(c) Effect of confinement, Y/d, on circumferential average Nusselt profile, $\overline{Nu}_c$: H/d = 4 and Re = 100000.

no increase in $\overline{Nu}_{c10}$ with confinement in the range of Y/d up to 3, but $\overline{Nu}_{c10}$ increases sharply with Y/d above 3 for close nozzle spacings, $H/d \leq 2$.

The $\overline{Nu}_{c10}$ - Y/d relationship shown on Figure 4.46 is for the conditions of Figure 4.45. The increase of $\overline{Nu}_{c10}$ is large over the Y/d range of 3 - 5.75, particularily for H/d = 1. The present data do not extend to a sufficiently high value of Y/d to determine the maximum value that the circumferential average Nusselt number would reach. It appears from Figure 4.46 that though use of a sufficiently large confinement surface there is the potential to increase $\overline{Nu}_{c10}$ by perhaps 50% for H/d = 2, by more than 100% for H/d = 1. If an ideally designed confinement plate could eliminate the effect of thermal degradation, the $\overline{Nu}_{c10}$ results shown in Figure 4.30 for H/d = 1 and an entrainement factor, F = 0, would indicate that the theoretical maximum is near 125% increase in average heat transfer.

A correlation for average circumferential Nusselt number, $\overline{Nu}_c$, when the extent of confinement is Y/d = 5.75, in a form similar to Equation 4.9, obtained using the nonlinear regression procedure described in Section 4.2.2, is as follows:

$$\overline{Nu}_c = \left[0.367-0.007\left(\frac{S}{d}\right)^{0.30}\left(\frac{y}{d}\right)^{0.13}\left(\frac{H}{d}\right)^{1.41}F\right]Re^{0.63}\left(\frac{S}{d}\right)^{-0.12}\left(\frac{y}{d}\right)^{-0.62} \quad (4.16)$$

which is valid over the range

$$60000 \leq Re \leq 118000$$
$$1 \leq H/d \leq 4$$
$$3 \leq y/d \leq 11$$
$$3 \leq S/d \leq 8 \text{ (or } 1.5 \leq x/d \leq 4)$$
$$0.95 \leq F \leq 1.35$$

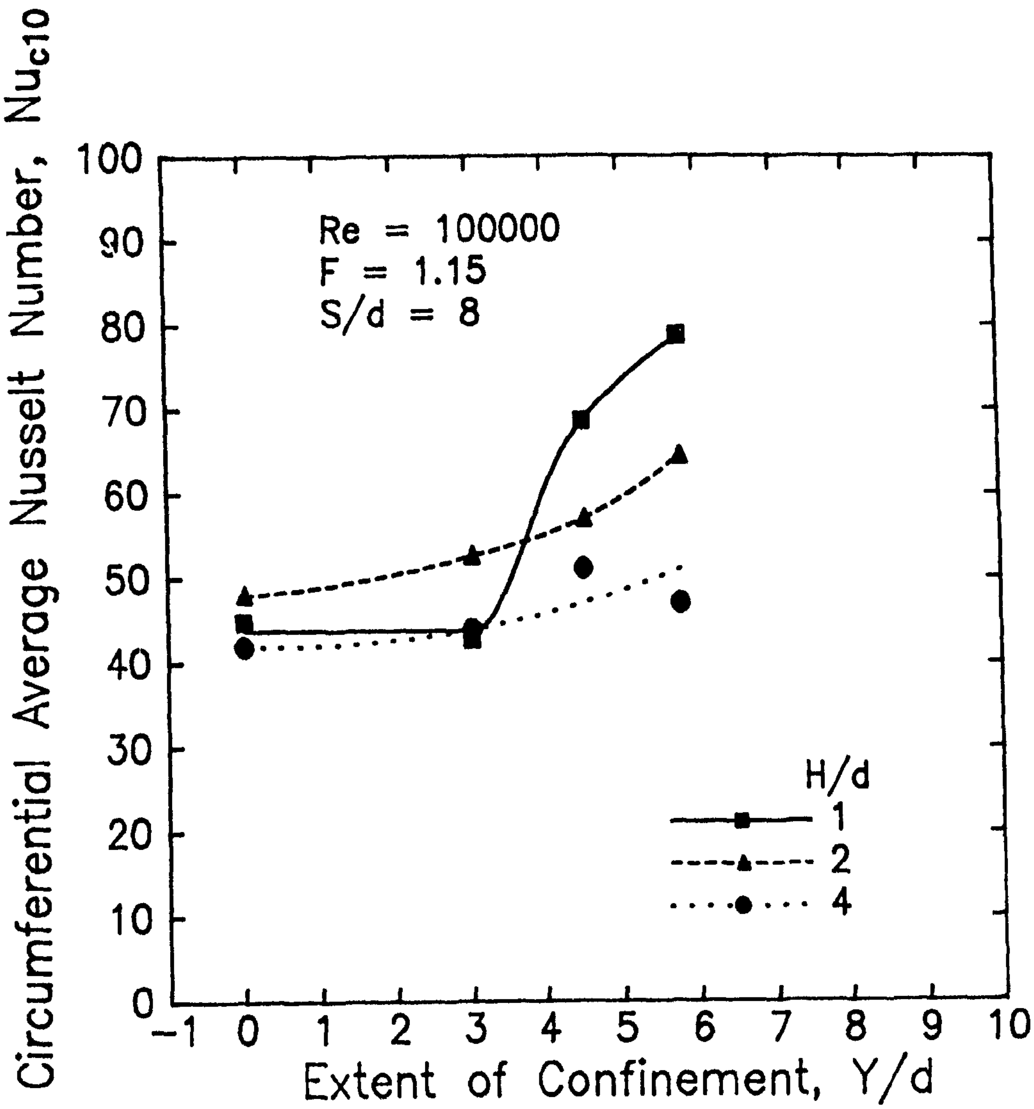

Figure 4.46 Effect of extent of confinement, Y/d, and nozzle spacing, H/d, on circumferential average Nusselt number for $(y/d)_a = 10$, $\overline{Nu}_{c10}$.

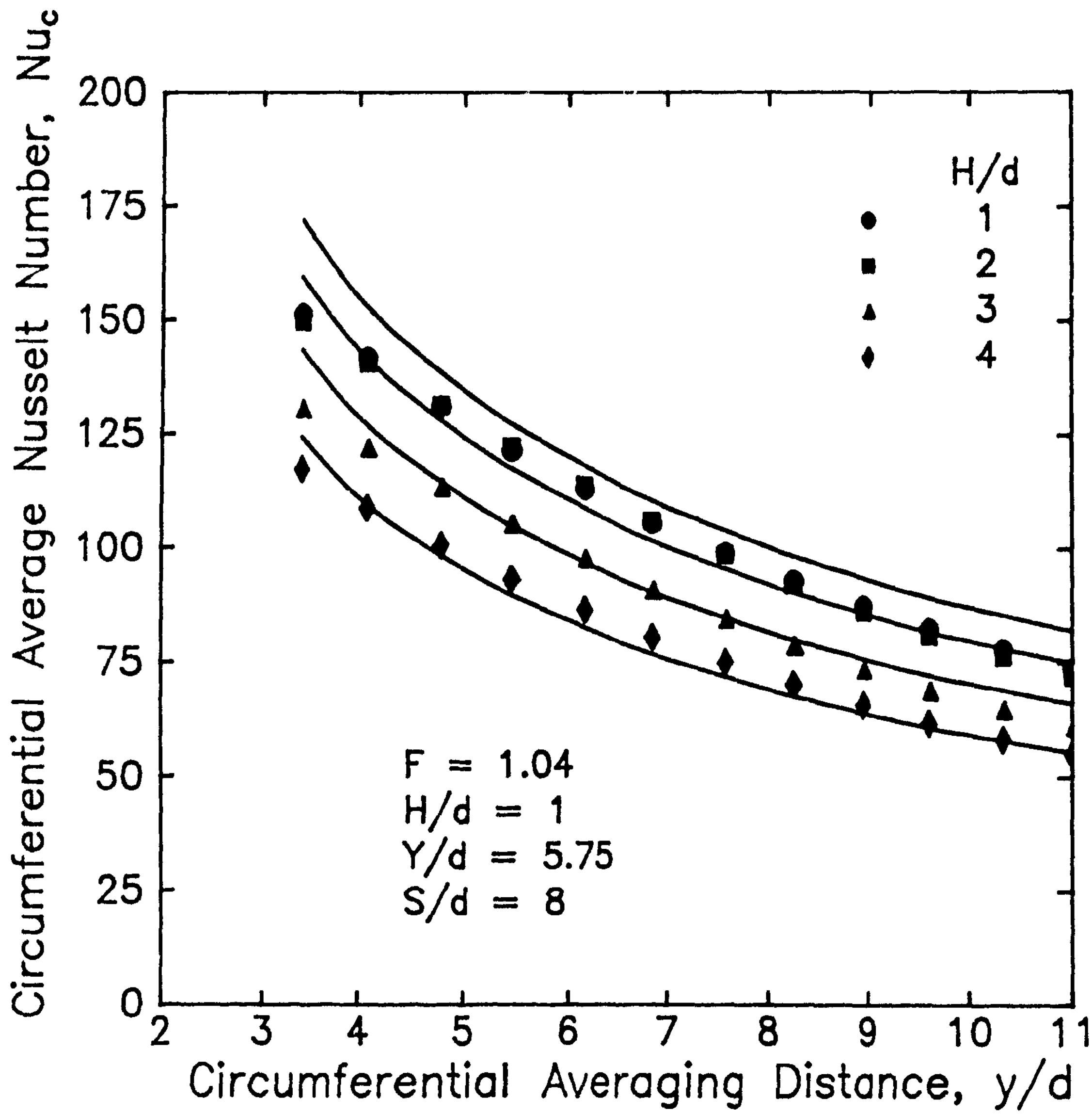

Figure 4.47(a) Comparison of $\overline{Nu}_c$ measurements with those from Equation 4.16: Effect of H/d for Re = 100000, F = 1.04.

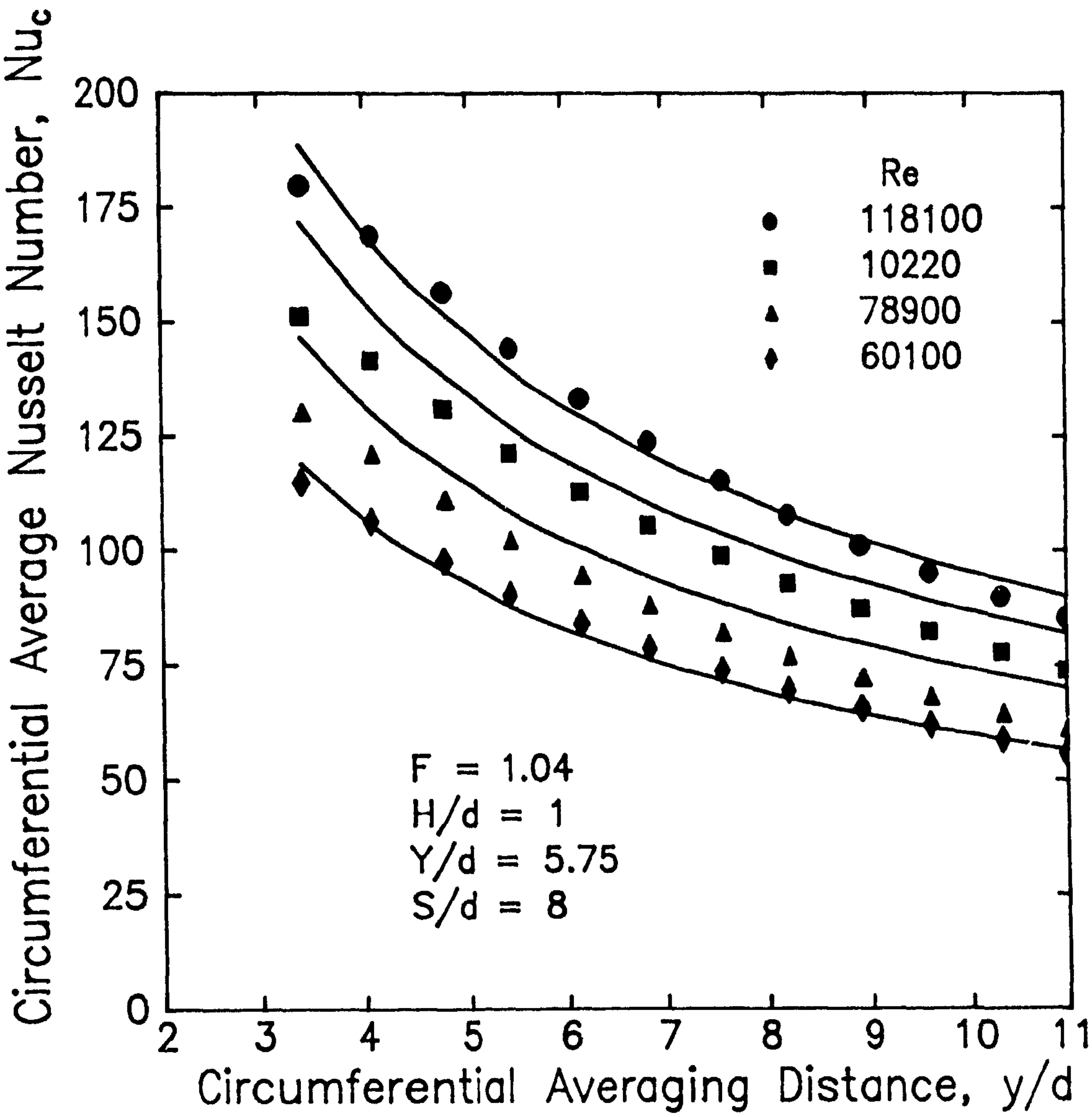

Figure 4.47(b) Comparison of $\overline{Nu}_c$ measurements with those from Equation 4.9: Effect of Re for H/d = 1, F = 1.04.

Figures 4.47(a) to 4.47(b) illustrate the effectiveness of the proposed correlations in the representation of the experimental data for $\overline{Nu}_c$.

In summary, under conditions when entrainment is unimportant, i.e. when the ambient temperature is closer to the jet temperature than to that of the impingement surface temperature, confinement reduces the heat transfer rate. Under conditions typically encountered in calender control, entrainment should definitely be avoided, thus confinement would be greatly beneficial.

4.6 Effect of Multiple Rows of Offset Nozzles

When round jets are arranged in a row, as typical for many calender control systems, the nozzle-to-nozzle spacing, S, becomes a compromise between the larger heat transfer achieved with a closer inter-nozzle spacing, and the corresponding diminished heat transfer per nozzle with the interference between the wall jets from closely spaced jets. For large spacing, in the range $S/d = 10$, the detrimental effect of jet-to-jet interference is small. In some calender control systems, however, spacings as low as $S/d = 4$ are used.

Kan[1986] argued that non-uniform heat transfer in the axial direction associated with impinging jets would result in a "bumpy" roll. As shown in Chapter 5, the high thermal conductivity of cast iron calender rolls is sufficient to damp such any axial differences in calender roll surface temperature and correspondingly in roll diameter.

Pelletier et al.[1984, 1987] showed that for $S/d = 4$ the heat transferred per nozzle is considerably lower than that for $S/d = 8$. To use the heat transfer potential of each jet more effectively, their analysis indicated an advantage for the use of two rows of jets, spaced at $S/d = 8$, but offset between the rows by $S/d = 4$ and separated in the circumferential direction such that the minimum spacing between the nozzles was 8d. Thus nozzles would be spaced on equilateral triangles with sides of 8d, as illustrated on Figure 4.48. The experimental test of that analysis is now presented though comparison between a single row of nozzles with S/d = 4 and two staggered rows with a spacing of S/d = 8.

4.6.1 Circumferential variations of local Nu

Heat transfer under nozzle arrays is best illustrated with the aid of contour graphs, Figures 4.49 and 4.50 showing lines of constant local Nusselt number. In both in-line and staggered nozzle arrangements there are nozzles at axial positions x/d = -4, 0, 4. For staggered arrays, the jets are seen to spread with much less interference that for the in-line arrays. Consequently the contours for Nu = 50, for example, enclose a much greater area in the staggered configuration, Figure 4.50, than with in-line nozzles, Figures 4.49.

The heat transfer area for in-line nozzles is limited by the neighboring jets. The staggered configuration, with an increased nozzle-to-nozzle separation, subjects more of the calender roll surface to higher heat transfer. Where this improvement occurs can be observed by comparing the circumferential heat transfer profiles for the in-line jets, Figure 4.51, and staggered jets, Figure 4.52, at the axial positions,x/d, of 0 and ±2, i.e. axial locations directly under a jet and midway between two jets. With the staggered configuration, at a given axial position the calender roll experiences heat transfer from both rows of jets, resulting in the higher heat transfer efficiency.

The effect of confinement on the Nu profiles for the in-line and staggered geometry can be observed by comparing the size of the Nu = 50

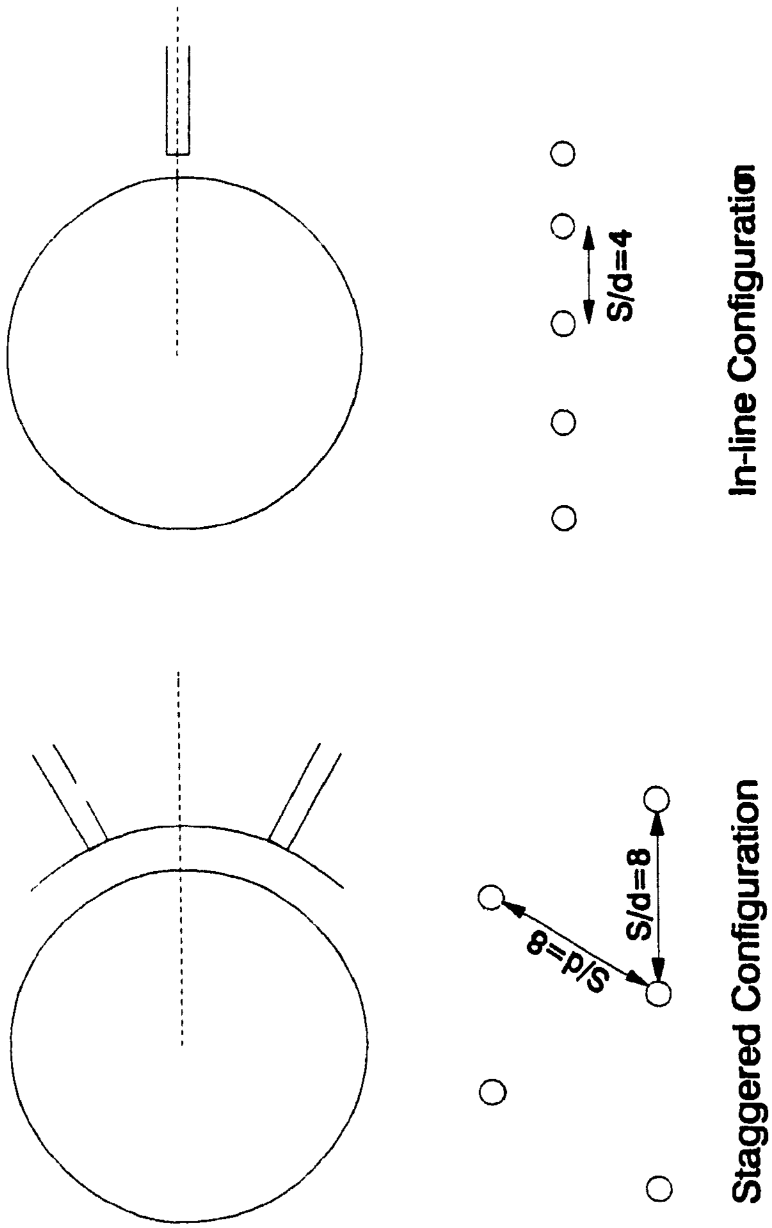

Figure 4.48 Comparative staggered and in-line nozzle configurations.

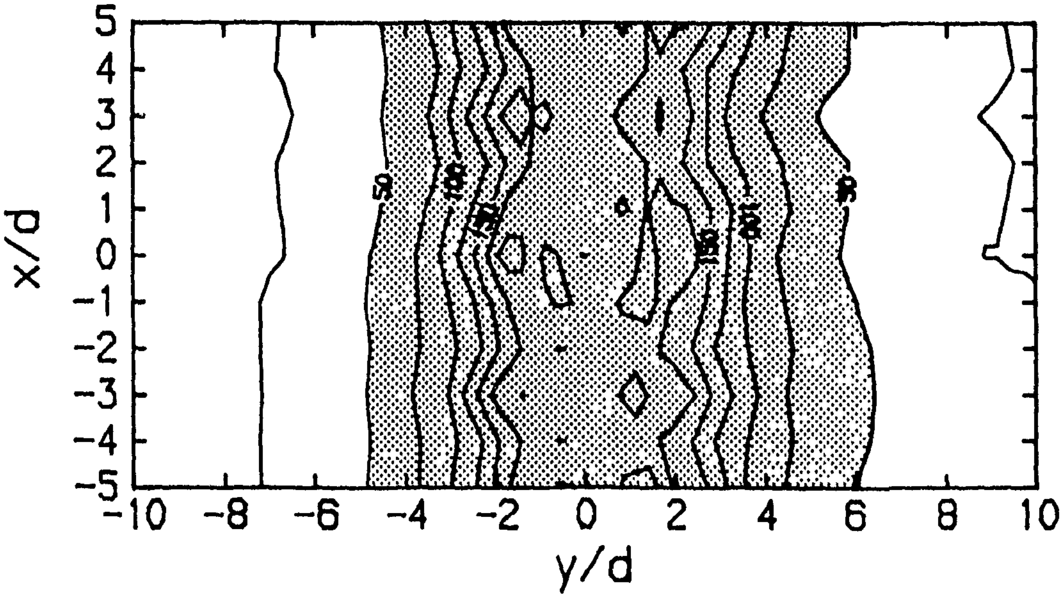

(a) unconfined

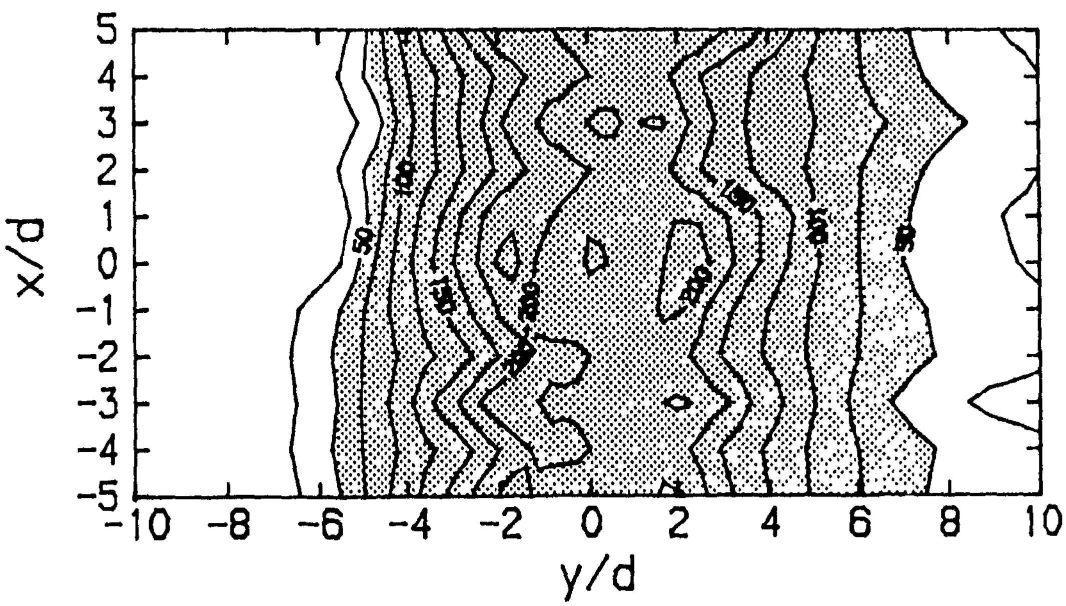

(b) confined

Figure 4.49 Contour plots of local Nusselt number for a single, in-line row of impinging jets: Re = 100000, H/d = 2, S/d = 4, F = 1.05.

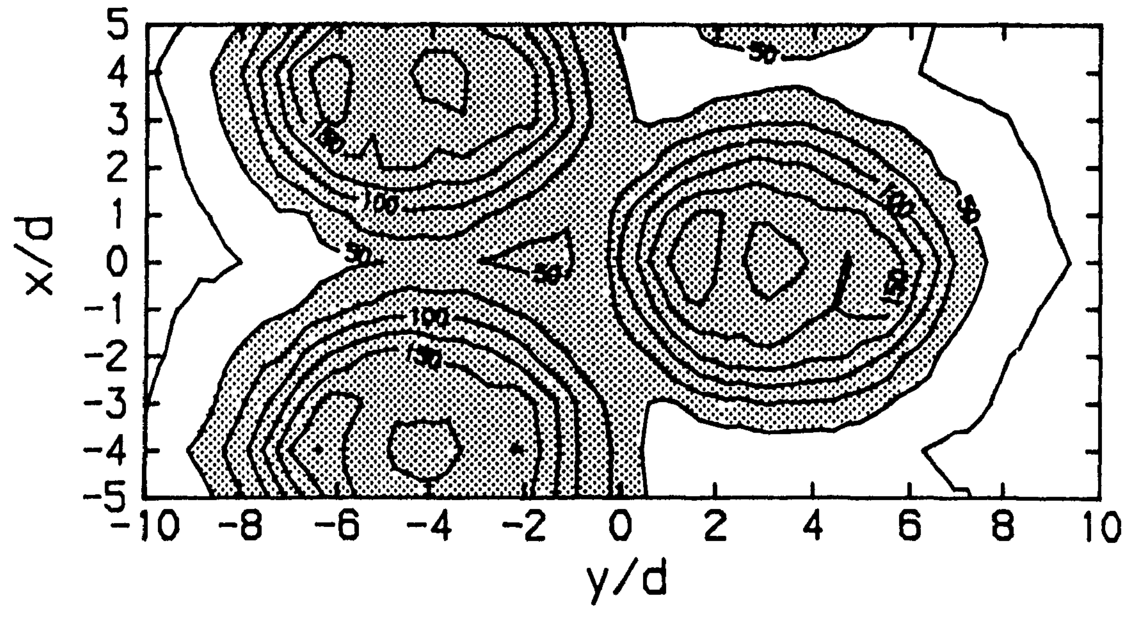

(a) unconfined

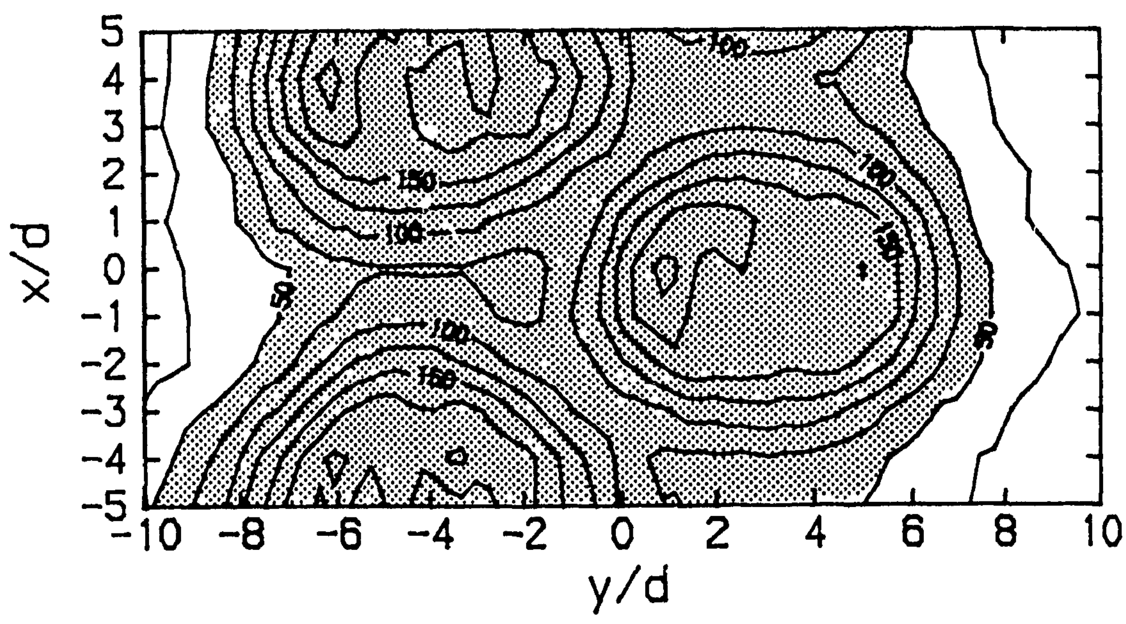

(b) confined

Figure 4.50 Contour plots of local Nusselt numbe: for the staggered configuration of impinging jets: Re = 100000, H/d = 2, effective S/d = 8, F = 1.05.

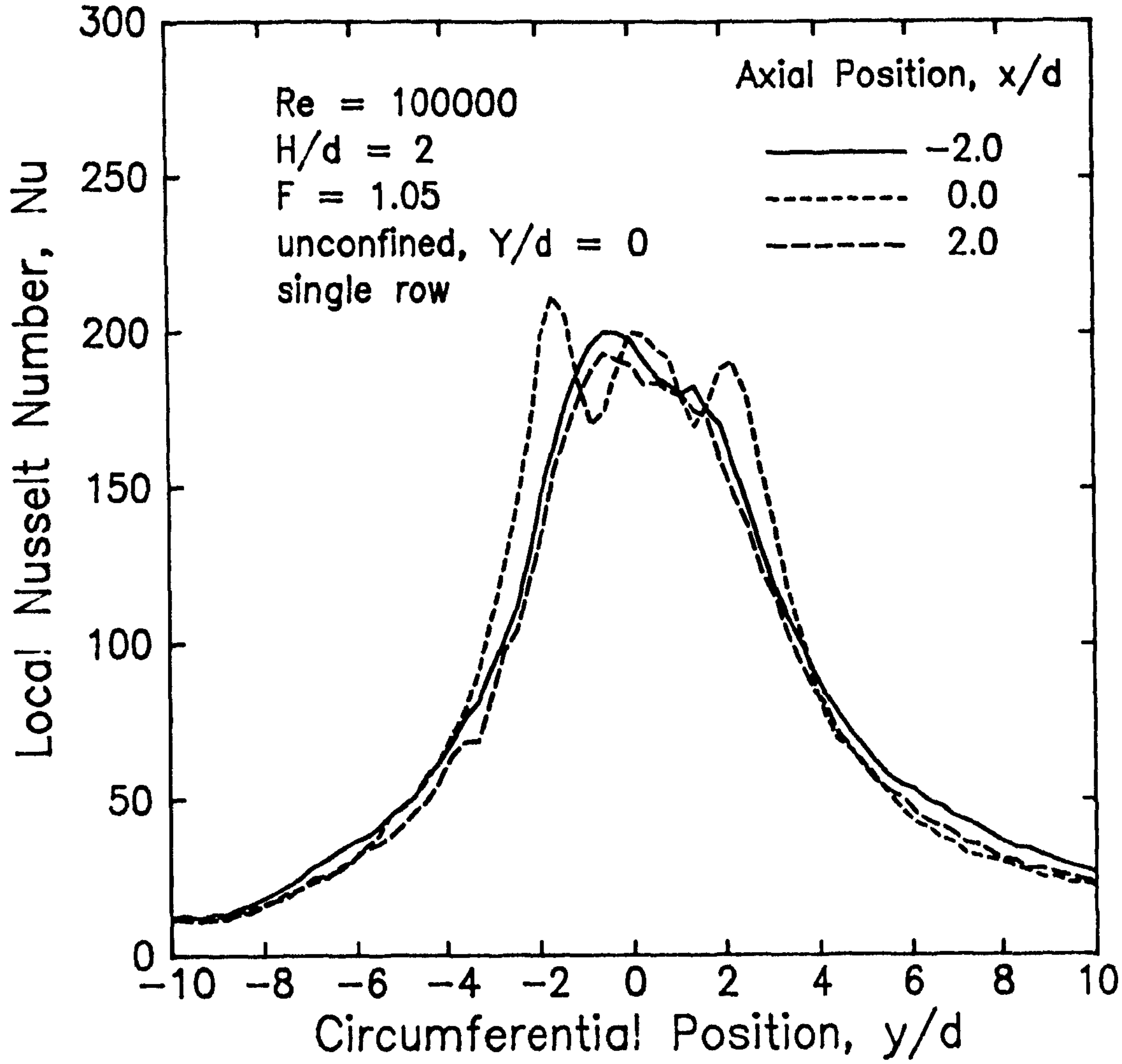

Figure 4.51 Circumferential profiles of local Nusselt number for a single, in-line row of unconfined jets: H/d = 2, Re = 100000.

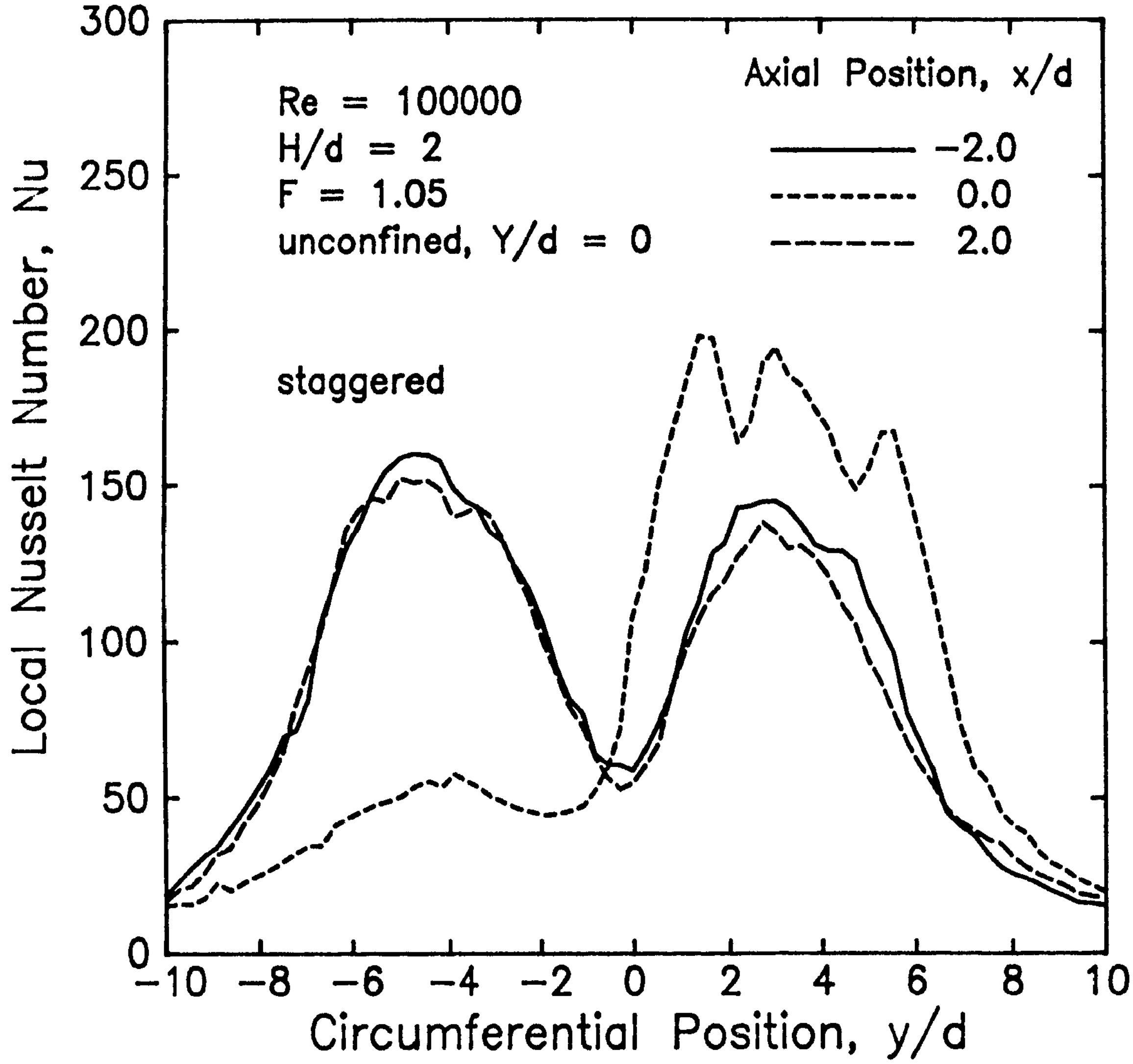

Figure 4.52 Circumferential profiles of local Nusselt number for the staggered configuration of unconfined jets: H/d = 2, Re = 100000.

contours in Figures 4.49 and 4.50. Thus the Nu ≥ 50 area in Figure 4.49(b) exceeds that in Figure 4.49(a) and that in Figure 4.50(b) exceeds that in Figure 4.50(a), consistent with the observations made in Section 4.5.

4.6.2 Circumferential Average Nusselt Number

Figures 4.53 and 4.54 provide the quantitative comparison of the in-line and staggered configurations for impingement heat transfer at a calender roll. This circumferential average $\overline{Nu}_c$ extends in the axial direction $(x/d)_a = \pm 2$ from the nozzle centerline (corresponding to a nozzle-to-nozzle spacing, S/d = 4), with circumferential averaging distance varying up to $(y/d)_a = \pm 10$. For the staggered configuration the averaging starts at a position mid-way between the two rows of nozzles and for this reason the average is lower until an averaging distance, $(y/d)_a = \pm 4$. At that point, as shown in Figure 4.53, the two averages include the heat transfer of effectively one impinging jet, and thus are equal. For $(y/d)_a \geq \pm 4$, Figure 4.54, the staggered configuration reaches a maximum average heat transfer at $(y/d)_a = 6$. The most relevant comparison is for $(y/d)_a = 10$, a circumferential position by which most of the heat transfer to the calender roll has been accomplished. Figures 4.53 and 4.54 indicate that the improvement in total heat transfer at the calender roll, $\overline{Nu}_{c10}$, by the staggered configuration is 30% for either confined or unconfined jets.

Also shown in Figures 4.54 and 4.55 are the $\overline{Nu}_c$ profiles for a single row of impinging jets with a nozzle to nozzle spacing, S/d = 8. As can be observed, keeping a single row of jets and changing S/d from 8 to 4 only resulted in 34% and 26% increases in $\overline{Nu}_{c10}$ for the unconfined and confined cases. Staggering the jets and maintaining an effective

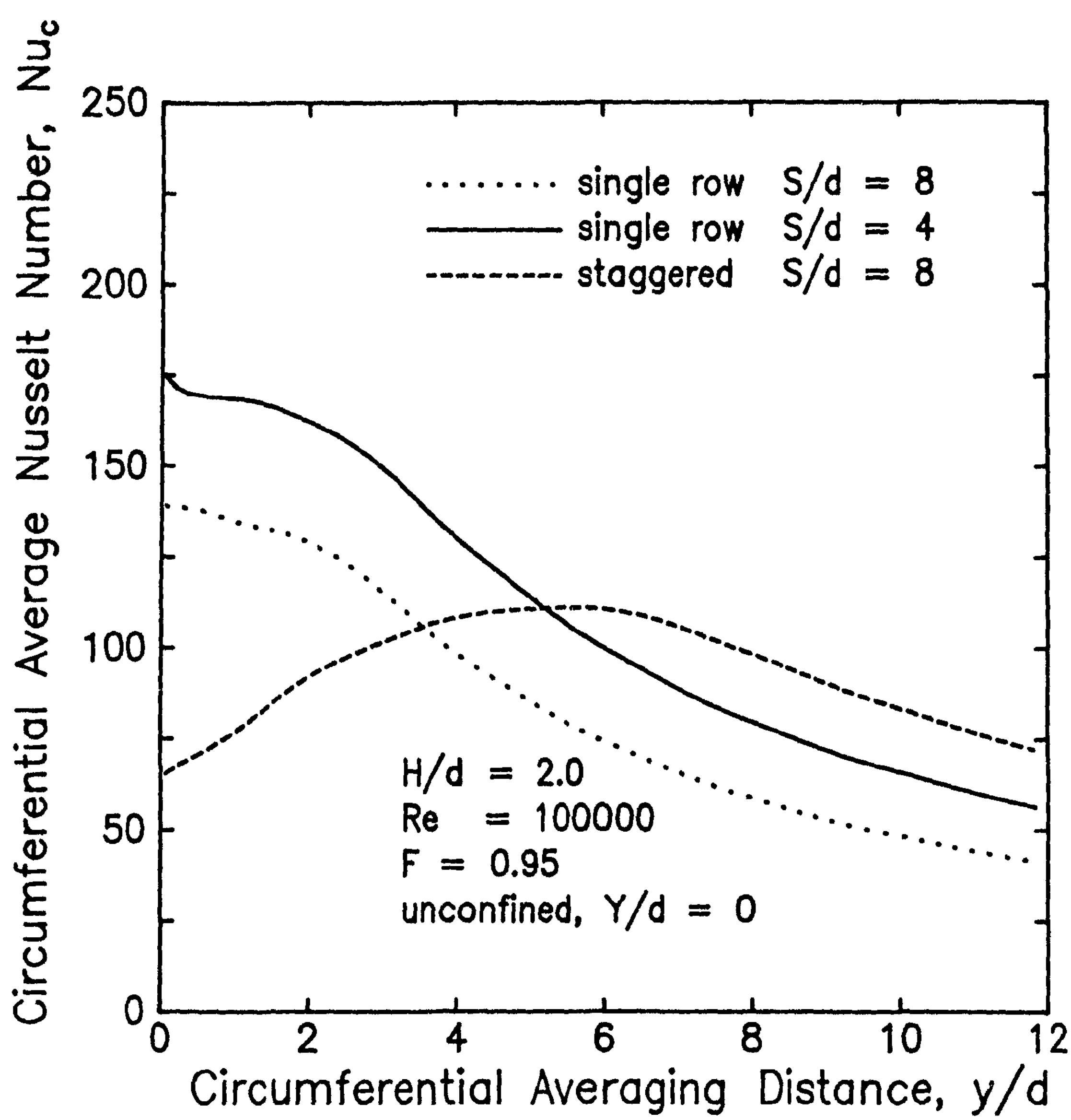

Figure 4.53 Comparison of circumferential profiles of $\overline{Nu}_c$ for the single row and staggered nozzle configurations: unconfined jets.

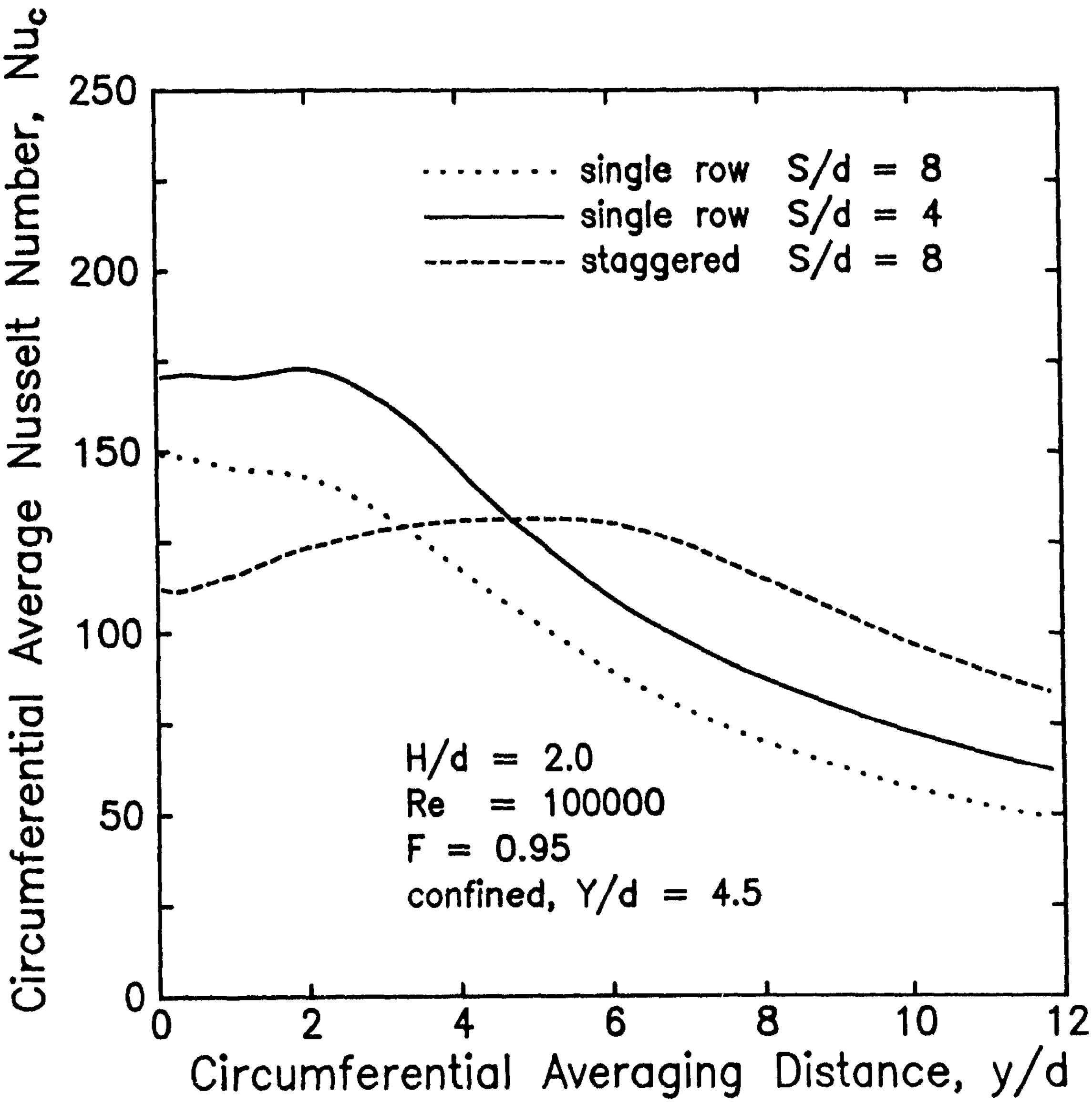

Figure 4.54 Comparison of circumferential profiles of $\overline{Nu}_c$ for the single row and staggered nozzle configurations: confined jets.

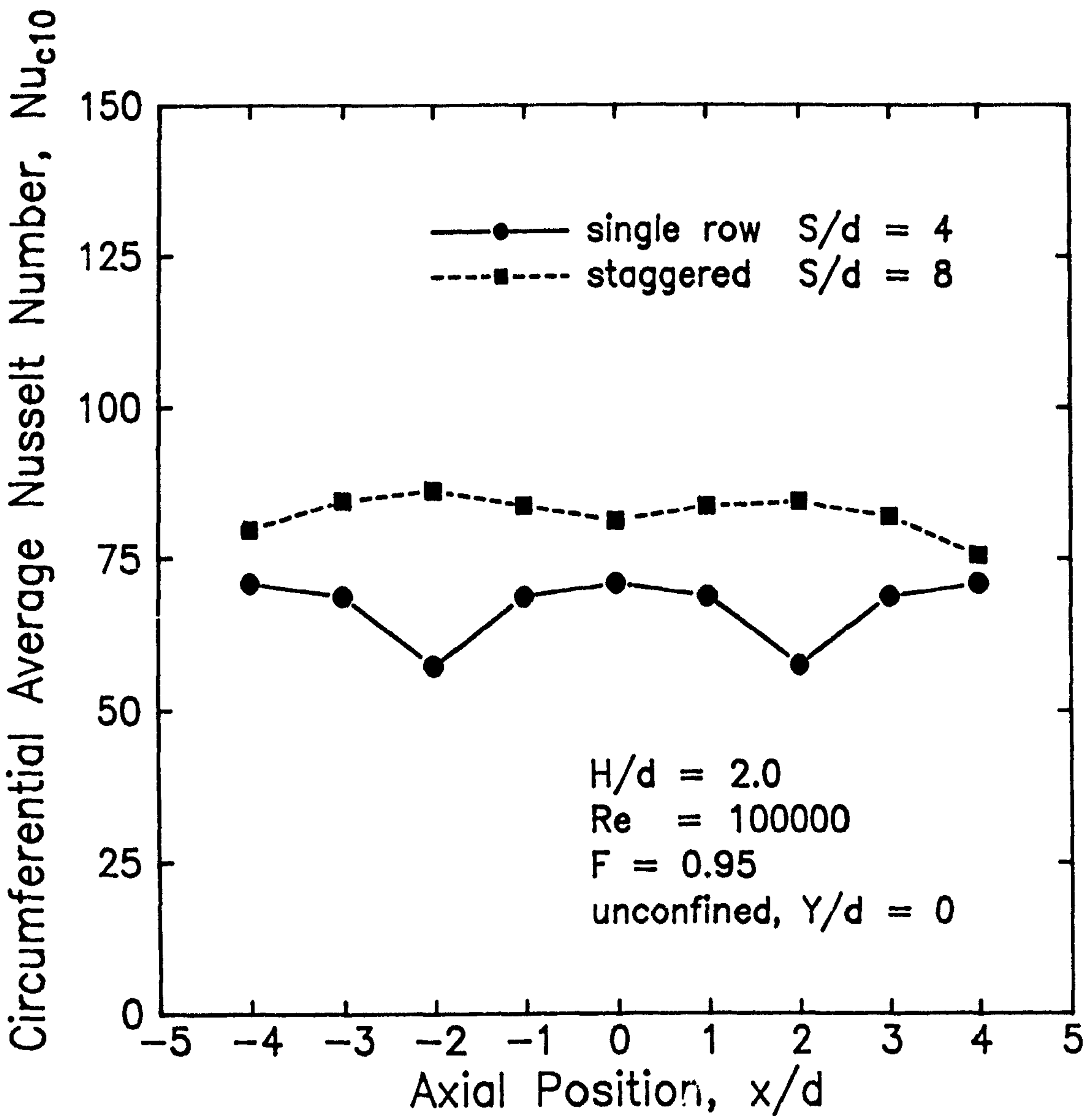

Figure 4.55 Comparison of axial profiles of $\overline{Nu}_{c10}$ (circumferential averaging distance, $y/d_c = \pm 10$) for the single row and staggered nozzle configurations: unconfined jets.

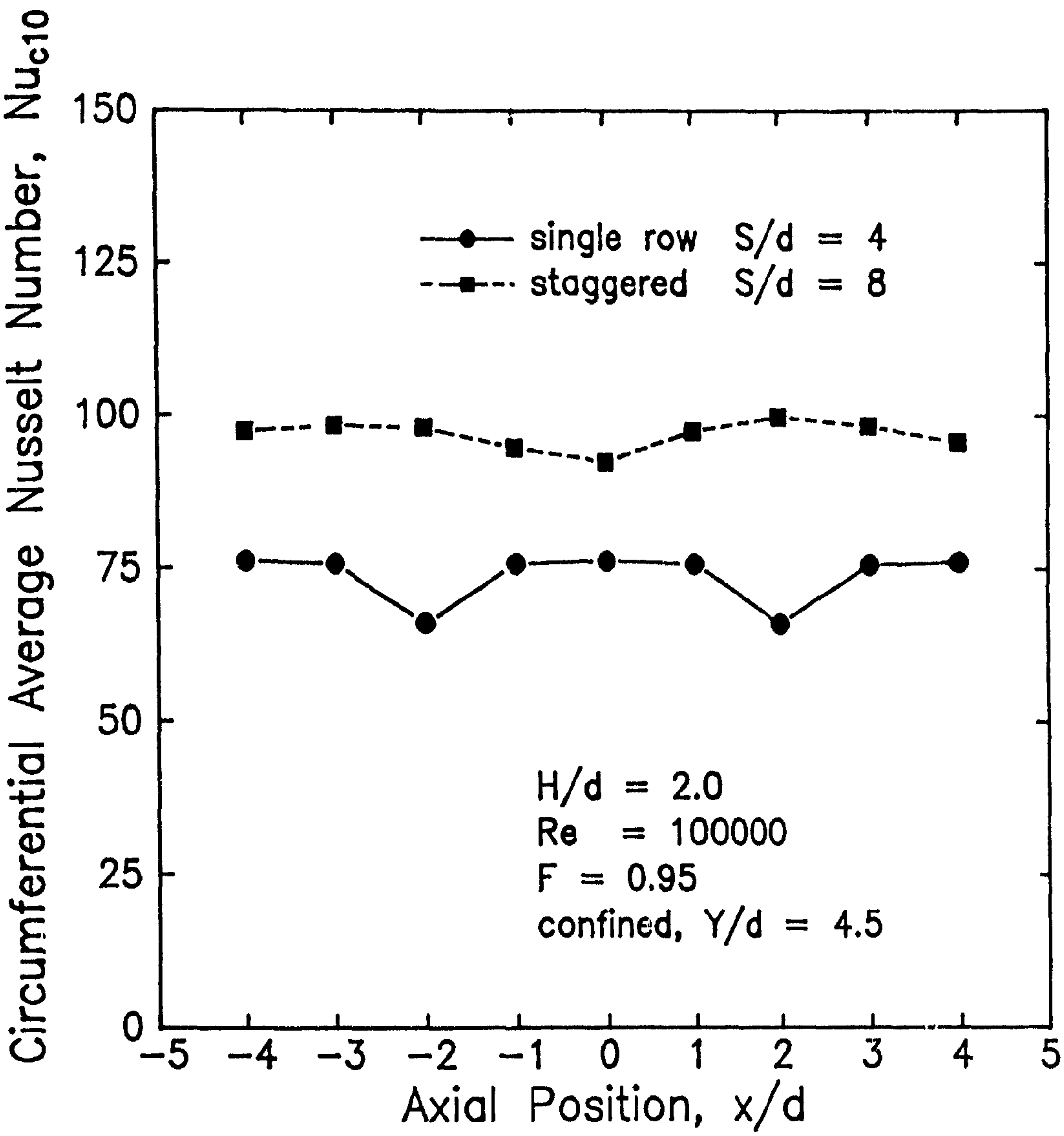

Figure 4.56 Comparison of axial profiles of $\overline{Nu}_{c10}$ (circumferential averaging distance, $y/d_c = \pm 10$) for the single row and staggered configurations: confined jets.

nozzle to nozzle separation of 8 resulted in increases of 73% and 69% respectively.

These improvements in heat transfer are further illustrated through the axial profiles of local values of $\overline{Nu}_{c10}$. Figures 4.55 and 4.56 show that for the staggered configuration of both unconfined and confined jets,the axial profile of circumferential average heat transfer is both higher and more uniform with improvements in $\overline{Nu}$ of improvements of 22% and 33% respectively. Although the improvements measured here are somewhat lower than those predicted analytically by Pelletier et al.[1987], it is significant that their predication of an advantage of staggered over in-line nozzle configurations has now been confirmed by direct measurement.

4.7 Conclusions

1. It has been shown that the published data on impingement heat transfer for axisymmetric jets are generally applicable to the calender control problem, provided the entrainment of ambient air is correctly treated.

2. The effect of surface motion and the accompanying air flow was found to have no significant effect on impingement heat transfer over the range of the nondimensional surface motion parameter, $0.027 < M_{vs} < 0.64$.

3. Entrainment of ambient air by axisymmetric jets, as used for calender control, can reduce the impingement heat transfer by as much as 65% when the jet to ambient temperature difference is equal to or larger than the jet to impingement surface temperature difference.

4. For the stagnation and average Nusselt number, comprehensive regression equations were developed which incorporate the effect of

entrainment.

5. The effect on average heat transfer of jet orientation relative to the calender roll was found to be negligible over the range of the variables considered, i.e. impingement position from 60° to 120° relative to the outgoing nip, and nozzle inclinations from -45° to 35° relative to impingement normal to the wall.

6. Confinement of the impingement flow by a plate parallel to the roll surface can produce substantial improvements, by as much as doubling the heat transfer, through reduction of the strongly deleterious effect of thermal entrainment for temperatures in the range relevant to paper machine calender control. The extent of the confinement surface should be as large or larger than 5.75d, the maximum extent tested in the present study.

7. The switch from an in-line row of nozzles to a staggered configuration for the nozzles results in a higher heat transfer rates and a correspondingly higher jet heat transfer efficiency. For conditions typical in the calender control application, measured heat transfer rates were higher by 22% and 33% for unconfined and confined jets respectively.

CHAPTER 5

HEAT TRANSFER AND THERMAL DEFORMATION IN PAPER MACHINE CALENDER ROLLS

5.1 Introduction

In the manufacture of paper two requirements are that the paper be uniform in thickness and have an acceptable surface finish. Production of the desired surface characteristics and the final control on uniformity of thickness is accomplished by calendering the paper. A calender stack, Figure 5.1, is essentially a rolling mill, a vertical array of cast iron rolls. Paper, from the dryer section, passes through successive nips from top to bottom of the calender stack. The weight of the rolls compresses the paper. The final sheet thickness and surface finish is controlled by adjusting the nip pressure and local roll surface temperature.

The change in paper thickness is determined by a complex interaction of the paper and the calendering parameters, of which pressure in the nips and temperature of the paper are the most important. Figure 5.2 shows these parameters and their multiple interactions as represented by Lyne et al. [1976].

Control of the calendering process in the cross machine (CD) direction is required because the final sheet thickness is affected by variation in sheet properties (i.e. web temperature, moisture content and basis weight) and variation in the nip load (due to grinding tolerances on calender rolls and to CD temperature variations). Machine direction streaks of low or high thickness paper, when built up over a

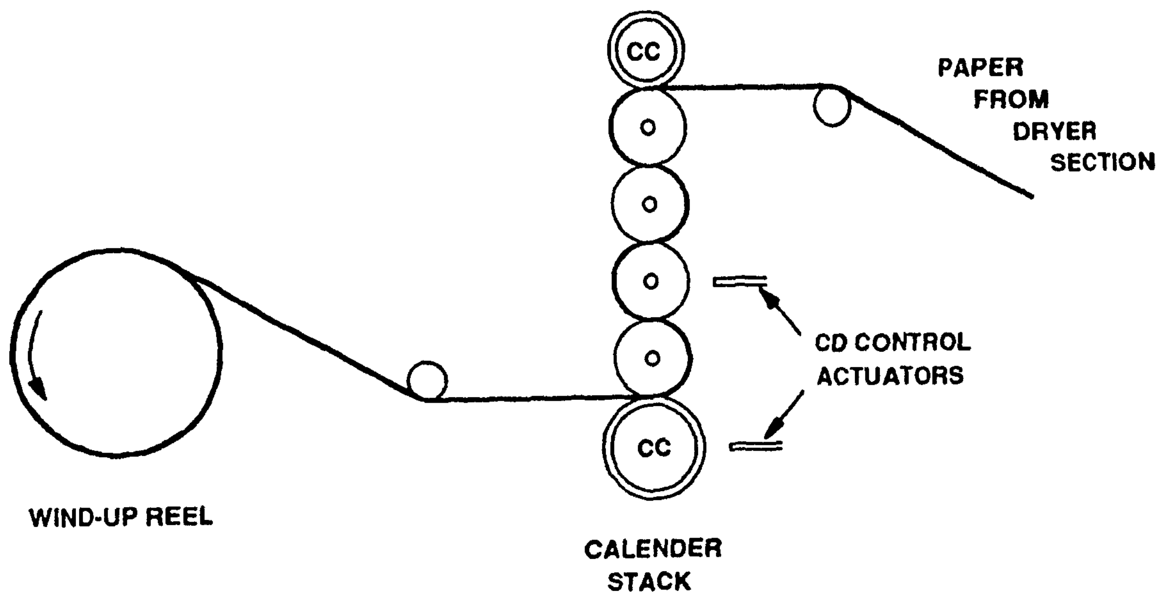

Figure 5.1 A paper machine calender stack.

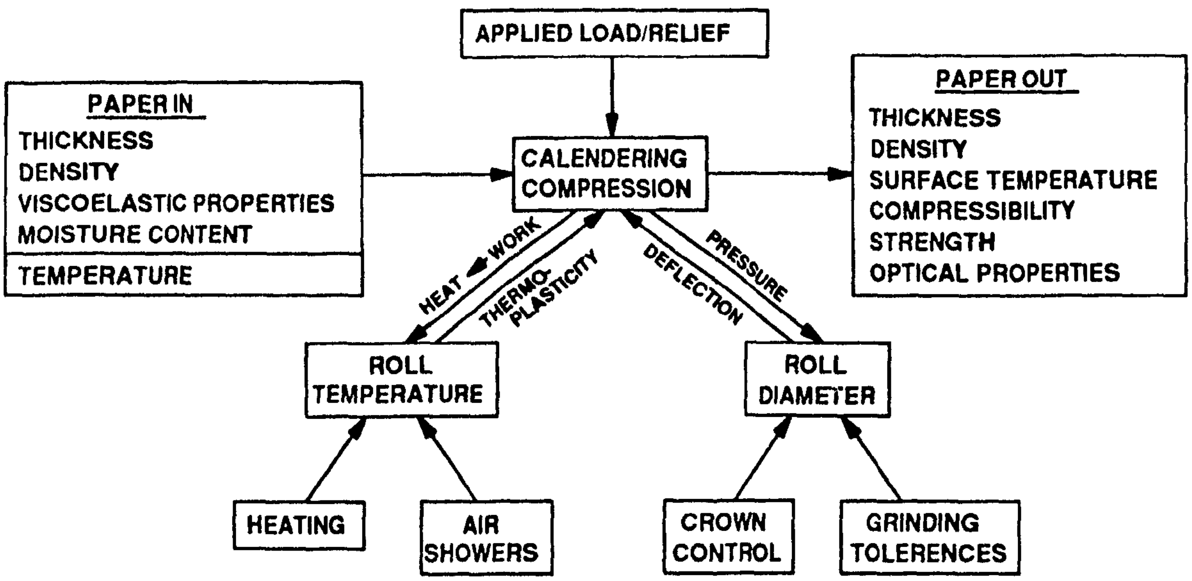

Figure 5.2 Paper - calender roll interactions.

large number of revolutions, produce soft or hard zones in the windup reel which in turn cause unacceptable problems during high speed unwinding for printing. Calender control provides a means of correcting small variations in sheet thickness in the cross machine direction.

Colley and Peel [1972] calculated that a calender roll radius change of only 1.5μm would produce paper of uniform final thickness from incoming paper differing in basis weight by 5%. The challenge of cross machine direction control can be appreciated by noting that this micron-level control of local calender roll radius must be achieved in a modern paper machine, of width about 6m running at about 15m/s, with calender rolls typically 0.3 - 0.6m in diameter and paper thickness, in the case of newsprint, about 60μm.

The correction of cross machine thickness variations is accomplished by:

i. use of a variable crown roll, a roll fitted with hydraulic devices capable of varying the roll diameter, useful for correcting paper thickness over wide streaks, and/or

ii. control of the local calender roll temperature using systems of heating/cooling air jets, induction heaters or friction pads, these control actuators providing local adjustment of roll diameter by thermal deformation.

The complex interaction of the operating parameters on the outgoing paper thickness have been understood qualitatively by papermakers, who have been adjusting cross machine direction profiling systems manually for years. This considerable body of practical knowledge does not however provide the quantitative basis to optimize existing calender stack operations or to design better control systems.

The thermoelastic deformation of hollow and solid cylinders has been studied extensively (Boley [1972], James [1964], Valentin and Carey

[1970], Emery and Carson [1971] amongst others) where the primary concern has been the behavior of nuclear fuel rods. By contrast there has been little quantitative investigation of the thermoelastic response of calender rolls to calender control actuators. The few such studies have simplified the problem by specifying either roll surface temperature boundary conditions, Brierly et al. [1975], or roll deformations, Haglund [1975]. Neither study provides evidence as to whether these boundary conditions are realistic, and moreover, roll surface temperature and roll deformation are in reality dependent variables.

The objective of the present work is to provide a quantitative basis for calender control system design and optimization, through development of a numerical simulation for a calender roll including the control actuators. Thus this simulation links the heat transfer of the control actuators with the thermal deformation of the calender roll. Moreover, as the limited amount of previous work on calender roll deformation has been entirely concerned with steady state simulation, the objectives of the present study include unsteady state simulation because thermal deformation response time is a centrally important control characteristic. The control system model presented here allows investigation of the following parameters associated with roll deformation:

A. Thermal effects
   i. external surface heat transfer profiles
   ii. heat flux to/from paper web
   iii. internal heat transfer

B. Roll geometry effects
   i. external roll diameter
   ii. shell thickness
   iii. roll type (i.e. solid, shell)

5.2 Literature Review

The comprehensive steady state calendering equation of Crotogino [1980] relates thickness reduction in a calender nip to the properties of the incoming paper web (temperature, moisture content, density) and to the operating conditions of the calender stack (machine speed, nip load, roll diameter). As this calendering equation is valid only for cross machine average conditions it is not relevant to the problem considered here, local control in the cross machine direction.

Based on the paper thickness reduction equations of Peel and co-workers [1969, 1972], Haglund [1975] proposed a steady state numerical model. Haglund's model describes the effects that cross direction variation in the calendering and paper web properties have on the outgoing sheet thickness profile. The local cross machine calendering conditions are linked using the line pressure distribution, the resulting calender roll deflection and the local roll deformation. This model requires conversion from the measurable applied line pressure, P_{line}, to the resulting pressure distribution in a calender nip. Haglund [1975] accomplished this using the simplification suggested by Robertson and Haglund [1974], where the pressure pulse in the nip is approximated by a rectangular pulse. The model produced the interesting prediction that the load concentration due to an incoming streak of high basis weight could result in an outgoing streak of low thickness. Although the occurrence of this unexpected result has yet to be documented in actual calendering practice, the difficulty of defining the pseudoplastic properties of paper makes it impossible to discount the possibility. The model also indicated that calender control would require adjustment of the calender roll radius in the range $\Delta r \leq 1\ \mu m$.

This magnitude of roll radius change would appear to be too low since the grinding tolerances on calender rolls are larger than 1 μm.

Brierly et al. [1975], using a steady state finite difference numerical technique, predicted the temperature distribution within the roll and the local thermal deformation in roll radius of a hollow calender roll. Their thermal boundary conditions are a specified uniform temperature on the heated internal surface and a specified temperature profile on the external surface of the roll. Their roll external surface temperature profile is triangular, varying linearly between the peak and the base value of roll surface temperature, T_{sp} and T_{sb}, over the width, W_T, of the temperature peak. All surfaces were specified as being free from externally applied stresses. Brierly et al. found that for surface temperature peak width, W_T, greater than 250-500mm the maximum roll deformation, Δr_p, was unaffected by W_T. They proposed an empirical correlation for the peak difference in roll radius, Δr_p, as a function of the peak difference in roll surface temperature, ΔT_{sp}, and temperature peak width, W_T, in the form

$$\frac{\Delta r_p}{\Delta T_{sp}} = k \left\{ 1 - \exp \left[-\left(\frac{W_T}{\lambda}\right)^p \right] \right\} \tag{5.1}$$

where

Δr_p - peak difference in roll radius

ΔT_{sp} - peak difference in roll surface temperature, $|T_{sp} - T_{sb}|$

W_T - width of the surface temperature peak

k, λ, p - parameters dependant on roll geometry and internal temperature

Application of the above equation to actual calendering conditions was not verified. Moreover, a basic shortcoming of this method is that the temperature profile at the surface of the calender roll, T_s, specified by Brierly et al., is not an independent variable. Rather, it is the operating conditions of the calender stack and the control actuators which are the independent variables. To be of practical value, a simulation must be based on the actual independent variables of the system.

Lyne et al. [1976] used holographic interferometry to measure the steady state thermal deformation of a pilot scale solid calender roll (0.5m dia. x 1.1m long) under the influence of a heating impinging air jet. With peak surface temperature difference, ΔT_{sp}, between 1 to 2 $^\circ$C, the surface temperature peak width was of the order of 0.3m. They found the peak difference in roll radius, Δr_p, varied linearly with ΔT_{sp}, with a proportionality $\Delta r_p / \Delta T_p = 1.4 \mu m/^\circ C$.

Previous studies make little mention of the effect of calender roll type (i.e. shell or solid) or internal calender operating parameters (i.e. heated, unheated, crown controlled) on the thermal roll deformation associated with calender control actuators. Mitchell and Sheahan [1978] reported a very much slower response for a solid calender roll as compared to a shell type roll. Lyne et al. [1976], acknowledging the effect of roll type, speculated that unheated hollow rolls would have a higher thermal sensitivity, i.e. a larger change in radius per degree change in roll surface temperature than either solid or heated rolls.

In summary, the literature provides some useful isolated observations about cross machine direction profiling and some approaches to partial modeling of steady state thermal deformation. However these results are incomplete, sometimes conflicting and provide no quantitative information on response time of the local roll deformation. Thus previous work does not provide the quantitative basis required to optimize existing control systems or to guide the design and positioning of new, high performance calender control systems.

5.3 Mathematical Model

The system for which steady and unsteady state numerical simulations were obtained is shown in axial and radial sections as Figure 5.3 and 5.4. For the axisymmetric coordinate system (r,z), Figure 5.3, the origin is located at the intersection of the center lines of the roll and the controlling actuator. The section being simulated is sufficiently far from the ends of the calender roll to exclude end effects. A specified repeating sequence of cooling and heating control actuators is located symmetrically, in the axial direction, on either side of the origin. The base case repeating sequence comprises a line of 9 identical actuators, either all heating or all cooling, and one controlling actuator producing the opposite thermal effect. The repeating sequence provides sufficient spacing between the controlling actuator jets that calender conditions under one actuator are unaffected by the next controlling actuator. Although detailed results of the simulation are given for the case where the actuators are impinging jets of cooling or heating air, the model is general and could be used for any actuators for which the heat flux between the actuator and the roll surface can be expressed quantitatively, e.g. a water mist evaporator. The use of induction heaters can be approximated with this model or it could be modified by the addition of a heat generation term to Equations 5.2(a) and 5.2(b).

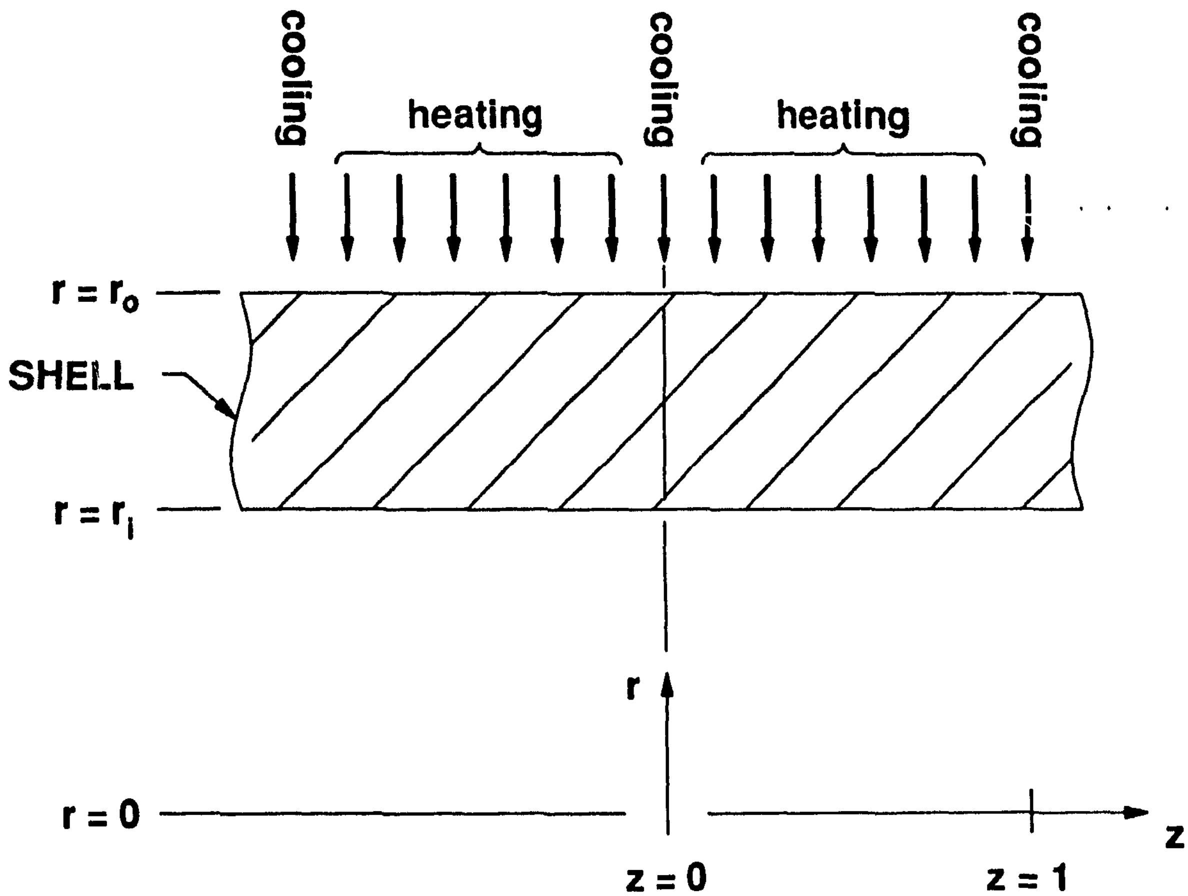

Figure 5.3 Calender control system: axial section.

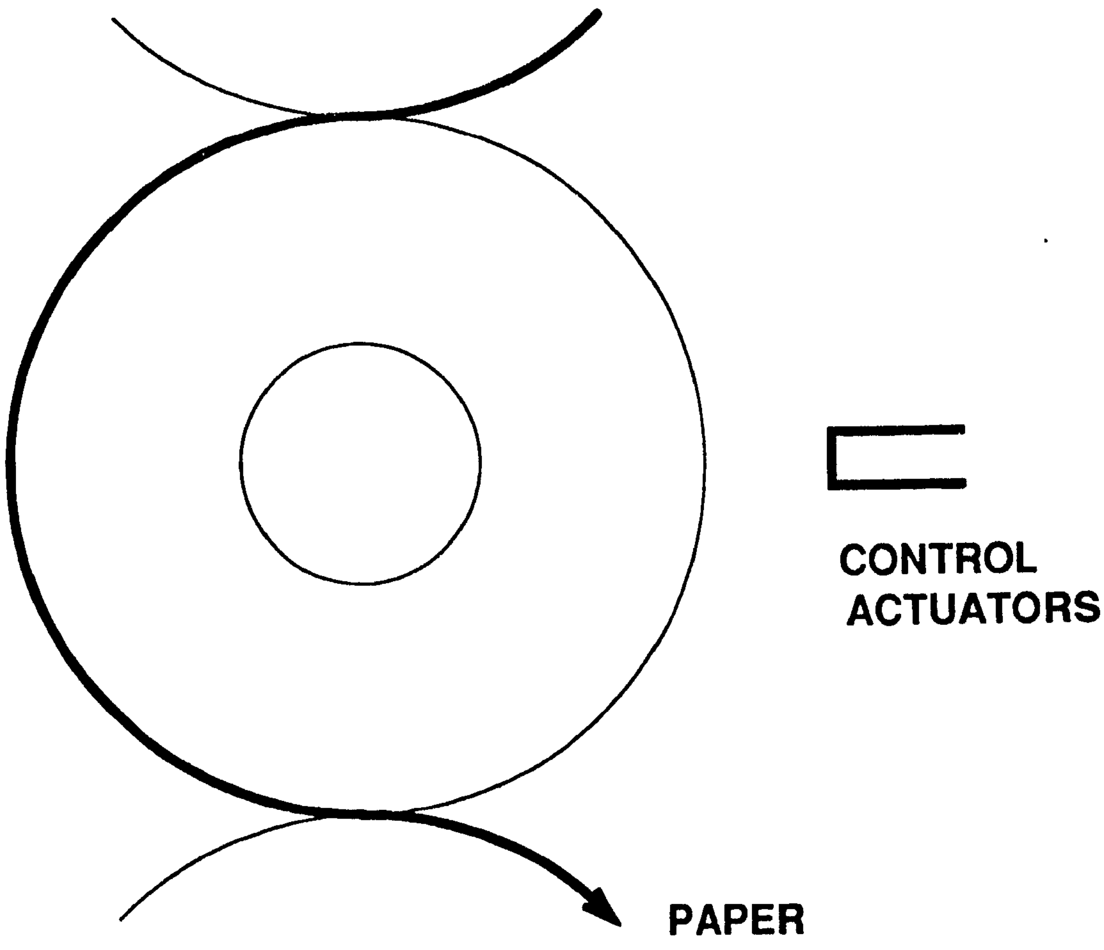

Figure 5.4 Calender control system: radial section.

5.3.1 Equations of State

The governing Fourier equations without heat generation, Equations 5.2a and 5.2b, are:

unsteady-state

$$\frac{1}{r}\frac{\partial}{\partial r}\left(rk \frac{\partial T}{\partial r} \right) + \frac{\partial}{\partial z}\left(k \frac{\partial T}{\partial z} \right) = \rho C \frac{\partial T}{\partial t} \qquad (5.2a)$$

steady-state

$$\frac{1}{r}\frac{\partial}{\partial r}\left(rk \frac{\partial T}{\partial r} \right) + \frac{\partial}{\partial z}\left(k \frac{\partial T}{\partial z} \right) = 0 \qquad (5.2b)$$

The corresponding relations for equilibrium stress, σ, Equations 5.3, are:

$$\left.\begin{aligned} \frac{1}{r}\frac{\partial}{\partial r}(r\sigma_{rr}) + \frac{\partial}{\partial z}(\sigma_{rz}) + \frac{1}{r}\sigma_{\vartheta\vartheta} &= 0 \\ \frac{\partial}{\partial z}(\sigma_{zz}) + \frac{1}{r}\frac{\partial}{\partial r}(r\sigma_{rz}) &= 0 \end{aligned}\right\} \qquad (5.3)$$

The stress-strain relationship is given by the Duhamel-Neumann law, Equations 5.4,

$$\left.\begin{aligned} \sigma_{rr} &= \frac{E\nu}{(1+\nu)(1-2\nu)}(\varepsilon_{rr}+\varepsilon_{\vartheta\vartheta}+\varepsilon_{zz}) + \frac{E}{(1+\nu)}\varepsilon_{rr} - \frac{E\alpha T}{(1-2\nu)} \\ \sigma_{\vartheta\vartheta} &= \frac{E\nu}{(1+\nu)(1-2\nu)}(\varepsilon_{rr}+\varepsilon_{\vartheta\vartheta}+\varepsilon_{zz}) + \frac{E}{(1+\nu)}\varepsilon_{\vartheta\vartheta} - \frac{E\alpha T}{(1-2\nu)} \\ \sigma_{zz} &= \frac{E\nu}{(1+\nu)(1-2\nu)}(\varepsilon_{rr}+\varepsilon_{\vartheta\vartheta}+\varepsilon_{zz}) + \frac{E}{(1+\nu)}\varepsilon_{zz} - \frac{E\alpha T}{(1-2\nu)} \\ \sigma_{rz} &= \frac{E}{(1+\nu)}\varepsilon_{rz} \end{aligned}\right\} \qquad (5.4)$$

The strains in Equations (5.4) are related to the radial, u_r, and axial, u_z, displacements by Equations 5.5.

$$\left.\begin{aligned} \varepsilon_{rr} &= \frac{\partial u_r}{\partial r} & \varepsilon_{\vartheta\vartheta} &= \frac{u_r}{r} \\ \varepsilon_{zz} &= \frac{\partial u_z}{\partial z} & \varepsilon_{rz} &= \frac{1}{2}\left(\frac{\partial u_r}{\partial z} + \frac{\partial u_z}{\partial r}\right) \end{aligned}\right\} \tag{5.5}$$

5.3.2 Simplifying Assumptions

i) Calender roll physical properties are assumed homogeneous and isotropic. As calender rolls are generally chill cast, a layer of chilled iron extends about 10 mm from the outside surface. There is a large difference in thermal conductivity, $\lambda = 58W/m^{\circ}C$ for grey cast iron, $\lambda = 21W/m^{\circ}C$ for chill cast. Since the chill iron thickness is less than 10% of the total shell thickness, the assumption of uniform conductivity (weighted average) will not have a significant effect on the temperature distribution.

ii) The physical properties of the calender roll, λ, α, ν and E, are taken to be independent of temperature, a good assumption for the small temperature differences involved.

iii) The effect on thermal deformation of residual stresses, created during manufacturing, was neglected. These stresses are linearly additive to the numerically predicted thermal stresses.

iv) The elastic stress waves produced in the calender roll by its rotary motion under the line load from the rolls higher in the calender stack can be neglected since the rate of propagation in iron is about 5km/sec, Kolsky [1953]. The corresponding response time, 0.0002s, is three orders of magnitude smaller than the period of rotation.

v) Roll deformation due to gravity and rotation is negligible. Brierly et al. [1975] estimated the critical peripheral speed at which centrifugal forces cause plastic deformation to be about 146m/s, far beyond the 15m/s typical of a high speed paper machine).

5.3.3 Boundary Conditions

(a) Thermal boundary and initial conditions

There are two radial boundary conditions, i.e. at the exterior (Equations 5.6-5.8) and interior (Equations 5.9-5.11) surfaces of the roll, two axial boundary conditions (Equation 5.12) and an initial condition (Equation 5.13).

The heat transfer experienced by the external surface of the calender roll, Equation 5.6, has two components, q_c and q_p, each applying to half the roll circumference, Figure 5.4. The half of particular interest in this study, q_c, is defined by the calender control actuators, the other half by heat transfer between the roll and the paper web due to latent and sensible heat effects of the web, q_p. In the axial direction, the half of the roll exposed to the control actuators experiences the repeating sequence of heating and cooling actuators in the cross machine direction.

$$\lambda \frac{\partial T}{\partial r}\bigg|_{r = r_o} = \frac{\left(h_c(z) \;(T_j - T_s) + \dfrac{q_p}{2\pi r_o} \right)}{2} \tag{5.6}$$

For impinging jet type actuators the heat transfer under each actuator, the $h_c(z)(T_j - T_s)$ term in Equation 5.6, is described by a circumferentially averaged Nusselt number, $\overline{Nu}_c$. For use in this numerical simulation, the axial $\overline{Nu}_c$ data for base case used in Chapter 4, a unconfined single roll of jets, Re = 100000, S/d = 8, as shown in Figure 4.55, was represented as a function of axial distance from the nozzle centerline, as follows

$$\overline{Nu}_c = \frac{a'}{1 + b'\left(\frac{x}{d}\right)^{c'}} + d' \tag{5.7}$$

In the axial direction this equation has the bell shape characteristic of $\overline{Nu}_c$ profiles. The values of the parameters a', b', c' and d' used were those detailed in Chapter 4 for the following typical impingement calender control system conditions with unconfined jets:

entrainment factor, F = 1
jet Reynolds number, Re = 100,000
nozzle diameter, d = 25.4mm
nozzle-to-impingement surface spacing, $H/d \leq 4$
nozzle-to-nozzle spacing, $S/d \leq 8$

For these conditions, the parameters of Equation 5.7 as determined in Chapter 4, give:

$$\overline{Nu}_c = \frac{94.68}{1 + 0.019\left(\frac{x}{d}\right)^{2.09}} - 38.84 \tag{5.8}$$

For a control system using confined jets with H/d = 2, the value of $\overline{Nu}_c$ is 33% higher.

The boundary condition for the half of the calender roll wrapped by the paper, Figure 5.4, is the $q_p/2\pi r_o$ term in Equation 5.6. The q_p term for contact heat transfer between the roll surface and the paper, difficult to specify, could involve several factors, i.e. sensible and latent effects for the paper web and compressive heating in the nips. As this study focusses on the effect of control actuators on the exposed half of the calender roll, the paper side heat transfer assumptions of Aro [1985] are used. Thus the effect of roll-paper heat transfer from heat generated by compression in the nips is assumed negligible. As for sensible and latent heat effects, the assumptions of Aro for a roll without internal heating, are:

i) no change in sheet moisture content.

ii) no change in sheet temperature.

i.e. no sensible or latent heat effects. Thus for an unheated roll, $q_p = 0$. For internally heated rolls, Aro assumed:

i) sheet moisture content decreases by 0.2%

ii) sheet temperature increases by 9.3°C

The present model may of course use any other paper side boundary conditions.

For the case of an internally heated calender roll, specification of the radial boundary condition at the internal surface is by the heat transfer coefficient, h_i, from the heating medium at a bulk temperature, T_b.

$$\left.\frac{\partial T}{\partial r}\right|_{r = r_i} = h_i\,(T_b - T_i) \tag{5.9}$$

For a solid roll or a center-bored or shell (double-wall) type roll which is unheated, $h_i = 0$. Otherwise h_i was obtained using McAdams' correlation:

$$Nu = 0.023\ Re^{0.8}\ Pr^{n} \tag{5.10}$$

where: $n = 0.4$ (for heating), 0.3 (for cooling)

In the case of a double-walled temperature controlled shell type roll, Figure 5.5, the equivalent diameter, d_e, for both Nusselt and Reynolds number is:

$$d_e = 2(r_i - r_d) \tag{5.11}$$

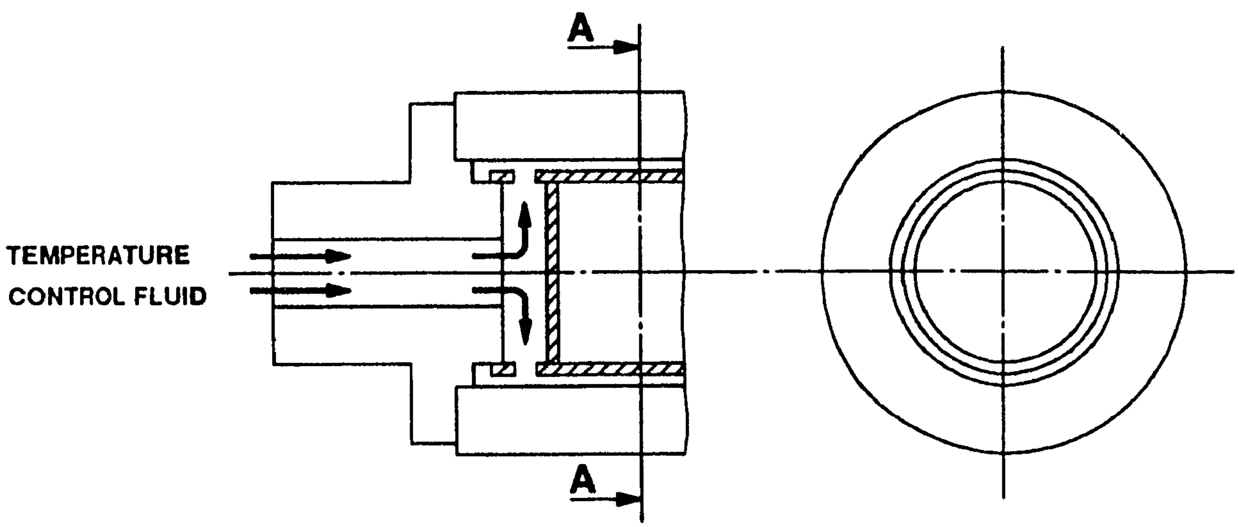

DOUBLE WALLED ROLL

Figure 5.5 A double walled, internally heated roll.

where r_d is the outside radius of the displacement body. For the double-walled roll the heating medium flow rate is fixed at 8L/s of 150°C water with a gap width, $r_i - r_d$ = 60mm, again those documented by Aro [1985] in his numerical study of calender roll edge effects. These assumptions yield an internal heat transfer coefficient, $h_i \cong 11000$. To simplify the data analysis, over a large range of roll diameters and shell thickness, this value of h_i was used for all heated roll cases.

The axial boundary conditions for the numerical simulation, Equation 5.12, are by contrast quite simple, i.e. no axial heat transfer at the centerline of the controlling actuator,

$$\left.\frac{\partial T}{\partial z}\right|_{z\,=\,0,\ell} = 0 \tag{5.12}$$

where ℓ is the length of calender roll occupied by one repeating set of actuators. As noted earlier, this simulation is valid at axial positions sufficiently far from the extremities of the roll to exclude end effects such as heat transfer changed by the absence of paper and the presence of the calender roll journal.

The initial condition for the unsteady state solution was taken as the temperature distribution (Equation 5.13) for the steady state solution with either a row of heating jets all with nozzle exit temperature T_j = 150°C or a row of cooling jets all with T_j = 20°C.

$$T\big|_{t\leq 0} = T(r,z) \tag{5.13}$$

The condition imposed at t = 0 was a repeating sequence of either 1 cooling jet at T_j = 20°C and 9 heating jets at T_j = 150°C, or 1 heating jet and 9 cooling jets at these values of T_j. The jet-to-jet spacing, S, was generally taken as S = 4d = 100mm, in some cases as S = 8d = 200mm, as listed subsequently in Table 5.1. These conditions before and after

$t = 0$, although arbitrary, provide a standard basis for the determination of the characteristic response time of calender rolls.

(b) Stress equilibrium boundary conditions

In the r-direction

At $r = r_i, r_o$ and $0 \le z \le \ell$

$$\left.\begin{aligned} \sigma_{rr} &= 0 \\ \sigma_{rz} &= 0 \end{aligned}\right\} \qquad (5.14)$$

In the z-direction

- symmetry boundary

$$\left.\begin{aligned} v &= 0 \\ \sigma_{rz} &= 0 \end{aligned}\right\} \quad \begin{aligned} & z = 0 \\ & r_i \le r \le r_o \end{aligned} \qquad (5.15)$$

- no traction boundary condition

$$\left.\begin{aligned} \sigma_{zz} &= 0 \\ \sigma_{rz} &= 0 \end{aligned}\right\} \quad \begin{aligned} & z = \ell \\ & r_i \le r \le r_o \end{aligned} \qquad (5.16)$$

The boundary conditions specified in Equations 5.14 to 5.16 express the absence of external forces at all radial and axial boundaries of the calender roll, i.e. the no-traction boundary conditions. For this case the roll can expand freely, axially and radially, responding to the temperature and stress distributions within the calender roll.

5.3.4 Solution Method

(a) Steady State solution

The steady-state temperature field and corresponding stress and displacement profiles were determined by solving Equations 5.2(b), 5.3 and 5.4 simultaneously using IMSL PDE PROTRAN©, which is a general purpose, two dimensional, finite element procedure. The pseudo-fortran source code for the PDE PROTRAN© finite element method is given in Appendix D.

Although PDE PROTRAN© greatly simplifies the coding of numerical problems, specification of the boundary conditions for the present problem involves difficulties. In calender roll operation there is a temperature gradient through the roll wall. Under the no-traction boundary condition at $z = \ell$, the inside to outside surface temperature difference for an internally heated roll causes differential axial expansion of the roll, resulting in a distortion of the calender roll called the "oxbow effect", Figure 5.6. This roll distortion is an artifact of the no-traction boundary condition which is valid only at the edge of a roll and not at internal boundaries. Attempts to remove the oxbow effect in the solution domain, which is located away from the calender roll edges, by modifying the no-traction boundary condition to one of uniform axial expansion at the $z = \ell$ boundary were unsuccessful. Previous work by Rothenbacher and Vomhoff [1982] on internal heat transfer from peripherally bored calender rolls, has shown that the oxbow effect is limited to a distance less than 1 roll diameter from the end of a roll. As this effect is not relevant to the present study it was eliminated by extending the axial dimensions of the simulation to not less than 2 roll diameters. Although effective, this procedure greatly increased the required processing time.

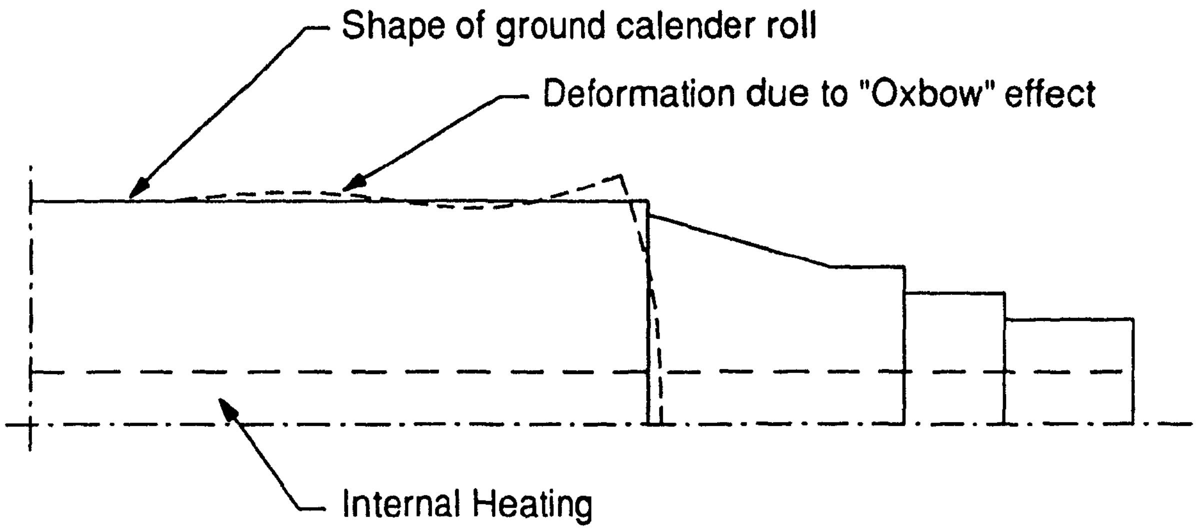

Figure 5.6 The "oxbow" effect.

(b) Unsteady State Solution

An analytical solution is available for thermal deformation when a cylinder behaves as an assembly of disks which are physically separate but thermally connected. The elastic deformation of shells and solid rolls for this case when there are no externally applied forces, commonly referred to as the plane strain solution, is

$$u_r = \frac{\alpha}{r(1-\nu)} \left\{ (1+\nu) \int_{r_i}^{r_o} T\, r\, dr + \frac{(1-3\nu)\, r_o^2 + (1+\nu)\, r_i^2}{r_o^2 - r_i^2} \int_{r_i}^{r_o} T\, r\, dr \right\} \qquad (5.17)$$

Equation 5.17 is central to the solution of the unsteady state case, for which the temperature and stress distributions were considered to be uncoupled, i.e. that the stress distribution is constantly in equilibrium with the temperature profile. The temperature distribution, $T(r,z,t)$, was obtained by solving Equation 5.2 using the finite volume method of Patankar[1980]. Equation 5.17 can then be used to approximate the roll deformation, $u_r(z,t)$. The validity of the approximation of uncoupling the temperature and stress distribution equations is tested for the present case in Section 5.5. The fortran source code for the finite volume procedure is given in Appendix C.

5.3.4 Validation of the Numerical Models

(a) Steady State Model

Of the studies of thermoelastic deformation of hollow and solid cylinders, only that of Brierly et al.[1975] examined conditions approximating those for paper machine calender stacks. Their numerical results for a steady state simulation by the finite difference method were for specified internal and external temperature profiles. Their conditions were rerun with the current numerical procedures as a validation of the latter. The temperature boundary conditions specified by Brierly et al. correspond to the following values of parameters:

$$q_p = 0$$

$$\left.\begin{matrix} h_i \\ h_c \end{matrix}\right\} = \infty$$

In practice, $h_i = h_c = 10^5$ is a suitably large number. Their external temperature profile was specified as

$$T_s = T_{sp} - \frac{2\,z}{W_T}\,\Delta T_{sp} \qquad 0 \le z \le \frac{W_T}{2}$$

$$T_s = T_{sb} \qquad \frac{W_T}{2} \le z \le \frac{\ell}{2}$$

The run of Brierly et al. which was rerun here was one for which the thermal boundary conditions and roll geometry gives large axial surface temperature gradients, a test case which has the greatest opportunity to expose differences. The conditions used were:

$$\ell = 0.625\text{m}$$

$$W_T = 0.0625\text{m}$$

$$T_{sb} = 50^\circ\text{C}$$

$$T_{sp} = 70^\circ\text{C}$$

$$\Delta T_{sp} = |T_{sm} - T_{sp}| = 20^\circ\text{C}$$

$$T_b = 30^\circ\text{C}$$

It is demonstrated that the steady state temperature fields obtained here using the finite volume (difference) and finite element methods, Figures 5.7 and 5.8 respectively, do not differ significantly from the results of Brierly obtained with a finite difference method.

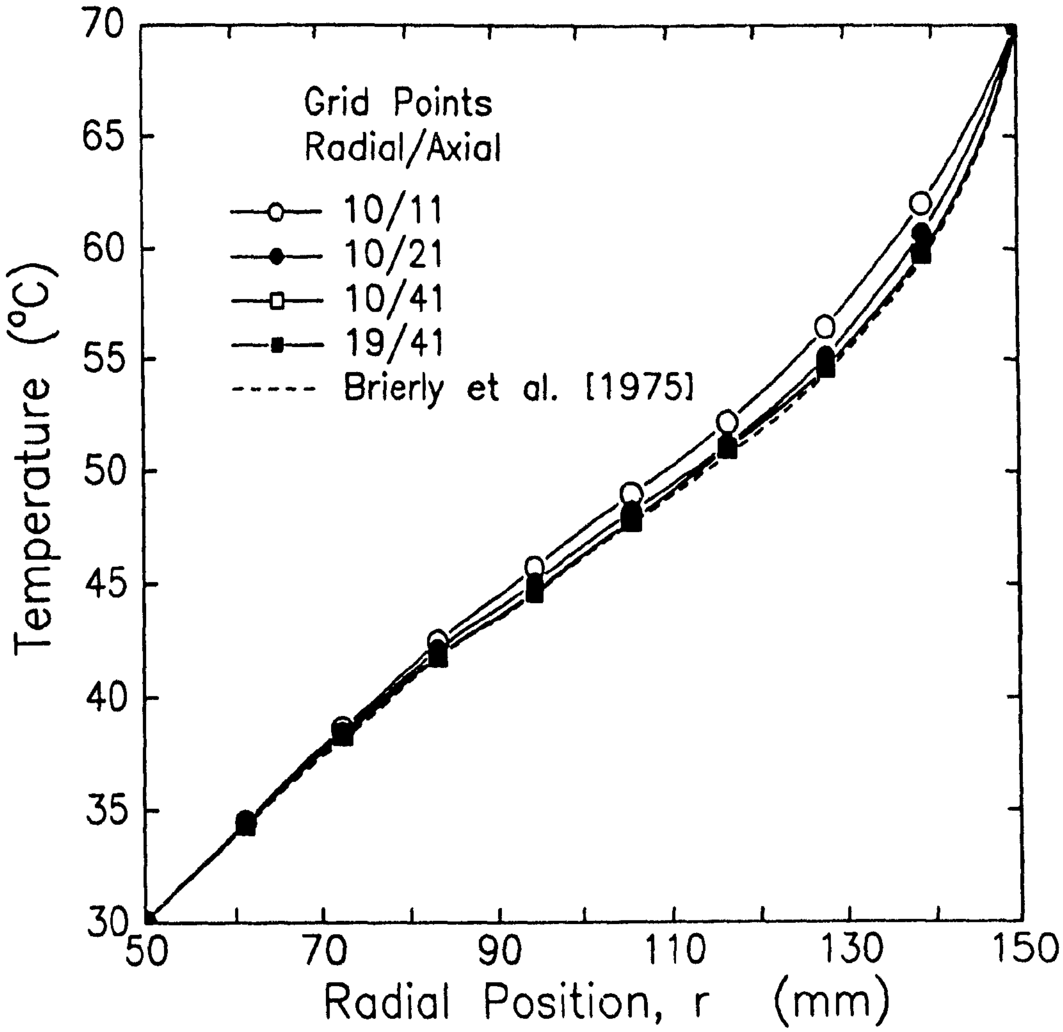

Figure 5.7 Grid independent temperature field (finite volume).

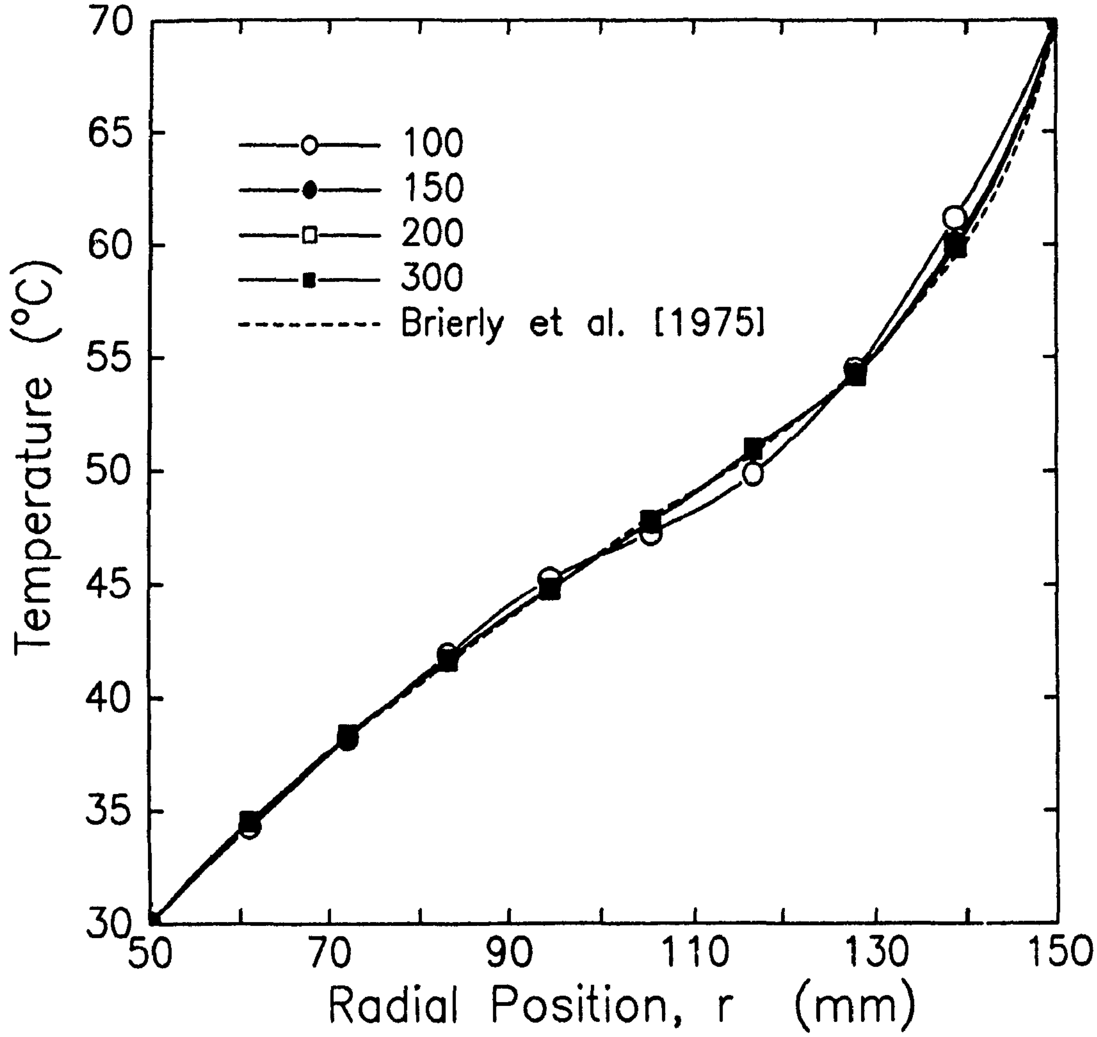

Figure 5.8 Grid independent temperature field (finite element).

Further, the lack of an effect of grid spacing with the large ΔT_{sp} justifies the use of the grid spacings selected for subsequent runs, i.e. 100 node per meter in the axial and radial directions.

A comparison of profiles of steady state roll deformation as predicted by the current simulation and by Brierly et al., Figure 5.9, shows that the differences, $\leq$ 5%, are not significant. Brierly et al. found their displacement field to be grid dependent and estimated the errors to be in the range ±1% to ± 2.75%. The roll deformation predicted by either method is seen to be less, as must be the case, than the plane strain solution, Equation 5.17. Although not shown, the deformations predicted in all three cases converge, as expected, for peak widths, W_T, greater than 5m.

The only experimental measurement of thermal deformation is that of Lyne et al. [1976] for a pilot scale calender roll (solid, 0.5m dia. x 1.1m long) using a single round or slot heating jet. At steady state they observed a surface temperature peak width, W_T, in the order of 300mm for a peak difference in roll surface temperature, ΔT_{sp}, of 1° to 2°C. They characterized the steady state deformation of roll radius under a single jet as $1.4\mu m/\Delta T_{sp}$. Using the approximation of a Brierly-type triangular profile of surface temperature, which closely approximates the axial temperature distribution observed by Lyne et al.,along with the measured ΔT_{sp}, the resulting thermal deformation calculated using the current model is shown in Figure 5.10. The peak value of the predicted roll deformation profile agrees closely with that measured by Lyne et al. For the very modest values of calender surface peak temperature difference obtained by Lyne et al., ΔT_{sp} of 1 or 2°C, Figure 5.10 also shows that the thermal stresses are sufficiently small that the plane strain solution closely approximates the present

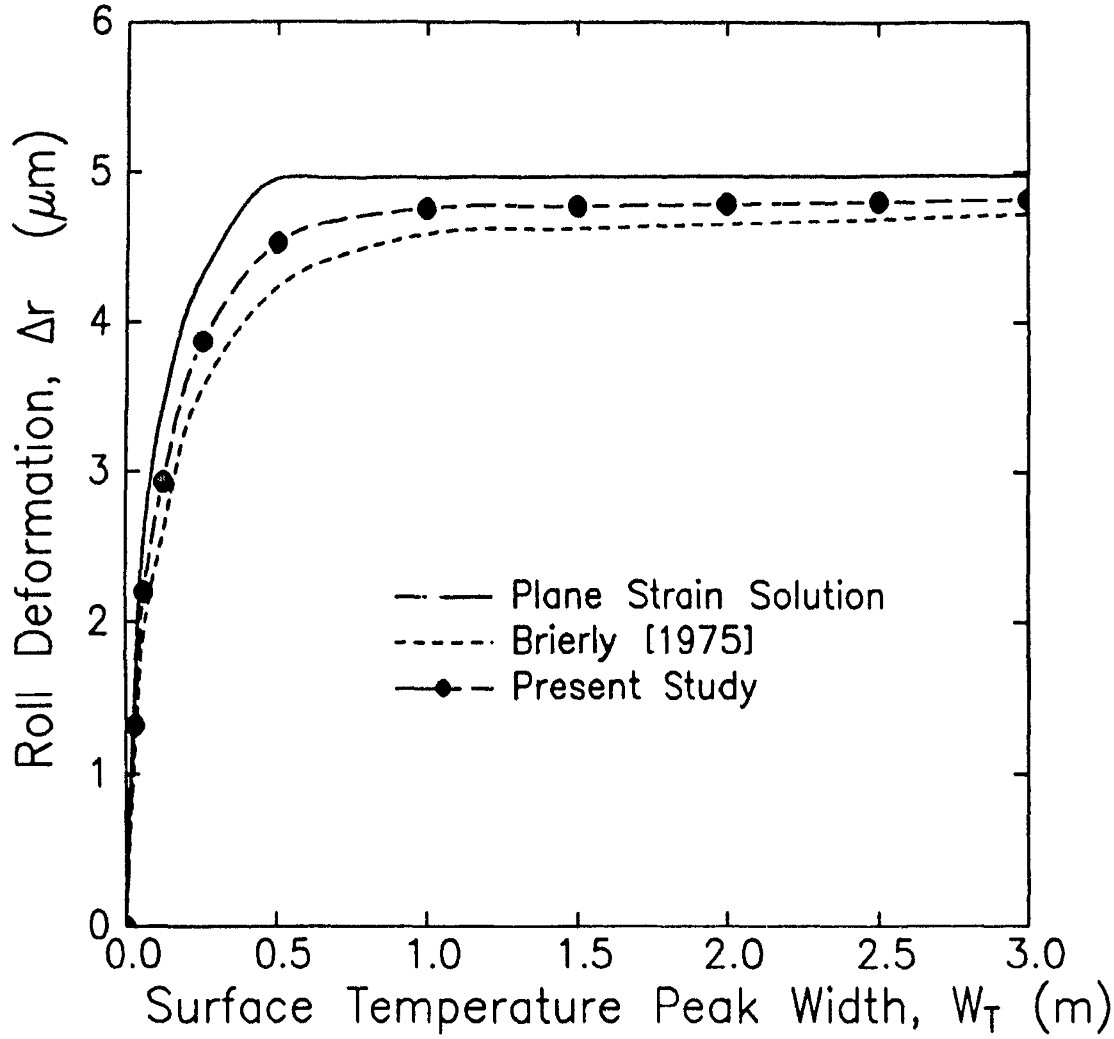

Figure 5.9 Comparison with roll deformation simulation of Brierly et al.

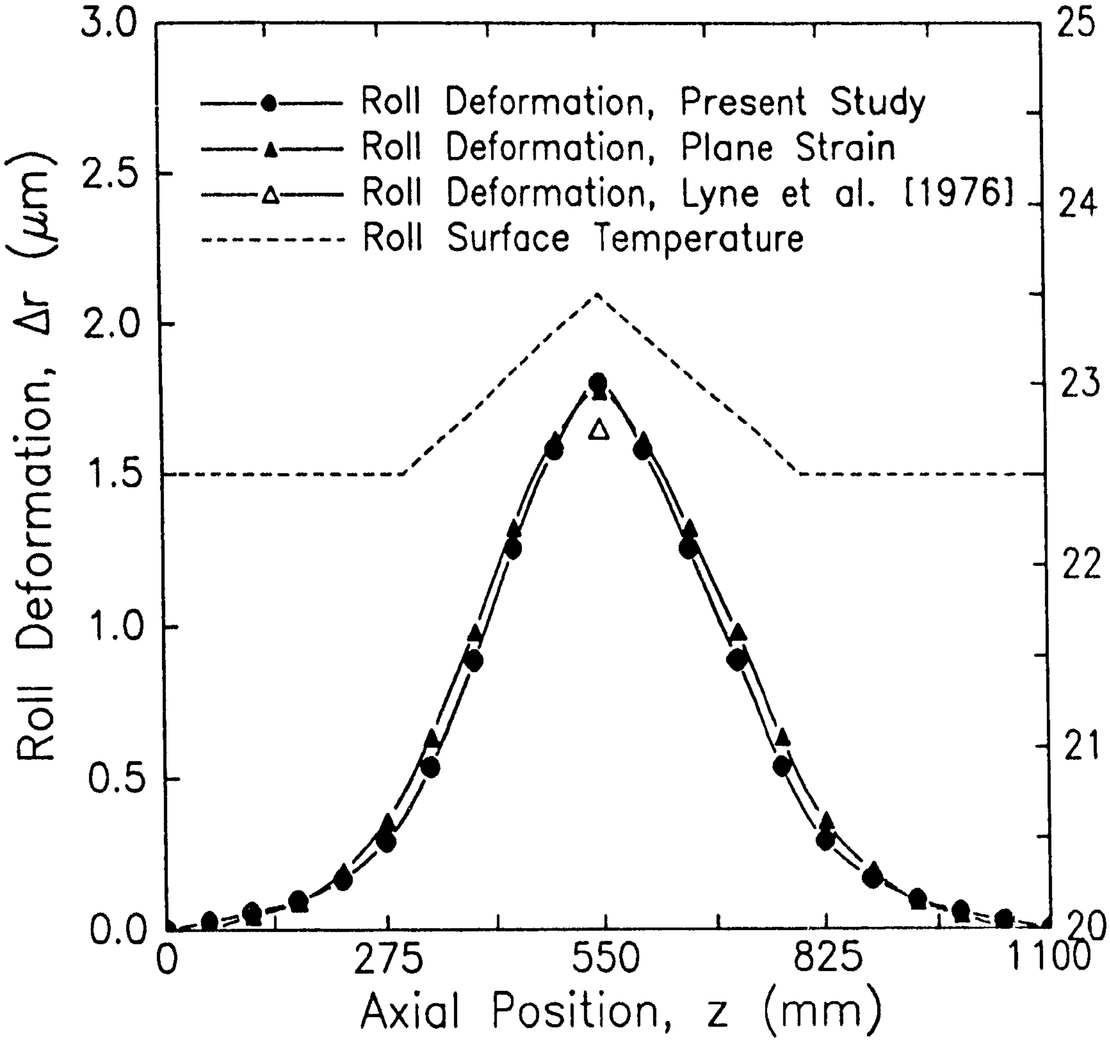

Figure 5.10 Comparison with roll deformation measurement of Lyne et al.

simulation. Under conditions encountered on paper machine calender stacks, axial surface temperature differences may reach 10°C, for which the plane strain solution can be inadequate.

Roll response is characterized as either the local or peak value, Δr or Δr_p, of deformation and as the width of this deformation, $W_{\Delta r}$, as illustrated in Figure 5.11. As the deformation, Δr, is a distributed variable in the z-dimension, a specific definition is required for $W_{\Delta r}$. For consistency, the definition of characteristic width of deformation used here is that of Verasalo [1984], i.e. $W_{\Delta r}$ is the z-direction width over which $\Delta r \geq \Delta r_p/3$. As will become apparent, the local deformation approximates a normal distribution, thus $W_{\Delta r}$ would correspond to $W_{\Delta r} = 1.48\ \sigma$.

Figure 5.12 gives the axial profiles of local roll deformation produced with the control jet, a single cooling jet at $T_j = 20°C$ in a row of heating jets at $T_j = 150°C$, for the case of heated (with 150°C water) double-walled rolls of fixed outside radius, $r_o = 250mm$ and various shell thickness, s. Roll deformation obtained assuming the plane strain solution (Equation 5.17) is also shown. The values of ΔT_{sp} calculated by the model are recorded on Figure 5.18. Relative to the idealized plane strain solution for an assembly of physically separate thin disks, in the real case the thermal stresses act to reduce the maximum value of the roll deformation, Δr_p, and to increase the width of the region of roll deformation, $W_{\Delta r}$. Thus the numerical simulation of the plane strain solution, gives values of Δr_p about 5% too large. On the same basis, the approximation of $W_{\Delta r}$ by the plane strain solution varies from about 25% too low for s = 100mm, to negligible difference as a solid roll is approached, Figure 5.13. The error in the plane strain approximation decreases as shell thickness increases because, for the

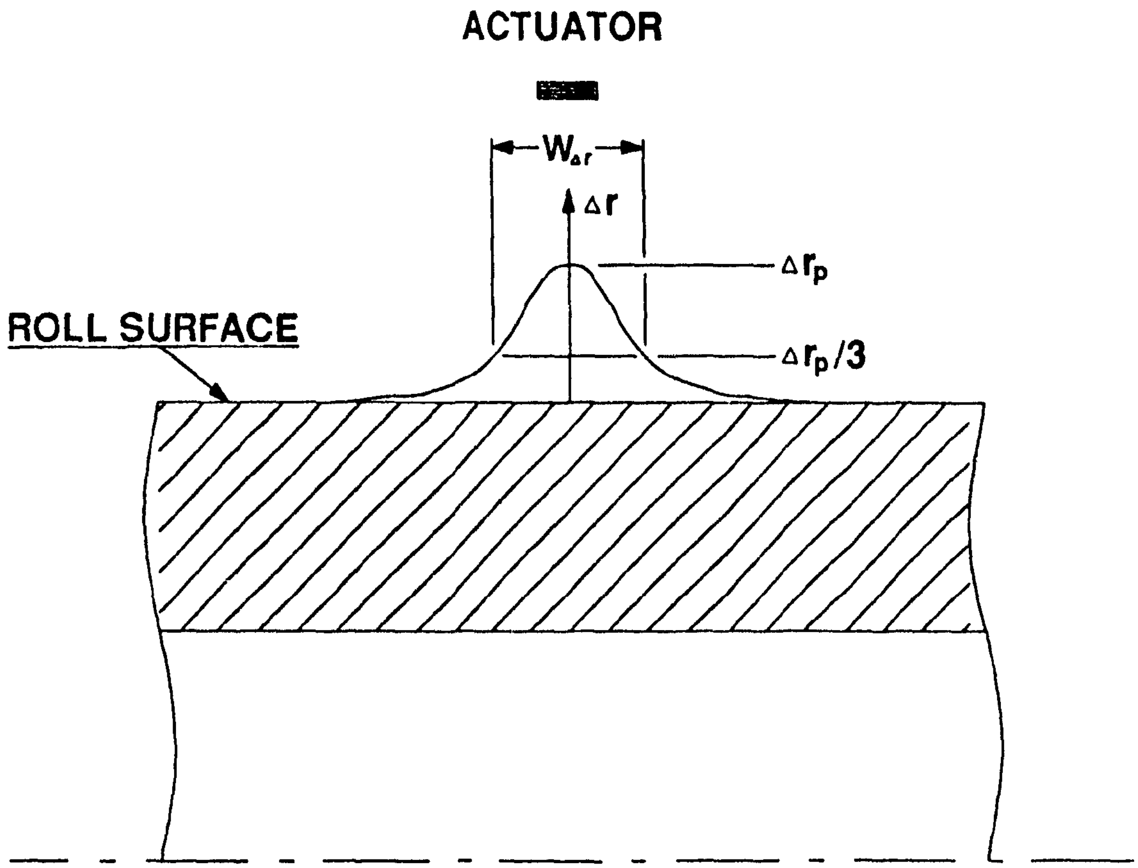

Figure 5.11 Definition of characteristic width of roll deformation, $W_{\Delta r}$.

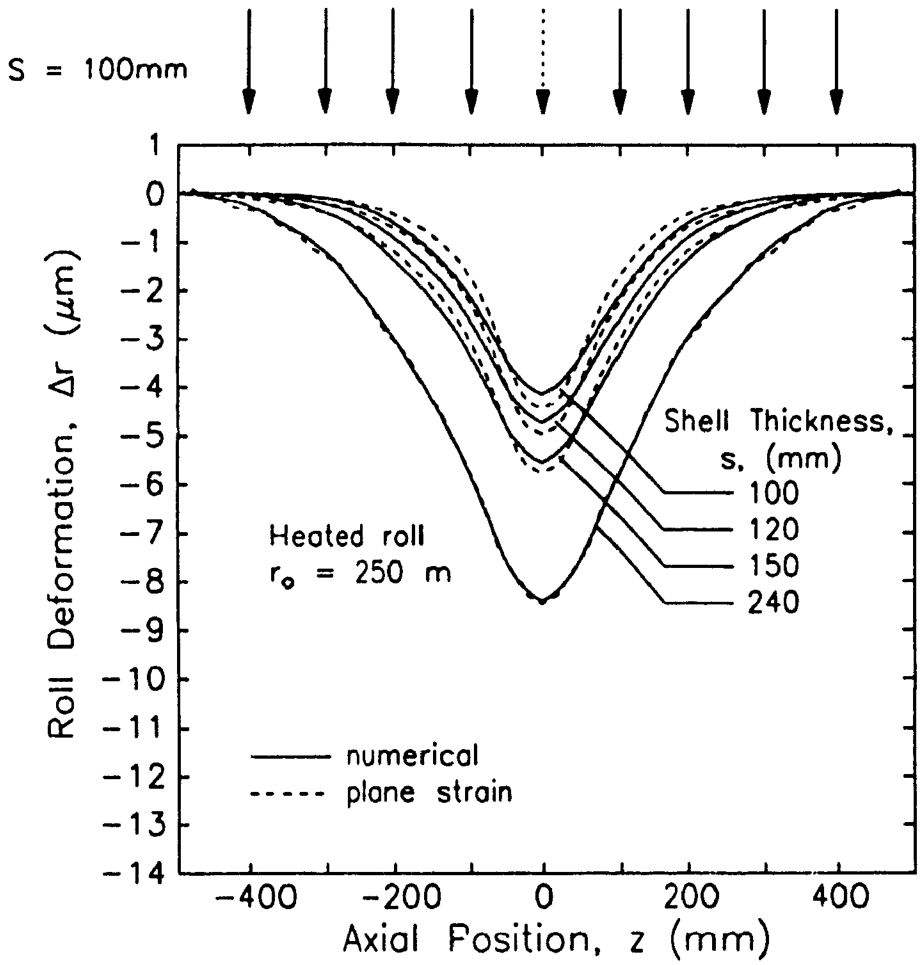

Figure 5.12 Profiles of local roll deformation, by numerical simulation and plane strain solution: Internally heated roll, r_o=250 mm.

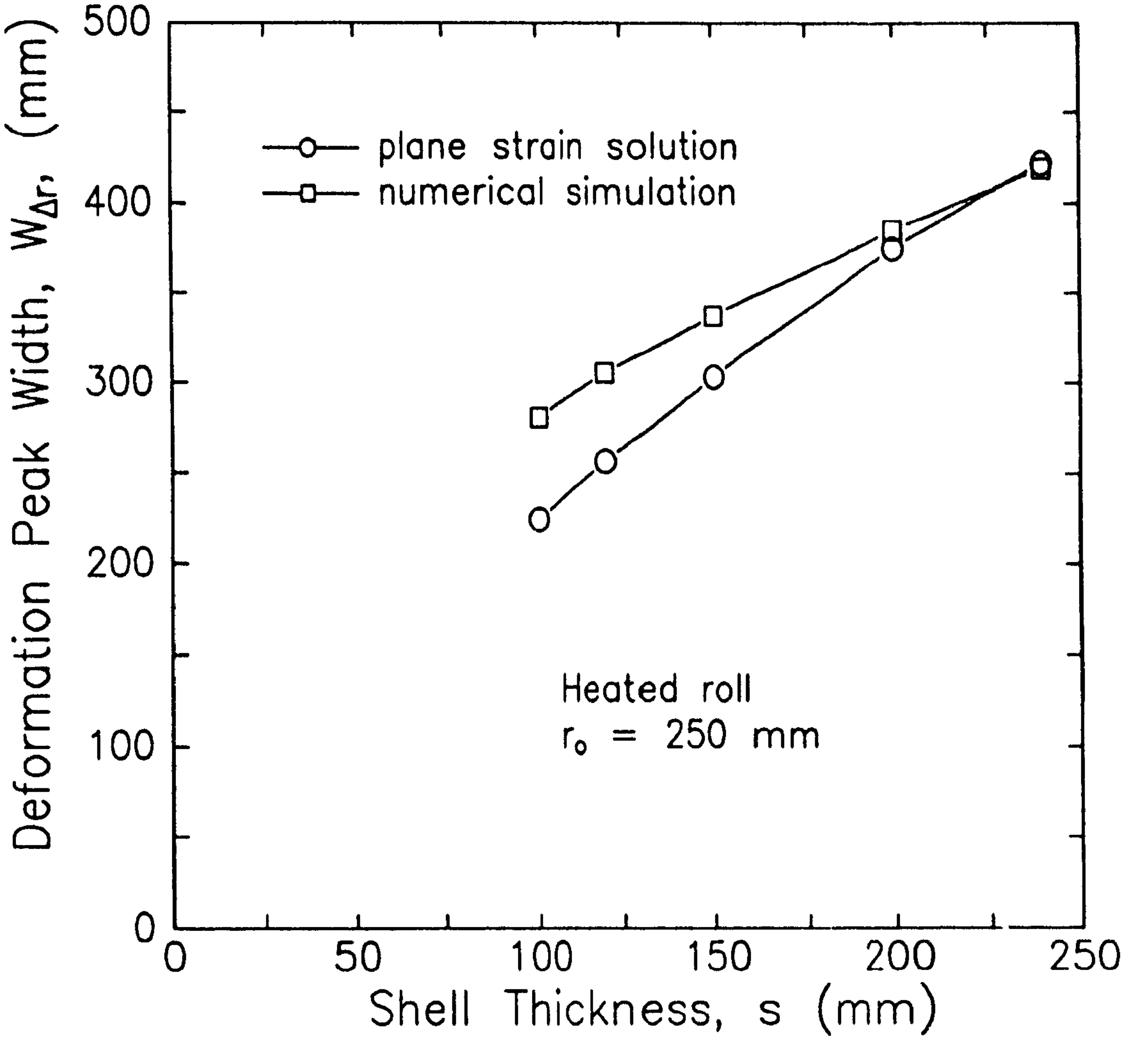

Figuree 5.13 Width of deformation, by numerical simulation and planestrain solution: internally heated roll, r_c=250 mm.

boundary conditions used, the temperature gradients and thus the thermal stresses decrease correspondingly.

For local control of sheet thickness in the cross machine direction,the characteristic width of the roll deformation, $W_{\Delta r}$, with a single control jet is of central importance because this value defines the minimum width of strip over which control of sheet thickness may be effected. The axial heat flux, q_z, through the high conductivity cast iron roll spreads the thermal effect of the control jet so that, for the heated roll cases of Figures 5.12 and 5.13, the control width, $W_{\Delta r}$, is about 300-400 mm, i.e., about 3-4 times the jet-to-jet spacing of S = 100 mm.

(b) Unsteady State Model

Although the finite volume procedure used to solve the unsteady state model converges on the steady state solution, the validity of the unsteady state behavior predicted by the model must be validated. For this geometry, validation can be readily accomplished by judicious choice of general boundary conditions for the numerical simulation. Two classic textbook examples of one dimensional unsteady state thermal behavior, for which analytical and tabular solutions exist, can be simulated with the two dimensional finite difference procedure. These are:

i. Sudden change in temperature of the fluid surrounding a semi-infinite cylinder initially at a constant temperature

ii. Sudden change in temperature of the fluid surrounding a semi-infinite slab initially at a constant temperature

Both cases can be calculated using an internal heat transfer coefficient, $\bar{h}_i = 0$, a constant value for the external heat transfer coefficient with $h_c \neq f(z)$. The semi-infinite cylinder is an obvious subset of the current simulation, while the thermal behavior of a semi-infinite slab is approached, in cylindrical coordinates, as $r_o/r_i \rightarrow 1.0$. In the case of the semi infinite slab, the boundary at r_i corresponds to the center plane of the slab. The temperature-time history for both cases were tabulated in the numerical results of Heisler [1947], commonly presented as Heisler charts.

The predicted temperature-time history at the centerline of the cylinder and the slab are presented in Figures 5.14(a) and 5.14(b) and are in good agreement with the results obtained from Heisler charts.

In summary, these results establish that the finite element steady state and finite difference transient models presented here produce reliable, grid independent predictions, consistent with the limited amount of previous work.

5.4 Numerical Simulation of Steady State Thermal Deformation

The effects at steady state of roll design and operating variables for systems of impinging jets used as calender control actuators were determined by numerical simulation.

5.4.1 Conditions Used in Numerical Simulations

The operating conditions for which the steady state numerical simulation were performed are listed in Table 5.1

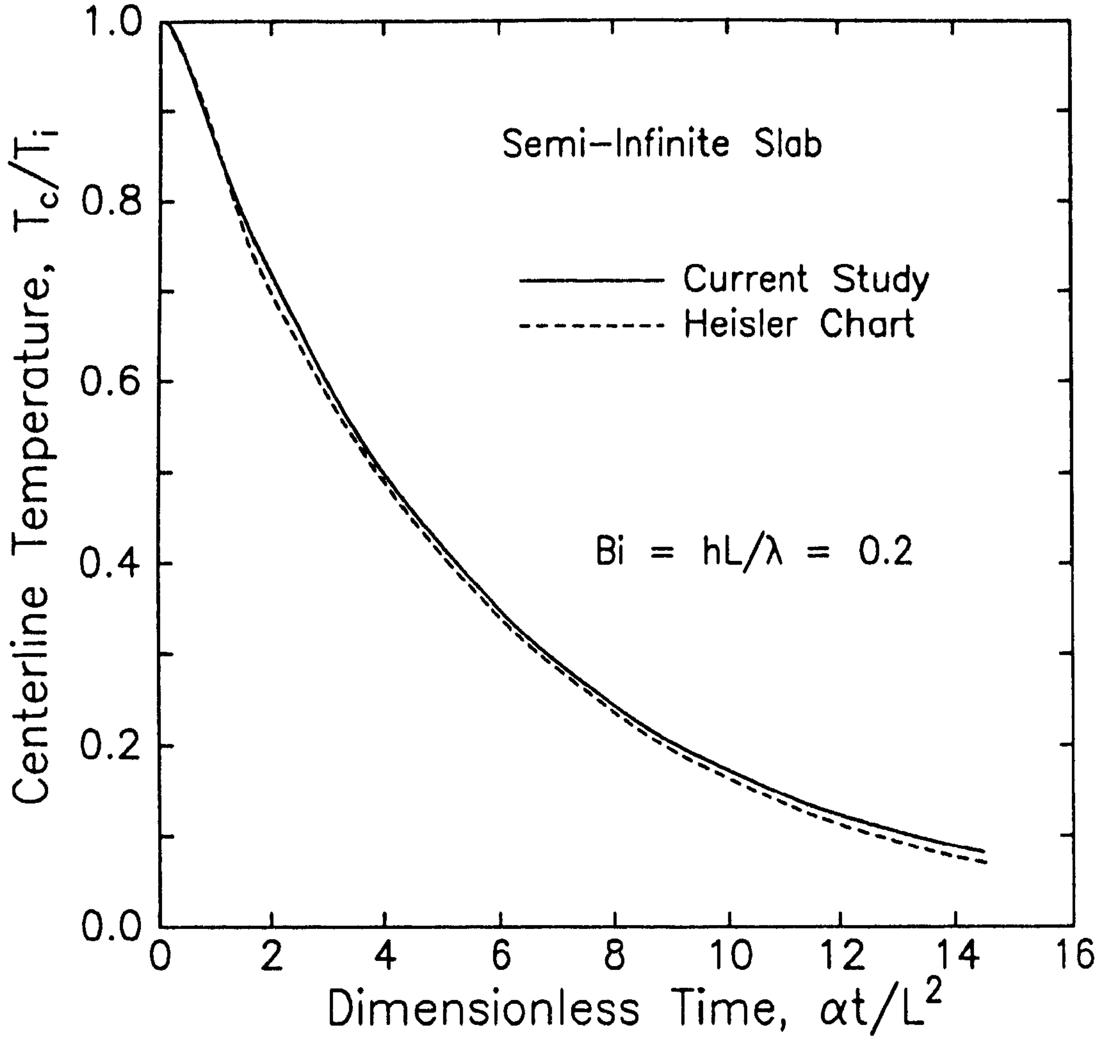

Figure 5.14(a) Comparison of unsteady state response obtained using the finite volume model with results from Heisler charts: semi-infinite slab, $r_i/r_o \rightarrow 1.0$

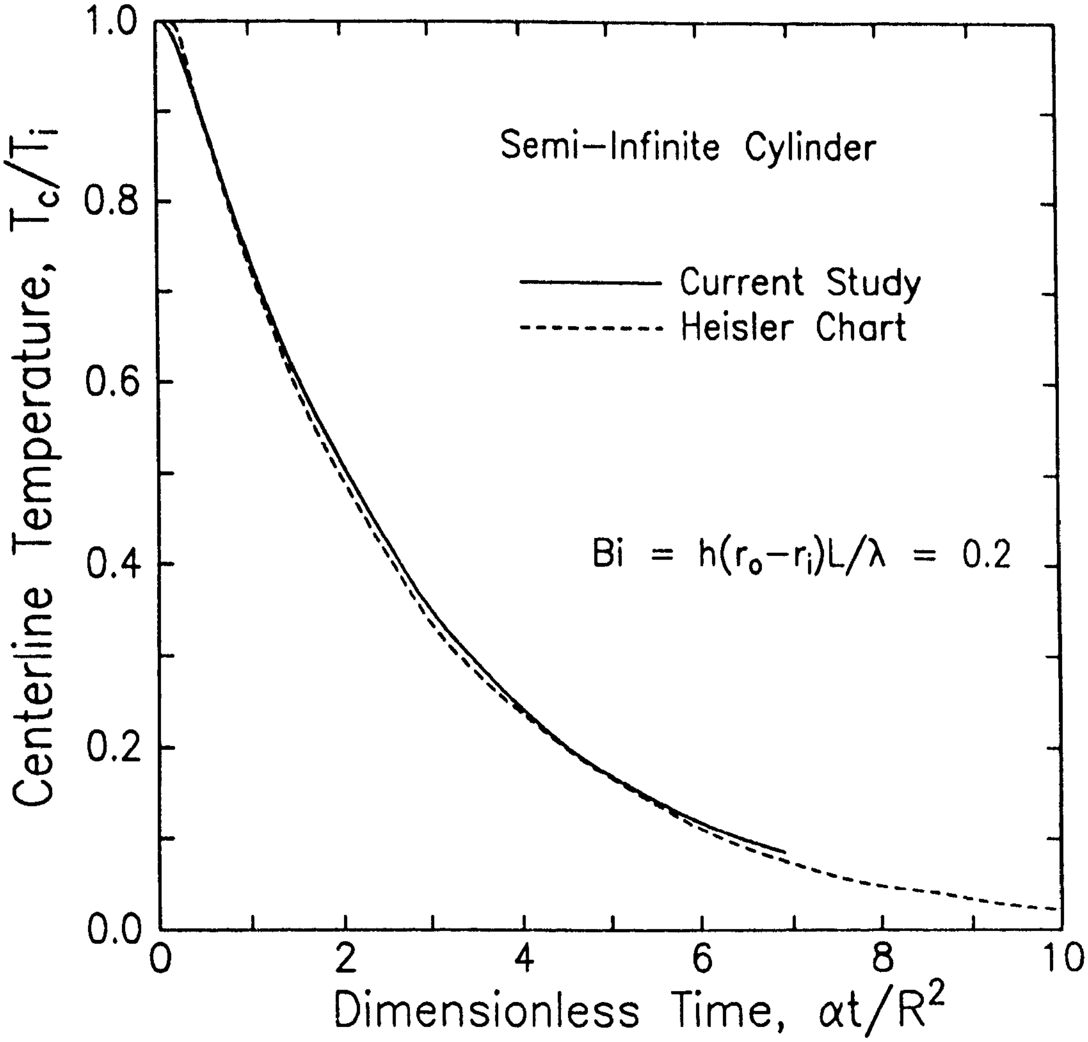

Figure 5.14(b) Comparison of unsteady state response obtained using the finite volume model with results from Heisler charts: semi-infinite cylinder, $r_i \to 0.0$

Table 5.1 Conditions for steady state numerical simulations

External Diameter r_c (mm)	Shell Thickness s (mm)	Internal Heated/ Unheated	Jet-to-Jet Separation S (mm)	Number of heating jets/ cooling jets	Comment
250	100	heated	100	9-1	
250	120	heated	100	9-1	
250	150	heated	100	9-1	
250	200	heated	100	9-1	
250	240	heated	100	9-1	
250	100	unheated	100	9-1	
250	120	unheated	100	9-1	
250	150	unheated	100	9-1	
250	180	unheated	100	9-1	
250	250	unheated	100	9-1	(1)
250	120	heated	200	9-1	
250	120	heated	200	9-1	(2)
250	120	heated	200	9-1	(3)
250	120	heated	100	9-1	
250	120	heated	100	9-2	
250	120	heated	100	9-3	
250	120	heated	100	1-9	
250	120	heated	100	2-9	
250	120	heated	100	3-9	
250	120	heated	100	9-1	(4)
250	120	heated	200	9-1	
270	120	heated	100	9-1	
300	120	heated	100	9-1	
300	150	heated	100	9-1	

(1) solid roll

(2) sharp Nusselt number profile

(3) extremely sharp Nusselt number profile

(4) confined impinging jets

5.4.2 Equivalence of Heating and Cooling Control Jets

The equivalence of heating and cooling control jets with respect to steady state deformation, Δr, is as expected for unheated rolls because, with $q_p = 0 = q_i$, the boundary conditions are symmetric. However, the subsequent displays of results show that the absolute magnitude of the thermal deformation for heating and cooling control jets is generally indistinguishable even for the case of heated rolls. Here the boundary conditions are not symmetric because radial heat flux within such rolls is always outward from the heated core whereas the direction of convective flux at the roll surface reverses with a switch between heating and cooling control jets. Inspection of the radial and axial temperature profiles at $t \leq 0$ with those at steady-state provides insight into this behavior.

Figures 5.15 to 5.15a show the profiles of radial temperature at $z = 0$ and of axial temperature at r_o, i.e. T_s, in each case at both $t \leq 0$ and at steady state. While Figures 5.15 and 5.15a are for a shell thickness, s, of 100 mm, the corresponding profiles for 120 and 150mm shells are shown as Figures 5.16 and 5.16a, and Figures 5.17 and 5.17a. Visually from Figures 5.15-5.17(a), comparison of the profiles between the initial and the steady state conditions indicates the same shift occurs for heating and cooling control jets, although the direction of the shift is of course opposite. As the boundary conditions are not symmetric, it is of interest to examine this behavior.

With an internally heated calender roll subjected to either all heating jets or all cooling jets for the $t \leq 0$ condition, the roll assumes a steady state temperature distribution which satisfies the heat balance at the surface, $r = r_o$, where

$$q_i + q_c + q_p = 0$$

When all heating jets are used, the $|q_p|$ heat sink is satisfied by two heat sources, $|q\ |$ and $|q_c|$. When all cooling jets are used, the single source $|q_i|$ satisfies the two heat sinks, $|q_c|$ and $|q_p|$. These $t \leq 0$ conditions are seen as the highest and lowest profiles on both the radial temperature profiles, Figures 5.15, 5.16 and 5.17, and the axial profiles of T_s, Figures 5.15a, 5.16a and 5.17a. The steady state control

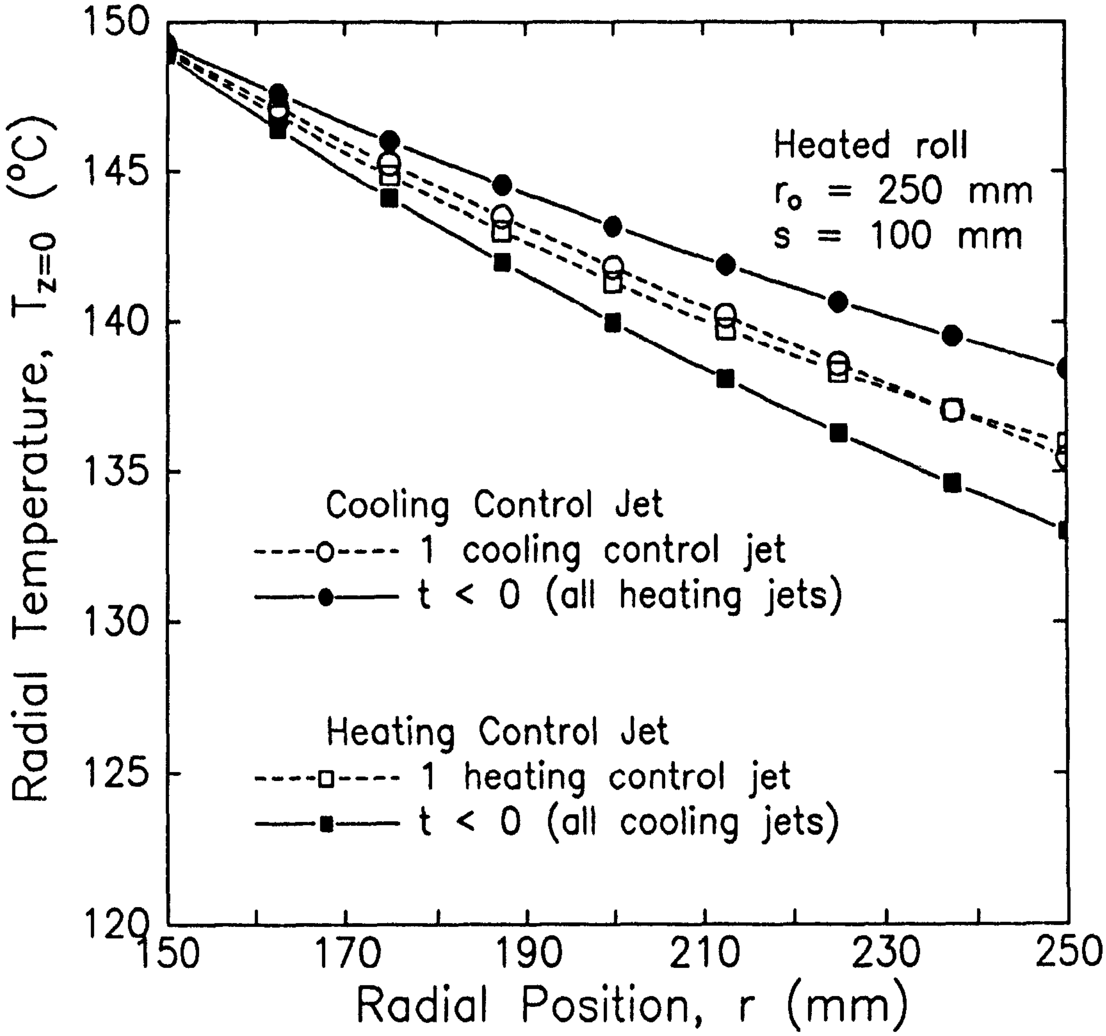

Figure 5.15 Radial temperature profiles at initial and final steady state for heated roll with heating and cooling control jet: r_o = 250 mm, s = 100 mm.

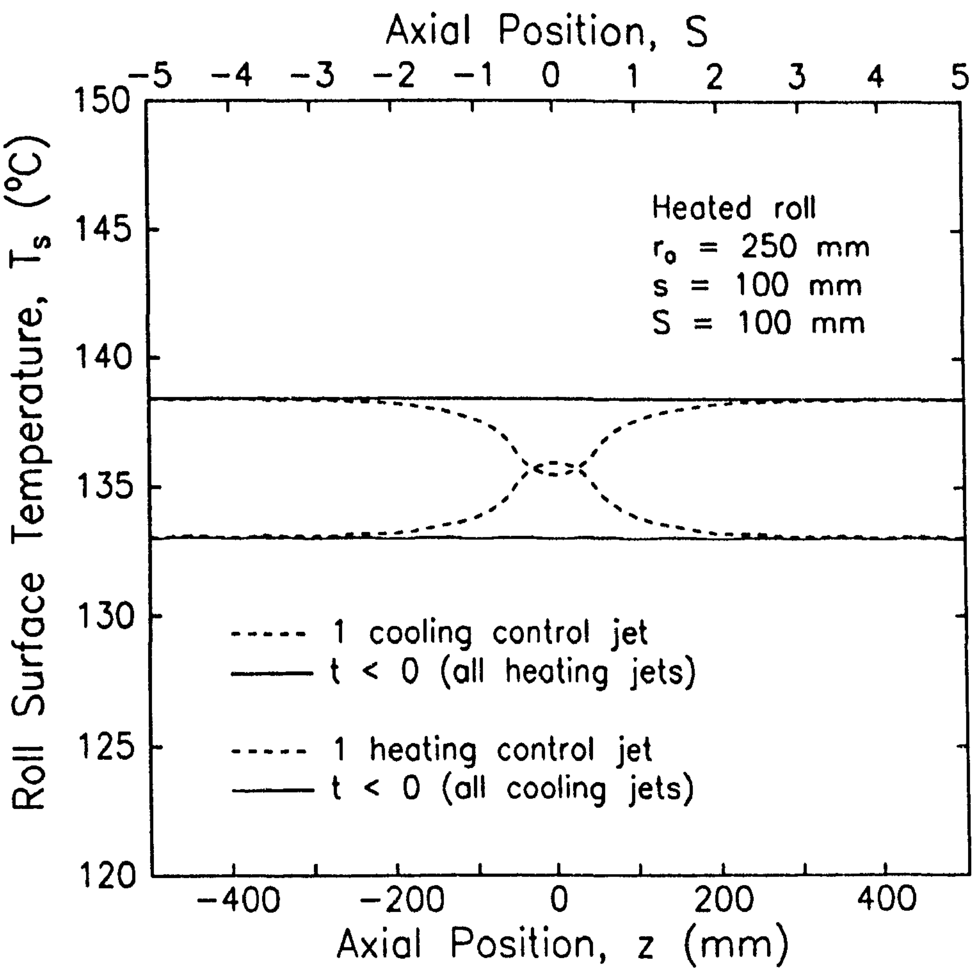

Figure 5.15(a) Axial surface temperature profiles at initial and final steady state for heated roll with heating and cooling control jet: r_o = 250 mm, s = 100 mm.

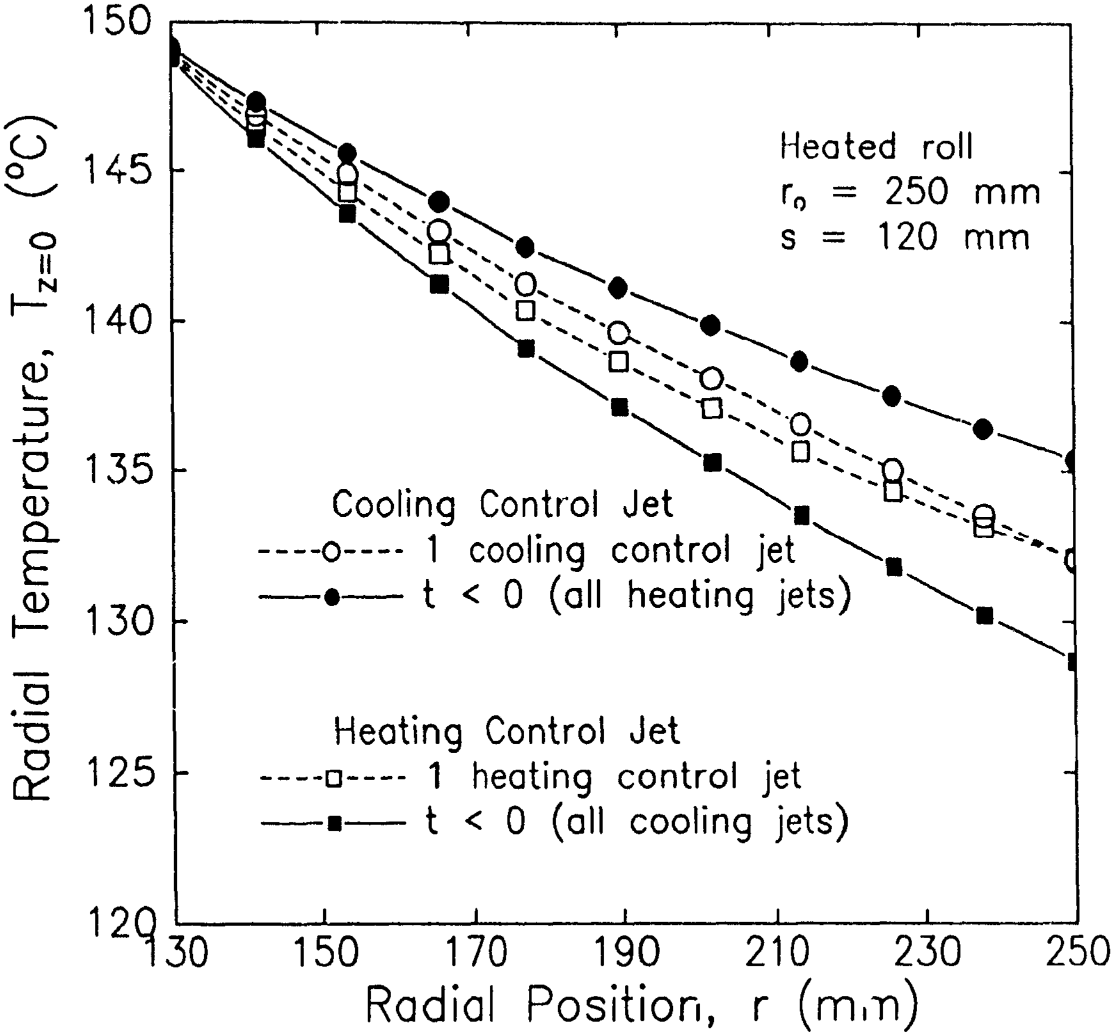

Figure 5.16 Radial temperature profiles at initial and final steady state for heated roll with heating and cooling control jet: r_o = 250 mm, s = 120 mm.

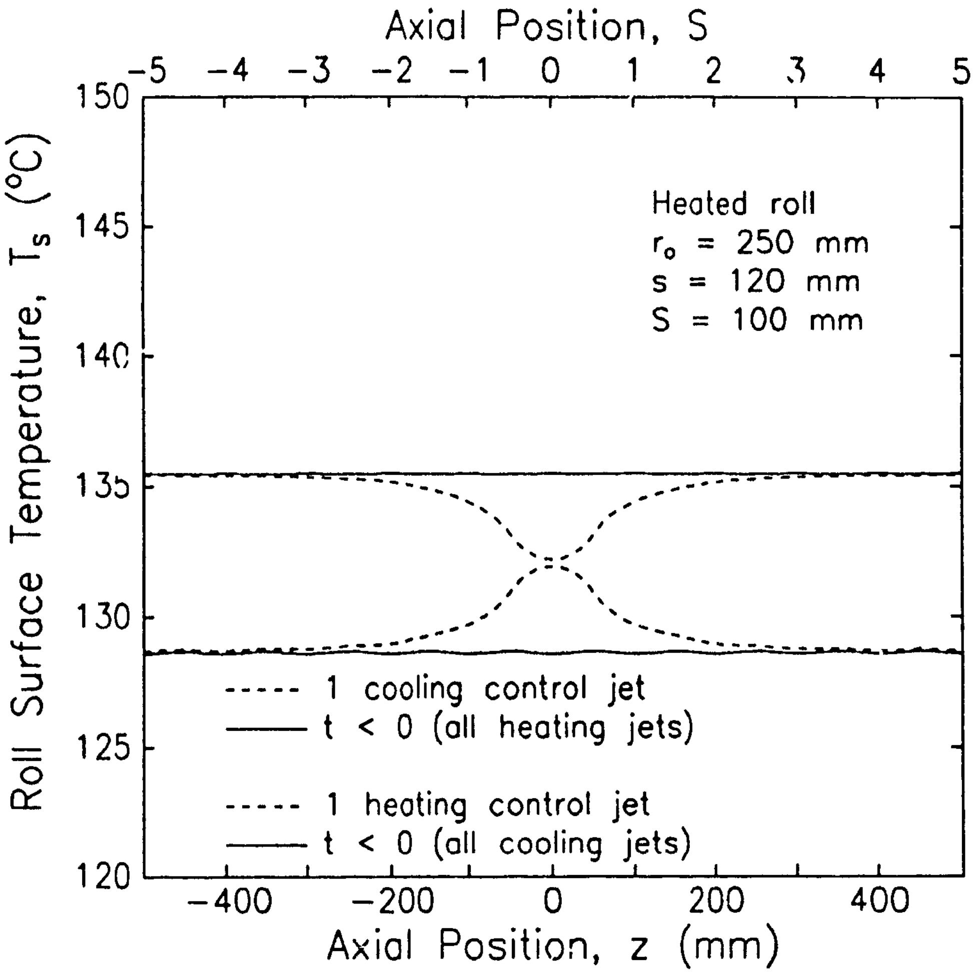

Figure 5.16(a) Axial surface temperature profiles at initial and final steady state for heated roll with heating and cooling control jet: r_o = 250 mm, s = 120 mm.

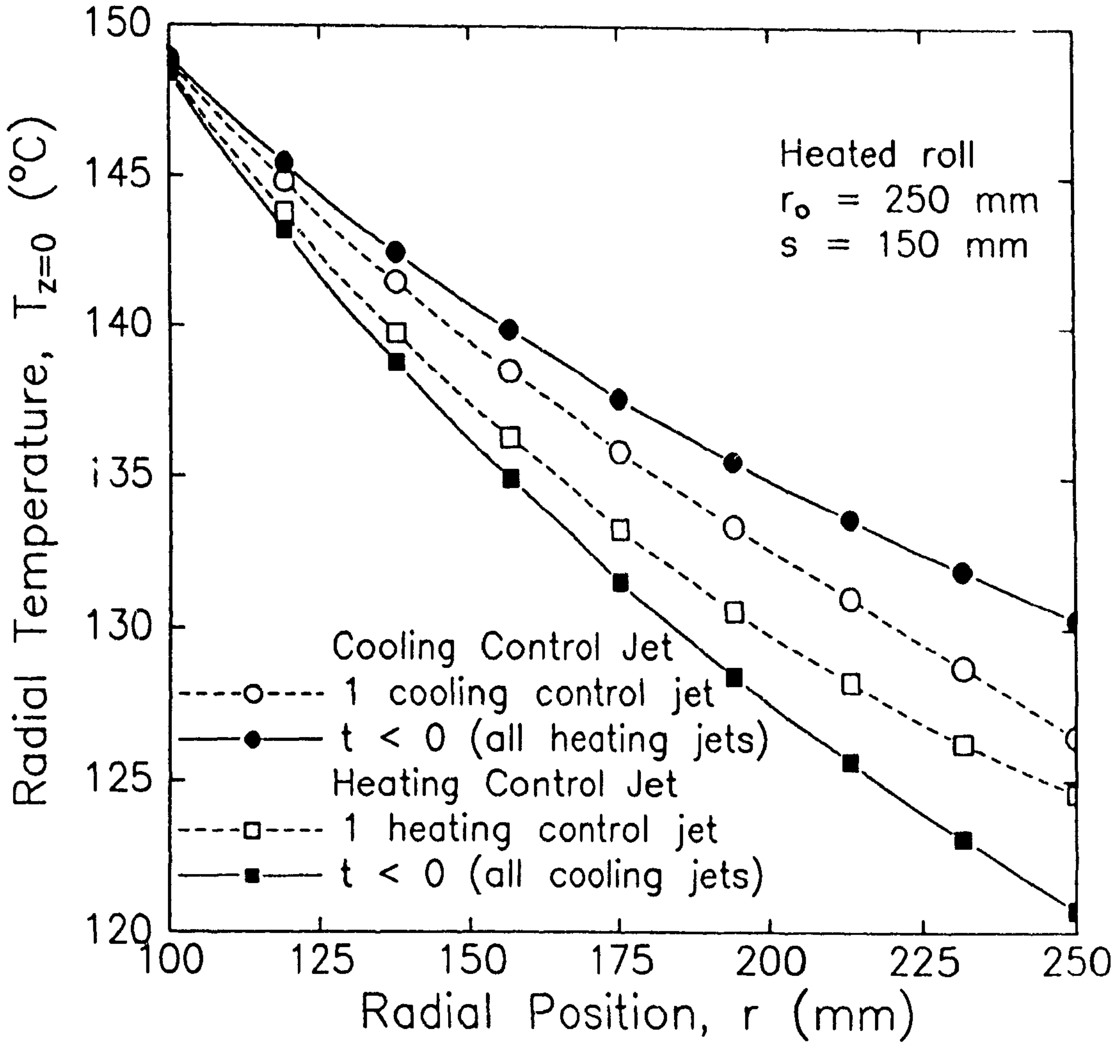

Figure 5.17 Radial temperature profiles at initial and final steady state for heated roll with heating and cooling control jet: r_o = 250 mm, s = 150 mm.

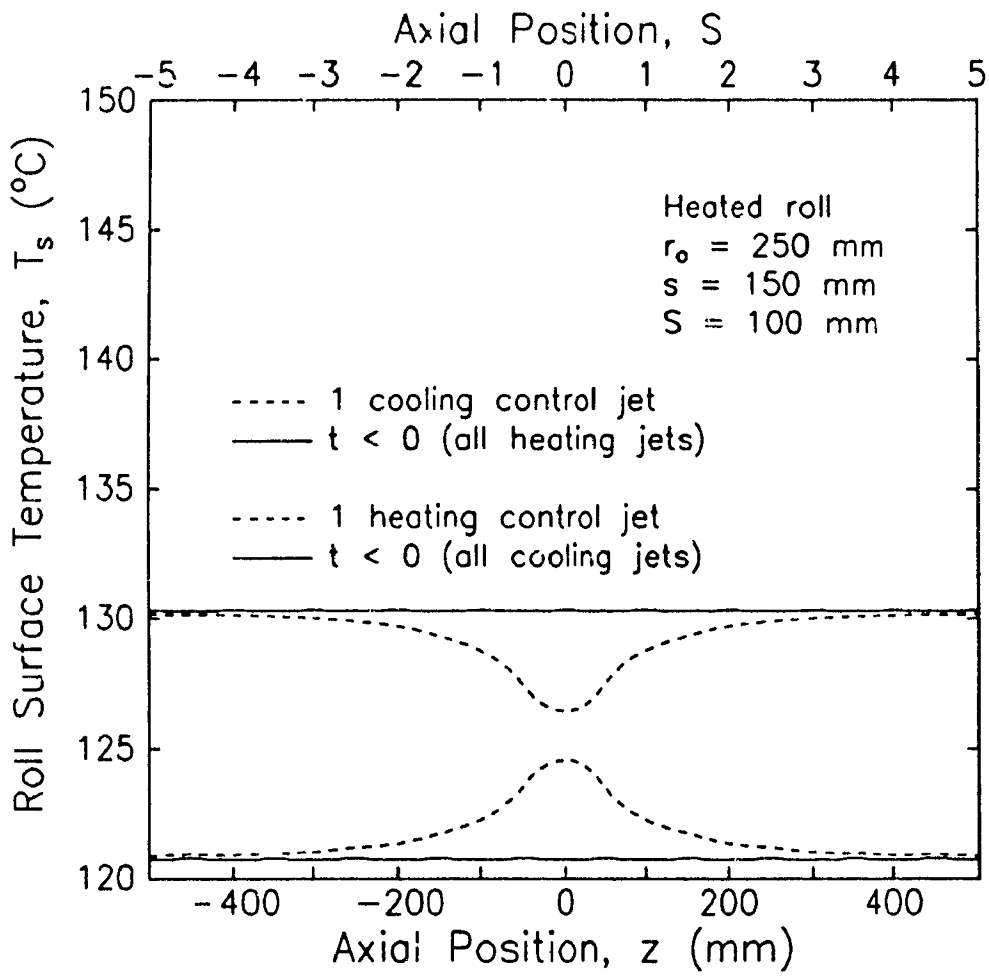

Figure 5.17(a) Axial surface temperature profiles at initial and final steady state for heated roll with heating and cooling control jet: r_c = 250 mm, s = 150 mm.

condition raises the lowest profile or decreases the highest profile, relative to the t ≤ 0 initial condition profiles, thereby producing the interior pair of radial or axial profiles. The relative importance of the three heat fluxes at the t ≤ 0 initial condition is shown in Table 5 2.

Table 5 2 Heat Balance at t≤0 at the Surface of an Internally Heated Calender Roll

	Initial Condition: All Heating Jets			Initial Condition: All Cooling Jets		
	Shell Thickness, s, mm			Shell Thickness, s, mm		
Heat Flow, W/m	100	120	150	100	120	150
q	7795	7674	7472	11467	11354	11146
q_c	405	526	728	-3267	-3154	-2946
$q_p^{(-)}$	-8200	-8200	-8200	-8200	-8200	-8200

$^{(-)}q_p$ is constant by virtue of the choice of paper side boundary condition.

For the initial condition of all heating jets, the relative importance of q and q_c in satisfying the single heat sink, q_p, is apparent, witn q_c providing only 5-10% of the heat transfer required by the paper side boundary condition. Likewise, for the initial condition of all cooling jets, the split of the single heat source, q, between the two heat sinks, q_c and q_p is still dominated by the paper side heat transfer. Also, comparison of the magnitudes of q and q_c indicates the large extent to which the calender roll surface temperature, T, is dominated by radial conduction from the heated core and the paper web This conclusion is quantitatively evident from the observation, Figures 5.15-5.17, that with the roll heating fluid at 150°C, the switch between all heating jets at 150°C and all cooling jets at 20°C never moves the roll surface temperature beyond the range 121 - 138°C.

For the initial condition of all cooling jets, the axial profiles of roll surface temperature, T_s, shown in Figures 5.15a, 5.16a and 5.17a are not straight lines but display a barely perceptible periodic ripple which is associated with the location of the cooling jets at the axial positions 0, ±S, ±2S, ±3S and ±4S. In the associated control mode with one heating jet, the same ripple in T_s persists except in the region dominated by the heating jet. This T_s ripple must be present also for the initial condition of all heating jets, but in this case with q acting in the same direction as the dominant q term, the amplitude of the ripple is too small to be detected.

The value of the peak difference in roll surface temperature, ΔT_{sp}, is seen as the difference between the peak temperature, T_{sp}, and the base temperature, T_{sb}, on Figures 5.15a, 5.16a, 5.17a. These values of ΔT_{sp} are displayed on Figure 5.18. For the thickest shell, s = 240mm, the basic non-equivalence of the heating and cooling control jet cases with a heated roll can be seen on Figure 5.18, with of course the cooling control jet producing a larger roll surface temperature peak, ΔT_{sp}, which would be accompanied by a correspondingly larger thermal deformation peak, Δr_p These differences between the heating and cooling control jet cases are very small even for the extreme case of s = 240mm, and soon become undetectably small for the thinner shells generally used in industrial practice.

With unheated calender rolls, $q_i = 0 = q_p$, so that the heating and cooling control jet cases are always equivalent for steady state roll temperatures and thermal deformation. Thus for unheated rolls, all results in the present study done with heating or cooling control jets

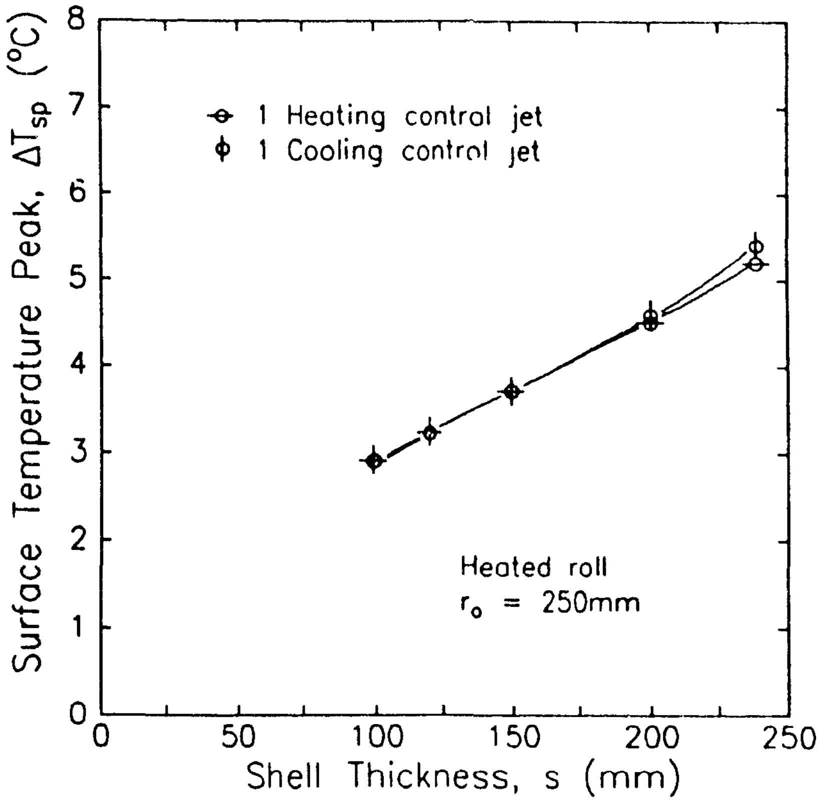

Figure 5.18 Peak difference in roll surface temperature, ΔT_{sp}, for a heating and a cooling control jet

are in fact applicable in either case. In principle, this equivalence does not apply for heated rolls. However, the present quantitative analysis shows that the non-equivalence is so small for conditions of industrial relevance that even for heated rolls, all results with heating and cooling control jets could, in practice, be used for either case

5.4.3 Effect of Roll Design

For the case of unheated rolls with a single control jet, profiles of local roll deformation, $\Delta r'$, for various shell thicknesses are illustrated in Figure 5.19. The much larger steady state deformation for unheated rolls than for heated rolls is clearly evident by comparison with the profiles shown earlier as Figure 5.12.

Figure 5.20 shows that, for heated and unheated rolls, the effect of shell thickness, s, on peak roll deformation, Δr_p, is just the opposite. As the shell thickness approaches the roll radius, Δr_p for heated and unheated rolls converge as expected, since the area available for internal heat transfer approaches zero. For the commonly used shell thickness of 120mm it is highly significant that Δr_p is 2.2 times higher with the unheated calender roll, Figure 5.20. For solid calender rolls, the dashed line between the results for the two solid rolls on Figure 5.20 indicates the extent of the increase in Δr_p associated with the use of smaller roll diameters.

The peak deformations obtained with a heated calender roll are consistant with the values quoted by Verkasalo[1984], i.e. 2 - 5.5μm for a double walled roll and 3 - 6μm for a center-bored roll. Verlasko made no mention of the effect of shell thickness, s, other than the implied

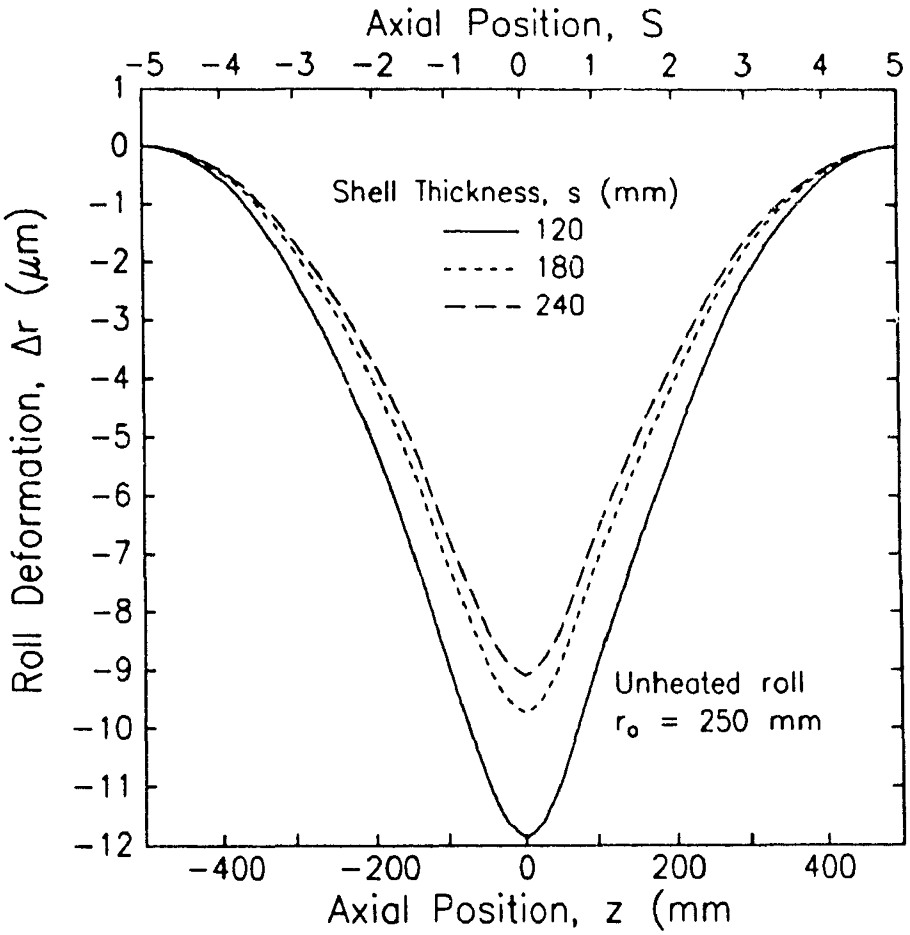

Figure 5.19 Profiles of local roll deformation: unheated roll, r_o 250mm

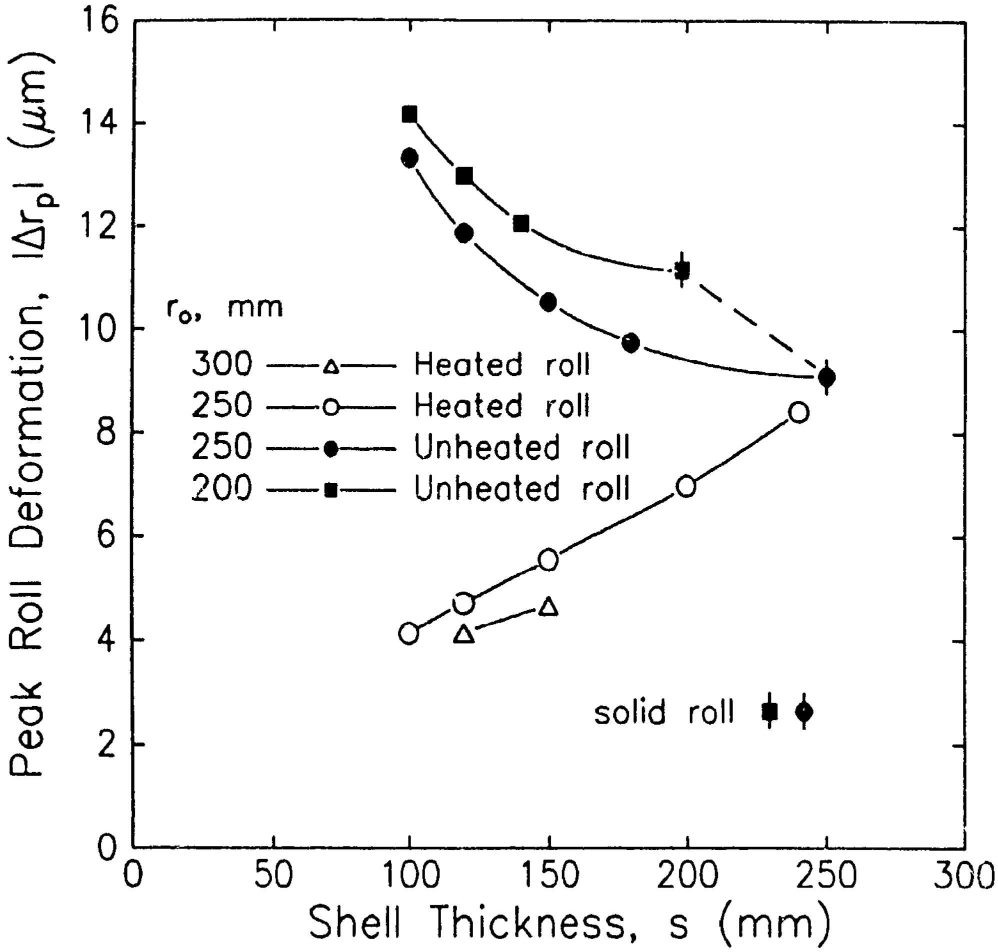

Figure 5.20 Effect of shell thickness on peak roll deformation forheated and unheated rolls.

differences due to shell wall thickness changes between the two types of rolls. There must be an effect of shell thickness, s, since thermal deformation is a function of the length over which a temperature change is made.

Figure 5 21 shows that the magnitude of the characteristic width of the roll deformation, $W_{\Delta r}$, and again the opposite effects of s on $W_{\Delta r}$ for heated and unheated rolls. With unheated rolls the larger values of Δr_c, Figure 5 20, naturally give larger values of $W_{\Delta r}$, Figure 5 21, with these differences disappearing as $s \rightarrow r$ The values of $W_{\Delta r}$ obtained are consistent with the values quoted by Verkasalo [1984] For double-walled and center-bored rolls, he claims $W_{\Delta r}$ is in the range 340 to 424 mm, with the larger values of $W_{\Delta r}$ being for the center-bored rolls As mentioned earlier, Verkasalo does not consider the effect of shell thickness amde evident in the present work For solid rolls, the significant improvement in peak deformation, Figure 5 20, is seen on Figure 5 21 to be obtained with no penalty as to width of deformation

Figure 5.22 shows the effect of external roll radius, r_o, on the profiles of local roll deformation, Δr, for heated rolls of shell thickness 120mm with a single control jet When r is increased by 20% the peak roll deformation, Δr_c, decreases by 12% while the characteristic width, $W_{\Delta r}$, decreases, as is typical, by a smaller proportion, in this case about 5%

For unheated rolls, where the internal wall is considered adiabatic, roll deformation is larger than with the equivalent heated roll, Figure 5 20, due to the absence of an internal heat source In the absence of q_i the response of the roll surface to the control jet is now limited only by axial heat transfer, q_z, between the region beneath the control jet and the surrounding region Thus with unheated rolls,

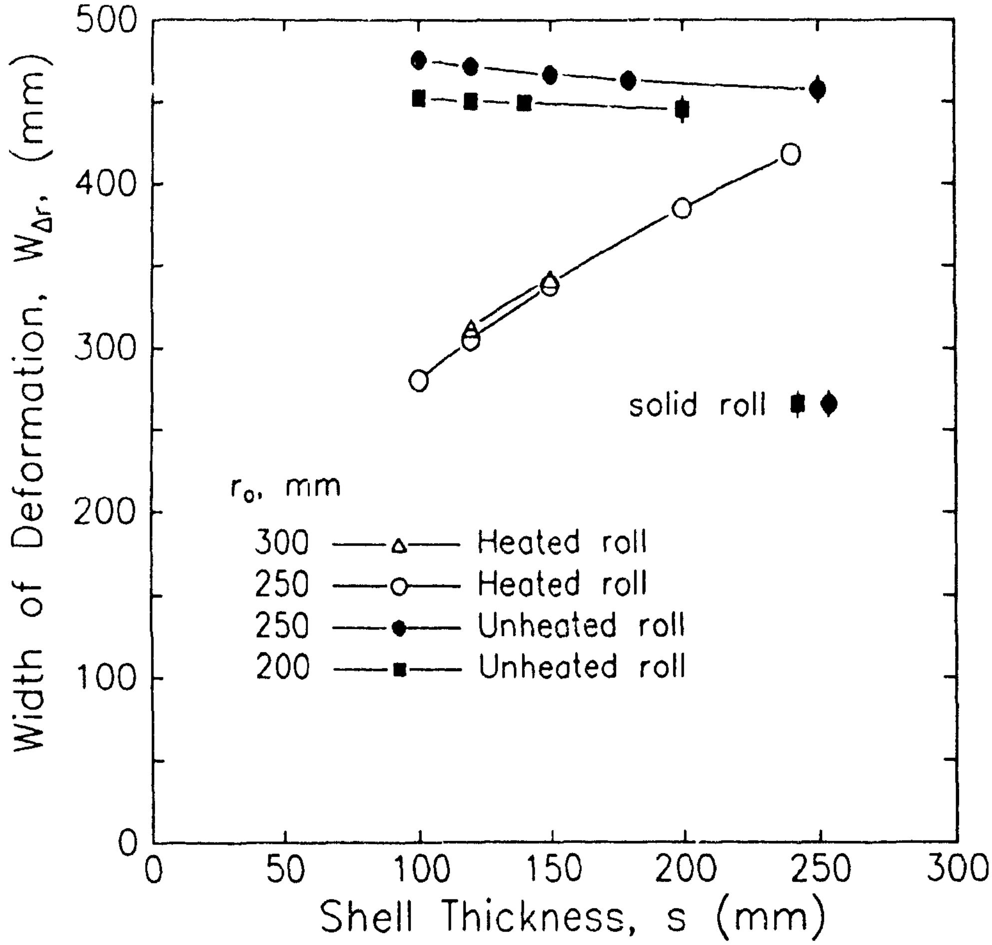

Figure 5.21 Effect of shell thickness on width of deformation for heated and unheated rolls, r_c=250 mm.

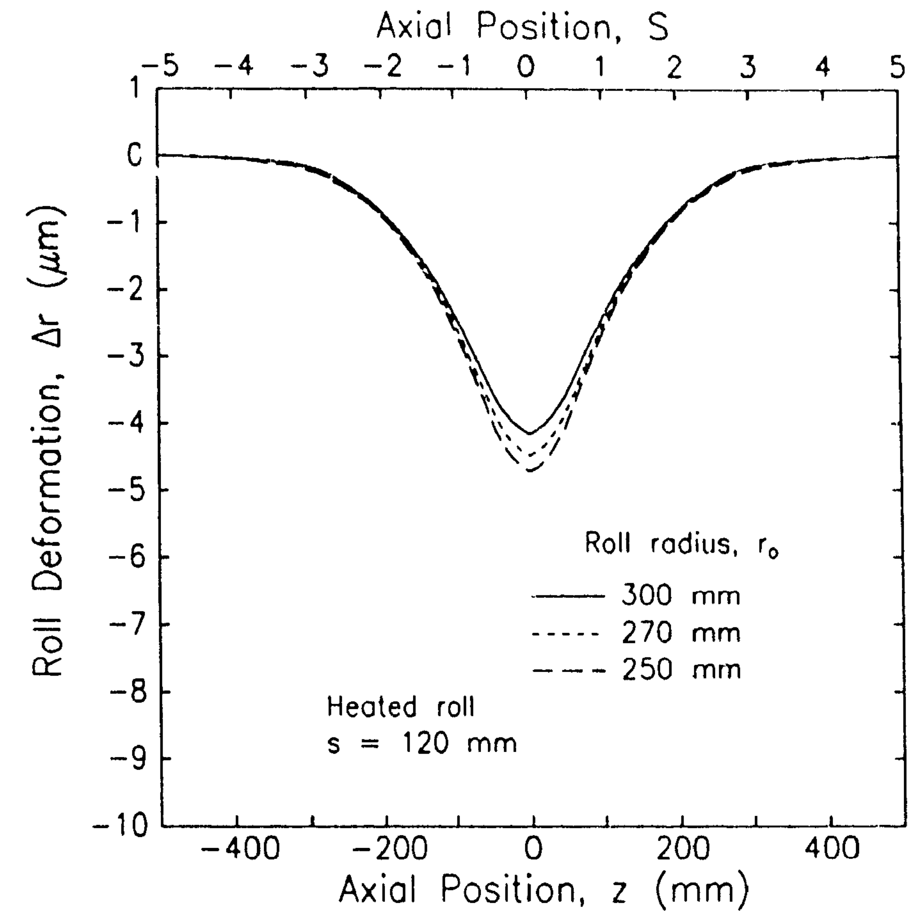

Figure 5.22 Profiles of local roll deformation Effect of external roll radius, s = 120 mm, for a heated roll.

increasing $\bar{s}$ at constant r_o increases the axial heat transfer area relative to that for heat transfer from the control jet, hence increases q_j relative to q_c, which reduces the temperature difference that the control jet produces, thereby decreasing roll deformation, Δr.

The higher roll deformation obtainable with unheated rolls is particularly interesting for control purposes. For example, in an existing calendering configuration where a control system of impinging jets is installed on a heated roll, the advantage of a much higher control bandwidth could be obtained by simply moving the control system to an unheated roll.

5.4.4 Calender Control Deformation Index

A single index of calender roll deformation performance is desirable because what is required is a control system with high peak roll deformation, Δr_p, but low width of deformation, $W_{\Delta r}$. The results recorded in Figures 5.19 to 5.22 indicate invariably a trade-off between these two desirable criteria, i.e. conditions which give high Δr_p, as is desired, also give high $W_{\Delta r}$, a negative characteristic for local control. Therefore inspection of the effect of a variable on Δr_p and $W_{\Delta r}$ provides no guidance as to the net effect on control characteristics. However the absolute value of the ratio of these two characteristics, $\left| W_{\Delta r}/\Delta r_p \right|$, i.e. millimeters of width of deformation per micron of peak deformation, provides a deformation characteristic which is relevant to control. This ratio is therefore termed the calender control deformation index, I_D. In Table 5.2 the corresponding values of $W_{\Delta r}$, Δr_p and control index, $I_D = \left| W_{\Delta r}/\Delta r_p \right|$, are given for the cases recorded in Figures 5.12 - 5.13 and 5.19 - 5.22. By definition, the lower the I_D value the better the control characteristics.

Table 5.3 Calender control deformation index

(a) Internally heated roll, r_o = 250mm, S = 100mm.

Shell thickness s, mm	$W_{\Delta r}$ mm	Δr_p µm	I_D mm/µm
100	278	-4.14	67
120	305	-4.72	65
150	337	-5.55	61
200	385	-6.97	55
240 (almost solid)	421	-8.41	50

(b) Unheated roll, r_o = 250mm, S = 100mm.

Shell thickness s, mm	$W_{\Delta r}$ mm	Δr_p µm	I_D mm/µm
100	475	-13.32	36
120	472	-11.88	40
150	466	-10.53	44
180	462	-9.74	47
250 (solid)	457	-9.10	50

(c) Internally heated roll, s = 120mm, S = 100mm.

Roll radius, r_o mm	$W_{\Delta r}$ mm	Δr_p µm	I_D mm/µm
200	290	-5.58	52
250	305	-4.72	65
270	317	-4.48	71
300	356	-4 16	86

(d) Unheated roll, s = 120mm, S = 100mm.

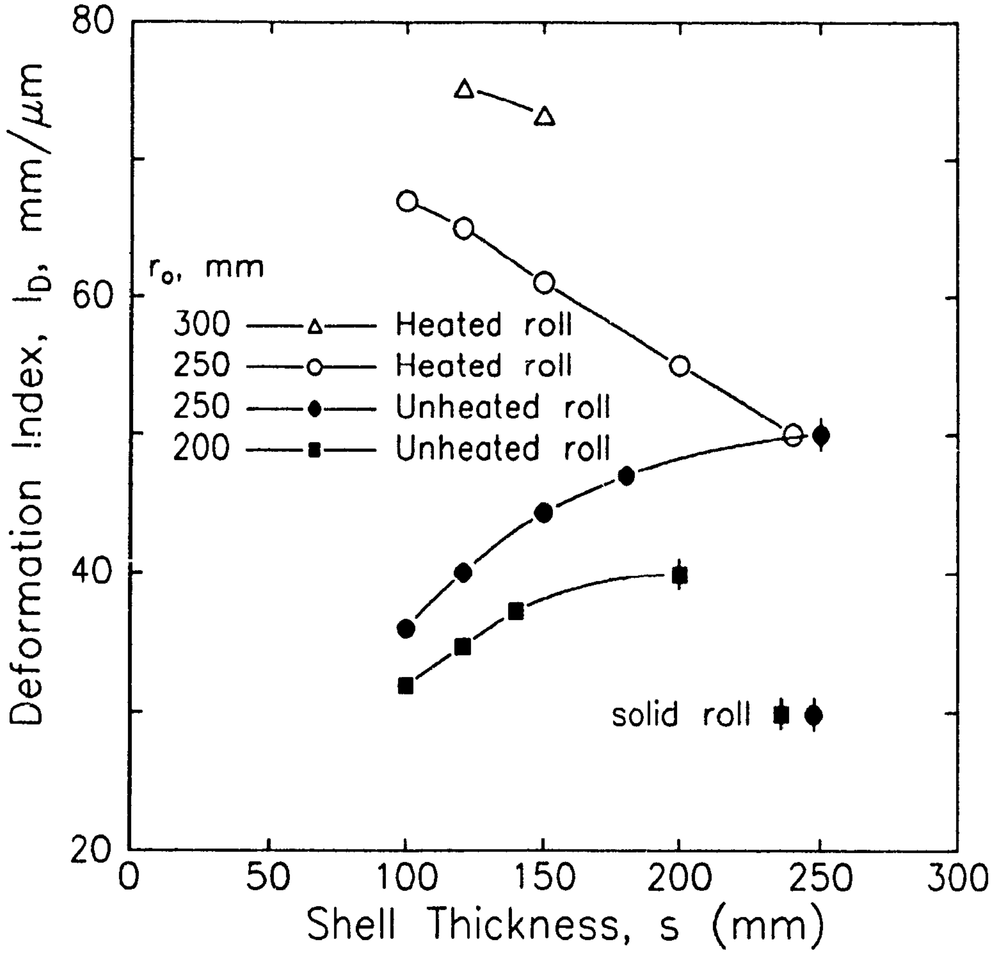

Figure 5.23 Effect of shell thickness on calender control deformation index for heated and unheated rolls of r_i = 250 mm.

Roll radius, r_o mm	$W_{\Delta r}$ mm	Δr_D µm	I_D mm/µm
200	450	-12.98	35
250	472	-11.88	40
270	480	-11.55	42
300	490	-11.16	44

For internally heated rolls, the values of the deformation index, I_D, found in Table 5.3 show that increasing the shell thickness produces an improvement (i.e. a decrease) in the deformation index for values of shell thickness in the range 100 to 150mm.

For a fixed shell thickness in the range commonly found in existing heated calender rolls, s = 120mm, the results in Table 5.2(c) indicate a substantial improvement in I_D as roll radius is decreased. For a calender roll of fixed radius, the opposite effects of shell thickness on deformation index for heated and unheated rolls, apparent in Table 5.2 (a) and (b), are portrayed on Figure 5.23. With unheated rolls, the deformation index improves strongly with reduction in shell thickness Moreover, for a 250mm radius hollow roll, Figure 5.23 illustrates the dramatic improvement in calender control deformation index to be obtained by switching from heated to unheated rolls.

Clearly the system with the highest control potential, considering the desirability of both high local roll deformation and narrow control width, is a small diameter unheated roll of minimum practical shell thickness. Of the specifications for unheated rolls tested here , Table 5.2(b) and (d), those giving the best (lowest) value of the deformation index, I_D of about 35mm/µm, are fortunately also those which give the highest absolute value of the peak roll deformation, Δr_p of about 13 µm.

It has been traditional practice in the paper industry to avoid placing calender control equipment on adjustable crown rolls (such as Crown Controlled or Nipco© rolls) because these rolls are already assisting in the control process through hydraulically produced roll deformation. However, hydraulically actuated adjustable crown rolls have control widths, $W_{\Delta r}$, in the order of meters while impinging jet control systems provide control widths, $W_{\Delta r}$, in the range 300 - 500mm, Figure 5.21, Table 5.2. The bandwidths of under 500mm associated with unheated shell rolls can probably be extended to adjustable crown type rolls , although internally, such rolls may not be completely adiabatic.

Although peripherally bored heat transfer rolls were not simulated in this study, the current results provide guidance concerning this roll design. The high internal heat transfer and thin effective shell thickness of such rolls would clearly result in a small thermal deformation, Figure 5.20, and a poor control index, Figure 5.23, making these rolls a poor choice for calender control.

5.4.5 Effect of Actuator Heat Transfer Profile

Kan [1986] and Hilden and Randle [1984] recommended higher control actuator resolution in the cross machine direction in order to produce the "ideal" step function temperature profile at the roll surface. They claimed this strategy would provide larger calender roll deformation directly at the actuator centerline and a uniform roll diameter between actuators. As shown in Chapter 4, for jet-to-jet separation of $S/d \leq 8$ the circumferentially averaged local heat transfer between jets is relatively uniform. Moreover, the effect of axial heat conduction in the calender roll is high, as shown by the finding that the characteristic width of the roll deformation, $W_{\Delta r}$, is about 3 - 5 times that of the jet-to-jet spacing, $\underline{S}$ = 100mm. High axial heat transfer damps the surface temperature profile and, consequently, the profile of thermal deformation, Δr.

To provide a quantitative analysis of this effect, roll deformation was calculated for three heat transfer profiles as boundary conditions Profile #1 of Figure 5.24 is that for an impinging jet obtained experimentally in Chapter 4 and represented by equation 5 12. The other profiles were arbitrarily chosen to approach a step function heat transfer profile while maintaining the same heat flux per actuator as for Profile #1. In the extreme case, Profile #3, half the area between actuators has no heat transfer. The calculated profiles of roll deformation, Figure 5.24, show that concentrating the heat flux to effectively a step function profile around the actuator results in an increase in the roll deformation directly at the actuator centerline by only ≈ 12%, with less than 12% decrease in control width, $W_{\Delta r}$ (Table 5.4). An impinging jet heat transfer profile is seen to give values of roll deformation, control width and deformation control index which are almost as good as those for the ideal case of a step function heat flux profile.

Table 5.4 Effect of heat transfer profile on roll deformation characteristics of a heated roll with r_o = 250mm, s = 120mm, S = 200mm (S/d = 8).

Heat Transfer Profile	$W_{\Delta r}$ mm	Δr_r µm	I_c mm/µm
1. impinging jet	348	-7.26	48
2. medium	320	-8.00	40
3 extreme	309	-8 65	36

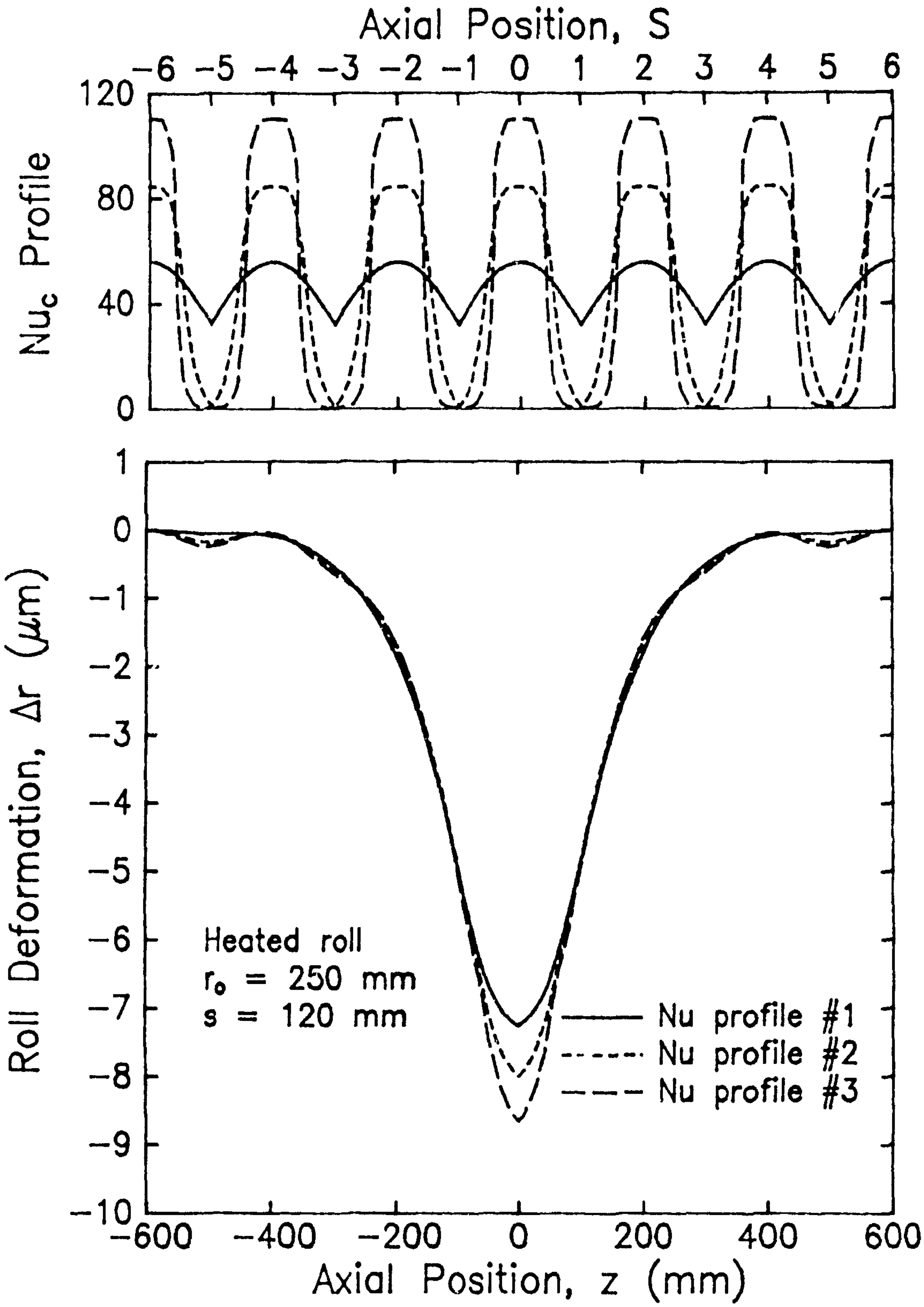

Figure 5.24 Profiles of local roll deformation: alternative Nusselt number profiles, r_o = 250 mm, s = 120 mm.

Thus the more nearly step function heat flux profile with induction heaters as the CD control actuator, pointed out by Kan and by Hilden and Randle as advantageous, is seen to be an advantage with minimal quantitative effect. On the other hand, impinging jets provide the unique control advantage of ready access to either a cooling or a heating control flux. As for the concern of previous investigators that bell shaped heat transfer profiles would create a "bumpy" roll, the present analysis demonstrates that for impinging jets, the maximum "bump" in roll diameter between actuators, Figure 5.24, is less than 0.3 μm. Such concerns are clearly groundless.

5.4.6 Effect of Actuator Arrangement

Two parameters describing actuator arrangement are the jet-to-jet separation, S, and the number of adjacent control jets used. Increasing S increases the jet heat transfer efficiency, i.e., more heat transfer per jet. Increasing the number of adjacent control jets affects the profile of local roll deformation.

(a) Effect of number of adjacent control jets

For a jet-to-jet spacing S of 100mm, Figure 5.25 and Table 5.5 show the roll deformation of a heated roll with various numbers, N, of adjacent cooling or heating control jets. The use of N = 2 results in increasing by a factor of 1.7 the peak roll deformation, Δr_p, relative to that produced by a single control jet. For N = 3, Δr_p is that 2.1 times that for a single control jet. For S = 100mm, r_o = 250mm and s = 120mm, the values of Δr_p produced by using 1, 2 and 3 adjacent control jets are, respectively, 39%, 65% and 82% of the maximum deformation possible (i.e. that with all jets at the control jet

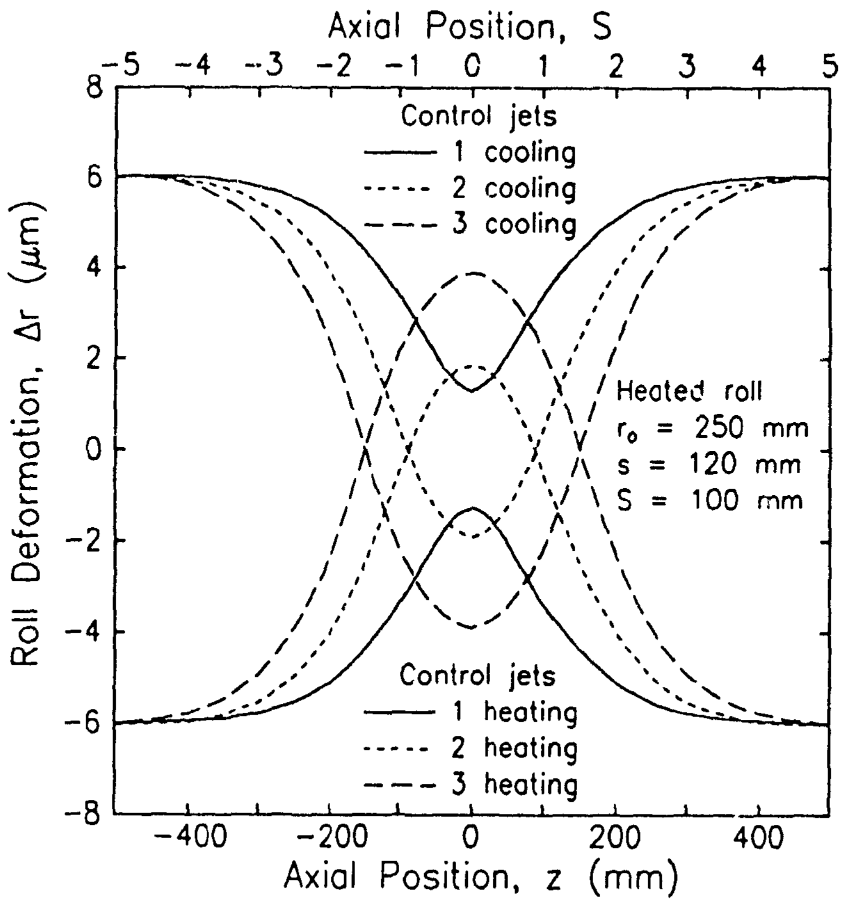

Figure 5.25 Profiles of local roll deformation for heating and cooling control jets, r_o = 250 mm, s = 120 mm, S = 100 mm.

condition. From Figure 5 25 it would appear that an axial distance of about 700mm would be required to go from minimum roll diameter (a row of cooling control jets) to maximum roll diameter (a row of heating control jets) With the high thermal conductivity of the calender roll, W_{Δ}. is about 300mm for S =100mm, so closer spacing of the control jets will clearly have little influence on local deformation. Typical commercial practice is to place calender control actuators at axial separations in the range 80 to 200 mm. The high degree of coupling between the effects of neighboring control actuators, illustrated by the present results, provides the basis for rational design of CD caliper process control schemes.

Table 5.5 Effect of number of adjacent control jets on the roll deformation characteristics of a heated roll with r_o = 250mm, s = 120mm, S = 100mm.

Control jet	N, Number of adjacent control jets	$W_{\Delta r}$ mm	Δr_p µm	I_o mm/µm
heating	1	305	4.73	65
	2	357	7.97	45
	3	422	9 91	42
cooling	1	300	-4.70	64
	2	351	-7.95	44
	3	416	-9.89	42

Under the conditions tested, the absolute magnitude of the deformation achieved by 1, 2 or 3 adjacent heating jets surrounded by cooling jets is indistinguishable from that obtained for cooling control jets in a row of heating jets. This effective equivalence of heating and cooling control jets on heated rolls was explained in Section 5.4 2.

(b) Effect of jet-to-jet separation

As detailed in Chapter 4, for a single row of impinging jets a jet-to-jet spacing of S less than 8d (200mm) results in decreased jet heat transfer efficiency. Figure 5.26 and Table 5.6 show the effect of jet-to-jet spacing on roll deformation characteristics by comparing the case of a single control jet at a spacing of S/d = 8, i.e. S = 200mm, with that obtained for control with 2 adjacent jets at a standard spacing of S/d = 4, S = 100 mm. The air flow rate per jet is the same in the two cases. The maximum roll deformation, Δr_p, with 2 control jets and S/d=4 is only 8% greater than that with a single control jet at double the S/d. As the calender roll deformation index, I_D, is also essentially the same between the two cases, there is no advantage in narrower jet-to-jet spacing.

Table 5.6 Effect of jet-to-jet spacing, S, on roll deformation characteristics of a heated roll with r_o = 250mm, s = 120mm.

Jet-to-jet Spacing, S mm	$W_{\Delta r}$ mm	$\lvert \Delta r_p \rvert$ µm	I_D mm/µm
100	356	7.97	45
200	348	7.26	47

On an operating calender, Mitchell and Sheahan [1976] observed that the maximum difference in roll surface temperature under jets spaced at S/d=8 was only 15% less than that for S/d=4. Thus the conclusion reached from the present numerical simulation is identical to that obtained from the measurements by Mitchell and Sheahan on an industrial calender. Considering the important disadvantage of use of double the amount of air with the S = 4d spacing and the negligible control advantage of the narrower spacing, a jet-to-jet spacing closer than S = 8d appears uneconomic.

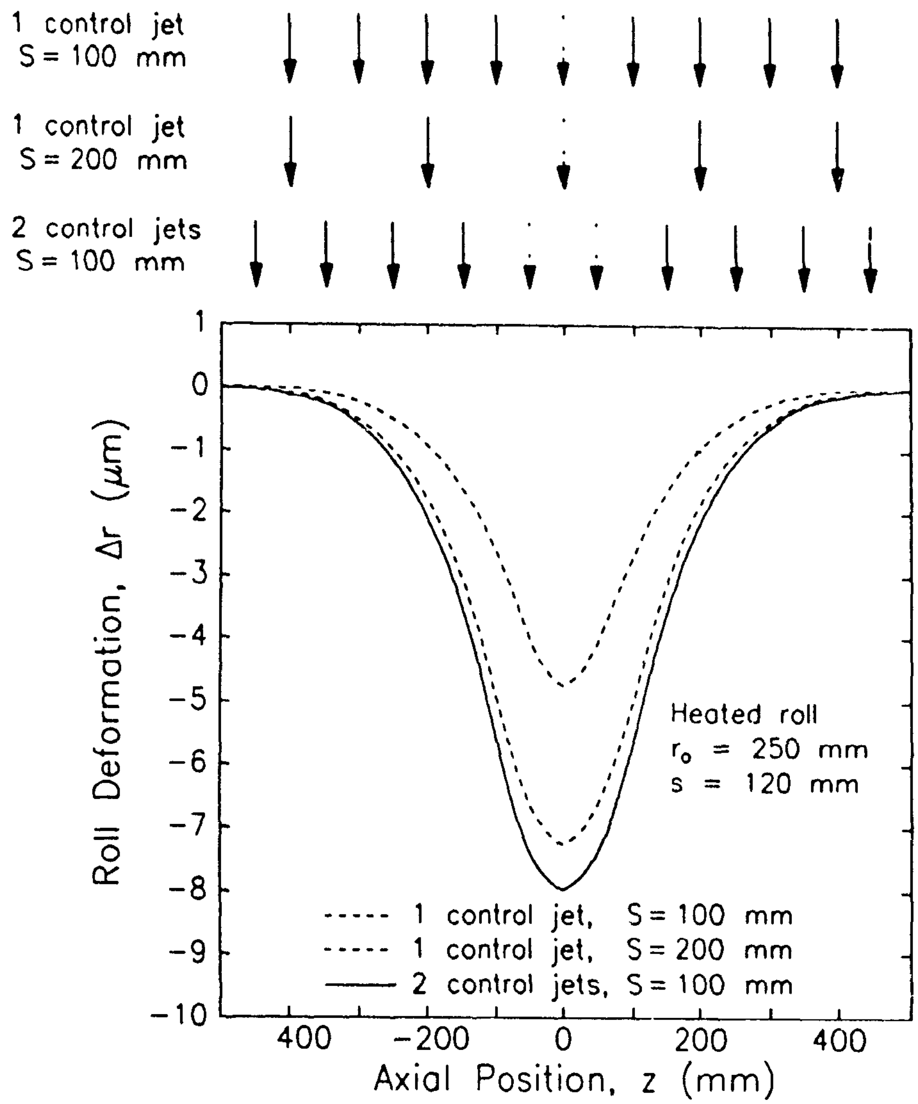

Figure 5 26 Profiles of local roll deformation Effect of jet-to-jet spacing, r_o = 250 mm, s = 120 mm

5.4.7 Effect of Jet Confinement

The effect of placing at the nozzle exit a confinement plate, concentric with the calender roll, continuous in the cross machine direction and extending 5.75d in the circumferential direction on either side of the nozzle centerline was reported in Chapter 4. Those results demonstrate that, for H/d = 2, use of such a confinement plate increases the circumferentially averaged heat transfer coefficient by 33% (Figure 4.45(b)). To determine the influence of jet confinement on local roll deformation, the axial heat transfer boundary condition for the jets, Equation 5.8, was modified simply by increasing $\overline{Nu}_c$ by 33%.

With the associated 33% increase in local heat transfer from use of confinement, Figure 5.27 and Table 5.7, there is a corresponding substantial improvement in both peak roll thermal defo\rmation, Δr_p, and calender roll deformation index, I_D, in both cases by about 23%.

Table 5.7 Effect of jet confinement on roll deformation characteristics of a heated roll with r_o = 250 mm, s = 120 mm, S = 100 mm

Jet Confinement	$W_{\Delta r}$	$\lvert\Delta r_p\rvert$	I_D
	mm	µm	mm/µm
without confinement	305	4.72	65
with confinement	299	5.84	51

The use of a confinement surface on impinging jet calender control systems was recommended in Chapter 4 for reasons of heat transfer energy efficiency. This advantage is now supplemented by the documented substantial improvement in CD calender control characteristics with confined jets. For existing unconfined impingement calender control systems, this improvement can easily be realized by retrofitting a confinement surface at the nozzle exit.

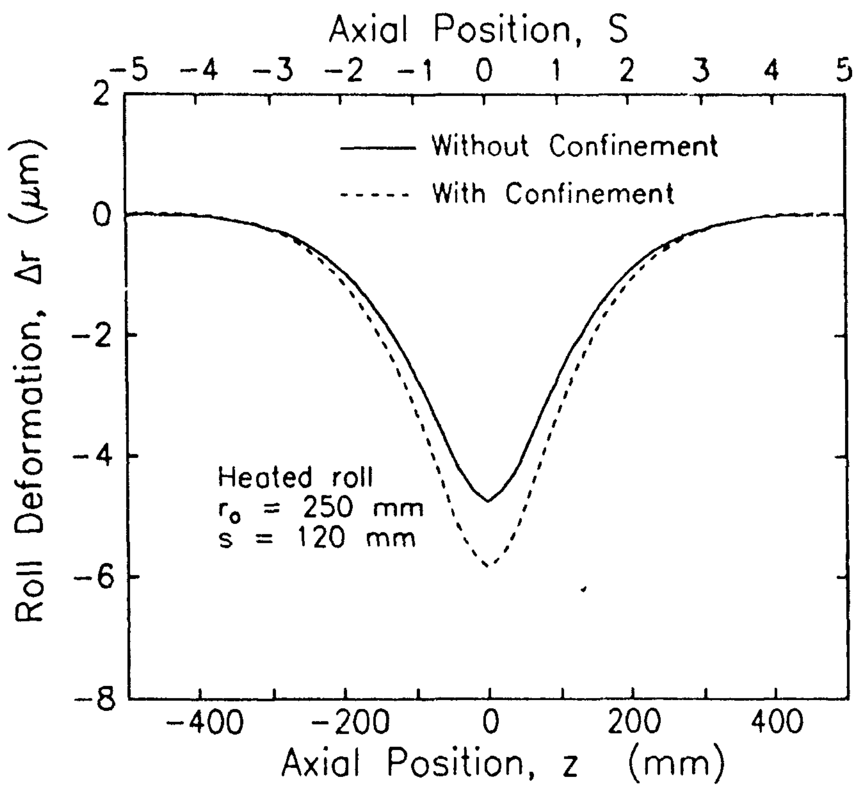

Figure 5.27 Effect of jet confinement on local roll deformation profile.

5.5 Numerical Simulation of Unsteady State Thermal Deformation

The desired characteristics of a system for cross-machine direction control are large steady state thermal deformation over a narrow strip of the calender roll and a short response time to each new steady state control objective. The previous section dealt with the former aspect while the present section deals with the second of these two control characteristics.

5.5.1 Analytical Solution

Analytical solutions are readily available for the transient thermal behavior of a semi-infinite cylindrical body of constant thermal conductivity when subjected to axially uniform convective heat transfer boundary conditions, i.e. no axial variation in heat transfer coefficients, h_i and h_c, or heat transfer fluid temperature. The solution, Equation 5.18, takes the form of a Bessel equation,

$$T(r,t) = \sum_{m=0}^{\infty} e^{-\alpha\beta_m^2 t} K_0(\beta_m, r) \cdot \int_a^b r' K_0(\beta_m, r')\, F(r')\, dr' \qquad (5.18)$$

where $$K_0(\beta_m, r) = \frac{R_0(\beta_m, r)}{\sqrt{N}}$$

$$R_0(\beta_m, r) = \frac{J_0(\beta_m r)}{k\,\beta_m J_0'(\beta_m b) + h_c J_0'(\beta_m b)} - \frac{Y_0(\beta_m r)}{k\,\beta_m Y_0'(\beta_m b) + h_i Y_0'(\beta_m b)}$$

$$N = \frac{b^2}{2}\left[1 + \frac{h_c^2}{k^2\beta_m^2}\right] R_0^2(\beta_m, r_o) - \frac{a^2}{2}\left[1 + \frac{h_i^2}{k^2\beta_m^2}\right] R_0^2(\beta_m, r_i)$$

Solving Equation 5.18 requires solving for the roots of Equation 5.19

where β_m are the roots to the transcendental equation

$$\frac{-\beta k\ J_0'(\beta r_i) + h_i J_0(\beta r_i)}{\beta k\ J_0'(\beta r_o) + h_o J_0(\beta r_o)} - \frac{-\beta k\ Y_0'(\beta r_i) + h_i Y_0(\beta r_i)}{\beta k\ Y_0'(\beta r_o) + h_o Y_0(\beta r_o)} = 0 \qquad (5.19)$$

This unwieldy equation applies only to the case of one dimensional, radial heat transfer. With respect to providing insight concerning thermal response of the body to changes in the boundary conditions, this analytical solution offers no advantage over a numerical solution. For the case of interest here, furthermore, the external thermal boundary condition is non-uniform axially, which makes this a two-dimensional problem.

5.5.2 Conditions Used in Numerical Simulations

The conditions for which the unsteady state simulation was made are listed in Table 5.8.

5.5.3 Results of Unsteady State Simulation Model

The tracking of process disturbances with minimum time lag, desired for optimum control characteristics, requires use of calender rolls with minimum response time. The response of a calender roll to a change in the control actuator heat transfer from a row of identical jets to a repeating sequence of either 1 cooling jet and 9 heating jets, or 1 heating jet and 9 cooling jets, is illustrated by following the time response of the deformation at the centerline of the control jet, $\Delta r|_{z=0}$. The steady state limit of $\Delta r|_{z=0}$ is the peak roll deformation, Δr_p as used in Section 5.4. The close agreement of steady-state peak

Table 5.8 Conditions for unsteady state numerical simulations

External Diameter r_o (mm)	Shell Thickness s (mm)	Internal Heated/ Unheated	Jet-to-Jet Separation S (mm)	Number of heating jets/ cooling jets	Comment
150	80	heated	100	9-1	
150	100	heated	100	9-1	
200	80	heated	100	9-1	
200	100	heated	100	9-1	
200	120	heated	100	9-1	
200	140	heated	100	9-1	
250	80	heated	100	9-1	
250	100	heated	100	9-1	
250	120	heated	100	9-1	
250	140	heated	100	9-1	
300	80	heated	100	9-1	
300	100	heated	100	9-1	
300	120	heated	100	9-1	
300	140	heated	100	9-1	
200	80	heated	100	1-9	
200	100	heated	100	1-9	
200	120	heated	100	1-9	
200	140	heated	100	1-9	
250	80	heated	100	1-9	
250	100	heated	100	1-9	
250	120	heated	100	1-9	
250	140	unheated	100	1-9	
200	100	unheated	100	9-1	
200	120	unheated	100	9-1	
200	140	unheated	100	9-1	
200	200	unheated	100	9-1	solid roll
250	100	unheated	100	9-1	
250	120	unheated	100	9-1	
250	140	unheated	100	9-1	
250	250	unheated	100	9-1	solid roll

roll deformation, Δr_p, predicted using with the plane strain solution (i.e. Equation 5.2(a) and 5.17) with that from the complete numerical model (i.e. Equation 5.2(b), and 5.3, 5.4 and 5.5), was shown in Figure 5.12. This good agreement at steady state between the approximate and exact solutions and the excellent unsteady state thermal behavior predicted by the approximate model permits the simplification of the unsteady-state model. Under the conditions examined here it is therefore legitimate to obtain the transient response of a calender roll using the plane strain solution, i.e. Equation 5.2(a) to solve for the temperature field and Equation 5.17 to determine the instantaneous roll deformation Thus all the unsteady state results are obtained by application of the plane strain approximation to the transient state.

Figures 5.28 to 5.35 show the development of roll surface deformation at the control jet centerline, $\Delta r|_{z=0}$, from the time of switching from a row of identical jets to one of the control modes noted above. Figures 5.28 to 5.33 are for heated shell type rolls of various external diameter and shell thickness. Figures 5.34 and 5.35 are for unheated calender rolls. In Figures 5.32 and 5.33 the control jet is a single heating jet in a row of cooling jets, while all other figures show the complimentary case of a single cooling jet in a row of heating jets. A jet-to-jet spacing of S/d = 4 is used throughout, corresponding to a separation, S, of 100mm between the center lines of the impinging jets issuing from nozzles of diameter d = 25mm. The nozzle exit temperatures of the jets, T_j, of 20°C and 150°C and the values of all other operating conditions are as specified in Section 5.3.3.

5.5.4 Simulation Results as Deformation Time Constant

The transient response of a calender roll illustrated in Figure 5.28 to 5.35, by the development of the peak value of roll surface deformation, $\Delta r|_{z=0}$ can be represented in the form of an exponential decay:

$$\Delta r = \Delta r_p (1 - e^{-t/\tau}) \qquad (5.20)$$

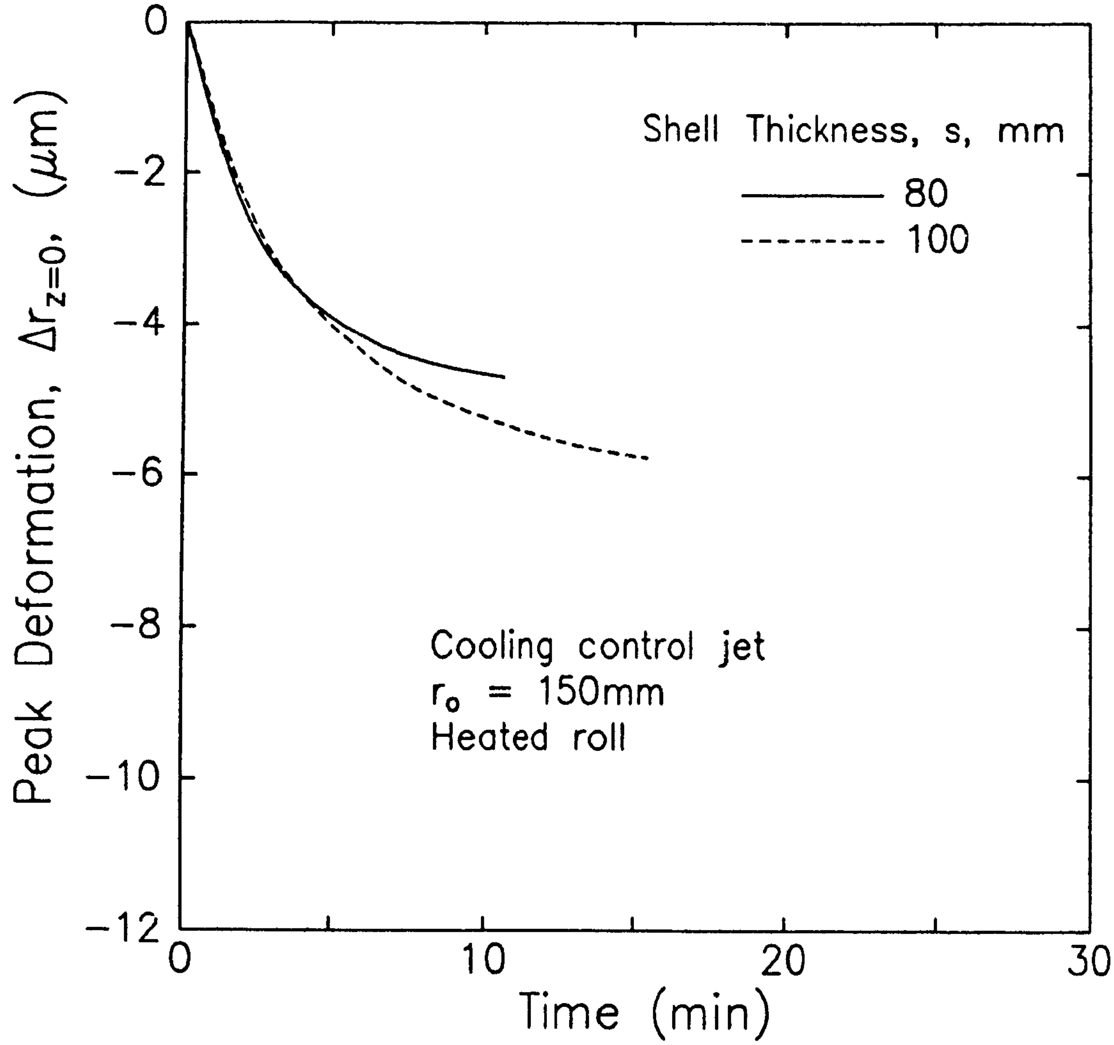

Figure 5.28 Peak deformation response: Cooling control jet on an internally heated roll, r_o=150mm.

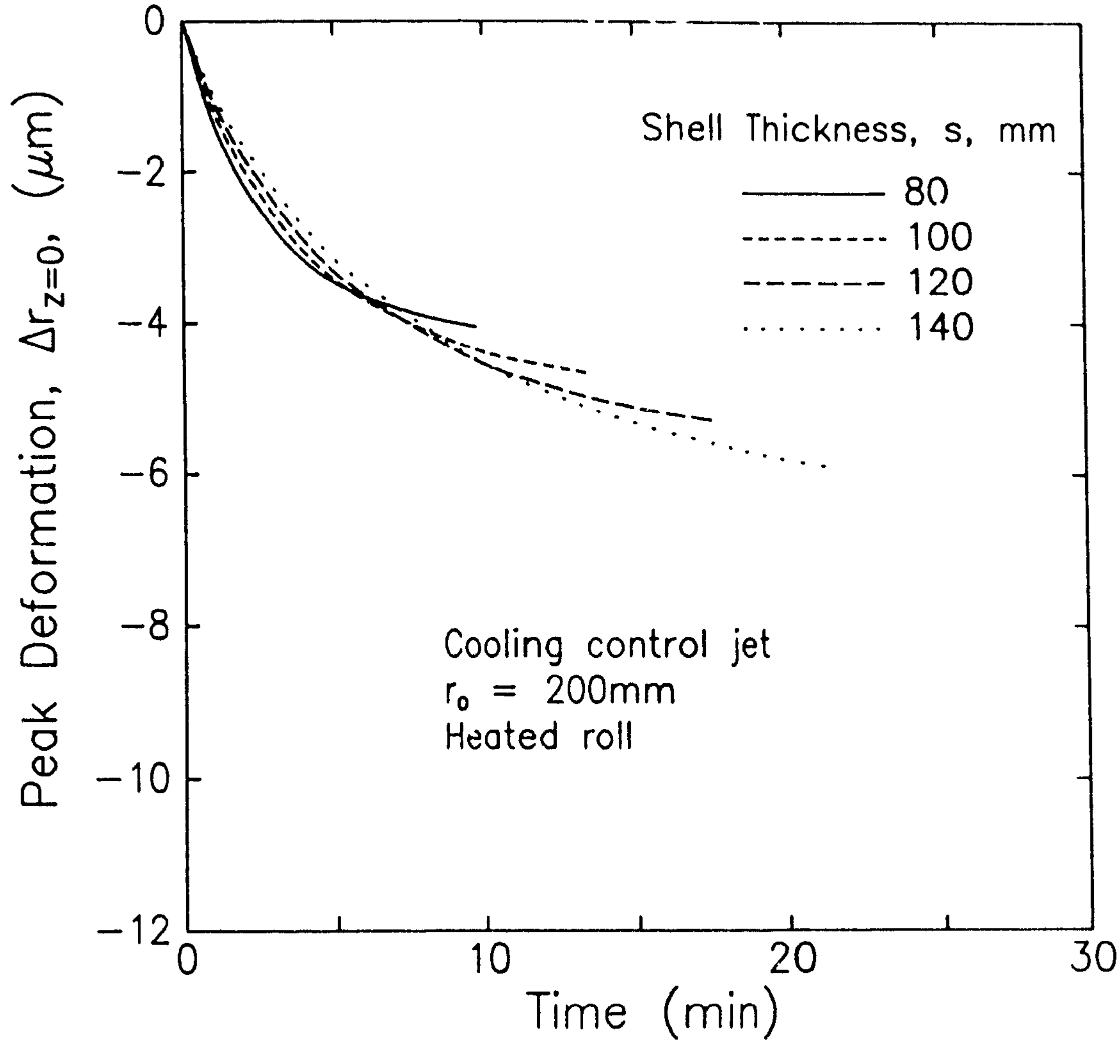

Figure 5.29 Peak deformation response: Cooling control jet on an internally heated roll, r_o=200mm.

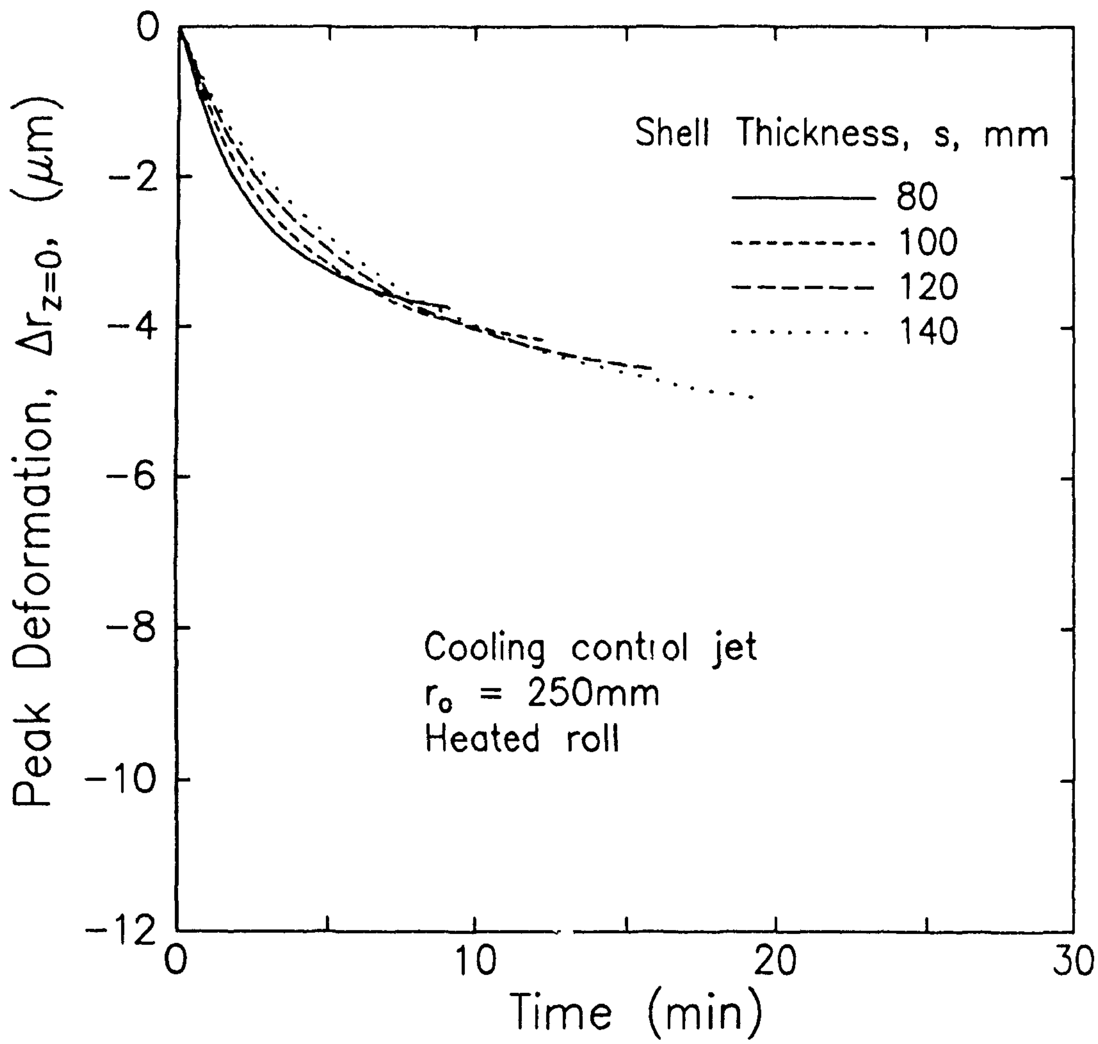

Figure 5.30 Peak deformation response: Cooling control jet on an internally heated roll, r_o=250mm.

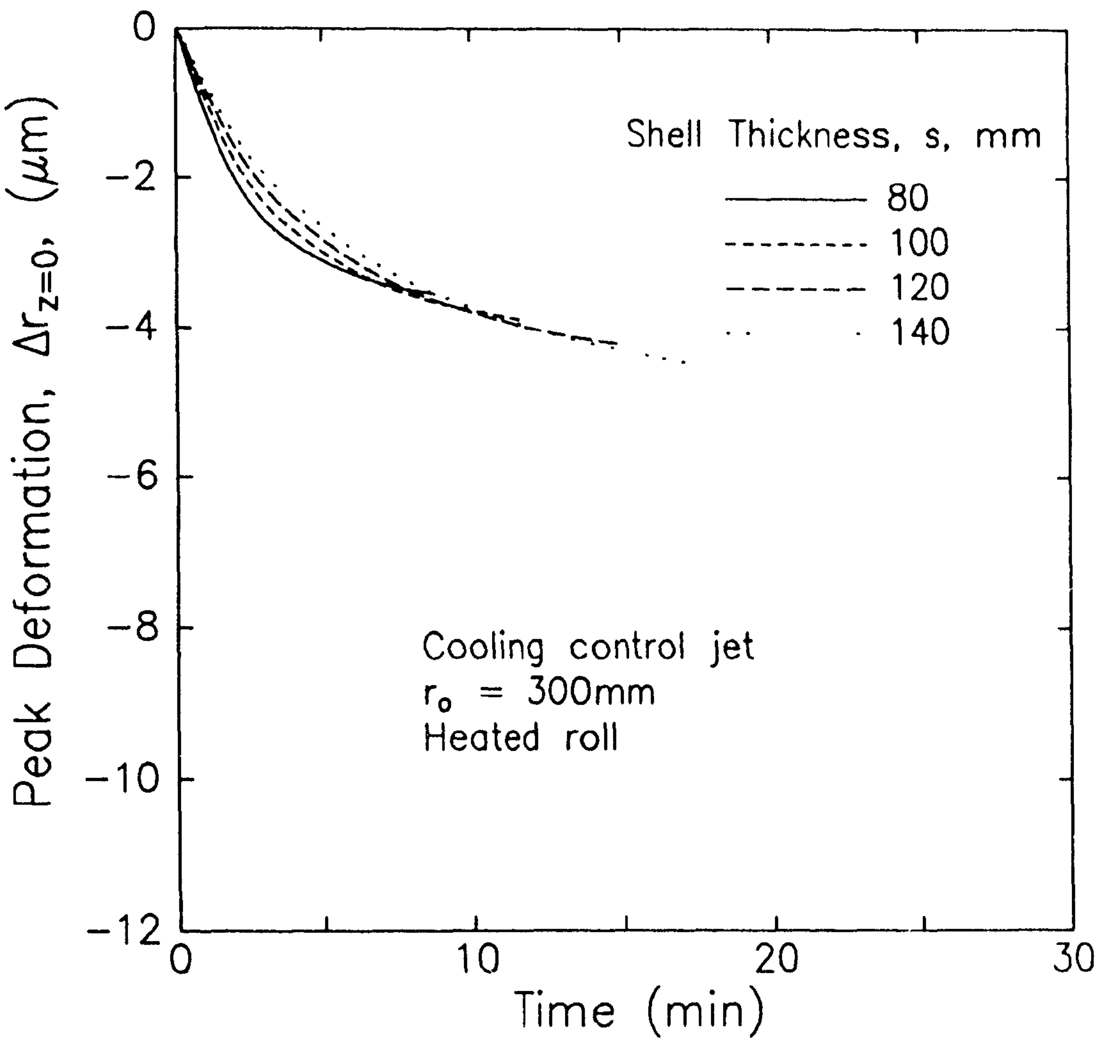

Figure 5.31 Peak deformation response: Cooling control jet on an internally heated roll, r_o=300mm.

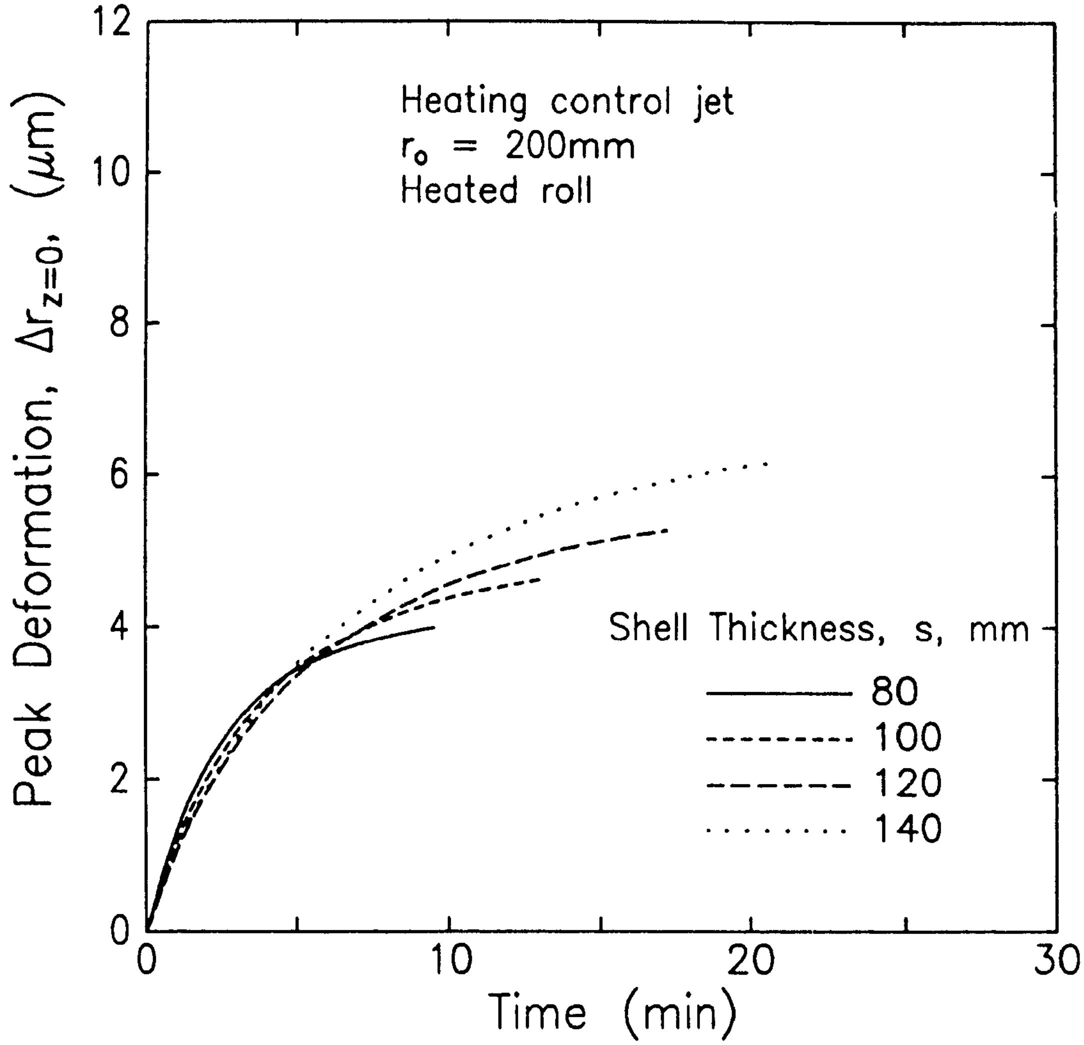

Figure 5.32 Peak deformation response: Heating control jet on an internally heated roll, r_o=200mm.

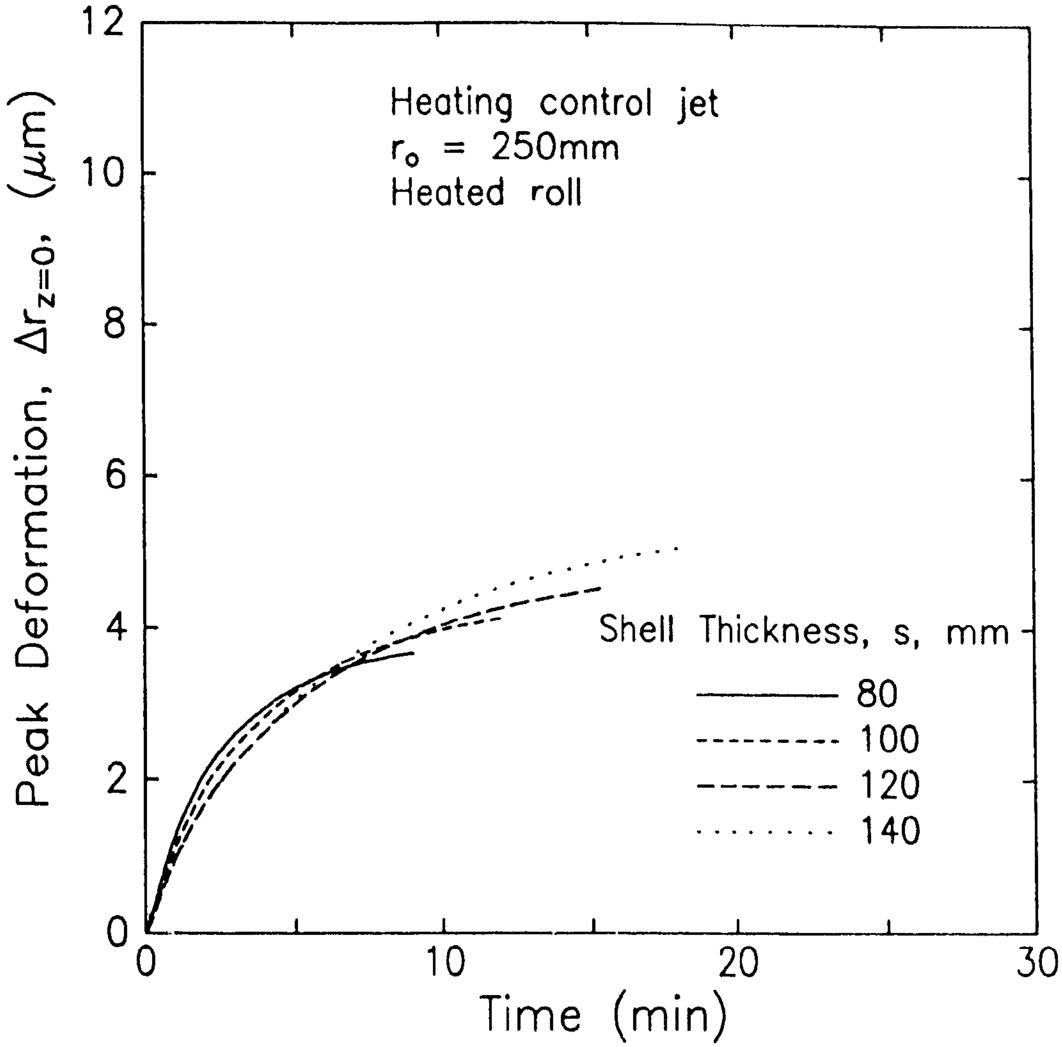

Figure 5.33 Peak deformation response: Heating control jet on an internally heated roll, r_o=250mm.

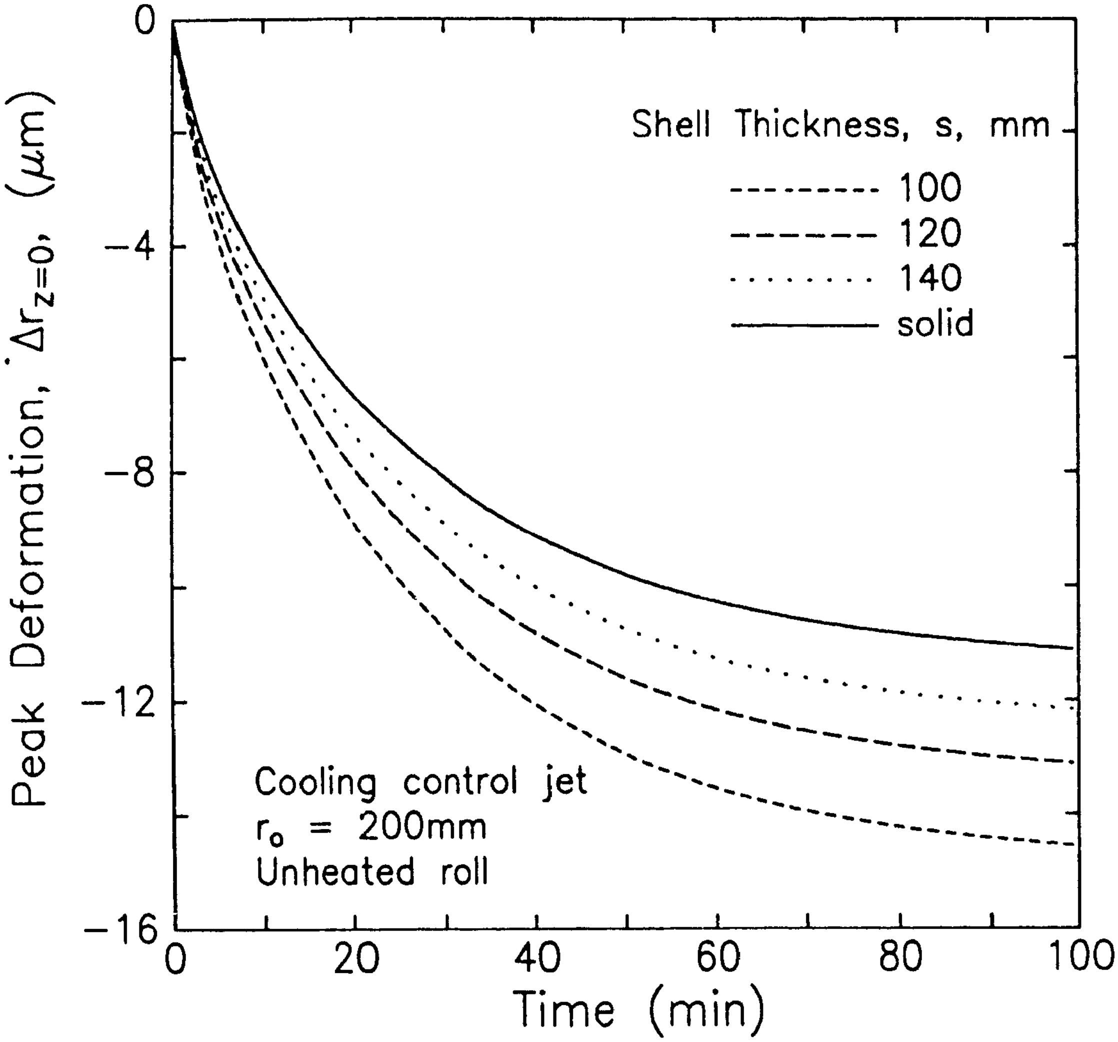

Figure 5.34 Peak deformation response: Cooling control jet on an unheated roll, r_o=200mm.

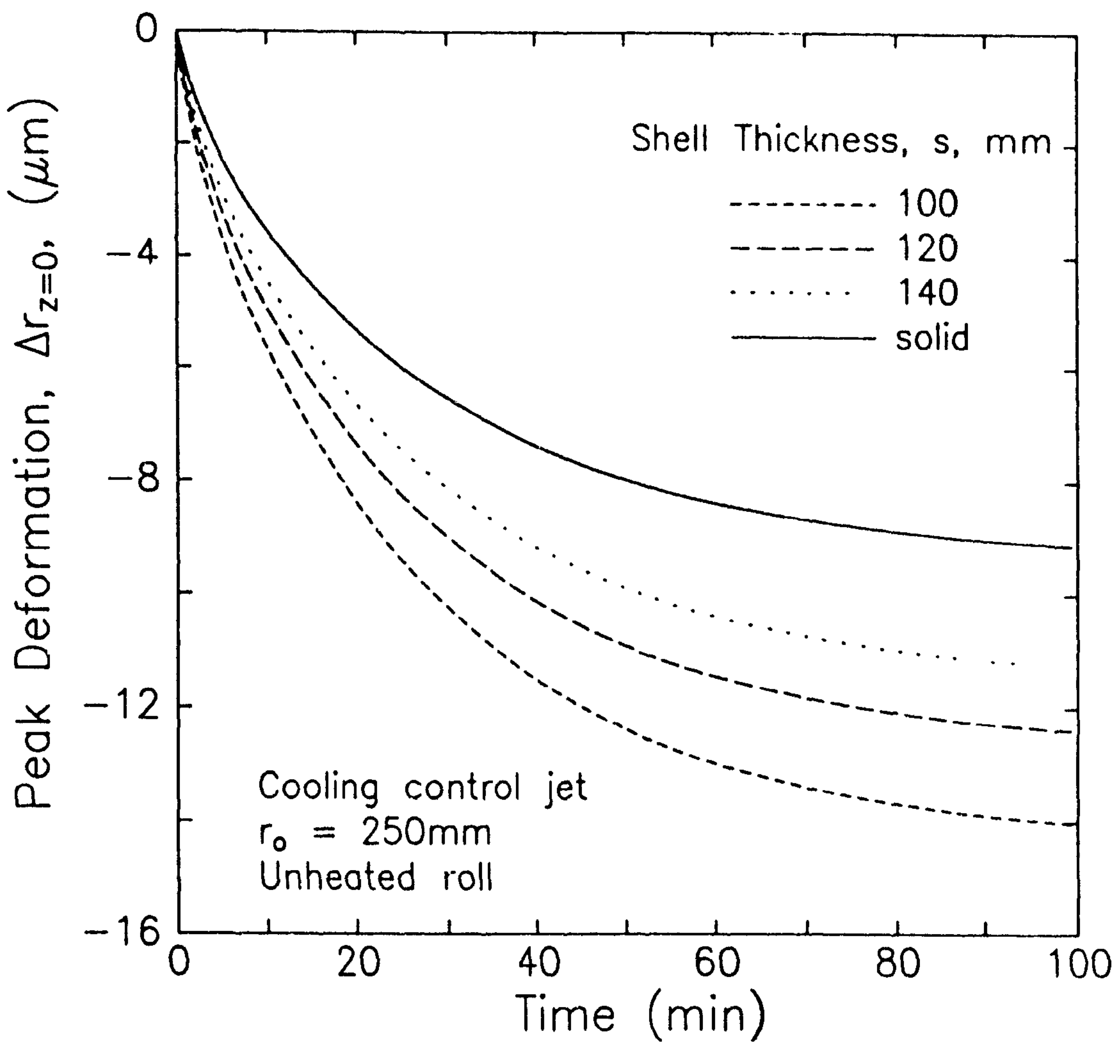

Figure 5.35 Peak deformation response: Cooling control jet on an unheated roll, r_o=250mm.

where the deformation time constant, τ, and the peak roll deformation, Δr_p, depend on the geometrical and thermal boundary condition. Desirerable control characteristics are a high value of peak deformation and of low deformation time constant. Figure 5.36(a) and (b) show comparisons of time histories of numerically predicted values of $\Delta r|_{z=0}$, with the fit obtained by Equation 5.20. As the agreement is excellent, the values of τ and Δr_p obtained by fitting Equation 5.20 to the time history results displayed in Figures 5.28 to 5.35 can be considered a satisfactory representation of the system.

Figures 5.37 to 5.40 display the results as expressed in terms of Equation 5.20. These simulations cover the range of parameters $150 \le r_o \le 300$ mm and $80 \le s \le 140$ mm for internally heated rolls with heating and cooling control jets, and for unheated rolls with cooling control jets. As already noted, results with heating and cooling control jets are either exactly equivalent or are effectively equivalent.

A comparison of steady-state peak roll deformations obtained for a heated roll under heating and cooling control jets is shown in Figure 5.38. The near equivalence of heating and cooling control jets with a heated roll, established in Section 5.4.5, is again illustrated. Peak roll deformation obtained by steady-state simulation (Section 5.4) compares well with that obtained by expressing the unsteady state thermal deformation in terms of Equation 5.20.This agreement further supports the correctness of the approximate transient model based on the plane strain assumption, i.e. Equations 5.2(a) and 5.17, and representation of these results using Equation 5.20.

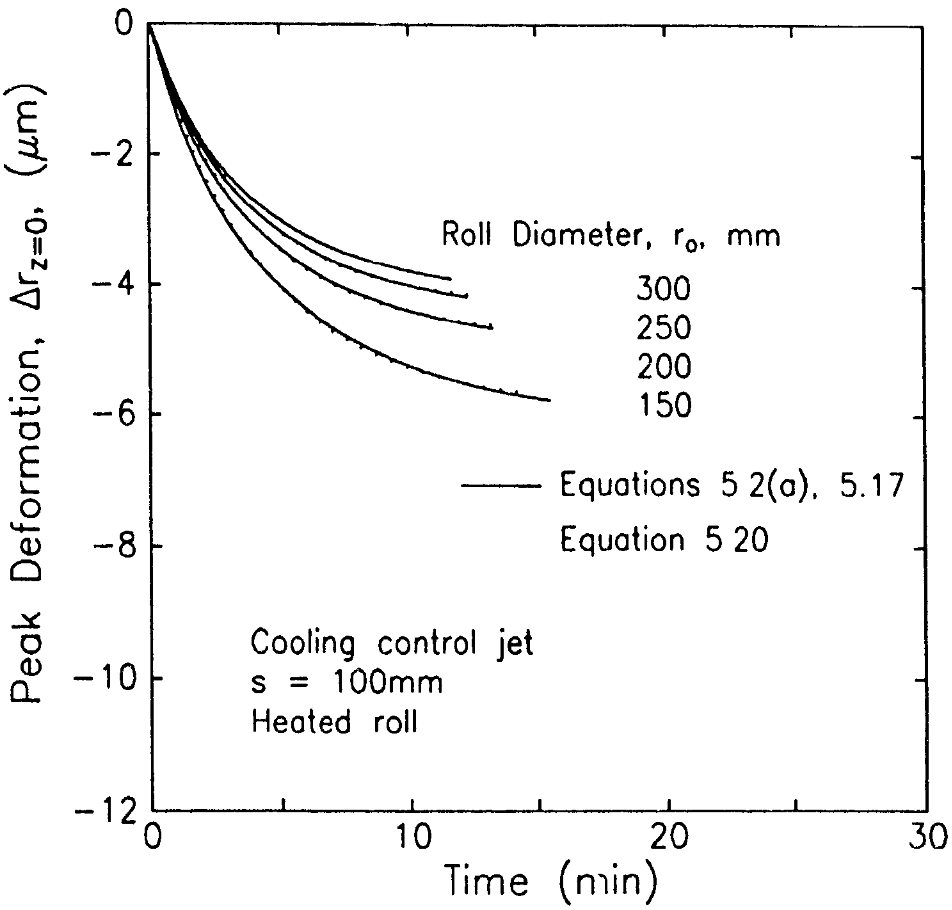

Figure 5.36(a) Comparison of time histories of the numerically predicted values of $\Delta r|_{z=0}$ with the fit obtained using Equation 5.20: cooling control jet on heated roll, s = 120mm.

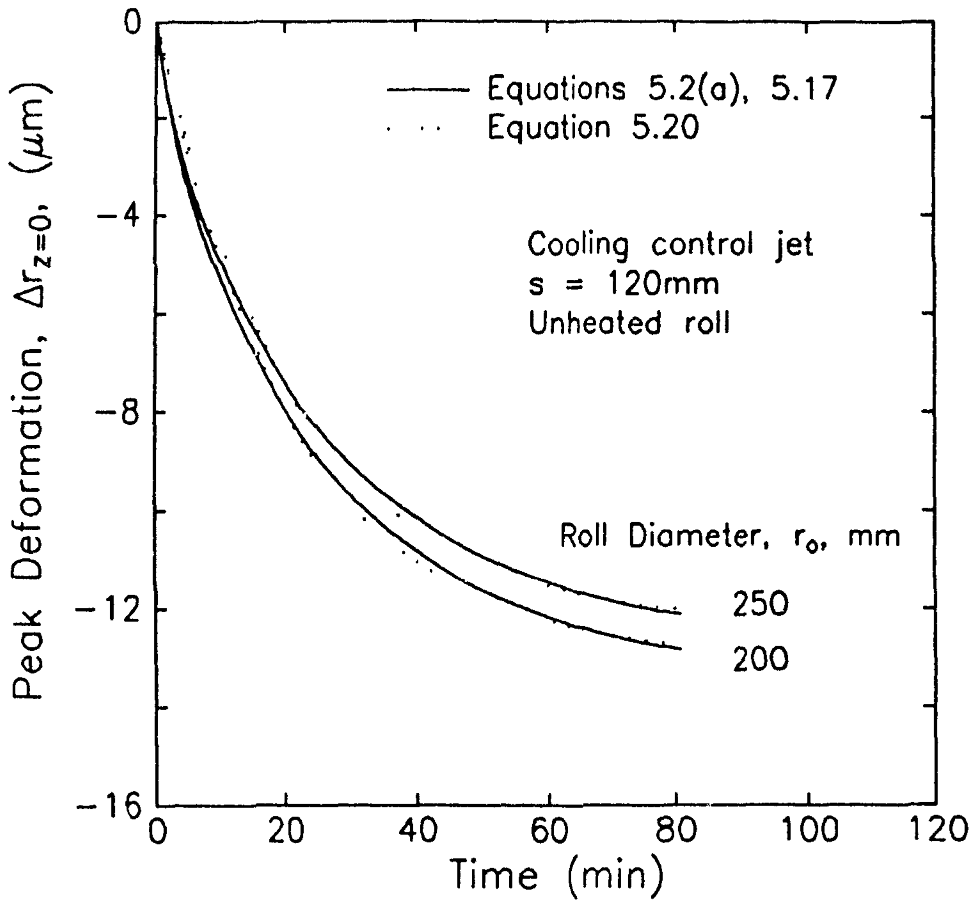

Figure 5.36(b) Comparison of time histories of the numerically predicted values of $\Delta r|_{z=0}$ with the fit obtained using Equation 5.20: cooling control jet on unheated roll, s = 120mm.

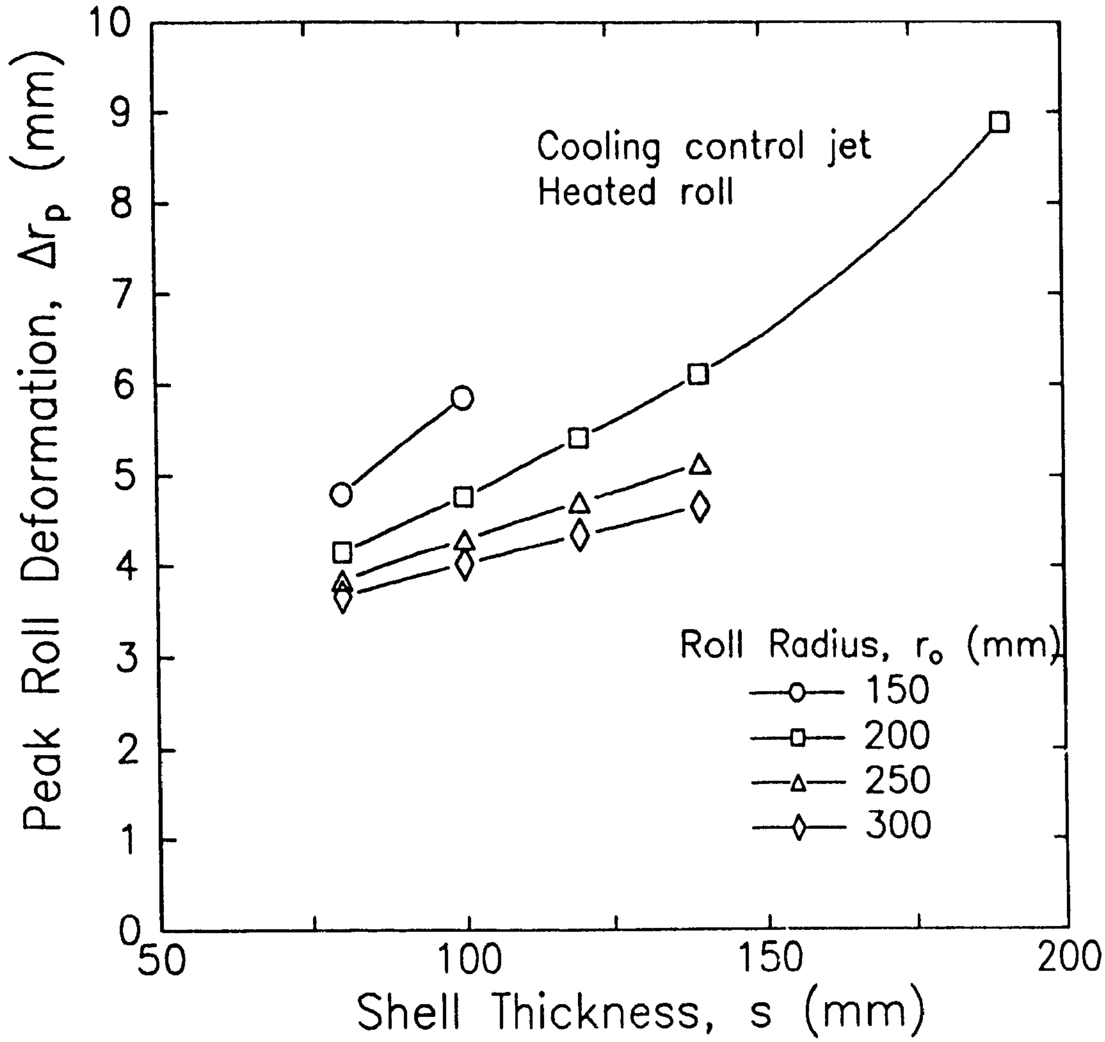

Figure 5.37 Effect of shell thickness and roll radius on peak roll deformation for heated rolls, cooling control jet.

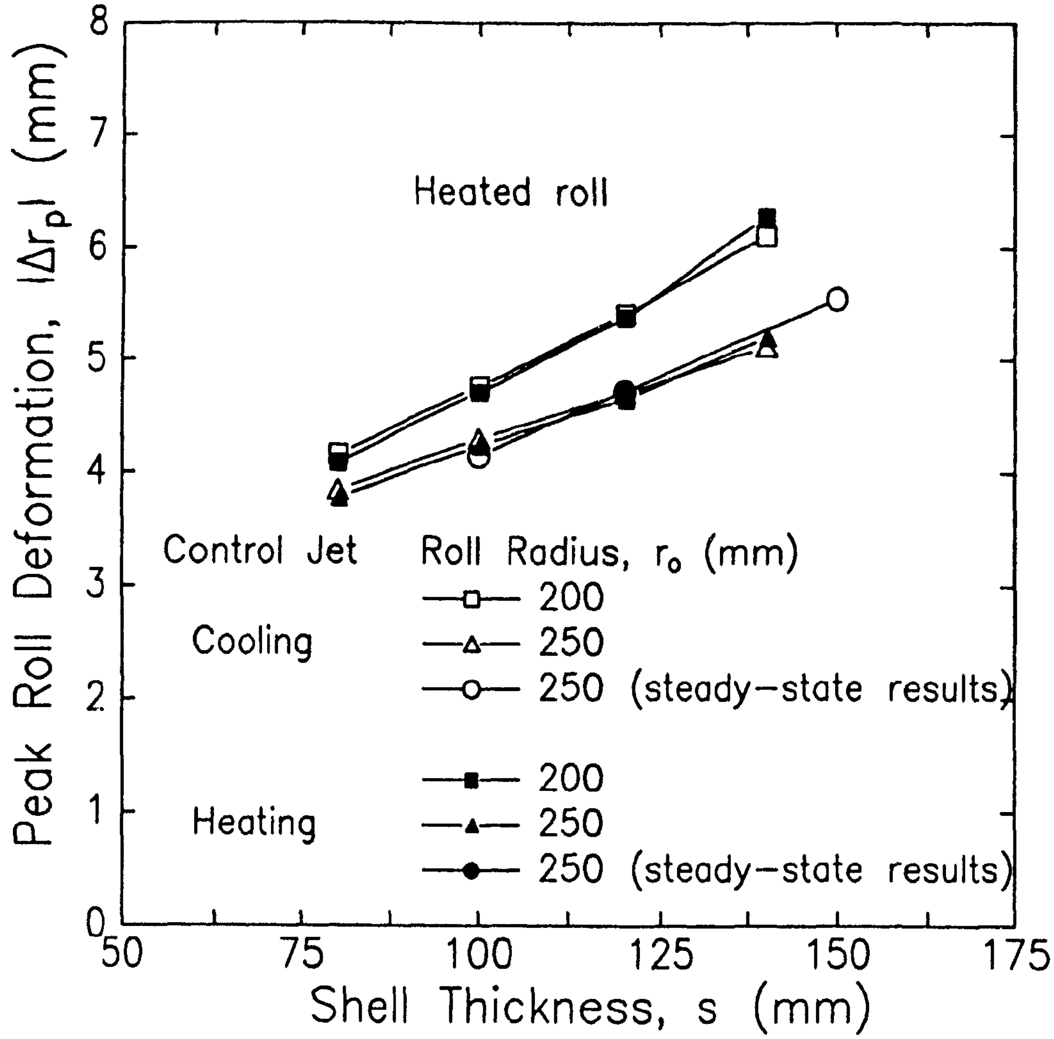

Figure 5.38 Comparison of peak roll deformations obtained with steadystate and unsteady state simulations.

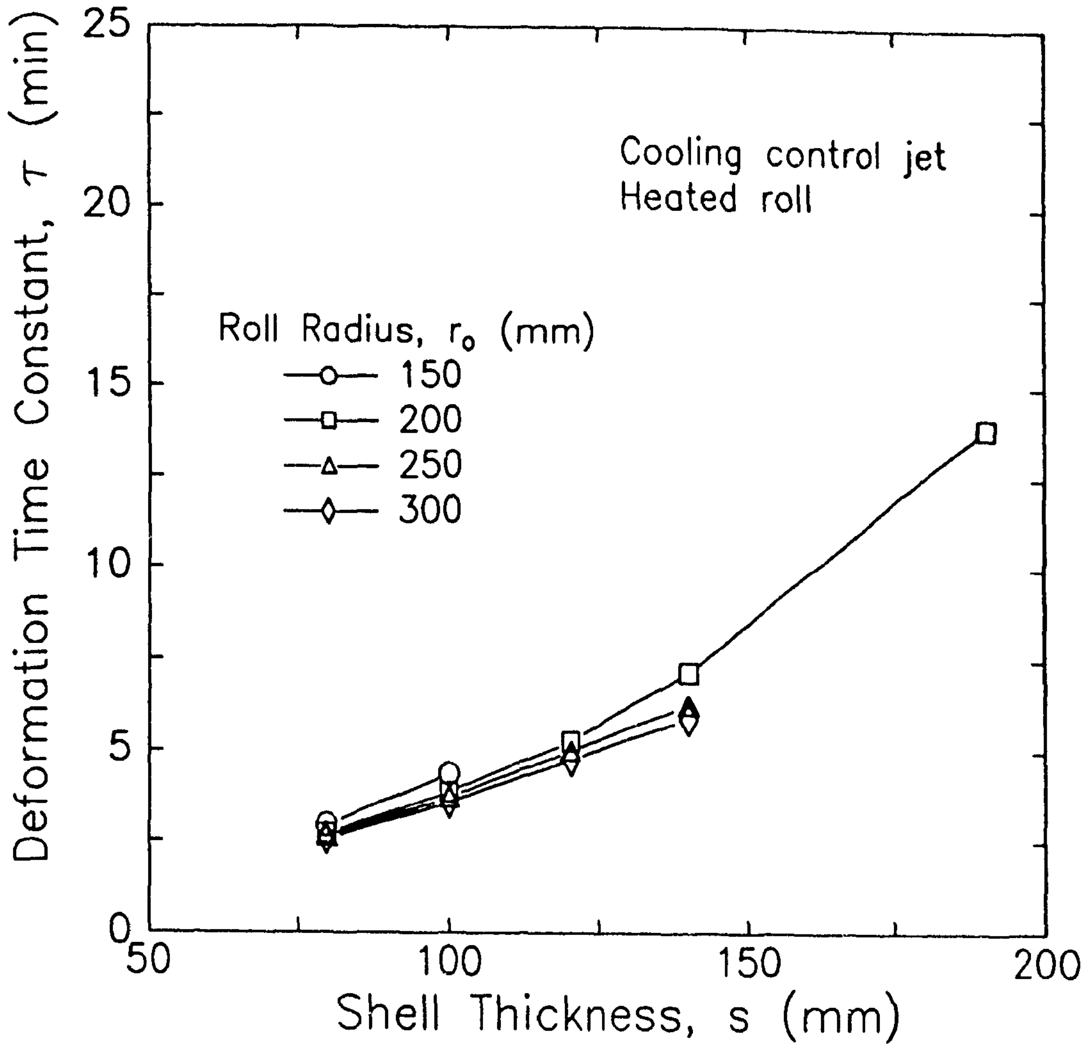

Figure 5.39 Effect of shell thickness and roll radius on deformation time constant for heated.

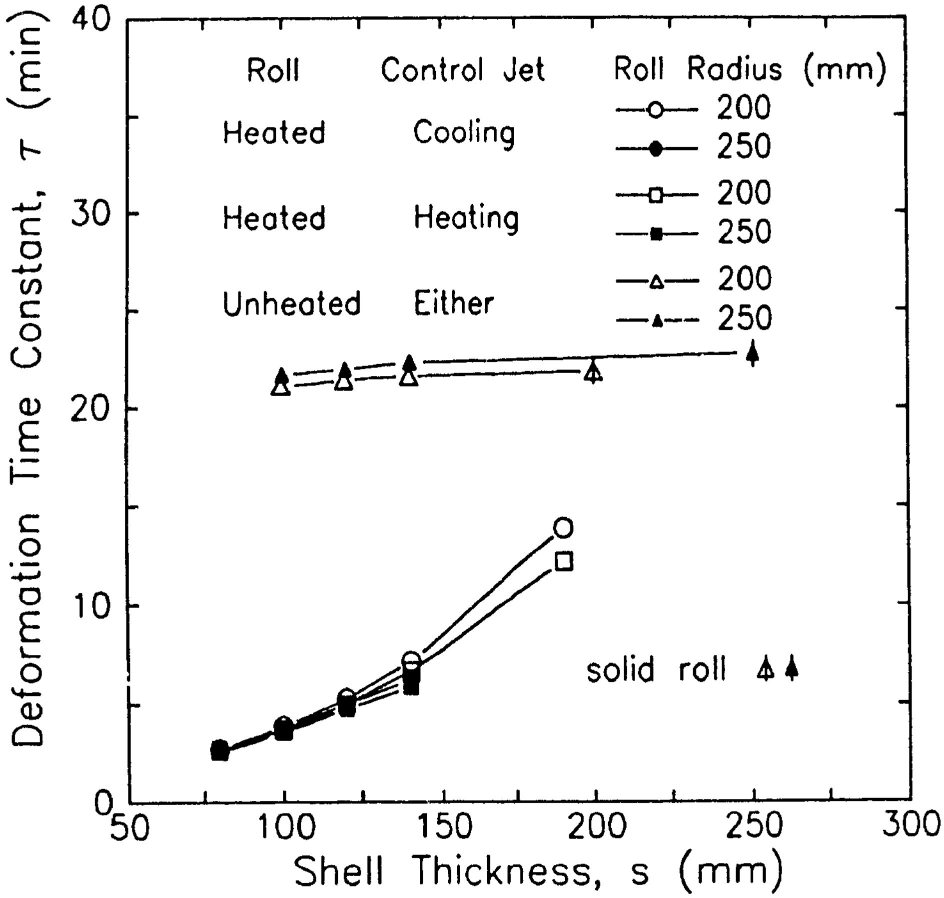

Figure 5.40 Comparison of deformation time constant obtained with heating and cooling control jets.

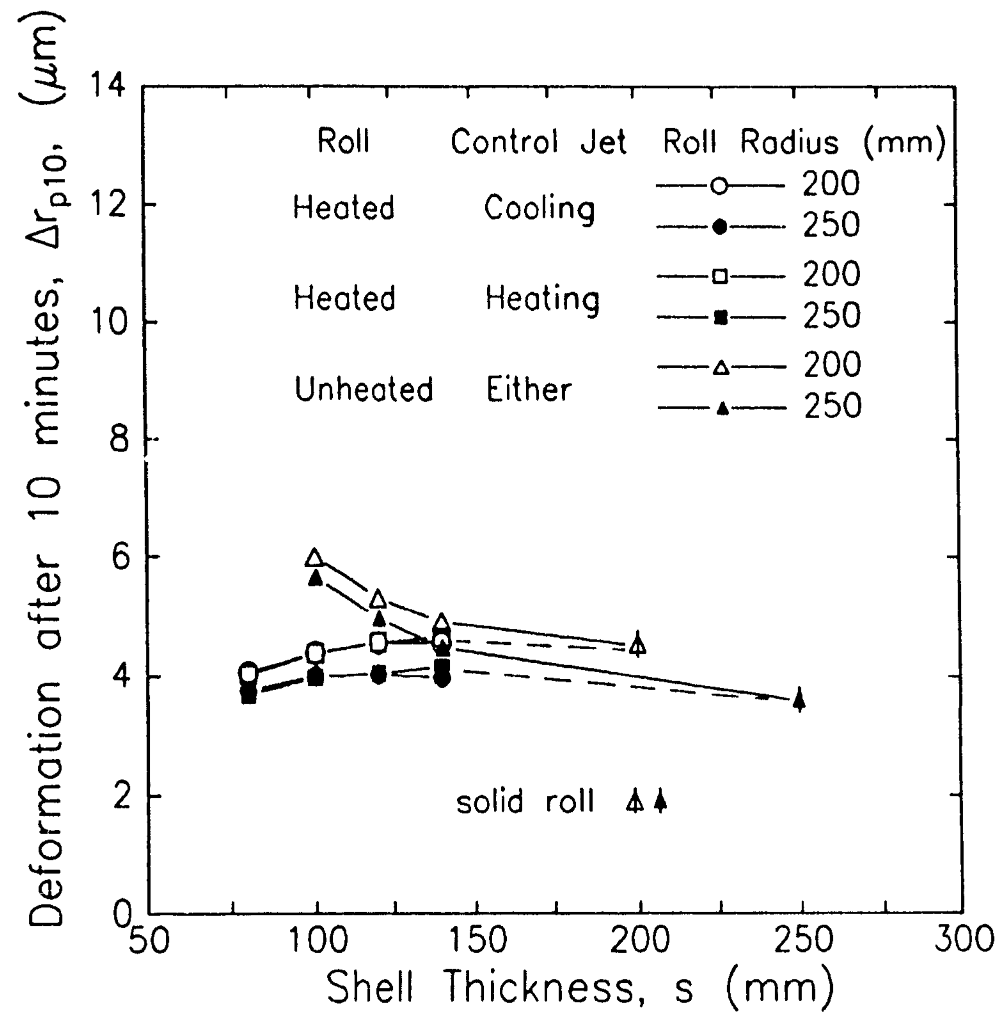

Figure 5.41 Comparison of the roll deformation, 10 minutes after the control action, Δr_{p10}, obtained with heating and cooling control jets.

With a heated roll, the cooling control jet data of Figure 5.39 indicate that the deformation time constant, τ, for constant shell thickness is little affected by r_o. Increasing r_o from 200 to 300mm improves the time constant, but only by less than 10%. The effect of shell thickness on τ at constant r_o is much stronger. Thus for r_o = 250mm the time constant is greatly improved, in fact is reduced by more than 50%, for a decrease in shell thickness from 140 to 80mm. These $\partial\tau/\partial r_o$ and $\partial\tau/\partial s$ effects both reflect an increase in the external roll surface heat transfer area for the control jet, relative to the mass of the metal shell. Heat conduction out through the metal shell attenuates the rate at which deformation of the roll surface is obtained in response to a step change in convective heat transfer rate by the control jet at the roll surface.

The deformation time constant for unheated rolls is much greater than for heated rolls and is little affected by either roll diameter or shell thickness, Figure 5.40, with $\tau \cong$ 21-23min, much higher than determined for heated rolls As a heated roll of r_o = 200mm approaches a solid roll (increasing shell thickness) Figure 5.40 shows that τ increases exponentially because, as $s \rightarrow r_o$, the deformation time constant must approach that shown for a solid roll.

Since the the peak deformation is different for all cases, it is inappropriate to compare the maximum peak deformation and time constant separately. Although unheated rolls have comparatively large time constants, the roll deformations are also much larger. For control to be effective on calender stack, the response to the control action should occur within a 10 minute period. Using this somewhat arbitrary time period, the deformation achieved in a 10 minute period, Δr_{p10}, gives a means of comparing overall transient control characteristics.

Figure 5.41 shows the peak roll deformation obtained within 10 minutes of the control action. For rolls of equal diameter, the thermal deformation after 10 minutes is always greater for unheated rolls. As expected, the heated and unheated results converge as the shell thickness increases and approaches that of a solid roll.

For heated roll there is a modest maximum roll deformation near a shell thickness of 140mm. As shell thickness increases, the thermal influence of the internal heat transfer on Δr_{p10} decreases, due to the increased separation and a decrease in the internal heat transfer area. Thus initially an improvement in the deformation is observed. As the shell thickness is increased further, the relative importance of axial heat conduction increases, due to a larger available heat transfer area. This results in a small decrease in Δr_{p10} behavior as the heated roll results approach that for unheated rolls.

5.6 Summary

The thermal deformation of calender rolls under unsteady-state conditions was numerically simulated using finite volume and finite element techniques, for which grid independent solutions were ascertained. The effect of calender roll design and of control system design and operation on steady state and transient response of calender rolls was thereby determined.

The only previous numerical study required the use of an assumed surface temperature profile, which in practice is an unknown dependant variable. A key feature of the present simulation is the avoidance of that assumption by linking the thermal deformation to the heat transfer characteristics of the control actuator being used. The present, more comprehensive simulation, when adapted to specified surface temperature boundary conditions, closely reproduces the results of the previous simulation.

As shown, the deformation time constant of a calender roll decreases with decreasing shell thickness due to a smaller thermal mass which must be heated or cooled. This criteria applies for both heated and unheated rolls. For a given roll design, however the increased penetration depth into the shell of the heat transfer associated with the control actuators with unheated calender rolls results in larger time constants than for heated rolls.

The transient behavior of calender rolls, as characterized by Δr_{p10}, the peak roll deformation, 10 minutes after the control action, indicates that in most cases optimum transient behavior for calender control purposes is observed on unheated roll. For heated rolls there is a broad maxima where a heated roll with a large shell thickness would have a larger Δr_{p10} than a solid roll of equal diameter.

Although the effect from thermal stresses associated with axial temperature gradients must be taken into consideration for most typical calender control situations, the plane strain solution given by Equation 5 16 is a very good approximation for control purposes.

The local steady state deformation of calender rolls was characterized in the radial direction as roll deformation, Δr, and the peak deformation, Δr_p, and in the axial direction by the characteristic width of this deformation, $W_{\Delta r}$. The simulation was carried out for a wide range of calender roll design parameters, including roll diameter, shell thickness, unheated rolls and internally heated rolls. As for the system of control actuators, the simulation investigated the use of heating and cooling air jets as the control actuator(s), various heat transfer profiles, variations in the number of control jets used, variations in the jet-to-jet spacing and the difference between confined and unconfined jets.

Because there is generally a trade-off between the desirability for calender control for purposes of a high peak roll deformation, Δr_p, and a low width of deformation, $W_{\Delta r}$, a criterion is proposed for the evaluation of alternative systems. The recommended characteristic, denoted the calender control performance index, I_c, is the ratio $W_{\Delta r}/\Delta r_p$, i.e. the width of deformation in millimeters per micron of peak deformation.

The investigation of numerous roll designs indicates that the most desirable steady-state and transient control characteristics are provided by unheated rolls of small diameter and of minimum practical shell thickness.

The placement of calender profiling equipment on adjustable crown rolls should not be discounted as has been traditional practice. The performance of the control system is complicated by the presence of hydraulic crown control but considering the thin shell wall and adiabatic internal boundary condition, the adjustable crown roll may be an optimal control position location. The high heat transfer characteristics and relatively thin effective shell thickness associated with the peripherally bored type of heated rolls make such rolls unsuitable for cross machine direction calender control.

As to design parameters for air jet control systems, a switch from unconfined to confined jets yields a 33% increase in the heat transfer, which in turn results in almost as large an improvement in peak roll deformation, Δr_p, with no loss in the calender control performance index, I_c. The addition of a confinement surface to many existing calender control systems involving unconfined jets is a relatively easy and inexpensive method to obtain a substantial improvement in calender control performance.

The present investigation also indicates that there is negligible control advantage to using jet-to-jet spacing, S, of less than 0.2m, while closer spacings than that have the disadvantage of wasting a large amount of air.

The concern recorded in some previous work as to the production of a "bumpy" roll between impinging jets, reflecting the axial non-uniformity of the actuator heat transfer profile, is shown in the present study to be groundless. It appears that the previous work did not appreciate the magnitude of the role played by axial heat conduction in calender control systems.

Finally, although the present numerical simulation has been demonstrated for a cross direction control system with local control effected by impinging unconfined jets of heating and cooling air, the simulation is sufficiently general to be readily used with other control actuators such as induction heaters or water mist coolers.

CHAPTER 6

THE EFFECT OF ACTUATOR POSITION ON PERFORMANCE OF A CD CALENDER CONTROL SYSTEM: AN EXPERIMENTAL STUDY ON A COMMERCIAL CALENDER

6.1 Introduction

The optimum position of an actuator system in a calender stack for local control of web thickness is a commercially important, yet unresolved issue. The rather limited technical literature on this subject agrees that the position of the actuator system is a significant parameter in the performance of a cross-machine (CD) calender control system. However there is considerable disagreement as to the optimum position and little convincing experimental evidence to support any of the stated opinions.

An experimental study was carried out on a commercial newsprint calender to provide better insight into the effect of the vertical positioning of actuators on the response time and magnitude of the response of a CD calender control system. The experiments were performed on only one calender configuration and, strictly speaking, are valid only for it and other similar configurations. However, together with the experimental and numerical results presented by Journeaux[1990], the data presented here provide a somewhat broader insight than the literature which has so far been published on this subject.

6.2 Literature Review

Traditionally the calender control nozzles, or "calender cooling nozzles" as they were called, were placed on the exposed rolls of the entering side of the calender stack. This gave the backtender easy access to the nozzles and avoided the potential problem of condensation water dripping on the calendered paper. As described by Janett[1955], this practice gradually changed to positioning the nozzles on the third and fourth roll from the bottom of the stack, which is currently the prevalent practice. Janett commented: "It now becomes apparent that air should be supplied to the first roll above the queen roll on the entering side of the calender stack, and on the second roll above the Queen roll on the leaving side of the stack, with the necessary headers on both sides. In addition, a considerable number of papermakers feel it desirable to supply air to the queen roll on the leaving side of the stack". It is apparent from these remarks that positioning was based on undocumented practical experience and that papermakers are engaged in a constant struggle to get better performance from their control systems.

Kahoun et al.[1965] suggested that papermakers might make better use of cooling air by applying it to the paper web entering the calender rather than to the calender rolls. Using this approach, they were able to make substantial improvements in the thickness profile on a paper-machine over a period of 40 minutes.They claimed that an equivalent response with air blowing on a calender roll might take as long as 2-6 hours, which is unrealistically long. The alleged reduction in the response time (from several hours to under an hour) was attributed to a higher heat transfer efficiency from the air to the paper and from there to the calender rolls, as well as the ability of the cooler paper to affect more than one calender roll.

Lyne et al.[1976] made measurements on the commercial calender shown in Figure 6.1. They observed a 1.5°C surface temperature change and a 1.5μm change in web thickness after blowing 27°C air for 30 minutes, at maximum flow rate, onto the 1.0m diameter crown-controlled

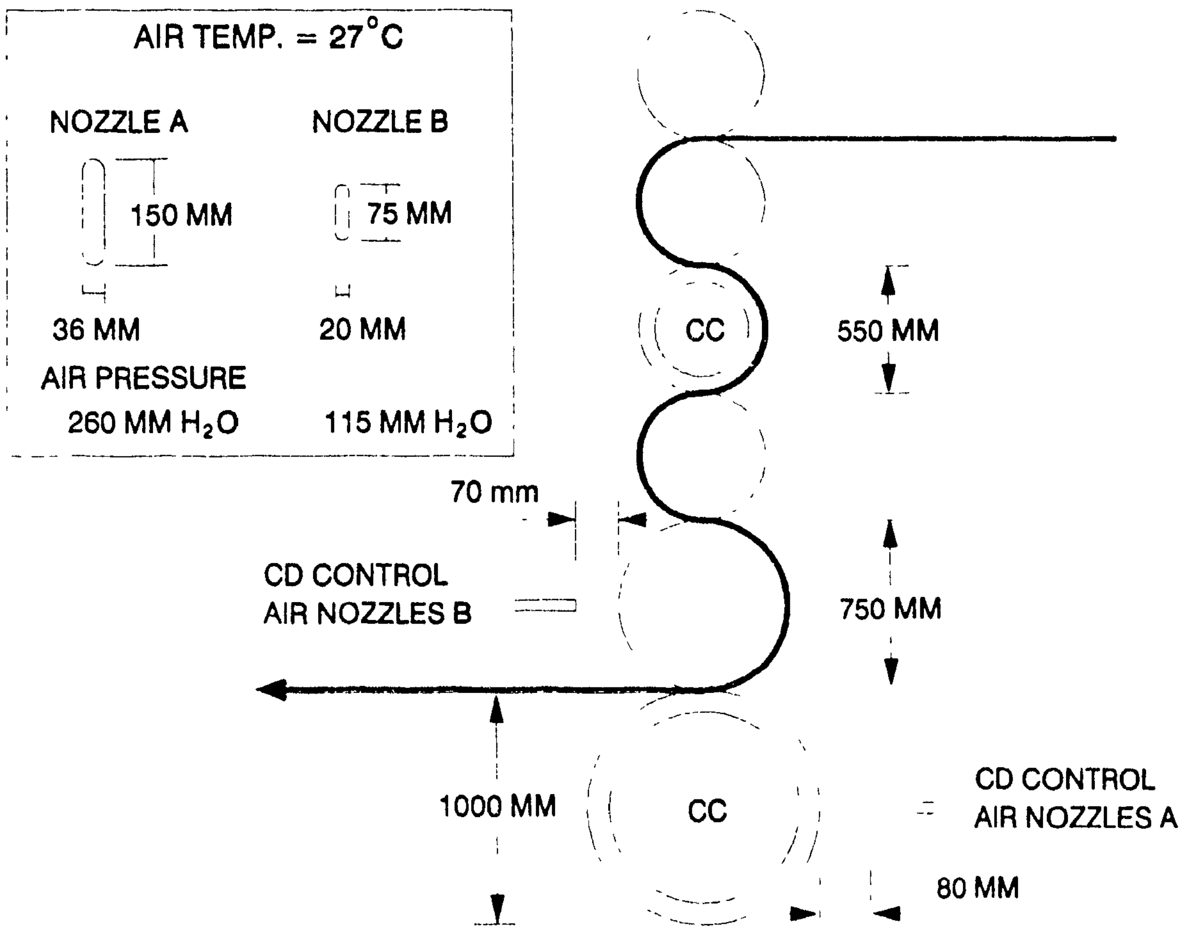

Figure 6.1 Calender stack configuration used by Lyne et al [1976]

king roll operated at $6^{\circ}C$. No measurable effect was observed by their companion experiment carried out on the 0.75m diameter solid queen roll at $55^{\circ}C$. Based on these experimental results and the following reasoning, they recommended the king roll as the optimum location for paper thickness control:

i. Heat transfer from the roll surface to/from the travelling web is minimized.

ii. Thickness adjustments are final rather than the beginning of an iterative effect as occurs in the upper nips of a calender stack (less thickness reduction at one spot in a nip resulting in more compression at that spot in the following nip).

iii. When using cold air jet showers, general stack cooling is avoided.

Their comparison of results between control jets on the king and queen roll was inappropriate because of the large differences in nozzle size, mass flow; rate, and jet Reynolds number. For the low pressure air jet from the small nozzle on the queen roll, the heat transfer rate would have been only about 15% of that on the king roll. The consequent low response on the queen roll would evidently have been below that measurable by their technique.

From experiments performed on the newsprint calender shown in Figure 6.2 Mitchell and Sheahan[1978] found control jets acting on the crown-controlled king roll to be 50% more effective at producing web caliper changes than when located on the center-bored third roll. The air supply system provided air at $28^{\circ}C$ in the nozzle headers while the roll surface temperatures averaged $54^{\circ}C$. They agreed with the comments and conclusions presented by Lyne et al.

Fjeld and Hickey[1981] approached the problem of actuator location using largely undisclosed reasoning based on control theory. Their

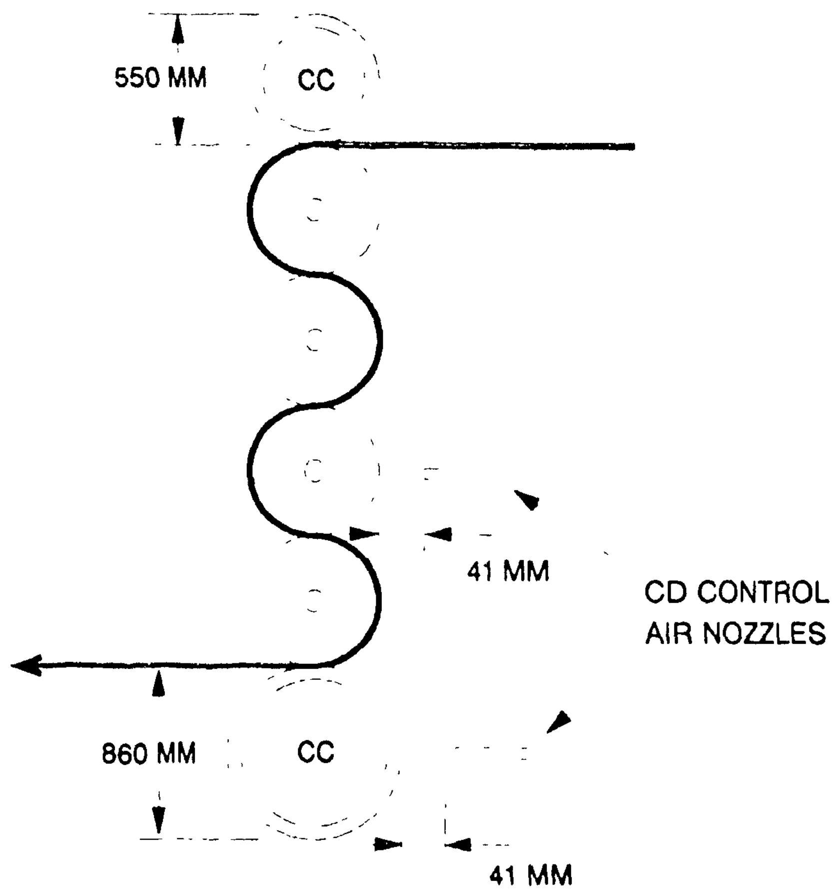

Figure 6.2 Calender stack configuration used by Mitchell and Sheahan[1978].

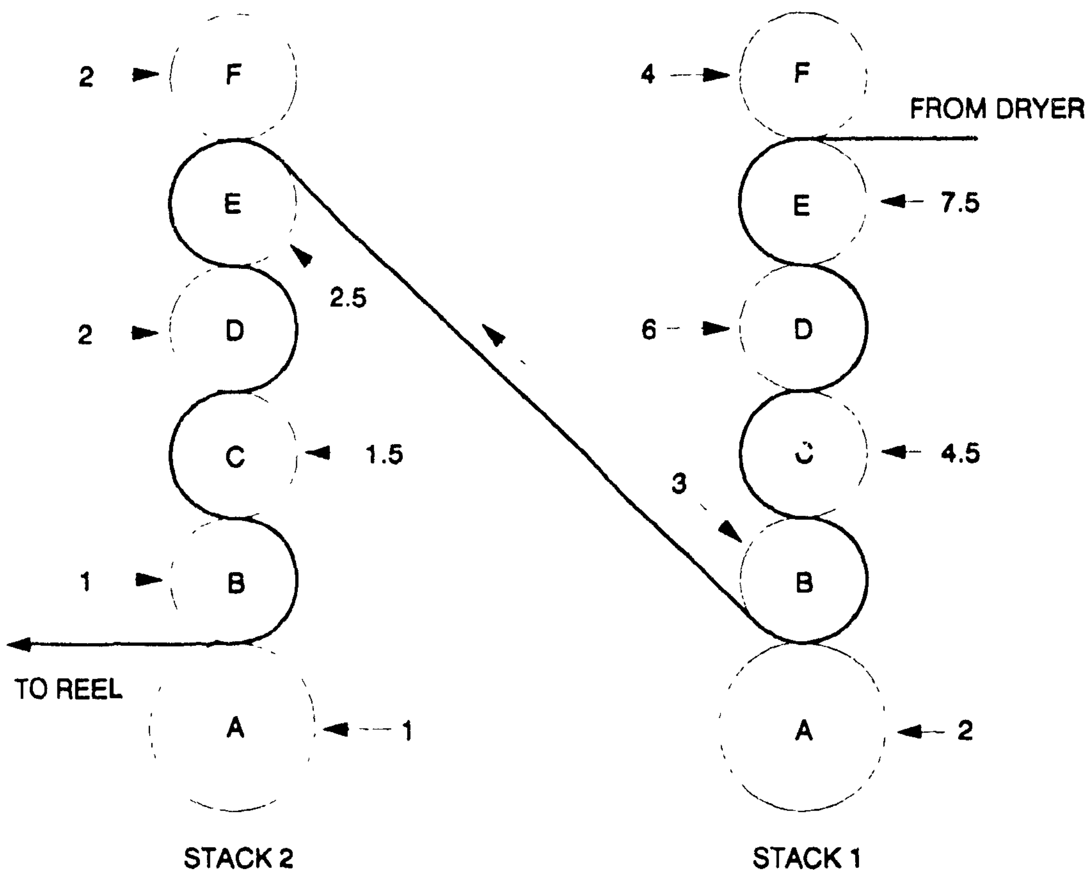

Figure 6.3 Relative actuator sensitivity according to Fjeld and Hickey[1981].

recommendations are summarized in Figure 6.3 in terms of estimated relative control improvement as a function the control actuator position in a double calender. According to their analysis, actuators placed higher in the stack are more effective because they provide:

i. high system response time and good spatial resolution in the cross machine direction;

ii. a wide control band;

iii. highest potential of relative decrease in caliper.

In their analysis, Fjeld and Hickey assume that a thickness correction made in the top nip is as effective as one made in lower nips because under feedback control the location where the correction is made is irrelevant. However that argument, which holds provided the actuator can make the changes called for by the control system, says nothing about the magnitude of this change. This magnitude depends on the process, which in this case is highly non-linear. As the bulk duction is much greater in the top nips than in the bottom of the calender, a much larger roll reflection is needed in the top nips to produce the same permanent thickness change.

In summary, the placement of CD control actuators recommended by Lyne et al[1976] and Mitchell and Sheahan[1978] is on the king roll, by Fjeld and Hickey[1981] on the second roll from the top of the stack, and by Kahoun et al.[1965] is on the web entering the stack. They all agree that the traditionally prefe-red location on the third and fourth rolls from the bottom, as described by Janett[1955], is not the optimum.

The available literature makes little mention of the effect of calender roll type (i.e. shell or solid) or internal calender operating parameters (i.e. heated, unheated, crown controlled) on the thermal roll deformations associated with caliper control actuators. Mitchell and

Sheahan[1978] noted the very much slower response of a solid calender roll as compared to a shell type roll. Lyne et al.[1976] acknowledge the effect of roll type and speculated that unheated hollow rolls would have a larger change in radius per $^{\circ}$C than either solid or heated rolls.

Thus the published literature takes little consideration of the effect of roll design and, moreover, provides conflicting results which therefore do not provide the needed guidance in the design of high performance calender control systems or in the optimization of existing control systems.

6.3 Mill Calender Stack Configuration

The experiments were carried out on the double calender of a 3.7m wide commercial newsprint machine operating at a speed of 500m/min, producing a 45-47g/m^2 roto-news sheet from a furnish containing 53% thermomechanical pulp, 32% stone groundwood and 15% semi-bleached kraft pulp.

This calender, shown in Figure 6.4, is described in Table 6.1. The calender stacks were identical with the exception of the king roll, a solid roll in the first stack, a hydraulically pressured, variable-crown roll in the second stack. All rolls above the king roll were center-bored (100mm) and, with the exception of the top rolls in each stack, were steam-heated. The steam pressure was varied to adjust the average thickness of paper produced during the five days of mill trials, as shown in Table 6.2.

On each roll CD thickness control was automatically controlled by two rows of cooling air jets. The jet-to-jet spacing was 200mm, with the two rows on each stack offset by 100mm to provide an effective jet-to-jet spacing of 100mm. The nozzles in the CD control system were

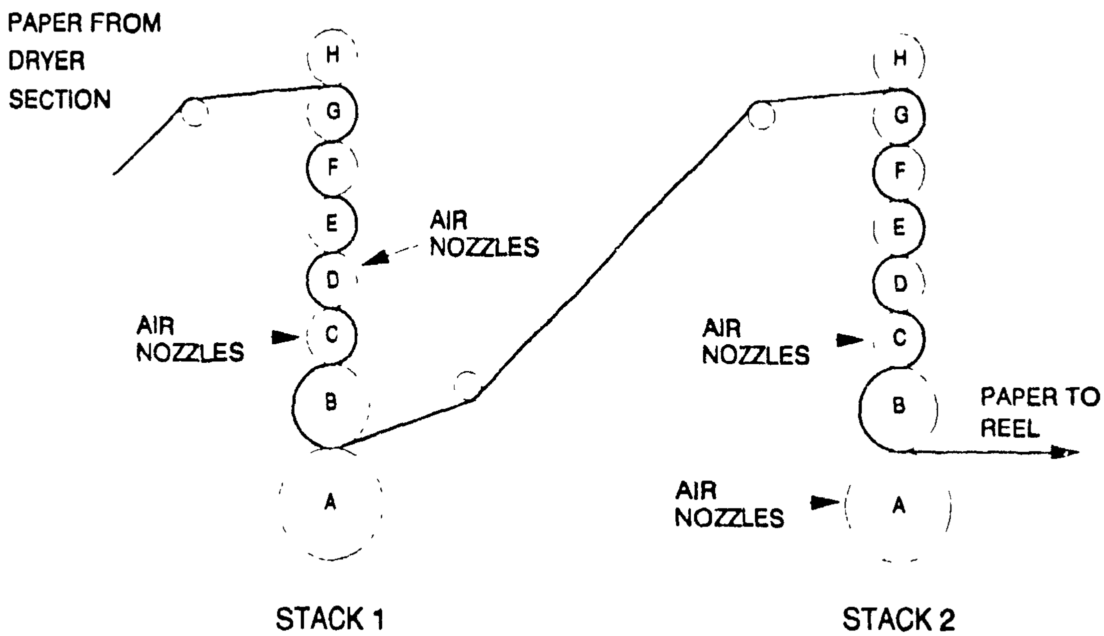

Figure 6.4 Calender stack configuration for present study

13mm diameter, set at a nozzle-to-roll separation, H, of 100mm corresponding to a non-dimensional nozzle-to-roll separation of H/d = 8.

6.3.1 Experimental Procedures

The following procedure was used:

i. For each trial a cross-machine location was chosen near the center of the machine, which had a relatively flat and stable web thickness profile as measured by the CD control system.

ii A test nozzle, Figure 6.5, attached to a compressed air line at 18°C was placed on the roll to be investigated, mounted at the center of the experimental region with a nozzle-to-roll separation of H = 50mm, giving H/d = 2.

iii. The control system cooling air showers in the experimental region were turned off and the web thickness was allowed to drop.

iv. When the web caliper reached a minimum the test air nozzle was turned on and the change in web thickness, as measured by the CD control system, was recorded as a function of the elapsed time.

A nozzle exit velocity of 200m/s, corresponding to a jet Reynolds number of 343000, was used in the test nozzle. Although much higher than normally used in calender control air showers, this jet flow rate provided faster system response time and a web thickness change sufficiently large to be readily separated from the background noise associated with normal mill operation.

Axial profiles of roll surface temperature were measured using an intra-red pyrometer fitted with an emissivity converter, Figure 6.6. The emissivity converter, required since the chilled iron surface of the calender rolls has a low emissivity, consists of a thin blackened teflon strip mounted on a bracket in front of the lens of the pyrometer. The teflon strip contacts the roll and assumes the roll surface temperature very quickly. The pyrometer measures the temperature of the Teflon strip.

Table 6.1 Calender Stack Configuration

Roll Position	Stack #1 Roll type	Stack #1 Diameter (m)	Stack #1 Weight (kg)	Stack #2 Roll type	Stack #2 Diameter (m)	Stack #2 Weight (kg)
H	steam(off)	0.356	5000	steam(off)	0 356	5000
G	steam	0.356	5000	steam	0.356	5000
F	steam	0.356	5000	steam	0.356	5000
E	steam	0.356	5000	steam	0.356	5000
D	steam	0.356	5000	steam	0.356	5000
C	steam	0.356	5000	steam	0 356	5000
(queen) B	steam	0.457	7273	steam	0.457	7273
(king) A	solid	0.711	—	swimming	0.711	-

Table 6.2: Operating Conditions During the Trials

	Date	Basis Wt. g/m^2	Caliper (μm)	Steam Pressure (psig)
Day 1	June 7/85	46.0	70.0	3
Day 2	June 8/85	46.0	70.0	3
Day 3	Sept 2/85	46.9	62.1	5
Day 4	Sept 4/85	46.9	62.1	5
Day 5	Nov 3/85	45.4	64.8	4

6.4 Results

The experiments, very time consuming, required five days. The paper machine operating conditions did vary somewhat from day to day, as suggested by the basis weight, paper thickness and steam pressure values listed in Table 6.2. The average roll surface temperatures observed during days 3 and 4 are listed in Table 6.3.

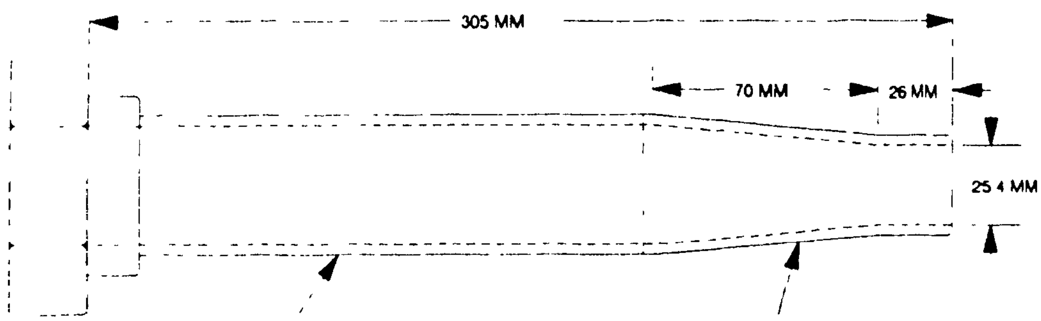

Figure 6.5 The test nozzle.

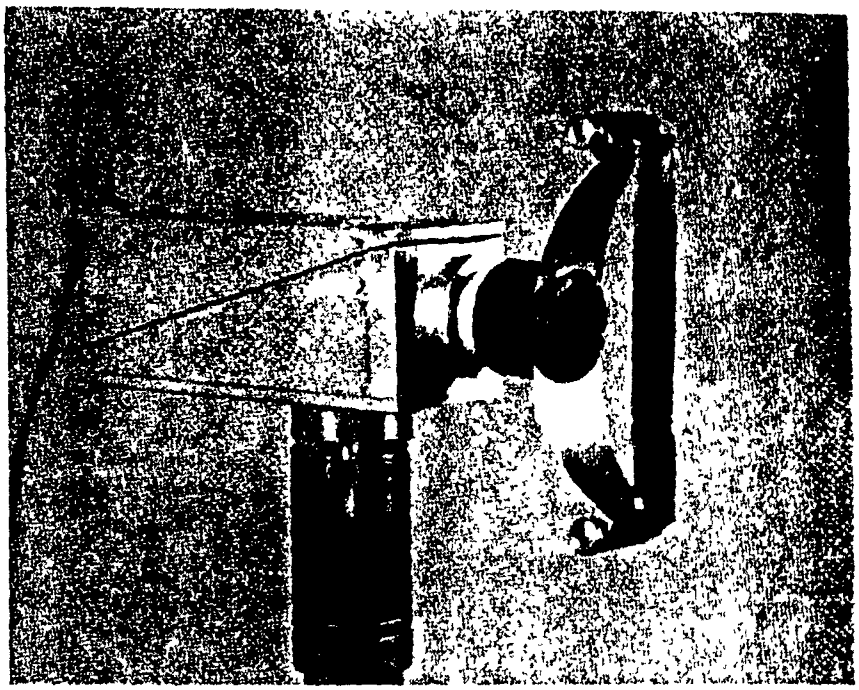

Figure 6.6 The infra-red pyrometer with emissivity converter.

Table 6.3 Calender Roll Surface Temperatures Observed During Days 3 and 4.

Roll Position	Surface Temperatures (°C) Stack #1	Stack #2
H	--	--
G	--	--
F	82	83
E	88	85
D	86	87
C	89	87
(queen) B	81	82
(king) A	66	65

The effect of nozzle position for results obtained during days 1 and 2 are shown on Figures 6.7 and 6.8, and for days 3 and 4 on Figure 6.9. During the first two days Roll B1 was not accessible. In addition to the measurements made on Roll B1, the repeat measurements made on Roll C1 provide an estimate of the reproducibility of the measurements.

For the series of measurements performed on day 5, shown in Figure 6.10, the experimental nozzle was moved successively to different positions in Stacks 1 and 2 for a further comparison of the effectiveness of these positions.

The control air jet produced much smaller changes in web thickness when located on the second stack, Figure 6.8, than on the first stack, Figures 6.7 and 6.9. The largest effect was with the control jet on Roll B1, the queen roll, with progressively smaller effects on Rolls C1 and D1 Roll A1, the solid king roll, and Roll F1, near the top of the stack, showed very weak response to the control air jet.

The reproducibility of results is illustrated with measurements made on Rolls C1 and D1 For Roll C1, Figure 6.9 demonstrates the consistency between the two measurements made on day 4 and those made on

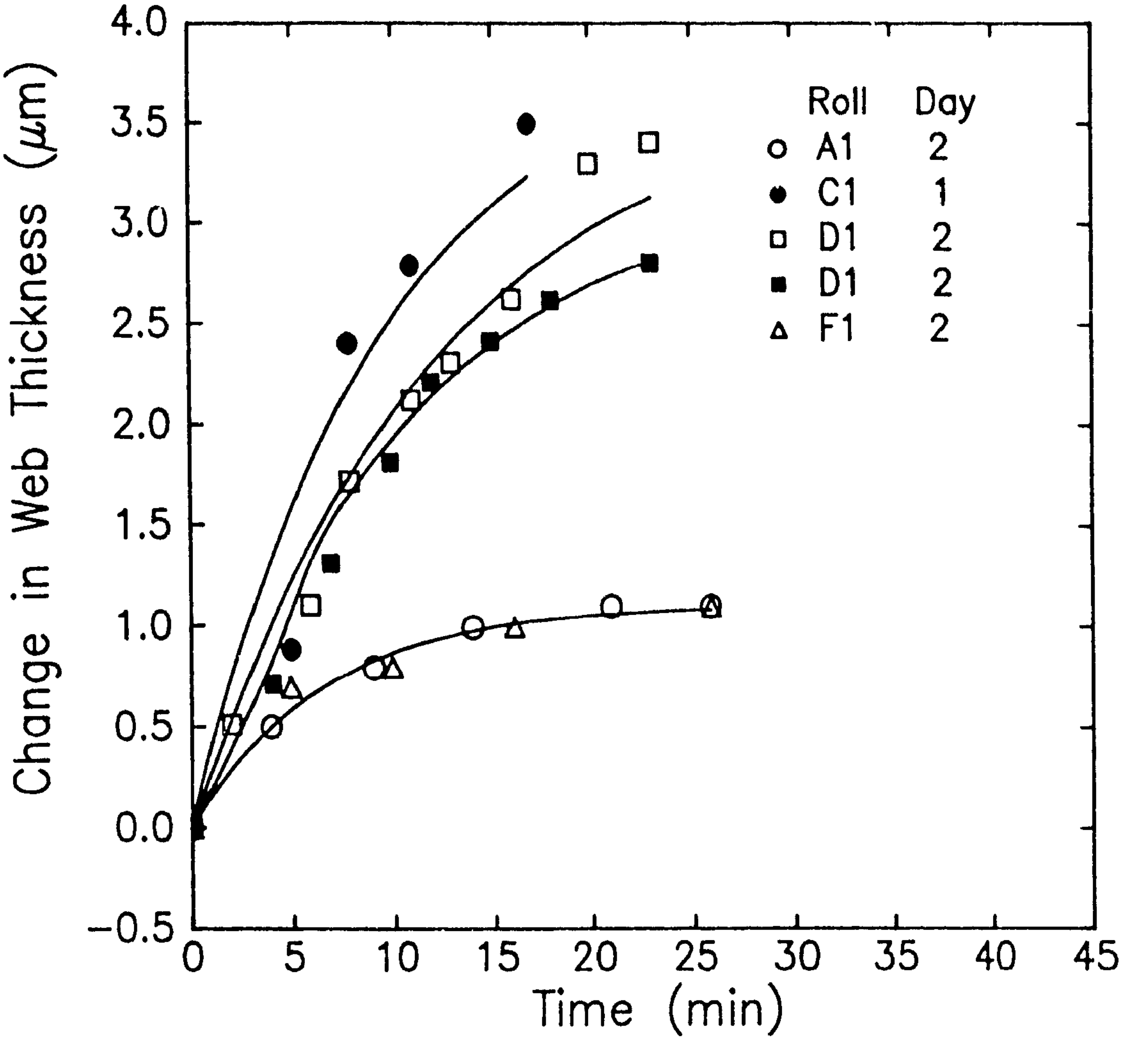

Figure 6.7 Paper thickness changes with a control air jet at various locations in the first calender stack: Days 1 and 2.

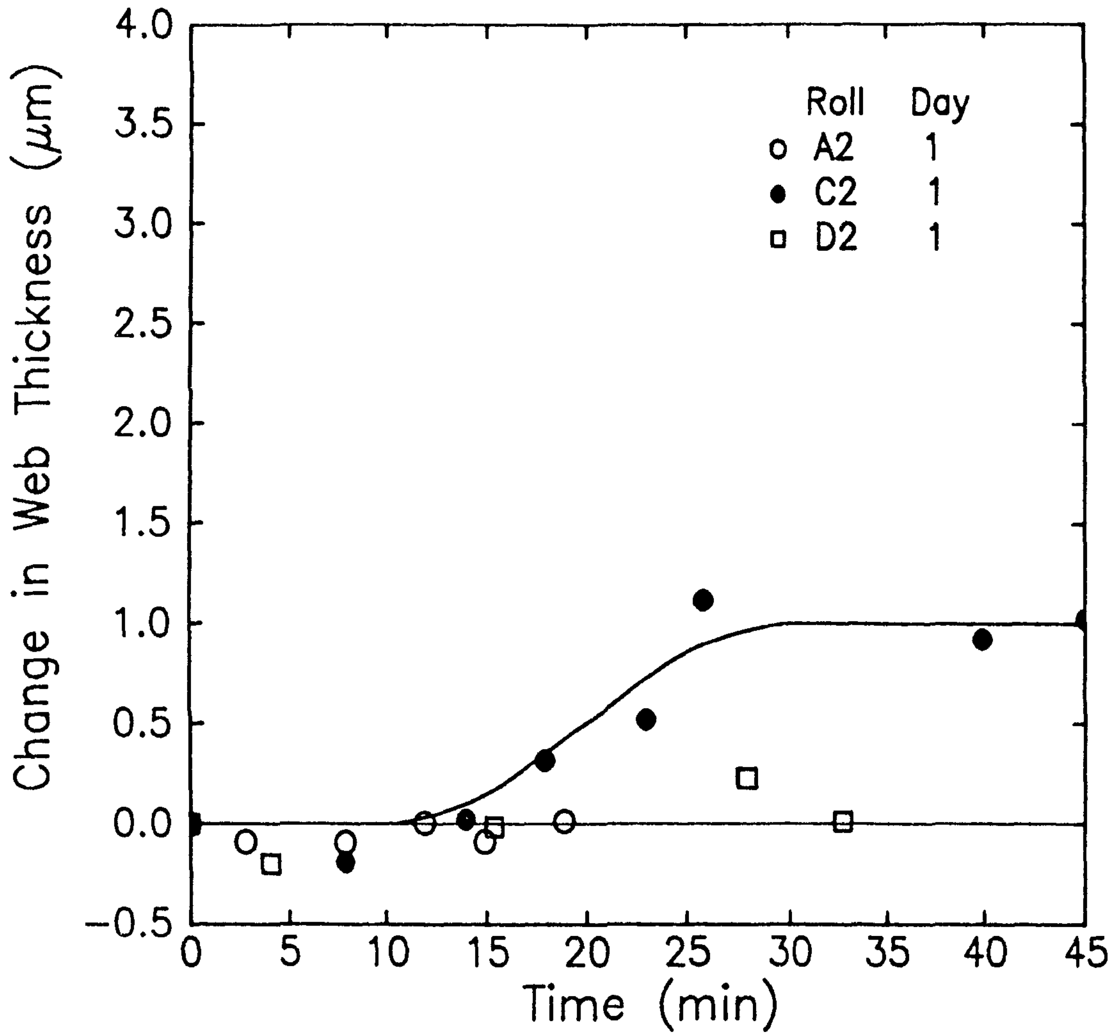

Figure 6.8 Paper thickness changes with a control air jet at various locations in the second calender stack: Day 1.

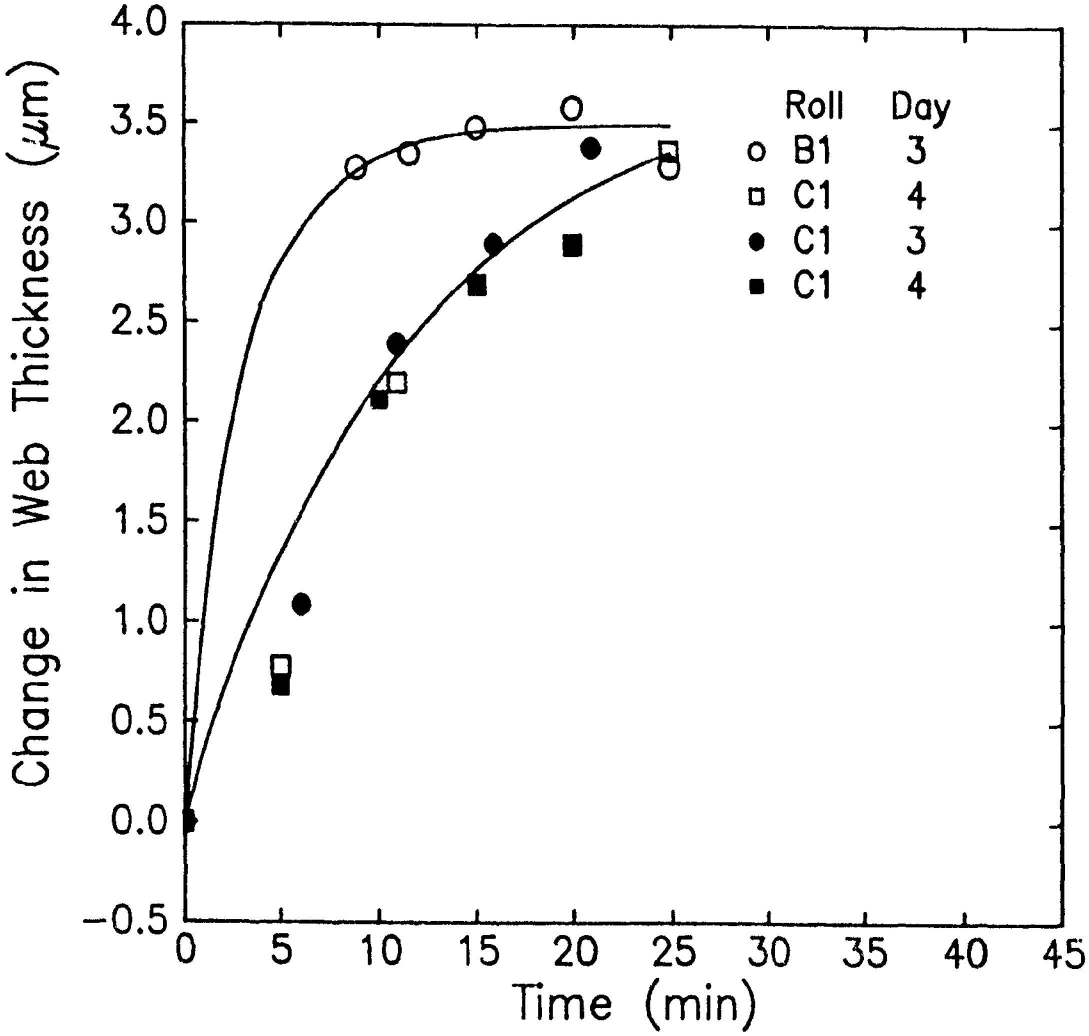

Figure 6.9 Paper thickness changes with a control air jet at various locations in the first stack: Days 3 and 4.

day 3. The response of Roll C1 is slightly stronger on day 1, Figure 6 7, most likely as a consequence of some difference in operating conditions of the paper machine and calenders. The two measurements made on Roll D1 on day 2, Figure 6.7, are in very good agreement. In summary, satisfactory reproducibility of measurements made on the same day and on different days is establisned.

A further illustration of the relative effectiveness of the various nozzle locations is snown in Figure 6.10. At t = 0 the automatic calender control cooling system was turned off at the axial region being considered and the web thickness allowed to drop. After 10 minutes the test nozzle was moved to position C1, and thereafter at periods of approximately 10 minutes the nozzle was moved to a new roll but at the same axial position. The four positions tested, two in each stack, corresponded to the placement of the calender control air showers in this machine. With the test nozzle, only locations in the first stack are effective for control, i.e. produce increases in the web thickness, while the two positions in the second calender stack are totally ineffective. While it is difficult to measure roll deformation directly, roll surface temperature changes on two similar calender rolls indicates the relative deformation of the rolls. Axial roll surface temperature profiles were measured immediately before and after cooling air was applied with the control test nozzle on Rolls C1 and C2 on day 1. As the results, shown in Figure 6.11, indicate that the magnitude of temperature change achieved on both rolls was similar, the magnitude of roll deformation would likewise have been similar. Yet the change in paper thickness achieved with Roll C1 was much larger than that achieved with Roll C2.

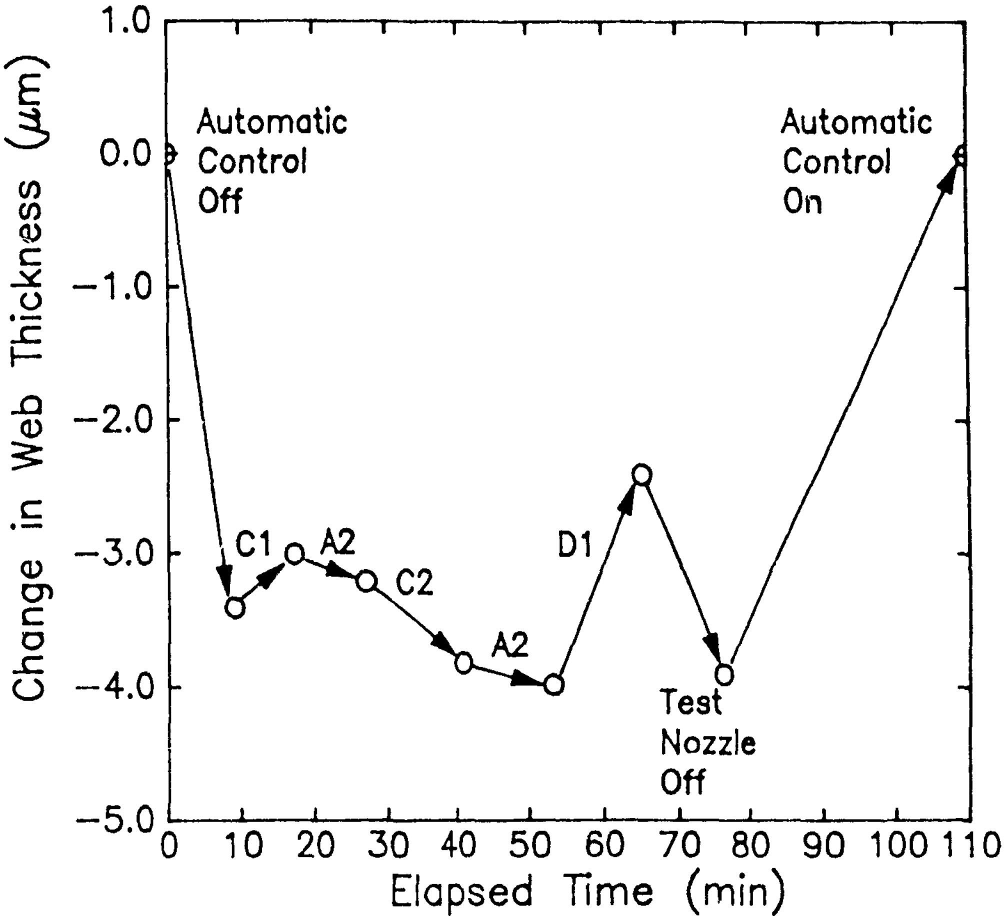

Figure 6.10 Paper thickness changes with the [illegible] air jet at various locations

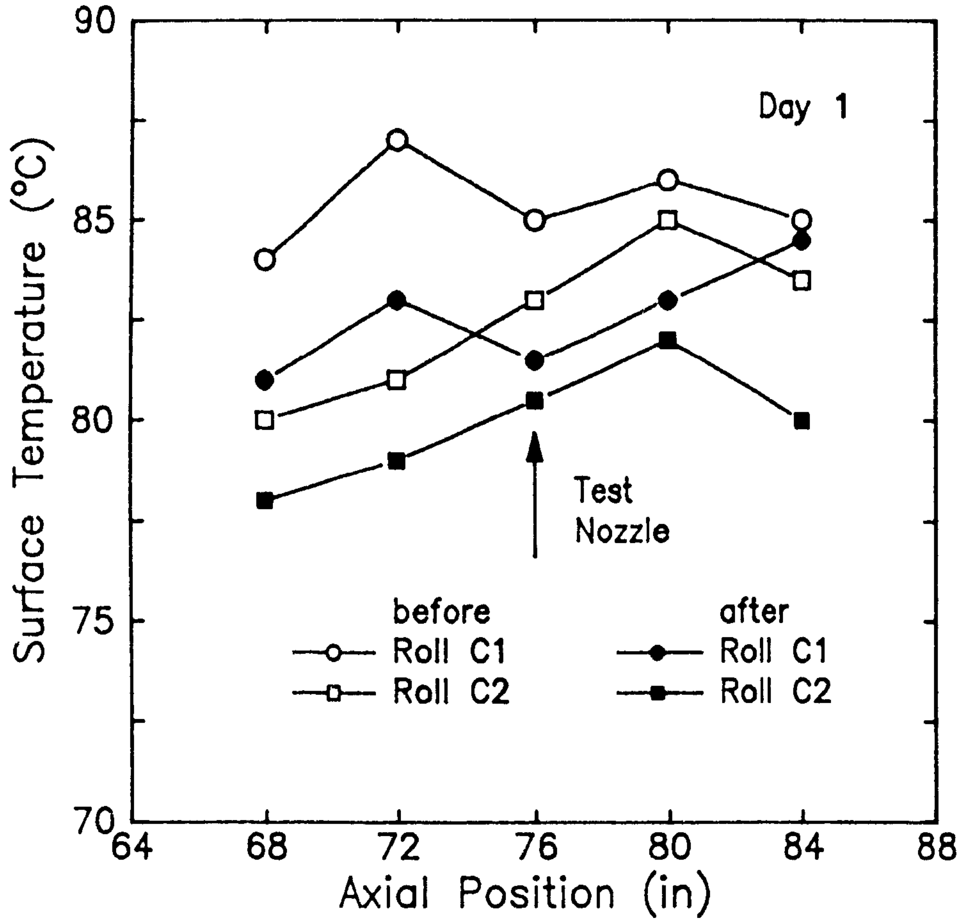

Figure 6 11 Roll surface temperature profiles before and after application of the control air jet.

6.5 Discussion

The web thickness response, Figures 6 7, 6 8 and 6 9, to the standardized control change is for rolls that differ in four ways, i e in two aspects of position and two aspects of roll geometry With respect to position, the rolls differ as to location within a stack and which of the two stacks As to geometry, rolls differ in diameter and in shell thickness. Moreover, there are two components to the control response, i.e. the steady state limit and the rate of approach to this limit. These two aspects of the control response are now analyzed relative to the four variables, two concerning position and two concerning roll geometry.

The most pronounced aspect of the results is the very low response for rolls located in the second stack, Figure 6.8 calender roll surface temperature measurements, Figure 6.11, confirm that temperature response, and hence the deformation response, of rolls in the first and second stack are indistinguishable Thus the weak response in the second stack is a consequence of the small potential for thickness reduction in this stack. As can be shown using the calendering equation of Crotogino et al.[1980, 1983], when two identical calender stacks are used in series the reduction in average thickness in the second stack is negligible near the top, and even near the bottom, thickness reduction is only small. Effective local control of thickness can only be accomplished in nips which have potential for significant reduction in average bulk. If the second stack was operated at higher nip loads, significant reduction in average bulk would occur near the bottom of the second stack. Under these conditions, actuators located near the bottom nips of the second stack would be most effective, but the present study clearly shows that CD local control should be carried out on the first calender stack.

Another striking aspect of the results is the demonstrated low effectiveness of calender control when applied to the king roll, Figure 6.7 This finding contradicts the recommendations of Lyne et al [1976] and Mitchell and Sheahan[1978] that the king roll is the preferred location The conclusions of Lyne et al appear to be the consequence of the lack of consistent test conditions on the different rolls in their experiments and to differences in design of these rolls, rather than to roll position in the stack. They supported their conclusion with the argument that for thickness corrections to be final, web thickness control should be performed on the king roll. This argument is not valid because corrections performed by control on the queen roll are just as final. Moreover, any local change in diameter of the king roll affects only one nip while the same diameter change on all other rolls effects two nips. This intrinsic feature places calender control on the king roll, and by extrapolation, the top roll, at a severe disadvantage relative to that on the adjacent rolls.

The theoretical study of local thermal deformation of calender rolls under CD control conditions by Journeaux[1990] shows that for rolls of the same diameter, unheated rolls with thin shells have a larger deformation than heated thick-walled rolls. The king roll on most calenders is a large diameter variable-crown roll, a favorable design for good control response. The complete lack of response from Roll A, a variable-crown roll, Figure 6.8, establishes that this design advantage is insufficient to compensate for the double disadvantage of location, i e the king roll position, on the second stack. All subsequent discussion therefore relates to control alternatives on the first calender stack

Figures 6.7 and 6.9 indicate that, for the same control change, the steady state web thickness response with control on the king roll was only 1/4-1/3 of that with control effected on one of the rolls immediately above it. This is well beyond the factor of 2 difference that might result from a local change in diameter of the king roll affecting only a single nip instead of two nips as for the other rolls. Roll geometry differences must therefore be the source of the response difference beyond that associated with being the last roll in the stack. The two factors differentiating this king roll from rolls higher in the stack in are.

(i) it is a solid roll, and

(ii) it is of much higher diameter - 56% larger than the queen roll and double the size of the other rolls.

In his study of the local thermal deformation of calender rolls under CD control conditions, Journeaux[1989] has shown that, for the same control change, the steady state thermal deformation of solid rolls decreases with increasing roll diameter. Thus the low web thickness response associated with being the last roll in the stack and therefore acting on but a single nip, is further reduced because of the much larger diameter of this king roll relative to the rolls above it.

When rolls of identical geometry and thermal condition in the first calender stack are subjected to the same control change, Figure 6.7 shows that the roll in the position two rolls above the king roll, Roll C1, yields a steady state web thickness change slightly larger than the roll located three rolls, Roll D1 above the king roll, and 3.5 times larger than the deformation on Roll F1. This finding contradicts the results of the theoretical study by Fjeld and Hickey[1981], which indicate that the control response decreases the lower the roll is located in a stack. Since the trend of control sensitivity with roll position in a stack as reported here is based on direct measurements with a mill calender, the contrary prediction of Fjeld and Hickey, based on a control theory analysis, is evidently in error.

A good CD control system is characterized both by a large change in local web thickness at steady state after a control actuator change, the criterion used in the above discussion, and by a fast response to an actuator change. The present set of measurements on the first calender stack, Figures 6.7 and 6.9, indicates that for all but one of the combinations tested, 50% of the steady state response occurs in about 6-7 minutes. The interesting exception is that, for the control jet located on the queen roll, Roll B1 on Figure 6.9, 50% of the steady state response occurs in only about 2-3 minutes. Comparing control on this queen roll to that on the roll immediately above it, this large difference in dynamic response contrasts with the small difference in steady state response, Figure 6.9. Relative to the rolls located higher in the stack this queen roll differs in two ways, i.e. it has a larger diameter, 457mm compared to 356mm, and a larger shell thickness, 179mm compared to 128mm. The numerical study of Journeaux[1990] on local thermal deformation of calender rolls found that the deformation time constant for a heated roll with a cooling control jet, i.e. the conditions of the mill calender of the present investigation, was fairly insensitive to roll diameter but decreased substantially with smaller shell thickness. This trend is opposite of that observed in this study. It seems unlikely that the improved response time observed with control performed on the queen roll would be due entirely to its position in the stack. Unfortunately, the difficulty in placing the impingement jet on the queen roll precluded a replicate being performed at that position and this potentially interesting finding must remain unsubstantiated.

6.6 Conclusions

Experiments on the double calender stack of a production newsprint machine made to determine the most suitable position for CD control actuators on the rolls of this calender led to the following conclusions:

1. Measurements of control sensitivity made on a calender in a mill have the advantage of corresponding directly to operating conditions in industrial practice, in contrast to published theoretical analyses or measurements on laboratory calenders The associated disadvantage of these mill calender measurements is that interpretation of such results is complicated because the two aspects of control response, steady state and dynamic response, are affected by two position variables (which of two stacks and roll position within a stack) as well as by three design variables (roll diameter, shell thickness, and whether heated or unheated).

2 The king roll and the top roll in the stack were shown to be the poorest choices for the placement of control actuators Control on these rolls suffers from the disadvantage that only a single nip is affected while all other rolls affect two nips

3. When two identical calenders are used in succession, the actuators should be placed on the first stack as very little local control of web thickness is obtained in the second stack The second stack might be suitable only if it was operated at much higher nip loads than the first stack. Subsequent conclusions relate therefore to

control on the first calender stack.

4 The queen roll and the rolls immediately above it produce the strongest steady state response to a control change. When the actuators are placed on rolls higher in the calender stack, which in this mill calender are of identical design and thermal condition, the steady state response with control on the second roll above the queen roll is slightly less than for the roll immediately above the queen roll.

5. When choosing the location for control actuators it is essential to consider the several calender roll design variables noted in item 1 For example the results of the present mill calender measurements combined with the theoretical study of Journeaux indicate that locating control actuators on an unheated thin walled roll (e g. a variable-crown roll) situated above the queen roll would be superior to local CD control effected on a thick-walled queen roll

CHAPTER 7

CONCLUSIONS

7.1 Contributions to Knowledge

1. Applicability of published impingement data to the calender control problem

It is demonstrated that the published data on impingement heat transfer for axisymmetric jets, usually with flat, stationary impingement surfaces, is generally applicable to the calender control problem, with a cylindrical impingement surface rotating at high speed, provided the entrainment of ambient air is properly treated

2. Effect on impingement heat transfer of entrainment by unconfined jets

Entrainment of ambient air by unconfined, axisymmetric jets, as used for calender control, can reduce impingement heat transfer by 65% when the absolute jet to ambient temperature difference, $|T_j - T_a|$, is equal to the absolute jet to impingement surface temperature difference, $|T_j - T_s|$. This study establishes that the entrainment factor, F, the ratio of those two temperature differences

$$F = \frac{T_j - T_a}{T_j - T_s}$$

scales the effect on impingement heat transfer of entrainment of ambient fluid by unconfined and confined jets.

3 Effect of impingement surface motion· axisymmetric impinging jets

The absence of a significant effect of surface motion on heat transfer under axisymmetric impingement jets was documented for impingement surface speeds up to the high levels relevant to paper machine calenders. This finding is in sharp contrast to the strong effect of impingement surface motion and the accompanying air flow on the heat transfer performance of slot jets measured by Polat[1988] and van Heiningen[1982]. Polat observed that for slot jets, on a rapidly moving impingement surface, $M_{vs} = 0.34$, average heat transfer was about 25% lower than that for a stationary surface. The present study, using axisymmetric jets, found that impingement surface motion had no significant effect on heat transfer over the range of the nondimensional surface motion parameter from effectively zero up to $M_{vs} = 0.64$.

4 Effect of jet orientation

The effect on average heat transfer of jet orientation relative to the rotating cylinder was found to be negligible over the range of the variables considered: i.e. circumferential impingement position from 60° to 120°, relative to the out-going nip, and nozzle inclinations from -45° to 35°, relative to impingement normal to the surface. In the case of circumferential impingement position, provided that the jet center line remains at least 10d from the in-going or out-going nip, no effect of position would be expected. As for nozzle inclination, a slight maximum in average heat transfer is apparent at $\psi = 0^{\circ}$ (normal to the surface) for $H/d = 2$ but this maximum does not appear for nozzle spacings of $H/d = 4$ or higher.

5. Comprehensive correlations for heat transfer Unconfined jets

Local and average heat transfer under unconfined axisymmetric jets impinging on a moving surface were determined for the range of variables:

$$1 \le H/d \le 8$$
$$22000 \le Re \le 118000$$
$$-0.1 \le F \le 1.35$$
$$S/d = 4,\ 8$$

Correlations were obtained for stagnation and average heat transfer under those conditions. In correlations for average heat transfer, two basically different averaging areas were used The radially averaged Nu_r gives an average rate relative to the geometry of the jet nozzle, as is commonly used in the axisymmetric impinging jet heat transfer literature. The circumferentially averaged $\overline{Nu}_c$ provides the average rate relative to the geometry of the impingement surface, a cylindrical surface in the present study. Of these two bases for an average, Nu_c is the average which is most relevant to the design of calender control systems.

6. Effect of impinging jet confinement

Confinement of the impingement flow by a plate coincident with the nozzle exit and parallel to the roll surface can produce substantial improvements, by as much as doubling the heat transfer This increase in heat transfer by a confinement surface results from reduction of the strongly deleterious effect of thermal entrainment for temperatures in the range relevant to paper machine calender control. The extent of the confinement surface on either side of the nozzle center line should be as large or larger than 5.75d, the maximum extent tested in the present study. In existing calender control systems using confined air jets, the addition of a confinement plate of width ±5.75d would improve average heat transfer by approximately 80% for H/d = 1, by 33% for H/d = 2, and by 15% at H/d = 4. Wider confinement plates, particularly on the downstream side of the nozzle, could give even greater improvement.

7. Comprehensive correlations for heat transfer: Unconfined jets

Local and average heat transfer under confined axisymmetric jets impinging on a moving surface were determined for the following range of variables:

$$1 \le H/d \le 4$$
$$60000 \le Re \le 118000$$
$$0.95 \le F \le 1.35$$
$$Y/d = 0,\ 3,\ 4.5,\ 5.75$$
$$S/d = 4,\ 8$$

Correlations for the circumferentially averaged heat transfer are provided.

8. Comparison of a staggered array with an in-line row of nozzles

The switch from an in-line row of nozzles to a staggered configuration for the nozzles results in a higher heat transfer rate and a correspondingly higher jet heat transfer efficiency. For conditions typical in the calender control application, measured heat transfer rates for the staggered array were higher by 22% and 33% for unconfined and confined jets respectively.

9. Thermal deformation of calender rolls under control actuators

The steady-state and unsteady-state thermal deformation of calender rolls under control actuator conditions was determined by numerical simulation using finite volume and finite element techniques.

The effect of calender roll design and of control system operation was thereby established. The only previous numerical study required use of an assumed surface temperature profile, which in practice is an unknown dependant variable. A key feature of the present simulation is the avoidance of that assumption by linking the thermal deformation directly to the heat transfer characteristics of the control actuator being used.

10. Steady-state thermal deformation of calender rolls

The local steady state deformation of calender rolls was characterized in the radial direction as roll deformation, Δr, and its maximum value, the peak deformation, Δr_p, and in the axial direction by the characteristic width of this deformation, $W_{\Delta r}$. The simulation covers a wide range of calender roll design parameters, including roll diameter, shell thickness, unheated rolls and internally heated rolls. As for the system of control actuators, the simulation investigated the use of confined and unconfined air jets of various spacings as control actuators, as well as various actuator heat transfer profiles, the limit being effectively flat profiles as would correspond to the use of electrical heaters as control actuators.

The findings indicate that the most desirable steady state control characteristics are provided by unheated rolls of small diameter and of minimum practical shell thickness.

The placement of calender profiling equipment on adjustable crown rolls should not be discounted, as has been traditional practice. The performance of a control system installed on a hydraulic crown roll is difficult to calculate precisely, but in view of the thin shell wall and adiabatic internal boundary condition, an adjustable crown roll may be an optimal choice for positioning the control system. By contrast, the high internal heat transfer characteristics of peripherally bored, heated rolls make them unsuitable for cross machine direction calender control.

Although the simulation was demonstrated for local control by impinging jets, the simulation is sufficiently general to be readily adapted for use with other control actuators such as induction heaters or water mist coolers.

11 Calender control performance index

Because of the trade-off in calender control between the desirability of a high peak roll deformation, Δr_p, and a low width of deformation, $W_{\Delta r}$, a criterion is proposed for the evaluation of alternative roll designs. The recommended characteristic, denoted the calender control performance index, I_c, is the ratio $W_{\Delta r}/\Delta r_c$, i.e. the width of deformation in meters per micron of peak deformation. Thus a good system for calender control, an unheated calender roll with a diameter of 400mm and a shell thickness of 120mm, gives a performance index of about I_c = 35m/μm while a poor control system, an heated calender roll with a diameter of 600mm and a shell thickness of 120mm, gives values of this control index in the range I_c = 86m/μm.

12 Addition of confinement plate to existing control system

For conditions measured in the present study, a switch from unconfined to confined jets in an existing calender control system using unconfined jets could yield a 33% increase in the heat transfer, for a nozzle to calender roll spacing, H/d, of 2 (even higher if closer H/d are possible), almost as large an improvement in peak roll deformation, Δr_p, with no loss in the calender control performance index, I_c. The addition of a confinement surface to many existing industrial calender control systems involving unconfined jets would be a relatively easy and inexpensive method to obtain a substantial improvement in calender control performance.

12. Unsteady-state thermal deformation of calender rolls

The numerical simulation shows that for rolls of equal diameter and shell thickness, the thermal deformation 10 minutes after the control action is taken, is always greater for unheated rolls. For heated rolls there is a broad optimum where a heated roll with a large shell thickness should have a larger Δr when compared to a solid roll of equal diameter.

13. Optimum actuator-to-actuator spacing

The simulation documents a negligible control advantage [illegible] actuator-to-actuator spacing, S, of less than 0.2m, while closer spacings yet have the disadvantage of wasting a large amount of air.

The concern reported in previous work as to the production, between impinging jets, of a "bumpy" roll, reflecting the axial nonuniformity of the actuator heat transfer profile, is shown in the present study to be groundless. Previous studies underestimated the magnitude of axial heat conduction in calender control systems.

14. Positioning of control actuators on calender stacks

When two identical calenders are used in succession, as is the practice on some paper machines, the actuators should be placed on the first stack as very little local control of web thickness is obtained in the second stack. The second stack might be suitable only if it was operated at much higher nip loads than the first stack. Subsequent conclusions relate therefore to control on the first calender stack.

Tests carried out on an industrial paper machine calender stack indicate that the bottom roll (king roll) and the top roll are the poorest choices for the placement of control actuators. Control on these rolls suffers from the disadvantage that only a single nip is affected while all other rolls affect two nips.

At intermediate positions, the "queen" roll, second from the bottom, and the two rolls immediately above it, produced the strongest steady state response. With identically designed calender rolls, the steady-state response decreased with position above the queen roll, with the fourth roll above the queen roll yielding only 30% of the response of the roll immediately above the queen roll.

When choosing the location for control actuators it is essential to consider the several calender roll design variables (roll diameter, roll thickness, and whether heated or unheated). For example, the results of the present study indicate that locating control actuators on an unheated thin walled roll (e.g. a variable-crown roll) situated above the queen roll would be superior to the local control effected on a thick-walled queen roll.

7.2 Recommendations for Future Work

1. The design of confinement plates should be investigated to optimize the heat transfer in the calender roll control configuration.

2. The flow and temperature domain associated with the entrainment flow, both with the jet and with the impingement surface motion, should

be measured.

3. The performance characteristics of evaporative cooling as a calender control system should be determined in order to evaluate their usefulness.

4. The compressibility of paper under the dynamic conditions experienced in a calender nip should investigated. This information would allow the direct coupling of local calender roll deformation to resulting in-nip and recovered paper thickness

5 The internal heat transfer characteristics of internally heated calender rolls need to be adequately documented

REFERENCES

Baines W.D and Peffer J.F., "Shear Stress and Heat Transfer at a Stagnation Point", Int J Heat and Mass Transfer, 19, 21-26, [1976]

Black J. and Hardisty H., "Heat and Mass Transfer in Ink Drying and Infra-Red Dryness Measurement", 6th Thermodynamics and Fluid MEchanics Conv , Univ of Durham, [1976]

Boissevain M , "Dewater Southern Flattens Caliper Profiles with Calender Control Actuator", Paper Trade J., 170, [1986]

Boley B A , "Survey of Recent Developments in the Fields of Heat Conduction in Solids and Thermo-Elasticity", Nucl. Eng. and Design, 18, 377-399, [1972]

Boley B A and Weiner J.H , "Theory of Thermal Stresses", Wiley (New York, New York), 272-306, [1960]

Brierly P , Hopkins G and J D Peel, "Thermal Deformations of Machine Calender Rolls", Proc Symp. on Calendering/SuperCalendering of Paper (Manchester, England), Paper 5.3, [1975]

Bryan W P , "How to Get More Cooling from Calender Stack Cooling Systems", Paper Trade Journal, Jan 10, 36-37, [1972]

Chapman D L T and Peel J.D , "Calendering Processes and the Compressibility of Paper: Part 1", Paper Technol., 10, 2, T116-124, [1969]

Cherewick H R and Walker O.J , "Automatic Reel Building", Am. Peper Ind , 56, 3, 26-30, [1974] Colley J. and Peel J D , "Calendering Processes and the Compressibility of Paper: Part 2 - The Effects of Moisture Content and Temperature on the Compressive Creep Behaviour of Paper", Paper Technol , 13, 5, T166-173, [1972]

Crotogino R H , "Towards a Comprehensive Calendering Equation", JPPS, 6, 4, TR89-94, [1980]

Crotogino R.H., "Machine Calendering - Recent Advances in Theory and Practice", Trans. Tech Sect. CPPA, 7, 4, TR75-87, [1981]

Crotogino R H. and Gratton M.F , "Hard-nip and SOft-nip Calendering of uncoated Groundwood Papers", Pulp Paper Can , 88, 12, T461-T469, [1987]

Crotogino R H., Hussain S M and McDonald J D , "Mill Application of the Calendering Equation", JPPS, 9, 5, TR128-133, [1983]

Crotogino R H , Weiss G R , Visentin J and Dulas L "State of the Art in CD Calender Control",

Crow S.C and Champagne F H "Orderly Structure in Jet Turbulence", J Fluid Mechanics, 48, part 3, 547-491, [1971]

D'Amato D A , "Temperature Controlled Rolls - One Key to Successful Calendering Operation", Paper Trade Journal, 164, 19, 41-46, [1980]

den Ouden, C. and Hoogendoorn C J , "Local Convective Heat Transfer Coefficients for Jets Impinging on a Plate, Experiments Using a Liquid Crystal Technique", Int. Heat Transfer Conf , Tokyo, Paper MA 2 5, [1974]

Derezinski S J., "Digital Computer Simulation of Paper Calendering", Proc Tappi Paper Finishing and Converting Conf , [1981] Donaldson, du P.C. and Snedeker, R.S., " A Study of Free Jet Impingement: Part I", J. Fluid Mechanics, 45, part 2, 281, [1971]

Donaldson, du P.C., Snedeker, R.S. and Margolis, D.P., " A Study of Free Jet Impingement: Part II - Free Jet Turbulent Structure and Impingement Heat Transfer", J. Fluid Mechanics, 45, part 3, 477, [1971]

Emery, A.F.and Carson, W.W., "An Evaluation of the Use of the Finite Element Method in the Computation of Temperature", J. Heat Transfer, 94, 5, 136-145, [1971]

Fechner, G. "Warmeubertragung bei Senkrencht auftreffendem Strahl an der Platte und am Rohr", Dissertation T.U. München, [1971]

Fjeld, M and Hickey W P., "Die Querprofilregelung am Kalander: Praxisbezogene Betrachtungen über den Einstaz von Lüftdusen", Das Papier, 30, 1, 4-13, [1984]

Florschuetz L.W. and Metzger D.E., " Effects of Initial Crossflow Temperature on Turbine Cooling with Jet Arrays", Heat and Mass Transfer in Rotating Machinery XIV International Centre for Mass Transfer Symp., Dubrovnik, Yugoslavia, [1982]

Folayan C., "Impingement Cooling", Ph.D. Thesis, Imperial College, London, [1976]

Gardon, R. and Cobonpue J., "Heat Transfer Between a Flat Plate and Jets of Air Impinging on It", Proc. 2nd Int. Heat Transfer Conf., ASME, 454-460, [1962]

Gardon R. and Akfirat J.C., "The Role of Turbulence in Determining the Heat Transfer Characteristics of Impinging Jets", Int. J. Heat Transfer, 8, 1261-1272, [1965] Gardon, R. and Akfirat J.C., "Heat Transfer Characteristics of Impinging Two-Dimensional Air Jets", J. Heat Transfer, 88, 101-108, [1966]

Goldstein, R.J. and Franchett M.E., "Heat Transfer From a Flat Surface to an Oblique Impinging Jet", J. Heat Transfer, 110, 84-90, [1988]

Haglund L. and Robertson G., " Local Thickness Reduction in a Calender Nip - An Experimental Study", Svensk Papperstidning, 14, 521-530, [1974]

Haglund L., "Profile Model for a Calender Nip", Proc. Symp. on Calendering/SuperCalendering of Paper (Manchester, England), Paper 5.1, [1975]

Hardisty H., " Drying Printed Ink Coatings by Impinging Air Jets", Drying '80, vol. I, Hemisphere Publishing Corp., 367-375, [1980]

Higham J.D., "Therma-Jet Exceeds Performance Targets in Caliper Control", Paper Age, 1, 24-25, (Jan 1986]

Ho, C.Y. et al., "Thermophysical Properties of Polystyrene and Poly (Vinyl Chloride)", Cezairliyan, A. ed., Proceedings of the Seventh Symposium on Thermophysical Properties, May 10-12, Gaithersburg, MD, (ASME), 198-218, [1977]

Holik H., "Zur Prallströmtrocknung von Papier", Das Papier, [illegible], 6, 423-429, [1971]

Hollworth, B.R. and Gero L.R., "Entrainment Effects on Impingement Heat Transfer: Part II - Local Heat Transfer Measurements", J. Heat Transfer, 107, 910-915, 1985

Hollworth, B.R. and Wilson S.I., "Entrainment Effects on Impingement Heat Transfer Part I - Measurement of Heated Jet Velocity and Temperature Distributions and Recovery Temperature on Target Surface", J. Heat Transfer, 106, 797-803, 1984

Huang, B., "Heat Transfer under an Inclined Slot Jet Impinging on a Moving Surface", Ph.D Thesis, Chem Eng. Dept., McGill University, [1988]

Hyrak P., "Heat Transfer from a Row of Jets Impinging on a Concave Semi-Cylindrical Surface, 6th Int. Heat Transfer Conf., 2, 67-72, [1968]

Ioffe A.V and Ioffe A.F., "Measurement of the Thermal Conductivity of Semiconductors in the Vicinity of Room Temperature," Soviet Physics, 3, 11, 2163-68, [1958]

Janett, L C , "Calender Cooling on the Modern Paper Machine", Tappi, 38, 7, 433-436, [1955]

Kahoun, J B , Zurowitch, W. and Newby, L , "System for the On-Machine Measurement and Control of Paper Caliper", Tappi, 48, 7, 60A-65A, [1958]

Kan C E , "A New Caliper Control Actuator - It's Evolution, Process and Application Results", Proc. Tappi Paper Finishing and Converting Conf., [1986]

Kerekes R J , " Speed and Loading Effects in a Calender Nip", Trans. Tech Sect. CPPA, 2, 3, 88-91, [1976]

Kezios S.P., "Heat Transfer in the Flow of a Cylindrical Air Jet Normal to an Infinite Plate", Ph.D. Thesis, Illinois Institute of Technology, [1956]

Koopman, R N. and Sparrow E.M., "Local and Average Transfer Coefficients due to an Impinging Row of Jets", Int. J. Heat and Mass Transfer, 19, 673-683, [1976]

Korger M. and Krizek F., "Mass Transfer Coefficient in Impingement Flow from Slotted Nozzles", Int. J. Heat and Mass Transfer, 9, 337-344, [1966] Korger M. and Krizek F., "Verfahrenstechnik" (Maine), 6, 223-228, [1972]

Larive R. and Lindstrom R., "The Calcoil: A New Approach for Better Cross-machine Control", Pulp Paper Can., 87, 3, T125-T127, [1986]

Lyne, M.B., Haglund L. and Bjelkhagen H , "Control of Machine Calender Roll Diameter with Air Showers - An Experimental Investigation", Svensk Papperstid, 79, 8, 251-284, [1976]

Mackin G.E., Keller E.L. and Baird P.K , "Effects of Calendering Pressure on Sheet Properties", Paper Trade J., 113, 1, 53-61, [1941]

Mardon J., Monahan R E., Carter R A. and Wilder J E., "Dynamic Consolidation of Paper During Calendering and Dynamic Compressibility of Paper", Trans. Symp. Tech. Sect. Brit. Paper and Board Makers Assn, [1965]

Martin H., "Heat and Mass Transfer Between Impinging Gas Jets and Solid Surfaces", Advances in Heat Transfer, 13, Academic Press, [1977]

Maxwell R.W. and Nash K L , "Convective Mass Transfer From Stationary and Moving Surfaces Using a Mercury Evaporation Technique", Int J Heat and Mass Transfer, 16, 385-393, [1973]

Metzger D.E. and Grochowsky L D , "Heat Transfer Between an Impinging Jet and a Rotating Disk", Trans. of ASME, J Heat Transfer, 99, 663-667, [1977]

Mitchell J.G. and Sheahan D K., "The Control of Reel Building with Calender Stack Air Showers, CPPA Tech. Sect., Spring Conf. Jasper, Alberta, [1978]

Murray B.C. and Patten T D., "Heat Transfer Under an Array of Impinging Jets, 6th Int. Heat Transfer Conf., Toronto, [1978] Nakatogawa T., Nishiwaki N., Kiraki M. and Torii K., "Heat Transfer of Round Jets Impinging Normally on a Flat Plate", Int. Heat Transfer Conf , Paris, Paper FC 5 2, [1970]

Obot N.T., "Flow and Heat Transfer for Round Turbulent Jets Impinging on Permeable and Impermeable Surfaces", Ph.D. Thesis, Chem. Eng. Dept., McGill University, [1980]

Patankar S.V., "Numerical Heat Transfer and Fluid Flow", Hemisphere, Washington, D C [1980]

Pelletier L , "Impingement Heat Transfer to a Stack of Rotating Cylinders", M. Eng Thesis, Chem. Eng. Dept., McGill University, [1984]

Pelletier L., Douglas W J.M. and Crotogino R.H., "CD Calender Control with Air Jets - An Experimental Study of Impingement Heat Transfer", J. Pulp Paper Science, 13, 2, 49-55, [1987]

Polat S., "Transport Phenomena Under Jets Impinging on a Moving Surface with Throughflow", Ph D. Thesis, Chem. Eng. Dept , McGill University, [1988]

Popiel Cz O , Tuliszka E and Buglaslawski O., "Heat Transfer from a Rotating Disk in an Impinging Air Jet", Int. Heat Transfer Conf., Tokyo, [1974]

Poreh M. and Cermak J E , "Flow Characteristics of a Circular Submerged Jet Impinging Normally on a Smooth Boundary", 6th Mid-Western Conf. on Fluid Mechanics, Univ. of Texas, 198, [1959]

Saad N.R., "Flow and Heat Transfer for Multiple Impinging Slot Jets", Ph.D. thesis, Chem. Eng Dept , McGill University, [1981] Schauser J.J. and Eustis R.H., "The Flow Developement and Heat Transfer Characteristics of Plane Turbulent Impinging Jets, Technical Report No. 3, Mech. Eng Dept., Stanford Univ , [1963]

Schlunder E.U. and Gnielinski V., "Warme-und Stoffubertragung zwishen Gut und aufprallendum Dusenstrahl, Chemie-Ingenieur-Technik, 39, 9/10, 578-584, [1967]

Streigel S.A. and Diller T.E., "The Effects of Entrainement Temperature on Jet Impingement Heat Transfer", J. Heat Transfer, 106, 27-33, [1984]

Subba Raju K. and Schunder E.U., "Heat Transfer Between an Impinging Jet and a Continuously Moving Flat Surface", Warme-und Stoffubertragung, Thermo- and Fluid Dynamics, 10, 131-136, [1977]

Tani J. and Komatsu Y., "Impingement of a Round Jet on a Flat Surface", 11 Int. Conf on Applied Mech , 672, [1966]

van Heiningen A.R P , "Heat Transfer Under an Impinging Slot Jet", Ph D Thesis, Chem. Eng. Dept , McGill University, [1982]

Valentin R A and Carey J J, "Thermal Stresses and Displacements in Finite Heat Generating Circular Cylinders", Nucl Eng and Design, 12, 277-290, [1970]

Verkasalo M , "Thermo Rolls in Newsprint Calendering", Valmet Application Notes, [1984]

Vlachopoulos J. and Tomich J F., " Heat Transfer from a Turbulent Hot Air Jet Impinging Normally on a Flat Plate", Can J Chem Eng , 41, 462-466, [1971]

APPENDIX A

Signal Noise Reduction

The noise levels in the heat flux sensor signal was reduced to about +/- 10 μV on a peak-to-peak signal of 1 V (after a gain of 2500) by the following measures:

- use of low noise instrumentation
  - a. amplifier with 3 μV rms RTI and 2 mV RTO for a 10 kHz bandwidth.
  - b slip ring assembly with 2 5 μV noise per ring with 12 mA into 350 Ω
- use of low pass filter to remove any noise above the Nyquist frequency
- use of a common ground shared between all instrumentation and equipment.
- use of shielded cables for all inter-instrumentation leads

APPENDIX B

Schematic of the Data Acquisition Program

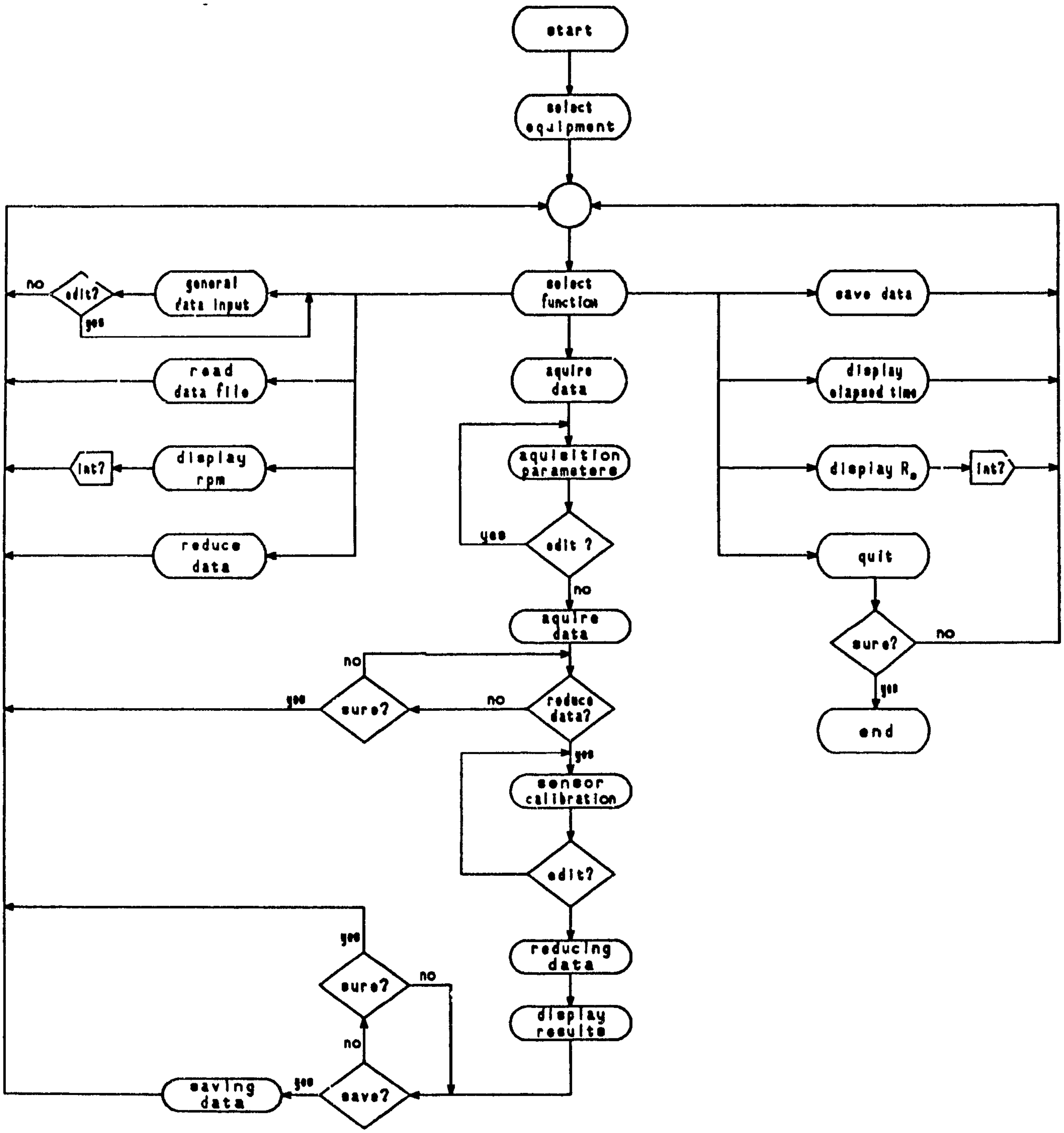

Figure B.1 Schematic of the data acquisition program

APPENDIX C

Thermophysical Properties of Polyvinylchloride

Accurate values of the thermal properties of the substrate were required for the calculation of the surface heat flux. However, the thermophysical properties of PVC are not well documented and the available experimental data for some properties are widely divergent and subject to large uncertainty. Ho et al. [1977] presented a comprehensive compilation and critical evaluation of the available experimental data and recommended values for the thermal conductivity, λ, specific heat, Cp, and thermal diffusivity, α, of PVC with or with only a few percent of stabilizer and plasticizer but without filler. But, since it was not possible to obtain the exact composition of the PVC used in the construction of the model calender stack and the heat flux sensor, it was necessary to determine experimentally the required thermophysical properties.

1. Thermal Conductivity

The thermal conductivity of PVC was determined using the transient method developed by Ioffe and Ioffe [1958]. The test apparatus is shown in Figure C.1. Due to the low conductivity of the PVC the apparatus was modified to improve the accuracy low thermal conductivities by:

i. using a sample with a large surface area to sample thickness, typically with an area of 19 cm^2 and thickness of .2 -.5 cm thick. This maximizes the heat flux, Q, and increases the accuracy of the ΔT measurement.

ii. using a vacuum in the chamber surrounding the sample and upper

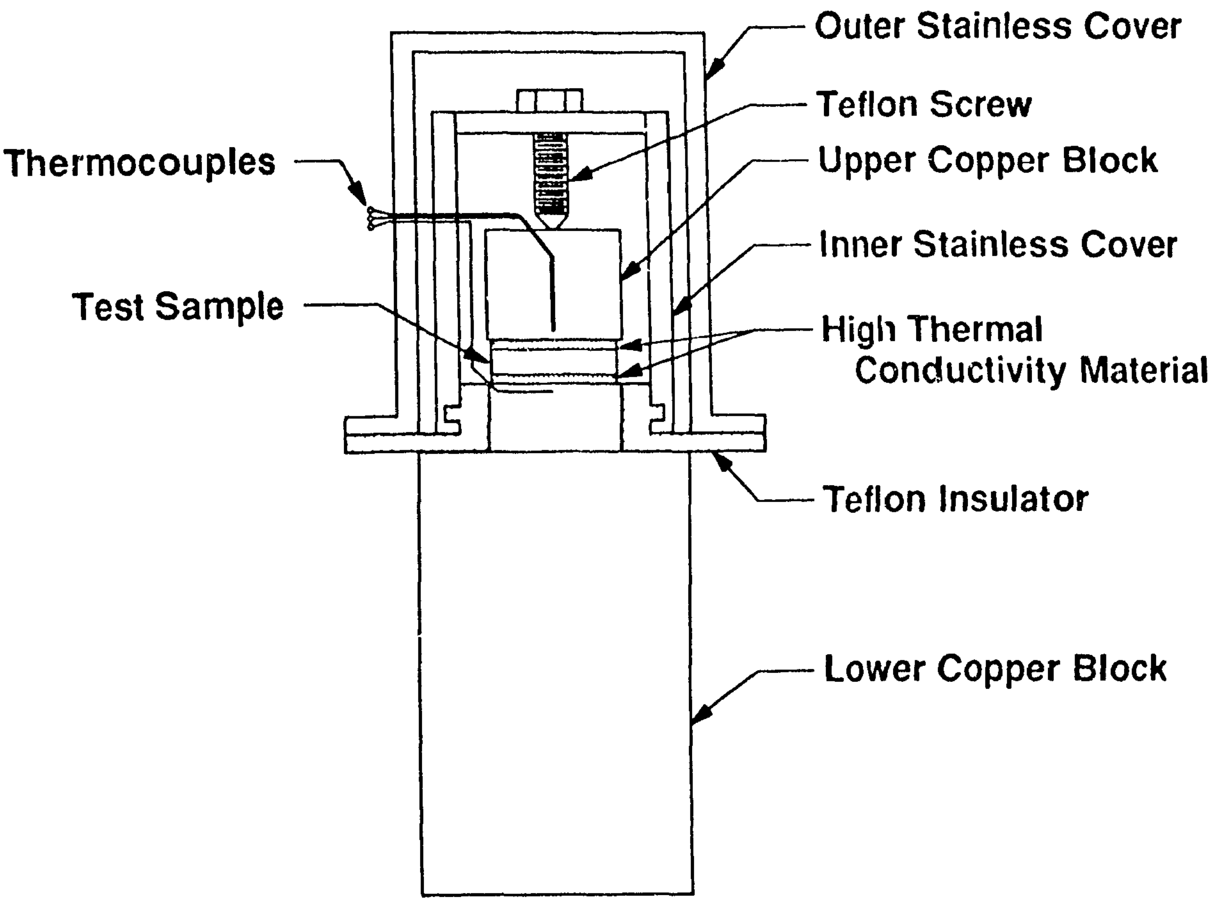

Figure C.1 Test assembly for thermal conductivity measurements using transient method of Ioffe and Ioffe[1958] copper block, minimizing heat losses from the upper copper block through the air spaces.

The experimental procedure used has been described by van Heiningen [1982]. The measurement of λ involves the measurement of the temperature of the upper block, T_u, along with the temperature difference across the sample (T_u-T_l). A typical signal output is shown in Figure C.2. When (T_u-T_l) reaches a maximum (A-B), $\frac{\Delta T_u}{t}/(T_u-T_l)$ remains constant. The slope of the T_u curve during that interval (C-D) is measured and the thermal conductivity, λ, can be calculated using

$$\lambda = \frac{Cp\left(\frac{\Delta T_u}{\Delta t}\right)}{(T_u-T_l)} \left(\frac{L_s}{A}\right) \tag{C.1}$$

where

λ	-	sample thermal conductivity (W/m/°C)
Cp	-	heat capacity of upper block (J/°C)
L_s	-	sample thickness (m)
A	-	sample area (m^2)
T_u	-	temperature of upper block (°C)
T_l	-	temperature of lower block (°C)
ΔT_u	-	temperature change of upper block during time interval, Δt (°C)

The accuracy of the experimental apparatus was verified using Pyrex and teflon samples where the thermal conductivities were found to be 1.14 and 0.23 W/m/K respectively, within 6% of the reported literature values. The reproducability of the experiments was within 5%.

The measurements of λ obtained for PVC are compared with the

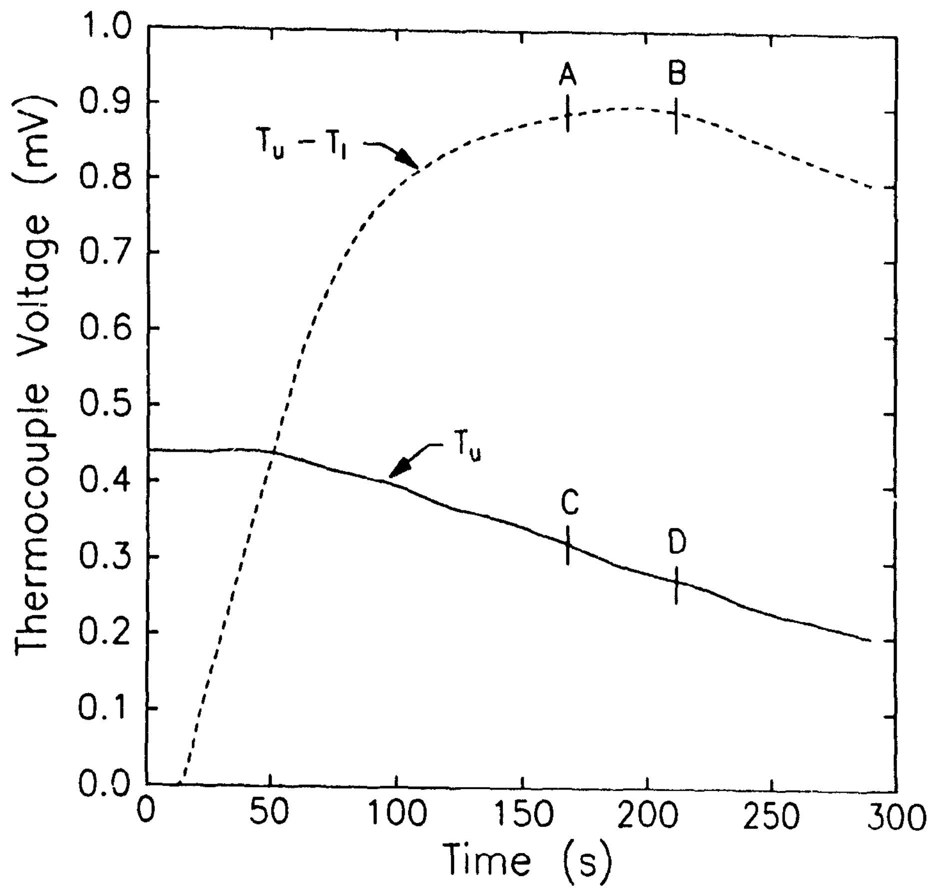

Figure C.2 Typical output from the thermal conductivity apparatus recommended values of Ho et al. [1977] shown in Figure C.3. The reproducability of the experiments was found to be within 3%. The results lie within 3% of the recommended values provided by Ho et al. The temperature dependance of λ over the temperature range of interest, 280K - 320K, was represented using

$$\lambda = 0.128 + 0.0001\,T \qquad (C.2)$$

where λ and T are W/m/K and K respectively.

2. Heat Capacity

The heat capacity of the PVC was determined using a Differential Scanning Calorimeter (DSC) and standard procedures (O'Neill [1966]). The heat capacity versus temperature profile for the range 300K to 350K is shown in Figure C.4. The reference material used for the measurements was synthetic sapphire (Al_2O_3). The temperature dependance of C_p over the temperature range of interest, 280K - 320K, was represented using

$$Cp = -171.7 + 3.75\,T \qquad (C.3)$$

where Cp and T are J/kg/K and K respectively.

3. Density

To obtain a value for the thermal diffusivity, using the heat capacity and thermal conductivity measured previously, the density must be measured. Using weight and volume measurements, the density was found to be $1400 kg/m^3$ with a reproducability of ±2% which is in good agreement

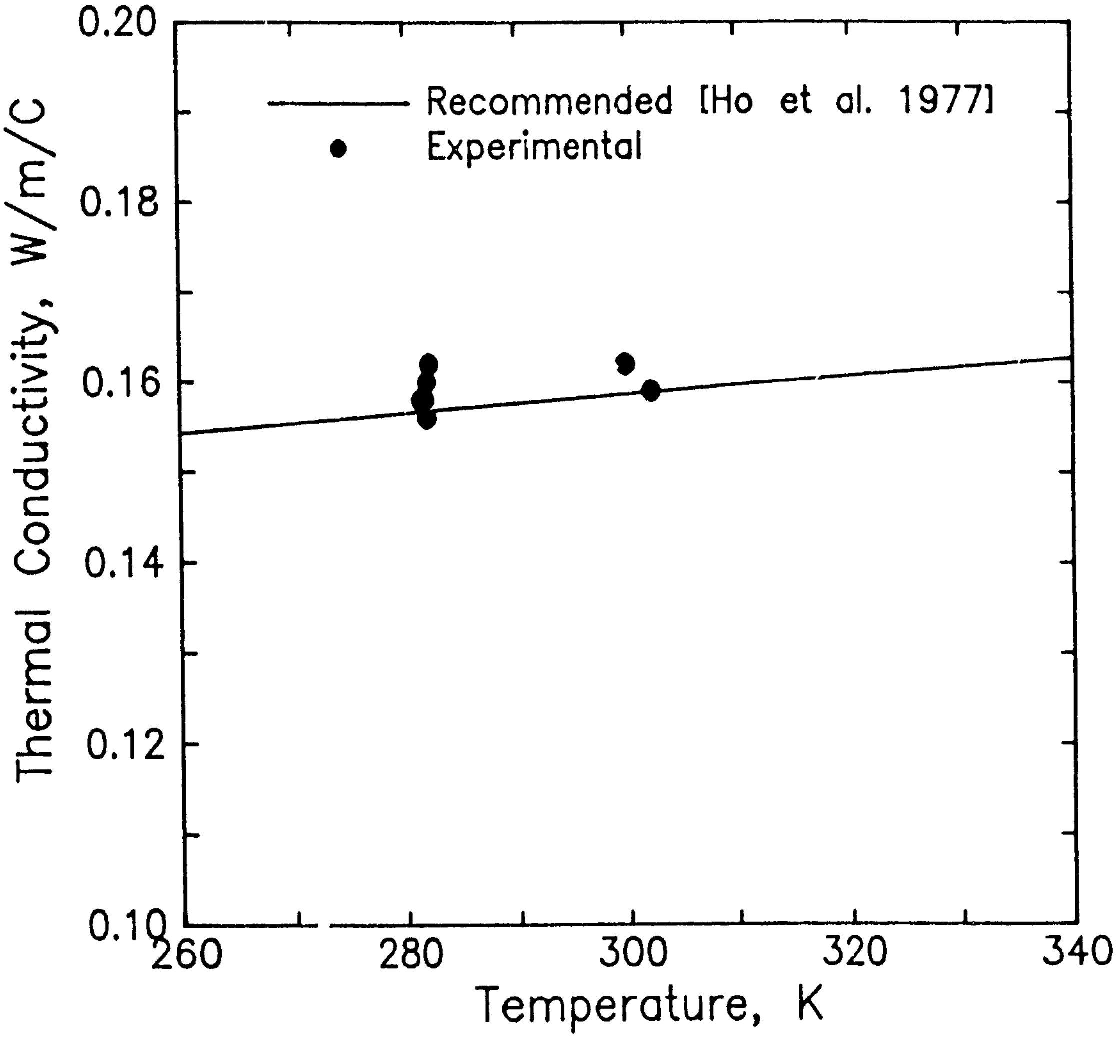

Figure C.3 Measured thermal conductivity of PVC as compared to recommended values

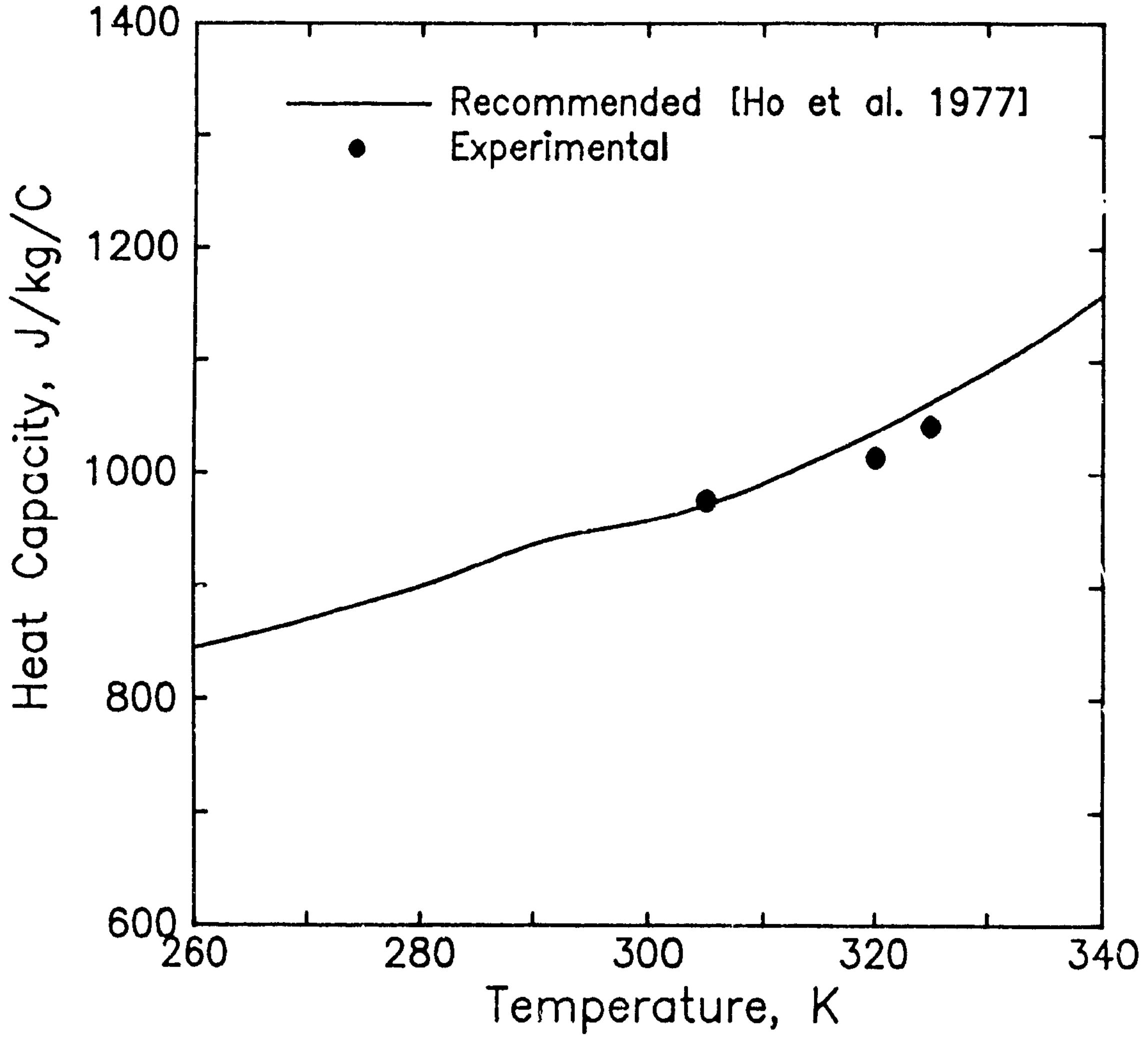

Figure C.4 Measured heat capacity of PVC as compared to recommended values with the recommended values of Ho et al, Figure C 5. The temperature dependance of ρ over the temperature range of interest, 280K - 320K, was represented using

$$\rho = 1492.9 - 0.312\ T \tag{C 4}$$

where ρ and T are kg/m^3 and K respectively.

4. Conclusions

The experimental values compare favorably with the recommended values, indicating either the absence of additives (ie. fillers and/or stabilizers and plasticizers) or that the additives used did not affect the thermophysical properties.

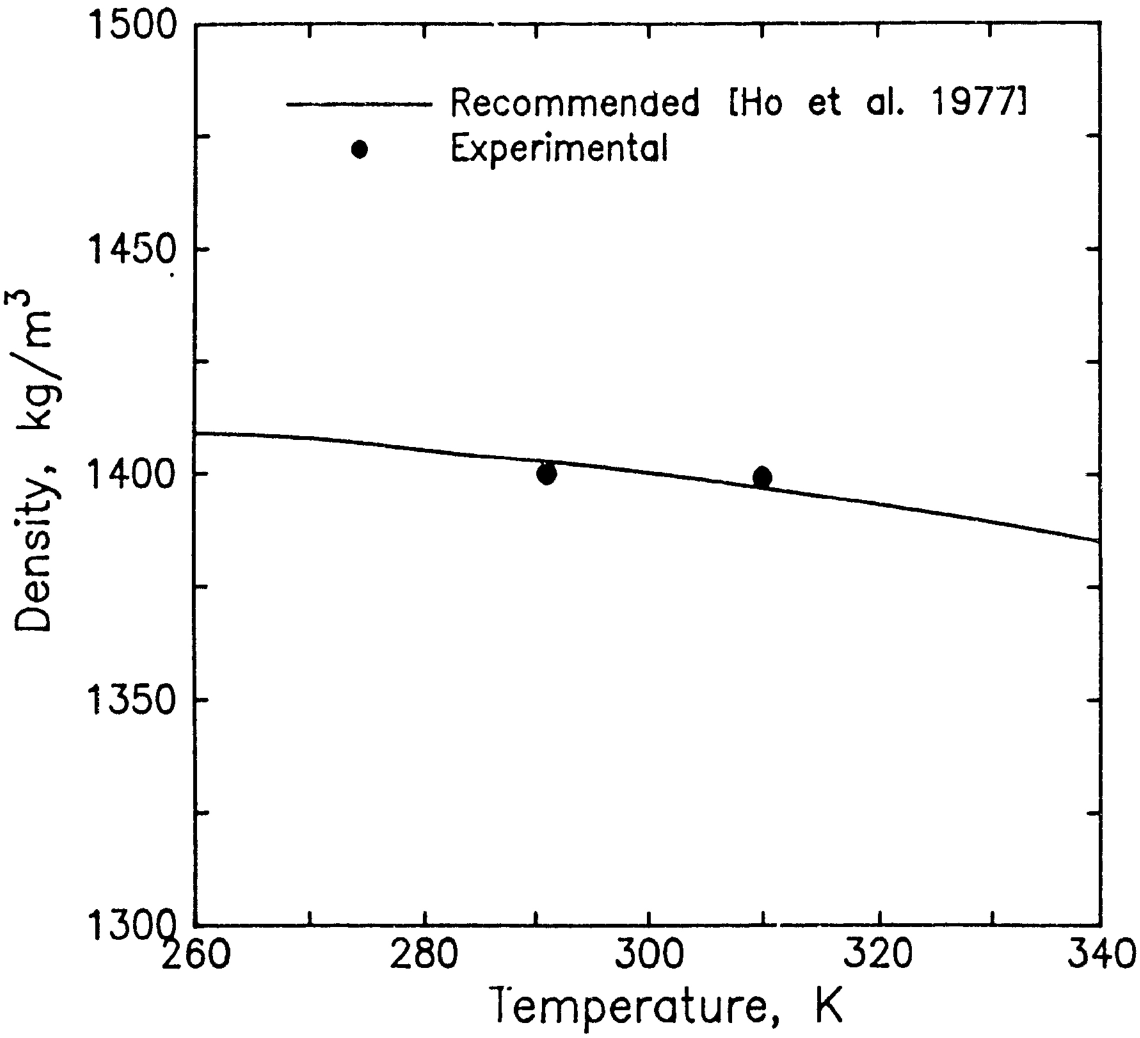

Figure C.5 Measured density of PVC as compared to recommended values

APPENDIX D

Source Code for Finite Volume Unsteady-State Simulation

The finite volume unsteady-state simulation program was written using FORTRAN-77 (Microsoft Fortran version 3.31) and should compile with little or no modification using any FORTRAN-77 compiler.

```
C     PROGRAM NONDIMENSIONAL HEAT TRANSFER IN A CYLINDER
      IMPLICIT REAL*8(A-H),REAL*8(J-Z)
      REAL*8 L
      INTEGER*2 KOUNT1,KOUNT2,M,N,M1,N1,MF,NF,J,curve
      CHARACTER*1 filr1a(12),filr2a(12),filr3a(12)
      CHARACTER*12 FILER1,FILER2,FILER3,FILEN,ftemp
      DIMENSION texpan(50,3),NU(50),f(50)
      DIMENSION XP(50),YP(50),B(50),C(50),D(50)
      DIMENSION TRIGL(3000)
      COMMON/HTCOEF/HP,HI,HNO,HZ1,HZN,FLX,HJ(50)
      COMMON/TEMPER/TJ(50),TJET(50),TIN(50),TP(50),T(50,50,3),TZ1,TZN
      COMMON/PROPERT/K(50),RHO(50),CP(50)
      COMMON/GRIDNO/M,N,M1,N1,R(50),Z(50),DELT
      COMMON/COEF/AE(50,50),AW(50,50),AN(50,50),AS(50,50),
     #            APO(50,50),AP(50,50),B1(2,50),B2(50,2)
      equivalence (filer1,filr1a),(filer2,filr2a),(filer3,filr3a)

C Properties are for grey iron portion of roll
c      kroll=36.34    - Jakko Aro thesis
c      kgrey  = 58.0 \  SHW design technical data
c      kchill = 20.0 /    (date of issue: 1980)
c      cproll=544
c      droll=7334.9
c      clinexp= 11.34e-6
c      Pratio = 0.27

C Initial values for array pointers
      ITOLD=1
      ITNEW=2
      ITRES=3
      press=101330.0
      kgray  = 58.0
      kchill = 21.0
      WRITE(*,*) '# of simulations to perform: '
      read (*,*) insim
      write(*,*) 'depth of chill in gridlines: '
      read (*,*) ix
      open(2,file='dimhtsim.dat')
C
C File should not use the extentions .RLT or .ARR or .UST
C  these are use by the program
      OPEN(3,FILE='prn:')
      do 9999 ifiler = 1,insim
      read(2,'(a)') filen
```

```
      open(1,file=filen,status='old')
C Read in the description of the Simulation Conditions
      read(1,*) clinexp
      read(1,*) pratio
      read(1,*) rpm
      read(1,*) M
      read(1,*) N
      read(1,*) RI
      read(1,*) RO
      read(1,*) L
      read(1,*) ITMAX
      read(1,*) IRMAX
      read(1,*) critr1
      read(1,*) critr2
      read(1,*) nozdia
      read(1,*) DELT
      read(1,*) TZ1
      read(1,*) TZN
      read(1,*) HP
      read(1,*) HI
      read(1,*) HNO
      read(1,*) HZ1
      read(1,*) HZN
      read(1,*) FLX

      read(1,*) ijcnst
      if(ijcnst.eq.1) then
         READ(1,*) (TJet(J),J=1,N)
      else
         read(1,*) temp
         do 110 J=1,N
 110     tJet(J)=temp
      endif

      read(1,*) ipcnst
      if(ipcnst.eq.1) then
         READ(1,*) (TP(J),J=1,N)
      else
         read(1,*) temp
         do 115 J=1,N
 115     tp(J)=temp
      endif

      read(1,*) iicnst
      if(iicnst.eq.1) then
         READ(1,*) (TIN(J),J=1,N)
      else
         read(1,*) temp
         do 118 j=1,n
 118     tin(j)=temp
      endif

      read(1,*) ikcnst
      if(ikcnst.eq.1) then
```

```
         READ(1,*)  (k(i),i=1,M)
      else
         read(1,*) ktemp
         do 120 i=1,M
 120     k(i)=ktemp
      endif
      do 122 i=m,m-ix+1,-1
 122     k(i)=kchill

      read(1,*) ircnst
      if(ircnst.eq.1) then
         READ(1,*)  (rho(i),i=1,M)
      else
         read(1,*) rtemp
         do 130 i=1,m
 130     rho(i)=rtemp
      endif

      read(1,*) icpnst
      if(icpnst.eq.1) then
         READ(1,*)  (cp(i),i=1,M)
      else
         read(1,*) cptemp
         do 140 i=1,m
 140     cp(i)=cptemp
      endif

      read(1,*) CURVE

C
C This contains the spline fit information for the Nu profiles
C at the surface.
C
      read(1,*) INUPRF
      read(1,*) ISPLN
      IF(ISPLN.EQ.1) THEN
         read(1,'(A)') ftemp
         open(4,file=ftemp,status='unknown')
         READ(4,*)  INUM
         READ(4,*)  (XP(I),YP(I),I=1,INUM)
         READ(4,*)
         READ(4,*)  (B(I),C(I),D(I),I=1,INUM-1)
         CLOSE(4)
      ELSE
         read(1,*) incnst
         if(incnst.eq.1) then
            READ(1,*)  (nu(j),j=1,n)
         else
            read(1,*) nutemp
            do 150 j=1,n
 150        nu(j)=nutemp
         endif
      ENDIF

C Read in starting Temperature profile if required
```

```
C or Initialize Temperature array and Thermal Expansion Array
      read(1,*) ITPROF

      if(ITPROF.eq.1) then
         read(1,'(A)') ftemp
         open(4,file=ftemp,status='old')
         read(4,*) mf,nf
         if((mf.ne.m).or.(nf.ne.n)) then
            write(*,*) m,mf,n,nf
            write(*,*) 'Temperature File Array Size Does Not Match'
            write(*,*) 'Specifications Given In Description.'
            write(*,*) 'Simulation Was Skipped.'
            goto 9999
         endif
         read(4,*) clinexp,pratio
         read(4,*) (r(i),i=1,m)
         read(4,*) (z(j),j=1,n)
         read(4,*) ((T(I,J,1),I=1,M),J=1,N)
         READ(4,*) (TEXPAN(J,1),J=1,N)
         CLOSE(4)
         DO 160 I=1,M
         DO 160 J=1,N
         DO 160 IK=2,3
 160     T(I,J,IK)=T(I,J,1)
      ELSE
          read(1,*) TINTER
         DO 170 J=1,N
         TEXPAN(J,1)=0.0
         DO 170 IK=1,3
         DO 170 I=1,M
         T(I,J,IK)=TIN(1)-(i-1)/(m-1)*tinter
170      continue
      ENDIF
      CLOSE(1)

C For Plane strain poisson ratio and coef of Linear expansion in equation
C are modified since the equation is one for plane stress
C Under these conditions the calender roll is under plane strain
C Thermal Expansion is given by equation 9.10.4 in Theory of Thermal
C Stresses by Boley, B.A. and Weiner, J.H. page 290 TA405.5 B64

c        prat=pratio
c        clnex = clinexp
      clnex = clinexp*(1+Pratio)
      Prat = Pratio/(1-Pratio)
C Constants for calculation of Thermal Expansion
C
      TECST1 = ((1-prat)*RO**2 + (1+prat)*RI**2)/(Ro**2-Ri**2)
      TECST2 = clnex/ro
      TECST3 = 1+prat
      write(*,*) tecst1, tecst2, tecst3

C Initialization of the various variables and arrays

C Calculate grid node Position arrays
```

```
      DELR=(RO-RI)/(M-1)
      DELZ=L/(N-1)
      M1=M-1
      N1=N-1
      DO 210 J=1,N
 210  Z(J)=(J-1)*DELZ
      DO 220 I=1,M
 220  R(I)=(I-1)*DELR+RI
      filer1 = filen
      filer2 = filen
      filer3 = filen
      filr1a(9)  = '.'
      filr1a(10) = 'R'
      filr1a(11) = 'L'
      filr1a(12) = 'T'
      filr2a(9)  = '.'
      filr2a(10) = 'A'
      filr2a(11) = 'R'
      filr2a(12) = 'R'
      filr3a(9)  = '.'
      filr3a(10) = 'U'
      filr3a(11) = 'S'
      filr3a(12) = 'T'
c      OPEN(9,FILE=filer3,STATUS='UNKNOWN')

      WRITE(3,2011) M, filen
      WRITE(3,2021) N
      WRITE(3,2026) L
      WRITE(3,2031) RI
      WRITE(3,2036) RO
      WRITE(3,2039) nozdia
      WRITE(3,2041) DELT
      WRITE(3,2071) TAMB
      WRITE(3,2091) HP
      WRITE(3,2096) HI
      WRITE(3,2101) HNO
      WRITE(3,2106) FLX

      IF(INUPRF.EQ.1) then
C Hot Jet Bounded by Hot Jets
         DO 310 J=1,N

         ZTEMP=Z(J)/nozdia
            IF(ISPLN.EQ.1) THEN
               DO 320 I=1,INUM
               IF(ZTEMP.LT.XP(I)) THEN
                  IP=I-1
                  GOTO 330
               ENDIF

 320           CONTINUE

 330           NU(J)=YP(IP)+B(IP)*(ZTEMP-XP(IP))
     #                     +C(IP)*(ZTEMP-XP(IP))**2
     #                     +D(IP)*(ZTEMP-XP(IP))**3
```

```
              else

                 cst1 = 94.68
                 cst2 = 0.019
                 cst3 = 2.09
                 cst4 = -38.84
                 nu(j) = cst1/(1+cst2*ztemp**cst3) + cst4

              ENDIF
              HJ(J)=NU(J)*thmcair(tjet(j))/NOZDIA*20*nozdia/3.14159/r(m)
 310      CONTINUE

       ELSEIF(INUPRF.EQ.2) THEN
C Alternating Hot and Cold Jets with Simular Nu Profiles
          if(n/2*2.eq.n) then
             inend=n/2
          else
             inend=n/2+1
          endif

          do 350 j=1,inend
           ZTEMP=Z(J)/nozdia
             IF(ISPLN.EQ.1) THEN
                DO 360 I=1,INUM
                IF(ZTEMP.LT.XP(I)) THEN
                   IP=I-1
                   GOTO 370
                ENDIF

 360            CONTINUE

 370            NU(J)=YP(IP)+B(IP)*(ZTEMP-XP(IP))
     #                   +C(IP)*(ZTEMP-XP(IP))**2
     #                   +D(IP)*(ZTEMP-XP(IP))**3
             else

                cst1 = 94.68
                cst2 = 0.019
                cst3 = 2.09
                cst4 = -38.84
                nu(j) = cst1/(1+cst2*ztemp**cst3) + cst4
                nu(n-j+1) = nu(j)

             ENDIF
             HJ(J)=NU(J)*thmcair(tjet(j))/NOZDIA*20*nozdia/3.14159/r(m)
             HJ(n-j+1)=NU(J)*thmcair(tjet(n-j+1))/NOZDIA*
     *                                   20*nozdia/3.14159/r(m)
 350      CONTINUE

       ELSEIF(INUPRF.EQ.3) THEN
C No Jets, Roll Turning in Stagnant Air at Specified RPM
C Nu relation is as given by Fechner
          densa=density(tamb,press)
          visa=visair(tamb)
          Rerot=2*RO*(2*PI(15)*RO*RPM/60)*Densa/VISA
```

```
        Nurot=0.0226*Rerot**0.8
        DO 380 J=1,N
        NU(j) = NuRot
 380    HJ(J)=Nurot*thmcair(tamb)/(2*RO)

      ELSEIF(INUPRF.EQ.4) THEN
C Specifed h, HJ=NU(J), mainly for testing purposes
        DO 390 J=1,N
 390    HJ(J)=HNO
      ENDIF

c      if(tp(1).ne.0.0) then
c         densa=density(tp(1),press)
c         visa=visair(tp(1))
c         Rerot=2*RO*(2*PI(15)*RO*RPM/60)*Densa/VISA
c         Nurot=0.0226*Rerot**0.8
c         Hp = Nurot*thmcair(tp(1))/(2*RO)
c      endif

      CALL ABCOEF(CURVE)


      DO 520 J=1,2
      WRITE(*,2550) (B2(I,J),I=1,M)
 520  WRITE(*,*)
      DO 530 I=1,2
      WRITE(*,2550) (B1(I,J),J=1,N)
 530  WRITE(*,*)


C Write out array of A's to file 'UNSTEADY.PRN'
c      DO 540 I=1,M
c      DO 540 J=1,N
c 540  WRITE(*,2560) I,J,AN(I,J),AS(I,J),AE(I,J),AW(I,J),
c     #               APO(I,J),AP(I,J)

      DO 550 I=1,M
 550  F(I) = T(I,1,1)*R(I)
      CALL SIMPSON(F,RI,RO,M,TRORG)


C Steadystate Criteria
      CRIT1 = CRITR1*N*M
C Convervgence criteria
      CRIT2 = CRITR2*N*M
      WRITE(*,*) CRIT1,CRIT2

      DO 5000 KOUNT1 = 1 , ITMAX

         DO 5500 KOUNT2 = 1 , IRMAX

C Solve in one direction J = 1 to N
         CALL SWEEP1(ITNEW,ITOLD,T)

C then in the other J = N to 1
```

```
      CALL SWEEP2(ITNEW,ITOLD,T)

      RES=0.0
      DO 610 I=1,M
      DO 610 J=1,N
610   RES=RES+ABS(T(I,J,ITNEW)-T(I,J,ITRES))

      IF(RES.LT.CRIT2) GOTO 5600

C Update pointers
      ITEMP=ITNEW
      ITNEW=ITRES
      ITRES=ITEMP
5500  CONTINUE

5600  CHANGE=0
      DO 620 I=1,M
      DO 620 J=1,N
 620  CHANGE=CHANGE+ABS(T(I,J,ITNEW)-T(I,J,ITOLD))

      WRITE(*,*) kount1,crit1,change,kount2

      DO 640 I=1,M
 640  F(I)=T(I,1,itnew)*R(I)
      CALL SIMPSON(F,RI,RO,M,TRIGL(KOUNT1))

      IF(CHANGE.LT.CRIT1) GOTO 5100

C Update pointers
      ITEMP=ITOLD
      ITOLD=ITNEW
      ITNEW=ITRES
      ITRES=ITEMP
5000  CONTINUE
5001  CONTINUE

C Print out profiles

5100  TIME=KOUNT1*DELT
      WRITE(3,2130) TIME,CHANGE
      WRITE(3,2135) RES,KOUNT2

      MM=M
      IF(M.GE.10) MM=9
      WRITE(3,2140) (I,I=1,MM)
      DO 710 J=1,N
 710  WRITE(3,2145) J,(T(I,J,ITNEW),I=1,MM)
      IF(M.LE.9) GO TO 799

      MM=M
      IF(M.GE.19) MM=18
      WRITE(3,2140) (I,I=10,MM)
      DO 720 J=1,N
 720  WRITE(3,2145) J,(T(I,J,ITNEW),I=10,MM)
      IF(M.LE.18) GO TO 799
```

```
      MM=M
      IF(M.GE.28) MM=27
      WRITE(3,2140) (I,I=19,MM)
      DO 730 J=1,N
 730  WRITE(3,2145) J,(T(I,J,ITNEW),I=1,MM)
      IF(M LE.27) GO TO 799

      MM=M
      IF(M.GE.37) MM=36
      WRITE(3,2140) (I,I=28,MM)
      DO 740 J=1,N
 740  WRITE(3,2145) J,(T(I,J,ITNEW),I=1,MM)
      IF(M.LE.36) GO TO 799

      MM=M
      IF(M.GE.46) MM=45
      WRITE(3,2140) (I,I=37,MM)
      DO 750 J=1,N
 750  WRITE(3,2145) J,(T(I,J,ITNEW),I=1,MM)
      IF(M.LE.45) GO TO 799

 799  CONTINUE

C Calculate roll expansion
      do 800 j=1,n
         DO 810 I=1,M
 810     F(I)=T(I,J,itnew)*R(I)
         CALL SIMPSON(F,RI,RO,M,TRint)
         texpan(j,2) = TECST2*(TECST3*TRint+TECST1*TRint)
         TEXPAN(J,3) = TEXPAN(J,2)-TEXPAN(J,1)
         write(*,*) trint
 800  continue

      write(3,*)
      write(3,2500)
      do 510 j=1,n
 510  WRITE(3,2510) j,Z(J),TIN(J),TP(J),Tjet(j),NU(J),hj(j),texpan(j,3)

      write(3,*)
      write(3,2520)
      do 515 I=1,M
 515     WRITE(3,2530) i,R(I),k(i),cp(i),rho(i)

      DO 830 I=1,M
 830  F(I)=T(I,1,itnew)*R(I)
      CALL SIMPSON(F,RI,RO,M,TRint1)

      tr95 = 0.95*(trint1-trorg)+trorg
      if(trint1.gt.trorg) then
         do 850 i = 1,itmax
          if(tr95.lt.trigl(i)) goto 870
 850     continue
      else
         do 860 i = 1,itmax
```

```
        if(tr95.gt.trigl(i)) goto 870
 860      continue
      endif
 870  continue

      rtim95= i*delt
      write(3,*)
      write(3,2570) rtim95
      write(3,*) char(12)
9998  OPEN(4,FILE=filer2,STATUS='UNKNOWN')
      WRITE(4,*) m,n
      write(4,*) clinexp,pratio
      write(4,*) (r(i),i=1,m)
      write(4,*) (z(j),j=1,n)
      WRITE(4,*) ((T(I,J,ITold),I=1,M),J=1,N)
      WRITE(4,*) (TEXPAN(J,2),J=1,N)
      CLOSE(4)

9999  continue
      STOP

2011  FORMAT(' # of Grid Points in r-Direction? ',I2,20x,a15)
2021  FORMAT(' # of Grid Points in z-Direction? ',I2)
2026  FORMAT(' Axial Length of Jet Zone = ',F8.5)
2031  FORMAT(' Internal surface radius  = ',F8.5)
2036  FORMAT(' External surface radius  = ',F8.5)
2039  FORMAT(' Nozzle Diameter          = ',F8.5)
2041  FORMAT(' Time step forward        = ',F8.5)
2051  FORMAT(' Internal temperature = ',F8.4)
2061  FORMAT(' Paper  temperature   = ',F8.4)
2071  FORMAT(' Amb. air temperature = ',F8.4)
2081  FORMAT(' Jet Temperature      = ',F8.4)
2091  FORMAT(' Nu (Crotogino) paper  <-->  cylinder = ',F15.7)
2096  FORMAT(' h  (McAdams)   inter. <-->  cylinder = ',f15.7)
2101  FORMAT(' Nu (Fechner) amb. air <--> cylinder  = ',F15.7)
2106  FORMAT(' Flux due to evap. and heatup         = ',f15.7)

2130  FORMAT('-Time = ',F15.6,'   Change = ',F10.6)
2135  FORMAT(' Residual = ',F8.6,' after ',I3,' Loops')
2140  FORMAT('0',7X,' R(',8(I2,')   R('),I2,')')
2145  FORMAT(1(' Z(',I2,') ',9(F7.3,1X)))

2400  FORMAT(f8.4,2x,6pf6.3)

2500  Format(3x,'j',3x,'z(j)',2x,'Tin(j)',2x,'Tp(j)',1x,'Tjet(j)',
     &     2x,'Nu(j)',2x,'Hj(j)',3x,'Th. Expan.')
2510  FORMAT(2x,i2,4(f7.3,1x),f6.2,1x,f6.2,3x,6pf8.3)
2520  Format(1x,' i     R(i)     Kroll(i)    CProll(i)    Density(i)')
2530  FORMAT(2x,i2,1x,f7.4,3x,f7.4,5x,f7.3,5x,f7.2)
2550  FORMAT(5(F9.3,2X))
2560  FORMAT(1X,I2,1X,I2,2X,6(F8.3,1X))
2570  FORMAT(1x,' Response Time (95%) ->  ',f8.2)

      END
```

```
      SUBROUTINE ABCOEF(CURVE)

C The Coefficients calculated are for a uniform grid spacing only.
C The changes for a none uniform grid are simple but there are
C several. References to DELZ, DELZ2, DELR, DELR2 have to be changed
C to explicitly calculate the required difference.
C The routine calculates the A's and B's for Cartesian and Cylindrical
C Coordinates.
C If CURVE = 1 coefficients for cylindrical coordinates are made.
C otherwise cartesian coordinates are used.
C Property variation are in in the R direction only.

      IMPLICIT REAL*8(A-H,J-Z)
      IMPLICIT INTEGER*2(I)
      INTEGER*2 M,N,M1,N1,CURVE,J
      DIMENSION RHOCP(50)

      COMMON/HTCOEF/HP,HI,HNO,HZ1,HZN,FLX,HJ(50)
      COMMON/TEMPER/TJ(50),TJET(50),TIN(50),TP(50),T(50,50,3),TZ1,TZN
      COMMON/PROPERT/K(50),RHO(50),CP(50)
      COMMON/GRIDNO/M,N,M1,N1,R(50),Z(50),DELT
      COMMON/COEF/AE(50,50),AW(50,50),AN(50,50),AS(50,50),
     #            APO(50,50),AP(50,50),B1(2,50),B2(50,2)

      kintf(k1,k2)=2*k1*k2/(k1+k2)

      CPI = 4.0*ATAN(1)
      DELZ=Z(2)-Z(1)
      DELZ2=DELZ/2

      DELR=R(2)-R(1)
      DELR2=DELR/2

      FX=FLX*DELZ

      do 300 I=1,M
300   rhocp(i)=rho(i)*cp(i)
      write(*,*) 'Calculating As and Bs'
      IF(CURVE.eq.1) then

         DO 200 J=1,N
            B1(1,J) = 2*CPI*R(1)*DELZ*HI*TIN(j)
200         B1(2,J) = 2*CPI*R(M)*DELZ*((HJ(J)*TJET(J)+HP*TP(j))/2) + FX
         write(*,*) cpi,r(1),r(m),delz,hi,tin(1),hj(1),tjet(1),hp,tp(1),
     #      fx
         B1(1,1) = B1(1,1)/2
         B1(1,N) = B1(1,N)/2
         B1(2,1) = B1(2,1)/2
         B1(2,N) = B1(2,N)/2

         DO 205 I=2,M-1
            B2(I,1) = 2*CPI*R(I)*DELR*HZ1*TZ1
205         B2(I,2) = 2*CPI*R(I)*DELR*HZN*TZN
         B2(1,1)= CPI*(R(1)*DELR+(DELR2)**2)*HZ1*TZ1
         B2(M,1)= CPI*(R(M)*DELR-(DELR2)**2)*HZ1*TZ1
```

```
      B2(1,2)= CPI*(R(1)*DELR+(DELR2)**2)*HZN*TZN
      B2(M,2)= CPI*(R(M)*DELR-(DELR2)**2)*HZN*TZN


      AR = 2*CPI*DELZ/DELR
      AZ = 2*CPI*DELR/DELZ
      AT = 2*CPI*DELR*DELZ/DELT

C Calculate internal A's
      DO 220 I=2,M-1
         DO 225 J=2,N-1
            AE(I,J)=AR*kintf(k(i),k(i+1))*(R(I)+DELR2)
            AW(I,J)=AR*kintf(k(i),k(i-1))*(R(I)-DELR2)
            AN(I,J)=AZ*k(i)*R(I)
            AS(I,J)=AN(I,J)
            APO(I,J)=AT*R(I)*rhocp(i)
            AP(I,J)=AE(I,J)+AW(I,J)+AN(I,J)+AS(I,J)+APO(I,J)
 225     CONTINUE
 220  CONTINUE


C Calculate corner A's
C Lower Left
      AE(1,1)   = 2*CPI*(R(1)+DELR2)*DELZ2/DELR*kintf(k(1),k(2))
      AW(1,1)   = 0.0
      AN(1,1)   = CPI*(R(1)*DELR+(DELR2)**2)/DELZ*K(1)
      AS(1,1)   = 0.0
      APO(1,1)  = CPI*(R(1)*DELR+(DELR2)**2)*DELZ2*rhocp(1)/DELT
      AP(1,1)   = AE(1,1)+AW(1,1)+AN(1,1)+AS(1,1)+APO(1,1)
    #             + CPI*(R(1)*DELR+(DELR2)**2)*HZ1
    #             + 2*CPI*R(1)*DELZ2*HI
C Top Left
      AE(1,N)   = AE(1,1)
      AW(1,N)   = 0.0
      AN(1,N)   = 0.0
      AS(1,N)   = AN(1,1)
      APO(1,N)  = APO(1,1)
      AP(1,N)   = AE(1,1)+AW(1,1)+AN(1,1)+AS(1,1)+APO(1,1)
    #             + CPI*(R(1)*DELR+(DELR2)**2)*HZN
    #             + 2*CPI*R(1)*DELZ2*HI

C Lower Right
      AE(M,1)   = 0.0
      AW(M,1)   = 2*CPI*(R(M)-DELR2)*DELZ2/DELR*kintf(k(m),k(m-1))
      AN(M,1)   = CPI*(R(M)*DELR-(DELR2)**2)/DELZ*K(m)
      AS(M,1)   = 0.0
      APO(M,1)  = CPI*(R(M)*DELR-(DELR2)**2)*DELZ2*rhocp(m)/DELT
      AP(M,1)   = AE(M,1)+AW(M,1)+AN(M,1)+AS(M,1)+APO(M,1)
    #             + CPI*(R(M)*DELR-(DELR2)**2)*HZ1
    #             + 2*CPI*R(M)*DELZ2*(HP+HJ(1))/2
C Top Right
      AE(M,N)   = 0.0
      AW(M,N)   = AW(M,1)
      AN(M,N)   = 0.0
      AS(M,N)   = AN(M,1)
```

```
      APO(M,N)  = APO(M,1)
      AP(M,N)   = AE(M,1)+AW(M,1)+AN(M,1)+AS(M,1)+APO(M,1)
     #            + CPI*(R(M)*DELR-(DELR2)**2)*HZN
     #            + 2*CPI*R(M)*DELZ2*(HP+HJ(N))/2

C Calculate border A's
      DO 230 I=2,M-1
C Bottom
         AE(I,1)=AE(I,2)/2
         AW(I,1)=AW(I,2)/2
         AN(I,1)=AN(I,2)
         AS(I,1)=0.0
         APO(I,1)=APO(I,2)/2
         AP(I,1)=AE(I,1)+AW(I,1)+AN(I,1)+AS(I,1)+APO(I,1)
     #            +2*CPI*R(I)*DELR*HZ1
C Top
         AE(I,N)=AE(I,N-1)/2
         AW(I,N)=AW(I,N-1)/2
         AN(I,N)=0.0
         AS(I,N)=AS(I,N-1)
         APO(I,N)=APO(I,N-1)/2
         AP(I,N)=AE(I,N)+AW(I,N)+AN(I,N)+AS(I,N)+APO(I,N)
     #            +2*CPI*R(I)*DELR*HZN

 230  CONTINUE

      DO 235 J=2,N-1
C Left
         AE(1,J)=AE(1,1)*2
         AW(1,J)=0.0
         AN(1,J)=AN(1,1)
         AS(1,J)=AS(1,N)
         APO(1,J)=APO(1,1)*2
         AP(1,J)=AE(1,J)+AW(1,J)+AN(1,J)+AS(1,J)+APO(1,J)
     #            +2*CPI*R(1)*DELZ*HI
C Right
         AE(M,J)=0.0
         AW(M,J)=AW(M,1)*2
         AN(M,J)=AN(M,1)
         AS(M,J)=AS(M,N)
         APO(M,J)=APO(M,1)*2
         AP(M,J)=AE(M,J)+AW(M,J)+AN(M,J)+AS(M,J)+APO(M,J)
     #            +2*CPI*R(M)*DELZ*(HP+HJ(J))/2

 235  CONTINUE

    else
      DO 530 J=1,N
         B1(1,J)=HI*TIN(j)*DELZ
 530     B1(2,J)=(HJ(J)*TJET(J)+HP*TP(j))*DELZ/2 + FX
      B1(1,1)=B1(1,1)/2
      B1(1,N)=B1(1,N)/2
      B1(2,1)-B1(2,1)/2
      B1(2,N)=B1(2,N)/2
```

```
      DO 535 I=1,M
        B2(I,1) = HZ1*TZ1*DELR
535     B2(I,2) = HZN*TZN*DELR
      B2(1,1)= B2(1,1)/2
      B2(M,1)= B2(M,1)/2
      B2(1,2)= B2(1,2)/2
      B2(M,2)= B2(M,2)/2

      AR=DELZ/DELR
      AZ=DELR/DELZ
      AT=DELR*DELZ/DELT

C Calculate internal A's
      DO 750 I=2,M-1
        DO 755 J=2,N-1
          AE(I,J)=AR*kintf(k(i),k(i+1))
          AW(I,J)=AR*kintf(k(i),k(i-1))
          AN(I,J)=AZ*k(i)
          AS(I,J)=AN(I,J)
          APO(I,J)=AT*rhocp(I)
          AP(I,J)=AE(I,J)+AW(I,J)+AN(I,J)+AS(I,J)+APO(I,J)
755     CONTINUE
750   CONTINUE


C Calculate corner A's
C Lower Left
      AE(1,1)=AR/2*kintf(k(1),k(2))
      AW(1,1)=0.0
      AN(1,1)=AZ/2*k(1)
      AS(1,1)=0.0
      APO(1,1)=AT/4*rhocp(1)
      AP(1,1)=AE(1,1)+AW(1,1)+AN(1,1)+AS(1,1)+APO(1,1)
    #         +HZ1*DELR/2+HI*DELZ/2
C Top Left
      AE(1,N)=AE(1,1)
      AW(1,N)=0.0
      AN(1,N)=0.0
      AS(1,N)=AZ/2*k(1)
      APO(1,N)=AT/4*rhocp(1)
      AP(1,N)=AE(1,N)+AW(1,N)+AN(1,N)+AS(1,N)+APO(1,N)
    #         +HZN*DELR/2+HI*DELZ/2
C Lower Right
      AE(M,1)=0.0
      AW(M,1)=AR/2*kintf(k(m),k(m-1))
      AN(M,1)=AZ/2*k(m)
      AS(M,1)=0.0
      APO(M,1)=AT/4*rhocp(m)
      AP(M,1)=AE(M,1)+AW(M,1)+AN(M,1)+AS(M,1)+APO(M,1)
    #         +HZ1*DELR/2+(HJ(1)+HP)/2*DELZ/2
C Top Right
      AE(M,N)=0.0
      AW(M,N)=AW(M,1)
      AN(M,N)=0.0
      AS(M,N)=AZ/2*k(m)
```

```
      APO(M,N)=AT/4*rhocp(m)
      AP(M,N)=AE(M,N)+AW(M,N)+AN(M,N)+AS(M,N)+APO(M,N)
     #         +HZN*DELR/2+(HJ(N)+HP)/2*DELZ/2

C Calculate border A's
      DO 760 I=2,M-1
C Bottom
         AE(I,1)=AE(I,2)/2
         AW(I,1)=AW(I,2)/2
         AN(I,1)=AN(I,2)
         AS(I,1)=0.0
         APO(I,1)=AT/2*rhocp(I)
         AP(I,1)=AE(I,1)+AW(I,1)+AN(I,1)+AS(I,1)+APO(I,1)
     #         +HZ1*DELR
C Top
         AE(I,N)=AE(I,N-1)/2
         AW(I,N)=AW(I,N-1)/2
         AN(I,N)=0.0
         AS(I,N)=AS(I,N-1)
         APO(I,N)=AT/2*rhocp(I)
         AP(I,N)=AE(I,N)+AW(I,N)+AN(I,N)+AS(I,N)+APO(I,N)
     #         +HZN*DELR

 760  CONTINUE

      DO 765 J=2,N-1
C Left
         AE(1,J)=2*AE(1,1)
         AW(1,J)=0.0
         AN(1,J)=AN(1,1)
         AS(1,J)=AS(1,N)
         APO(1,J)=AT/2*rhocp(1)
         AP(1,J)=AE(1,J)+AW(1,J)+AN(1,J)+AS(1,J)+APO(1,J)
     #         +HI*DELZ
C Right
         AE(M,J)=0.0
         AW(M,J)=2*AW(M,1)
         AN(M,J)=AN(M,1)
         AS(M,J)=AS(M,N)
         APO(M,J)=AT/2*rhocp(m)
         AP(M,J)=AE(M,J)+AW(M,J)+AN(M,J)+AS(M,J)+APO(M,J)
     #         +(HJ(J)+HP)/2*DELZ

 765  CONTINUE

      endif

      RETURN
      END



      SUBROUTINE SWEEP1(IN,IO,T)
      IMPLICIT REAL*8(A-H),REAL*8(J-Z)
```

```
      INTEGER*2 M,N,M1,N1,J,JP1,JM1,IM1
      DIMENSION T(50,50,3)
      COMMON/COEF/AE(50,50),AW(50,50),AN(50,50),AS(50,50),
     #            APO(50,50),AP(50,50),B1(2,50),B2(50,2)
      COMMON/TDMAVA/P(50),Q(50)
      COMMON/GRIDNO/M,N,M1,N1,R(50),Z(50)

C Solve for temperature at J=1 boundary
      P(1)=AE(1,1)/AP(1,1)
      Q(1)=(AN(1,1)*T(1,2,IN)+APO(1,1)*T(1,1,IO)
     *     +B1(1,1)+B2(1,1))/AP(1,1)
      DO 20 I=2,M-1
      IM1=I-1
      DEN=AP(I,1)-AW(I,1)*P(IM1)
      P(I)=AE(I,1)/DEN
      Q(I)=(AN(I,1)*T(I,2,IN)+APO(I,1)*T(I,1,IO)+B2(I,1)
     *      +AW(I,1)*Q(IM1))/DEN
   20 CONTINUE
      DEN=AP(M,1)-AW(M,1)*P(M1)
      P(M)=0.0
      Q(M)=(AN(M,1)*T(M,2,IN)+APO(M,1)*T(M,1,IO)
     #     +B1(2,1)+B2(M,1)+AW(M,1)*Q(M1))/DEN
      CALL TDMAT(T,1,IN)

C Solve for internal temperature distribution
      DO 10 J=2,N-1
      JP1=J+1
      JM1=J-1
      P(1)=AE(1,J)/AP(1,J)
      Q(1)=(AN(1,J)*T(1,JP1,IN)+AS(1,J)*T(1,JM1,IN)+APO(1,J)*T(1,J,IO)
     *     +B1(1,J))/AP(1,J)
      DO 21 I=2,M-1
      IM1=I-1
      DEN=AP(I,J)-AW(I,J)*P(IM1)
      P(I)=AE(I,J)/DEN
      Q(I)=(AN(I,J)*T(I,JP1,IN)+AS(I,J)*T(I,JM1,IN)+APO(I,J)*T(I,J,IO)
     *      +AW(I,J)*Q(IM1))/DEN
   21 CONTINUE
      DEN=AP(M,J)-AW(M,J)*P(M1)
      P(M)=0.0
      Q(M)=(AN(M,J)*T(M,JP1,IN)+AS(M,J)*T(M,JM1,IN)+APO(M,J)*T(M,J,IO)
     #     +B1(2,J)+AW(M,J)*Q(M1))/DEN
      CALL TDMAT(T,J,IN)
   10 CONTINUE

C Solve for temperature at J=N boundary
      P(1)=AE(1,N)/AP(1,N)
      Q(1)=(AS(1,N)*T(1,N1,IN)+APO(1,N)*T(1,N,IO)
     *     +B1(1,N)+B2(1,2))/AP(1,N)
      DO 22 I=2,M-1
      IM1=I-1
      DEN=AP(I,N)-AW(I,N)*P(IM1)
      P(I)=AE(I,N)/DEN
      Q(I)=(AS(I,N)*T(I,N1,IN)+APO(I,N)*T(I,N,IO)+B2(I,2)
     *      +AW(I,N)*Q(IM1))/DEN
```

```
   22  CONTINUE
       DEN=AP(M,N)-AW(M,N)*P(M1)
       P(M)=0.0
       Q(M)=(AS(M,N)*T(M,N1,IN)+APO(M,N)*T(M,N,IO)
      #      +B1(2,N)+B2(M,2)+AW(M,N)*Q(M1))/DEN
       CALL TDMAT(T,N,IN)

       RETURN
       END

       SUBROUTINE SWEEP2(IN,IO,T)
       IMPLICIT REAL*8(A-H),REAL*8(J-Z)
       INTEGER*2 M,N,M1,N1,JP1,JM1,IM1
       DIMENSION T(50,50,3)
       COMMON/CCEF/AE(50,50),AW(50,50),AN(50,50),AS(50,50),
      #            APO(50,50),AP(50,50),B1(2,50),B2(50,2)
       COMMON/TDMAVA/P(50),Q(50)
       COMMON/GRIDNO/M,N,M1,N1,R(50),Z(50)

C Solve for temperature at J=N boundary
       P(1)=AE(1,N)/AP(1,N)
       Q(1)=(AS(1,N)*T(1,N1,IN)+APO(1,N)*T(1,N,IO)
      *      +B1(1,N)+B2(1,2))/AP(1,N)
       DO 22 I=2,M-1
       IM1=I-1
       DEN=AP(I,N)-AW(I,N)*P(IM1)
       P(I)=AE(I,N)/DEN
       Q(I)=(AS(I,N)*T(I,N1,IN)+APO(I,N)*T(I,N,IO)+B2(I,2)
      *       +AW(I,N)*Q(IM1))/DEN
   22  CONTINUE
       DEN=AP(M,N)-AW(M,N)*P(M1)
       P(M)=0.0
       Q(M)=(AS(M,N)*T(M,N1,IN)+APO(M,N)*T(M,N,IO)
      #      +B1(2,N)+B2(M,2)+AW(M,N)*Q(M1))/DEN
       CALL TDMAT(T,N,IN)

C Solve for internal temperature distribution
       DO 10 J=N-1,2,-1
       JP1=J+1
       JM1=J-1
       P(1)=AE(1,J)/AP(1,J)
       Q(1)=(AN(1,J)*T(1,JP1,IN)+AS(1,J)*T(1,JM1,IN)+APO(1,J)*T(1,J,IO)
      *      +B1(1,J))/AP(1,J)
       DO 21 I=2,M-1
       IM1=I-1
       DEN=AP(I,J)-AW(I,J)*P(IM1)
       P(I)=AE(I,J)/DEN
       Q(I)=(AN(I,J)*T(I,JP1,IN)+AS(I,J)*T(I,JM1,IN)+APO(I,J)*T(I,J,IO)
      *       +AW(I,J)*Q(IM1))/DEN
   21  CONTINUE
       DEN=AP(M,J)-AW(M,J)*P(M1)
       P(M)=0.0
       Q(M)=(AN(M,J)*T(M,JP1,IN)+AS(M,J)*T(M,JM1,IN)+APO(M,J)*T(M,J,IO)
      #      +B1(2,J)+AW(M,J)*Q(M1))/DEN
       CALL TDMAT(T,J,IN)
```

```
   10  CONTINUE

C Solve for temperature at J=1 boundary
       P(1)=AE(1,1)/AP(1,1)
       Q(1)=(AN(1,1)*T(1,2,IN)+APO(1,1)*T(1,1,IO)
      *      +B1(1,1)+B2(1,1))/AP(1,1)
       DO 20 I=2,M-1
       IM1=I-1
       DEN=AP(I,1)-AW(I,1)*P(IM1)
       P(I)=AE(I,1)/DEN
       Q(I)=(AN(I,1)*T(I,2,IN)+APO(I,1)*T(I,1,IO)+B2(I,1)
      *       +AW(I,1)*Q(IM1))/DEN
   20  CONTINUE
       DEN=AP(M,1)-AW(M,1)*P(M1)
       P(M)=0.0
       Q(M)=(AN(M,1)*T(M,2,IN)+APO(M,1)*T(M,1,IO)
      #      +B1(2,1)+B2(M,1)+AW(M,1)*Q(M1))/DEN
       CALL TDMAT(T,1,IN)

       RETURN
       END

       SUBROUTINE TDMAT(T,J,IN)
C TDMA procedure as described in Patankar

       IMPLICIT REAL*8(A-H),REAL*8(J-Z)
       INTEGER*2 M,N,M1,N1,J
       DIMENSION T(50,50,3)
       COMMON /TDMAVA/P(50),Q(50)
       COMMON /GRIDNO/M,N,M1,N1,R(50),Z(50)
       T(M,J,IN)=Q(M)
       DO 10 I=M1,1,-1
       T(I,J,IN)=P(I)*T(I+1,J,IN)+Q(I)
   10  CONTINUE
       RETURN
       END


       function thmcair(temp)
       implicit real*8(a-h,j-z)
c
c  This correlation for the thermal conductivity of air is valid over
c  the range of 250 deg. K to 400 deg. K (-25 to 130 deg. C)
c  The correlation was obtained by fitting a polynomial to
c  the thermal conductivity data given by Touloukian,Liley and Saxena
c  in Thermophysical Properties of Matter, IFI/Plenum,
c  New York, 1970.
c
c    temperature input is to be given in deg. C.
c    internal to the function, the temperature is
c    converted to deg. K.
c    thermal conductivity is in W/m*C
c
       t=temp+273.15
       thmcair=(-8.98737e-3+1.057024e-3*t-5.21e-7*t*t)/10.
```

```
      return
      end
c
c
      function visair(temp)
      implicit real*8(a-h,j-z)
c
c  This correlation for the viscosity of air is valid over
c  the range of 250 deg. K to 400 deg. K (-25 to 130 deg. C)
c  The correlation was obtained by fitting a polynomial to
c  the viscosity data given by Touloukian,Liley and Saxena
c  in Thermophysical Properties of Matter, IFI/Plenum,
c  New York, 1970.
c
c    temperature is to be given in deg. C.
c    internal to the function, the temperature is
c    converted to deg. K.
c    viscosity is in N/s*m^2
c
      t=temp+273.15
      visair=1.2147081+0.0679118*t-0.0000340*t*t
      visair=visair*1.E-6
      return
      end
c
      function density(temp,pres)
      implicit real*8(a-h,j-z)
c
c  The ideal gas law is used to predict gas density.
c  The relationship is valid over the temperature
c  range 200 deg. K to 1500 deg. K and for pressures
c  up to a few atmospheres. MW air = 28.97
c
c    temperature is to be given in deg. C.
c    internal to the function, the temperature is
c    converted to deg. K.
c    pressure is in Pa.
c    density is in kg/m**3
c
      t=temp+273.15
      density=pres/t*0.003484
      return
      end



      SUBROUTINE SIMPSON(F,A,B,N,SINTEG)

      IMPLICIT REAL*8(A-H,J-Z)
      IMPLICIT INTEGER*2(I)
      INTEGER*2 I,M,N
      DIMENSION F(1)

      M=(N-1)/2
```

```
      IF((2*M).EQ.N) THEN
         WRITE(*,100)
100      FORMAT(' INTEGRAL CANNOT BE CALCULATED. N MUST BE ODD.')
         RETURN
      ENDIF

      H=(B-A)/(2.*M)

      EVEN=0.0
      DO 10 I=2,N-1,2
10    EVEN=EVEN+F(I)
      EVEN=4*EVEN

      ODD=0.0
      DO 20 I=3,N-2,2
20    ODD=ODD+F(I)
      ODD=2*ODD

      SINTEG = H/3*(F(1)+EVEN+ODD+F(N))
      RETURN
      END



      Function pi(n)
C Listing from BYTE  May 1987 page 22
      Implicit real*8(a-h,j-z)
      integer*2 N
      fnp(s,p)=(p+s/p)/2
      fns(s)= fnp(s,fnp(s,dsqrt(s)))
      s=fns(3)
      p=2
      do 10 k=1,n
      s=fns(s+2)
   10 p=2*p/s
      pi=p+p/s
      return
      end
```

APPENDIX E

Source Code for Finite Element Steady-State Simulation

This source code was developed using IMSL's PDE PROTRAN, a FORTRAN pre-processor. A description of PDE PROTRAN is avialable in the reference by *******.

```
/INFO MVS CL(62) R(MUSIC) TI(80) MSGL(0)
// EXEC PROTRAN,PARM.FORT='NOSF,NOTF'
//PREPROXX.SYSIN DD *
C
C TSTRESS
$      DECLARATIONS
        IMPLICIT DOUBLE PRECISION (A-H,O-Z)
        DOUBLE PRECISION MATRIX TSOL(11,51),USOL(11,51),VSOL(11,51)
        DOUBLE PRECISION VECTOR EXPPS(51), EXPRL(51), TSURF(51)
        DOUBLE PRECISION VECTOR YLOC(51), XLOC(11)
        DOUBLE PRECISION VECTOR NU(51), HJET(51)

C DEFINE COORDINATE SYSTEM
$      FORTRAN
       X1 = 0.13
       X2 = 0.25
       X12= (X1+X2)/2
       YJZ= 0.1
       Y1 = 0.0
       Y2 = Y1+YJZ/2
       Y12= (Y1+Y2)/2
       Y3 = Y2+YJZ
       Y23= (Y2+Y3)/2
       Y4 = Y3+YJZ
       Y34= (Y3+Y4)/2
       Y5 = Y4+YJZ
       Y45= (Y4+Y5)/2
       Y6 = Y5+YJZ
       Y56= (Y5+Y6)/2
       Y7 = Y6+YJZ
       Y67= (Y6+Y7)/2
       Y8 = Y7+YJZ
       Y78= (Y7+Y8)/2
       Y9 = Y8+YJZ
       Y89= (Y8+Y9)/2
       Y10    = Y9+YJZ
       Y910   = (Y9+Y10)/2
       Y11    = Y10+YJZ
       Y1011 = (Y10+Y11)/2
       Y21    = Y11+YJZ/2
       Y1112 = (Y11+Y21)/2
       NX = 11
       NY = 51
C
       TIN     =  150.0
       TJ1     =  20.0
```

```
      TJ2     =  150.0
      XHIN    =  11000.0
      VNU     = 0.27
      ALPHA   = 11.34E-6
      XN      = VNU
      XA      = ALPHA
      TECST1 = ((1-XN)*X2**2+(1+XN)*X1**2)/(X2**2-X1**2)
      TECST2 = XA/X2
      TECST3 = 1 + XN
      DIA     =  0.0254
      PI      = 3.141592654
      PI2     = 2*PI
      CAIR1= CAIR(TJ1)
      CAIR2= CAIR(TJ2)
      CST11= 94.68*CAIR1/DIA
      CST12= 94.68*CAIR2/DIA
      CST2 = 0.019
      CST3 = 2.09
      CST41= 38.84*CAIR1/DIA
      CST42= 38.84*CAIR2/DIA
      FLUX = 8200.0
      RI    = X1 + 0.0001
      RO    = X2 + 0.0001
      RDIA2= 20.*DIA/PI

$     PDE2D

      PRECISION = DOUBLE
      UNKNOWNS = ( T, U, V )

' PARTIAL DIFFERENTIAL EQUATION

      A = ( X*COND*TX,
     &      X*((E1+E2)*UX+E2*U/X+E2*VY-E3*(T-TEMPO)),
     &      X*E1/2*(UY+VX) )
      B = ( X*COND*TY,
     &      X*E1/2*(UY+VX),
     &      X*((E1+E2)*VY+E2*U/X+E2*UX-E3*(T-TEMPO)) )
      F = ( 0.0,
     &      -((E1+E2)*U/X+E2*UX+E2*VY-E3*(T-TEMPO)),
     &      0.0 )

      DEFINE

         ====
         COND    =  58.0
         VNU     -  0.27
         ALPHA   = 11.34E-6
         EM      =  20.0E7
         E1 = EM/(1+VNU)
         E2 = E1*VNU/(1-2*VNU)
         E3 = EM*ALPHA/(1-2*VNU)
         TEMPO = 0.0
         ====
```

```
GLOBAL
  ====
    COMMON /TEMP/ TIN, TJ1, TJ2, FLUX
    COMMON /DIMX/ X1,X2,X12
    COMMON /DIMY1/ Y1,Y2,Y3,Y12,Y23,Y4,Y5,Y34,Y45,Y6,Y7,Y56,Y67
    COMMON /DIMY2/ Y8,Y78,Y9,Y89,Y10,Y910,Y11,Y1011,Y21,Y1112
    COMMON /HTCOEF/ CST11,CST12,CST2,CST3,CST41,CST42,XHIN
    COMMON /CONST/ RI, RO, DIA, RDIA2, PI, PI2
    ====
  UC = (140.0, 0.0, 0.0)

! BOUNDARY CONDITIONS

  GB = (1, 0.0, 0.0, -1.0E15*V)
&      (2, 0.0, 0.0, 0.0)
&      (3,XHIN*RI*(TIN-T), 0.0, 0.0)
&      (4, RO*(TJ1-T)/2*(RDIA2/RO)*
&        (CST11/(1+CST2*(ABS(Y-Y1)/DIA)**CST3)-CST41)-FLUX/(PI2),
&          0.0, 0.0)
&      (5, RO*(TJ2-T)/2*(RDIA2/RO)*
&        (CST12/(1+CST2*(ABS(Y-Y23)/DIA)**CST3)-CST42)-FLUX/PI2,
&          0.0, 0.0)
&      (6, RO*(TJ2-T)/2*(RDIA2/RO)*
&        (CST12/(1+CST2*(ABS(Y-Y34)/DIA)**CST3)-CST42)-FLUX/PI2,
&          0.0, 0.0)
&      (7, RO*(TJ2-T)/2*(RDIA2/RO)*
&        (CST12/(1+CST2*(ABS(Y-Y45)/DIA)**CST3)-CST42)-FLUX/PI2,
&          0.0, 0.0)
&      (8, RO*(TJ2-T)/2*(RDIA2/RO)*
&        (CST12/(1+CST2*(ABS(Y-Y56)/DIA)**CST3)-CST42)-FLUX/PI2,
&          0.0, 0.0)
&      (9, RO*(TJ2-T)/2*(RDIA2/RO)*
&        (CST12/(1+CST2*(ABS(Y-Y67)/DIA)**CST3)-CST42)-FLUX/PI2,
&          0.0, 0.0)
&      (10,RO*(TJ2-T)/2*(RDIA2/RO)*
&        (CST12/(1+CST2*(ABS(Y-Y78)/DIA)**CST3)-CST42)-FLUX/PI2,
&          0.0, 0.0)
&      (11,RO*(TJ2-T)/2*(RDIA2/RO)*
&        (CST12/(1+CST2*(ABS(Y-Y89)/DIA)**CST3)-CST42)-FLUX/PI2,
&          0.0, 0.0)
&      (12,RO*(TJ2-T)/2*(RDIA2/RO)*
&        (CST12/(1+CST2*(ABS(Y-Y910)/DIA)**CST3)-CST42)-FLUX/PI2,
&          0.0, 0.0)
&      (13,RO*(TJ2-T)/2*(RDIA2/RO)*
&        (CST12/(1+CST2*(ABS(Y-Y1011)/DIA)**CST3)-CST42)-FLUX/PI2,
&          0.0, 0.0)
&      (14,RO*(TJ1-T)/2*(RDIA2/RO)*
&        (CST11/(1+CST2*(ABS(Y-Y21)/DIA)**CST3)-CST41)-FLUX/PI2,
&          0.0, 0.0)

! INITIAL TRIANGLULATION

  VERTICES = (X1,Y1) (X2,Y1) (X2,Y2) (X1,Y2)
&   (X12,Y12) (X2,Y3) (X1,Y3) (X12,Y23)
```

```
     &  (X2,Y4)  (X1,Y4)  (X12,Y34)
     &  (X2,Y5)  (X1,Y5)  (X12,Y45)
     &  (X2,Y6)  (X1,Y6)  (X12,Y56)
     &  (X2,Y7)  (X1,Y7)  (X12,Y67)
     &  (X2,Y8)  (X1,Y8)  (X12,Y78)
     &  (X2,Y9)  (X1,Y9)  (X12,Y89)
     &  (X2,Y10)  (X1,Y10)  (X12,Y910)
     &  (X2,Y11)  (X1,Y11)  (X12,Y1011)
     &  (X2,Y21)  (X1,Y21)  (X12,Y1112)

      TRIANGLES = (1,2,5,1) (2,3,5,4) (3,4,5,0) (4,1,5,3)
     &  (4,3,8,0) (3,6,8,5) (6,7,8,0) (7,4,8,3)
     &  (7,6,11,0) (6,9,11,6) (9,10,11,0) (10,7,11,3)
     &  (10,9,14,0) (9,12,14,7) (12,13,14,0) (13,10,14,3)
     &  (13,12,17,0) (12,15,17,8) (15,16,17,0) (16,13,17,3)
     &  (16,15,20,0) (15,18,20,9) (18,19,20,0) (19,16,20,3)
     &  (19,18,23,0) (18,21,23,10) (21,22,23,0) (22,19,23,3)
     &  (22,21,26,0) (21,24,26,11) (24,25,26,0) (25,22,26,3)
     &  (25,24,29,0) (24,27,29,12) (27,28,29,0) (28,25,29,3)
     &  (28,27,32,0) (27,30,32,13) (30,31,32,0) (31,28,32,3)
     &  (31,30,35,0) (30,33,35,14) (33,34,35,2) (34,31,35,3)

 ' TRIANGULATION REFINEMENT
      NTRIANGLES = 132

 ' OUTPUT
      GRIDPOINTS = (11,51)
      PRINTSOLUTION
      SAVEARRAY = (TSOL,USOL,VSOL)

 $    FORTRAN
        DELX  =  (X2-X1)/(NX-1)
        DELY  =  (Y21-Y1)/(NY-1)
        M     =  (NX-1)/2
        H     =  (X2-X1)/(2*M)

        DO 5 I = 1,NX
   5      XLOC(I) = X1 + (I-1)*DELX
        DO 30 J = 1,NY
           YLOC(J) = (J-1) *DELY + Y1
           IF(YLOC(J).LE.Y2) THEN
             HJET(J)= CST11/(1+CST2*(ABS(YLOC(J)-Y1)/DIA)**CST3)-CST41
             NU(J)   = HJET(J)*DIA/CAIR1
           ELSEIF(YLOC(J).LE.Y3) THEN
             HJET(J)= CST12/(1+CST2*(ABS(YLOC(J)-Y23)/DIA)**CST3)-CST42
             NU(J)   = HJET(J)*DIA/CAIR2
           ELSEIF(YLOC(J).LE.Y4) THEN
             HJET(J)= CST12/(1+CST2*(ABS(YLOC(J)-Y34)/DIA)**CST3)-CST42
             NU(J)   = HJET(J)*DIA/CAIR2
           ELSEIF(YLOC(J).LE.Y5) THEN
             HJET(J)= CST12/(1+CST2*(ABS(YLOC(J)-Y45)/DIA)**CST3)-CST42
             NU(J)   = HJET(J)*DIA/CAIR2
```

```
            ELSEIF(YLOC(J).LE.Y6) THEN
              HJET(J)= CST12/(1+CST2*(ABS(YLOC(J)-Y56)/DIA)**CST3)-CST42
              NU(J)   = HJET(J)*DIA/CAIR2
            ELSEIF(YLOC(J).LE.Y7) THEN
              HJET(J)= CST12/(1+CST2*(ABS(YLOC(J)-Y67)/DIA)**CST3)-CST42
              NU(J)   = HJET(J)*DIA/CAIR2
            ELSEIF(YLOC(J).LE.Y8) THEN
              HJET(J)= CST12/(1+CST2*(ABS(YLOC(J)-Y78)/DIA)**CST3)-CST42
              NU(J)   = HJET(J)*DIA/CAIR2
            ELSEIF(YLOC(J).LE.Y9) THEN
              HJET(J)= CST12/(1+CST2*(ABS(YLOC(J)-Y89)/DIA)**CST3)-CST42
              NU(J)   = HJET(J)*DIA/CAIR2
            ELSEIF(YLOC(J).LE Y10) THEN
              HJET(J)= CST12/(1+CST2*(ABS(YLOC(J)-Y910)/DIA)**CST3)-CST42
              NU(J)   = HJET(J)*DIA/CAIR2
            ELSEIF(YLOC(J).LE.Y11) THEN
             HJET(J)= CST12/(1+CST2*(ABS(YLCC(J)-Y1011)/DIA)**CST3)-CST42
             NU(J)   = HJET(J)*DIA/CAIR2
            ELSE
              HJET(J)= CST11/(1+CST2*(ABS(YLOC(J)-Y21)/DIA)**CST3)-CST41
              NU(J)   = HJET(J)*DIA/CAIR1
            ENDIF
            WRITE(6,1000)  J, YLOC(J), NU(J), HJET(J)
 1000       FORMAT(2X,I2,2X,F10.6,2(2X,F11.6))
            TSURF(J) = TSOL(NX,J)
            EXPRL(J) = USOL(NX,J)*1.0E6


            EVEN = 0.0
            DO 10 I = 2, NX-1,2
  10        EVEN = EVEN + TSOL(I,J)*XLOC(I)
            EVEN = 4 * EVEN
            ODD = 0.0
            DO 20 I = 3, NX-2,2
  20        ODD = ODD + TSOL(I,J)*XLOC(I)
            ODD = 2 * ODD
            TINT=H/3*(TSOL(1,J)*XLOC(1)+EVEN+ODD+TSOL(NX,J)*XLOC(NX))
            EXPPS(J)=TECST2*(TECST3*TINT + TECST1*TINT)*1.0E6
  30     CONTINUE

      XRL = EXPRL((NY-1)/2+1)
      XPS = EXPPS((NY-1)/2+1)
      DO 40 J = 1, NY
      RL = EXPRL(J) - XRL
      PS = EXPPS(J) - XPS
      WRITE(6,1010) J, YLOC(J),TSURF(J), EXPRL(J), RL, EXPPS(J), PS
 1010 FORMAT(2X,I2,2X,F10.6,2X,F11.6,4(2X,F10.6))
  40  CONTINUE
$     END

      FUNCTION CAIR(T)
      REAL T
' CALCULATE CONDUCTIVITY OF AIR
      TK = T + 273.15
      CAIR = (-8.98737E-3 + 1.05702E-3 * TK- 5.21E-7 * TK*TK)/10
```

```
$       END
/*
//GO PLOT DD DSN=CY4Q.TEMPER1,DISP=(NEW),UNIT=ONLN
```

APPENDIX F

Error Analysis of Nusselt and Reynolds Number

The total rms errors of a Nusselt and Reynolds numbers can be variable can be expressed as:

$$\frac{1}{f}\,\delta f = \sqrt{\sum_{i=1}^{n}\left(\frac{\partial f}{\partial x_i}\,\frac{\delta x_i}{f}\right)^2} \qquad \text{(F.1)}$$

1. Nusselt Number

The Nusselt number is defined as:

$$Nu = \frac{hd}{k_j} \qquad \text{(F.2)}$$

where

$$h = \frac{q}{T_j - T_s} \qquad \text{(F.3)}$$

$$q = \frac{k_s\,(T_s - T_1)}{\Delta x} = k_s\,\frac{\Delta T_s}{\Delta x} \qquad \text{(F.4)}$$

T_1 = temperature one grid point in from the surface

Therefore

$$Nu = \frac{\Delta T_s}{(T_j - T_s)}\;\frac{d}{\Delta x}\;\frac{k_s}{k_j} \qquad \text{(F.5)}$$

Differentiation of Equation (A?.5) with respect to the experimental variables yields the individual error terms

$$\frac{1}{Nu}\,\frac{\partial Nu}{\partial T_j}\,\delta T_j = -\frac{1}{(T_j - T_s)}\,\delta T_j$$

$$\frac{1}{Nu}\frac{\partial Nu}{\partial T_s}\delta T_s = \frac{1}{(T_j - T_s)}\delta T_s$$

$$\frac{1}{Nu}\frac{\partial Nu}{\partial \Delta T_s}\delta \Delta T_s = \frac{1}{\Delta T_s}\delta \Delta T_s$$

$$\frac{1}{Nu}\frac{\partial Nu}{\partial d}\delta d = \frac{1}{d}\delta d$$

$$\frac{1}{Nu}\frac{\partial Nu}{\partial \Delta x}\delta \Delta x = -\frac{1}{\Delta x}\delta \Delta x$$

$$\frac{1}{Nu}\frac{\partial Nu}{\partial k_j}\delta k_j = -\frac{1}{k_j}\delta k_j$$

$$\frac{1}{Nu}\frac{\partial Nu}{\partial k_s}\delta k_s = \frac{1}{k_s}\delta k_s$$

The error in Nu associated with the effect of entrainment measured using the entrainment factor, F, was estimated to be ≅ 8%. The rms error involved in the ΔT_s term was estimated to be 1% based on the sensor calibration and data aquisition resolution. Thus, including these additional errors, under typical experimental conditions, the total percent rms error in Nu was calculated to be 8.5%.

2. Reynolds Number

In a simular fashion, the definition of Reynolds number is

$$Re = \frac{\rho_j V_j d}{\mu_j} \tag{F.6}$$

where the jet velocity is based on the static pressure measured at a distance upstream of the nozzle exit, and was correlated using the equation

$$V_j = 26.438 \sqrt{\frac{P_s T_j}{P_b}} \qquad (F.7)$$

Thus the individual error terms can be defined as:

$$\frac{1}{Re} \frac{\partial Re}{\partial d} \delta d = \frac{1}{d} \delta d$$

$$\frac{1}{Re} \frac{\partial Re}{\partial P_b} \delta P_b = \frac{\left(\frac{\partial(\rho_j V_j)}{\partial P_b}\right)}{\rho_j V_j} \delta P_b$$

$$\frac{1}{Re} \frac{\partial Re}{\partial P_s} \delta P_s = \frac{\left(\frac{\partial(\rho_j V_j)}{\partial P_s}\right)}{\rho_j V_j} \delta P_s$$

$$\frac{1}{Re} \frac{\partial Re}{\partial T_j} \delta T_j, = \left[\frac{\left(\frac{\partial(\rho_j V_j)}{\partial T_j}\right)}{\rho_j V_j} - \frac{\left(\frac{\partial \mu_j}{\partial T_j}\right)}{\mu_j}\right] \delta T_j$$

The resulting total rms error in Re for typical operating conditions was calculated to be less than 5% over the range 40,000 ≤ Re ≤ 120,000.